Ground-Source Bridge Deck Deicing and Integrated Shallow Geothermal Energy Harvesting Systems

George Allen Bowers, Jr.

Dissertation submitted to the faculty of the
Virginia Polytechnic Institute and State University
in partial fulfillment of the requirements for the degree of

Doctor of Philosophy
In
Civil Engineering

C. Guney Olgun, Chair
Joseph E. Dove
Matthew B. Mauldon
Cristopher D. Moen

February 12, 2016
Blacksburg, VA

Keywords: Geothermal Energy, Bridge Deck Deicing, Energy Pile, Geothermal Borehole, Sustainability
Copyright © 2016, George Allen Bowers, Jr.

Ground-Source Bridge Deck Deicing and Integrated Shallow Geothermal Energy Harvesting Systems

George Allen Bowers, Jr.

ABSTRACT

Shallow geothermal energy (SGE) systems are becoming increasingly popular due to both their environmental and economic value. By using the ground as a source and sink for thermal energy, SGE systems are able to more efficiently heat and cool structures. However, their utility beyond structural heating and cooling is being realized as their applications now extend to slab and pavement heating, grain and agricultural drying, and swimming pool temperature control. Relatively recently, SGE systems have been combined with deep foundations to create a dual purpose element that can provide both structural support as well as thermal energy exchange with the subsurface. These thermo-active foundations provide the benefits of SGE systems without the additional installation costs.

One of the novel applications of thermo-active foundations is in bridge deck deicing. Bridge decks experience two main winter weather related problems. The first of which is preferential icing, where the bridge freezes before the adjacent roadway because the bridge undergoes hastened energy loss due to its exposed nature. The second problem is the accelerated deterioration of concrete bridge decks resulting from the application of salts and other chemicals that are used to prevent accumulation and/or melt the frozen precipitation on roads and bridges. By utilizing the foundation of a bridge as a mechanism by which to access the shallow geothermal energy of the subsurface, energy can be supplied to the deck during the winter to melt and/or prevent frozen precipitation.

An experimental ground-source bridge deck deicing system was constructed and the performance is discussed. Numerical models simulating the bridge deck and subsurface system components were also created and validated using the results from the numerical tests. Furthermore, the observed loads that result in a foundation from bridge deck deicing tests are shown. In order to better design for these loads, tools were developed that can predict the temperature change in the subsurface and foundation components during operation. Mechanisms by which to improve the efficiency of these systems without increasing the size of the borehole field were explored. Ultimately this research shows that SGE can effectively be used for bridge deck deicing.

Ground-Source Bridge Deck Deicing and Integrated Shallow Geothermal Energy Harvesting Systems

George Allen Bowers, Jr.

ABSTRACT

Bridge decks experience two main winter weather related problems. The first of which is preferential icing, where the bridge freezes before the adjacent roadway because the bridge undergoes hastened energy loss due to its exposed nature. The second problem is the accelerated deterioration of concrete bridge decks resulting from the application of salts and other chemicals that are used to prevent accumulation and/or melt the frozen precipitation on roads and bridges. This research project addresses those concerns by proposing a sustainable system that prevents the bridge deck from freezing during the winter by using shallow geothermal energy harvested by the foundations of the bridge deck.

Near-surface or shallow geothermal energy has been used for space heating and cooling of buildings and it also presents a unique alternative for heating and deicing bridge decks. A schematic of the concept is shown in the figure below. The bridge sub-structure is converted to a thermoactive foundation by installing circulation tubes in the foundation elements, creating energy piles, and in the embankment. As fluid is circulated in the system, heat energy can be extracted from the ground and supplied to the deck. The ground acts as a heat source because the temperature of the ground remains relatively constant throughout the year, especially at depths greater than 6-10 m (20-30 ft). During the winter, the ground temperature is warmer than the atmospheric temperature, thus providing a source of thermal energy. During the summer the system can be operated to collect the thermal energy of the bridge deck and inject it into the ground to replace the energy that was used during the winter and to raise the temperature of the ground for more efficient operation of the system.

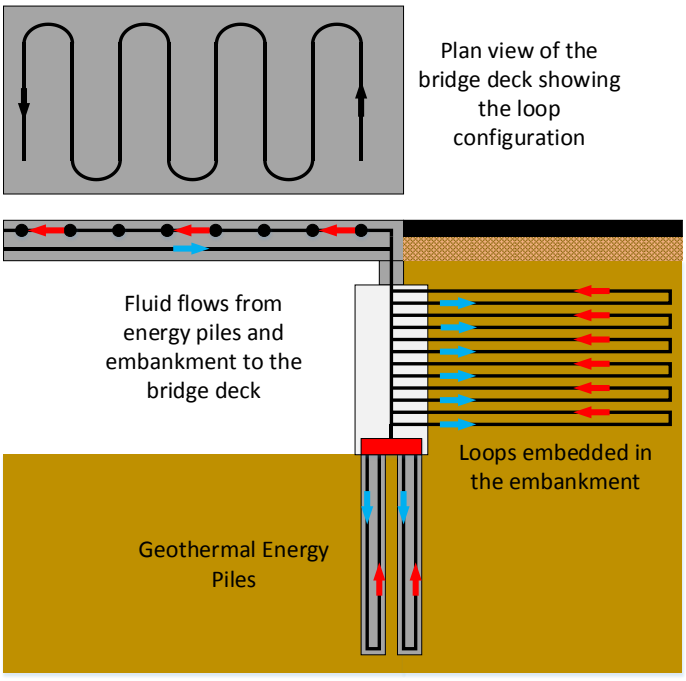

The fluid can be pumped directly from the foundation to the bridge deck (passive system), or can travel to a heat pump (active system), which then uses the energy from the fluid to more efficiently heat the circulation fluid in the bridge deck. Because heat pump operation can be energy intensive, necessitate the availability of an external power source, and add complexity to the system's configuration, passive systems are desirable. Due to the fact that in the passive configuration the highest possible

temperature of the circulation fluid is the ground temperature, there are obvious operational limitations.

There is still significant hesitation on the part of bridge designers and transportation authorities to adopt alternate bridge deck deicing technology, especially passively configured geothermal systems, for several reasons. These reasons include lack of published case studies showing the operational capability of such systems; lack of understanding of how these system will perform under a variety of conditions; uncertainty regarding how both the installation and operation of a hydronic system will affect the structural integrity of the bridge deck; and, in systems which utilize thermoactive foundations, the range of thermally induced stresses that the foundation will experience due to system operation.

Through experimental and numerical studies, this research addresses all of the above questions. It includes the design, construction, and operation of a small-scale bridge deck deicing system using thermal energy harvested by a thermoactive foundation. Numerical models are then developed and calibrated based on the results of the experimental studies and are then used to develop a comprehensive understanding of how both the ground and bridge deck responds to system operation.

Dedicated to my wife Ashley

who shows me every day the love and

compassion of Christ.

ACKNOWLEDGEMENTS

In his work *Epitome of Copernican Astronomy & Harmonies of the World,* the great astronomer and mathematician Johannes Kepler suddenly interrupts his writings with the following refrain that I would like to echo:

> *Accordingly let this do for our envoi concerning the work of God the Creator. It now remains that at last, with my eyes and hands removed from the tablet of demonstrations and lifted up towards the heavens, I should pray, devout and supplicating, to the Father of lights: O Thou Who dost by the light of nature promote in us the desire for the light of grace, that by its means Thou mayest transport us into the light of glory, I give thanks to Thee, O Lord Creator, Who hast delighted me with Thy makings and in the works of They hands have I exulted. Behold! Now, I have completed that work of my profession, having employed as much power of mind as Though didst give to me; to the men who are going to rea those demonstrations I have made manifest the glory of Thy works, as much of its infinity as the narrows of my intellect could apprehend.*
>
> *Great is our Lord and great His virtue and of His wisdom there is no number: praise Him, ye heavens, praise Him, ye sun, moon, planets, use every sense for perceiving, every tongue for declaring your Creator. Praise Him, ye celestial harmonies, praise Him, ye judges of the harmonies uncovered… and thou my soil, praise the Lord thy Creator, as long as I shall be; for out of Him and through Him and in Him are all things… [both sensible and the intelligible]; for both whose whereof we are utterly ignorant and those which we know are the least part of them; because there is still more beyond. To Him be praise, honor, and glory, world without end. Amen.*

I also thank my family, without whom this endeavor would not have been accomplished; my family who loves me, thinks too much of me, prays for me, makes me laugh, consoles me, lifts me up, gives me strength, and whom I will always treasure in my heart: My wife, whom has borne the brunt of the sacrifice this research has required with understanding and compassion. My parents, whose love and encouragement propel me to always give me best and not to worry about the rest. My sister, who always reminds me life is to be enjoyed, not accomplished. My grandparents, who have left a legacy far more valuable than anything this world can offer, and in whose steps I strive to follow. My uncle, aunt, and cousins who are my second family and ascribe me far more honor than I deserve. My wife's family, who have adopted me as their own and loved me during this journey.

I would like to thank my advisor and PhD committee. Dr. Olgun not only gave me the opportunity to begin researching as an undergraduate, but talked me into continuing on to a PhD and has provided so much guidance along the way. Dr. Dove, Dr. Mauldon, and Dr. Moen, likewise, have been an integral part of my academic journey and have provided wisdom, encouragement, and friendship.

I would like to thank those who have made the research possible: The National Science Foundation for their support of me as a Graduate Research Fellow (grant no. DGE-0822220), their support of the research project "The Use of Energy Piles for Sustainable Energy" (CMMI-0928807), and the "GOALI: Long-Term Thermo-Mechanical Performance and Group Effect Considerations for Design of Energy Piles" project (CMMI-110752). These grants supported the installation of the field test and made the research possible. The Via Foundation also funded me as a graduate student at Virginia Tech, and to the Via family I am truly grateful. In addition, the NSF supported my attendance at an international workshop they sponsored, the "International Workshop on Thermo-active Geotechnical Systems for Near-Surface Geothermal Energy:

From Research To Practice, Lausanne, Switzerland" (CMMI-1249656). I would also like to thank Christopher Fox and REHAU for donating the PEX tubing and fittings; ConRock for donating the concrete to build the deck; and Charles Elks and Mechanical Equipment Sales for providing the fluid circulation pumps and much advice on how to construction the circulation system. Brett Farmer and Dennis Huffman provided their time and expertise and were invaluable in the construction of the actual deck. Sherif Abdelaziz also assisted in the construction of the deck and setup of the instrumentation system. Layne GeoConstruction and Fatih Catalbas were instrumental in the energy pile field installation and testing.

Finally, to all of my colleagues and friends along the way – Craig Shillaber, Soheil Kamalzare, Melis Sutman, Tolga Ozudogru, Alfonso Rivera, Mertcan Geyin, Dan VandenBerge, Andrew Bain, and many others – thank you for help and for making the process enjoyable. It was a pleasure to work alongside each of you.

TABLE OF CONTENTS

LIST OF FIGURES

LIST OF TABLES

1. INTRODUCTION

1.1. OVERVIEW

Shallow geothermal energy (SGE) systems are becoming increasingly popular due to both their environmental and economic value. By using the ground as a source and sink for thermal energy, SGE systems are able to more efficiently heat and cool structures. However, their utility beyond structural heating and cooling is being realized as their applications now extend to slab and pavement heating, grain and agricultural drying, and swimming pool temperature control. Relatively recently, SGE systems have been combined with deep foundations to create a dual purpose element that can provide both structural support as well as thermal energy exchange with the subsurface. These thermo-active foundations provide the benefits of SGE systems without the additional installation costs.

One of the novel applications of thermo-active foundations is in bridge deck deicing. Bridge decks experience two main winter weather related problems. The first of which is preferential icing, where the bridge freezes before the adjacent roadway because the bridge undergoes hastened energy loss due to its exposed nature. The second problem is the accelerated deterioration of concrete bridge decks resulting from the application of salts and other chemicals that are used to prevent accumulation and/or melt the frozen precipitation on roads and bridges. By utilizing the foundation of a bridge as a mechanism by which to access the shallow geothermal energy of the subsurface, energy can be supplied to the deck during the winter to melt and/or prevent frozen precipitation. The construction of such a system is discussed in Chapter 2. The system was operated over the course of several years and the performance of the system is discussed in Chapter 3.

The creation of thermo-active foundations does, however, introduce additional loads that have not traditionally been considered must now be accounted for in design. The loads that result in a foundation from bridge deck deicing tests are observed and discussed in Chapter 4. In order to better design for these loads, tools must be developed that can predict the temperature change in the subsurface and foundation components during operation. The development of numerical and analytical tools are discussed in Chapter 5. Another notable difference between a SGE system and thermo-active foundation is that the size of the system is likely to be controlled by foundation design. Thus, mechanisms by which to improve the efficiency of systems that have pre-defined geometries are explored in Chapter 6.

Finally, in order for ground-source bridge deck deicing systems to be feasible, they must be understood. Chapter 7 describes the creation of a 3-dimensional numerical model that is validated using experimental tests from Chapter 3. The model is capable of modeling these system to predict system performance. The model is then used in Chapter 8 to perform a parametric analysis in order to develop a comprehensive understanding of how these systems respond to various factors.

1.2. RESEARCH QUESTIONS REGARDING SHALLOW GEOTHERMAL ENERGY AND BRIDGE DECK DEICING SYSTEMS

The driving goal of this research is to better understand shallow geothermal energy and ground source bridge deck deicing systems on both a fundamental and practical level. Specifically, this entails several components. The first of which is developing a comprehensive understanding of the physical processes involved in ground-source bridge deck deicing. After the physical processes are understood and are sufficiently characterized, parameters of significance to the system are identified. Once the parameters

are identified, their effects are quantified and trends developed. Each of these components are described below:

Physical Processes: The physical processes are inclusive of all the physics that govern the operation and performance of a ground source bridge deck deicing system. These processes need to be understood in both the bridge deck and subsurface components of the system on a fundamental level.

Quantifying Parametric Significance: After characterizing the physical processes, the effect of various parameters to the system are quantified. Realize that in quantifying these parameters, it is not the effect the parameters have on the system that is studied, rather it is how the parameters affect the physical processes that in turn control the system, which is studied. Significant parameters include geometric characteristics, material properties, and environmental conditions.

Developing Trends: After the significance of the system parameters are quantified, trends are developed that characterize system performance. Again, keep in mind that these trends are fundamentally representations of how the physical processes change and interact during system operation. An example trend that could be developed is the effect of wind speed on required ground temperature for different geometric configurations.

1.3. INCLUDED PAPERS

This dissertation primarily consists of six journal papers, some of which have been, and some of which will be submitted for publication. The topic of each paper and the associated journal (if one has been selected) is given below:

- Chapter 3 – The thermal performance of a small-scale bridge deck deicing system under bridge deck deicing and thermal recharge operations.
    - Overview: This chapter documents the performance of the experimental BDD system during numerous operations in both the summer and winter. Results include bridge deck surface and internal temperatures, operating fluid temperatures, and the rate of bridge deck heating.
    - Journal: ASCE Journal of Cold Regions Engineering *(to be submitted)*
- Chapter 4 – Experimental investigation of energy pile response under heating and cooling loads for bridge deck deicing applications.
    - Overview: Whereas Chapter 3 documents what happens to the bridge deck and overall system performance during BDD operations, this chapter focuses on the thermally induced stresses and strains in the energy piles that result from BDD operation.
    - Journal: DFI Journal *(in review)*
- Chapter 5 – Numerical and analytical investigation of subsurface response to heat exchange operations in shallow geothermal energy systems.
    - Overview: This chapter primarily deals with developing an analytical model that is then validated using a numerical model that was calibrated from an experimental field test. The model is then used to replicate experimental results.
    - Journal: Geothermics *(to be submitted)*

- Chapter 6 – Optimization of shallow geothermal energy systems through selective borehole utilization.
    - Overview: A 2D numerical model is used to represent a field of borehole heat exchangers. Optimization of the system is then obtained by selectively operating certain boreholes.
    - Journal: Applied Thermal Energy *(to be submitted)*
- Chapter 7 – 3-Dimensional bridge deck deicing numerical model: model development and calibration.
    - Overview: Chapter 6 details the development and calibration of a 3D numerical model for BDD operations. It explains the associated physics and then uses two experimental cases for model validation.
    - Journal: *To be selected*
- Chapter 8 – Numerical investigation of shallow geothermal energy bridge deck deicing systems.
    - Overview: This chapter utilizes the model developed in Chapter 6 to evaluate the performance of multiple BDD systems under a variety of conditions. Recommendations are then given for design and methods for increasing system performance are discussed.
    - Journal: *To be selected*

Two additional chapters are included in order to give a comprehensive understanding of this research project. Chapter 2 describes the design, construction, layout, and data processing of the experimental bridge deck deicing system and Chapter 9 provides a summary of the research.

2. EXPERIMENTAL SETUP

2.1. INTRODUCTION

The field testing site is located at the Virginia Tech's Geotechnical Research Facility on Price's Fork Road in Blacksburg, VA. There are several components; the energy pile subsystem, the bridge deck subsystem, the circulation subsystem, and the data acquisition subsystem. Each will be explained in this Chapter.

2.2. ENERGY PILES

2.2.1. Layout and Pile Properties

The energy piles were installed for a previous project (Abdelaziz 2013). A total of five piles were installed, each to a depth of 30.5 m (100 ft). The piles are 25.4 cm (10 in) in diameter with a single 2.54 cm (1in) rebar in the middle. The layout of the piles is shown in Figure 2-1. In addition to the five piles, four observation boreholes were drilled to monitor the temperature in the ground.

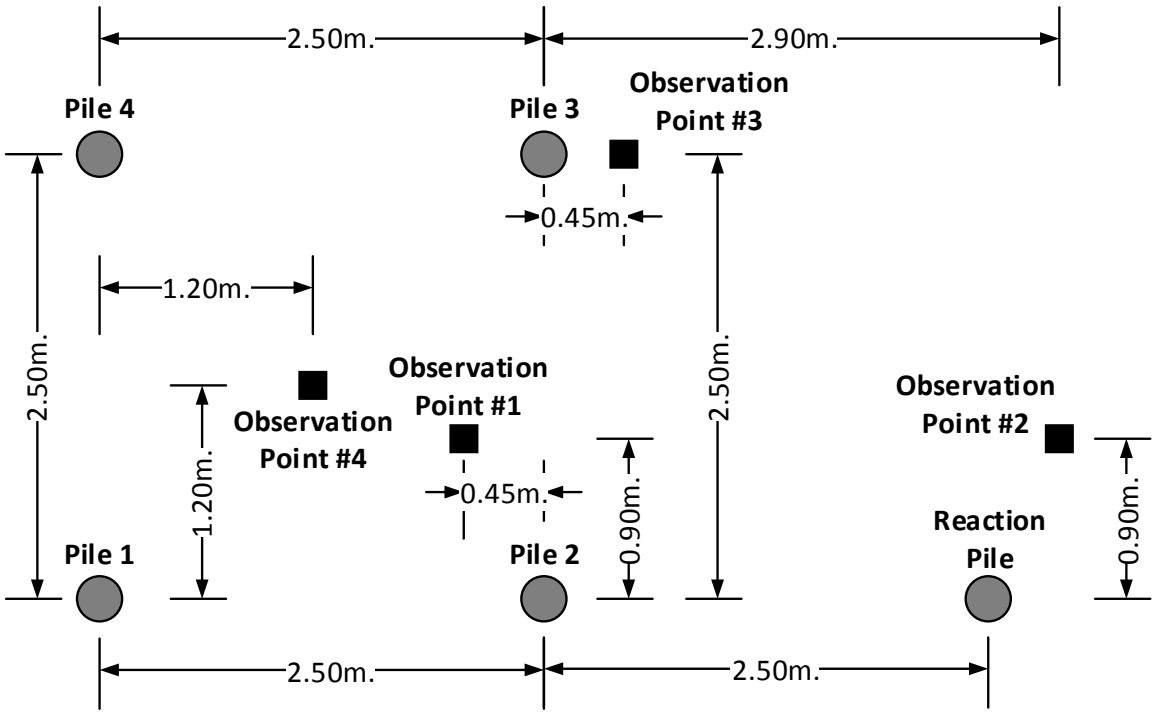

Figure 2-1. Field layout of the energy piles and observations wells (redrawn after Abdelaziz 2013).

The specifics of the circulation tubing in each pile is given in Table 2-1. Furthermore, Piles 2 and 3 are equipped with vibrating wire strain gauges. The strain gauge locations, as well as the locations of the temperature sensors in the observation boreholes is also given in the table below.

Table 2-1. Summary of energy pile components (data taken from Abdelaziz 2013).

Element	Depth (m)	Tube and Size		Sensor Type	Depth of Sensors (m)
		Type	Loop		
Pile 1	30.5	HDPE – 19mm	Single	-	-
Pile 2	30.5	HDPE – 19mm	Single	Thermocouple	3.0, 6.0, 9.1, 12.2, 15.2, 18.3, 21.3, 24.4, 27.4, 30.5
Pile 3	30.5	PEX – 25.4mm	Single	Thermocouple	3.0, 6.0, 9.1, 12.2, 15.2, 18.3, 21.3, 24.4, 27.4, 30.5
Pile 4	30.5	PEX – 25.4mm	Double	-	-
Observation Borehole 1	30.5	-	-	Thermistors	3.0, 6.0, 9.1, 12.2, 15.2, 18.3, 22.9, 27.4, 30.5
Observation Borehole 2	30.5	-	-	Thermistors	3.0, 6.0, 9.1, 12.2, 15.2, 18.3, 22.9, 27.4, 30.5
Observation Borehole 3	15.2	-	-	Thermistors	3.0, 6.0, 10.7, 15.2
Observation Borehole 4	36.5	-	-	Thermistors	3.0, 6.0, 9.1, 12.2, 15.2, 18.3, 21.3, 24.4, 27.4, 30.5, 33.5, 36.6

In addition, Pile 2 was extensively tested and is well characterized in terms of its structural properties. The depth specific pile tangent moduli is given as:

Table 2-2. Tangent moduli values for Pile 2 (data taken from Abdelaziz 2013).

Depth (m)	E_{pile} (kPa/με)
3.0	69.34
6.0	60.61
9.1	34.76
12.2 – 30.5	40.07 – 0.0269ε

2.2.2. Subsurface Properties

The subsurface at the site consists of two distinct layers. The top layer is a silty sand that extends to a depth of roughly 14.5m. Below that is a weak shale. While the piles and observation boreholes were being installed, observations were made as to the depth of the shale layer. The table below summarizes these observations. The thermal properties were estimated using the results from field thermal conductivity tests, however it assumed the ground was a homogeneous medium. Thus, for the purposes of this research they provide little value and are not included in this report.

Table 2-3. Observed depth of the silty sand layer (data taken from Abdelaziz 2013).

Element	Depth to Shale Layer (m)
Pile 1	14.3
Pile 2	12.8
Pile 3	17.4
Pile 4	18.9
Reaction Pile	14.3
Observation Borehole 1	14
Observation Borehole 2	17.7
Observation Borehole 3	>15.2
Observation Borehole 4	12.5

2.3. BRIDGE DECK

2.3.1. Design

2.3.1.1. Overview

There were several objectives in determining the proper design for the bridge deck. One was to replicate a typical bridge deck that could be found in Virginia. The size also needed to be large enough such that boundary effects would not control the behavior of the system. Another objective was to be able to test different bridge deck deicing system configurations. Thus, it was decided to build a 2.6 m x 3.05 m (8.5 ft x 10 ft) model bridge deck in two 1.3 m x 3.05 m (4.25 ft x 10 ft) halves that could be operated independently from each other. Each half would be identical except for the circulation tube spacing. One half would have tubes spaced 20.3 cm (8 in) apart, and the other half would have tubes spaced 30.5 cm (12 in) apart. The plan view of each half of the bridge deck is shown in Figure 2-2 and Figure 2-3. A simple cross section is also shown, but the exact details of the cross section are given in the next section.

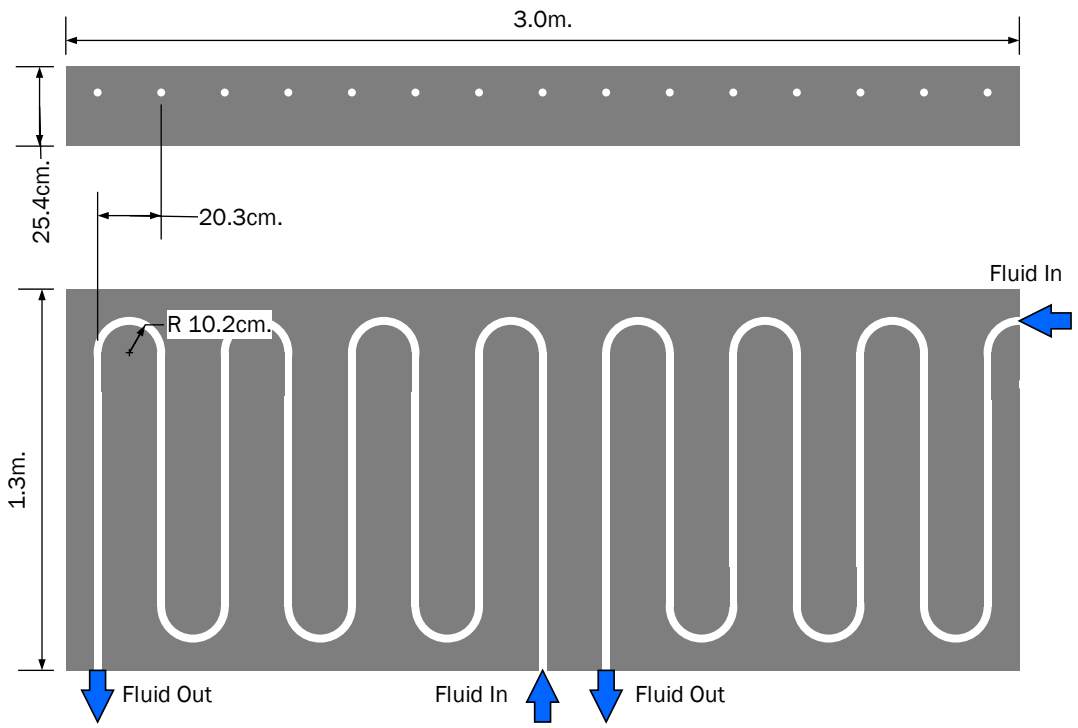

Figure 2-2. Plan view of the slab with circulation tubes spaced 20.3 cm (8 in) apart.

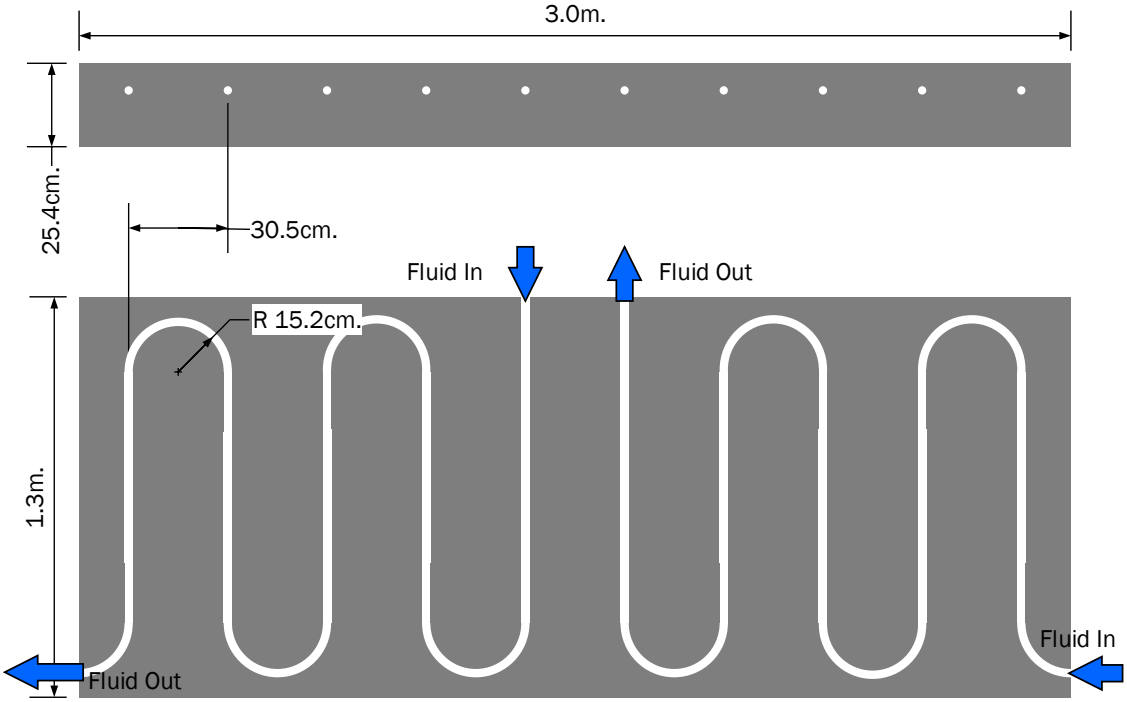

Figure 2-3. Plan view of the slab with circulation tubes spaced 30.5 cm (12 in) apart.

In order to monitor temperatures in the slab, 36 thermistors were installed. The type, location, and installation of the thermistors will be discussed in a later section.

2.3.1.2. Cross-Sectional Details

The slab is 0.254 m (10 in) thick. The rebar placement and spacing was determined based on ACI design code for reinforced concrete slabs. There are two layers of reinforcement. The bottom layer consists of #4 steel rebar (0.5 in. OD) spaced at 20.3 cm (8 in.) both longitudinally and transversely. The bottom of the layer is 3 in. from the bottom of the slab. The top layer of reinforcement also consists of #4 steel rebar also spaced 20.3 cm in the longitudinal and transverse directions. The bottom of the top layer is located 2.5 in. below the surface of the deck. The circulation tubes are attached to the bottom of the top layer of reinforcement. Cross sectional views detailing the above are shown in Figure 2-4 and Figure 2-5.

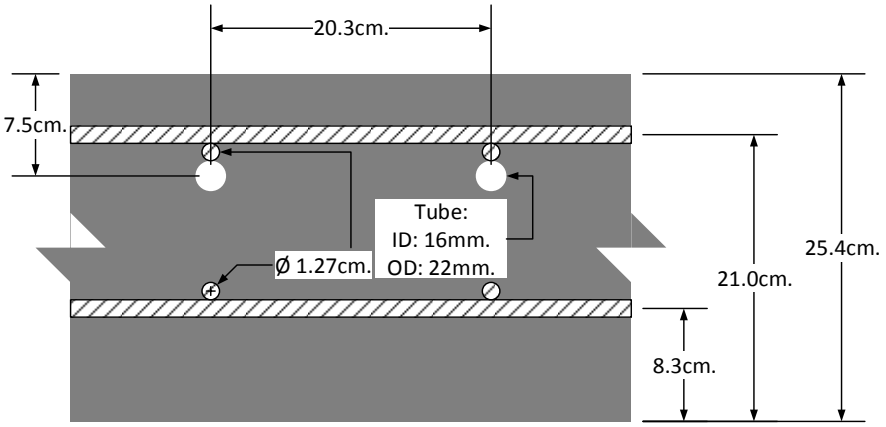

Figure 2-4. Cross-sectional details of the slab with circulation tubes spaced 20.3 cm apart.

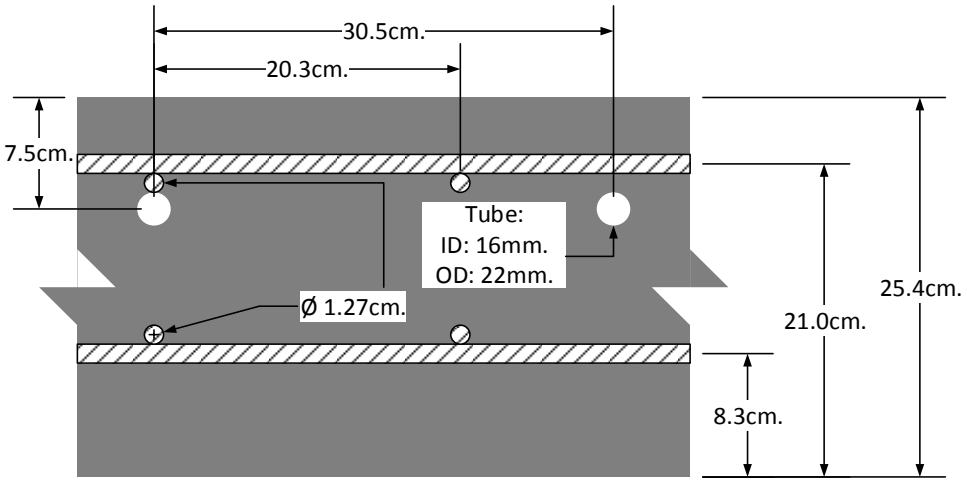

Figure 2-5. Cross sectional details of the slab with circulation tubes spaced 30.5 cm apart.

2.3.2. Construction

The model bridge deck was constructed during the winter and spring of 2012. In order to elevate the bridge deck, it was constructed on top of stacked concrete masonry units and pressure treated 4x4's. Two cast-in-place deck forms were used for the bottom of the deck. The corrugation of the forms was 5 cm (2 in) wide and 5 cm deep. The outer form for each half of the deck was created using 2 in x 10 in timbers. This is shown in Figure 2-6. In order to prevent thermal interference between the two halves of the deck, a strip of 2.54 cm (1 in) green-foam insulation was placed between the two halves, which is also shown in Figure 2-6.

Figure 2-6. Photographs showing the formwork for the two halves and elevation from the ground (left) and the insulation used to prevent thermal interference between the two halves (right).

The two layers of rebar were placed in the forms using spacers to keep them at the appropriate depth. The circulation tubes were attached to the bottom of the top layer of rebar. The rebar and circulation tubes are shown in Figure 2-7.

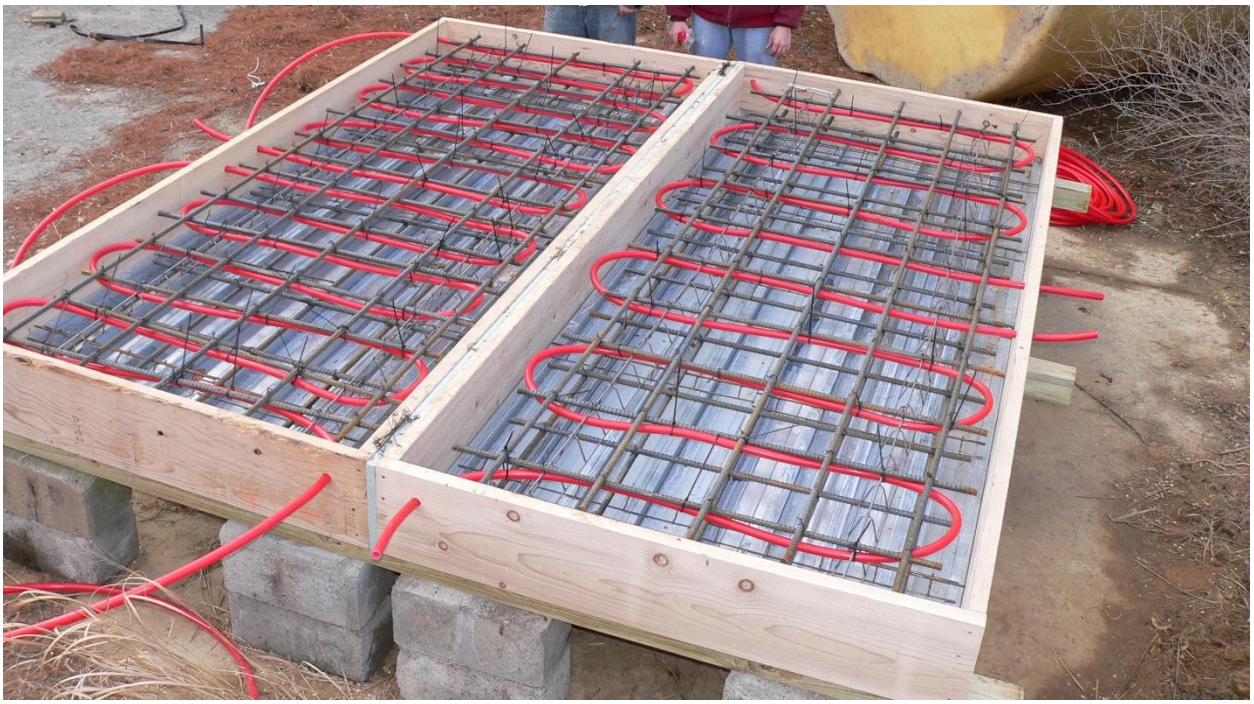

Figure 2-7. Addition of the two levels of rebar and circulation tubes to the formwork.

Depending on their location, the sensors were either attached directly to the rebar, circulation tubes, or a spacer made of rebar as shown in Figure 2-8.

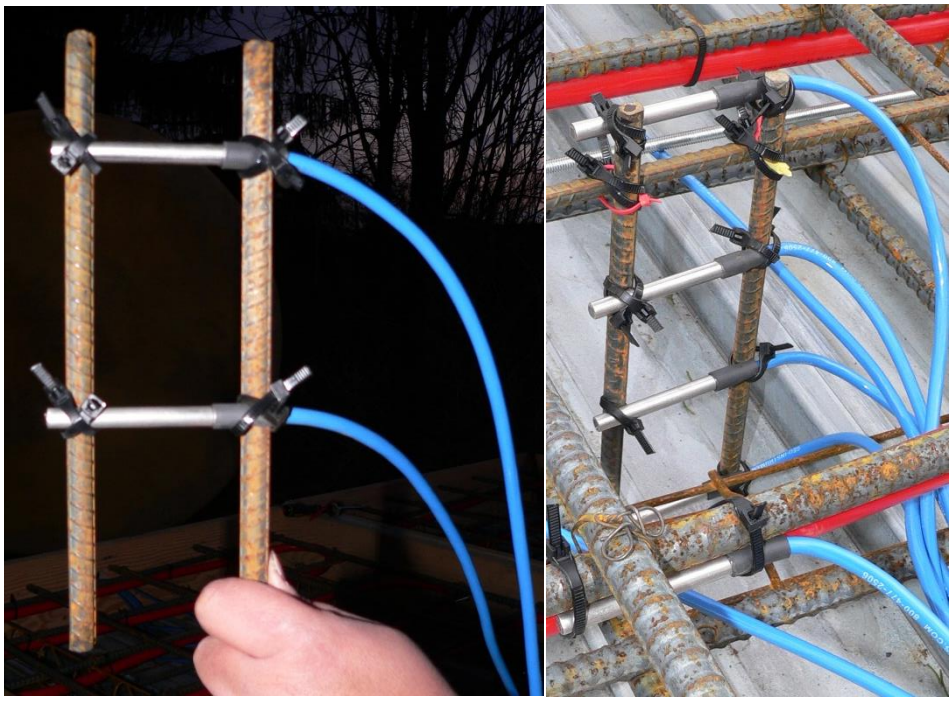

Figure 2-8. Attachment of thermistors to a spacer made of rebar that is placed vertically in the bridge deck to record temperatures at selected depths.

An A4 concrete mix was used, which is typical for Virginia bridge decks. The concrete was poured into the form and the leftover concrete was used to create a smaller slab of the same depth as the model slab with no reinforcement and a single thermistor to be used as a temperature control. These are shown in Figure 2-9 and Figure 2-10.

Figure 2-9. Poured model bridge deck slab. Note that the green foam insulation was added to the outer walls of this slab after the concrete set.

Figure 2-10. The smaller control slab used for temperature control.

During the summer of 2012, a black covering was applied to the 30 cm spaced side by individuals not authorized to perform the research. This covering was finally removed the summer of 2014 with an angle grinder. The photographs below show what the side looked like with the covering and then after the covering was removed.

Figure 2-11. The 30 cm spaced slab with and without the black covering.

2.3.3. Bridge Deck Material Properties

The table below summarizes the material properties of all components of the bridge deck.

Table 2-4. Material properties of the bridge deck components.

Parameter	Value	Unit	Source
Concrete - A4 General Mix			
Density	2360	kg/m^3	Measured by Schnabel
Thermal Conductivity	3.0	W/m/K	ACI (2002)
Specific Heat Capacity	880	J/kg/K	COMSOL (2015)
Coefficient of Thermal Expansion	1.00E-05	1/K	COMSOL (2015)
Young's Modulus	2.50E+07	MPa	COMSOL (2015)
Compressive Strength (28 days)	35.0	MPa	Tested by Schnabel
Compressive Strength (56 days)	43.9	MPa	Tested by Schnabel
Rebar - Grade 40			
Density	7850	kg/m^3	COMSOL (2015)
Thermal Conductivity	44.5	W/m/K	COMSOL (2015)
Specific Heat Capacity	475	J/kg/K	COMSOL (2015)
Coefficient of Thermal Expansion	1.23E-05	1/K	COMSOL (2015)
Young's Modulus	2.00E+11	Pa	COMSOL (2015)
Poisson's Ratio	0.33		COMSOL (2015)
Diameter (#4 Bar)	12.7	mm	-
Spacing	20.3	cm	-
Circulation Tube - REHAU PEX O2 Barrier			
Density	930	kg/m^3	REHAU Specs
Thermal Conductivity	0.41	W/m/K	REHAU Specs
Specific Heat Capacity	2300	J/kg/K	Abdelaziz (2013)
Coefficient of Thermal Expansion (20^oC)	1.40E-04	1/K	REHAU Specs
Inner Diameter	17	mm	REHAU Specs
Outer Diameter	19	mm	REHAU Specs

2.4. FLUID CIRCULATIONS SYSTEM

The experimental setup has undergone two fluid circulation systems. The first system was created out of polyvinylchloride (PVC) pipe. This system was in operation from the winter of 2012 through the summer of 2014 and eventually deteriorated to the point of needing to be replaced. After the summer of 2014, a new circulation system was installed consisting of PEX tubing. In each case the circulation system is powered by two pumps. The characteristics of the fluid circulation systems are given below.

Both systems:

- Can operate each side of the deck independently of the other half
- Can selectively operate individual piles
- Can operate the pumps in parallel or series, depending on if the two sides of the deck are being used independently

First iteration only:

- Allowed for half of each side of the bridge deck to be operated independently. This feature was never used and thus not included in the second iteration.

Second iteration only:

- Allows for each side of the deck to be operated independently with two of the four piles. Previously, after exiting each side of the deck, the fluid was remixed before entering the piles. The second iteration keeps the fluid used for each side of the deck separate.

2.4.1. Circulation System Components

The circulation system contained several components. They are described briefly in this section.

Tubing (Iteration 1): Initially, PVC piping was used for the circulation system due to its low cost. 1" piping was generally used, unless specific sections needed ¾" piping. This whole system was insulated using foam. However, over the course of several seasons it began to rapidly deteriorate and was eventually replaced the winter of 2014-2015 with PEX tubing.

Tubing (Iteration 2): PEX tubing, donated by REHAU, was used to replace all the PVC components of the fluid circulation system. PEX was chosen due its better durability when compared with PVC, ease of installation (all connections are mechanical as compared to the solvent connections required by PVC), and its use in the industry. ¾" tubing was used, with brass and steel fittings.

Circulation Pumps: The fluid circulation system was powered by two 115V Grundfos UP 26-99 F circulation pumps, shown in the figure below. The pumps were donated by Mechanical Equipment Sales. The pump characteristic curve and technical details are given in Appendix 3A.

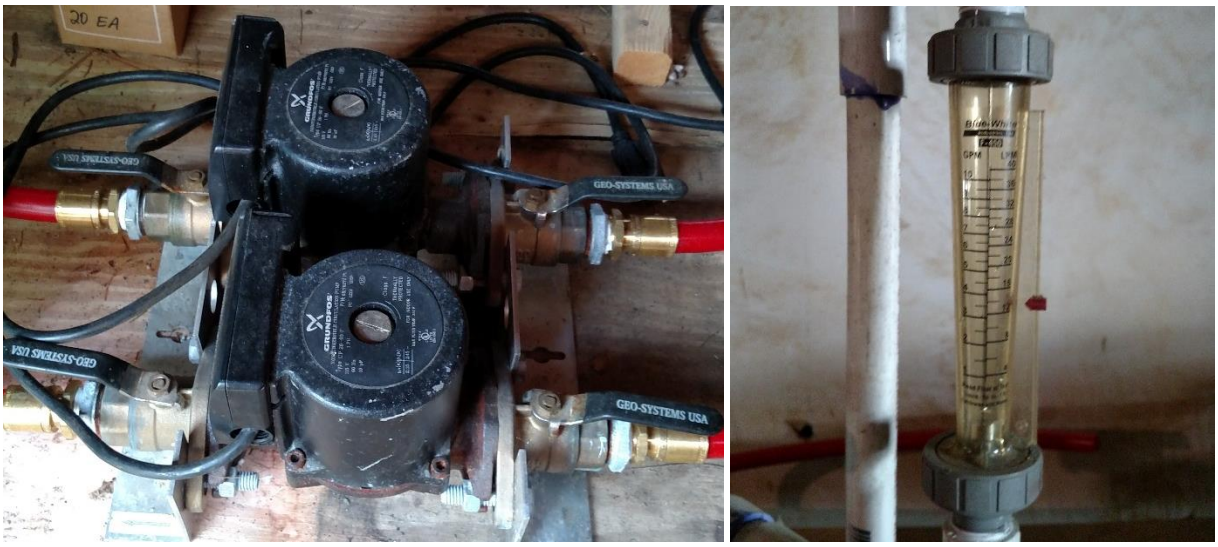

Figure 2-12. The circulation pumps used to power the system (left) and the flowmeter that was used to measure the volumetric flow rate (right).

Flowmeters: Blue-White Flowmeters, one of which is shown above, were used to measure the flow rate of the fluid. The first iteration contained four such that the flow for each half of each side of the bridge

deck could be monitored. With the second iteration, it was determined that being able to operate each half of each side was not needed. Thus, only two flowmeters are currently in use.

Fill Tank: The fill tank, shown below, is used as a reservoir for de-airing the system and to add antifreeze to the fluid. It is raised so that some pressure-head is created.

Figure 2-13. Fill tank that was used to add liquid and antifreeze to the system. It was also used for de-airing.

Control Shed: Originally the circulation pumps and some of the system controls were housed in waterproof boxes. These boxes began to deteriorate so a shed was constructed to house the dataloggers for the piles, the circulation pumps, the fill tank, and with the second iteration, all the valve controls.

Figure 2-14. The shed that was built to house the control equipment.

Expander Tank: An expander tank was originally part of the circulation system. But due to the fact that no significant pressure is ever created and that the fill tank can be used for de-airing, it was left out of the second iteration of the system.

Figure 2-15. An expander tank that was used for the first iteration of the system. It was not included when the system was rebuilt using PEX tubing.

2.4.2. Circulation System Layout

The circulation system configuration is shown in the series of figures below. There is a difference between the first and second iterations of the system, as shown in the diagrams, and as explained previously.

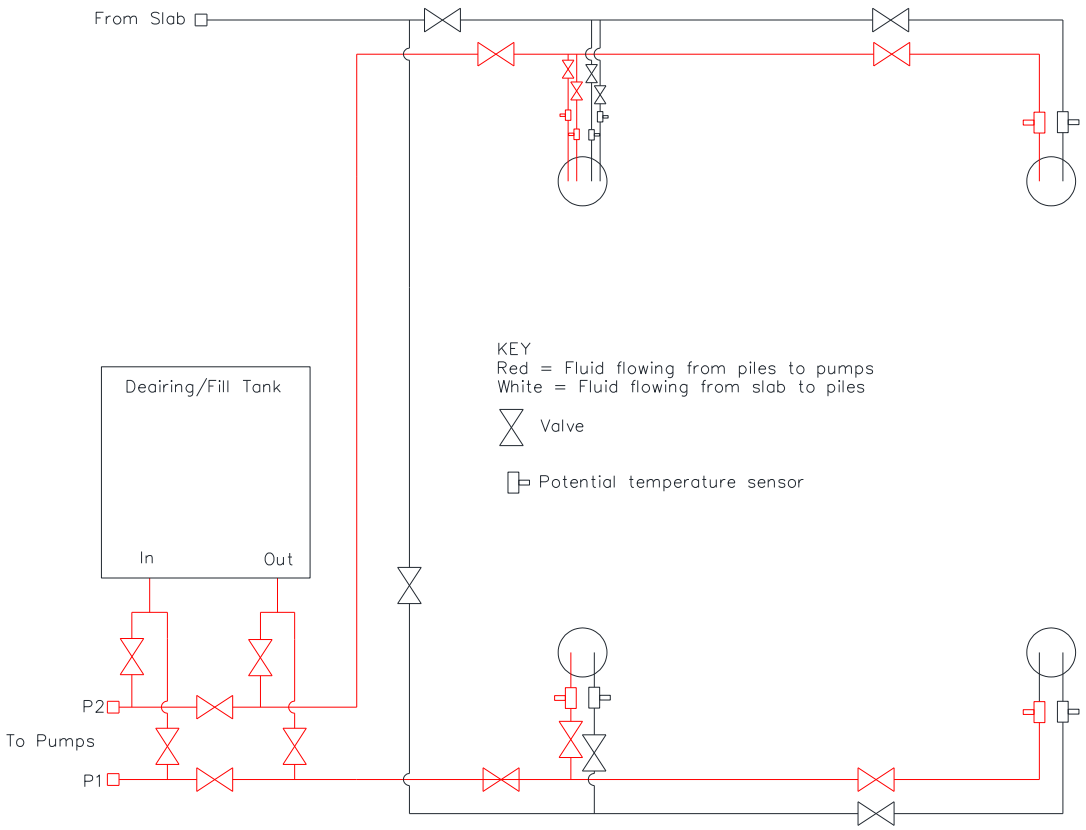

Figure 2-16. Pile circulation system layout, Iteration 1.

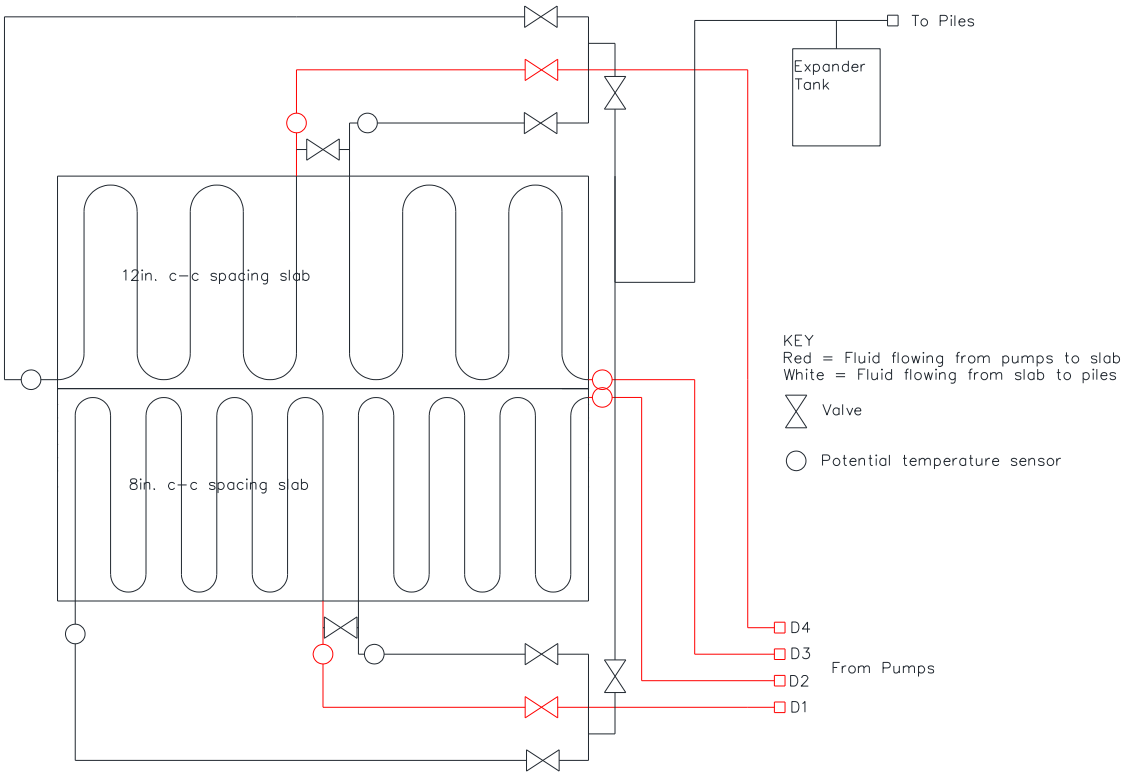

Figure 2-17. Slab circulation system layout, Iteration 1.

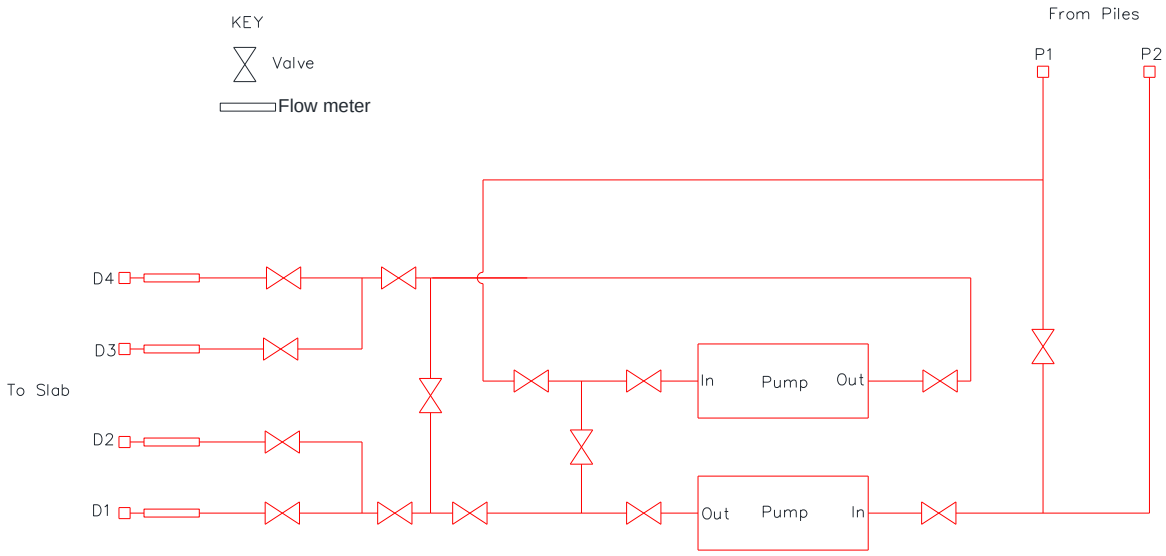

Figure 2-18. Pump circulation system layout, Iteration 1.

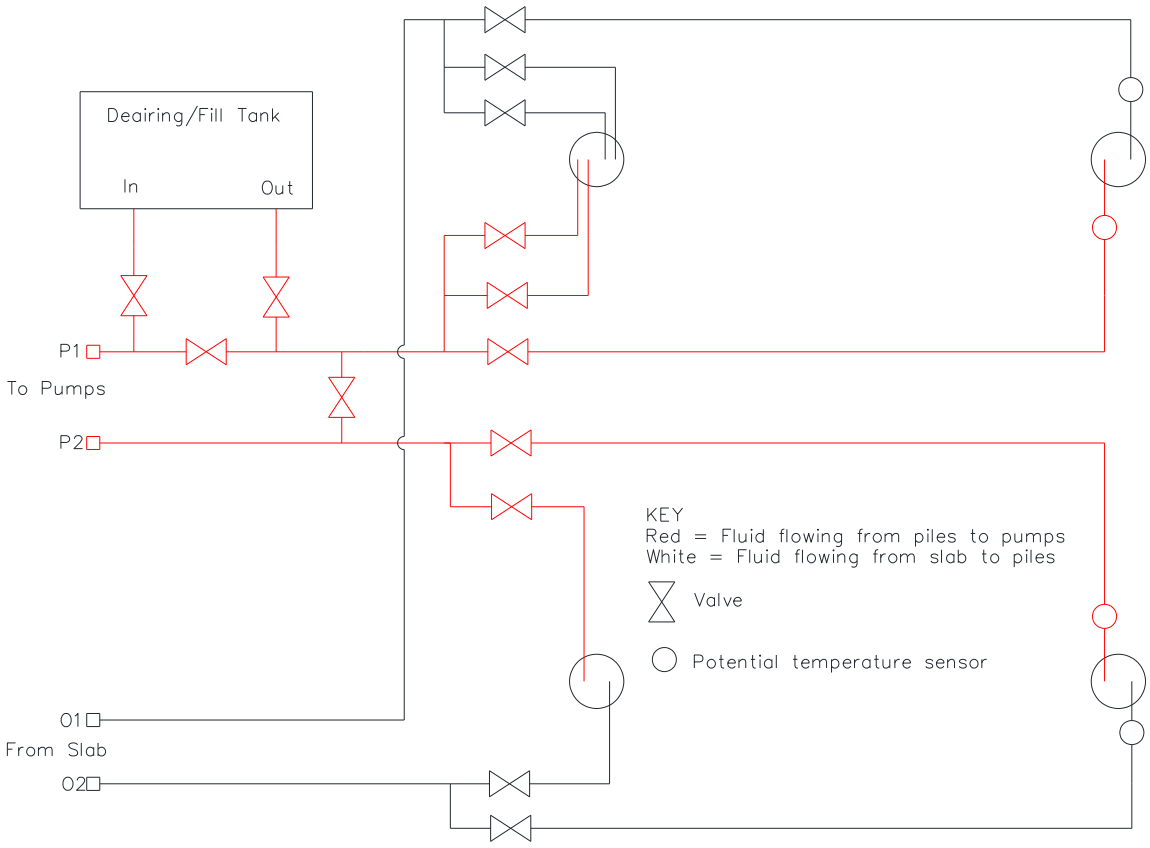

Figure 2-19. Pile circulation system layout, Iteration 2.

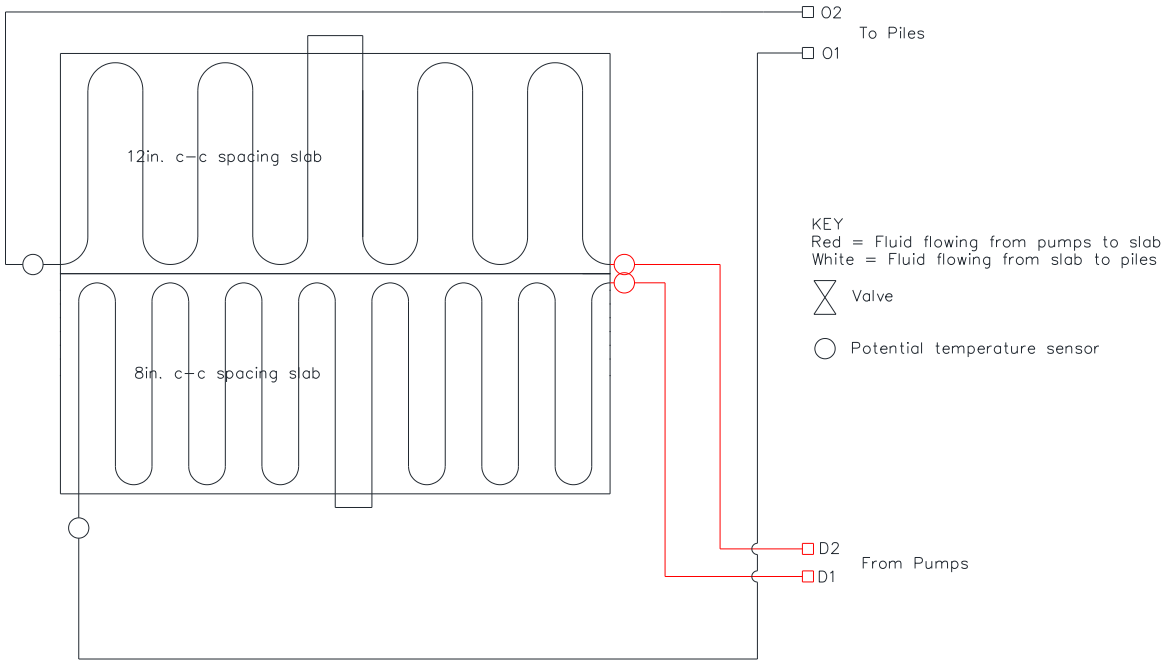

Figure 2-20. Slab circulation system layout, Iteration 2.

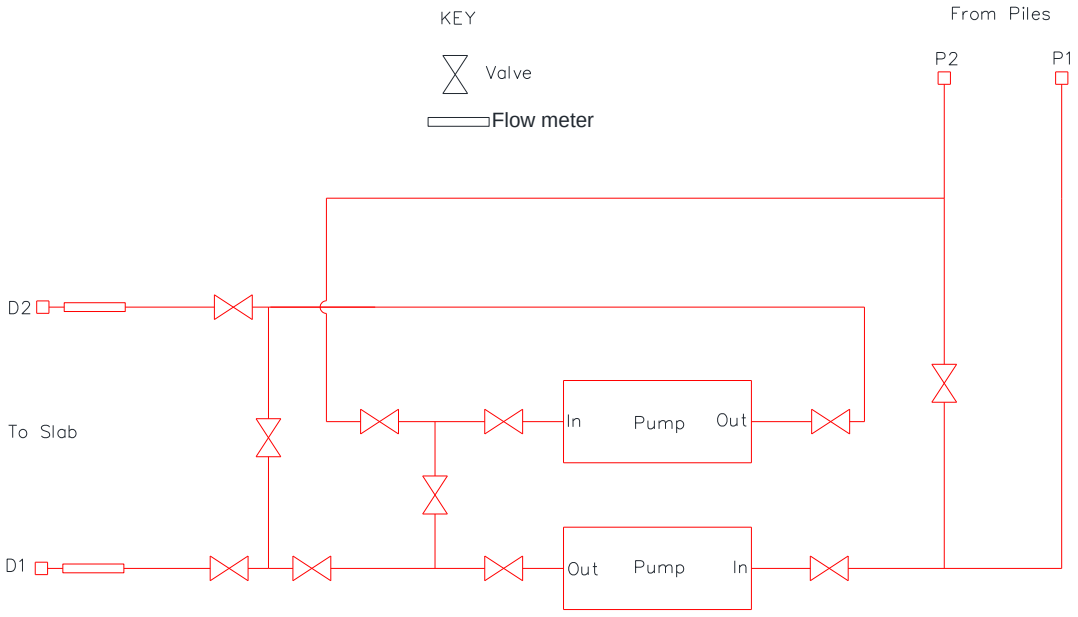

Figure 2-21. Pump circulation system layout, Iteration 2.

2.5. DATA COLLECTION SYSTEM

The data collection system for the bridge deck was provided by GeoInstruments. A total of 36 thermistors are located throughout the experimental slab. The thermistors are calibrated internally by the data logger, thus the output data consisted of the temperature measurements directly. The sensors were placed in four general locations in the deck's cross section: the top, the level of the circulation tube, the middle of the deck, and the bottom. This, as well as the specific depth measurements, are shown in Figure 2-22.

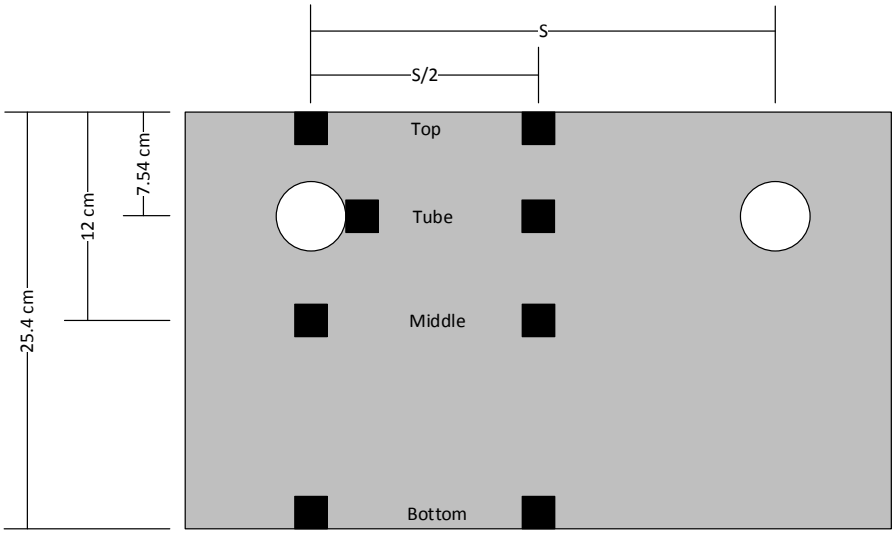

Figure 2-22. Sensor depths within the slab.

The sensors were placed in three general locations in plan view: on a circulation tube, between two circulation tubes, and in the radius of a bend in the circulation tube. This can be seen in Figure 2-23 and Figure 2-24.

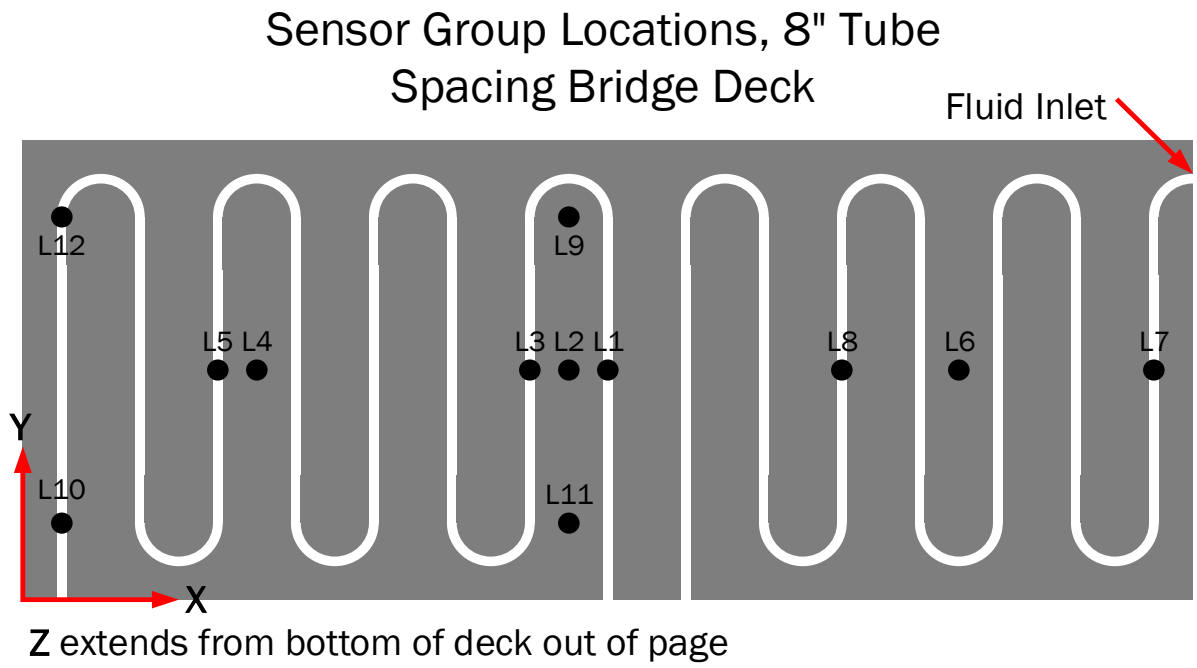

Figure 2-23. Plan view of sensor locations in the 20 cm side.

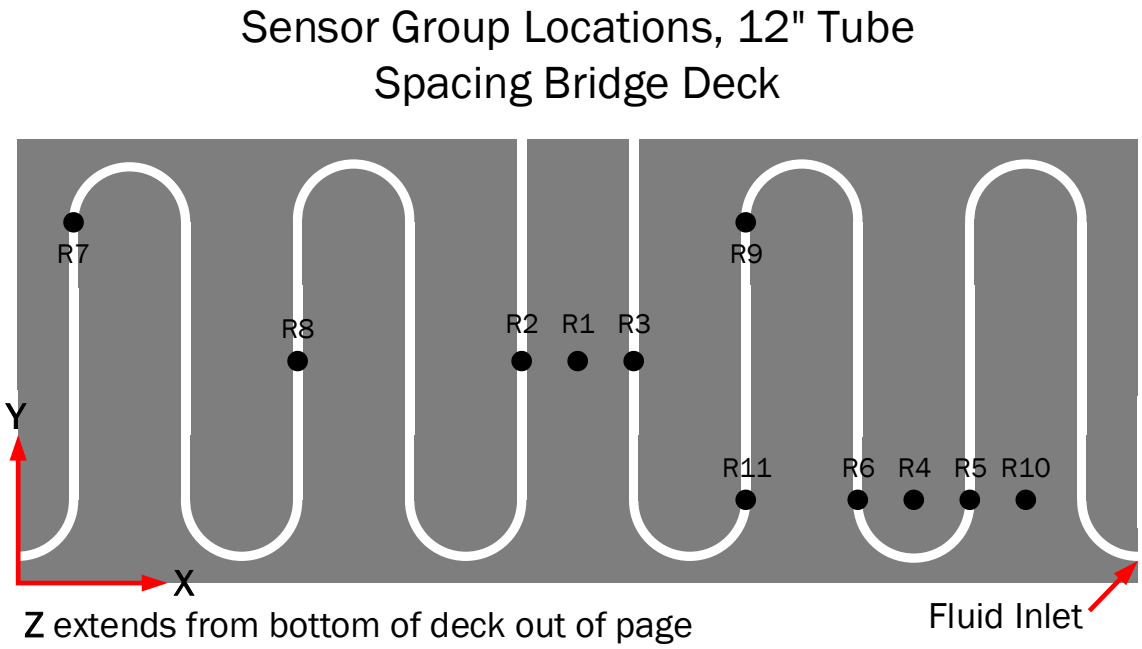

Figure 2-24. Plan view of the sensor locations in the 30 cm side.

The table below specifies exactly where each sensor is located.

Table 2-5. Spatial coordinates of the sensor locations within the slab.

Data Logger Channel	Location Code 1[1]	Location Code 2[2]	Depth	Coordinates x (cm)	y (cm)	z (cm)
1	L1	On	Top	152.4	65.0	25.4
2	L1	On	Tube	152.4	65.0	20.0
3	L1	On	Middle	152.4	65.0	12.0
4	L1	On	Bottom	152.4	65.0	0.0
5	L2	Between	Tube	142.2	65.0	20.0
6	L2	Between	Middle	142.2	65.0	12.0
7	L3	On	Tube	132.1	65.0	20.0
8	L3	On	Middle	132.1	65.0	12.0
9	L4	Between	Tube	61.0	65.0	20.0
10	L5	On	Tube	50.8	65.0	20.0
11	L6	Between	Top	243.8	65.0	25.4
12	L6	Between	Tube	243.8	65.0	20.0
13	L6	Between	Middle	243.8	65.0	12.0
37	L7	On	Tube	294.6	65.0	20.0
15	L8	On	Tube	294.6	65.0	20.0
16	L9	Radius	Middle	142.2	101.6	12.0
17	L10	On	Tube	10.2	65.0	20.0
18	L11	Between	Middle	142.2	65.0	12.0
19	L12	On	Tube	10.2	101.6	20.0
20	R1	Between	Tube	152.4	65.0	20.0
21	R1	Between	Top	152.4	65.0	25.4
22	R1	On	Middle	152.4	65.0	12.0
23	R1	On	Bottom	152.4	65.0	0.0
24	R2	On	Tube	137.2	65.0	20.0
25	R3	On	Tube	167.6	65.0	20.0
26	R4	Radius	Top	243.8	15.2	25.4
38	R4	Radius	Tube	243.8	15.2	20.0
28	R4	Radius	Middle	243.8	15.2	12.0
29	R5	On	Tube	259.1	15.2	20.0
30	R6	On	Tube	228.6	15.2	20.0
31	R7	On	Tube	15.2	106.7	20.0
39	R8	On	Tube	76.2	65.0	20.0
33	R9	On	Tube	198.1	106.7	20.0
34	R10	Between	Tube	274.3	15.2	20.0
35	R11	On	Tube	198.1	15.2	20.0
36	Control Slab		Tube			

[1]See Figure 2-23 and Figure 2-24 for Location Code 1

[2]'On' refers to a cross section with a deicing tube, 'Between' refers to a cross section between two deicing tubes, 'Radius' refers to the center of a bend between deicing tubes

2.6. OPERATIONAL SCHEDULE

The experimental setup was operated for several years during the course of this research. The days on which it was operated, and other operational parameters are shown in the table below.

Table 2-6. Log of system operation.

	Start		End			Deck Flowrate (gpm)		Pile Flowrate (gpm)			
Year	Date	Time	Date	Time	Length of Operation (h)	8" Spacing	12" Spacing	1	2	3	4
2013	12-Jun	13:30	12-Jun	17:10	3.67	3.5	4			7.5	
	15-Jun	14:15	15-Jun	19:30	5.25	3.5	4			7.5	
	17-Jun	13:32	17-Jun	17:05	3.55	3.5	4			7.5	
	25-Jun	12:29	25-Jun	20:40	8.18	3.5	4			7.5	
	26-Jun	12:00	26-Jun	20:00	8.00	3.5	4			7.5	
	28-Jun	11:25	28-Jun	19:25	8.00	3.5	4			7.5	
	29-Jun	12:00	29-Jun	20:00	8.00	3.5	4			7.5	
	16-Jul	12:00	16-Jul	15:00	3.00	3.5	4			7.5	
	23-Jul	12:00	23-Jul	20:00	8.00	3.5	4			7.5	
	2-Aug	11:00	2-Aug	19:00	8.00	3.5	4			7.5	
	27-Aug	8:00	27-Aug	19:00	11.00	3.5	4			7.5	
	28-Aug	8:00	28-Aug	17:00	9.00	3.5	4			7.5	
2014	6-Jan	10:45	8-Jan	15:45	53.00	5.5	0			5.5	
	15-Jan	7:45	16-Jan	7:45	24.00	5.5	0			5.5	
	21-Jan	7:00	24-Jan	7:45	72.75	5.5	0			5.5	
	27-Jan	16:30	31-Jan	11:00	90.50	5.5	0			5.5	
	12-Feb	7:15	14-Feb	14:00	54.75	5.5	0			5.5	
	3-Mar	7:10	3-Mar	15:00	7.83	5.5	0			5.5	
	17-Mar	18:30	18-Mar	15:22	20.87	5.5	0			5.5	
	26-Mar	6:00	26-Mar	8:30	2.50	5.5	0			5.5	
	26-May	10:00	26-May	20:00	10.00	6.75	7			5.5	
	27-May	12:00	27-May	20:00	8.00	6.75	7			All	
	29-May	9:30	29-May	11:00	1.50	9	0			9	
	2-Jun	14:00	2-Jun	20:00	6.00	6.75	7			All	
	3-Jun	14:00	3-Jun	20:00	6.00	6.75	7			All	
	4-Jun	14:00	4-Jun	20:00	6.00	6.75	7			All	
	16-Jun	14:00	16-Jun	20:00	6.00	6.75	7			All	
	17-Jun	14:00	17-Jun	20:00	6.00	6.75	7			All	
	18-Jun	14:00	18-Jun	20:00	6.00	6.75	7			All	
	19-Jun	14:00	19-Jun	20:00	6.00	6.75	7			All	
	20-Jun	14:00	20-Jun	20:00	6.00	6.75	7			All	
	24-Jun	14:00	24-Jun	19:00	5.00	6.75	7			All	

	25-Jun	14:00	25-Jun	19:00	5.00	6.75	7	All
	26-Jun	14:00	26-Jun	19:00	5.00	6.75	7	All
	27-Jun	14:00	27-Jun	19:00	5.00	6.75	7	All
	1-Jul	14:00	1-Jul	19:00	5.00	6.75	7	All
	2-Jul	14:00	2-Jul	16:10	2.17	6.75	7	All
	7-Jul	13:00	7-Jul	19:00	6.00	6.75	7	All
	8-Jul	13:00	8-Jul	16:10	3.17	6.75	7	All
2015	20-Feb	15:00	20-Feb	16:30	1.50	Y	Y	All
	20-Feb	16:30	22-Feb	15:00	46.50	4	0	4
	23-Feb	10:00	25-Feb	18:00	56.00	0	3.5	3.5
	23-Feb	16:50	26-Feb	18:45	73.92	4	0	4
	26-Feb	7:30	26-Feb	18:45	11.25	0	3.5	3.5
	4-Mar	17:45	6-Mar	13:00	43.25	4	0	4

2.7. DATA PROCESSING

Due to several years' worth of data, a program was created in Matlab to facilitate data viewing and retrieval. A graphical user interface (GUI) was created for each data set – the data set from the piles and the data set from the bridge deck – which allows the user to select the period of interest, desired sensor measurements, and for the piles, whether the data is to be plotted over time or over depth. Besides creating a plot of the data selected, the program also outputs the data range selected to an excel file.

2.7.1. Pile Data

The pile data GUI allows one to select the range of data, up to the hour, as well as which data points are specifically desired. It then generates a plot either vs time to look at how temperatures vary with time, or vs depth to look at temperature profiles at a particular location. The selected data is also output to an excel file for easy manipulation. While it only directly plots temperature data, it does output strain data at locations where strain was also measured.

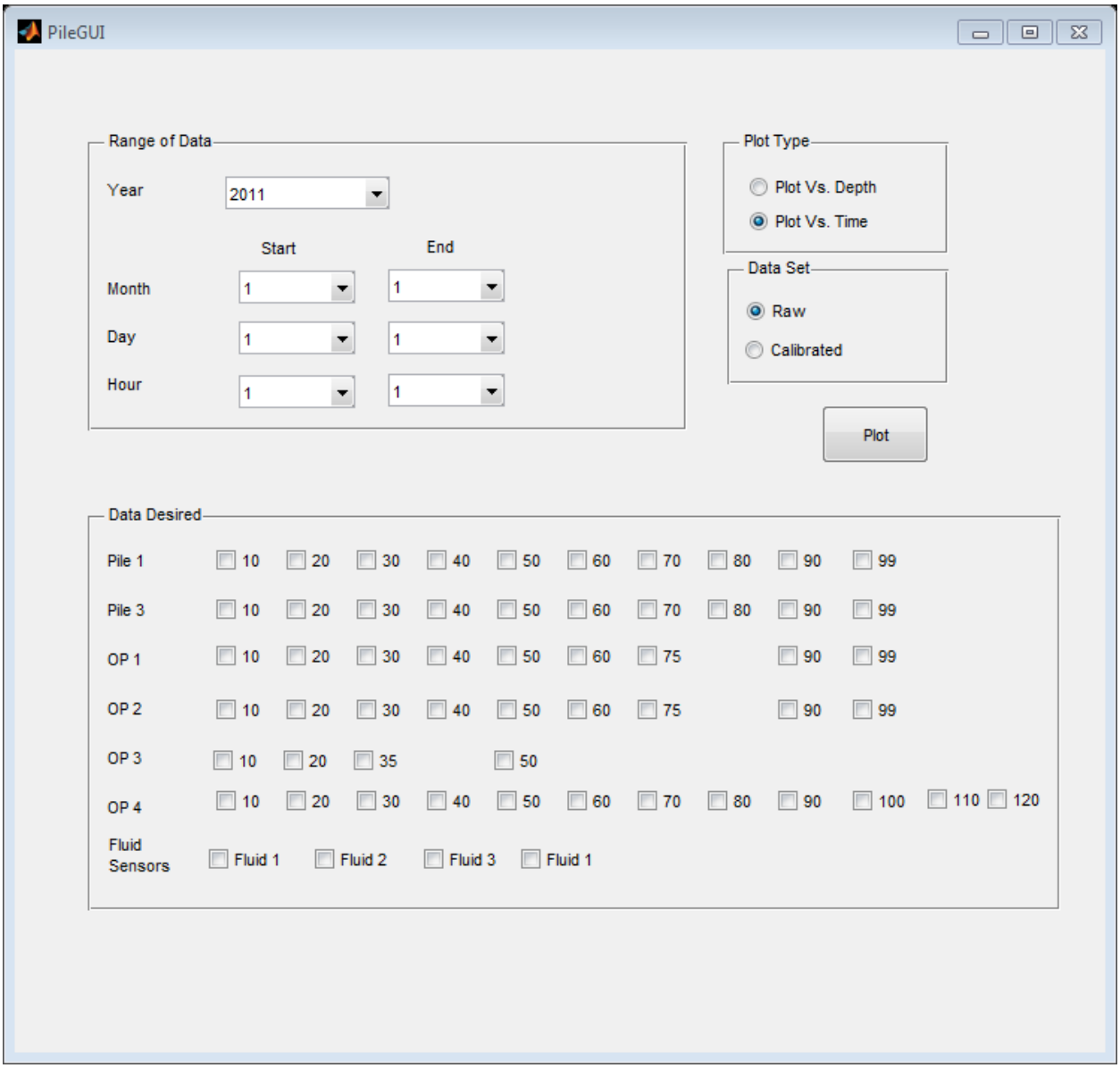

Figure 2-25. GUI to find, plot, and export the desired pile temperature and strain data.

2.7.2. Slab Data

The slab GUI is very similar to the pile GUI except that it does not plot vs depth, rather only time. It is to be used in conjunction with Figure 2-17, Figure 2-18, and Table 2-5 to acquire the correct sensor numbers.

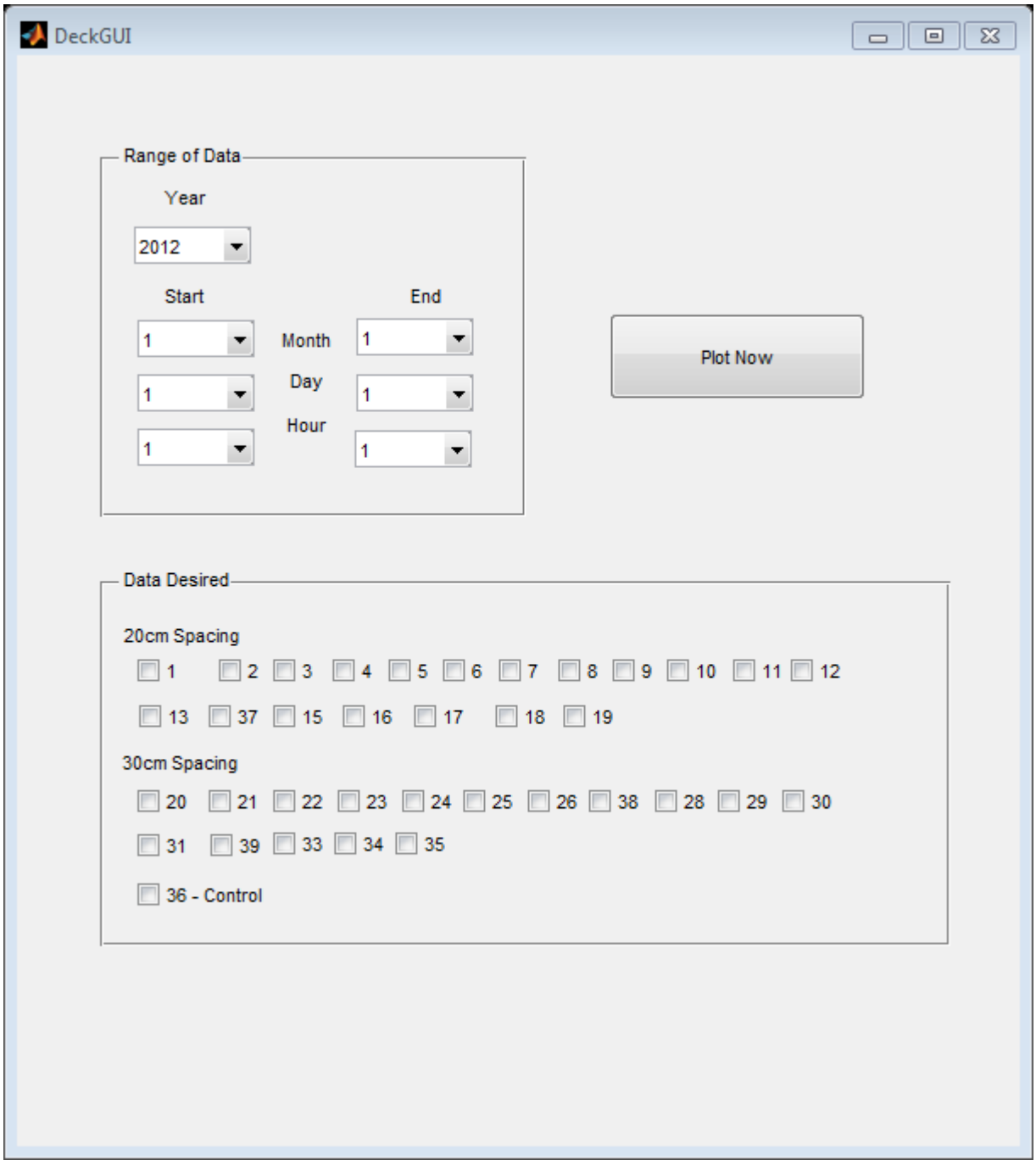

Figure 2-26. GUI to find, plot, and export the desired slab temperature data.

2.8. REFERENCES

Abdelaziz, S. L. (2013). "Deep Energy Foundations: Geotechnical Challenges and Design Considerations." Ph.D. Thesis, Virginia Polytechnic Institute and State University.

American Concrete Institute (ACI). (2002). “Guide to Thermal Properties of Concrete and Masonry Systems.” ACI 122R-02. American Concrete Institute.

COMSOL. (2015). “COMSOL MultiphysicsTM Version 5.1: User’s Guide and Reference Manual.” COMSOL Inc., Burlington, MA.

3. THE THERMAL PERFORMANCE OF A SMALL-SCALE BRIDGE DECK DEICING SYSTEM UNDER BRIDGE DECK DEICING AND THERMAL RECHARGE OPERATIONS

3.1. ABSTRACT

The icing of bridge decks during the winter poses a serious problem for motorists and transportation authorities. Icing is typically mitigated through the use of chemicals, including salts, which are corrosive to the bridge deck and harmful to the environment. Heating the bridge deck using shallow geothermal energy harvested by the bridge's foundation presents a unique opportunity to sustainably and efficiently solve this problem. These systems operate by circulating a fluid through tubes that were installed in the bridge's deep foundation, such as piles or drilled shafts. As the fluid circulates through the tubing in the foundation, it is heated by the ground, which below a certain depth maintains a constant temperature year-round. The heated fluid is then circulated through the bridge deck, heating the deck to prevent snow and ice accumulation and to melt snow or ice that has already accumulated. This paper presents the results of a small-scale bridge deck deicing system. Energy extracted from thermal piles was used to heat a model bridge deck during the winter. The system was able to both prevent accumulation and melt accumulated precipitation on the surface. The system was also operated during the summer to collect thermal energy and deposit it into the ground to replace the energy that was used during the winter. Also shown are the observed thermal gradients within the bridge deck resulting from naturally occurring environmental conditions as well as bridge deck deicing and thermal recharge operations.

3.2. INTRODUCTION

Highway bridges experience two major winter weather related problems. The first is preferential icing, which is when the bridge deck freezes before the rest of road as it loses thermal energy from the bottom as well as the top. This condition is dangerous for motorists and is attributed to hundreds of accidents and fatalities every year (Friar and Decker 1999). Transportation authorities rarely do more than erect warning signs as preferential icing is extremely hard to predict and the prevention of it would involve an excessive amount of salts and other chemicals applied either manually (which can be very expensive) or through a complicated automated control system (which is also expensive and prone to malfunctions, see Minsk (1999)). The second winter weather related problem results from the transportation authorities' attempts to prevent the accumulation of frozen precipitation (i.e. snow, ice) by using deicing chemicals and salts. One of the major factors that lead to accelerated deterioration of bridge infrastructure is the chloride attack from deicing salts (Baboian 1992; Cady and Weyers 1983). The landmark "Bridging the Gap" report ranks bridge deterioration the highest among the major problems facing the nation's bridge infrastructure (AASHTO 2008). It is estimated that the annual direct cost of bridge corrosion in the U.S. ranges between $6-$10 billion (Koch et al. 2002). The actual total cost can be as much as 10 times higher than this when indirect costs are also factored in (Yunovich et al. 2003). Furthermore, deicing salts and chemicals can be extremely damaging to the environment through surface runoff and infiltration to the groundwater. Although alternative methods for bridge deck deicing exist, they are often expensive, energy intensive, and non-sustainable.

Ground-source heating of bridge decks has the potential to decrease both the frequency of preferential icing and the use of chemical salts. A schematic of the concept is shown in Figure 3-1. The bridge sub-structure is converted to an energy foundation by installing circulation tubes in the foundation elements,

creating energy piles, and in the embankment (though not always). As fluid is circulated in the system, heat energy can be extracted from the ground and supplied to the deck. The ground acts as a heat source because the temperature of the ground remains relatively constant throughout the year, especially at depths greater than 6-10 m (20-30 ft). During the winter, the ground temperature is warmer than the atmospheric temperature, thus providing a source of thermal energy. During the summer the system can be operated to collect the thermal energy of the bridge deck and inject it into the ground to replace the energy that was used during the winter and to raise the temperature of the ground for more efficient operation of the system.

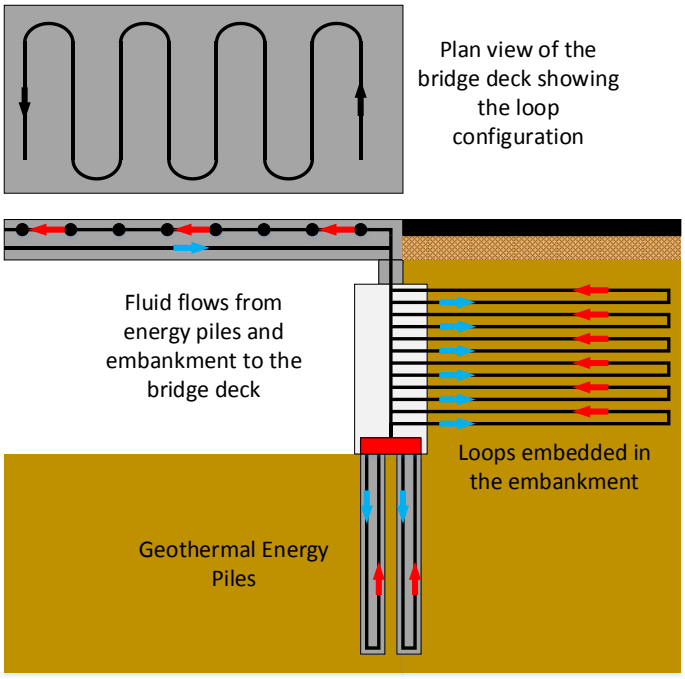

Figure 3-1. Conceptual schematic of ground-source bridge deck deicing (redrawn after Bowers and Olgun 2014).

The fluid can be pumped directly from the foundation to the bridge deck (passive system), or can travel to a heat pump (active system), which then uses the energy from the fluid to more efficiently heat the circulation fluid in the bridge deck (Liu et al. 2007). The main advantage of a passive configuration is that the only energy required is that to operate the circulation pumps, which could be produced on-site using a photo-voltaic array. This is contrasted with the energy required to operate a ground-source heat pump (GSHP) in an active configuration which would necessitate the availability of an external power source. Due to the absence of the heat pump, the highest possible temperature of circulation fluid is the ground temperature (around 13°C or 55°F in Blacksburg, VA) in a passive configuration, thus there are obvious operational limitations, which will be discussed in this paper. This temperature limitation also demonstrates that any increase in ground temperature obtained by operating the system during the summer greatly benefits passive systems.

This paper presents the results of several years' worth of experimental bridge deck deicing and thermal recharge tests using a ground-source bridge deck deicing system. The configuration of the system is described and then several bridge deck deicing case studies are presented that demonstrate the performance and operational limits of the system. A summary of the thermal recharge operations

performed is also given. Finally, an in-depth analysis as to the temperature gradients developed during both bridge deck heating and cooling operations is performed in an attempt to anticipate any detrimental thermally induced stresses that may result from system operation.

3.3. BACKGROUND

Several methods other than chemical bridge deck deicing have been developed and implemented and can generally fall into one of three categories: electric, heat pipe, or hydronic. There are several methods of using electricity to heat a bridge deck including buried electric cables, carbon fiber heating wire, and electrically conductive concrete. Minsk (1999) reports of two projects, one in West Virginia and one in Oregon, in which mineral-insulated cables were embedded several centimeters beneath the surface of the deck. The design heat outputs ranged from 516 W/m^2 to 753 W/m^2. Zhao (2010) used carbon fiber heating wire to successfully heat an experimental bridge deck, however, this technology has never been utilized in an actual bridge. Tuan (2008) reports of a bridge that was installed with electrically conductive concrete that is capable of producing 452 W/m^2 for deicing purposes. There are several drawbacks in utilizing heat generation from electrical resistivity, the main being that such methods necessitate the availability of an external power source.

One of the only reported instances where a heat pipe bridge deck deicing system was used was on a bridge in Virginia (Hoppe 2000). The system was designed with a heat output of 700 W/m^2 and was powered by a propane-fired boiler. As Hoppe (2000) highlights, there are many complexities with heat pipe systems including high operating temperatures (in order to vaporize the heat carrier fluid), small tolerances in construction (achieving the correct slopes for the condenser pipes), and as with electric systems, the necessity of an external power source (in this case propane and electricity).

Hydronic systems simply circulate a fluid through tubes that are installed underneath the surface of the bridge deck. Minsk (1999) describes several systems in Nebraska and Oregon that are heated using natural gas-fired boilers with a design heat flux of 530 W/m^2. There are several case studies of hydronic ground-source bridge deck heating, though none that use energy pile technology. Minsk (1999) documents a case where a bridge over the North Fork of Silver Creek in Oregon uses well water supplied to a heat pump, which is used in conjunction with a GSHP to hydronically heat the bridge deck. Another system in Texas utilizes a GSHP that is connected to a geothermal borehole field. The boreholes are 10.2 cm (4 in) in diameter and 53.6 m (176 ft) deep. The author notes that the system has been successfully used to prevent snow accumulation on the deck by circulating the fluid directly from the borehole field to the deck without the use of a heat pump, thus taking advantage of the passive configuration described previously.

Liu et al. (2003, 2007) built an experimental 18.3 m x 6.1 m (60 ft x 20 ft) bridge deck with an embedded hydronic heating system. The GSHP utilized a vertical closed-loop ground-source heat exchanger consisting of six 13 cm (5.25 in) diameter boreholes, each containing a single circulation loop. With the use of a heat pump, this system was able to successfully keep the deck snow-free during several winter storm events.

Yoshitake et al. (2011) reports of a bridge system in Japan that uses an underground water storage tank. The water is heated by the ground to roughly ground temperature and is then circulated through embedded tubes in the bridge decks when needed. This system does not incorporate a heat pump and relies on geothermal energy alone. The system is automatically controlled and is set to operate whenever

the lowest temperature in the bridge deck is less than 0.5°C. During several snow events, the system performed well and was able to prevent significant snow accumulation. The authors report utilizing thermal recharge during the summer to increase the temperature of the water in the tank by operating the system. This in turn increased the temperature of the ground around the tank.

One of the longest running hydronic geothermal bridge deck deicing projects is the SERSO system in Switzerland, which has been operating continuously from 1994 until the date of publication of Eugster (2007). It works by collecting thermal energy during the summer and storing it in 55,000 m^3 (71,939 yd^3) of rock, which is accessed by ninety-one 65 m 213 ft) BHEs. The heat energy is used to heat over 1,300 m^2 (13,993 ft^2) of roadway. The author reports that the typical heat output of the system is around 100 W/m and that it is operated preemptively to prevent snow and ice accumulation. This kind of operation (as opposed to melting already accumulated snow and ice) allows the system to operate without a GSHP. They have also found that they are usually able to collect more heat during the summer than what is needed during the winter and that heat collection during the summer serves to stabilize the road surface temperatures.

3.4. EXPERIMENTAL SET-UP

The experimental field test setup consists of a total of five micropiles, four of which are equipped with circulation loops along the full pile length for heat exchange. Test piles, 25.4 cm (10 in) in diameter, were installed to a depth of approximately 30.5 m (100 ft) at the Virginia Tech Geotechnical Research Facility. The energy piles are instrumented to measure strains and temperatures. In addition to the energy piles, there are four observation boreholes to measure the temperature of the ground surrounding the piles. A plan view of the piles and boreholes is given in Figure 3-2.

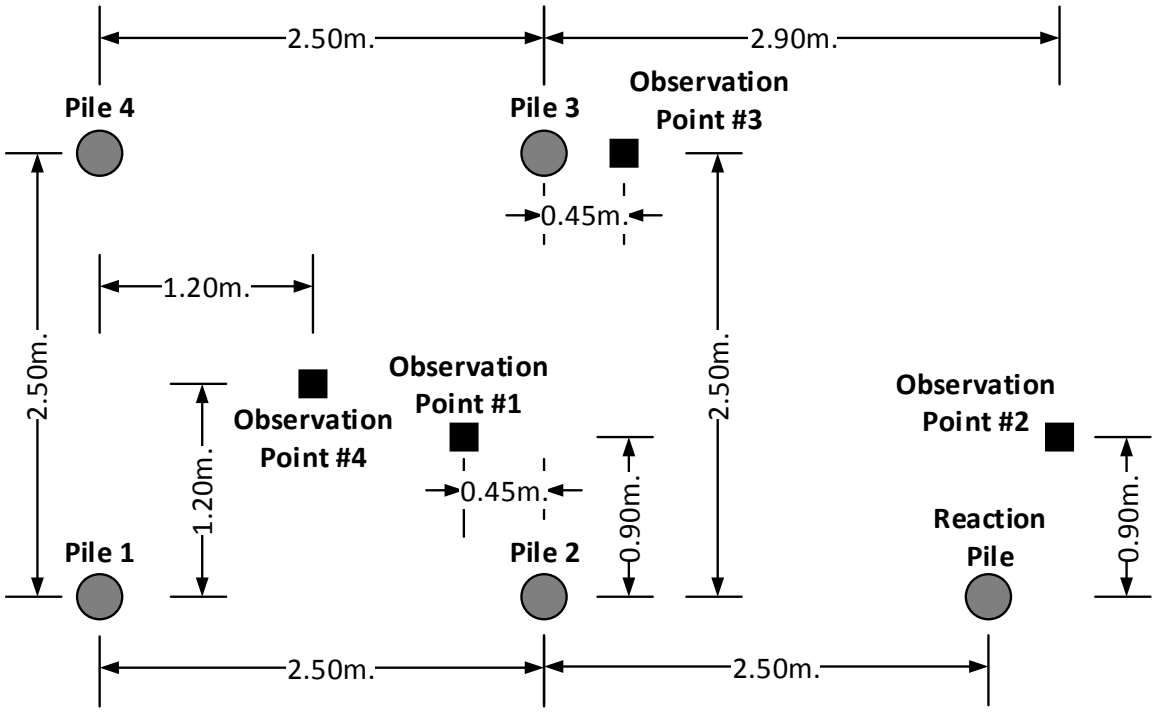

Figure 3-2. Plan view showing the spacing and locations of the energy piles and observation wells.

The piles are connected to a prototype 2.6 m x 3.0 m (8 ft x 10 ft) bridge deck, which is shown in Figure 3-3. The doubly reinforced 25 cm (10 inch) thick slab is elevated from the ground to simulate heat loss from the bottom face similar to a bridge deck. The test slab is divided into two 1.3 m x 3.0 m (4 ft x 10 ft) sections with an insulated separation in between. A 5 cm (2 in) thick clear concrete cover is present on top of the upper level reinforcement. PEX tubes with 16 mm (5/8 in) inner diameter (ID) are connected to the upper level reinforcement with 20 cm (8 in) and 30 cm (12 in) horizontal spacing in each section. Insulation has been added to the sides to simulate an adiabatic surface. The slab is heavily instrumented with thermistors to monitor the variation of temperature in both slab sections at different horizontal and vertical extents near the tubes. The locations where the reported temperatures in this paper were measured are shown in Figure 3-4.

Figure 3-3. Photograph of the experimental bridge deck during construction. The fluid circulation tubes are attached to the top layer of reinforcement and are spaced 20 cm apart on the left side and 30 cm apart on the right side.

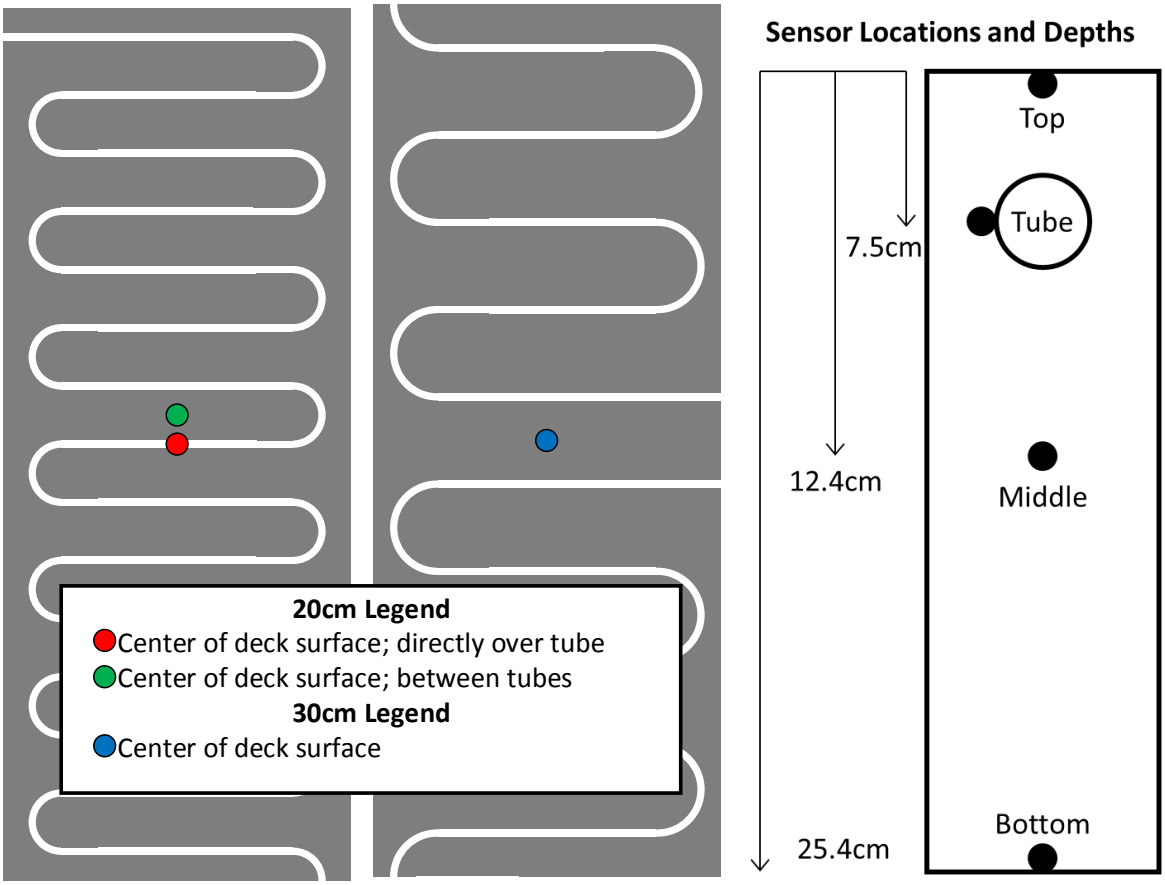

Figure 3-4. A plan and cross section view of the bridge deck showing the locations of the temperature sensors whose measurements are reported in this paper.

This system is powered by two geothermal circulation pumps and are configured such that they can be operated separately to control each side of the deck independently, or together in either parallel or series. The circulation fluid for bridge deck deicing tests is a mixture of 40% glycol by volume, and water. Water alone is used during the thermal recharge tests in the summer.

3.5. BRIDGE DECK HEATING TESTS

Bridge deck heating tests were performed during periods of winter storms It was also tested during periods where no storms were present, but the ability of the system to perform under certain environmental conditions was observed. There are two main performance metrics: energy and temperature. The amount of energy imparted to the deck by the circulating fluid is critical in determining how much energy is required of the ground during these storms. This can be calculated by multiplying the volumetric heat capacity of the circulation fluid by the volumetric flow rate and the temperature difference between the inlet and outlet. The temperature of the deck is critical as the surface temperature of the deck must be above 0^{o}C in order for the system to have a chance at melting the falling precipitation. Both energy imparted and surface temperature are given in the following analyses. Table 3-1 summarizes the heating tests and in-depth descriptions are below.

Table 3-1. List of bridge deck deicing experimental tests.

Dates	Length of Operation {Preheat, Storm, Melt Time} (h)	Cumulative Precipitation (cm)	Deck Performance
2/23-24/2015	15, 3, 0	0.6	100% clear; Temp above 0°C
1/21/2014	4, 5, 0	2.1	100% clear; temp above 0°C
1/27-28/2014	18, 7, 12	5.1	clear above tubes; temp above 0°C
2/25-26/2015	56*, 7, 0	7.6	clear 90% of storm; temp above 0°C
3/5-6/2015	17.25, 6, 20	10.7	Initially clear; Temp above 0°C
2/12-14/2014	7, 24, 22	45.7	Eventually melted; Temp above 0°C

*The system was turned on previously for the operation on 2/23-24/2014 and then left on for the storm the following day

3.5.1. Mild Winter Storm – 2/23-24/2015

A mild winter storm occurred on February 24, 2015 where, beginning at approximately 8:00 and continuing until 11:00, 0.6 cm of snow fell. This is a relatively small amount of snow, but it fell during a period of time when the ambient temperature was very cold, as can be seen in Figure 3-5. During the period of time the snow fell, the temperature of the control slab was below -5°C. The system was turned on in advance of the storm on 2/23/2015 at 17:00. Up to that point the surface temperature above the circulation tubes and between the circulation tubes was equal, but after operation began the surface temperature above the tubes became greater than the temperature between the tubes. And though temperatures at both locations continued to decrease, they remained above 0°C until the storm hit, at which point, aided by an increasing ambient air temperature, they increased to between 2°C and 5°C for the duration of the storm.

Figure 3-6 shows the condition of the deck surface at two points during the storm. The top photograph shows the deck on the morning of 2/24/2015 at 9:15, a little over an hour into the storm. As can be seen, over 80% of the deck is snow free and it was discovered that the snow that is present on the deck blew over from the other side, which was not heated. Thus, the deck is melting the falling snow as well as the snow that is drifting onto it. At 10:00, shown in the bottom photograph, the deck is completely clear and remained that way for the duration of the storm.

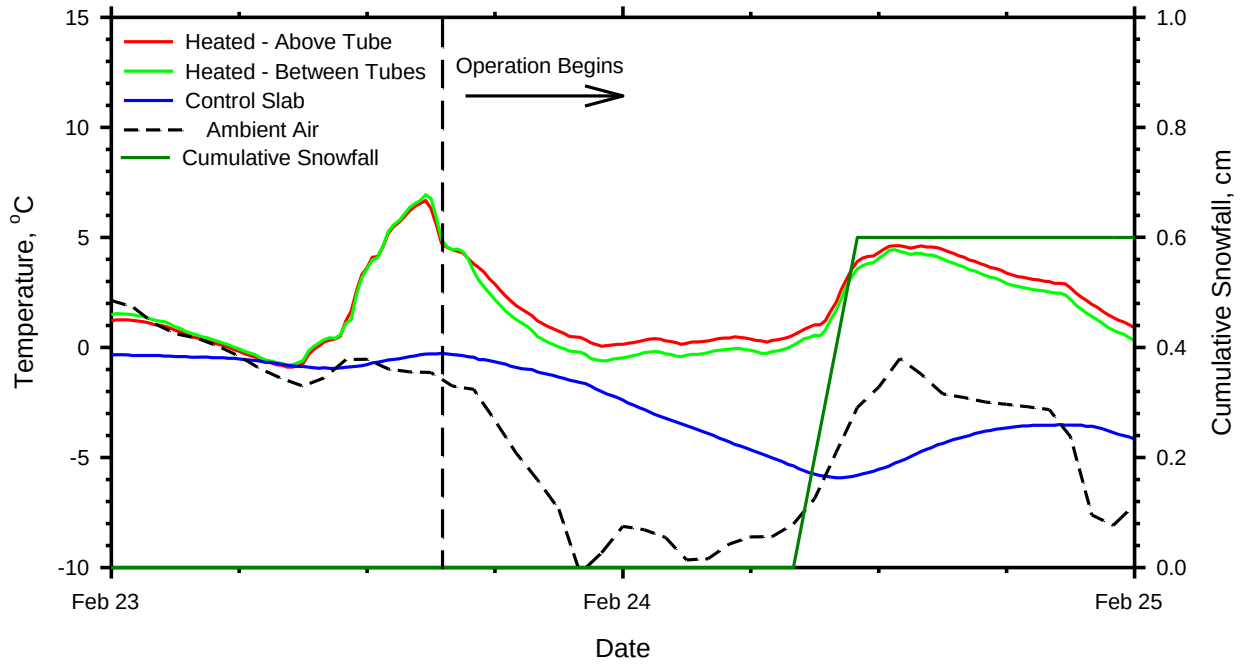

Figure 3-5. Surface temperatures of the heated and the temperature of the control slab during a mild winter storm on February 24, 2015.

Figure 3-6. Photographs of the heated bridge deck at 9:15 (top) and 10:00 (bottom) on the morning of 2/24/2015.

This experimental test shows that the system can keep a deck free from snow, even if the ambient temperatures are low. It should be noted, however, that the deck was turned on in advance of the storm, thus the surface temperatures were not permitted to become as low as they would have been the night preceding the storm as evidenced by the low temperature of the non-heated deck. It is likely that the system would not have worked if it were turned on the morning of the storm as it would have had to heat

the deck before the snow started falling instead of having the deck already heated and just maintaining the surface temperature. This system also showed that it could melt drifting snow, which often occurs after the roads have been cleared. Drifted snow presents a dangerous condition on bridges as it could easily freeze during the night.

3.5.2. Mild Winter Storm – 1/21/2014

A mild winter storm occurred on January 21, 2014 where, beginning around 11:00 and continuing until 16:00, approximately 2.1 cm (0.8 in) of snow fell. The system was turned on in advance of the storm at 7:00. Figure 3-7 shows the ambient air temperature, the temperatures of the surface of both the heated and unheated decks, as well as the cumulative amount of precipitation. Observe that the system was turned on when both the heated and unheated surfaces of the deck were decreasing. After beginning operation, the heated deck surface temperature increased to approximately 4°C (39°F) by the time the snow started to fall and maintained a temperature above 4°C for the duration of the event. The unheated deck maintained a temperature around 0°C (32°F). The system was able to keep the deck completely snow free for the entire duration of the test, whereas snow accumulated on both the unheated side and the control slab (Figure 3-8).

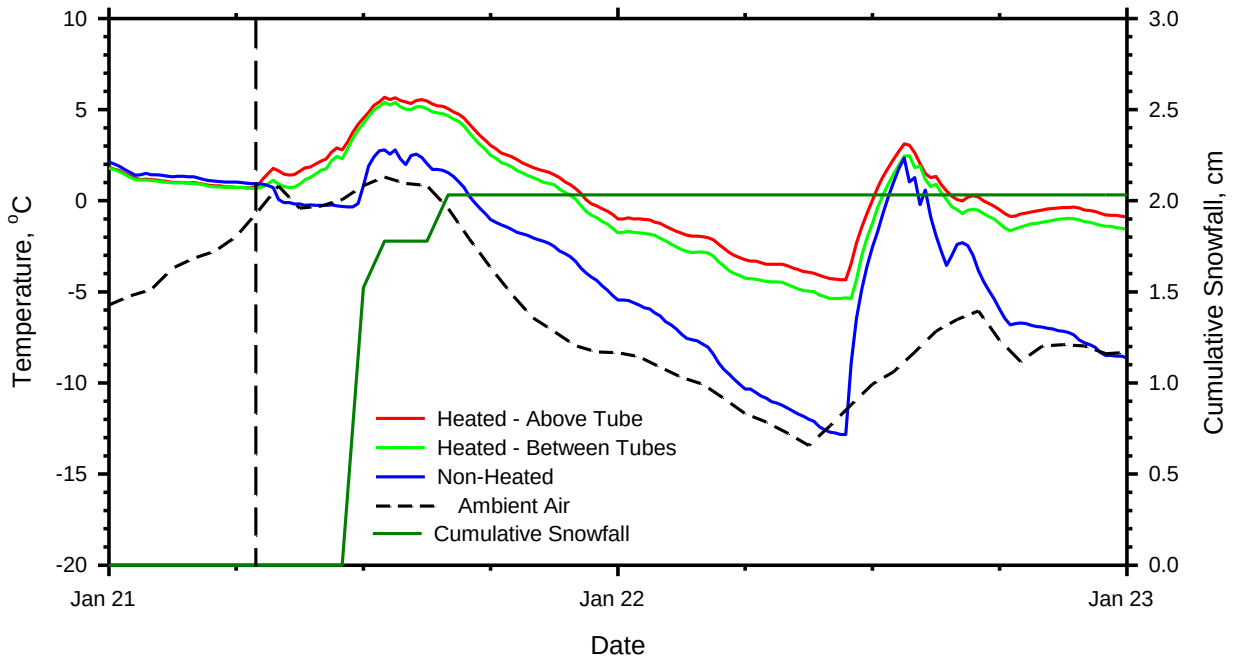

Figure 3-7. Surface temperatures of the heated and non-heated decks during a mild winter storm on January 21, 2014.

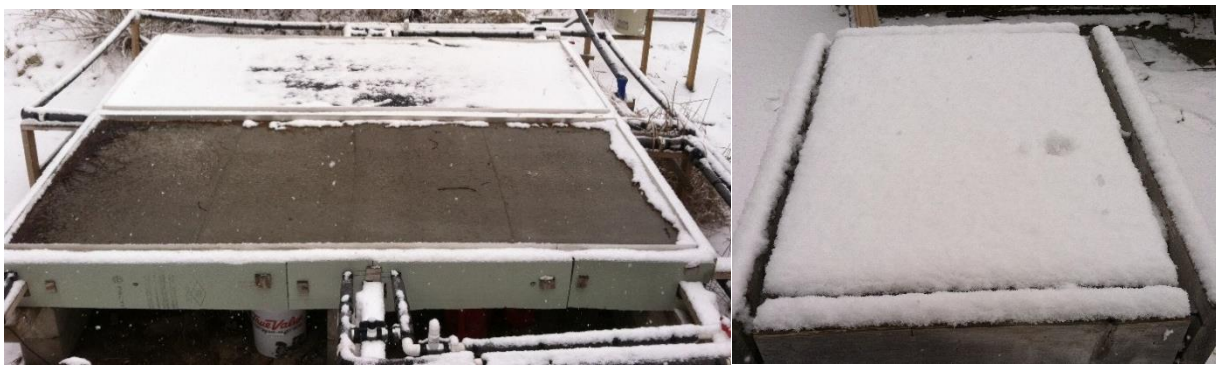

Figure 3-8. Photographs comparing performance of the heated deck vs. unheated deck (left) and the control slab (right) for the test that occurred on 1/21/2014.

This field test demonstrates the types of winter storms these systems are ideal for. In this case, the storm was relatively mild where a small amount of precipitation fell while the temperature was just below freezing. Despite the lack of severity of the storm, it is nevertheless dangerous for motorists especially in regards to bridges as though the roads may be clear, snow may very well be accumulating on bridges due to the lower temperatures at the surface of the bridge relative to the roads. This type of storm is, however, easily managed on roadways with deicing chemicals as they will keep the snow/slush from freezing and when combined with vehicular traffic, result in clear surfaces. Thus there is likely to be no mechanical removal which means if no chemicals are applied to bridges, in the absence of mechanical removal they must be able to maintain a snow free surface. And as this field test shows, they can.

3.5.3. Moderate Winter Storm – 1/27-28/2014

This field test occurred during a period of cold weather combined with 5.1 cm (2.0 in) of snowfall. The snowfall occurred on January 28, 2014 beginning around 16:00 and continuing until 23:00. The system was turned on preemptively on January 27, 2014 at 20:00. As shown in Figure 3-9, the system was turned on when the surface temperatures of both sides were below 0^{o}C and decreasing along with the ambient air temperature. For the next several days the ambient air temperature would remain well below 0^{o}C. The system was able to keep the surface temperatures of the deck from dropping any further before the storm arrived. By the time it started snowing, the surface temperatures above and between the tubes were greater than 0^{o}C and remained that way the entire duration of the storm whereas the surface temperature of the non-heated deck remained well below 0^{o}C. In fact, during the storm there is a 6 to 8^{o}C difference between the heated and non-heated sides.

The photographs of Figure 3-10 show the surfaces of the heated and non-heated sides during and after the storm. Figure 3-10a shows the deck at 16:30 on 1/27, shortly after the storm had started. There is approximately 0.75 cm of snow on the non-heated side and just a light dusting on the heated side. Figure 3-10b shows the deck at 7:30 the following morning (1/29), after the storm had ended. The deck surface above the tubes is clear whereas the surface between the tubes still has approximately 1 cm of snow. There is 5.1 cm of snow of the non-heated side. Figure 3-10c shows the deck at 17:30 on the evening of 1/29. There is still 5.1 cm of snow on the non-heated side whereas the heated side is clear.

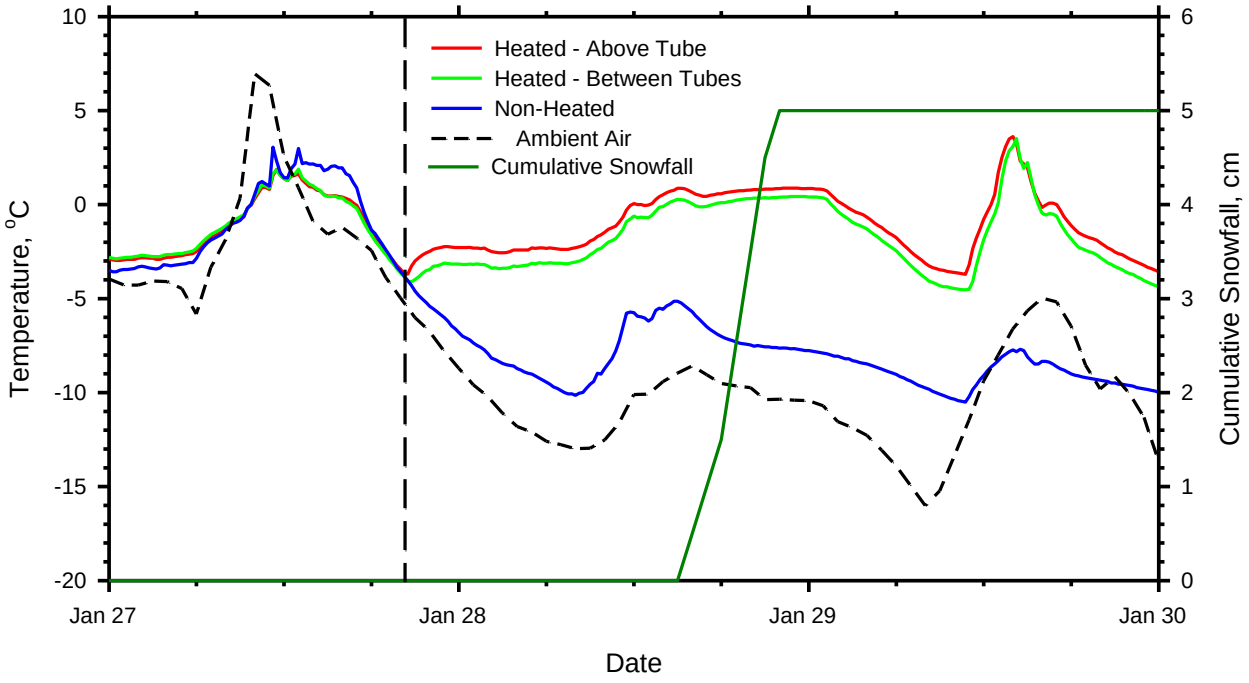

Figure 3-9. Surface temperatures of the heated and non-heated decks during a winter storm on January 28, 2014.

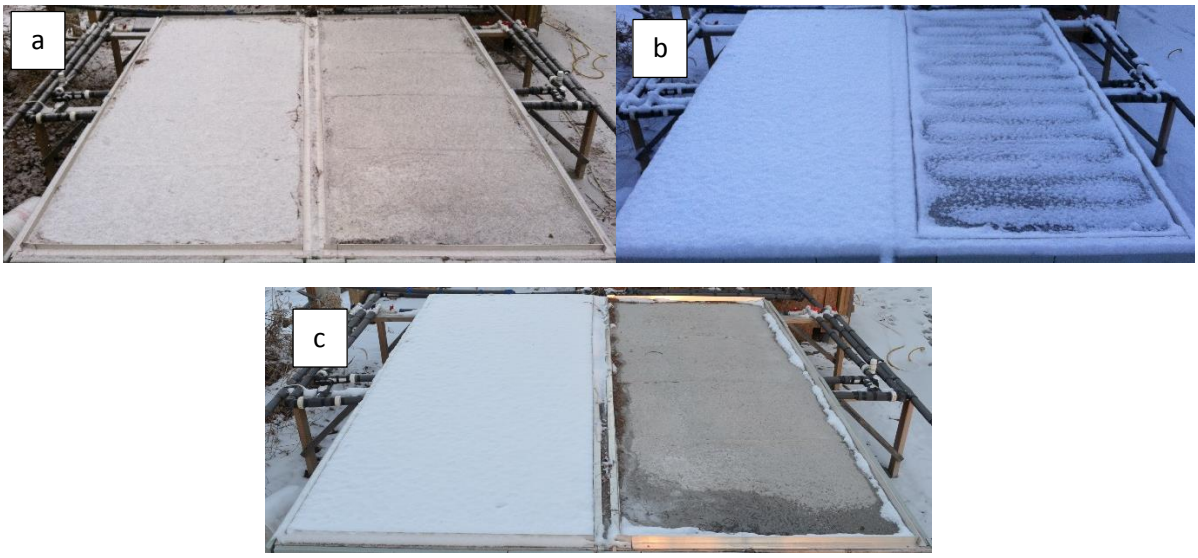

Figure 3-10. Photographs showing the deck surface at different times during the storm that occurred on 1/28-29/2014: a) 1/28/2014 16:30; b) 1/29/2014 7:30; c) 1/29/2014 17:30.

It can be observed from Figure 3-10 that although the deck surface temperature was above 0°C (see Figure 9), it was not high enough to keep the deck completely free. Initially, this may appear to be a failure, however several factors should be considered. The first is that with this low of temperature, deicing salts

are unlikely to work (Minsk 1998) and the roads will be just as dangerous as the bridges and thus require mechanical removal of the snow. As plows clear the roads (and bridges), because the surface temperature of the bridge is above 0°C, a snow-free surface will result. Secondly, as can be seen from Figure 3-9, the ambient air temperature remains well below freezing after the storm. A heated system prevents the surface of the deck from dropping as low, which will eventually melt any remaining precipitation whereas an unheated surface remains well below freezing.

3.5.4. Moderate Winter Storm – 2/25-26/2015

A moderate winter storm occurred on February 25-26, 2015 where 7.6 cm (3 in) of snow fell while the ambient air temperature was -2 to -3°C, as shown in Figure 3-11. The system had already been operating from a previous storm (Section 3.5.1) and remained on in anticipation of this storm. The non-heated deck had been operated previously with snow on the surface but was turned off at 18:00 on 2/25 before the storm. The previous operation is why the surface temperature is right around 0°C, as it had been melting the snow on the surface. By the time the storm began and the snow started to fall, the surface temperatures of the heated deck were above freezing and remained above freezing the entire storm. The surface temperature of the non-heated deck did not remain above freezing, and as a result snow accumulated on the surface.

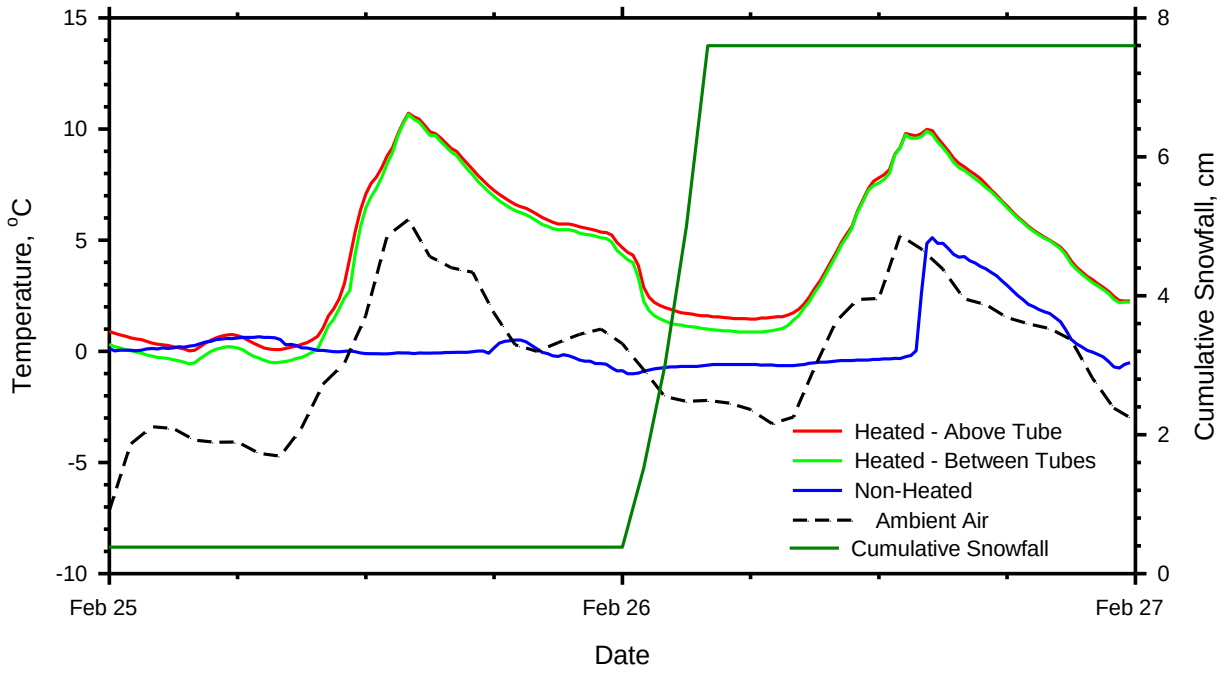

Figure 3-11. Surface temperatures of the heated deck and cumulative amount of snow that fell during the bridge deck deicing operation that took place on 2/25-26/2015.

The photographs in Figure 3-12 show the deck at several points during the operation. Figure 3-12a shows the deck at 2:30 on 2/26, which is about midway through the storm. Notice that roughly 60% of the deck is free from snow indicating that the storm conditions are right at the limit of what the system can handle as it is melting most snow as it is falling. Upon closer inspection, about 50% of the snow that is accumulating is doing so on debris (such as twigs and leaves) that wind had blown onto the deck. The

remaining 50% is accumulating in areas between the circulation tubes. There is 4.4 cm (1.75 in) of snow on the non-heated side. Figure 3-12b shows the deck at 7:30 on 2/26 after the storm had ended. It is free from snow, except that of which is on debris on the deck. There is 7.6 cm (3 in) of accumulated snow on the non-heated side. At this point in time the non-heated side was turned on and, in conjunction with warmer ambient temperatures, had melted the snow on the surface by 14:00 on 2/26 as shown in Figure 3-12c, at which point a spike in the surface temperature can be noticed (Figure 3-11).

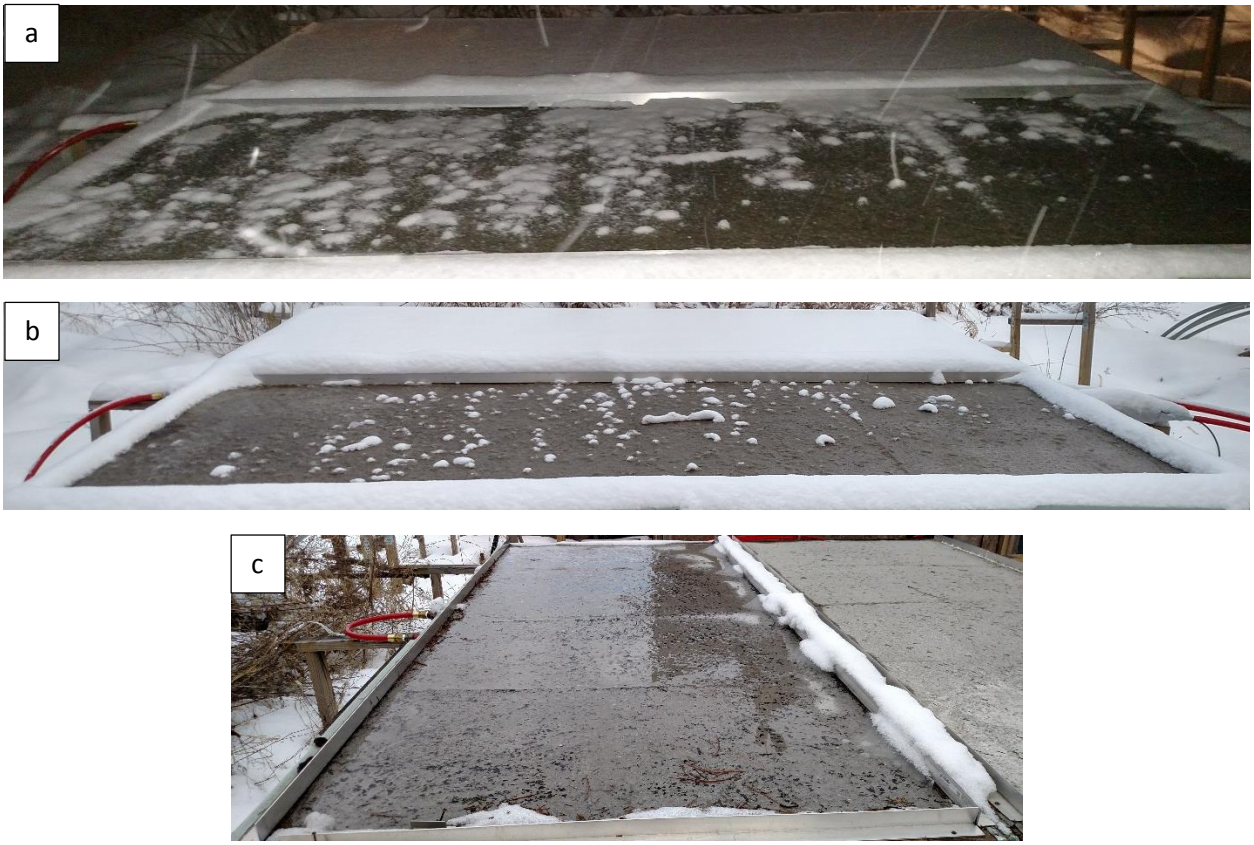

Figure 3-12. Photographs showing the deck surface at different times during the storm that occurred on 2/26/2015: a) 2/26/2015 2:30; b) 2/26/2015 7:30; c) the 30cm side at 2/26/2015 14:00.

One resource that was available during this storm was a thermal imaging camera. The following photographs show several images taken of the deck throughout the storm. Figure 3-13a shows the heated deck at 18:00 on 2/25. Notice that the entire deck is above freezing, and the outline of the circulation tubes can be seen. Figure 3-13b shows the non-heated deck at the same time, which is the point in time at which it was turned off. As a result, the outline of the circulation tubes can still be seen, although notice that the non-heated side of the deck is much colder than the heated side. Figure 3-13c shows the deck at 7:30 on the morning of 2/26. As can be seen, the surface temperature is right at freezing, which explains why it is clear. The dark spots are the specks of snow on the debris. The temperature of the top surface of the snow covering the non-heated side of the deck is several degrees below freezing as seen in Figure 3-13d, which was taken at 7:30 on 2/26. Figure 3-13e and Figure 3-13f are the heated and originally non-heated sides, respectively, at 14:00 on 2/26. As observed, the heated side has greatly increased in temperature and the temperature at the surface of the deck appears more uniform. The originally non-heated side was turned on at 7:30, and has finally cleared the 7.6cm of snow from the surface and the

surface temperature is a few degrees above freezing. The outline of the circulation tubes can be clearly seen.

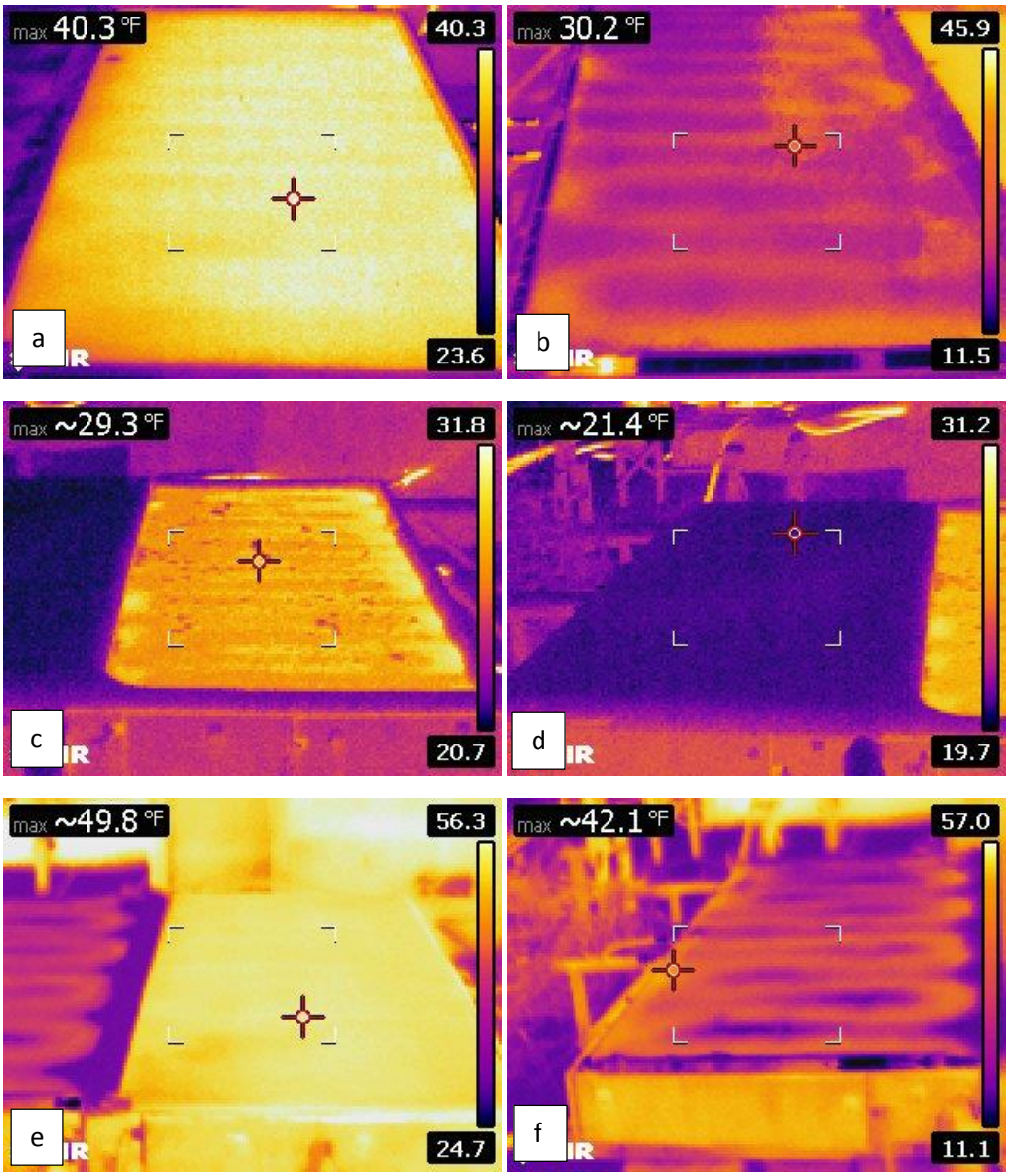

Figure 3-13. Thermal images of the bridge deck operation that occurred on 2/25-26/2015: a) 20cm side at 2/25 18:00; b) 30cm side at 2/25 18:00; c) 20cm side at 2/26 7:30; d) 30cm side at 2/26 7:30; e) 20cm side at 2/26 14:00; f) 30cm side at 2/26 14:00.

This was a valuable test for several reasons. First, it again proved the effectiveness of these systems in preventing snow accumulation during moderate storms where there are several centimeters of accumulation accompanied by temperatures a few degrees below freezing. In this case, the system was able to prevent accumulation on the majority of the surface. When combined with the mechanical removal from plows or even that caused by vehicular traffic, a snow free surface will result. Secondly, this test showed the upper limits of the system as the ambient temperature, snowfall rate, and preemptive

heating combined so that the rate at which the snow was melted at the surface was roughly equal to the rate at which it was falling.

3.5.5. Moderate Winter Storm – 3/5-6/2015

On March 5, 2015 6.9 cm of snow fell from 11:00 to 14:00, most of which fell from 11:00 to 13:00. This was a very dense snow, such that only 5.7 cm of snow depth was measured, however in terms of water content it was closer to 11 cm using the typical assumption that 0.1 cm of water equals 1 cm of snow. The snow fell during a period of time where the ambient air temperature continued to fall, as shown in Figure 3-14. The system was turned on the day before, March 4, at 17:45 while the ambient air and deck temperatures were around 8°C. Adding further stress to the system was the fact that the snow fall was preceded by rain events during the early morning hours of March 5th, which drew energy from the bridge deck. The surface temperatures of the heated deck were just over 5°C when it began to snow. They quickly dropped at the onset of the snow to 2°C above the tubes and 1°C between the tubes. This temperature drop is due to the fact that energy is now being required to melt the falling snow as well as heat the deck. Thus, the surface temperatures of the bridge deck decrease. The surface temperature of the non-heated deck was just over 2°C when it began to snow, but then quickly decreased to 0°C. This occurred because the energy of the deck was used to initially melt the snow as it was falling. But as soon as the temperature dropped to 0°C, there was no a longer a temperature gradient between the falling precipitation and the deck that was high enough to sustain the melting heat flux.

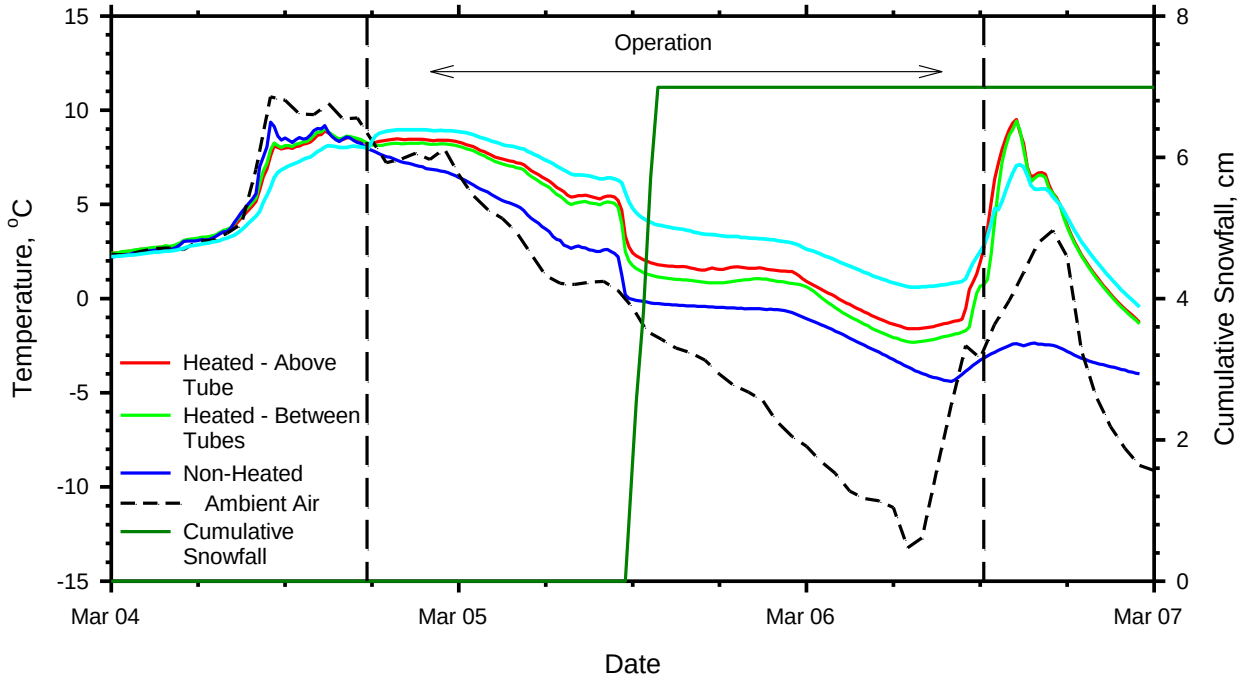

Figure 3-14. Surface temperatures of the heated and non-heated decks during the moderate winter storm that occurred on 3/5/2015.

Figure 3-15 shows the bridge deck at different points during and after the storm. Figure 3-15a was taken at 11:40 on the morning of 3/5. It can be observed that the heated side of the deck is still mostly clear whereas snow is accumulating on the non-heated side. Figure 3-15b was taken at 12:15 and shows that

snow has begun to accumulate on the heated side despite the surface temperatures remaining above 0°C. The depth was 1 cm and the layer at the snow-deck interface was slush. Thus the deck was heating the snow, just not at a rate equal to which it was falling. At this point there was 2.5 cm accumulated on the non-heated side. Figure 3-15c shows the deck at 15:15, the point at which the outline of the deicing tubes became clearly visible. There was 2.5 cm of snow above the tubes and 3.2 cm between the tubes whereas 6.9 cm had accumulated on the non-heated side. In Figure 3-15d, which was taken at 16:45, there is 1 cm of snow above the deicing tubes and 2.5 cm of snow between. At 19:30, which is shown in Figure 3-15e, a layer of ice had formed on the top surface of the snow due to its high water content and the rapidly falling ambient air temperature. The system was still melting the snow at the deck surface. This snow/slush mixture eventually turned to all ice at some point after midnight on the night of 3/5-6, as can be seen by the falling deck surface temperatures. It was still ice at 9:15 on the morning of 3/6, as shown in Figure 3-15f. After this point, aided by increasing ambient air temperatures, the deck surface heated to above 0°C and was able to melt the remaining the snow/ice such that at 12:00 (Figure 3-15g), the surface was clear above the circulation tubes and at 13:00, the deck surface was completely clear (Figure 3-15h).

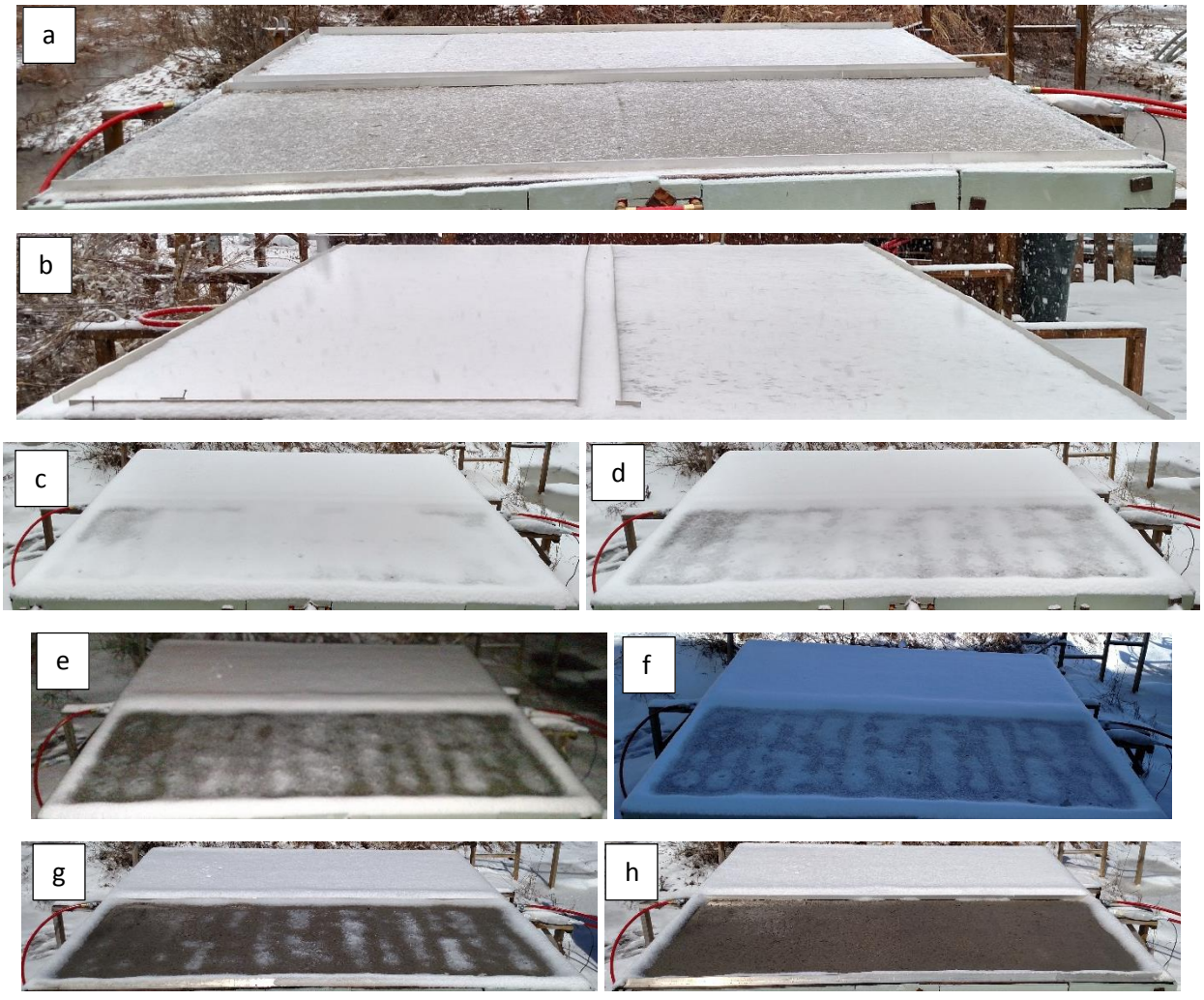

Figure 3-15. Conditions of the heated and unheated decks at different points in time from 3/5-6/2015: a) 3/5 11:40; b) 3/5 12:15; c) 3/5 15:15; d) 3/5 16:45; e) 3/5 19:30 f) 3/6 9:15; g) 3/6 12:00; h) 3/6 13:00.

Obviously, the formation of ice on the heated side is undesirable and can be directly attributed to the melting snow re-freezing as no ice was found on the non-heated side. This condition, however, will almost certainly not occur on actual highway bridges for two reasons. The first of which is drainage. The experimental bridge deck has poor drainage conditions, thus after the snow melts it tends to remain on the bridge deck and get reabsorbed into the snow to create slush. Actual bridges are designed to allow for adequate drainage. Secondly, the ice did not form on the surface of the snow until 19:15 on the evening of 3/5. This is over 5 hours after the end of the storm. A storm of this magnitude would also require mechanical snow removal for the roads, thus a plow would have cleared the snow/slush mixture from the bridge long before it had an opportunity to re-freeze.

3.5.6. Severe Winter Storm – 2/12-14/2014

The deicing capabilities of the bridge deck were tested from February 12-14, 2014 where the majority of the cumulative 45.7 cm (18 in) of snow fell over the course of 20 hours on the 12th and 13th. The ambient temperature during much of the snowfall was less than -2°C. As shown in Figure 3-16, the system was turned on in advance of the storm at 7:00 on the 12th. It was able to heat the deck to above freezing before the start of the storm whereas the surface temperature of the non-heated deck remained below 0°C. After the start of the storm, the surface temperature of the non-heated deck decreased substantially, whereas the surface temperatures above and between the circulation tubes of the heated deck only decreased slightly, and still remained above 0°C. The surface temperatures remained above 0°C the entire storm despite low ambient temperatures.

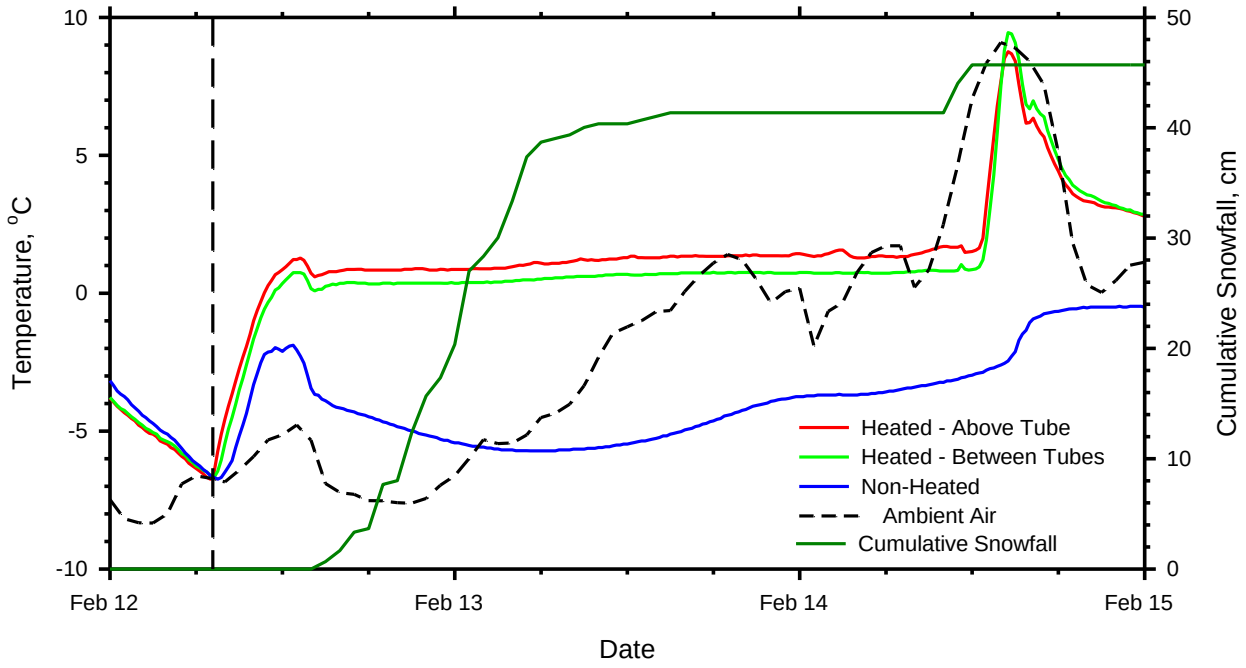

Figure 3-16. Surface temperatures of the heated and non-heated decks during a severe winter storm on February 12-14, 2014.

The photographs in Figure 3-17, show the deck at different points throughout the storm. Figure 3-17a, is at 16:00 on 2/12, shortly after the storm began. It can be observed that despite having a surface temperature greater than 0°C, snow is still accumulating on the surface of the deck. Measurements

revealed that there was 4.4 cm of snow on the non-heated deck and 2.5 cm of snow on the heated deck. So the system is melting the snow, just not a rate equal to which it is falling. The next photograph, Figure 3-17b, shows the deck at 11:00 on the morning of 2/14, which is the first time the site was accessible due to the excessively large snowfall. As can be seen, there is still snow on the heated side, though a significantly less amount than that which is on the non-heated side. At this point in time there is 34.5 cm (13 in) of snow on the non-heated side (though 45.7 cm of snow fell, after two days it has compacted and become more dense) and 7.6 cm (3 in) of snow on the heated side between the deicing tubes and between 0-3.8 cm (0-1.5 in) of snow over the circulation tubes. Figure 3-17c and Figure 3-17d show the deck at 12:00 and 13:00, respectively, on 2/12 and show the progressive melting of the snow on the heated side. Figure 3-17e shows the deck at 14:00 on 2/14, at which point all of the snow on the heated side had melted.

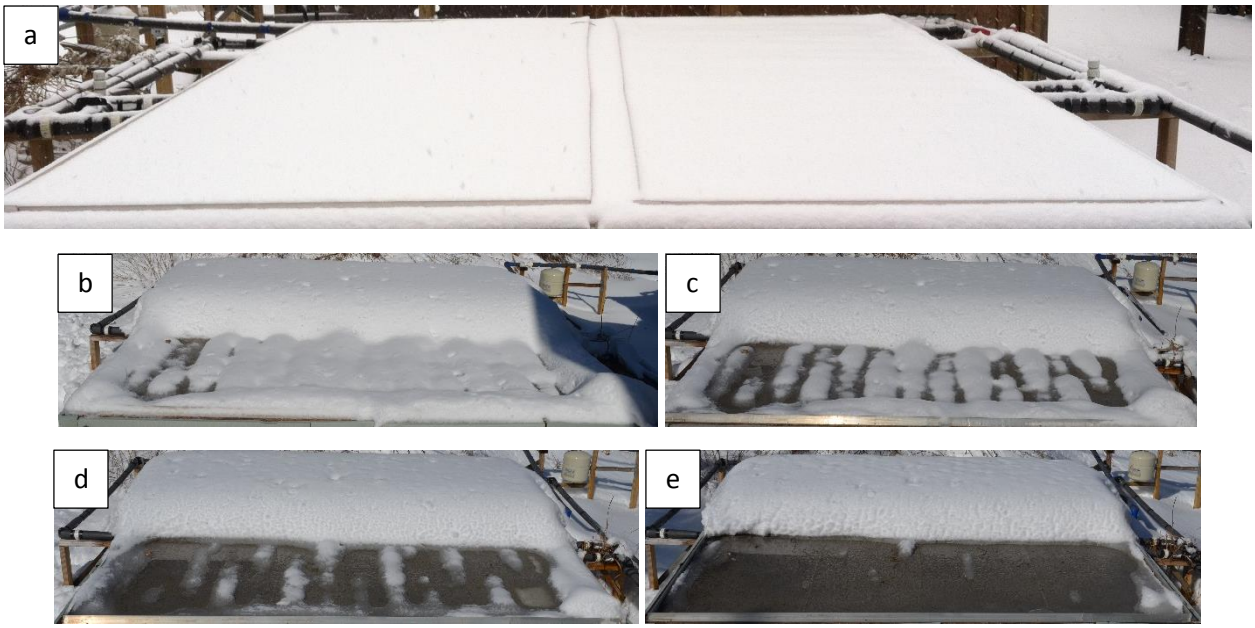

Figure 3-17. Photographs showing the surface condition of the bridge deck at different points in time during the heating test that occurred on February 12-14, 2014: a) 2/12 16:00; b) 2/14 11:00; c) 2/14 12:00; d) 2/14 13:00; e) 2/14 14:00.

Though the system was not able to keep the deck completely snow free the entire storm it was able to keep the surface temperature above freezing and did eventually melt all of the snow. As stated before, for large amounts of accumulation (generally more than 3 cm), plows will operate. For snows of this magnitude, plows must operate to remove the snow and clear the roads. Thus, when they encounter bridges, because the deck surface is above freezing and the system is melting the snow at the surface, a snow-free surface will result.

3.5.7. Severe Winter Weather – 1/6-8/2014

Blacksburg, VA experienced extremely cold weather during January 6-8, 2014 where the ambient air temperature dropped as low as -20°C (-4°F) at night. Though there was no precipitation during this period, the bridge deck deicing system was turned on to test the ability of the system to perform in extremely cold weather. In this test, the side of the bridge deck slab containing the 20 cm spaced circulation tubes was operated while the other side was left alone as a control. A single energy pile was used to supply heat

to the slab. Figure 3-18a shows the temperatures recorded at the surfaces and in the interiors of both slabs as well as the ambient air temperature during this period.

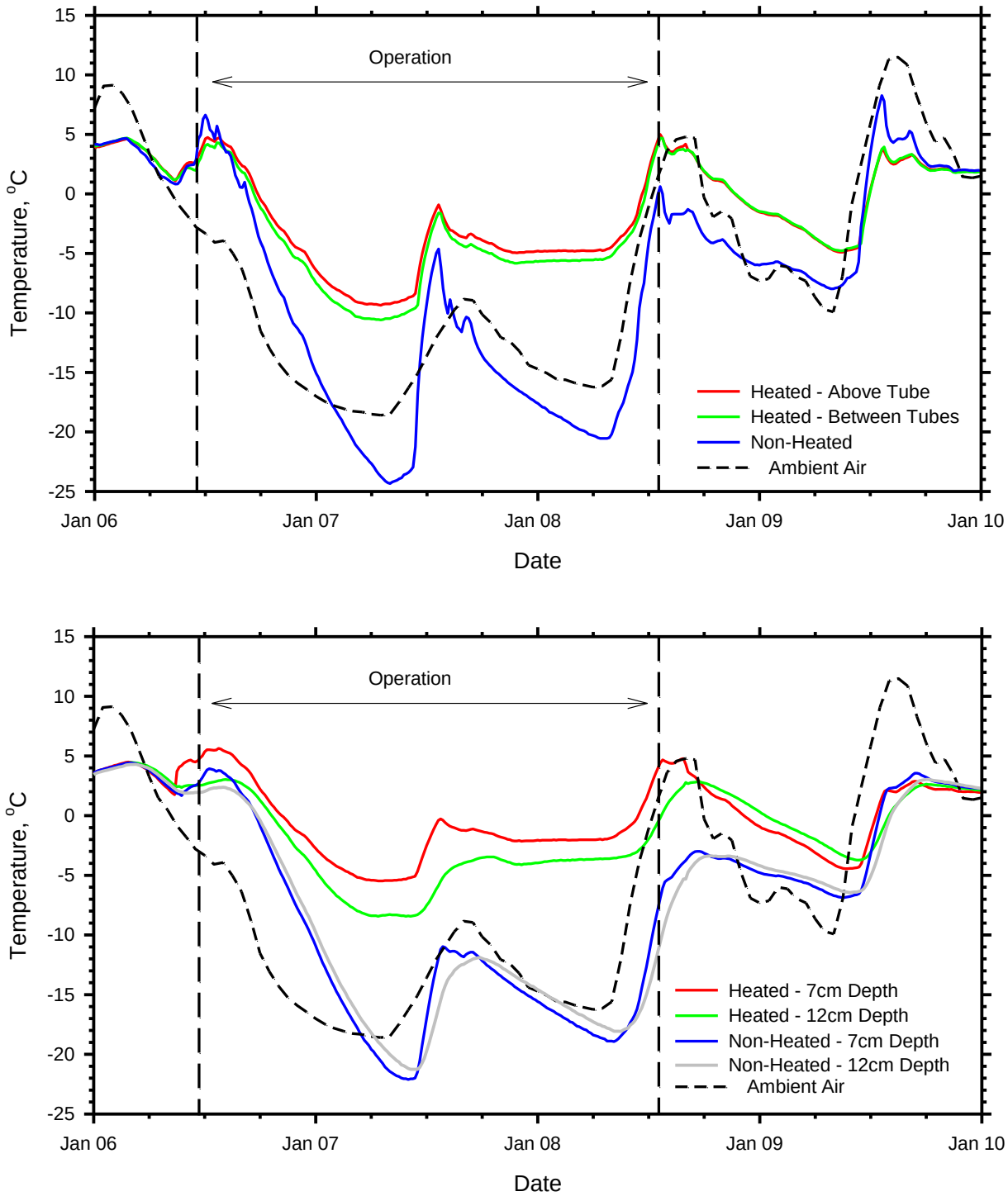

Figure 3-18. Surface temperatures (a, top) and interior temperatures (b, bottom) of the heated and non-heated decks during a period of extremely cold weather in January 2014.

From Figure 3-18a, several observations can be made. The first is that the bridge deck deicing system was able to significantly heat the slab, causing the surface temperature of the heated slab to be as much as 15°C (27°F) higher than the unheated slab. The same temperature difference is seen in the middle of the slab at depths of 7 and 12 cm, as shown in Figure 3-18b. If the volumetric heat capacity of the concrete is 2077 kJ/m^3 this difference in temperature corresponds to difference in energy of 31.3 MJ between the two decks. That value represents only the amount of energy retained within the slab and does not include the amount of energy that was lost by the heated slab to the environment. However, despite the significant difference between the performances of the two slabs, the system was not able to keep the surface temperature of the heated slab above 0°C (32°F) meaning that if any precipitation were to accompany this extreme cold weather event, it would accumulate on the surface of the deck. It should be noted, however, that these extreme environmental conditions are well outside the range of those expected during normal operation.

3.5.8. Severe Winter Weather – 2/20-22/2015

Another period of extremely cold weather occurred in Blacksburg, VA during February 20-22, 2015. This cold weather followed a snowstorm on 2/16-17/2015, during which almost 20 cm of snow fell. Unfortunately the system was non-operational for the snowstorm due to repair work. It was turned on after the snowstorm and during the period of cold weather to heat the deck and melt the snow that had accumulated on the surface. As shown in Figure 3-19, the system was turned on at 14:30 on 2/20. The ambient temperature for the preceding 4 days had never reached above 0°C and during the 19th and 20th, it was below -15°C. Thus, the temperature of the deck surface was very cold (-18°C) when the system was turned on. The system was then able to heat the surface of the bridge deck to above 0°C in about 9 hours despite the ambient air temperature dropping about 15°C during this same period of time. The highest temperature the surface of the non-heated deck reached was only -12°C.

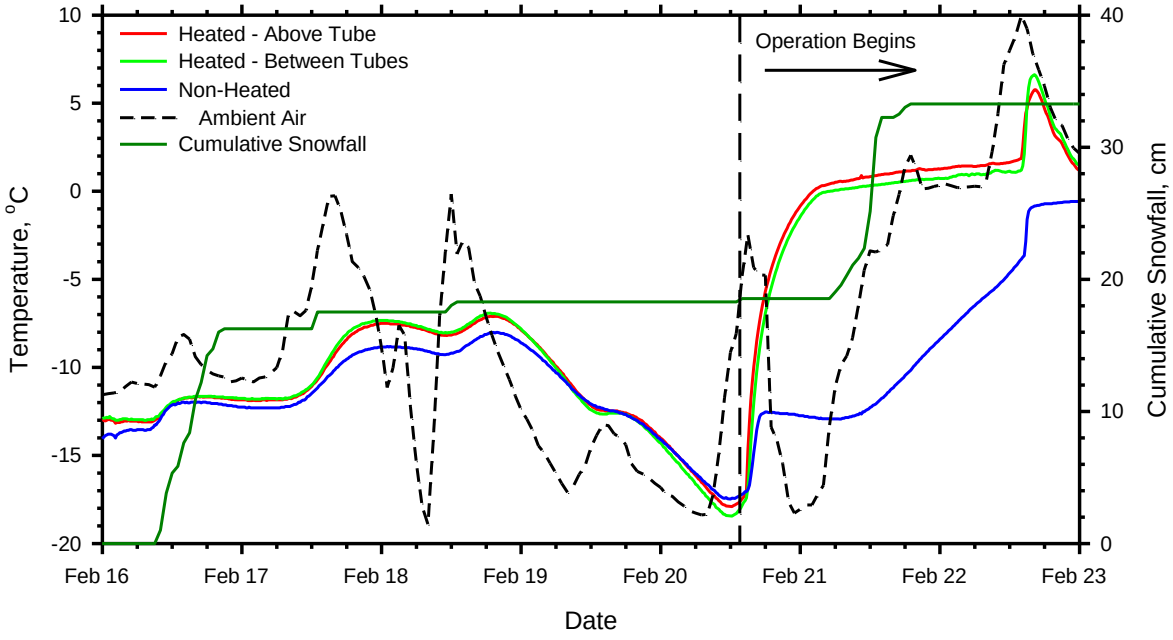

Figure 3-19. The surface temperatures of the heated and non-heated decks during a period of extremely cold weather and intense snowfall before and after operation on the heated deck begins during February 2015.

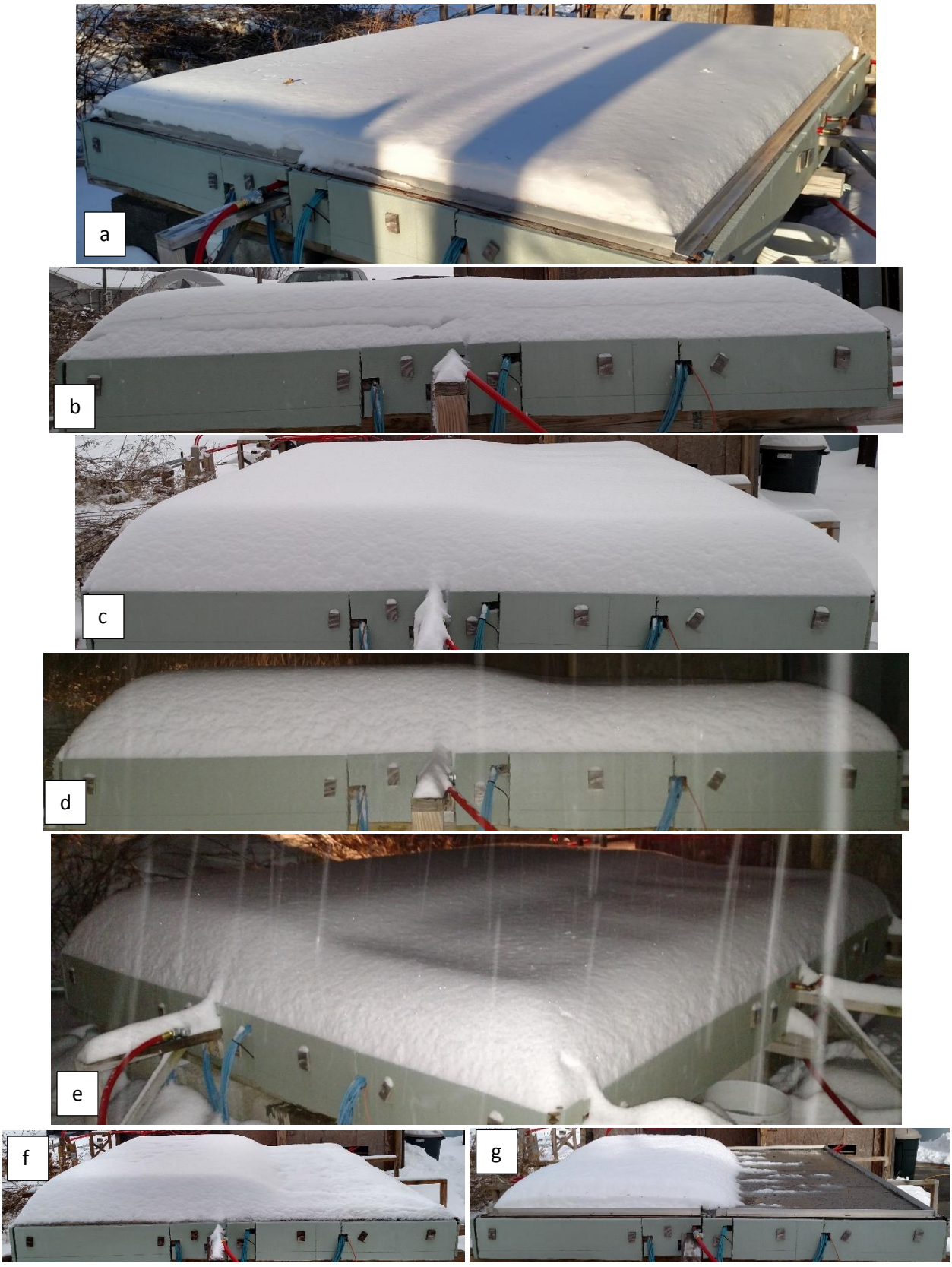

Figure 3-20. The condition of the heated and non-heated decks at different points in time during extreme winter weather in February 2015: a) 2/20 17:00; b) 2/21 10:00; c) 2/21 15:00; d) 2/21 19:30; e) 2/21 19:30; f) 2/22 7:30; g) 2/22 15:00.

More snow fell on 2/21. There was originally 16.5 cm of snow on both sides of the deck (Figure 3-20a) from the snow that occurred prior to 2/21 (the cumulative snowfall in Figure 3-19 reads around 18 cm – the difference is due to the settlement and densification of the snow). At 10:00 on 2/21 an additional 6.4 cm of snow had fallen bringing the total depth on the non-heated side to 22.9cm, whereas the heated side had only 20.3 cm. The slight difference in depths can be seen in Figure 3-20b. At 11:00, one hour later, a total of 24.1 cm of snow was on the non-heated side whereas the heated side had only 19.7 cm. Thus, between the hours of 10:00 and 11:00, the system was melting the snow at a faster rate than it was accumulating. At 15:00 on 2/21 there was 29.8 cm of snow on the non-heated side and 24.1c m on the heated side. That represents an increase of 5.7 cm of snow on the non-heated side and 4.4 cm on the heated side so though the system was melting the snow, it was at a slower rate than that at which the snow was accumulating between the hours of 11:00 and 15:00. Figure 3-20c shows the slab at this point in time and the difference in depth can be seen. At 19:30 on the evening of 2/21, which was near the end of the storm, there was 21.6 cm of snow on the heated side and 30.5 cm on the non-heated side. In Figure 3-20d, the difference in depths can be seen and in Figure 3-20e, the uneven surface resulting from more melting of the snow is shown. The following morning at 9:00 on 2/22 there was 11.4 cm of snow on the heated side (Figure 3-20f), at 12:30 there was 5.1 cm or less, and by 15:00 it was clear (Figure 3-20g).

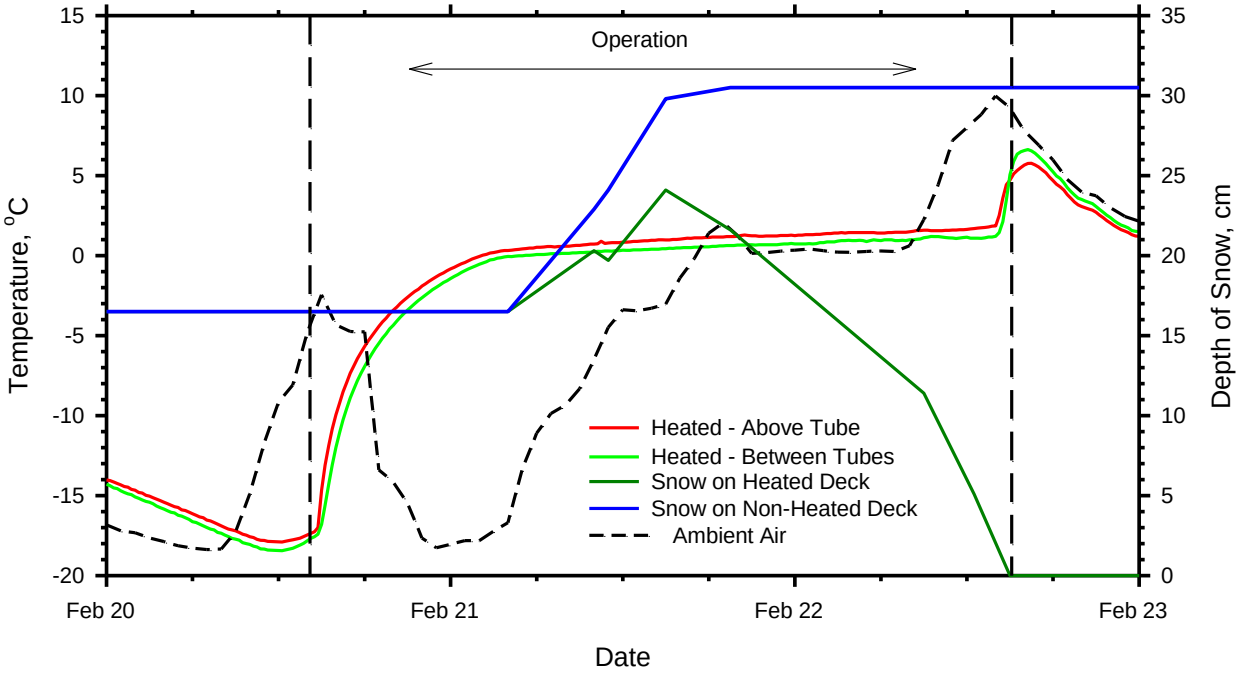

Figure 3-21. Amount of snow present on the heated and non-heated decks over the course of the heating operation that occurred from 2/20-22/2015.

Figure 3-21 compares the amount of snow on the heated and non-heated decks at the different times. The slopes of the lines indicate the average rate over the time interval at which the snow is either accumulating or melting. Observe that the rate of melting increases as the ambient air temperature increases. Also observe that by the time there is no snow left on the deck at 15:00 on 2/22, the surface temperatures rapidly increase by a couple of degrees.

3.5.9. Energy Analysis and the Ground's Response

Due to a problem with the fluid temperature sensors, accurate fluid temperatures were not obtained during the winter of 2014. The rate of energy imparted to the slab for the four tests that were reported from 2015 are shown in Figure 3-22. The test that occurred on 2/20-22/2015 had the highest rate followed by the test that occurred on 2/23-24/2015. The lowest energy rates were observed during the tests that occurred on 2/25-26/2015 and 3/5-6/2015. There is some variation during each test. The rate during the first test started very high and then decreased to around 100 W/m^2 for the remainder of the operation. The rate on 2/23-24/2015 was fairly consistent around 50 W/m^2 whereas the rate on 2/25-26/2015 started low (less than 25 W/m^2) but by the end of the operation was around 70 W/m^2. The rate during most of the operation on 3/5-6/2015 fluctuated between 60 and 20 W/m^2. In general the heating rates are lower than those of the active systems reported earlier (Section 3.3), but in line with those observed from other geothermal passive systems.

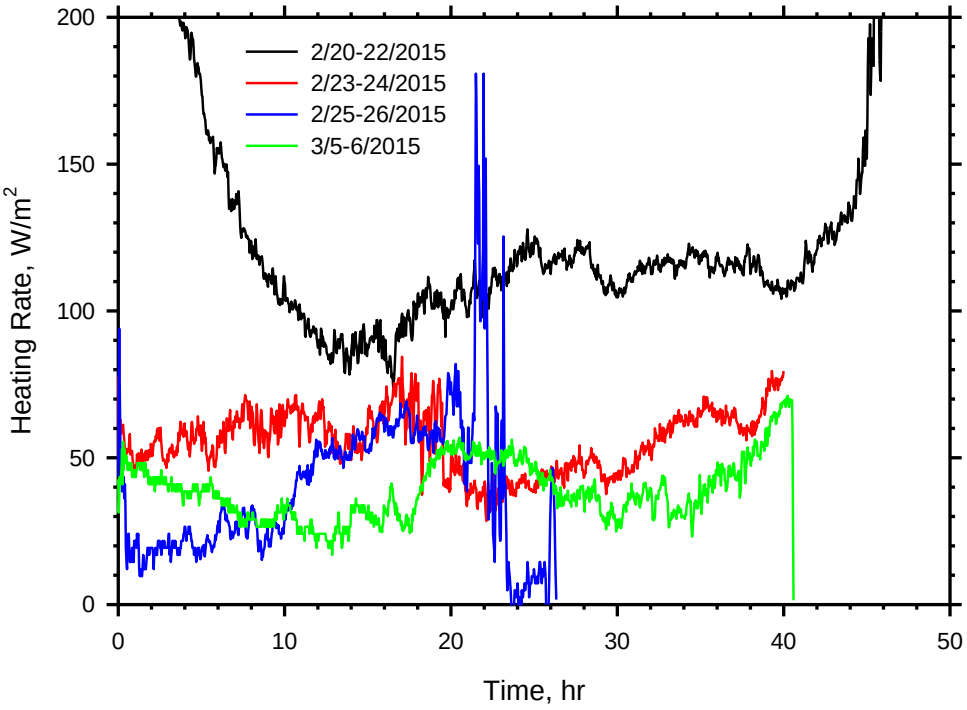

Figure 3-22. Rate of energy transfer from the circulation fluid to the bridge deck for the experimental tests during the winter of 2015.

Unlike active systems that can control the deck heating rate by controlling the inlet fluid temperature, the rate in passive systems is dependent on the temperature gradients that are present between the temperature of the deck and that of the fluid, as well as the difference between the fluid and the ground. A higher fluid temperature is always desirable, but fluid temperature alone does not indicate the degree of bridge deck heating. For example, Figure 3-23 shows the inlet fluid temperatures that were observed during the four tests. The highest inlet temperature actually corresponds to the lowest bridge deck heating rate. This is because the temperatures of the bridge deck were relatively high when the system was turned on. Also shown in Figure 3-23 is the top surface temperature of the bridge deck, which alone

is not totally indicative of the bridge deck temperature, but nevertheless gives a good approximation of the gradients involved. During the test with the highest inlet fluid temperature, because not much of a temperature gradient exists between the fluid and the deck, not as much energy could be imparted from the fluid to the deck. Furthermore, because of the higher fluid temperature, not as much energy could be imparted from the ground to the fluid, also because of a lower gradient. Contrast this with the lowest initial fluid temperature from Figure 3-23, which corresponds to the highest heating rate. In this case, the system was turned on when the deck was less than -15°C. So even though the fluid temperature was low, the gradient between the fluid and the deck was very high allowing for a higher heating rate. The lower fluid temperature also created a higher gradient between it and the ground, allowing more energy to be transferred to the circulation fluid. Additionally, this was the first test of 2015 meaning that the initial ground temperature was still high (relative to the initial ground temperature during the other tests), further aiding in the higher gradient. During the operation on 2/23-24/2015, a decrease in the gradient occurred around hour 20, whereas an increase occurred around hour 10 for the operation on 2/25-26-2015. It can be observed from Figure 3-22 that their heating rates decreased and increased, respectively.

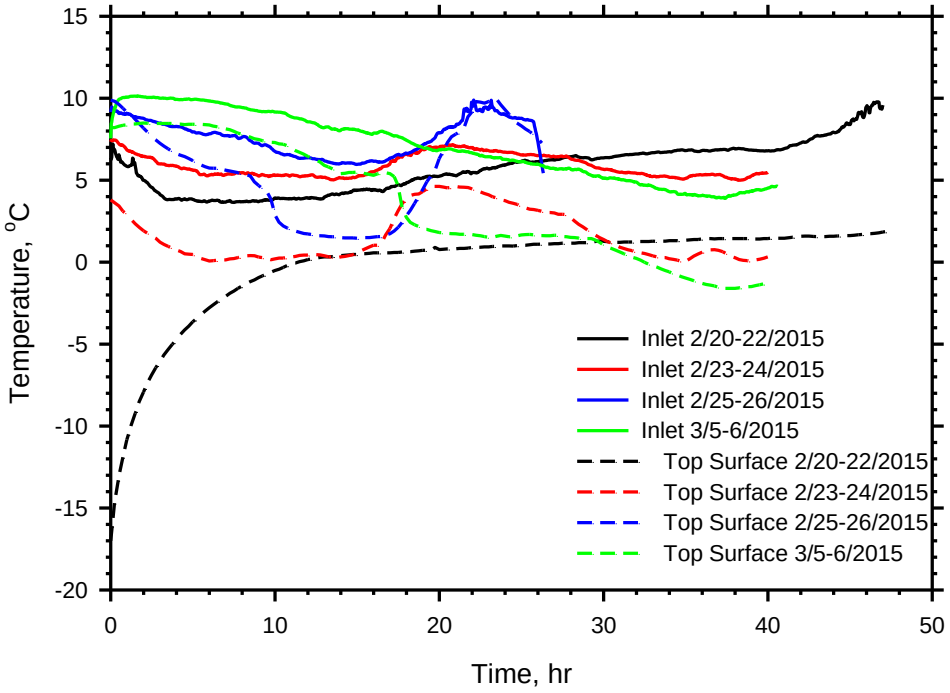

Figure 3-23. Inlet fluid and top surface temperatures of the bridge deck during the heating tests of 2015. The purpose is to show how it is the temperature difference between the fluid and the deck that contributes most to the deck heating rate as opposed to the temperature of the inlet fluid alone.

The extraction rates for the heating rates of Figure 3-22 are shown in Figure 3-24. The highest extraction rates were observed during the deicing test that occurred on 2/20-22/2015. The rates began above 50 W/m and then leveled off to 10-15 W/m for the remainder of the operation. The other operations had rates that were generally between 4-10 W/m. These are lower than the extraction rates that are typically utilized in GSHP systems, however, lower extraction rates are to be expected from passive system configurations.

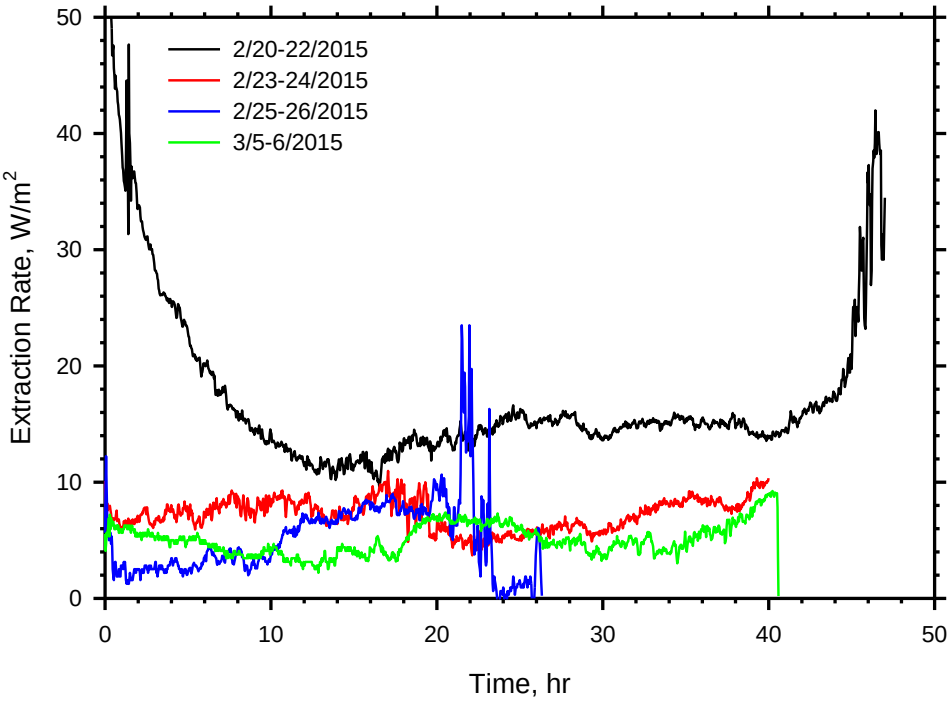

Figure 3-24. Rate of energy extraction for the pile for the bridge deck deicing tests.

Figure 3-25 presents the temperature at select depths in the pile that was used during these heating tests. Before the start of the first test, the temperature at every depth except 3.0 m and 6.1 m was between 12.5°C and 13.0°. The temperatures at depths 3.0 m and 6.1 m were both lower, which is to be expected during mid-winter due to atmospheric influence on ground temperature at shallow depths (Kusada and Achenbach 1965). Immediately after the first operation began, the temperatures at every depth in the pile decreased. The temperature decrease is greater in the shale, as explained in Bowers et al. (2015). After reaching a low, the temperatures gradually increased until the operation ends. The temperature decrease was between 1-2°C in the silty sand and between 3-4°C in the shale. The thermally induced stresses as a result of these operations are discussed in Chapter 4.

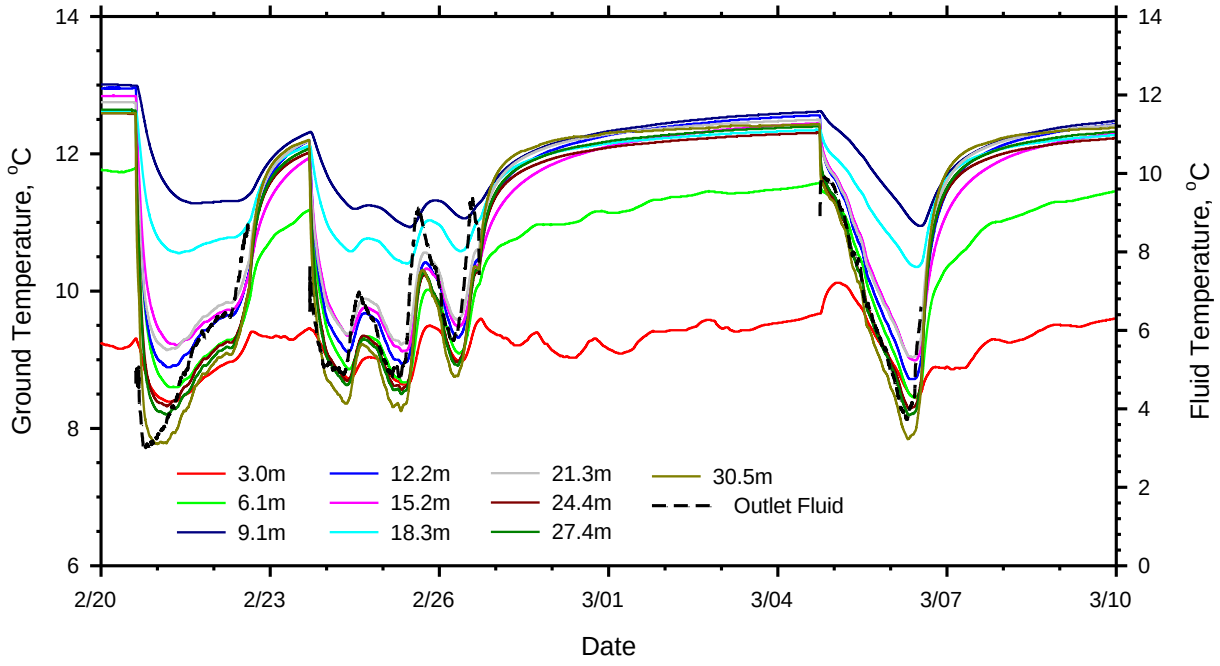

Figure 3-25. Temperatures in the piles that was used for the bridge deck heating tests of 2015 as well as the deck outlet fluid temperature, which shows the correlation in trends between the two.

The temperatures in the pile somewhat recovered between the first and second operations, but did not reach their starting values. They then decreased during the second operation, which included the tests on 2/23-24/2015 and 2/25-26/2015. After the end of the second operational period, the temperatures again recovered. Though there was more time (6 days) between the second and third operations as opposed to the first and second operations (1 day), they still did not reach their initial temperatures. The change in temperatures in the pile during the third operation are interesting as the temperature at the 3.0 m depth initially increases. The other depths decrease, but not as rapidly as in the previous operations. Also plotted in Figure 3-25 is the bridge deck outlet fluid temperature, which is the pile inlet fluid temperature. Note that it is plotted on a different scale than the ground temperatures so that their effects can be seen. The trend of the ground temperatures follow the outlet fluid temperature, which explains why the ground temperatures decrease so rapidly in operation 1, but very gradually in operation 3. This also explains why the 3.0 m depth initially increases during the third operation. The outlet fluid temperature is around 10°C whereas the ground temperature at 3.0 m depth is slightly below. This ultimately results in the temperature at the 3.0 m depth initially increasing.

There are several implications from these results. The first is that the rate of bridge deck heating is not solely dependent on the temperature of the ground, rather it is the gradient between the circulation fluid and the bridge deck. For example, the operation from 2/20-22/2015 had the lowest inlet fluid temperature but the highest deck heating rate. However, that it not to say the temperature of the ground is not significant. It is, as it controls the maximum value of the fluid temperature. Higher ground temperatures will result in higher fluid temperatures, which will in turn result in higher gradients between the fluid and the bridge deck. The ground temperatures present at the experimental site as well as the deck heating rates, though low, were sufficient in most cases to keep the temperature of the bridge deck

above freezing. Higher ground temperatures may result in higher heating rates, which may have allowed the system to keep the deck completely clear for some storms where snow did accumulate, however, it was noted that these storms would have necessitated mechanical removal anyway.

3.6. THERMAL RECHARGE OPERATIONS

As has been previously discussed, a possible way in which to increase the efficiency of ground-source bridge deck deicing systems is to perform thermal recharge operations during the summer, which is essentially bridge deck deicing in reverse. Instead of using the ground's thermal energy to heat the bridge deck, the thermal energy collected by the bridge deck from the sun is used to heat the ground in order to replace the energy that was used for deicing operations. Furthermore, if more thermal energy is injected into the ground during the summer than what was extracted during the winter, it could be possible to raise the temperature of the ground, thereby increasing the efficiency of these systems. 12 thermal recharge operations were conducted during the summer of 2013 and 21 thermal recharge operations were conducted during the summer of 2014 in order to explore this issue further. The operations lasted from 6 to 11 hours.

During the summer of 2013 energy was collected from both halves of the bridge deck and injected into Pile 3. During summer 2014, energy was also collected from both halves of the bridge deck, but injected into all of the energy piles. Figure 3-26a shows the rate at which energy was injected into Pile 3 on a few select days during the summer of 2013. The rates for almost all of the tests appear very jagged, much more so than the rates for bridge deck deicing. This is believed to be caused by a number of factors. The first is the flow rate, which was 7.5 gpm (28.4 L/min). When compared to the fluid flow rate for deicing operations of 3 gpm (11.4 L/min), any change in the temperature difference between the inlet and outlet fluid will be amplified by a factor greater than 2. Secondly, there was likely some interference between the fluid temperature sensor and the environment. Though this interference would affect mainly the magnitude of the inlet and outlet fluid temperatures equally resulting in no net change of the temperature difference between the two, it is probably responsible for some of the jaggedness especially as the least jagged rate, which occurred on 8/28, correlates to a test that was conducted on a cloudy day. In order to make the figure more readable, Figure 3-26b was created which displays the moving average using 20 minute intervals.

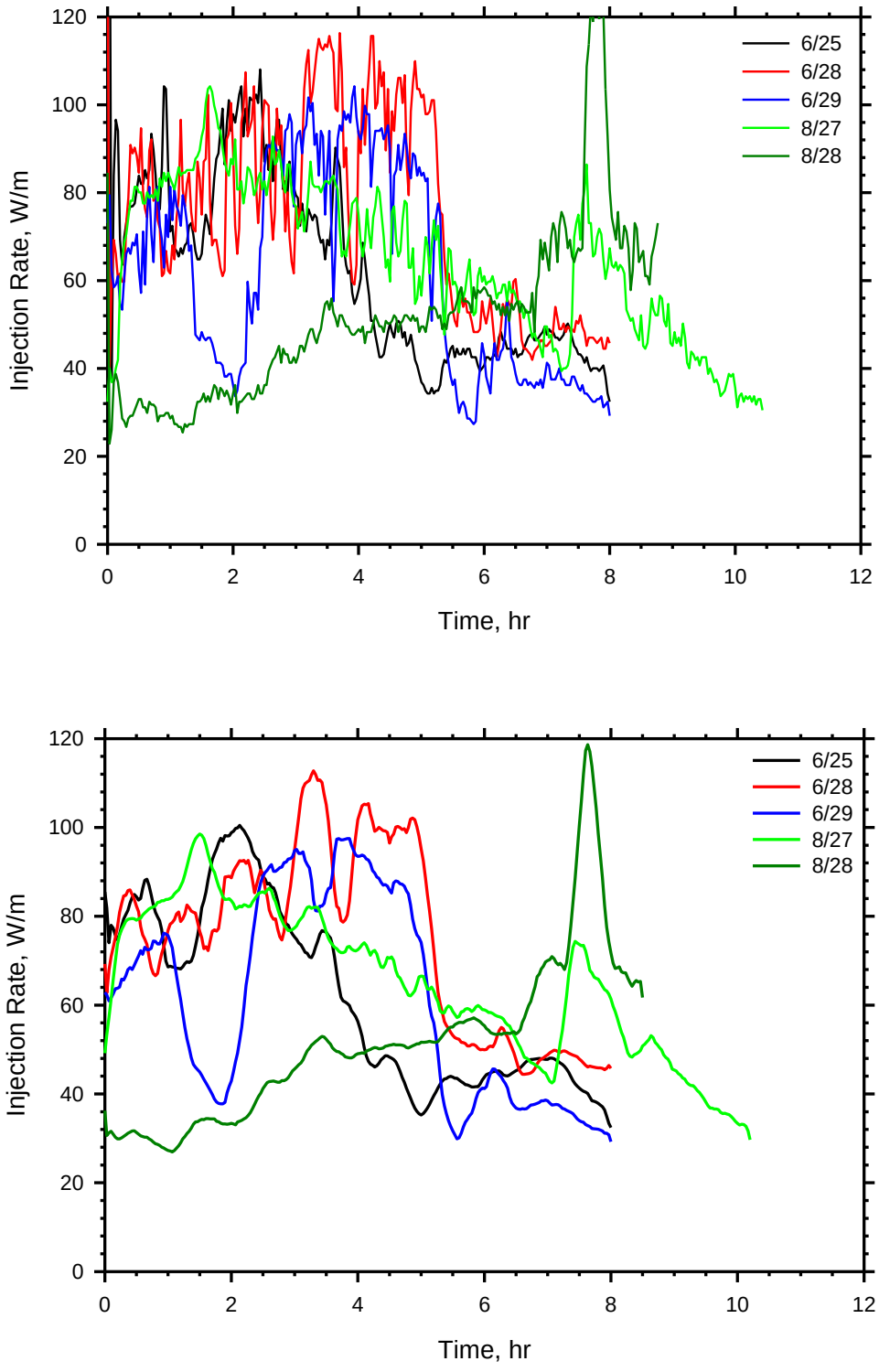

Figure 3-26. Rate at which energy was injected into Pile 3 during several thermal recharge operations during the summer of 2013 (a, top), and the averaged rate at which energy was injected into Pile 3 during several thermal recharge operations during the summer of 2013 (b, bottom).

The rates appear to mostly vary between 40 and 100 W/m, but there are several factors that affect the rates; the time the test was started and the temperature difference between the circulating fluid and the ground. These factors are interrelated. For example, the tests that occurred on 6/25, 6/28, and 6/29 were all initiated around 12:00 when the deck was warmer, which means the inlet fluid temperature would be warmer (as shown in Figure 3-27), and all begin with relatively higher rates. This is in contrast to the operation that occurred on 8/28 which was initiated at 7:40 when the deck and inlet fluid temperature was much cooler and resulted in lower initial rates. Furthermore, the fluid temperature during the operation on 8/28 remained low, which kept the rate low. The operation that occurred on 8/27 was also initiated earlier in the day at 8:00 and had a lower inlet fluid temperature. Yet unlike the operation on 8/28, it initially had a much higher rate. This occurred because it was the first recharge operation conducted in over 25 days, thus the ground temperatures had begun to stabilize. Therefore a high temperature gradient still existed between the incoming fluid and the ground (average ground temperatures are also shown in Figure 3-27). The next day (8/28) the ground temperatures did not have a chance to fully decrease, thus not as high a temperature gradient existed between the ground and the incoming fluid resulting in a lower injection rate. Notice that the relatively lower fluid temperature during 8/27 does result in a lower rate over time even though the rate begin high. Thus, from an energy perspective, it is better to start system operation later in the day when the temperatures are higher so that a higher temperature gradient is created between the inlet fluid and the ground and more energy can be injected. As will be explained in the next section, there are additional factors that must be considered when determining operational start time.

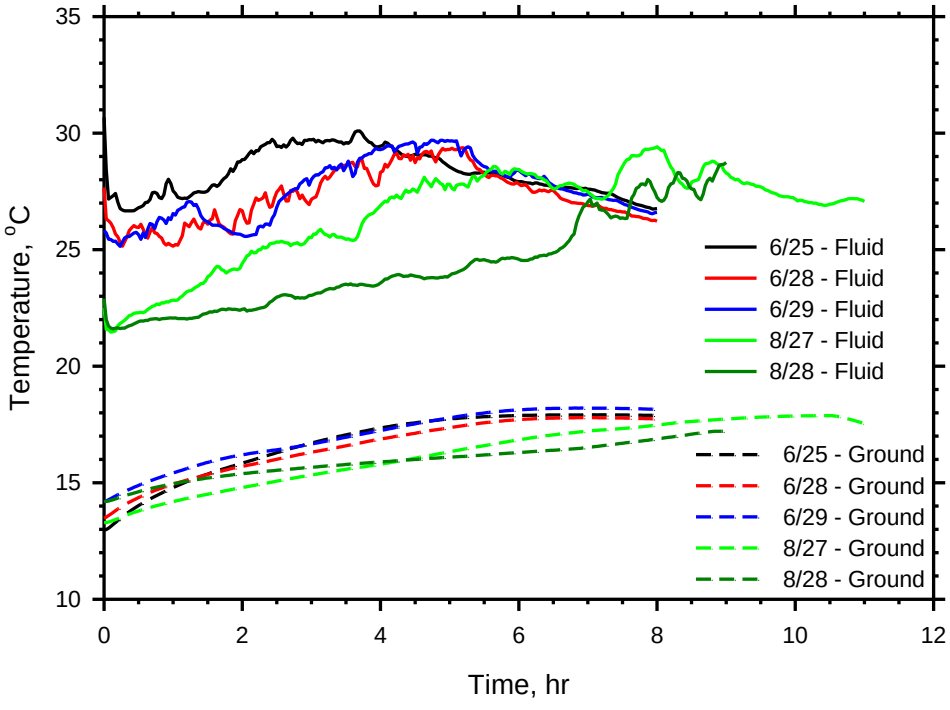

Figure 3-27. The inlet fluid temperature and average ground temperature for thermal recharge operations shown in Figure 3-26.

Figure 3-28 displays the heat collection rate of the bridge deck during each of these tests. Note that the inlet and outlet fluid temperatures of each bridge deck half were not measured directly because both halves were in operation for all of these tests. During this period, one of the halves had a black coating on the surface, which greatly increased the amount of solar radiation it absorbed as compared to the other half. Thus, the rate shown is an average rate for the two halves. The side with the black coating likely had a higher heating rate than the average shown in Figure 3-28, and the side without the coating likely had a heating rate lower than the average. Note that the average during most of the tests is between 130 and 225 W/m^2. This is a higher rate than what was used to heat the bridge deck (Figure 3-22), even if the actual rate of the side with only concrete is much less than the average of the two sides that is shown. This is possible because higher temperature gradients exist between the fluid and the ground during thermal recharge (Figure 3-27) than during bridge deck deicing (Figure 3-23). The implication of this is that not as many hours need to be spent recharging the ground during the summer as are used during deicing operations in the winter to replace the same amount of energy. In fact, if the operational periods are equal, more energy will be injected than what was extracted and it will be possible to raise the temperature of the ground.

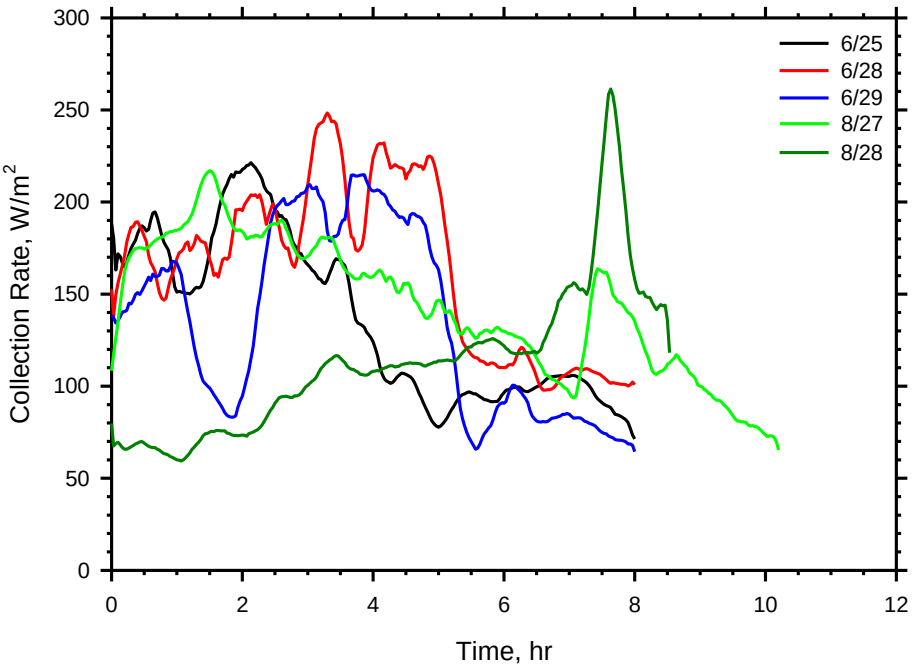

Figure 3-28. Rate at which the bridge deck collects energy during several thermal recharge operations during the summer of 2013.

In terms of system operational time covered in this study, about 85 hours of thermal injection occurred in 2013. In 2014, 320 hours of heat extraction operations and 105 hours of heat injection took place. In 2015, 220 hours of heat extraction took place. Thus extraction hours outnumbered injection hours by a factor of 2.8. Considering heat injection rates are 2 to 3 times higher than extraction rates, an equal amount of energy was likely exchanged. This will be discussed further in the following section.

3.6.1. Energy Injected and the Ground's Response

In order to evaluate the success of thermal recharge operations, it would be ideal to have had a year's worth of ground temperature data where no operations took place to establish a baseline. However, that was not available. Thus, the ground temperature was compared relative to a specific point in time. The chosen point in time was April 2013, before any thermal recharge operation took place.

Figure 3-29 displays the average monthly ground temperature for each month through April 2015 relative to the average monthly temperature of April 2013 for various depths in Pile 3. Note that some temperature variation in the shallower depths is expected due to atmospheric influence. However, depths beyond 12 m should remain relatively stable year round. Thus, any fluctuation of the average temperature at depths 12 m and greater is due to thermal injection or extraction operations. Notice that the average monthly temperatures increase due to heat injection during the summer of 2013. They decrease in the winter of 2013 – 2104 (months 7 – 9 in Figure 3-29) as heat is extracted for bridge deck heating. Following the decrease is an increase as heat energy flows back into the system from the surrounding ground. The temperatures again increase to above the initial temperature during the summer of 2014 due to thermal recharge operations. The increase, however, is not as great as the previous summer despite more thermal recharge operations (21 in 2014 as opposed to 12 in 2013). The reason for this is that energy was injected into only Pile 3 during 2013, whereas it was injected into all the energy piles during 2014. But because Pile 3 was used primarily for bridge deck heating during both 2014 and 2015, the average temperatures are lower than the initial temperatures 2 years prior, though not by much.

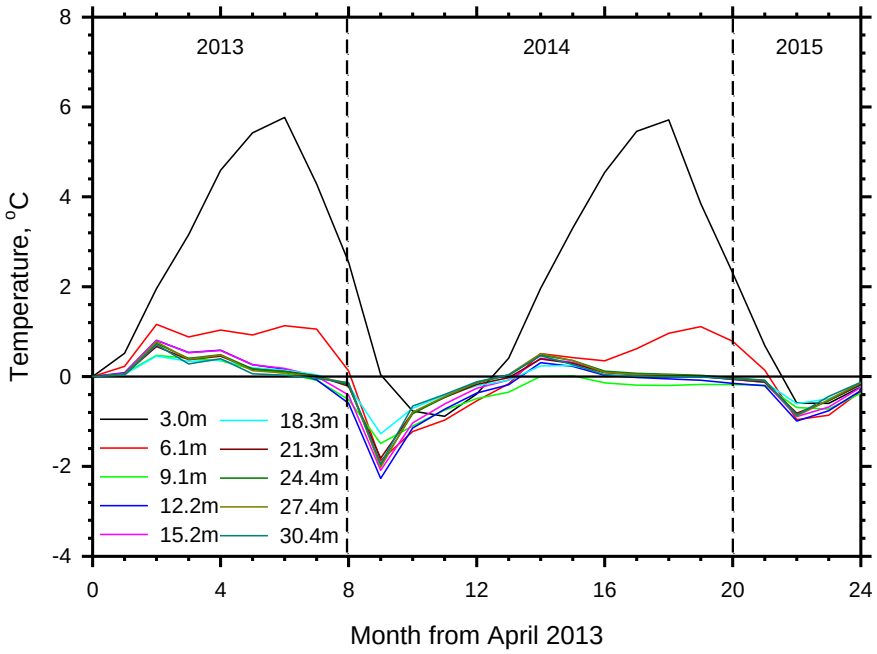

Figure 3-29. Change in average monthly temperatures of Pile 3 over time as compared to the average monthly temperature in April 2013.

Contrast this with what was observed in Pile 1, as shown in Figure 3-30. A temperature increase was observed during 2013 as injected energy from Pile 3 migrated to Pile 1. Because the energy was not injected directly into Pile 1, the increase in temperature is not as great. During 2014, Pile 1 was not used for heat extraction, though a decrease is observed due, again, to energy being extracted from Pile 3. During 2014, energy was injected directly into Pile 1 for thermal recharge, thus the temperature increased and remained positive until the winter of 2014 – 2015, where it decreased slightly due to heat extraction. After two years, the average temperatures in Pile 1 are higher than the initial temperatures.

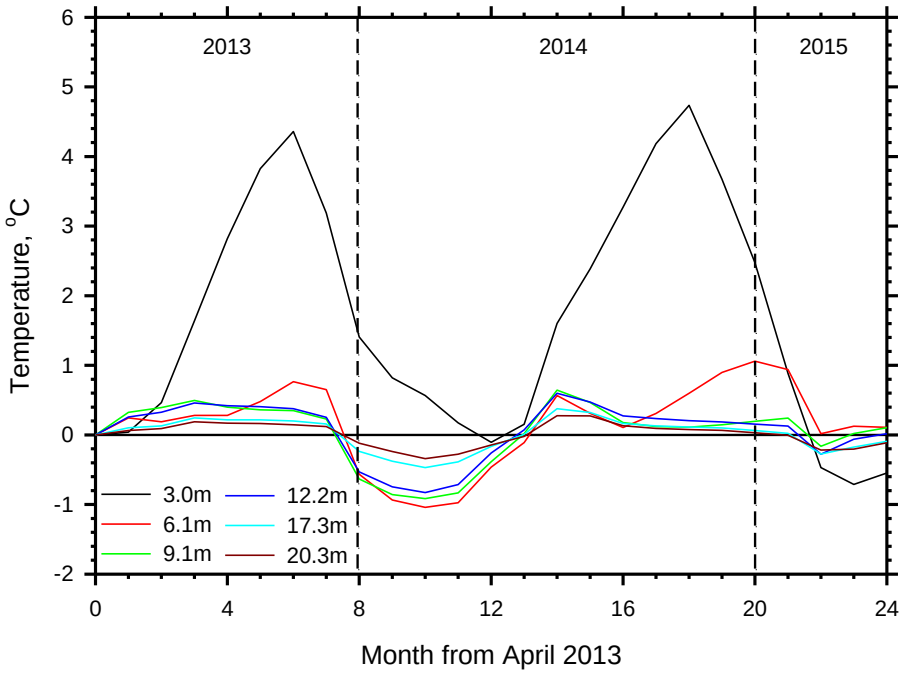

Figure 3-30. Change in average monthly temperatures of Pile 1 over time as compared to the average monthly temperature in April 2013.

Similar observations can be made from Figure 3-31, Figure 3-32, and Figure 3-33, which respectively display the relative temperature changes in OWs 1, 2, and 4. Observe that a decrease, though generally small, is observed after 2 years of operations for each OW. There are several reasons for this. The first is that it is possible that not as much energy was injected as extracted. Secondly, energy was not injected into the same piles that it was extracted from during 2014. As explained previously, energy was injected into all 4 piles during 2014 while only being extracted from Pile 3 during 2014 and Piles 1 and 3 during 2015. Thus, the energy that was injected into Piles 2 and 4 could have dissipated into the surrounding soil and, in essence, left the system resulting in a net decrease in energy around Piles 1 and 3 and the OWs. Thirdly, the temperature variations from the initial temperature are quite small, only a few tenths of a degree, which could simply be due to year-to-year fluctuations in the ground.

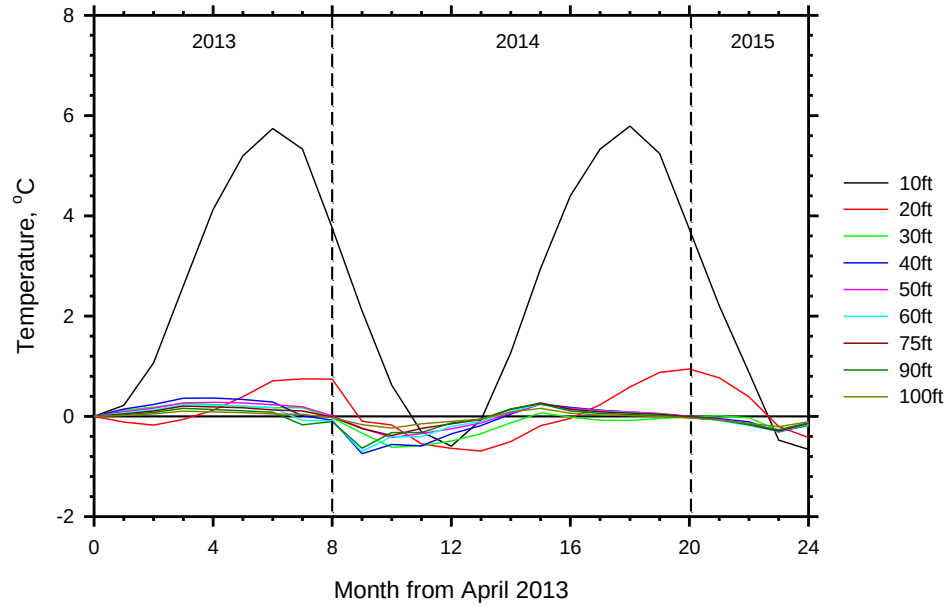

Figure 3-31. Change in average monthly temperatures of OW 1 over time as compared to the average monthly temperature in April 2013.

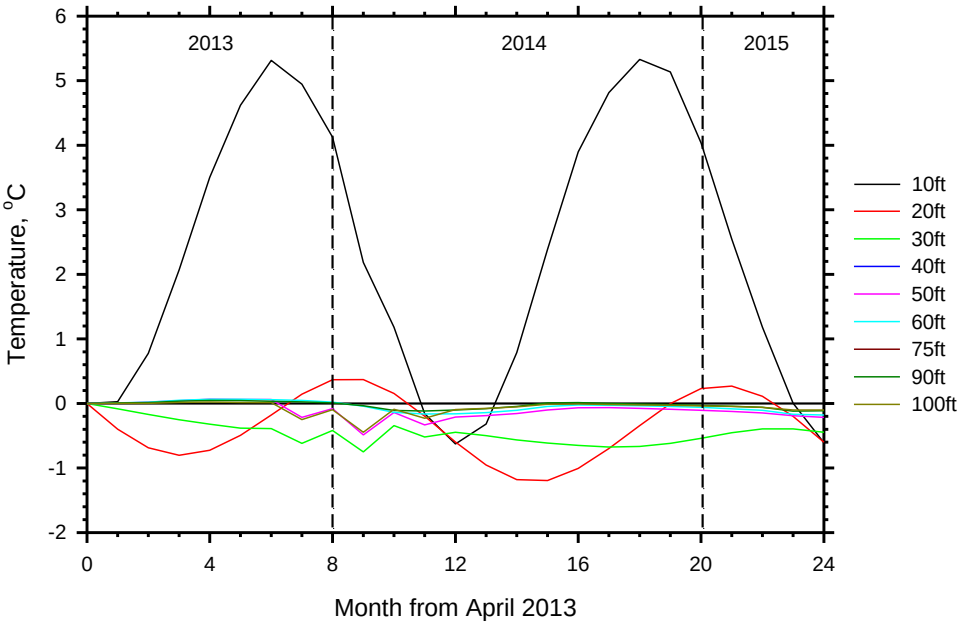

Figure 3-32. Change in average monthly temperatures of OW 2 over time as compared to the average monthly temperature in April 2013**.**

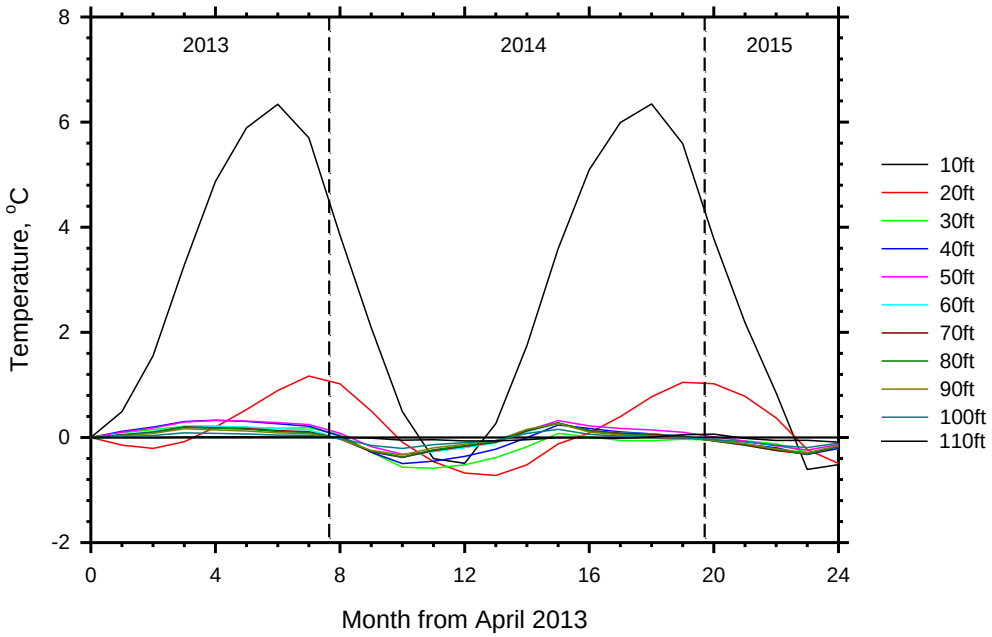

Figure 3-33. Change in average monthly temperatures of OW 4 over time as compared to the average monthly temperature in April 2013.

Ultimately, the experimental investigation in terms of thermal recharge performance is limited and there are several questions yet to be answered regarding thermal injection. The first is if the injected energy is still present during the winter, or if it dissipated to the surrounding soil. Secondly how much energy is injected near the surface, where it is difficult to discern because of the interference with the atmosphere. And finally, if energy is injected during more summer days than were considered in this study, will it make a significant difference on the ground temperatures during winter.

3.7. TEMPERATURE GRADIENTS IN THE BRIDGE DECK

A preliminary investigation was performed to ascertain whether or not a ground-source bridge deck deicing system will impose any significant structural challenges to the bridge deck overlay. There are two primary ways in which these systems could affect the bridge deck. The first is through the physical inclusion of the circulation tubes, and the second is through the temperature gradients created from the operation of these systems. The primary focus in this paper is the temperature gradients that were created and how they relate to current design guidelines.

The current AASHTO design methodology (AASHTO 2012) specifies maximum design temperature gradients for use in bridge decks. For a bridge located in Blacksburg, VA, the maximum design gradients are given in Figure 3-34. Observe that in the upper 10 cm, the maximum gradient is 1.64°C/cm, which occurs when the surface is warmer than the interior, and the minimum gradient is -0.49°C/cm, which occurs when the surface is cooler than the interior. The gradient for the remaining 15 cm is 0.41°C/cm and -0.12°C/cm. The experimental bridge deck contained four temperature sensors along the cross section, one at the surface, one at a depth of 7.3 cm, one at a depth of 13.4 cm, and one at the bottom of the slab. If a linear change in temperature relationship is assumed between the temperature sensors,

gradients can be created. Thus, the 'top' gradient refers to the gradient that exists between the surface of the deck and circulation tubes; the 'middle' gradient refers to the gradient between the circulation tubes and the sensor at mid-depth in the slab; and the 'bottom' gradient refers to the gradient in the bottom half of the slab.

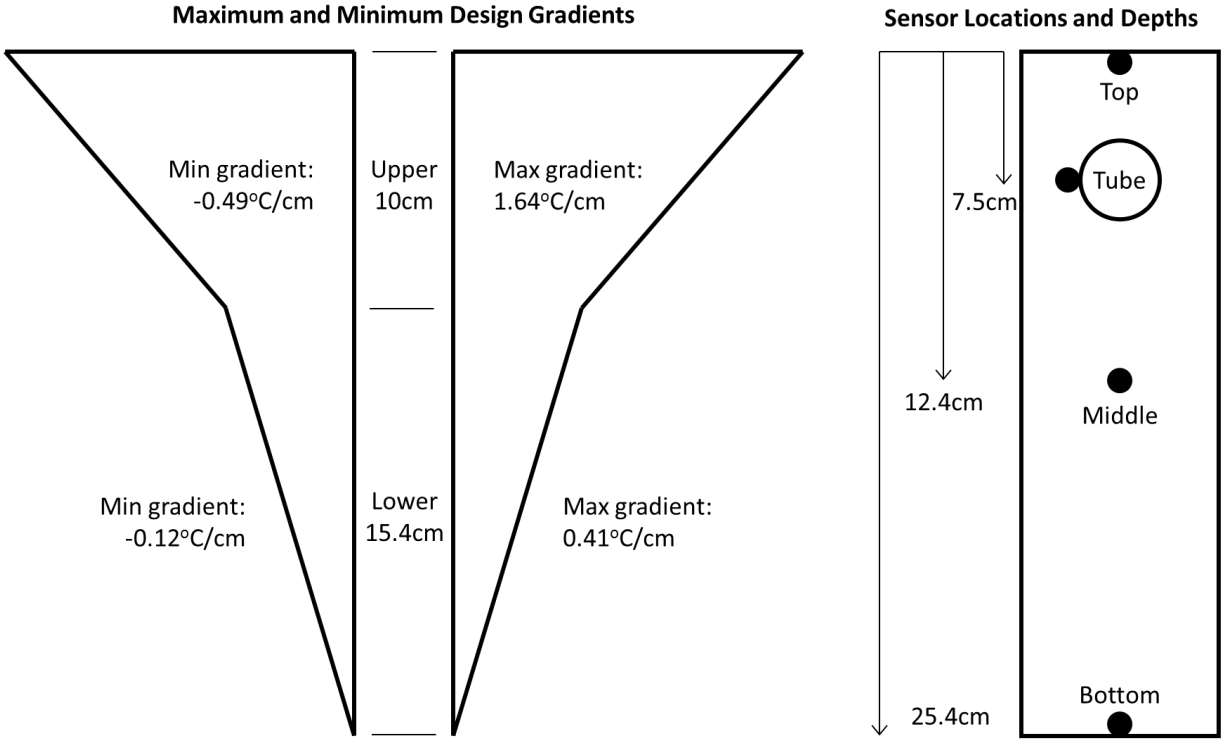

Figure 3-34. The maximum and minimum design temperature gradients (left) and the locations and depths of the temperature sensors in the slab (right).

3.7.1. Maximum Observed Gradients

The ten maximum observed top gradients from the summer of 2013 through the summer of 2015 in the upper 7.3 cm of the bridge deck are given in Table 3-2. Note that each day could only have one maximum gradient. That is there were gradients on 6/18/14 less than the maximum value of 0.92°C/cm but greater than 0.87°C/cm which occurred on 6/26/14, but because the maximum gradient of that day was already recorded, any gradients less than the maximum were ignored. There are a couple of interesting observations about this list. The first is that all occur during thermal recharge operations. Secondly, they all occur within a 30 minute window between 14:15 and 14:45. These observations will be discussed more fully in another section. Thirdly, and most importantly, the maximum value that was observed (0.92°C/cm) is lower than the design value of 1.64°C/cm.

Table 3-2. Maximum observed top gradients in the bridge deck.

Date	Top Gradient	Associated Tube Gradient	Operation
6/17/14 14:45	0.92	0.09	TR
6/18/14 14:45	0.92	0.13	TR
7/2/14 14:30	0.91	0.08	TR
7/1/14 14:30	0.90	0.11	TR
6/26/14 14:45	0.87	0.21	TR
6/16/14 14:15	0.86	-0.02	TR
6/24/14 14:45	0.85	0.03	TR
6/27/14 14:45	0.85	0.13	TR
6/2/14 14:15	0.85	0.41	TR
7/8/14 14:15	0.79	0.01	TR

The ten maximum observed middle gradients that occur between heights 12 cm and 18.1 cm are given in Table 3-3. Again, each day was only allowed to have one maximum value. There are also several interesting observations about the gradients on this list. The first is that all except the maximum occur during no operation (meaning these are naturally occurring gradients) during late spring and early summer. Secondly, though the range is larger than 30 minutes, they still all occur during the afternoon between the hours of 13:30 and 15:15. Thirdly, they are within the design value of 1.64°C/cm (technically the 'middle' point is located 2 cm below the top 10 cm of the slab and thus falls out of the zone, however it can be argued that the temperature cannot be known precisely at the 10 cm depth thus it is hard to tell if the gradient extends below 10 cm or not). Finally, the lowest middle gradient in Table 3-3 is greater than the highest top gradient in Table 3-2.

Table 3-3. Maximum observed tube gradients in the bridge deck.

Date	Tube Gradient	Associated Top Gradient	Operation
2/20/15 15:15	1.50	-0.74	BDD
4/28/15 14:30	1.42	0.50	None
5/11/15 14:15	1.39	0.52	None
5/5/15 14:30	1.39	0.51	None
5/24/15 13:30	1.35	0.52	None
5/13/14 14:15	1.34	0.43	None
5/12/14 14:15	1.33	0.45	None
4/21/14 14:30	1.32	0.45	None
5/18/14 14:00	1.32	0.42	None
6/11/15 15:15	1.31	0.47	None

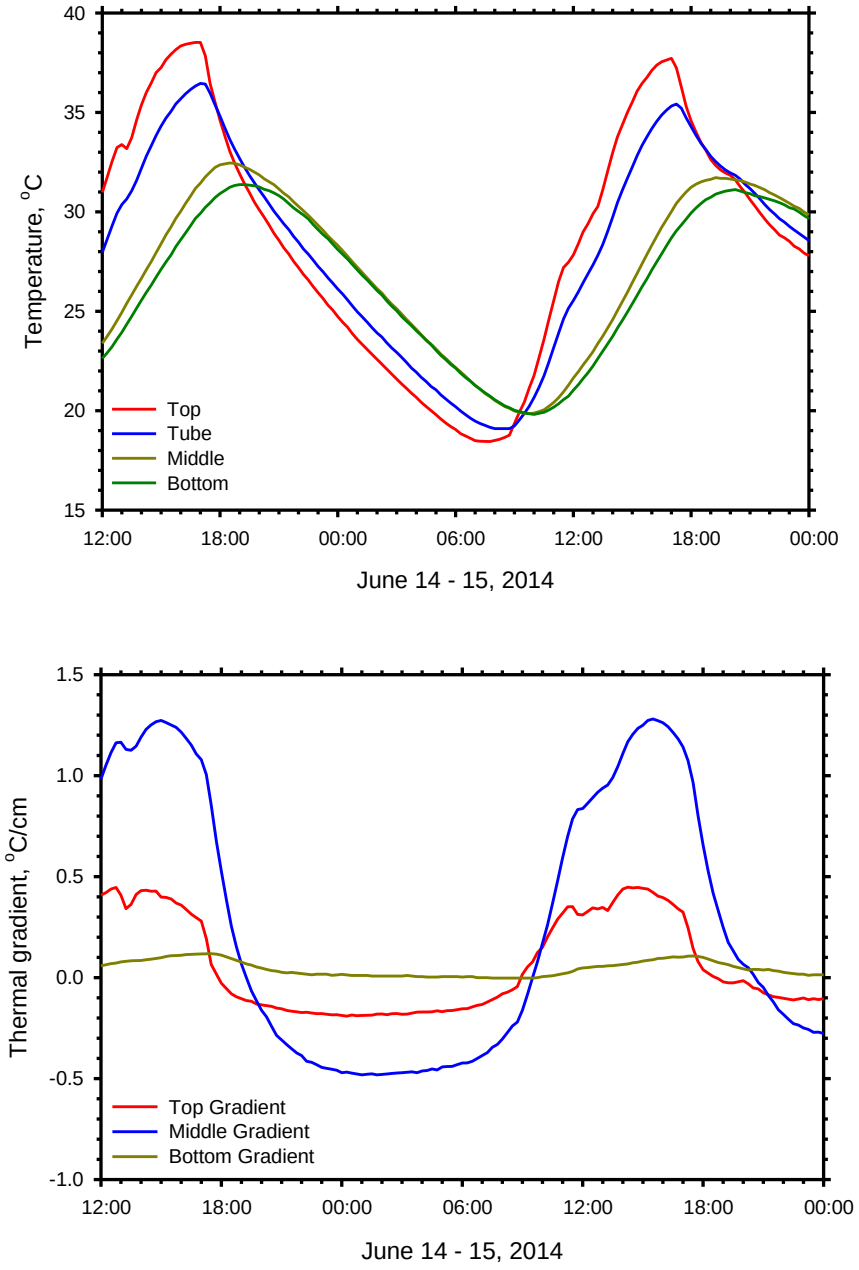

Figure 3-35. Top, tube, and middle temperatures for several warm summer days with no thermal recharge operations during summer of 2014 (a, top), and the thermal gradients that exist in the bridge deck during a summer day with no operation (b, bottom).

In order to understand what is happening within the slab, it is helpful to consider how temperatures within the slab change over time. Temperatures at different depths are shown in Figure 3-35a for a period of 36 hours between June 15 and 16, 2014 during which no operation occurred. Thermal gradients for the same period of time are shown in Figure 3-35b. From the experimental data, it appears that during the summer the surface of the deck becomes very warm between the hours of 12:00 and 18:00, creating a large gradient between the surface and tube locations. This gradient, however, is not the maximum that the

slab will experience. Rather, as the thermal energy from the surface dissipates further down the slab, a large gradient is created between the tube and middle depths. This is what is shown in Table 3-3. Also notice from Table 3-3 and Figure 3-35b that the associated top gradients are relatively small compared to the middle gradients indicating the surface and tube depths are closer to the same temperature. Later in the evening the thermal energy finally reaches the middle and bottom of the slab as the surface and tube locations begin to cool. The entire slab cools throughout the night until mid-morning when higher temperatures and solar radiation begin to heat the surface.

The maximum observed gradients in the deck occur in the late spring and early summer because the night temperatures are still relatively cold as compared to the daytime temperatures. Thus the slab cools significantly at night, but the surface is heated intensely during the day, leading to the large thermal gradients.

Thermal recharge operations disrupt this naturally occurring cycle by directly decreasing the temperature at the tube location during the day as can be seen in Figure 3-36a, which shows the thermal recharge operations that occurred from June 16-17, 2014. As the temperature at the tube depth decreases, a large gradient is created between it and the warm surface (Figure 3-36b). Each of the thermal recharge operations in Table 2 except for the last one were started at 14:00, meaning the maximum top gradients developed within 45 minutes after the operations began. From Figure 3-35a, this time of day (early afternoon) is also when the surface of the deck is very warm compared to the rest of the slab, which suggests that these high top gradients can be mitigated by selecting an earlier start time when the surface temperature is lower and the difference between it and the tube will be smaller. The operation that occurred on 7/8/14 was started at 13:00 and the top temperature gradient was lower. In all of the additional thermal recharge operations that had a start time earlier than 14:00, the maximum observed top gradient was 0.78°C/cm and occurred at 13:30 on 5/26/2014 when the system was turned on at 10:00.

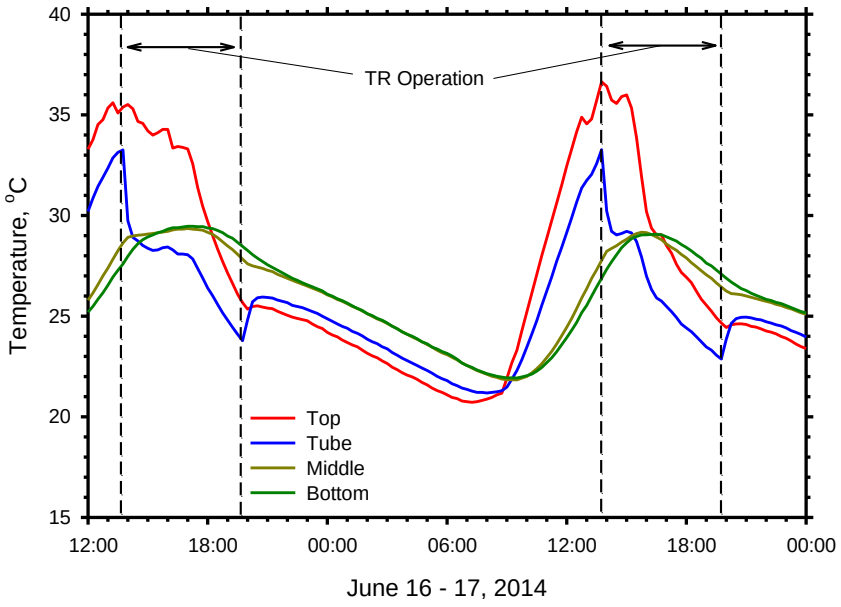

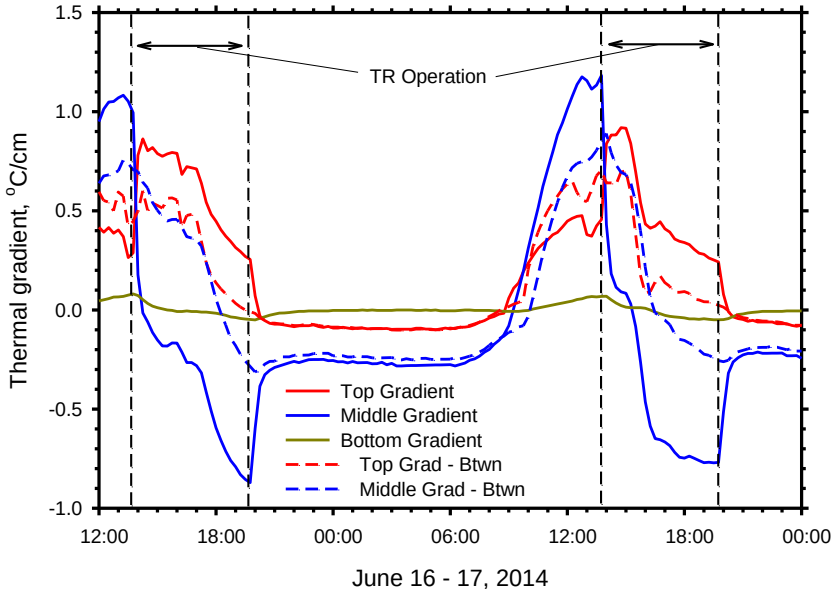

Figure 3-36. Temperatures within the bridge deck during the days with thermal recharge operations (a, top), and the thermal gradients in the bridge deck during two days with thermal operation. Gradients are shown for the cross section containing the deicing tubes (solid lines), and for the cross section with no deicing tubes (dashed line) (b, bottom).

There is a benefit, however, to developing the higher top gradients and that is that it prevents the development of the much higher middle gradients seen in Table 3-3 by lowering the temperature at the tube location. The drawback is the development of high negative temperature gradients in the middle of the deck, which will be discussed in the next section.

There is one more observation to be made about the thermal gradients observed in the slab. Whereas the middle gradients that occurred under no thermal recharge or BDD operation in Table 3-3 were present throughout the whole slab, the top gradients of Table 3-2 that occurred shortly after operation began were localized to cross sections containing a deicing tube. That is, they were not observed in cross sections without a deicing tube. Figure 3-36b compares the top and middle gradients in a section with the deicing tube and in one that is between two deicing tubes. The top gradient is lower in the cross section between circulation tubes whereas the middle gradient is higher. This is expected as the temperature decrease at the tube location in cross sections without a deicing tube is less than the decrease in the cross sections with a deicing tube thus the top gradient is smaller (not as much of a temperature difference between the top and tube locations) whereas the middle gradient is larger (larger temperature difference between the tube and middle locations).

The maximum middle gradient was the only tube gradient to occur during a system operation and deserves special discussion. This gradient occurred during the operation that occurred 2/20-22/2015 during severe winter weather (see 3.5.8). In this particular case, the deck was very cold (see the temperatures in Figure 3-37a), such that when the system was turned on, the much warmer fluid heated the tube location creating a large positive gradient that existed between it and the middle point and a large negative gradient that existed between it and the surface point. As shown in Figure 3-37b, these

large gradients persisted until the heat energy dissipated throughout the deck and decreased over time. More will be discussed about gradients during bridge deck deicing operations in the next section.

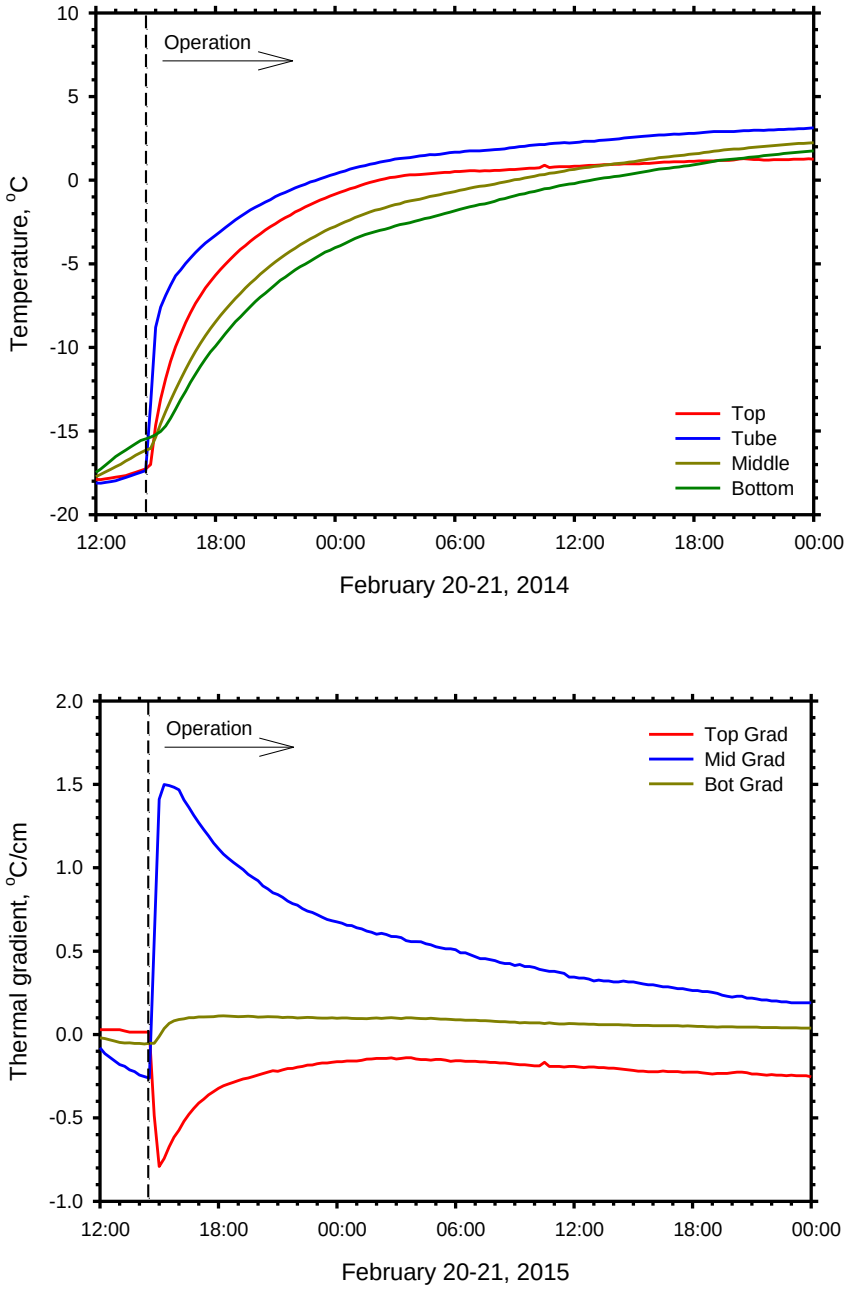

Figure 3-37. Temperatures within the bridge deck during the bridge deck heating operation on 2/20-22/2015. The highest observed middle gradient was associated with this operation (a, top), and the observed thermal gradients in the bridge deck during the bridge deck deicing operation on February 20-22, 2015 (b, bottom). Note that the maximum middle gradients and lowest top gradient were observed during this operation.

The bottom gradients have not been discussed. However, the highest temperature gradient in the bottom 12cm of the slab was only 0.16°C/cm and occurred on 6/11/2015 at 17:00 during no operation.

Ultimately it appears that thermal recharge operations may actually serve to help reduce temperature gradients in the bridge deck. Even though higher temperature gradients were observed near the top of the slab during thermal recharge operations, they served to prevent the even higher temperature gradients that would later exist between the tube and middle points if not for system operation. Furthermore, it has been shown that the high gradients near the top of slab can be reduced by selecting an earlier start time.

3.7.2. Minimum Observed Temperature Gradients

The six lowest observed temperature gradients in the top of the slab are given in Table 4. Note that the two lowest are lower than the design value of -0.49°C/cm. Those two cases will be discussed in detail later. All of the minimum gradients occurred during bridge deck deicing (or heating) operations. The top three in Table 3-4 all occurred in operations during extreme winter weather and the bottom three all occurred in the morning hours.

Table 3-4. Minimum observed top gradients in the bridge deck.

Date	Top Gradient	Associated Tube Gradient	Operation
2/20/15 15:00	-0.79	1.41	BDD
1/7/14 4:15	-0.54	0.60	BDD
1/6/14 23:45	-0.49	0.39	BDD
1/24/14 7:00	-0.46	0.47	BDD
2/12/14 7:30	-0.44	0.56	BDD
1/30/14 7:45	-0.42	0.23	BDD

Table 3-5. Minimum observed tube gradients in the bridge deck.

Date	Tube Gradient	Associated Top Gradient	Operation	Operation End Time
6/16/14 19:45	-0.87	0.25	TR	20:00
6/18/14 19:45	-0.80	0.26	TR	20:00
6/17/14 19:30	-0.77	0.25	TR	20:00
7/1/14 19:00	-0.77	0.31	TR	19:00
6/24/14 19:00	-0.71	0.26	TR	19:00
6/2/14 19:45	-0.70	0.19	TR	20:00
6/27/14 18:45	-0.69	0.27	TR	19:00
7/7/14 18:45	-0.68	0.28	TR	19:00
6/26/14 19:00	-0.66	0.30	TR	19:00

The ten lowest observed temperature gradients in the middle of the slab are given in Table 3-5. Observe that all of these occurred during thermal recharge operations. The time the thermal recharge operations ended is also given in Table 3-5, and it can be observed that the time of the lowest gradients all occur near the end of the operation. Furthermore, the gradients in Table 3-5 are all lower than the minimum design gradient.

In discussing the top gradients that occur during bridge deck deicing operations, as mentioned previously, the top three minimum gradients occurred during severe winter weather. The cause for the lowest gradient on 2/20/2015 at 15:00 has been discussed as resulting from the system being turned on when the deck was very cold. And as shown in Figure 3-37b, this gradient increases over time as the deck heats. The gradients that occur on 1/6/2014 and 1/7/2014 are actually a part of the same operation that was discussed as having occurred from 1/6-8/2014 in Section 3.5.7. As mentioned, there was no precipitation during this time, just extremely cold temperatures. Figure 3-38 displays the top, middle, and bottom gradients that were present in the bridge deck during this time. Also shown is the ambient air temperature. Notice that the lowest gradients occur when the ambient temperatures are low during the night, which cools the surface of the deck relative to the tube location. In actual applications, the system would not have been operated during this period of time because no precipitation was present. When precipitation is present with cold weather, similar to what occurred on 2/20-22/2014 and 3/4-6/2014, these low gradients do not develop because the precipitation acts as an insulation to the surface, which was discussed previously.

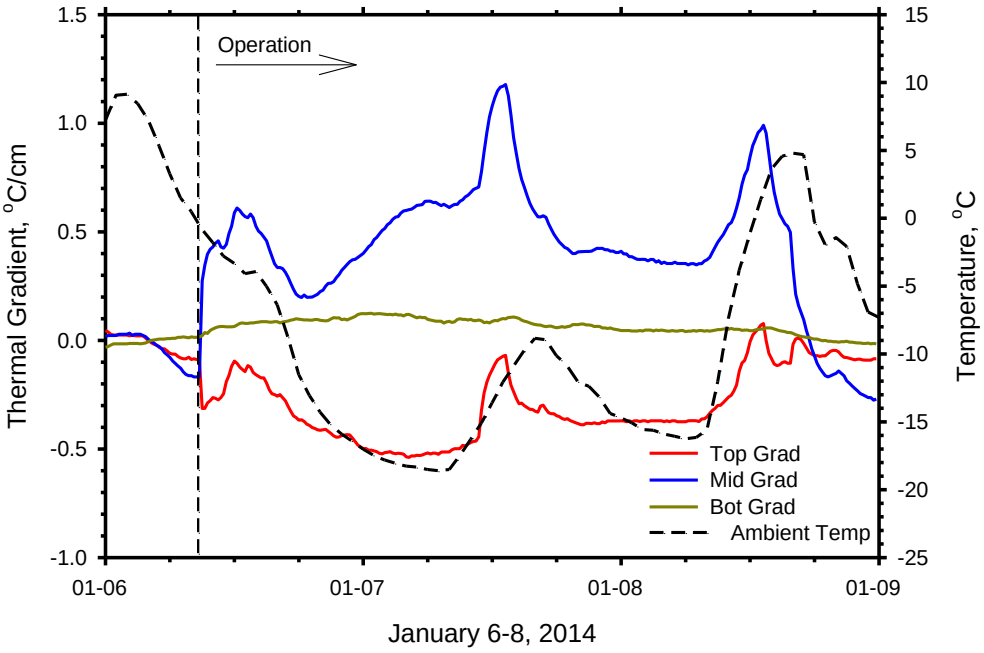

Figure 3-38. The thermal gradients within the bridge deck during the heating operation on 1/6-8/2014. There were low top gradients associated with this operation.

The three other low gradients in Table 3-4 are also a result of the surface of the deck being cooled relative to the tube location. They all occur in the early morning hours, which is typically the coldest period for

bridge deck surface temperatures (see Figure 3-35a). These gradients, however, are greater than the minimum design value.

As opposed to the minimum top gradients, all of which occur during BDD operations, the lowest middle gradients all occur during thermal recharge operations. They also all occur near the very end of operation. From Figure 3-36b, which was presented earlier, these low gradients typically develop later in the thermal recharge operation as the tube temperature decreases relative to the middle temperature. This temperature difference continues to increase (thus decreasing the gradient) until the system is turned off. From Figure 3-36b, it also appears these lower gradients are primarily concentrated in the cross-sections with circulation tubes.

The low gradients in the middle section can be avoided in much the same way the high gradients in the top section are avoided – by beginning system operation earlier in the day. The major advantage of this approach is that it allows the thermal energy to be collected by the thermal recharge operation before it is transferred deeper into the slab. This prevents the middle temperatures from increasing relative to the tube temperatures and thereby increasing the middle temperature gradient. For example consider Figure 3-39a, which shows the deck temperatures, and Figure 3-39b, which shows the thermal gradients for May 26, 2014. A thermal recharge operation occurred where the system was started at 9:00 and ended at 18:30. Notice the relative increase of the middle and bottom temperatures is not as great as in Figure 30a, where the thermal recharge operations began at 14:00. The thermal gradients in Figure 3-39b are also much different than those in Figure 3-36b. The middle thermal gradient is mostly positive and though it begins to decrease, is preventing from decreasing too far by the operation ceasing. The lowest value it reached it was -0.45°C/cm. If the operation were allowed to continue much longer, a lower gradient would have likely developed.

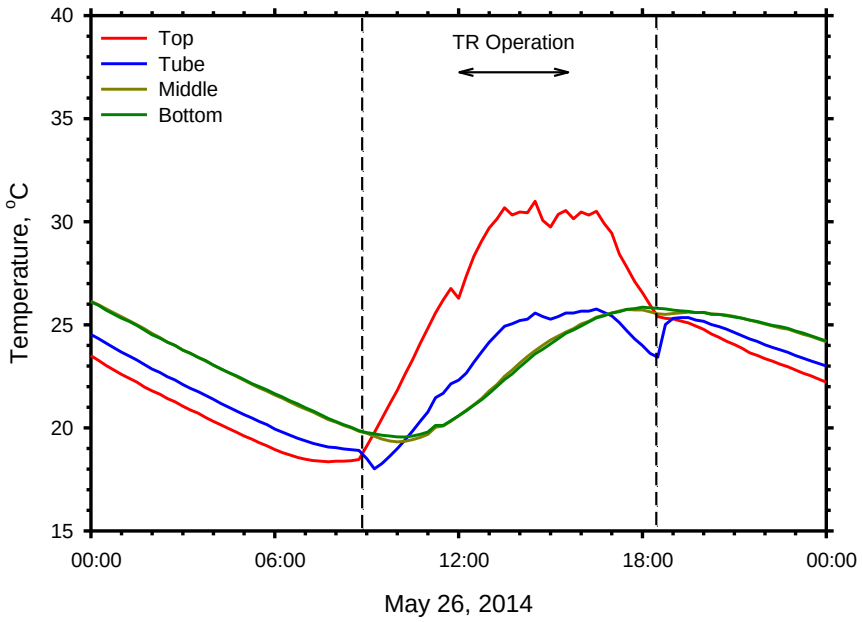

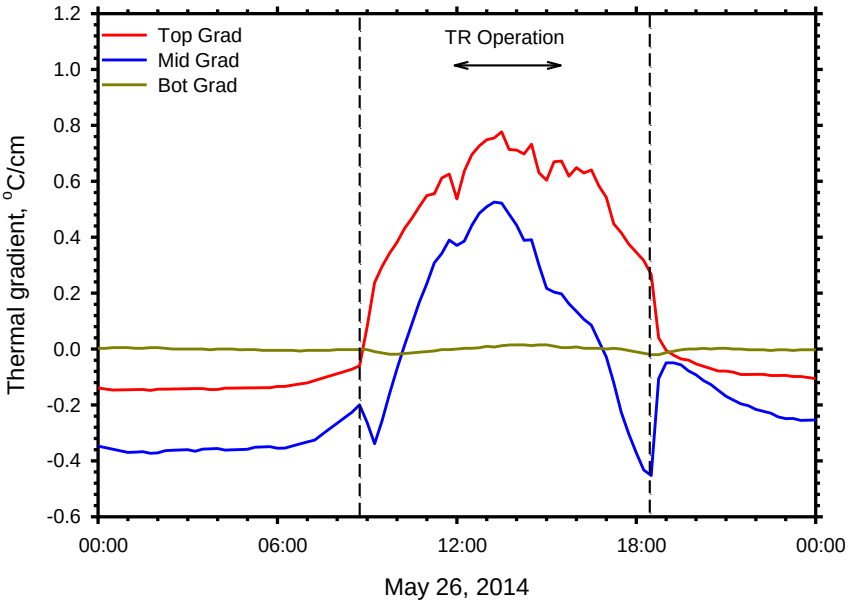

Figure 3-39. Temperatures within the bridge deck during a thermal recharge operation that was started and terminated earlier in the day (a, top), and thermal gradients within the bridge deck during a thermal recharge operation that was started and terminated earlier in the day. Note that both the high top gradients and the low middle gradients are avoided by performing thermal recharge operations earlier (b, bottom).

3.7.3. Conclusions Regarding Thermal Gradients

Bridge deck deicing and thermal recharge operations induce thermal gradients in the bridge deck. Whereas the observed positive thermal gradients are all below the recommended design value, several of the negative gradients were lower than the minimum design value. Thus negative gradients beyond those which are prescribed by current design guidelines should be taken into account when designing bridges that are to be equipped with BDD systems.

For the case of existing BDD systems or retrofitting existing bridges with a BDD system, however, there are operational guidelines that can be followed to reduce the severity of the gradients, and many times (if not every time) bring them within design guidelines. They are the following:

- For bridge deck deicing operations, large negative gradients can develop when the system is operated in extreme weather conditions. Caution should be taken when starting an operation when the bridge deck is very cold, and if possible, turn the system on before the deck temperatures are allowed to decrease substantially.
- For thermal recharge operations it is best to start and end the operation early. It is best to start the operation in the mid-morning hours before the deck temperatures have had a chance to substantially increase. This:
    - Prevents the surface temperature from increasing significantly relative to the tube and middle temperatures;

- Prevents the tube level temperatures from rising significantly relative to the middle level temperatures;
- Allows the system to collect the thermal energy before it dissipates deeper into the slab, increasing the middle and bottom temperatures and creating a large negative temperature gradient in the middle of the slab.

- The system should also be shut off early evening to prevent the tube level temperatures from dropping significantly relative to the middle level temperatures.

Also keep in mind that these systems, because they are ground-source and do not rely on a heat pump, deal with low temperature gradients in general. If a system which employs heat pumps and/or some other means to heat the fluid to higher temperatures, gradients larger than the ones presented in this paper are expected.

3.8. CONCLUSIONS AND RECOMMENDATIONS FOR PRACTICE

In this paper, the results from an experimental bridge deck deicing system were presented. The system, which was a passive configuration, used only the energy extracted from an energy pile to heat the deck during the winter. Performance during several winter storms of varying intensity, as well as during several episodes of severe winter weather was presented. Results were presented in terms of temperatures, energy, and photographs showing surface conditions of the heated slabs. Also considered in this experimental study was thermal recharge and it was shown that the ground could be heated using energy collected by the slab during the summer. Based on the results, the following conclusions and associated recommendations for practice are presented.

First, it is possible to perform bridge deck deicing operations without the use of a heat pump. The ground can supply the energy, and in a sense, is self-adjusting. In tests where the initial bridge deck temperature was very low and large amounts of energy were needed to heat it, higher heating rates were observed due to the temperature gradient between the deck and the ground. Though it is possible to heat the deck, it is important to consider the following points in terms of performance:

- For mild and moderate winter storms where there was no mechanical removal and/or no application of deicing chemicals the system was observed to keep the deck free from snow/ice accumulation. Thus, as a stand-alone system, passive ground-sourced bridge deck deicing operations can potentially increase the safety of bridges by maintaining a snow-free surface in most cases.

- For moderate to severe winter storms the system was not able to keep the deck completely free from snow/ice. However, it was, in all cases, able to keep the surface temperature of the deck above 0^{o}C. Thus, when seen as an aid to the mechanical removal process, a clear, snow-free surface will result. These systems should be expected to perform independently during such storms. Generally, this will be a non-issue as mechanical removal will be required.

- When the system was operated during no storm events, thermal gradients outside of the design gradients were observed. Thus care should be taken in cases where automated controls are used to operate the system whenever the temperature of the deck reaches a certain point as harmful gradients could result. This is expected to only be a problem during severe winter weather, thus

the frequency of these gradients will be few. New decks, however, should be designed for such gradients.

- Thermal recharge operations were successful in injecting thermal energy into the ground. The rate at which the energy was collected by the deck and injected into the ground was greater than the rate at which it was extracted. Thus, fewer hours of thermal recharge are required to replace the amount of energy that was used during bridge deck deicing. Any extra energy that is injected will serve to increase the temperature of the ground. Whether or not that energy is still available for deicing in the winter is a function of the thermal properties of the subsurface.
- Higher injection rates were observed for thermal recharge operations that occurred later in the day. However, harmful thermal gradients were also observed in thermal recharge operations that occurred later in the day. Thus, the recommendations from Section 3.7.3 should be considered to minimize harmful thermal gradients during operation.

3.9. REFERENCES

American Association of State Highway and Transportation Officials (AASHTO) (2008). "Bridging the Gap: Restoring and Rebuilding the Nation's Bridges." American Association of State Highway and Transportation Officials.

American Association of State Highway and Transportation Officials (AASHTO) (2012). "*AASHTO LRFD Bridge Design Specifications, Customary U.S. Units*.", American Association of State Highway and Transportation Officials (AASHTO), S.l.

Baboian, R. "Synergistic effects of acid deposition and road salts on corrosion." (1992). Proc., Symposium on Corrosion Forms and Control for Infrastruture, November 3, 1991 - November 4, 1991, Publ by ASTM, 17-29.

Bowers, Jr., G. and Olgun, C. (2014). "Ground-Source Bridge Deck Deicing Systems Using Energy Foundations." Geo-Congress 2014 Technical Papers: pp. 2705-2714.

Cady, P.D., and Weyers, R.E. (1983). "Chloride Penetration and the Deterioration of Concrete Bridge Decks." Cement, Concrete & Aggregate, Vol. 5, No. 2, pp. 81-87.

Eugster, W.J. (2007). "Road and Bridge Heating Using Geothermal Energy - Overview and Examples." Proc., European Geothermal Congress.

Friar, S., and Decker, R. (1999). "Evaluation of a fixed anti-icing spray system." Transportation Research Record(1672), 34-41.

Hoppe E.J., (2000). "Evaluation of Virginia's First Heated Deck Bridge." Virginia Transportation Research Council, Report No. VTRC 01-R8, December 2000.

Koch, G. H., Brongers, M. P. H., Thompson, N. G., Virmani, Y. P., and Payer, J. H. (2002). "Corrosion Cost and Preventive Strategies in the United States." FHWA, U.S. Department of Transportation, United States, 790p.

Kusuda, T., and Achenbach, P.R. (1965). "Earth temperature and thermal diffusivity at selected stations in the United States." ASHRAE Transactions, Vol. 71, Part 1, pp. 61-74.

Liu, X., Rees, S. J., and Spitler, J. D. (2003). "Simulation of a Geothermal Bridge Deck Anti-Icing System and Experimental Validation." 82nd Annual Meeting of the Transportation Research BoardWashington, DC.

Liu, X., Rees, S. J., and Spitler, J. D. (2007a). "Modeling snow melting on heated pavement surfaces. Part I: Model development." Applied Thermal Engineering, 27(5-6), 1115-1124.

Liu, X., Rees, S. J., and Spitler, J. D. (2007b). "Modeling snow melting on heated pavement surfaces. Part II: Experimental validation." Applied Thermal Engineering, 27(5-6), 1125-1131.

Minsk, L. D. (1998). Snow and ice control manual for transportation facilities, McGraw-Hill, New York.

Minsk, L. D. (1999). "Heated Bridge Technology: Report on ISTEA Sec. 6005 Program." FHWA, U.S. Department of Transportation, 51.

Tuan, C.Y. (2008). “Roca Spur Bridge: The implementation of an innovative deicing technology.” Journal of Cold Regions Engineering. Vol. 22, No. 1, 2008, pp. 1-15.

Yoshitake, I., Yasumura, N., Syobuzako, M., and Scanlon, A. (2011). "Pipe heating system with underground water tank for snow thawing and ice prevention on roads and bridge decks." Journal of Cold Regions Engineering, 25(2), 71-86.

Yunovich, M., Thompson, N. G., and Virmani, Y. P. (2003). "Life Cycle Cost Analysis for Reinforced Concrete Bridge Decks. Paper No. 03309." Proc., CORROSION/03.

Zhao, H.M., Wang, S.G., Wu, Z.M. and G.J. Che. (2010). “Concrete Slab Installed with Carbon Fiber Heating Wire for Bridge Deck Deicing”. ASCE Journal of Transportation Engineering. Vol. 136, No. 6, 2010, pp. 500-509.

4. EXPERIMENTAL INVESTIGATION OF ENERGY PILE RESPONSE UNDER HEATING AND COOLING LOADS FOR BRIDGE DECK DEICING APPLICATIONS

4.1. ABSTRACT

Energy piles are becoming an increasingly popular method of economically and efficiently accessing shallow geothermal energy for heating and cooling buildings. Energy piles are deep foundation elements integrated with circulation tubes, which allow them to serve as a heat exchanger in addition to their traditional role of structural support. In recent studies, the use of energy piles for deicing of bridge decks was investigated. Temperature-induced stresses that develop as a result of soil-pile interaction during heat exchange operations need to be evaluated for adequate design of energy piles. This paper presents the results from a series of full-scale field tests on an energy pile. These tests involve subjecting the energy pile to thermal loading using constant and variable energy injection/extraction rates. The resulting axial strains and stresses in the pile are presented and discussed within the context of soil-pile interaction under thermal loads. Conclusions are drawn about the behavior of energy piles under differing thermal loads and recommendations are given for their use as heat exchangers.

4.2. INTROUCTION

The icing of bridge decks in the winter is a major problem that creates dangerous driving conditions for motorists. Salts and other chemicals commonly used to deice bridge decks lead to accelerated corrosion of the bridge structure, threatening its structural integrity and can also have long-term life cycle impacts due to increased maintenance and repair costs (Koch et al., 2002; Granata and Hartt, 2009). Furthermore, salts and chemicals can be damaging to the environment through surface runoff and infiltration to the groundwater.

This paper presents the results of an experimental investigation that uses ground-source thermal energy to heat bridge decks. In the experimental studies, an energy pile was used to harvest thermal energy from the ground that was then used to heat a prototype bridge deck in the winter. During the summer, heat from the deck was injected into the ground through the energy pile. These operations induced temperature changes in the pile, which then led to the development of thermal loads. Tensile loads were observed during bridge deck heating (heat extraction) and compressive loads were observed during heat injection. The results of these tests are compared with other thermo-mechanical field tests performed on energy piles.

4.3. BACKGROUND

There are alternative methods to chemically deicing bridge decks including electric cables, heat pipes, electrically conductive concrete, and boiler-powered hydronic systems, however, these systems can require an extensive amount of input energy rendering them infeasible (Minsk 1999; Hoppe 2000; Tuan 2008). Several experimental and implemented systems use geothermal energy in conjunction with a heat pump (Ground-Coupled Heat Pump, or GCHP) to heat the bridge deck (Minsk 1999; Liu et al. 2007a, 2007b). Although more energy efficient than the previous systems, the GCHP systems still require additional energy to operate the heat pump and the costly addition of a borehole field.

Any feasible alternative to chemical deicing must meet two primary criteria: 1) it must not require significant energy/expense to operate, and 2) it must not be significantly more expensive to install. Using shallow geothermal energy taken directly from the ground to heat bridge decks without the use of any additional energy source has shown promise, which meets criteria (1). Shallow geothermal energy takes advantage of the fact that the temperature of the ground below a certain depth remains constant

throughout the year. In Blacksburg, VA, where the experimental tests in this paper were performed, after a depth of about 6m the temperature of the ground is a constant 11°C as shown in Figure 4-1 (Kusuda and Achenbach, 1965). Thus, during the winter, the ground temperature is warmer than the atmospheric temperature, thereby providing a source of thermal energy.

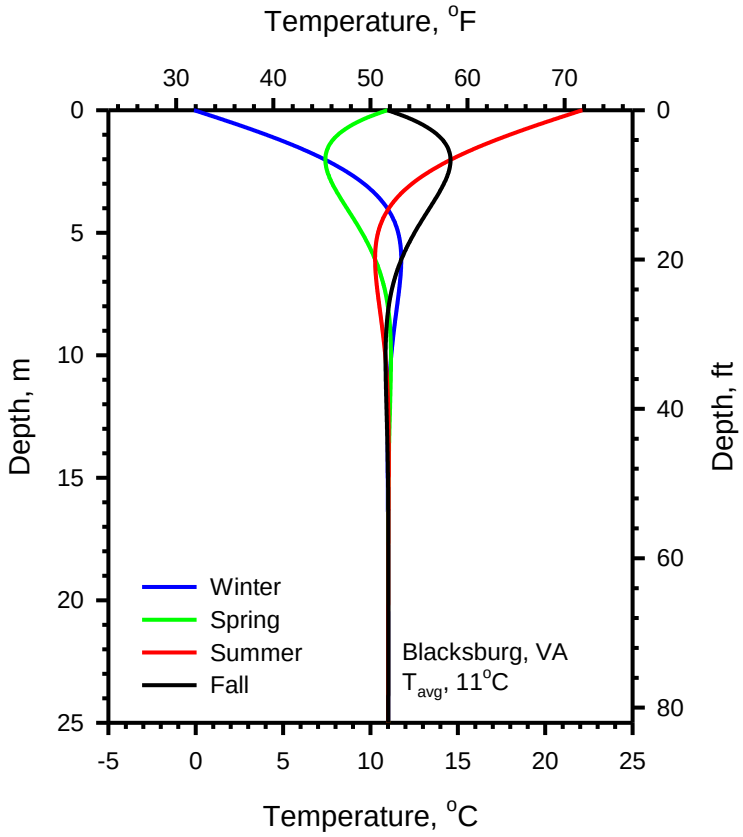

Figure 4-1. Temperature vs depth profile for Blacksburg, VA.

There are several methods of accessing shallow geothermal energy. One is geothermal boreholes, as mentioned previously. Another method is reported by Yoshitake et al. (2011) in which a bridge utilizes an underground water storage tank that contains water heated by the ground. This water is then circulated through the deck during the winter and is able to deice the surface. Both of these methods, however, do not meet criteria (2) as they require the costly addition of either a borehole field or an underground storage tank.

Because many bridges are supported by deep foundations, the use of energy piles to access shallow geothermal energy presents a unique opportunity in meeting requirements (1) *and* (2). Energy piles allow the already required deep foundation of the bridge to function for both structural support and in heat exchange operations with the ground. In this concept, the bridge sub-structure is converted to an energy foundation by installing circulation tubes in the foundation elements, creating energy piles. As fluid is circulated in the system, heat energy can be extracted from the ground and supplied to the deck. During the summer, the system can be operated to collect the thermal energy of the bridge deck and inject it into the ground to replace the energy that was used during the winter and to raise the temperature of the ground for more efficient operation of the system. A schematic of this system in shown in Figure 4-2 (redrawn after Bowers and Olgun 2014).

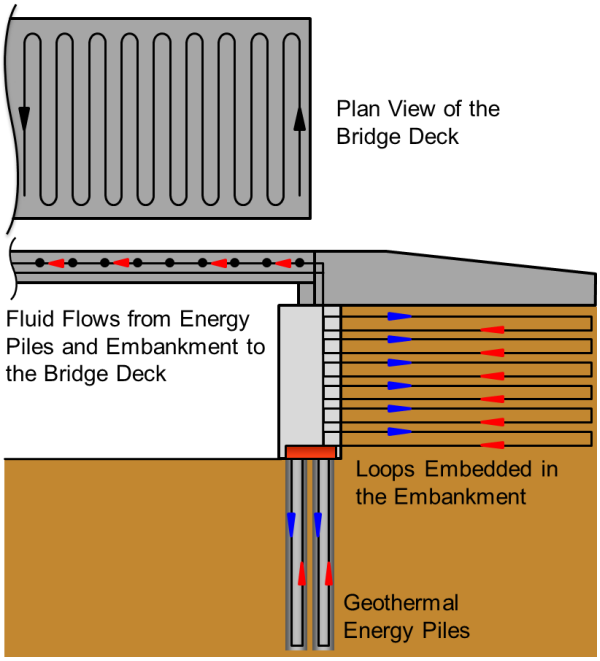

Figure 4-2. Schematic illustrating the concept of ground-source bridge deck deicing utilizing an energy foundation, which in this case includes the embankment and foundation piles (redrawn after Bowers and Olgun 2014).

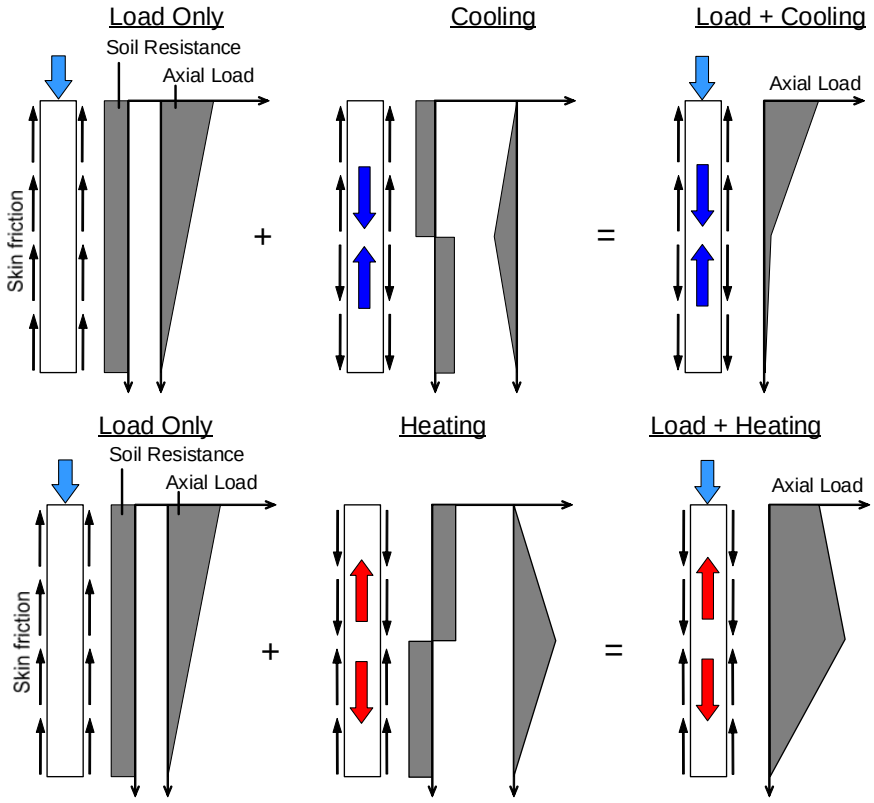

Figure 4-3. Schematic illustrating the effects of heating and cooling on the shaft resistance and axial load of a pile. Cooling loads can lead to the development of tensile loads in the pile whereas heating loads can lead to excessive compressive loads in the pile (redrawn after Bourne-Webb et al. 2009).

From a thermo-mechanical perspective, heat exchange operations with the ground will induce temperature change in the pile. Temperature change in the pile will lead the development of thermal loads in addition to the foundation loads. This has been observed in several experimental studies. Bourne-Webb et al. (2009) applied heating and cooling loads to an axially loaded pile. They observed tensile forces in the lower part of a pile shaft of an axially loaded pile undergoing cooling loads. Likewise they observed an increase of about 70% of the maximum head load in the pile during heating loads. Figure 4-3 demonstrates the types of thermal loads energy piles experience during heating and cooling cycles and their effects on both axial load and required shaft resistance.

4.4. VIRGINIA TECH EXPERIMENTAL PROGRAM

The use of energy piles for bridge deck deicing is being tested at the Virginia Tech Geotechnical Research Facility. Four energy piles were installed as part of a previous project (Abdelaziz 2013) in a subsurface that consists of a silty sand for the upper 12.2 m, below which is a weak shale layer. One of the piles has been studied extensively and is well characterized. This is the pile that was tested in the studies presented in this paper. The energy pile is a drilled micropile 30.5 m in length and 25.4 cm in diameter with a single HDPE circulation loop running along its length. The upper 9.1 m of the pile is cased in 0.64cm thick steel tubing. It is instrumented with vibrating wire strain gauges in the longitudinal direction every 3.0 m of depth that return values of both temperature and blocked strain. The blocked strain values are corrected for both location dependent effects in the pile cross section and differences in the thermal expansion coefficients of the steel gauge and the cement pile as discussed in Abdelaziz (2013). The corrected blocked strain values were then used to determine loads using the pile tangent moduli values given in Table 4-1. Note that the upper 9.1 m of the pile is controlled by the tangent modulus of the steel casing, hence the high values. Below that depth, the pile tangent modulus is strain dependent.

Table 4-1. Tangent moduli values.

Depth (m)	E_{pile} (kPa/με)
3.0	69.34
6.0	60.61
9.1	34.76
12.2 – 30.4	40.07 – 0.0269ε

The energy pile is connected to an experimental bridge deck. The bridge deck is 3.0 m X 2.4 m X 25.4 cm. It is doubly reinforced and contains PEX circulation tubes that are arranged in a serpentine configuration with a 30 cm spacing in one half and 20 cm in the other half. The circulation tubes are connected underneath the top layer of reinforcement. A single circulation pump is used to pump the fluid through the system. In the tests presented in this paper, the test pile was connected only to the side of the deck with the circulation tubes spaced 30 cm apart.

The deck was operated during winter storm events to test its deicing capabilities as well as during the summer to utilize thermal energy injection. One test each of deicing and thermal injection are presented in this paper. During the tests, the pile was not under any axial load and the pile head was free to move.

4.4.1. Bridge Deck Deicing

The bridge deck deicing test (heat extraction) took place February 23 – 26, 2015. This test actually consisted of two separate operations. The first occurred 2/23 – 2/25 for a total of 56 hours during a period of cold weather. The second test occurred on 2/25 for a total of 11 hours during a winter storm.

As can be seen in Figure 4-4, the system was able to successfully keep the temperature of the deck above freezing during both the cold period that occurred 2/23 – 2/25, and during the period of snow that occurred on 2/26. During this test, both the 20 cm and 30 cm sides of the deck were operated using separate energy piles. The photograph in Figure 4-5 shows the deck during the operation on 2/26. Observe that the left side of the deck, which contains the circulation tubes spaced 30 cm apart, is covered in snow whereas there is no snow on the right side, which contains the circulation tubes spaced 20 cm apart. Due to the rapid rate at which the snow fell, the system was not able to keep the left side of the deck completely free the entire storm, but the surface temperatures are above zero (see Figure 4-4), indicating that when combined with mechanical removal, the deck will be completely snow-free. However, because the side of the deck with tubes spaced 20 cm apart did remain free from snow the entire storm, a closer tube spacing is all that is needed.

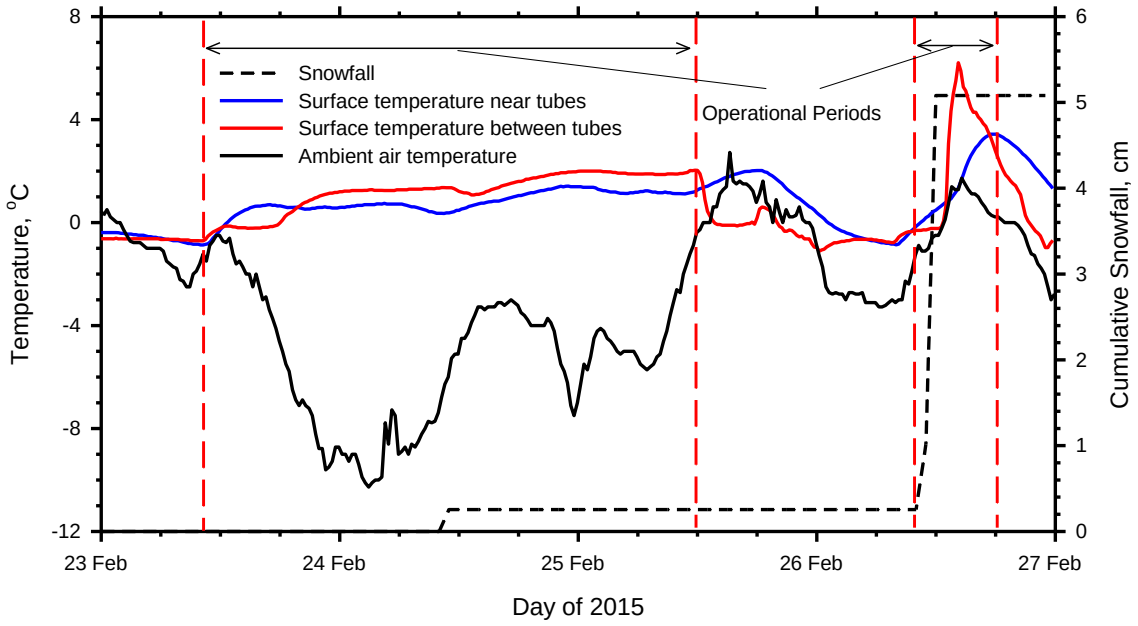

Figure 4-4. Weather conditions and the bridge deck surface temperatures of the side with the 30 cm-spaced circulation tubes during the deicing test that occurred February 23 – 26, 2015.

Figure 4-5. Photograph of the deck surfaces during the storm. The side with the 20 cm spaced tubes (right), which is powered by a separate energy pile, remained snow free the entire time whereas the side with the 30 cm spaced tubes (left), which is powered by the test pile, was able keep the deck above freezing and melt the snow after the storm.

4.5. THERMO-MECHNICAL RESPONSE OF THE ENERGY PILE

4.5.1. Heat Extraction (Bridge Deck Heating)

The following results were obtained from the bridge deck deicing (heat extraction) test that occurred during February 23-26, 2015. During this period of time, the system was operated twice, as shown in Figure 4-4, pumping fluid at a rate of 13.2 L/min (3.5 gal/min). By having two operations, the temperature and stress response as well as their successive response to the second operation can be observed. The temperature changes in the pile at select thermistor locations in the silty sand and shale layers are given in Figure 4-6. Observe that the temperatures do not completely recover between the two operations and that after the second operation, the temperatures have still not completely recovered after 48 hours. This demonstrates the necessity of thermal recharge during the summer. During successive operations, the efficiency of the system will decrease if the temperature of the ground has not sufficiently recovered. However, if the temperature of the ground can be increased, the efficiency lost from not having the temperatures completely recover is reduced.

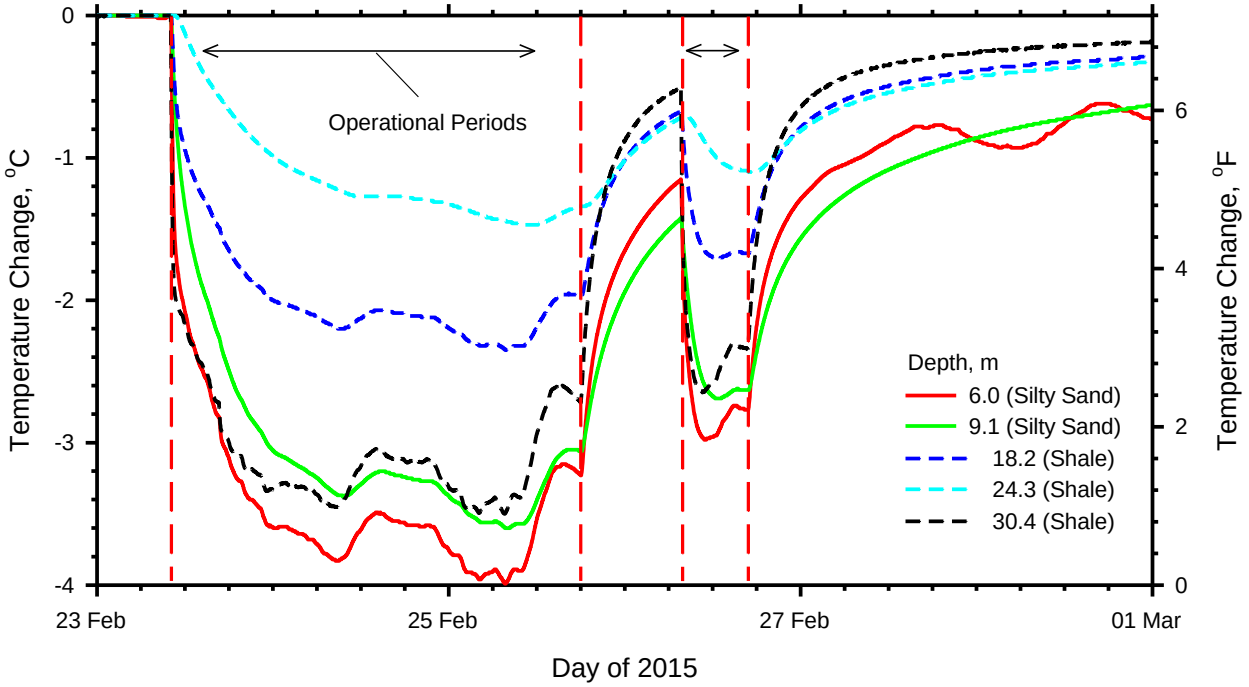

Figure 4-6. The temperature change in the pile at select thermistor locations in the silty sand and shale layers for the bridge deck deicing test (i.e. heat extraction operation). Note the recovery period between the two operations.

4.5.1.1. Development of Thermal Loads Caused by Pile Cooling (Heat Extraction)

The thermal loads were determined using the values of corrected blocked strain and tangent pile moduli as mentioned previously. The development of the thermal loads along the pile for the first operation are shown for various time steps in Figure 4-7. Note that geotechnical engineering convention is used when referring to stresses/loads so that negative values refer to tensile stresses/loads and positive values refer to compressive stresses/loads. The temperature change in the center of the pile for each of the times in Figure 4-7 is given in Table 2-1. The maximum load occurred approximately 24 hours after the start of operation. By the time the operation ended 56 hours after the start, the load profile had decreased from the maximum and is very similar to the profile that occurred 6 hours after the start.

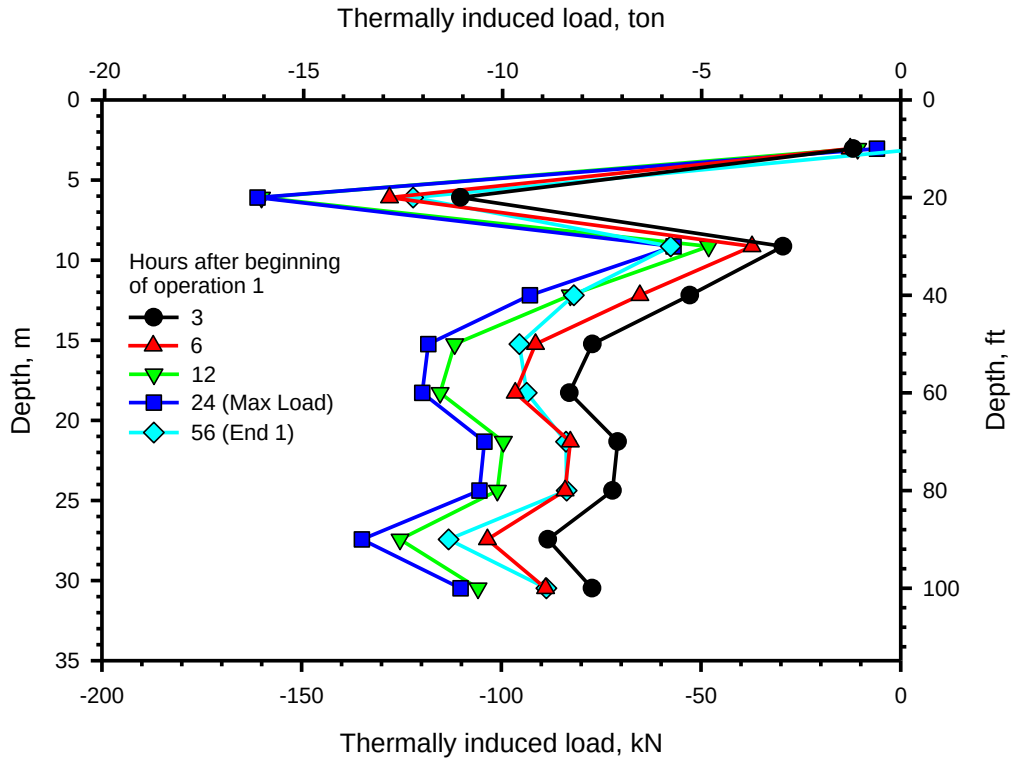

Figure 4-7. Thermally induced loads in the pile at certain points in time during the first operation of the bridge deck deicing test (i.e. heat extraction operation).

Table 4-2. Temperature change in the center of the pile during the first and second operations of the bridge deck deicing test.

Operation	Hours after start of operation	Temperature change at pile center, °C
1	3	-2.31
	6	-2.68
	12	-3.22
	24	-3.38
	56	-2.72
2	0	-0.51
	1.3	-2.30
	3.3	-2.64
	11.3	-1.34

4.5.1.2. Re-Initiation and Relaxation of Thermal Loads

After operating for 56 hours, the first operation ended. The second operation began after a 13.5 hour recovery period. The thermal loads developed during the second operation are shown in Figure 4-8. The points in time were selected based on the temperature change in the center of the pile such that they are similar to the ones from the first operation. The temperature change at the pile center is given in Table 4-2. Note that the load profile was not completely zero when operation 2 began and the reasons for this

will be discussed later. Also note that the load profile at the end of operation 2 is less than the maximum observed load, which occurred 3.3 hours after the start of the second operation and is similar to the load profile observed 6 hours after the start of operation 1. The maximum load experienced during the second operation is less than that of the one that occurred during the first operation.

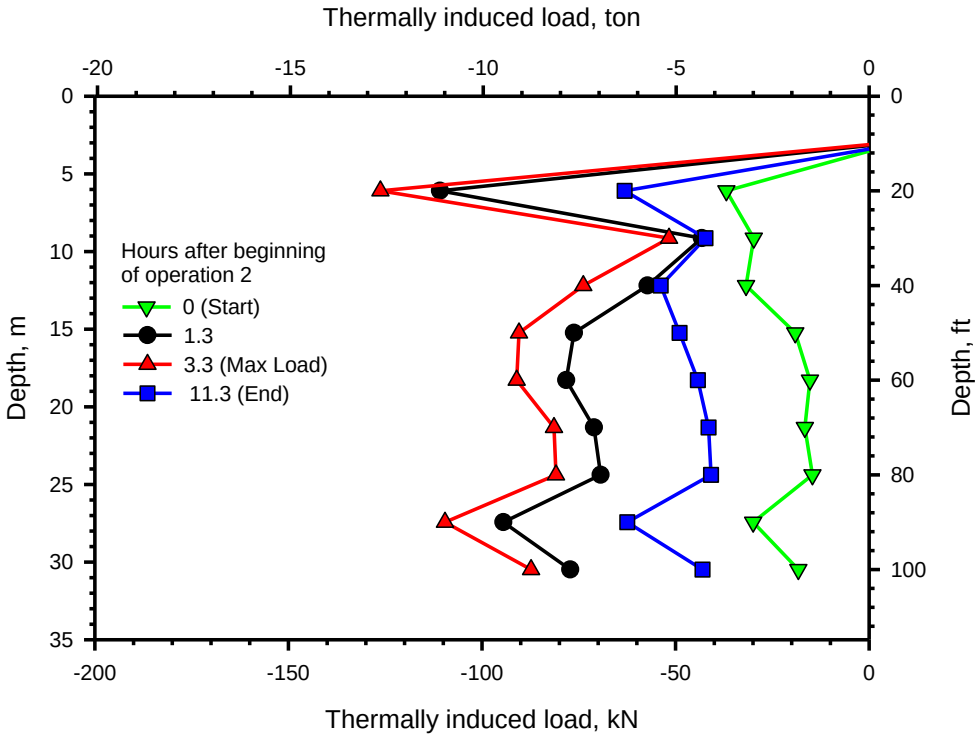

Figure 4-8. Re-initiation of thermal loads during the second operation of the bridge deck deicing test (i.e. heat extraction operation).

The relaxation of the thermal loads in the pile after the second bridge deck deicing operation ends is presented in Figure 4-9 and the temperature change at the pile center after the first and second operations is given in Table 4-3.

Table 4-3. Temperature change in the center of the pile after the end of the second operation.

Operation	Hours after end of operation	Temperature change at pile center, °C
1	0	-2.72
	2	-1.57
	12	-0.56
2	0	-1.34
	2	-0.94
	12	-0.42
	24	-0.29
	48	-0.20

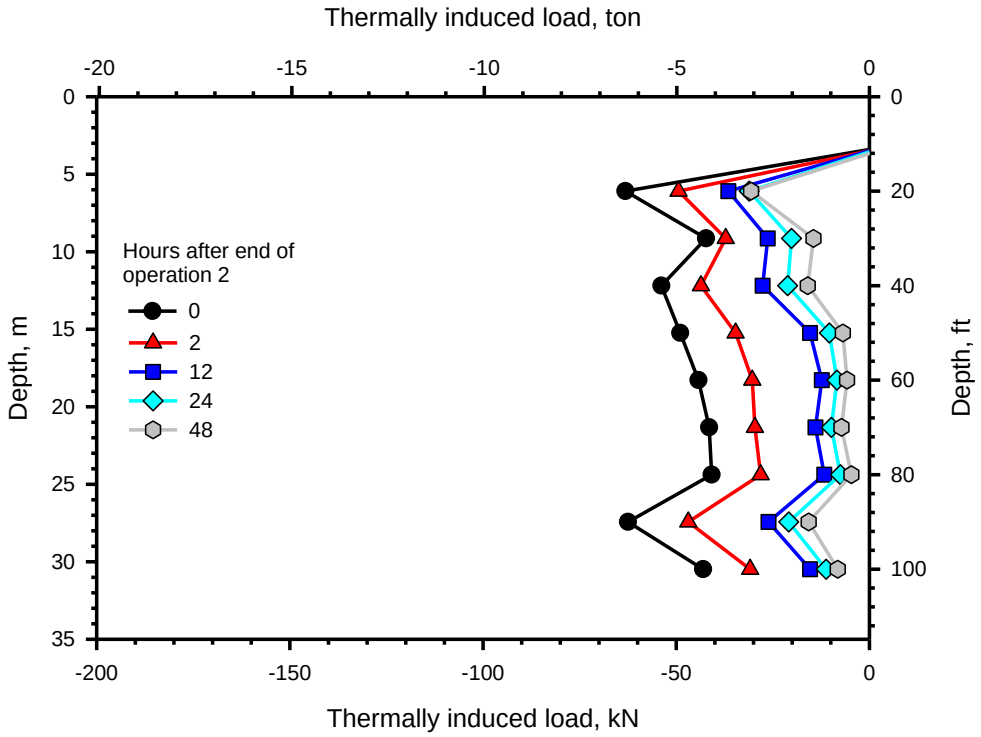

Figure 4-9. Relaxation of thermal loads in the pile after the second operation of the bridge deck deicing test (i.e. heat extraction operation).

4.5.1.3. Discussion of Results

Several observations can be made from the results during operation 1. The first is that the development of thermal loads in the pile occurs relatively quickly as roughly three-quarters of the maximum thermal load is observed just six hours after operation begins. This is directly related to the temperature decrease in the pile (Figure 4-6), which occurs almost immediately after operation begins. Secondly, the thermal loads in the pile remain relatively constant during operation with the thermal load profile at 12 hours being very similar to the thermal load profile at 24 hours (Figure 4-7). Again, this is related to the fact that the temperature change in the pile is relatively constant during this period of operation as well. The load profile at 56 hours, which is when operation 1 ends, is lower than the profiles at 12 and 24 hours due to the fact that the temperature change in the pile is not as great (see Table 4-2). Thirdly, the largest loads are seen at the 6.0 m depth. The 6.0 m depth is located in the middle of the section of the pile that contains a steel casing and due to the high tangent moduli of the pile in this section (because of the steel casing), relatively little strains can produce high values of stresses, as observed. Finally, the loading regime in the shale layer is relatively constant. The confinement and stiffness of the shale works to produce this more uniform load profile.

As operation 2 begins, temperature changes in the pile center that are similar to those that occurred during operation 1 produce similar load profiles to those observed in operation 1. The maximum load profile that occurred during operation 2 is less than that which occurred during operation 1, and is due to the lower temperature change in the pile.

After operation 1 ends, the loads in the pile quickly decrease. By the time the second operation begins, which is 13.5 hours after operation 1 ends, the loads have not fully recovered (that is, retreated back to zero). This is partly due to the fact that the temperatures have also not fully recovered after operation 1.

12 hours after the end of the second operation, most of the load in the pile has dissipated, however the rate at which it dissipates decreases as 48 hours after the end of operation 2, the loads within the pile have still not completely recovered.

The highest thermal load in the pile is -170 kN (tensile) and occurs at a depth of 6.0 m. This is 13% of the estimated maximum pile capacity magnitude (1334 kN compression). At 6.0 m depth, it is unlikely that enough of the load will have been taken by the soil above for the axial load to be low enough that the additional thermal load will cause the axial load to become tensile. However, the loads in the shale layer are between 100-120 kN. Under actual loading conditions, it is entirely possible that enough of the load will have been shed above for the tensile load from cooling to lead to tensile stresses in the lower portion of the pile, which would generate negative shaft resistance and increase the load in the upper portion of the pile.

4.5.2. Thermal Energy Injection

As mentioned previously, one of the ways in which ground-source bridge deck deicing systems can be made more efficient is by operating during the summer to inject thermal energy into the ground. When thermal heat energy is injected, the reverse happens from when energy is extracted. Specifically, the temperatures in the pile increase and it experiences compressive loads. Thermal injection operations were performed during the summer of 2014. Generally, each operation lasted between six and twelve hours during the day while the bridge deck was at its warmest. The system was then shut off during the night and then, depending on the weather conditions, operated again the following day. Thus, there was a cyclic behavior to these operations resulting in temperature fluctuations within the pile that resulted in the development and then relaxation of thermal loads. The results from a typical 48 hour period where the system was operated and then left idle and then operated again the following day are presented. The system was operated for ten hours on May 26, 2014 from 10:00 to 20:00. It was operated the following day, May 27, 2014 from 11:00 and lasting until 20:00. The temperature change observed in the pile at certain depths within the silty sand and shale layers during this time is shown in Figure 4-10.

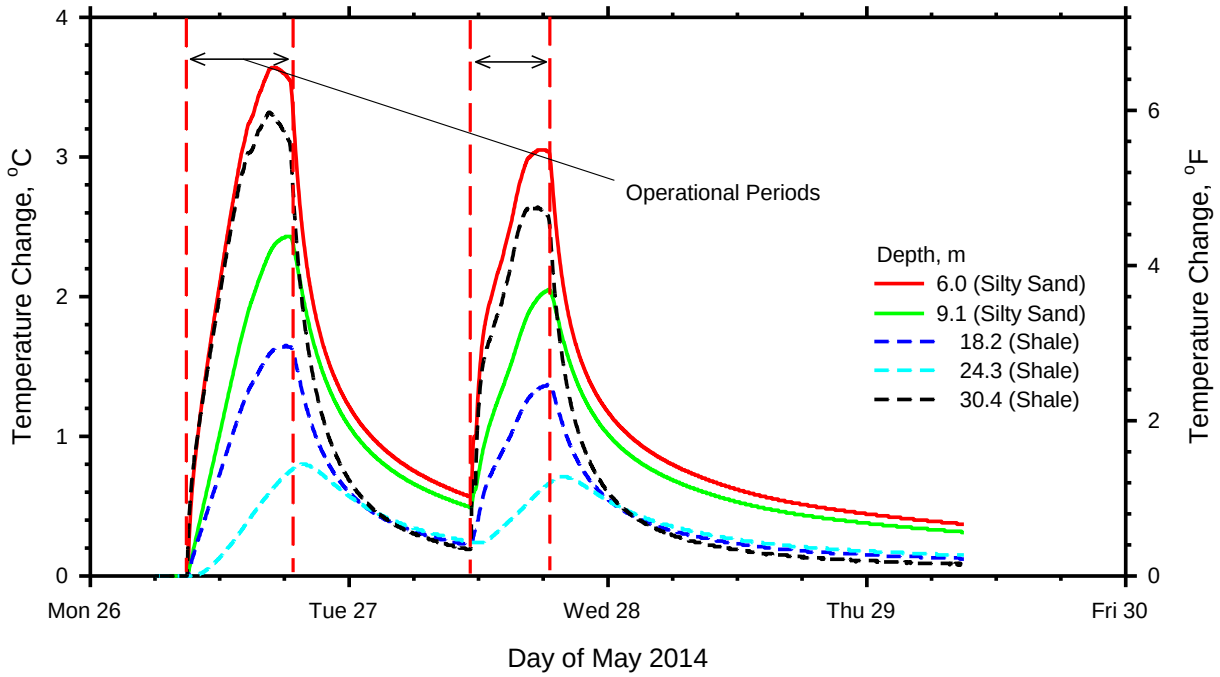

Figure 4-10. The change in temperature in the pile at select depths within the silty sand and shale layers during two recharge operations (i.e. heat injection operation) on successive days.

4.5.2.1. Development of Thermal Loads Caused by Pile Heating (Heat Injection)

The thermal loads at select points in time for the first operation is shown in Figure 4-11 and the temperature change at the pile center is given in Table 4-4 for operations 1 and 2. The maximum load was observed approximately 6 hours after the operation began. Operation 1 ended 10 hours after it began and the load profile at 10 hours is similar to the one at 2 hours.

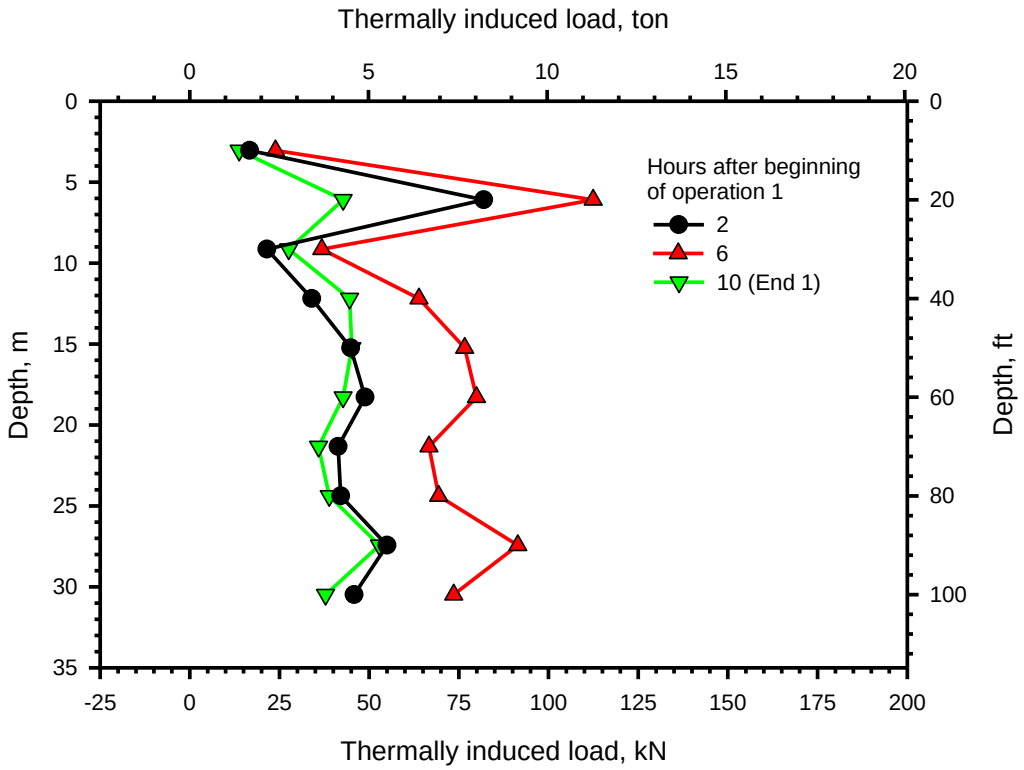

Figure 4-11. Thermally induced loads in the pile at certain points in time during the first operation of the heat injection test.

Table 4-4. Temperature change in the center of the pile during heat injection operations.

Operation	Hours after start of operation	Temperature change at pile center, °C
1	0	0.01
	2	2.00
	6	3.24
	10	1.75
2	0	0.19
	3.3	2.00
	6	2.63
	8	2.11

4.5.2.2. Re-Initiation and Relaxation of Thermal Loads

There was a 15 hour break between the first and second operation. The second operation also caused the development of thermal loads as shown in Figure 4-12. The thermal loads were similar in magnitude to those of operation 1 for similar temperature changes at the pile center. A 2.00°C temperature change occurred 2 hours after the beginning of operation 1 and 3.3 hours after the end of operation 2 (see Table 4-4). Both of the load profiles are similar. Similar to the first operation, the maximum load profile for the second operation also occurred about 6 hours after the start of operation, though it was not as great as the maximum load from the first operation.

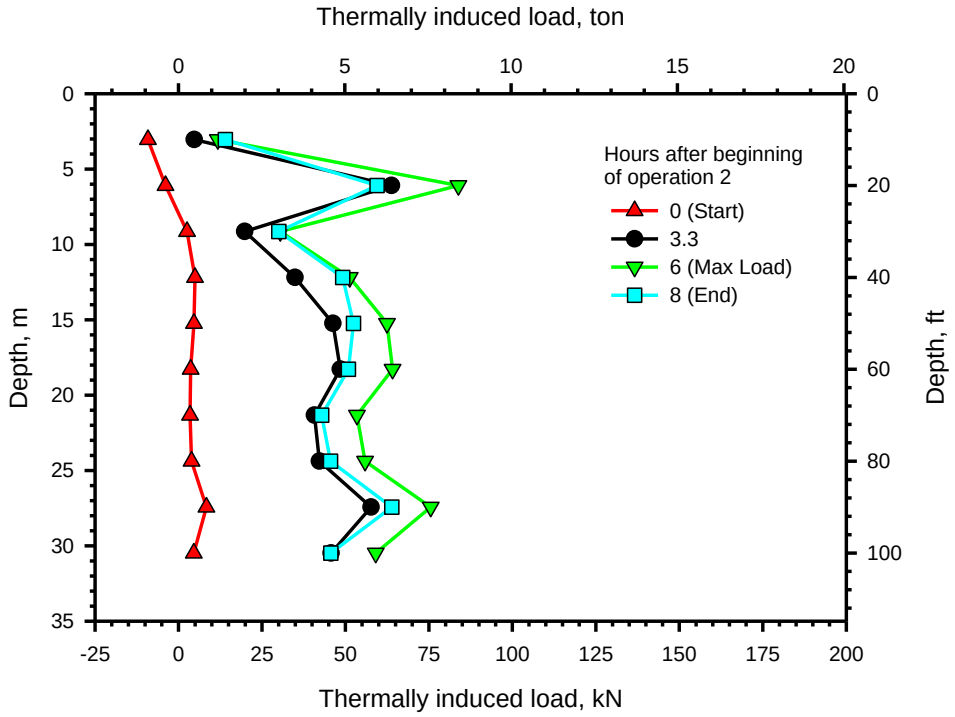

Figure 4-12. Re-initiation of thermal loads during the second operation of the heat injection test.

The relaxation of the loads in the pile after the end of the second operation is shown in Figure 4-13. The load profile at the end of operation 2 is slightly larger than the final load profile from operation 1 as is the temperature change in the pile center (Table 4-5). In comparison with heat extraction, after the end of 24 hours the absolute value of the temperature change in the pile center is less (0.13°C as compared to 0.29°C). In fact, the absolute value of the temperature change is greater 48 hours after heat extraction than 35 hours after heat injection. This is most likely related to the amount of time the system was operated as the amount of energy extracted during the heat extraction tests is much greater than the amount of energy injected during the heat injection tests.

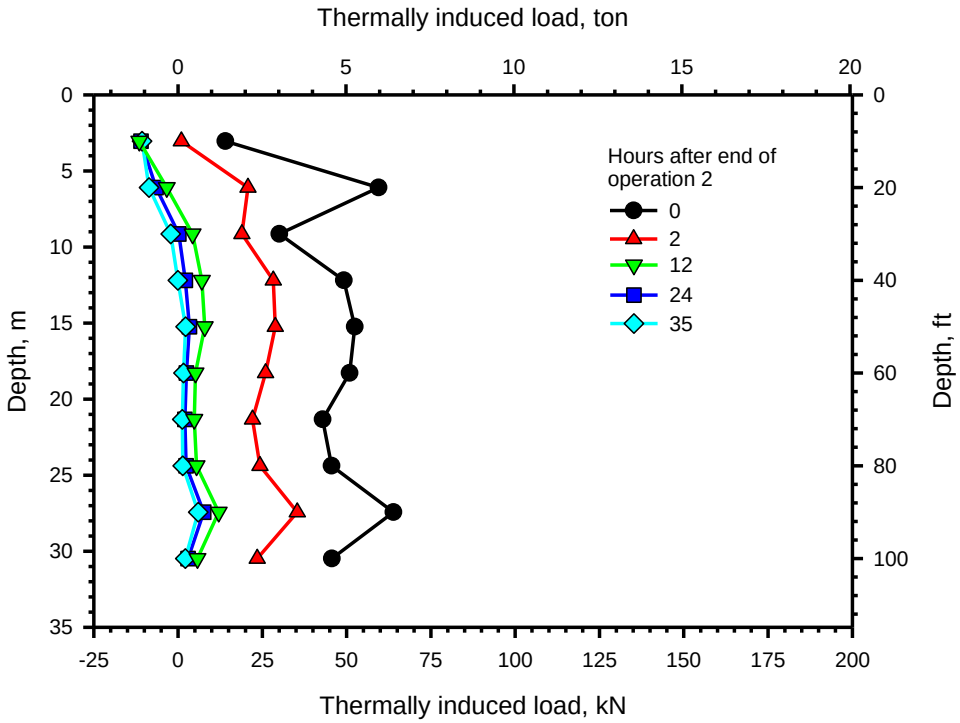

Figure 4-13. Relaxation of thermal loads in the pile after the second operation of the heat injection test.

Table 4-5. Temperature change in the pile center at certain points in time after the end of operations 1 and 2 for heat injection.

Operation	Hours after end of operation	Temperature change at pile center, °C
1	0	1.75
	2	1.03
	12	0.5
2	0	2.11
	2	1.1
	12	0.27
	24	0.13
	35	0.09

4.5.2.3. Discussion of Results

Several observations can be made from the results of heat injection. First, the results for heat injection almost mirror the results for heat extraction. In this case, the maximum temperature change observed in the pile center is about +3.3°C whereas it was -3.3°C for heat extraction. Likewise, there is a load concentration in most profiles at the 6.0m depth for heat injection, which is again due to the high pile tangent modulus resulting from the steel casing. Additionally, the strain and load profiles are relatively uniform in the shale layer. Also of interest is that the maximum stresses in the shale layer were in the range of -100 to -150 kN for heat extraction, whereas they are 100 to 120 kN for heat injection. One difference, however, is that due to the short operating period during heat injection (8 to 10 hours as

opposed to the 56 hours of operation for heat extraction), the loads in the pile did not have an opportunity to stabilize. The short operational period is also why the loads in the shale layer are more equal in magnitude to the loads at the 6.0 m, which was not the case with heat extraction. The shale layer has a higher thermal conductivity than the silty sand, thus the temperature changes are greater in that layer (see Figure 4-6 and Figure 4-10). Though the pile will eventually reach a roughly steady-state condition in terms of temperature change at the center, it takes longer than the 8 or 10 hours of operation to reach that point.

Several other observations can be made. First, the pile experienced a greater thermal load during the first operation as compared to the second. This is again related to the amount of induced temperature change in the pile as the temperature changes were greater during operation 1 than operation 2. When analyzing the recovery that occurs after the end of the second operation, the thermally induced loads have almost completely dissipated as well as the temperature differences at most depths (depths below 9.1 m) 35 hours after the end of operation. However, most of this reduction occurs in the first 12 hours after the end of operation as the load profile is only slightly greater than the one at 35 hours after the end of operation.

Also of interest is that the elevations between 3.0 m to 6.0 m depths along the pile experience negative (tensile) thermal forces after the end of each operation. These tensile stresses can be attributed to locked-in residual stresses after the heat injection operation ends. Mobilized shaft resistance due to the weight of the pile is reversed as a result of heat injection (see Figure 4-3) and a full-reversal is not achieved at the end of the heat injection operation and subsequent temperature dissipation. The reason that this is manifested as tensile stresses near the top of the pile is the lower level of mobilized stresses at these elevations. Residual stresses can easily reverse these smaller magnitude mobilized stresses resulting in tensile stresses. It should be understood that this issue would be different for a pile under structural load because the magnitude of mobilized shaft resistance will be different.

The maximum observed compressive load in the pile during these operations is 125 kN, and it occurs at the 6.1 m depth. While adding to the overall compressive load of the pile, it is unlikely that it will significantly affect the performance as the design load will be much less than the maximum load.

4.5.3. Comparison of Pile Heating and Cooling

Figure 4-14 shows the initial temperature profile in the pile and the temperature profiles that occur at the point of maximum observed load during the first operation of both the heat extraction and heat injection tests. Figure 4-15 presents the absolute value of the load in the pile for different changes in the pile center temperature. The load profiles were taken from the first operation for both pile heating and cooling. Additionally, they represent the first time the pile experiences that temperature change (that is, they represent the progressive heating/cooling of the pile). Note that it took 13.2 hours for the pile reach -3.38^{o}C temperature change during cooling, whereas it took 6.75 hours for the pile to reach +3.38^{o}C temperature change during heating.

The absolute values of the load profiles are remarkably similar for pile heating and cooling. They are most similar in the shale layer whereas the absolute values of the load during heating are slightly larger than those during cooling at lower temperature changes (≤2.0^{o}C) and less than those during cooling at higher temperature changes (>2.0^{o}C) in the silty sand layer.

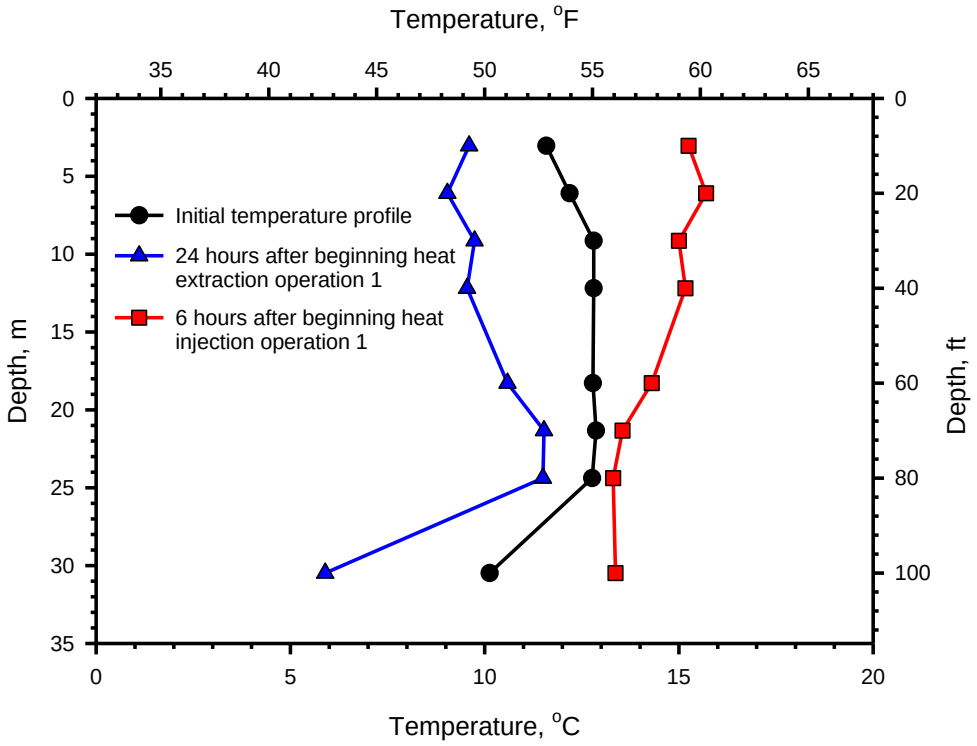

Figure 4-14. Comparison of the initial pile temperature profile with the temperature profiles occurring at the maximum observed load during heat extraction and heat injection.

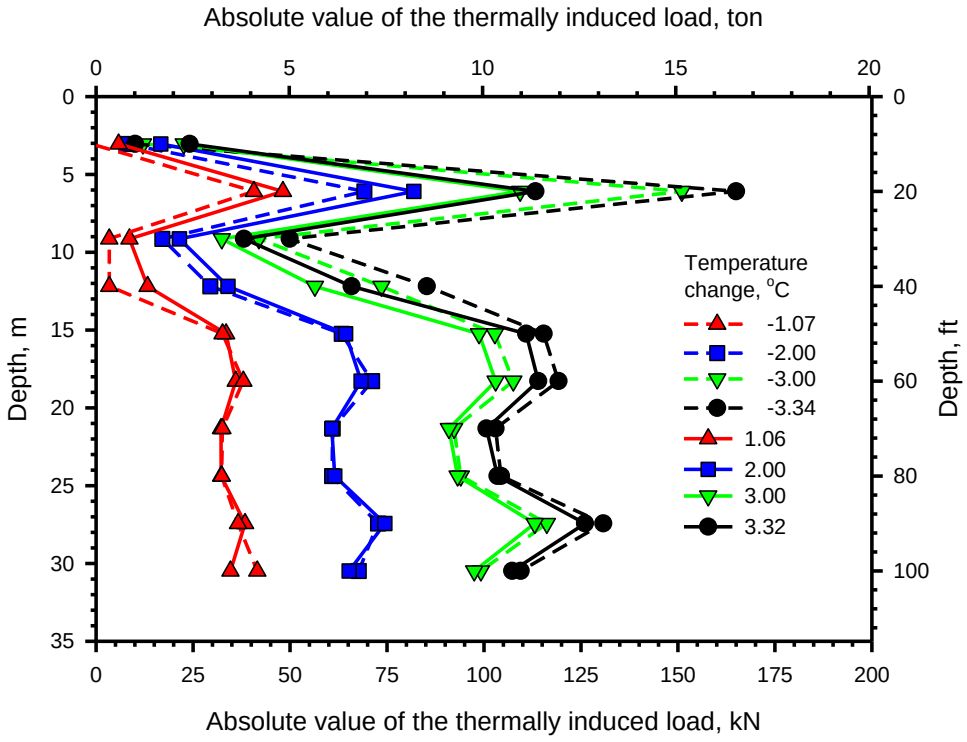

Figure 4-15. Comparison of the absolute values of the thermal loads for similar absolute values of temperature change in the center of the pile.

4.5.4. Comparison of Pile Response with other Thermo-Mechanical Field Tests

Figure 4-16 has been redrawn after Amatya et al. (2012) and Sutman et al. (2015) to include the results of the thermo-mechanical field tests presented in Abdelaziz (2013) while the pile was under load. The values shown are the axial stresses at the 6.0 m and 9.1 m depths. As shown, the axial stresses in the test pile at the 6.0 m depth for the given temperature changes are much larger than those observed from the other field tests. This is most likely related to the high pile tangent modulus at that depth. Also shown on the plot are lines representing constant axial stress increase with temperature change.

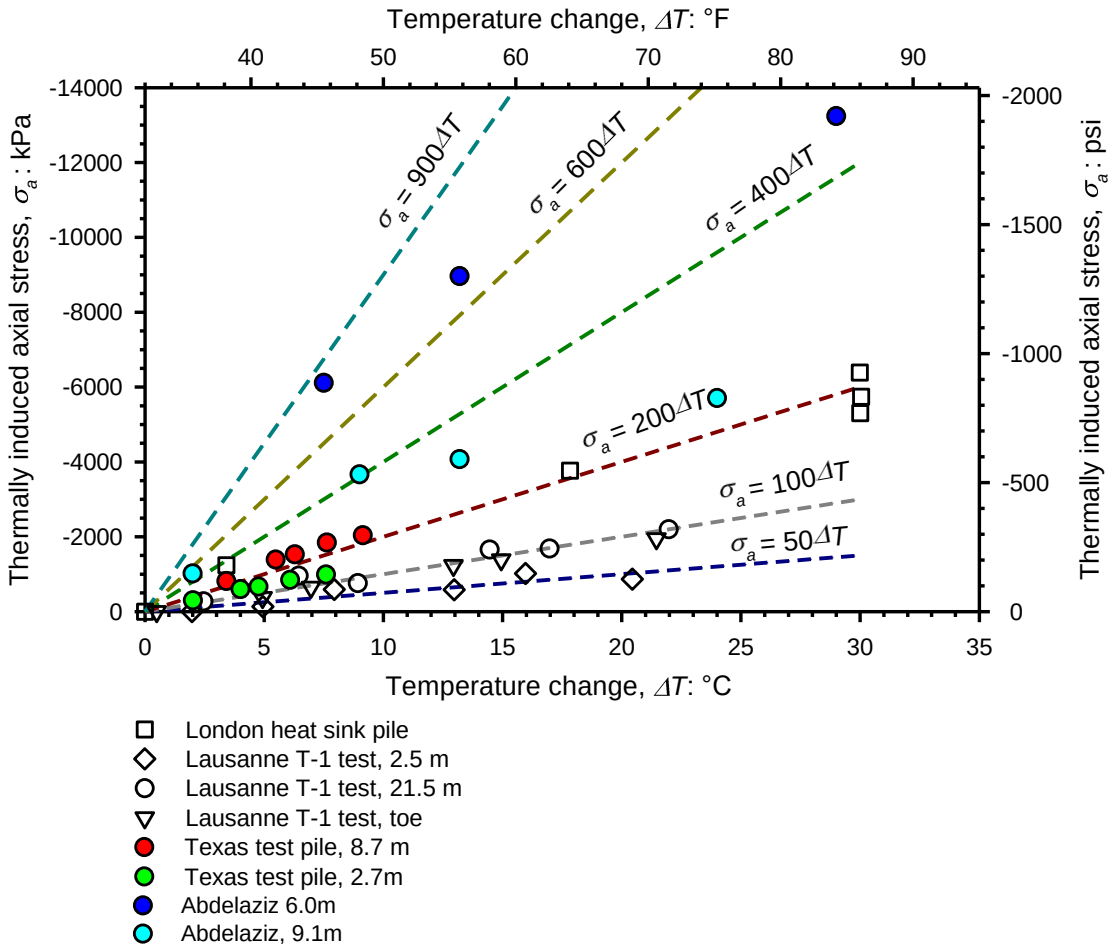

Figure 4-16. The thermally induced axial stress vs temperature change for the Virginia Tech test pile reported in Abdelaziz (2013) as compared to other field tests. Note that this figure follows the original developer's notation in that negative (-) values represent compressive stresses and positive (+) values represent tensile stresses. (Redrawn after Amatya et al. 2012 and Sutman et al. 2015).

Several of the previous energy pile load tests were performed by imposing large temperature variations on test these piles at extreme conditions. The tests that are presented in this paper are more reflective of regular operational conditions in which temperature variations are much lower compared to the previous field load tests. Therefore, as a result of the small temperature changes in the pile from the field tests presented in this paper, Figure 4-16 was redrawn by normalizing the y-axis by unit temperature change. This way the axial stress increase per unit temperature increase is shown along the y-axis. This value can be thought of as an equivalent thermal modulus and has units of stress per degree temperature change. This newly introduced parameter can be established as a new baseline to evaluate temperature-induced

stresses in an energy pile. Figure 4-17 shows the thermal moduli values of the previous field tests along with the thermal moduli values determined from the data of the heating field tests presented in this paper. Also shown in this figure are lines that represent the thermally induced axial stress per unit temperature change (thermal moduli) for fully fixed conditions for the piles presented in the figure. These lines are created by multiplying the pile tangent modulus by the thermal expansion coefficient of the pile and then dividing by unit temperature change. Because the pile tangent modulus is not constant with depth for the test pile used for the experiments in this paper, the lines representing the Virginia Tech pile gives the maximum stress under fully fixed conditions for only the 6.0 m and 9.1 m depths.

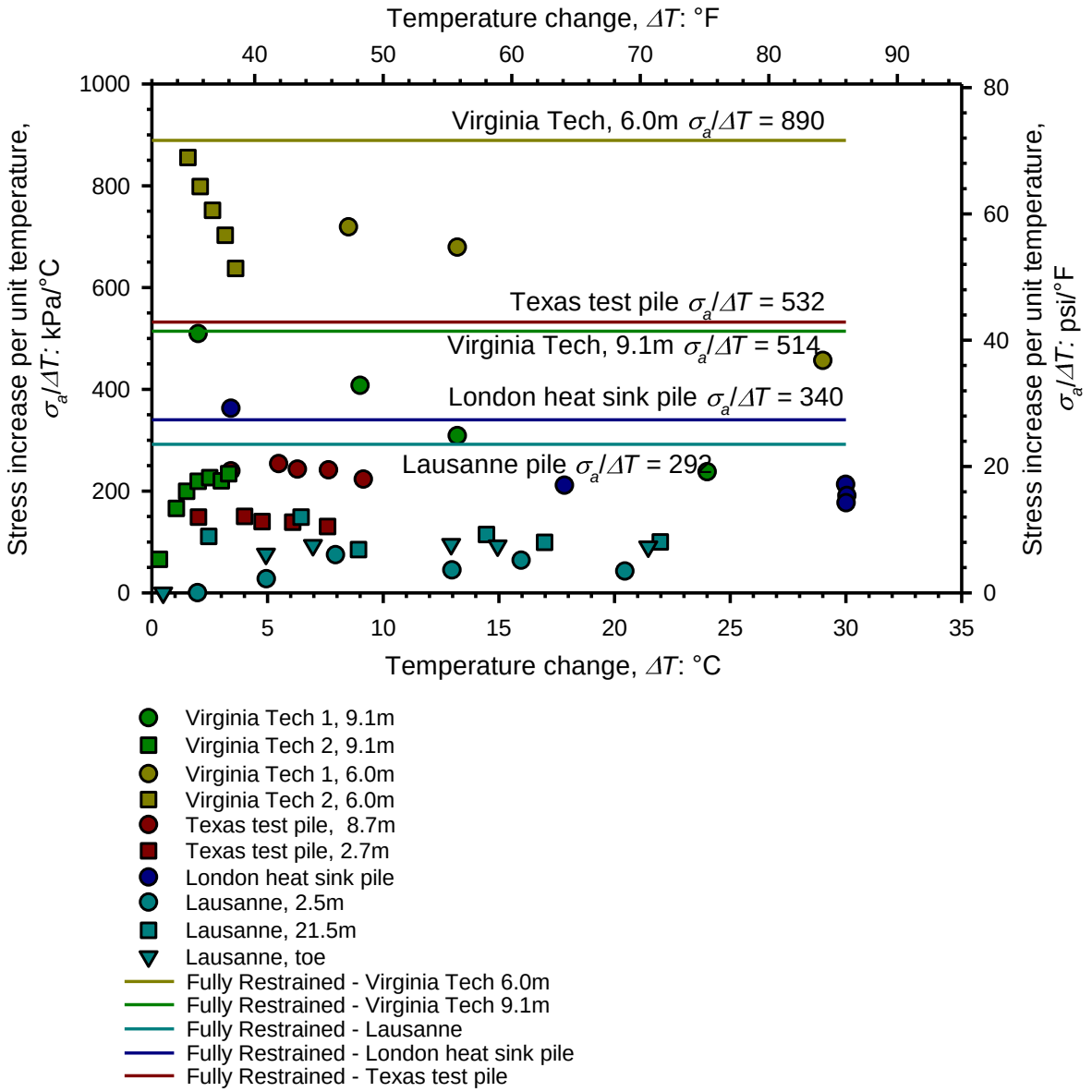

Figure 4-17. The thermal moduli values for the Virginia Tech field tests as compared to other reported field tests. Note that Virginia Tech 1 refers to the results reported in Abdelaziz (2013) and Virginia Tech 2 refers to the heat injection results from the tests presented in this paper.

From Figure 4-17, it is obvious that the thermal moduli values are much higher in the Virginia Tech test pile at the 6.0 m depth than in the piles from the other tests. This is, again, most likely from the high pile

tangent modulus value at that depth due to the presence of the steel casing, as explained earlier. The 9.1 m depth has thermal moduli values similar to a few of the other tests. Aside from the magnitude of the thermal moduli values, it is interesting to observe the variation in the thermal moduli for the different thermo-mechanical tests. The thermal moduli remains relatively constant for the two depths from the Texas test pile as well as the three depths reported for the Lausanne test pile, both of which were under load. The thermal moduli appears to gradually decrease for both the London heat sink pile and the Virginia Tech 1 pile at both depths. The thermal moduli decreases rapidly for the heat injection test (Virginia Tech 2) at the 6.0 m depth and actually increases at the 9.1 m depth. A possible explanation for the difference in trends at the two depths is that the stress initially develops in the section with the steel casing, which has a higher stiffness. As the pile progressively heats, other portions of the pile take proportionately more of the load, which is why the thermal moduli decreases in the section with the steel casing (6.0 m depth) and increases in the section below the steel casing (9.1 m depth), with a relatively lower pile tangent modulus. It is expected that at greater temperature changes under unloaded conditions that the thermal modulus would continue to decrease at the 6.0m depth, though not as rapidly. Furthermore, upon continued heating under unloaded conditions the thermal modulus would reach a maximum at the 9.1 m depth and then begin to decrease.

The fact that there is no load (the pile head is free to expand) for the heat injection test is clearly seen by the lower thermal moduli values when compared to the results from Virginia Tech 1, which was under load, at the 9.1 m depth. It is unfortunate that the lowest temperature change reported in Abdelaziz (2013) was 7.5^{o}C for the 6.0 m depth as it would be interesting to directly compare the trend in thermal moduli values under loaded and unloaded conditions at the 6.0 m depth. However, after beginning with roughly the same value, the trends indicate that the thermal moduli values decrease much quicker under unloaded conditions than loaded conditions at the 6.0 m depth.

4.6. CONCLUSIONS

Several conclusions can be drawn from this study. First, it has been clearly shown that energy piles can be used for the deicing of bridge decks without the aid of a heat pump. The energy extracted from the ground was sufficient to keep the surface temperature of the bridge deck above freezing for wider circulation tube spacing (30 cm), and was enough to keep the deck completely snow free for closer circulation tube spacing (20 cm). The next step is to match the energy demand from the bridge deck (which will vary depending on the storm) to the capacity of the energy piles to determine how many energy piles will be required for successful operation.

Secondly, the use of energy piles for bridge deck deicing (heat extraction) induces thermal loads in the pile, which are tensile. During thermal recharge operations (heat injection) in the summer, the induced thermal loads are compressive. For the range of temperature changes and thermally induced loads experienced, the absolute values of the temperature change in the pile are roughly the same for energy injection and extraction, thus the absolute values of the load profiles are similar. These loads develop from the opposing soil resistance (Figure 4-3), which may be an important soil-pile interaction issue. After each operation of either bridge deck deicing or thermal recharge, the thermal strains and loads dissipate as the temperatures recover and approach their starting value. However, this recovery is sometimes not complete between successive operations.

The thermal modulus was introduced as a parameter that can be used to characterize the development of thermally induced axial stresses in energy piles. Thermal moduli values differ for the same pile under loaded and unloaded conditions and can change for different values of temperature change. For the test pile presented in this paper, when compared with other tests performed on the same pile under loaded conditions, the thermal moduli values are both lower and display different trends as the temperature

change increases. Furthermore, they appear to more rapidly decrease in stiffer sections of the pile whereas they initially increase in less stiff sections.

Overall the results presented in this paper serve to further the understanding of thermally induced axial stresses in energy piles for different applications. The field deicing and thermal recharge experiments presented in this paper provide an example of the thermal loads expected from these types of operations. Future research may be necessary to evaluate the long term effects of these cyclic heat injection, recovery, and recharge operations that repeat seasonally. Even though no pile settlement was observed as a result of these operations, this case relates to a pile which is not under any load and only considers a relatively short testing period of 3-4 years. Thus, the long term behavior of these systems needs to be further investigated.

4.7. REFERENCES

Abdelaziz, S. L. (2013). "Deep Energy Foundations: Geotechnical Challenges and Design Considerations." Ph.D. Thesis, Virginia Polytechnic Institute and State University.

Amatya, B. L., Soga, K., Bourne-Webb, P. J., Amis, T., and Laloui, L. (2012). "Thermo-mechanical behavior of energy piles." Geotechnique, Vol. 62, pp. 503-519.

Bourne-Webb P.J., Amatya B., Soga K., Amis T., Davidson C., and Payne P. (2009). "Energy Pile test at Lambert College, London: Geotechnical and Thermodynamic Aspects of Pile Response to Heat Cycles." Geotechnique, Vol. 59, No. 3, pp. 237-248.

Bowers, Jr., G. and Olgun, C. (2014). "Ground-Source Bridge Deck Deicing Systems Using Energy Foundations." Geo-Congress 2014 Technical Papers: pp. 2705-2714.

Granata, R.D., and Hartt, W.H. (2009). "Integrity of Infrastructure Materials and Structures." FHWA-HRT-09-044, Federal Highway Administration, Washington, D.C.

Hoppe, E.J. (2000). "Evaluation of Virginia's First Heated Bridge." Virginia Transportation Research Council, Charlottesville, VA.

Koch, G.H., Brongers, P.H., Thompson, N.G., Virmani, Y.P, and Payer, J.H. (2002). "Corrosion Costs and Prevention Strategies in the United States." Report No. FHWA-RD-01/156, Federal Highway Administration, Washington, D.C., 2002.

Kusuda, T., and Achenbach, P.R. (1965) "Earth temperature and thermal diffusivity at selected stations in the United States." ASHRAE Transactions, Vol. 71, Part 1, pp. 61-74.

Liu, X., Rees, S. J., and Spitler, J. D. (2007a). "Modeling snow melting on heated pavement surfaces. Part I: Model development." Applied Thermal Engineering, 27(5-6), 1115-1124.

Liu, X., Rees, S. J., and Spitler, J. D. (2007b). "Modeling snow melting on heated pavement surfaces. Part II: Experimental validation." Applied Thermal Engineering, 27(5-6), 1125-1131.

Minsk, L. D. (1999). "Heated Bridge Technology: Report on ISTEA Sec. 6005 Program." FHWA, U.S. Department of Transportation, 51.

Sutman, M., Olgun, C. G., and Brettmann, T. (2015). "Full-Scale Field Testing of Energy Piles". Proceedings of the 2015 International Foundations Congress and Equipment Expo, pp. 1638-1647.

Tuan, C.Y. (2008). "Roca Spur Bridge: The Implementation of an Innovative Deicing Technology." Journal of Cold Regions Engineering, Vol. 22, No.1, pp. 1-15.

Yoshitake, I., Yasumura, N., Syobuzako, M., and Scanlon, A. (2011). "Pipe heating system with underground water tank for snow thawing and ice prevention on roads and bridge decks." *Journal of Cold Regions Engineering*, 25(2), 71-86.

5. NUMERICAL AND ANALYTICAL INVESTIGATION OF SUBSURFACE RESPONSE TO HEAT EXCHANGE OPERATIONS IN SHALLOW GEOTHERMAL ENERGY SYSTEMS

5.1. ABSTRACT

Ground-source heating of bridge decks is a promising technology that can drastically reduce the use of corrosive and environmentally unfriendly deicing salts. In this concept, the foundation system of the bridge substructure and the approach embankment are designed to access the ground as a renewable energy source. During the winter, heat energy is extracted from the ground and can be circulated as warm fluid through the tubing system within the bridge deck slab to prevent icing and freezing. Heat energy can be collected in the summer through circulation tubes embedded in the concrete bridge deck and stored in the ground for use in the winter. This paper presents experimental results from several tests performed using a model-scale bridge deck connected to energy piles. The results from the experiment were used in an analytical model of the ground to determine the ground's thermal properties. The finite line source, multi-layer analytical model introduces corrections for changing layer-dependent heating rates over time as well as atmospheric temperature influence in the upper soil layer. The ground thermal properties were then implemented in a 3D numerical model that was validated with the experimental tests. The utility of the analytical model in predicting temperature change as a result of heating operations consisting of differing lengths and rates within an energy pile field is shown.

5.2. INTRODUCTION

Ground-source heat pump (GSHP) systems are becoming an increasingly popular method of more efficiently heating and cooling buildings. GSHPs rely on shallow geothermal energy (SGE) to more efficiently operate as compared to traditional heat pump systems (Lund and Boyd 2016). SGE takes advantage of the relatively constant temperature of the ground that exists below a depth of 6-10 m. The applications of SGE, however, have the potential of extending beyond just GSHP systems to being used in diverse applications such as grain drying, greenhouse temperature regulation, and bridge deck deicing (Bowers and Olgun 2016, Minsk 1999, Lund and Boyd 2016). Furthermore, SGE systems are being incorporated into foundation elements such as piles, to create energy foundations, which are dual purpose elements that can be used for foundation support as well as SGE extraction (Brandl 2006, Bourne-Webb et al. 2009, Wood et al. 2009).

GSHP systems work by using the ground as either an energy source or an energy sink. Due to the stable temperatures of the ground, which after a certain depth are roughly equal to the average yearly temperature (Kusada and Achenbach 1965), the ground is warmer than the atmospheric air in the summer and cooler in the winter, which provides a considerable advantage over air-to-air heat pumps. As SGE is accessed, typically in a closed-loop fashion by circulating fluid through boreholes or energy foundations, the temperature of the ground changes. Depending on the type of operation, this change can serve to either increase or decrease the efficiency of the system. For example, during building heating, the ground experiences cooling as energy is withdrawn. As the ground continues to cool, the efficiency of the system decreases. However, a lower ground temperature results in more efficient operation for building cooling, which uses the ground as a heat sink. As long as heating and cooling operations are balanced and equal amounts of energy are being extracted and injected into the ground over a given year, long-term system efficiency is maintained. Problems arise when the loads are unbalanced and the ground is used primarily

for heating or cooling as the ground will progressively cool or heat, respectively, decreasing system efficiency.

Unbalanced loads can be problematic in climatic regions that are predominately hot (such as Miami) or cold (such as Chicago) as well as in applications that only require energy for a specific task, such as heating for bridge deck deicing. Thus, in order to accurately estimate the long-term performance of these systems, engineers need tools that predict the subsurface response in both the short and long terms.

This paper presents experimental results of the subsurface temperature response to field thermal conductivity tests (TCTs) and thermo-mechanical tests (TMTs). It also presents an analytical model that can be used to estimate the subsurface temperature response from such operations over the short and long terms. The model can account for non-homogenous subsurface materials and for non-constant heating and cooling loads. The model was validated using a numerical model and then used to replicate experimental subsurface responses from TCTs and TMTs.

5.3. BACKGROUND

Several tools and methods have also been developed to explore subsurface temperature change. Abdelaziz et al. (2014) developed a multilayer finite line source model for vertical heat exchangers. The model can account for multiple homogenous horizontal layers as opposed to just one and is further explained in subsequent sections. The model was validated with a finite element model and requires a constant heating rate. Although a significant improvement over the previous finite line source models, it is not capable of handling multiple operations of varying heating rates that would be performed during a year.

Ozudogru et al. (2014b) developed a 3D numerical model that is to be used for vertical heat exchangers. The model utilizes several simplifications regarding modeling fluid flow, symmetry, and domain discretization, which significantly decrease computational time. The results of the model were compared with those from an analytical model. The analytical model, while still assuming a homogenous subsurface, was able to account for varying heat rates. The 3D numerical model was validated in Ozudogru et al. (2014a) and compared with the results obtained by a finite difference model using the results from a thermal conductivity test. This model is implemented in this paper. While yielding good results, it is computationally inefficient to consider multiple heat exchangers and periods lasting longer than a few days, meaning it cannot be used to estimate the long-term performance of a borehole field or thermal pile group.

Several studies have examined the subsurface temperature change that is associated with SGE systems. Lazzari et al. (2010) examined the long-term performance of borehole heat exchanger (BHE) fields using 2-dimensional finite element models. In order reduce the models to 2D, a homogenous, infinite subsurface had to be assumed as well as negligible variation in the temperature distribution along the vertical direction. The authors considered a single BHE surrounded by infinite ground, a single line of infinite BHEs, two staggered lines of BHEs, and a square field of infinite BHEs. Using sine waves to represent the energy demand profiles, 50 years of operations were considered for different unbalanced cases. The authors concluded that long-term performance is negatively affected for every case except that of a single BHE, and especially for a square field of infinite BHEs.

Bowers et al. (2016) followed a similar approach to Lazzari et al. (2010) in using a 2D finite element model to represent a borehole grid. The purpose was to examine different injection and extraction scenarios

that would improve system performance for SGE system operation. Among their findings was that the average ground temperature within the vicinity of the BHEs could increase or decrease over time depending on both how much energy was injected/extracted as well as which boreholes were utilized. However, they only considered two years of operation.

De Paly et al. (2012) also examined the optimization of a BHE grid through the uneven distribution of heating loads. Their study considered 30 years of operation and employed a finite line source analytical model to represent the BHEs. Because of their assumption regarding a homogenous subsurface, they only considered a 2-dimensional cross section of the borehole grid. Beck et al. (2013) used a similar model to optimize a system, but primarily through the geometrical rearrangement. The authors also considered uneven load distribution to the BHEs, and developed an optimum geometric configuration for both scenarios (with and without uneven load distribution) considering a 30 year design life. Their model did include the vertical dimension, however it was not needed because they assumed a single-layer homogeneous subsurface.

Dupray et al. (2014) proposed a 2D finite element solution in examining the thermo-hydro-mechanical aspects of an energy pile foundation. They considered a total of five years of operation with both conventional and higher temperature operation. Although much of their focus was on the mechanical performance of the system, they reported that higher ground temperatures do not significantly increase the thermal loss. That is, if a system's efficiency is measured by the ratio of extracted energy to injected energy, higher ground temperatures do not significantly impact the rate at which energy leaves the system. They also found that because of thermal losses, the ground temperature progressively decreased even under balanced heating and cooling loads.

5.4. EXPERIMENTAL INVESTIGATION

5.4.1. Site Description

The field test setup consists of a total of five micropiles, four of which are equipped with circulation loops along the full pile length for heat exchange. The micropiles are 25 cm (10 in) in diameter and were installed to a depth of 30.5 m (100 ft) at the Virginia Tech Geotechnical Research Facility. Two of the energy piles are instrumented to measure strains and temperatures. Additionally, there are 4 observation boreholes located around the piles to measure ground temperature. A plan view of the piles and boreholes is given is Figure 5-1. The subsurface consists of a silty-sand (SP-SM) overlaying a shale. The depth of the silty-sand layer varies from pile to pile and from observation well to observation well. Table 5-1 gives the depths of the silty sand layer at each location.

The piles are connected to a prototype 2.4 m x 3.0 m (8 ft x 10 ft) bridge deck as shown in Figure 5-2. The doubly reinforced 25 cm (10 in) thick slab is elevated from the ground to simulate heat loss from the bottom face similar to a bridge deck. The test slab is divided into two 1.2 m x 3.0 m (4 ft x 10 ft) sections with an insulated separation in between. A 5 cm (2 in) thick concrete cover is present on top of the upper level reinforcement. PEX tubes with 16 mm (5/8 in) inner diameter (ID) are connected to the upper level reinforcement with 20 cm (8 in) and 20 cm (12 in) horizontal spacing in each section. Insulation has been added to the sides to simulate an adiabatic surface. The slab is heavily instrumented with thermistors to monitor the variation of temperature in both slab sections at different horizontal and vertical extents near the tubes.

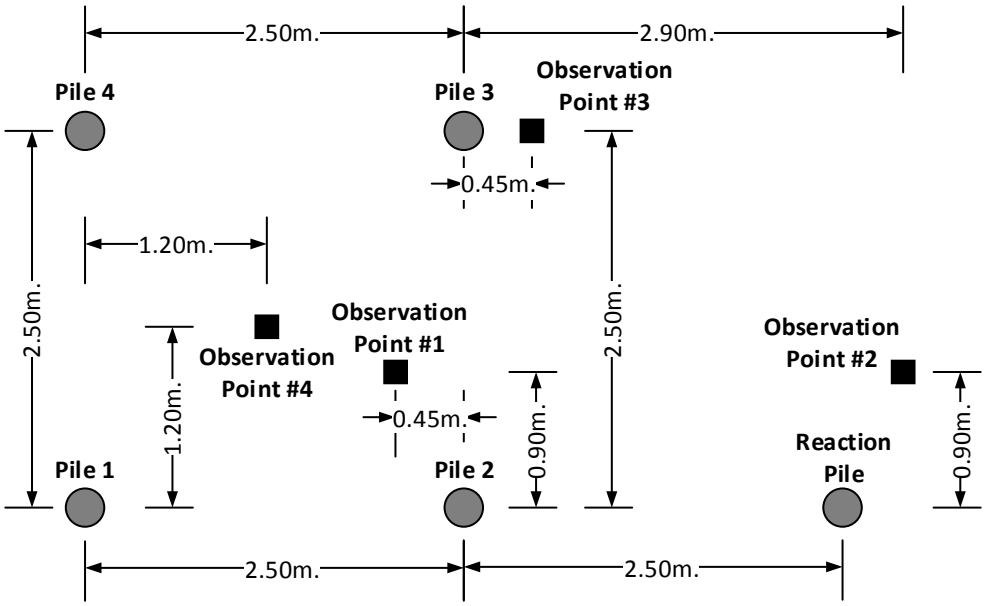

Figure 5-1. Plan view of pile and observation borehole layout.

Table 5-1. Depth of the silty sand layer at the piles and observation wells.

Location	Depth of Silty-Sand Layer (m)
Pile 1	12.8
Pile 2	14.3
Pile 3	17.4
Pile 4	18.9
Reaction Pile	14.3
OW 1	14
OW 2	17.7
OW 3	>15.3
OW 4	12.5

Figure 5-2. Photo of the prototype bridge deck during construction to show the circulation tubing connected to the reinforcement.

5.4.2. Thermal Conductivity and Thermo-Mechanical Tests

A total of seven tests were performed on the pile group reported in Abdelaziz (2013) and as described in Table 2. Five of these tests were thermal conductivity tests, where the heat injection rate was controlled and measured directly. The other two were thermo-mechanical tests where the pile was subjected to a variety of temperatures, thus the heat injection rate was not known directly. The heating rate can be determined, however, by using the difference between the inlet and outlet fluid temperatures and combined with the thermal and flow properties of the fluid. Figure 5-3 and Figure 5-4 show the inlet and outlet fluid temperatures over time for TMTs 1 and 2, respectively. Figure 5-5 and Figure 5-6 display the calculated heating rate of the pile. Observe that this changes over time. An approximation was used that took an average of the heating rate over a specified period of time. The approximations are also shown in Figure 5-5 and Figure 5-6. In total, the TCTs and TMTs span a period of over 200 days, which means that both the direct temperature response in the ground from the tests as well as the recovery periods in the ground can be observed. Additionally, because tests were performed on all 4 energy piles, and because there are four observation boreholes, many different radial distances from the heat source to the observation point in the ground can be observed.

Table 5-2. The thermal conductivity tests (TCT) and thermo-mechanical tests (TCT) performed on the pile group.

Start Date	Duration (hrs)	Type of Test	Pile	Heat Rate (W)
8/22/11	60	TCT	3	1845
10/29/11	310.2	TMT	2	See Figure 5-5
11/16/11	58.5	TCT	4	1852
11/23/11	384.7	TMT	2	See Figure 5-6
12/16/11	59.3	TCT	1	1810
1/18/12	3.4	TCT	2	4346
1/19/12	47.6	TCT	2	2603
2/18/12	49	TCT	2	2200

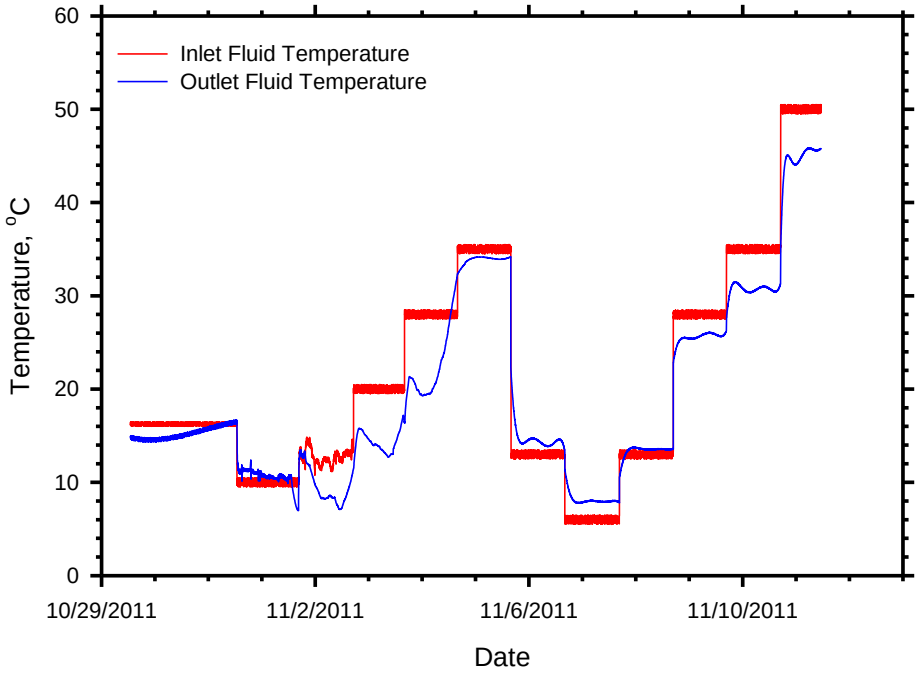

Figure 5-3. Inlet and outlet fluid temperatures for TMT-1.

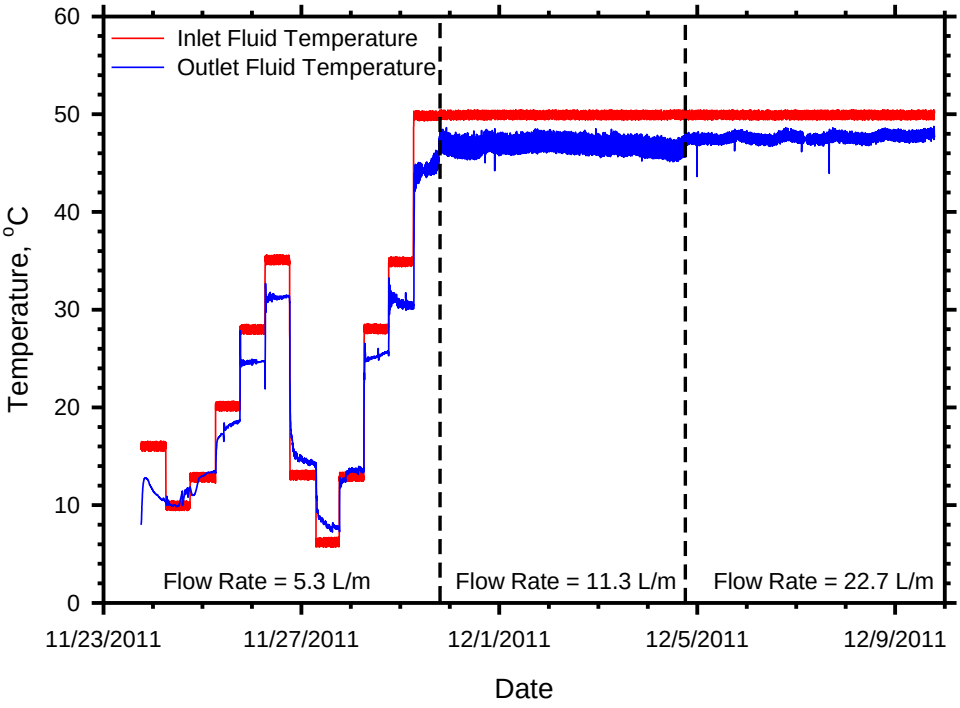

Figure 5-4. Inlet and outlet fluid temperatures for TMT-2.

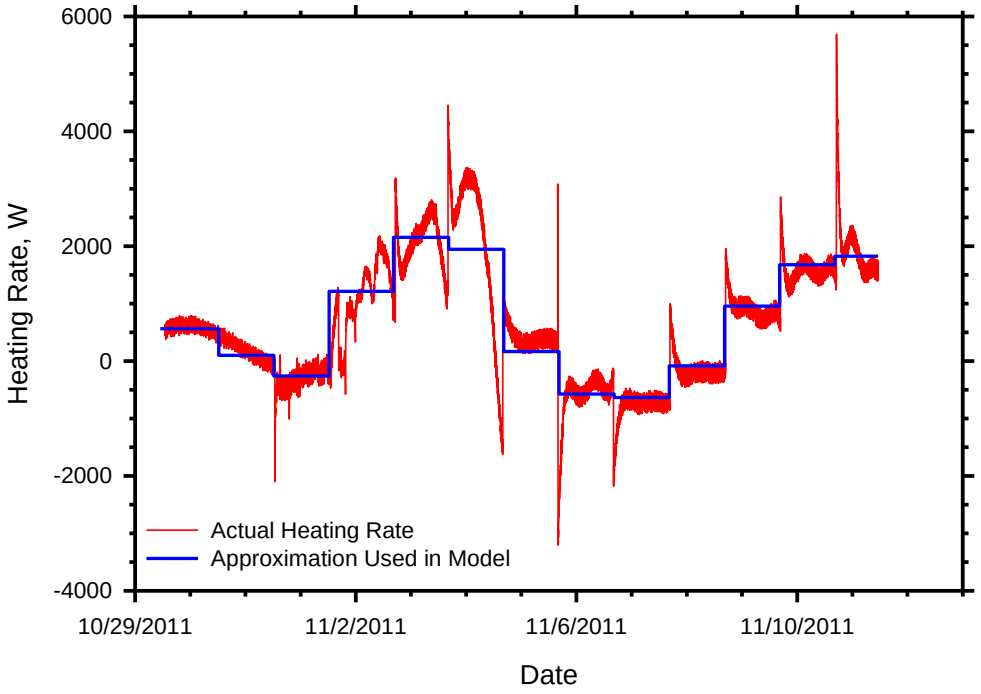

Figure 5-5. Actual heating rate as measured from the inlet and outlet fluid temperatures for TMT-1, as well as the approximated heat rate used in the analytical model.

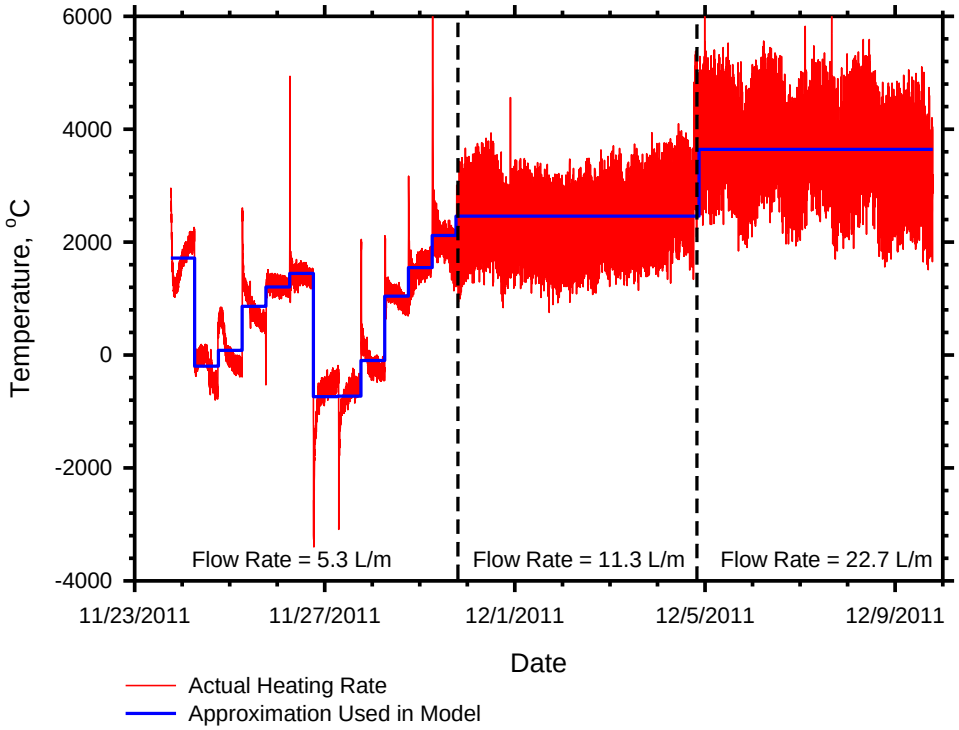

Figure 5-6. Actual heating rate as measured from the inlet and outlet fluid temperatures for TMT-2, as well as the approximated heat rate used in the analytical model.

5.5. ANALYTICAL MODEL DEVELOPMENT

In order to further study the ground's response to being heated and cooled, a multilayer finite line source model with variable heat rate was used. The development of that model is discussed in this section.

Table 5-3. Variables used in the analytical and numerical models.

Variable	Description
A	cross-section area (m^2)
C_A, C_B	factors in Equation 5-26
c_p	specific heat capacity (J kg^{-1} K^{-1})
d	diameter (m)
d_h	hydraulic diameter (m)
erfc	error function
Ei(*x*)	exponential integral
f_D	Darcy friction factor
h	depth of point of interest (m)
h_{int}	internal heat transfer coefficient (W m^{-1} K^{-1})
$(hZ)_{eff}$	effective heat transfer coefficient (W m^{-1} K^{-1})
H	length of heat exchanger (m)
k	thermal conductivity (W m^{-1} K^{-1})
Nu	Nusselt number
p	pressure (Pa)
q	heat (W)
q_{wall}	external heat exchange through pipe wall (W)
q'	heat flux per unit depth (W m^{-1})
q"	heat flux per unit area (W m^{-2})
r	radial distance between the heat source point and the point of interest (m)
Re	Reynold's number
S	distance that energy travels within a soil layer (m)
T	temperature (K)
T_{amp}	temperature amplitude (K)
t	time (s)
t_{now}	day of interest (d)
t_s	time scale (s)
t_{shift}	coldest day of the year (d)
V	volumetric flow rate (m^3 s^{-1})
u	tangential velocity (m s^{-1})
u	velocity field (m s^{-1})
x	depth of layer boundary (m)
z	depth of heat source point (m)
Z	wetted perimeter of pipe (m)
Greek Symbols	
α	thermal diffusivity (m^2 s^{-1})
ΔT(t)	temperature difference at time t (K)
ξ	distance between the actual point heat source and the point of interest (m)
ξ'	distance between the imaginary point heat source and the point of interest (m)
μ	dynamic viscosity (Pa s)
ρ	density (kg m^{-3})

Subscripts & Indices

avg	average
b	total number of energy sources
comp	composite section
ext	external
f	fluid
g	ground
i	soil layer number
j	energy source number
m	total number of soil layers
n	total number of heating loads
p	pipe
pi	pipe inner
po	pipe outer
tot	total
u	heating load number

The point heat source model was developed by Ingersol and Plass (1948) to determine the temperature change at a distance ξ and time *t* from a point source emitting constant heat *q*:

$$\Delta T(t) = \left(\frac{q\alpha}{k}\right)\left(\frac{1}{2\sqrt{\pi\alpha t}}\right)^3 \exp\left(-\frac{\xi^2}{4\alpha t}\right) \qquad \text{Equation 5-1}$$

The infinite line source (ILS) model is obtained by integrating the point heat source over a distance from negative infinity to infinity. Thus the temperature change at a given point a distance *r* from the line is:

$$\Delta T(t) = \frac{q}{4\pi k}\,\mathrm{Ei}\left(-\frac{r^2}{4\alpha t}\right) \qquad \text{Equation 5-2}$$

Zeng et al. (2002) then modified this approach to account for line sources of finite length by creating a heat sink *-q* of the same length as the finite line source and located directly opposite the ground surface boundary. This is obtained by integrating the line source over the length of the finite line and then adding the negative contribution from the imaginary source:

$$\Delta T(t) = \left(\frac{q}{4\pi k}\right)\int_0^H \left[\frac{\mathrm{erfc}\left(\sqrt{r^2+(z-h)^2}/2\sqrt{\alpha t}\right)}{\sqrt{r^2+(z-h)^2}} - \frac{\mathrm{erfc}\left(\sqrt{r^2+(z+h)^2}/2\sqrt{\alpha t}\right)}{\sqrt{r^2+(z+h)^2}}\right] dh \qquad \text{Equation 5-3}$$

Abdelaziz et al. (2014) accounted for the fact that when using the FLS model to simulate heat exchangers, the ground is usually not a homogenous medium and modified the FLS model to account for finite line heat sources in horizontal layers with different properties. This is done by accounting for the effects of both the primary and secondary segments of the heat exchanger on a point *r* distance from the heat source (Figure 5-7). The primary segment's contribution to the temperature change at a given point of depth *h* and within layer *i* is given as:

$$\Delta T_{1,i} = \frac{q}{4\pi k_i}\int_{x_i}^{x_{i+1}} \left[\frac{\operatorname{erfc}\left(\sqrt{r^2+(\xi-h)^2}/2\sqrt{\alpha_i t}\right)}{\sqrt{r^2+(\xi-h)^2}} - \frac{\operatorname{erfc}\left(\sqrt{r^2+(\xi+h)^2}/2\sqrt{\alpha_i t}\right)}{\sqrt{r^2+(\xi+h)^2}} \right] d\xi$$

Equation 5-4

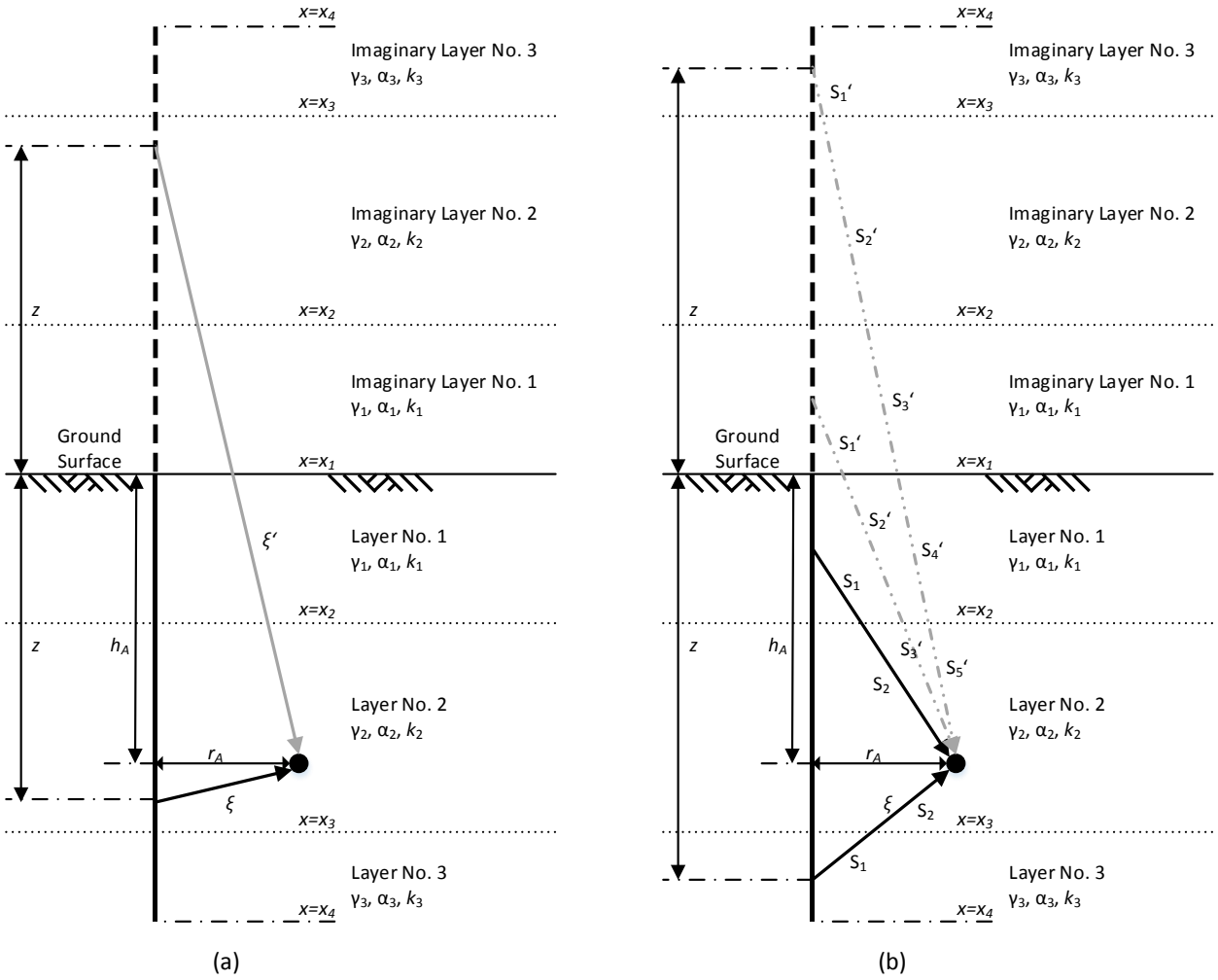

Figure 5-7. Multilayer finite line source model; (a) effect of the primary segment, and (b) effect of the secondary segments (redrawn after Abdelaziz et al. (2014).

The secondary segment's contribution is considered by creating composite properties for *k, γ, C_p,* and *α* based on the energy path of the point source along the line to the point of interest. The composite section properties are determined as follows:

$$\gamma_{comp.} = \sum_{i=1}^{N} \frac{S_i}{\sum S_i} \gamma_i$$ Equation 5-5

$$\frac{1}{k_{comp.}} = \sum_{i=1}^{N} \frac{(S_i / \sum S_i)}{k_i}$$ Equation 5-6

$$C_{p,comp.} = \sum_{i=1}^{N} C_{p,i} \frac{S_i \gamma_i}{\sum S_i \gamma_i}$$ Equation 5-7

$$\alpha_{comp.} = \frac{k_{comp.}}{C_{p,comp.} \gamma_{comp.}}$$ Equation 5-8

The contribution of all secondary segments to the temperature change at a point is given by:

$$\Delta T_{2,i} = \sum_{i=1}^{m} \frac{q}{4\pi} \int_{x_i}^{x_{i+1}} \left[\frac{\operatorname{erfc}\left(\rho / 2\sqrt{\alpha_{comp.} t}\right)}{k_{comp.} \rho} - \frac{\operatorname{erfc}\left(\rho' / 2\sqrt{\alpha'_{comp.} t}\right)}{k'_{comp.} \rho'} \right] d\rho$$ Equation 5-9

Where:

$$\rho = \sum_{i=1}^{N} S_i$$ Equation 5-10

Corrections are made to account for the effect of the layer dependent heat rate. Thus, the heat rate used within each soil layer is given as:

$$q_i = \frac{q}{2} \left(1 + k_i \frac{\sum_{i=1}^{m} L_i}{\sum_{i=1}^{m} k_i L_i} \right)$$ Equation 5-11

An adjustment is also made to account for the heat exchange between layers (see Abdelaziz et al. 2014 for details).

Yang et al. (2009) developed a method to account for a varying heat rate within an ILS model using step loading and superposition where for a series of different loads q_u that each last for $t_u - t_{u-1}$ as shown in Figure 5-8:

$$\Delta T(t_n) = \frac{q_1}{4\pi k} Ei\left(-\frac{r^2}{4\alpha t_n} \right) + \sum_{u=1}^{n-1} \frac{q_{u+1} - q_u}{4\pi k} Ei\left[-\frac{r^2}{4\alpha (t_n - t_u)} \right]$$ Equation 5-12

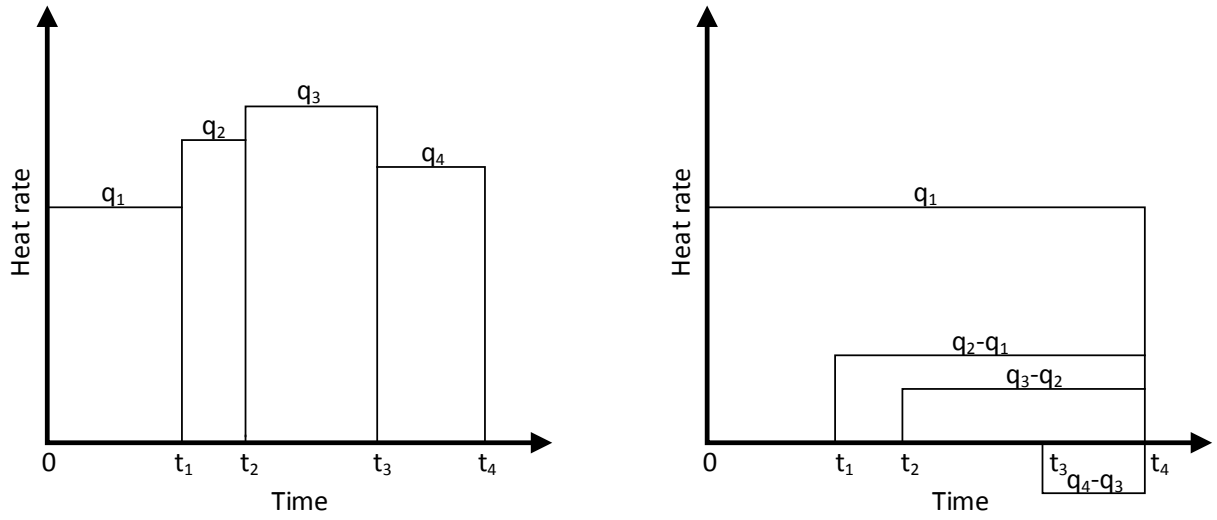

Figure 5-8. The superposition principle for varying heat rate (redrawn after Ozudogru et al. 2014b and Yang et al. 2009).

Ozudogru et al. (2014b) used the above model within the FLS framework to account for a heating period with constant rate q for a time t_1 and then a recovery period of time $(t_2 - t_1)$ to determine the temperature change at a point at time t_2:

$$\Delta T(t_2) = \frac{q}{4\pi k}\int_0^H \left[\frac{\operatorname{erfc}\left(\sqrt{r^2+(z-h)^2}/2\sqrt{\alpha t_2}\right) - \operatorname{erfc}\left(\sqrt{r^2+(z-h)^2}/2\sqrt{\alpha(t_2-t_1)}\right)}{\sqrt{r^2+(z-h)^2}} - \frac{\operatorname{erfc}\left(\sqrt{r^2+(z+h)^2}/2\sqrt{\alpha t_2}\right) - \operatorname{erfc}\left(\sqrt{r^2+(z+h)^2}/2\sqrt{\alpha(t_2-t_1)}\right)}{\sqrt{r^2+(z+h)^2}}\right] dh \quad \text{Equation 5-13}$$

Because the field test site consists of two distinct soil layers and because many different heating and cooling periods are simulated, the model in this paper modifies the one from Ozudogru et al. (2014b) to account for an arbitrary number of heating periods of varying heat rate in a multilayer medium. Thus, there will be effects from both primary and secondary segments and corrections made to the heat rate and for the interlayer heat exchange at each time step. The primary segment is given by:

$$\Delta T(t_n)_{1,i} = \frac{q_1}{4\pi k_i}\int_{x_i}^{x_{i+1}}\left[\frac{\operatorname{erfc}\left(\sqrt{r^2+(\xi-h)^2}/2\sqrt{\alpha_i t_n}\right)}{\sqrt{r^2+(\xi-h)^2}} - \frac{\operatorname{erfc}\left(\sqrt{r^2+(\xi+h)^2}/2\sqrt{\alpha_i t_n}\right)}{\sqrt{r^2+(\xi+h)^2}}\right]d\xi + \sum_{u=1}^{n-1}\frac{q_{u+1}-q_u}{4\pi k_i}\int_{x_i}^{x_{i+1}}\left[\frac{\operatorname{erfc}\left(\sqrt{r^2+(\xi-h)^2}/2\sqrt{\alpha_i (t_n-t_u)}\right)}{\sqrt{r^2+(\xi-h)^2}} - \frac{\operatorname{erfc}\left(\sqrt{r^2+(\xi+h)^2}/2\sqrt{\alpha_j (t_n-t_u)}\right)}{\sqrt{r^2+(\xi+h)^2}}\right]d\xi$$

Equation 5-14

The effect from the secondary segment is given by:

$$\Delta T(t_n)_{2,i} = \sum_{i=1}^{m}\frac{q_1}{4\pi}\int_{x_i}^{x_{i+1}}\left[\frac{\operatorname{erfc}\left(\rho/2\sqrt{\alpha_{comp.}t_n}\right)}{k_{comp.}\rho} - \frac{\operatorname{erfc}\left(\rho'/2\sqrt{\alpha'_{comp.}t_n}\right)}{k'_{comp.}\rho'}\right]d\rho + \sum_{u=1}^{n-1}\sum_{i=1}^{m}\frac{q_{u+1}-q_u}{4\pi}\int_{x_i}^{x_{i+1}}\left[\frac{\operatorname{erfc}\left(\rho/2\sqrt{\alpha_{comp.}(t_n-t_u)}\right)}{k_{comp.}\rho} - \frac{\operatorname{erfc}\left(\rho'/2\sqrt{\alpha'_{comp.}(t_n-t_u)}\right)}{k'_{comp.}\rho'}\right]d\rho$$

Equation 5-15

Boreholes are often part of a borehole field and energy piles are often a part of a pile foundation, thus do they rarely act alone. It is therefore necessary to consider the temperature change at a point in the ground from all sources. Superposition can be used such that the temperature change at a point in the ground with multiple energy sources is:

$$\Delta T(t)_{tot} = \sum_{j=1}^{b}\Delta T(t)_j$$

Equation 5-16

5.5.1. Accounting for the Time Dependence of the Layer Dependent Heating Rate

Equation 5-11 was found to yield poor agreement between numerical and analytical results, namely because it failed to account for the influence of several factors including time and the borehole thermal and geometric properties, which are especially important at early times in the operation. Thus, Equation 5-11 was modified to account for several factors. As explained in Abdelaziz et al. (2014), at the source (r = 0) by integrating over the length of heat exchanger, the infinite line source model (Equation 5-17) becomes :

$$q = 4\pi k t \cdot \Delta T$$

Equation 5-17

However, at the interface of the exchanger ($r = r_b$):

$$q = \frac{4\pi kt \cdot \Delta T}{e^{-r^2/4\alpha t}}$$ Equation 5-18

Thus the heat rate (q) is a function of the thermal conductivity of the soil layers, but also time (t), the thermal properties of the heat exchanger (α), and the radius of the heat exchanger. Therefore Equation 5-11 was modified as:

$$q_i = \frac{q}{3}\left(1 + \left(2 - f_q\right) + f_q k_i \frac{\sum_{i=1}^{m} L_i}{\sum_{i=1}^{m} k_i L_i}\right)$$ Equation 5-19

Where:

$$f_q = e^{-\frac{r_f r^2}{4\alpha t}} \{t > 0\}$$
$$f_q = 0 \{t = 0\}$$ Equation 5-20

This equation essentially does three things. First, it still accounts for the uniform heat rate inside of the GHE as well as the layer dependence of the heat rate outside of the GHE through the first and third terms inside of the parenthesis of Equation 5-19. Secondly, it increases the importance of the uniform heating rate inside of the GHE by introducing the second term. The reason for this will be shown Section 5.7. Thirdly, it introduces a factor, f_q, which accounts for various other parameters that impact the layer dependence of the heating rate.

Equation 5-11 assumes that the layer dependence of the heating rate is constant over time. In reality, the influence of the layers is minimal at the start and increases in importance as the operation goes on and a steady-state condition is reached inside the GHE. The factor f_q accounts for this time dependence by varying from 0 to 1. For low values of t, f_q is 0 resulting in a more equal distribution of the heat flux between the layers. As t increases, f_q approaches 1 which increases the importance of the layer dependence on the heating rate. Furthermore, it accounts for the thermal properties of the GHE indicating that a GHE with a lower thermal diffusivity would approach steady-state more slowly. Likewise, a GHE with a larger radius will also take longer to reach steady-state. The term r_f accounts for where the circulation tubes are located within the GHE and is:

$$r_f = \frac{r_{GHE}}{S_{tube}}$$ Equation 5-21

This accounts for the fact that GHEs will take longer to reach steady-state with tubes closer to the center of the GHE ($r_f \rightarrow \infty$, which results in $q_i = q$) than when they are closer to the edges ($r_f = 0$, which results in $f_q = 1$ for all t).

There is one significant disadvantage to using Equation 5-19, and that is that it can be computationally expensive when considering many operations over a large time interval, especially if smaller time steps are used. When a constant q_i is used for each layer, if the heat injection or extraction rate is constant one value can represent the entire operation. With this method q_i changes over time thus increasing the number of heating loads, n, from Equation 5-12 which increases the total number of steps by (n-1)·m for each time step, m, in Equation 5-14 and Equation 5-15. Because smaller time steps are needed in order for the added accuracy of Equation 5-19 to be effective, it is really only useful from a computational efficiency perspective when considering few operations and/or small time periods. Improved accuracy

from Equation 5-19 can be obtained, however, by setting f_q=1 and assuming a constant q_i over time for each layer. This was done in the replication of the experimental results which included 7 tests on 4 piles over the course of 250 days.

5.5.2. Influence of Atmospheric Energy Exchange

One obvious shortcoming of the analytical model is that it fails to account for the energy exchange that takes place between the ground and atmosphere, which influences the ground temperatures at shallower depths. Thus there is poor agreement between the observed temperature change in the ground and that which was predicted by the analytical model at depths less than 12.2 m when this temperature change is not accounted for (as will be shown in Section 5.7.2.1). Accounting for this exchange is challenging for several reasons. The first is that the rate of energy exchange between the ground and atmosphere is a function of the temperature gradient between the two as well as the thermal properties of the ground. This reduces to the differential Laplace equation. Approximations have been developed, however, for the determination of ground temperatures based on the atmospheric temperatures.

Kusuda and Achenbach (1965) showed that by assuming the earth is a homogenous heat-conducting medium with a constant thermal diffusivity and that the temperature of the surface exposed to the atmosphere varies periodically over time, heat conduction theory can be used to predict the temperature with depth. Specifically:

$$T_h = T_{g,avg} - T_{amp} e^{-x\left(\frac{\pi}{365*\alpha}\right)^{0.5}} \cos\left(\frac{2\pi}{365}\left(t_{now} - t_{shift} - \frac{x}{2}\left(\frac{365}{\pi\alpha}\right)^{0.5}\right)\right) \qquad \text{Equation 5-22}$$

By eliminating the $T_{ground,avg}$ term from the above equation, the change in temperature at depth is estimated. This equation was used to predict the temperature change in the ground from energy exchange with the atmosphere. Using superposition, the temperature change from the atmosphere can be added to the temperature change from the FLS model to get the total temperature change. There are, however, serious limitations to this method that must be addressed. The first is that when multiple layers are present in the ground with different thermal diffusivities, this can only account for the temperature change in the uppermost layer due to the assumption that the earth is a homogeneous semi-infinite heat conducting medium. For the ground profile from the experimental site presented in this paper, this is of little concern as the atmospheric induced temperature change is negligible below a depth of about 12 m. This limitation will cause problems for site conditions where the top layer is shallower.

The second major limitation of this model that must be realized is that it assumes the only influence on ground temperatures is that from the cyclical temperature variation at the surface due to the atmosphere. In reality, the average atmospheric temperatures differ from year to year, thus there will be slight variations in the ground temperature from what this model predicts. But more importantly, when ground temperatures are altered by heat exchange operations that occur with heat exchangers, the temperature gradients within the ground change, which will affect the amount of energy exchanged with the atmosphere. The effect will be most pronounced where the temperature gradients are most affected, which is close to the pile and near the ground surface.

5.6. NUMERICAL MODEL DEVELOPMENT

A three-dimensional model was developed to validate the analytical model using COMSOL Multiphysics™, a finite element simulation environment (COMSOL, 2015). This numerical analyses framework is based on the modeling approach developed and calibrated by Ozudogru et al. (2014b). The model consists of the entire borehole-soil system and utilizes several components. These components include an effective solid representing the fluid circulation pipes, a 1-dimensional line element through the middle of the fluid circulation pipes upon which fluid flow is determined, the thermal grout and the soil surrounding the energy pile (Figure 5-9). The geometric limits of the model are set far enough in order to eliminate potential boundary effects.

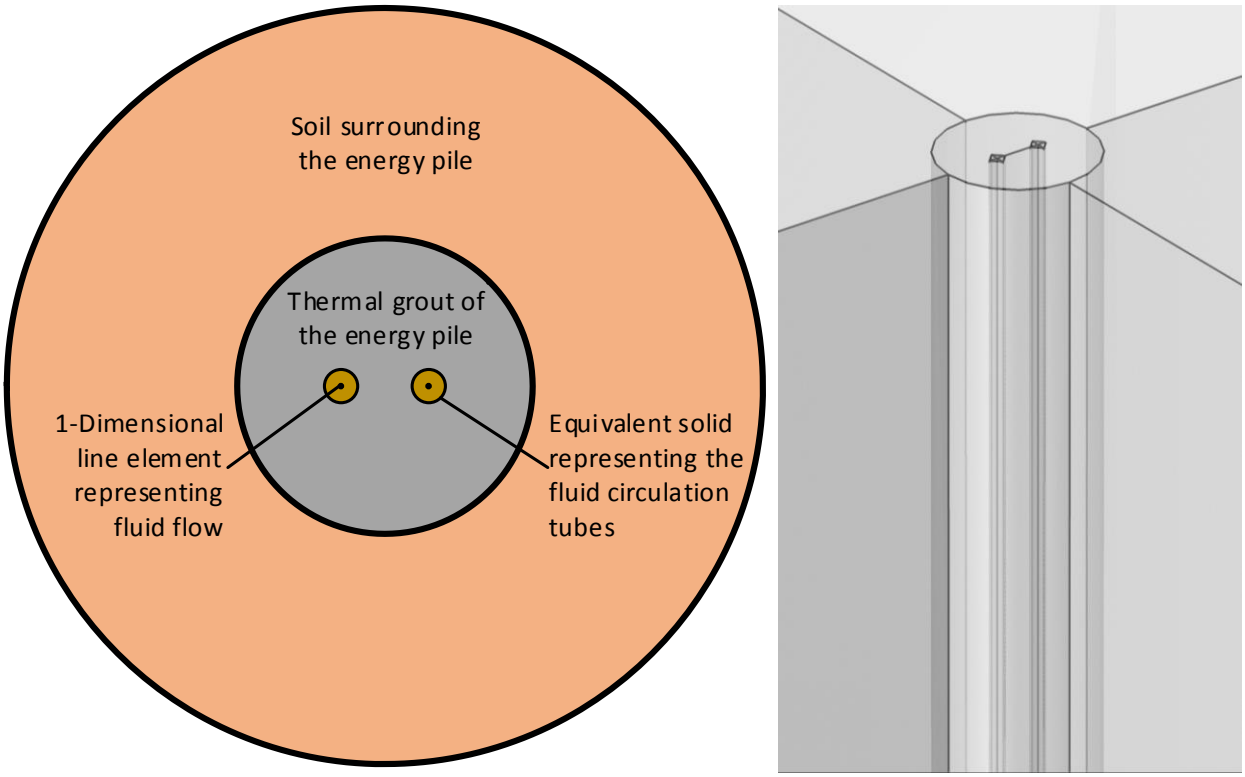

Figure 5-9. Geometric layout of the model and model domains.

Assuming there is no internal heat generation, heat conduction through the solid domains (slab, tube) is governed by the following differential equation:

$$\rho c_p \frac{\partial T}{\partial t} + \nabla \cdot (-\mathbf{k}\nabla T) = 0 \qquad \text{Equation 5-23}$$

Adiabatic surfaces are present at the outer radial and bottom boundaries of the ground which presents a Neumann boundary condition. This specifies the heat flux at the respective boundary is 0:

$$q" = (-\mathbf{k}\nabla T) = 0 \qquad \text{Equation 5-24}$$

To ensure this condition was present, the temperature along these boundaries were monitored to ensure they remained equal to the initial temperature. A Neumann condition was also applied to the ground surface. In reality, heat exchange occurs between the ground surface and the environment. However, due

to the short time periods considered in the studies using the numerical model and considering that the predominant direction of heat exchange will be in the horizontal direction, the heat exchange with the atmosphere is relatively minimal and an adiabatic surface can be used.

Because directly modeling fluid flow is a computationally expensive process and being able to directly model the flow of the fluid through the circulation pipes is not within the objectives of the model, the methodology of Ozudogru et al. (2014b) was followed. Thus, a 1D approximation of the fluid flow process was utilized using COMSOL's non-isothermal pipe flow module. According to this simplification, the energy equation that governs an incompressible fluid flowing in a pipe with no internal heat source is (COMSOL, 2015):

$$\rho A C_p \frac{\partial T}{\partial t} + \rho A C_p \mathbf{u} \cdot \nabla T = \nabla \cdot Ak\nabla T + f_D \frac{\rho A}{2d_h} |\mathbf{u}|^3 + Q_{wall} \quad \text{Equation 5-25}$$

In the equation above, the second term on the right hand side represents the friction heat dissipated due to viscous shear. The Darcy friction factor, f_D, can be estimated using the equation from Churchill (1997):

$$f_D = 8\left[\left(\frac{8}{\mathrm{Re}}\right)^{12} + (\mathrm{C_A} + \mathrm{C_B})^{-1.5}\right]^{\frac{1}{12}} \quad \text{Equation 5-26}$$

C_A and C_B are given by:

$$\mathrm{C_A} = \left[-2.457 \ln\left(\left(\frac{7}{\mathrm{Re}}\right)^{0.9} + 0.27\left(\frac{e}{d_h}\right)\right)\right]^{16} \quad \text{Equation 5-27}$$

$$\mathrm{C_B} = \left(\frac{37530}{\mathrm{Re}}\right)^{16} \quad \text{Equation 5-28}$$

The absolute surface roughness coefficient, e, is 0.0015mm for plastic pipes. The Reynold's number, Re, is given by:

$$\mathrm{Re} = \frac{\rho_f u d_h}{\mu_f} \quad \text{Equation 5-29}$$

In Equation 5-25, Q_{wall} is the radial heat transfer from the surroundings into the pipe and includes the effects of both the internal film resistance and thermal resistance from the pipe itself. It is given as:

$$Q_{wall} = (hZ)_{eff}(T_{ext} - T) \quad \text{Equation 5-30}$$

T_{ext} is the external temperature, in this case the temperature of the slab domain, and is what allows coupling of Equation 5-25 directly with the 3D heat transfer. In this case, the 3D model treats the fluid flow as a 1D line heat source. The $(hZ)_{eff}$ is the effective value of the heat transfer coefficient h, which includes the effects of the internal film resistance and the pipe thermal resistance, multiplied by Z, the wall perimeter. For circular, non-layered pipe cross sections, $(hZ)_{eff}$ is given by:

$$(hZ)_{eff} = \frac{2\pi}{\frac{2}{d_{pi}h_{int}} + \frac{\ln(d_{po}/d_{pi})}{k_p}} \quad \text{Equation 5-31}$$

Important to understand are two key assumptions in the determination of $(hZ)_{eff}$. The first is that there is an equal temperature distribution around the pipe and the second of which is that heat transfer through the pipe is quasi-static, or that it immediately assumes the temperature distribution across the pipe. In the equation above, the determination of h_{int}, the internal film heat transfer coefficient, is given by:

$$h_{int} = \mathrm{Nu}\frac{k_f}{d_h} \qquad \text{Equation 5-32}$$

Nu is the Nusselt number. For laminar pipe flow it is defined as 3.66 for circular pipe cross sections. For turbulent flow, it is determined as:

$$\mathrm{Nu} = \frac{(f_D/8)(\mathrm{Re}-1000)\mathrm{Pr}}{1+12.7(f_D/8)^{1/2}(\mathrm{Pr}^{2/3}-1)} \qquad \text{Equation 5-33}$$

Pr is the Prandtl number and is given by:

$$\mathrm{Pr} = \frac{C_{p,f}\mu_f}{k_f} \qquad \text{Equation 5-34}$$

As mentioned previously, the way the 1D pipe flow is typically coupled within the 3D numerical model is by integrating it as a line source element along the centerline of the tube. Ozudogru et al. (2014b) points out that this simplification produces two main coupling errors. The first is that by assuming the pipe is a 1D linear element, the temperature field of the borehole is coupled directly at that element whereas it should be coupled at a distance equal to pipe's outer radius. Secondly, by assuming the pipes themselves are linear elements, their volumetric heat capacities are neglected. Thus, Ozudogru et al. (2014b) developed a 'pseudo-pipe' approach to account for these coupling errors, which was implemented in this model. Under this approach a volumetric domain equal in size to the outer pipe radius is created. The domain consists of pseudo pipe elements, which have effective densities, defined by:

$$\rho_{p,eff} = \rho_p\left(\frac{d_{po}^2 - d_{pi}^2}{d_{po}^2}\right) \qquad \text{Equation 5-35}$$

The heat capacity of the pseudo pipe elements is equal to that of the actual pipe. The thermal conductivity, however, is anisotropic and is set to be very high (1000 W/(m·K)) in the radial direction as defined by the pipe's centerline and zero in the tangential direction.

This model was used to replicate a field thermal conductivity test (TCT 5 from Table 5-2) on Pile 1. The inlet temperature was coupled internally to the outlet temperature, that is, the inlet fluid temperature self-adjusted based on the outlet fluid temperature in the same way it occurs in the field. Thus, a constant temperature difference was maintained between the inlet and outlet fluid temperatures creating a constant heating rate.

The model geometry consists of a 30.48 m long micropile with a 25.4 cm diameter. Running along the length of the micropile is a single HDPE U-loop with an inner diameter of 3.404 cm and an outer diameter of 4.171 cm (i.e. wall thickness t = 3.84 mm). The soil domain consists of two layers to replicate field conditions. The top layer, which extends to a depth of 12.8 m, is a silty sand which is underlain by a shale. The material properties of the pipes, micropile, and soil are given in Table 1. The finite element mesh discretization of the model is performed using quadrilateral elements. The meshed domain is shown in

Figure 5-10. The soil domain extends 5m from the center of the model in the x and y directions and 5 m from the bottom of the energy pile.

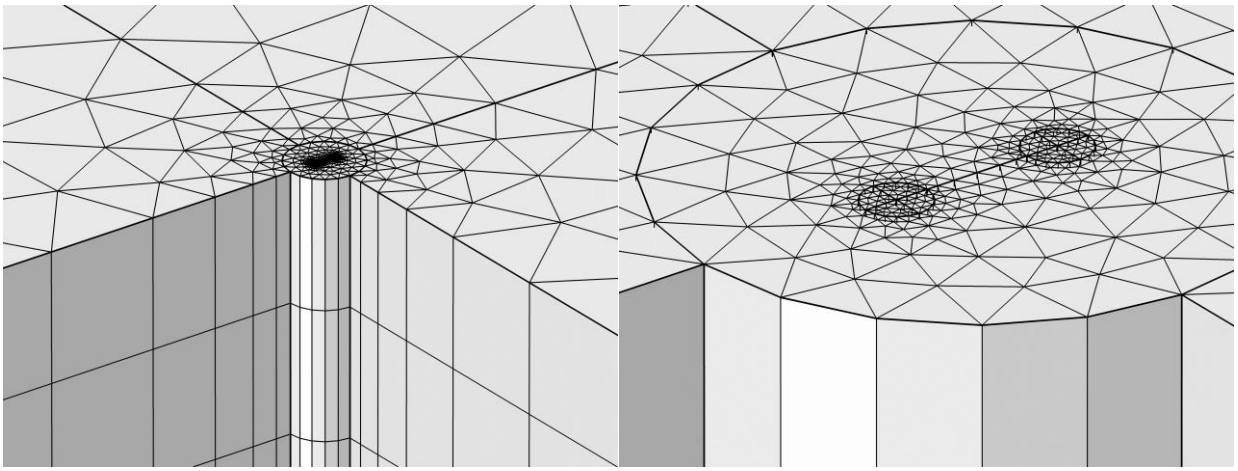

Figure 5-10. Meshed domain of the numerical model.

5.7. ANALYTICAL AND NUMERICAL MODEL CALIBRATION AND VALIDATION

Though there exists information regarding the thermal properties of the borehole materials (circulation pipes, borehole grout, circulation fluid), the thermal properties of the subsurface was not known. Thus, the analytical model was used to back calculate the thermal properties of the subsurface using the thermal properties and thermo-mechanical tests listed in Table 5-4 and Table 5-2, respectively. These properties were then verified using the numerical model by replicating the results of one of the thermal conductivity field tests.

Table 5-4. Parameters used in the analytical and numerical models.

Parameter	Ozudogru et al. (2015)	This Paper	Unit
Global Parameters			
Initial ground temperature	14.7	14.7	^{o}C
Heat rate per depth	72	72	W/m
Test duration	50	50	h
Circulation Fluid (Water)			
Flow rate	5.68	5.68	L/m
Dynamic viscosity	0.997	0.99	mPa·s
Thermal conductivity	0.6048		W/m·K
Specific heat capacity	4180		J/kg·K
Density	997.8		kg/m^3
Pipes (HDPE)[1]			
Thermal conductivity	0.40	0.51	W/m·K
Effective thermal conductivity	{1000, 1000, 0}[2]	{1000, 1000, 0}[3]	W/m·K
Specific heat capacity	2300	2300	J/kg·K
Density	940	945	kg/m^3
Effective density			kg/m^3

Pipe inner diameter	21.844	21.539	mm
Pipe wall thickness	2.413	2.413	mm
Shank spacing (center-to-center)	7.5	7.5	cm
Energy Pile[4]			
Thermal conductivity[5]	1.28	1.10	W/m·K
Specific heat capacity	880	880	J/kg·K
Density	1600	2000	kg/m^3
Diameter	25.4	25.4	cm
Length	30.48	30.48	m
Ground Layer 1 (Silty-Sand)			
Thermal conductivity	1.00	1.50	W/m·K
Specific heat capacity	1500	1500	J/kg·K
Density	1900	2000	kg/m^3
Layer thickness	12.80	12.8	m
Ground Layer 2 (Shale)			
Thermal conductivity	2.90	3.50	W/m·K
Specific heat capacity	1200	1200	J/kg·K
Density	2400	2000	kg/m^3

[1]The material properties for the HDPE pipe in this paper were taken directly from the manufacturer's data sheet. It did not give the thermal conductivity or heat capacity, thus typical values of HDPE were used.
[2]Directions are in the global x, y, and z directions where z is along the vertical axis of the borehole
[3]Directions are in the cylindrical material r, ϕ, and z directions where z follows the axis of the circulation tube
[4]In Ozudogru et al. (2014a), the authors listed this as a 'borehole', when it is actually an energy pile. Thus a higher density value was used more consistent with cast-in-place drilled micropiles.
[5]The thermal conductivity value used in Ozudogru et al. (2014a) is typical of that of concrete. However, Abdelaziz (2013) reports a value of 0.73W/m·K based on the dry density value of the concrete in the pile. Because this was based on a correlation, there is some room for fluctuation. However, the value 1.00W/m·K used in this paper is closer than 1.28W/m·K.

5.7.1. Numerical Model

The numerical model was calibrated to the field site using a thermal conductivity test (TCT-5 from Table 5-2) on Pile 1 reported in Abdelaziz (2013) and used to validate the material properties that were found using the analytical model. The test lasted for approximately 50 hours and a constant heat rate of 2.2 kW was applied to the pile (72 W/m). This test was chosen because it was the most controlled of the thermal conductivity tests and followed the 'Dutch procedure'. The initial temperature of the ground was taken as constant and reported as being 14.7°C. Ozudogru et al. (2014a) used this test to calibrate their finite element and finite difference models. Table 5-4 lists the material properties used in the models of Ozudogru et al. (2014a) as well as an additional set of parameters, which are also used to compute the results reported in this paper. There are two reasons for the additional set of parameters. First several of the energy pile and circulation tube material properties used do not match that which is reported in Abdelaziz 2013 so they were adjusted to more representative values. Secondly, the temperature changes in the ground using the parameters thermal properties reported in Ozudogru et al. (2014a) do not yield as good agreement with the observed experimental results as the second set of parameters. Throughout this paper, the results from both sets of parameters will be presented to show the differences.

Figure 5-11 presents the results of the model calibration using both sets of material properties from Table 5-4. Shown are the inlet and outlet fluid temperatures as compared with those observed experimentally. Though both sets of parameters yield excellent agreement to the experimental results, the parameters used in Ozudogru et al. (2014a) give slightly closer results. However, as will be shown in the subsequent section, the additional set of parameters yield better agreement to the experimental data when considering all of the TMTs and TCTs.

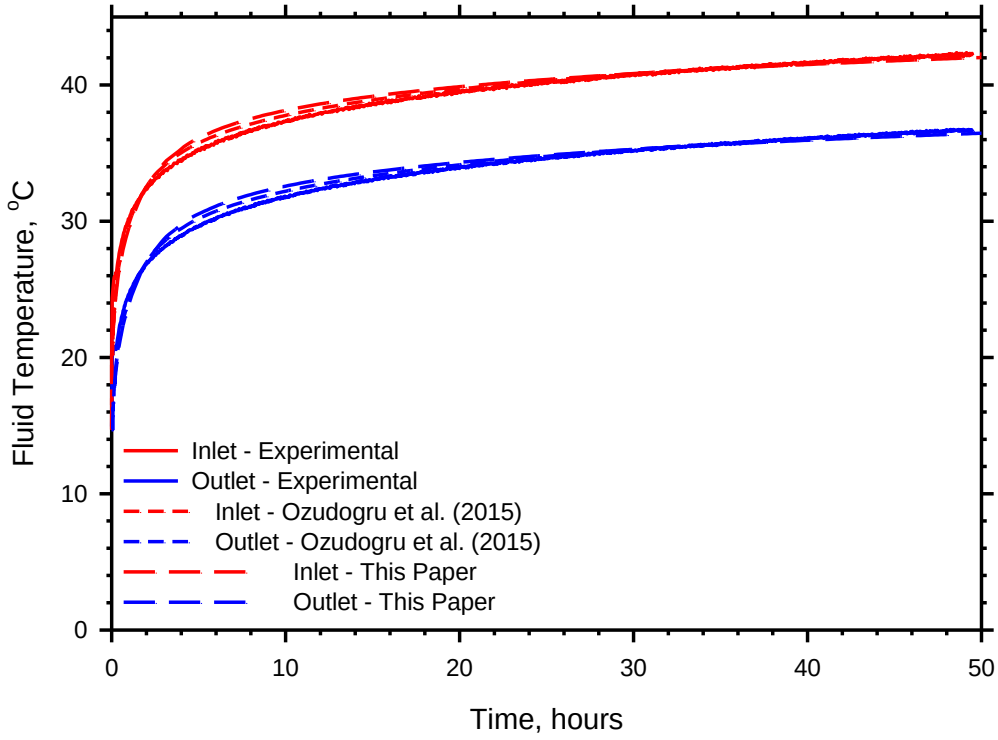

Figure 5-11. Comparison between the experimental results and those obtained through FE analysis using parameters from Ozudogru et al. (2015) and additional parameters found using the FLS model.

Figure 5-12 compares the temperature difference in the middle of the upper and lower soil layers 10, 50, and 168 hours after the start of the operation. It shows the temperature difference with distance from the soil-pile interface. The model is not symmetric as during a thermal conductivity test, the fluid traveling downward will generally be warmer than the fluid traveling upward. Thus, slightly more energy will be imparted to the side of the energy pile that contains the downward circulating fluid meaning that in the finite element model, the temperature vs distance from the pile will depend on which direction the distance is measured. Three different directions are measured and compared; one radially outward on the side containing the fluid flowing downward (known as the 'down' side), one radially outward from the side containing the fluid flowing upward (known as the 'up' side), and one from the side that is between the two tubes (known as the 'mid' side). As expected, for both the upper and lower soil layers, the temperature differences are greater on the down side of the pile, where the warmer fluid is flowing, followed by the up side where the relatively cooler fluid is flowing. The lowest temperatures are on the mid side where no fluid is flowing. The difference in temperature between the three locations decreases with distance from the interface. The differences between the down, up, and mid sides are greater in the upper layer, which is a function of different soil thermal properties, but mainly due to the fact that there

is a greater difference in temperature between the downward and upward traveling fluid in the upper layer (which is closer to the inlet and outlet) than the lower layer. After 168 hours, or one week after the start of the test, the differences are essentially non-existent regardless of distance from the pile.

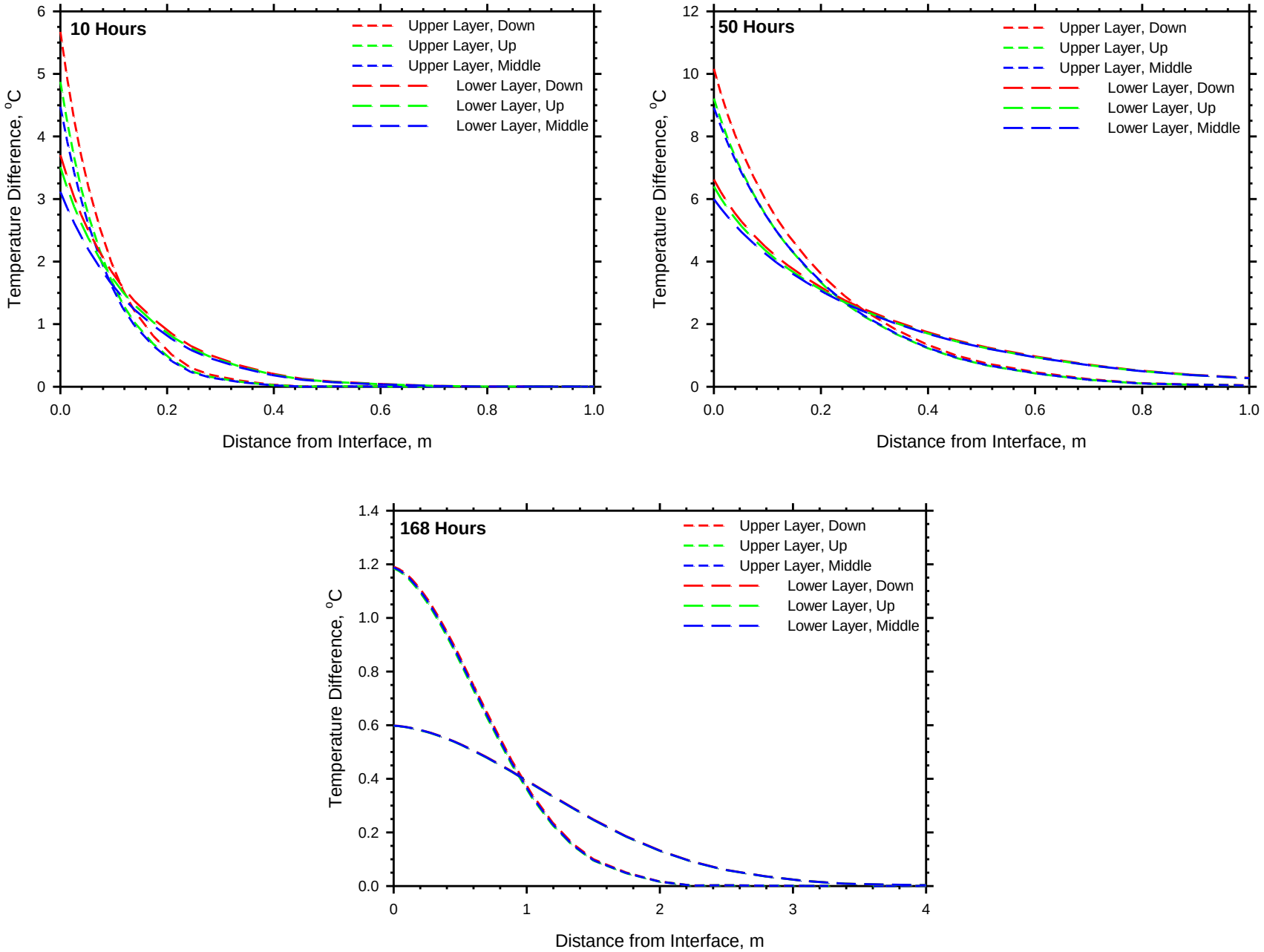

Figure 5-12. Temperature vs distance at the mid-depth in the upper (silty sand) and lower (shale) soil layers on the down, up, and middle sides of the pile at a) 10, b) 50, and c) 168 hours after start of operation.

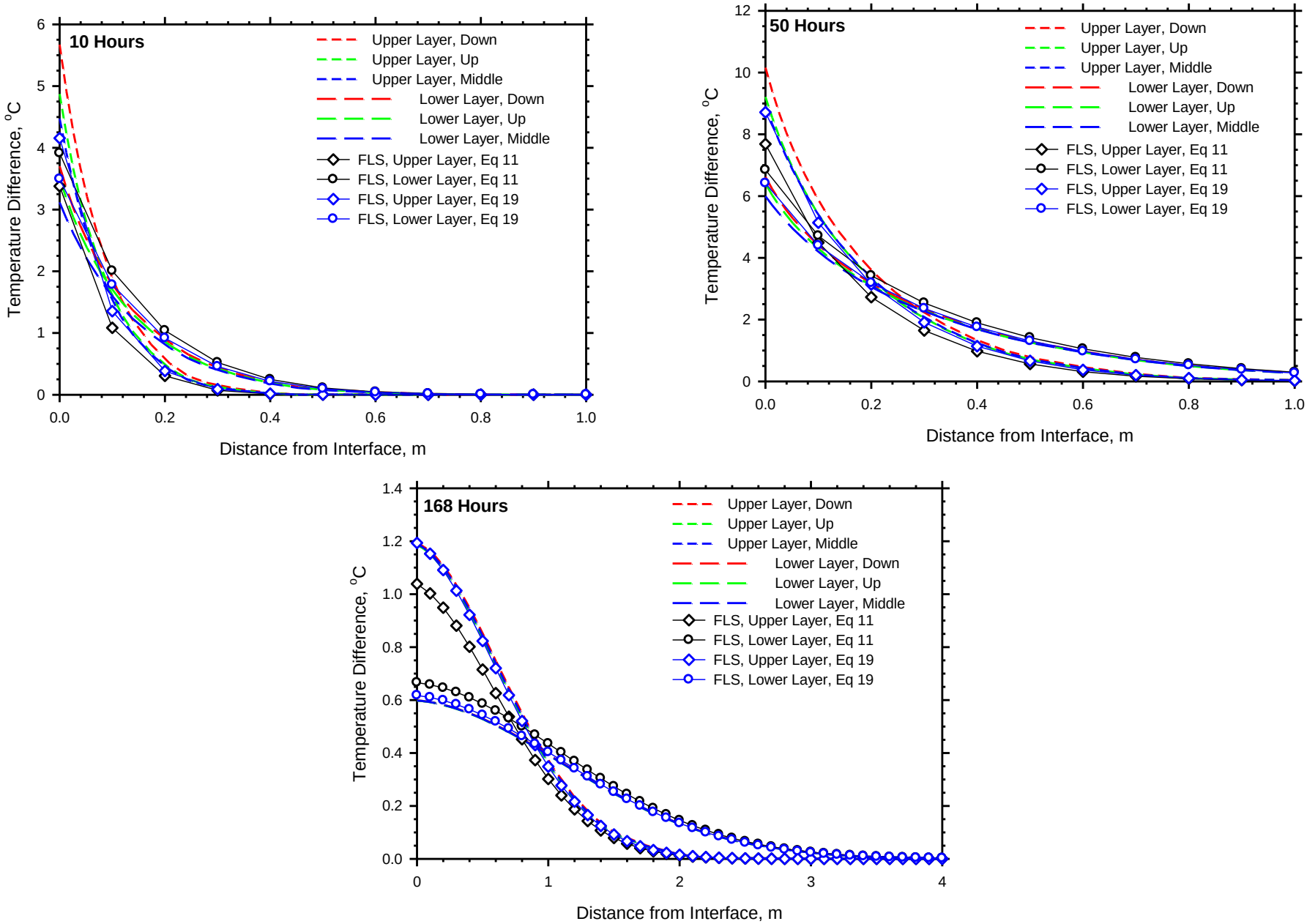

Figure 5-13. Temperature vs distance at the mid-depth in the upper (silty sand) and lower (shale) soil layers on the down, up, and middle sides of the pile and compared with the results from the analytical model at a) 10, b) 50, and c) 168 hours after start of operation.

Figure 5-13 shows the temperature changes observed from the FE model, but also includes the temperature changes as predicted by the analytical model using both Equation 5-11 and Equation 5-19 to determine the heating rate of the two layers. Several observations can be made. First, there is generally good agreement between the analytical and finite element models. The differences between the FE and FLS predictions are primarily a result of two factors. The first is that the FLS model represents a non-homogenous cylindrical heat source as a line heat source. This is going to introduce errors, especially near the pile-soil interface. Loveridge and Powrie (2013, 2014) and has shown that this difference is both a function of pile diameter and the placement of the circulation tubes within the pile. The second difference is the layer dependent heating rate (Equation 5-11 and Equation 5-19) used in the FLS model. As shown in Abdelaziz et al. (2014) and in Figure 5-14, there is a difference in the values determined by Equation 5-11 and those observed in FE models. In general, Equation 5-11 produced a value slightly high in the layer with the higher rate (the lower layer), and slightly lower value in the layer with the lower heat rate (the upper layer). Thus the FLS model slightly over predicts the temperatures in the lower layer and slightly under predicts them in the upper layer.

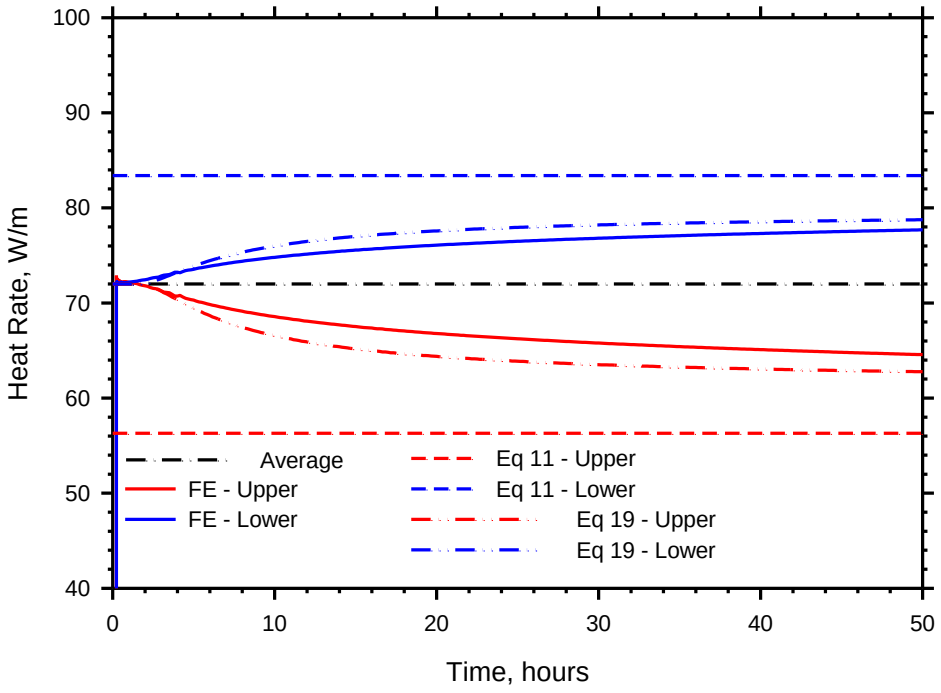

Figure 5-14. Heating rate in the upper and lower layers as determined by the FE model, Equation 5-11, and Equation 5-19.

In regard to the applicability of using Equation 5-11 this time-dependent heating rate, Abdelaziz et al. (2014) showed that it took almost 2 months for the heating rates observed in the FE model to approach those predicted by Equation 5-11. 2 months far exceeds the length of most continual heat injection or extraction operations. It especially exceeds the lengths of the relatively short bridge deck deicing and thermal recharge operations. A more accurate method was desired for the layer dependent heating rate, which is why Equation 5-19 was developed. Not only does it do a better job of capturing the time-rate effect of the layer dependence, the ultimate value each layer approaches is closer to the values in the FE model as well. As explained previously, this was accomplished by increasing the influence of the uniform

rate inside the GHE while accounting for the thermal and geometric properties of the heat exchanger over time. Figure 5-13 also includes the results from the FLS model using Equation 5-19. Note the much better agreement with the FE results.

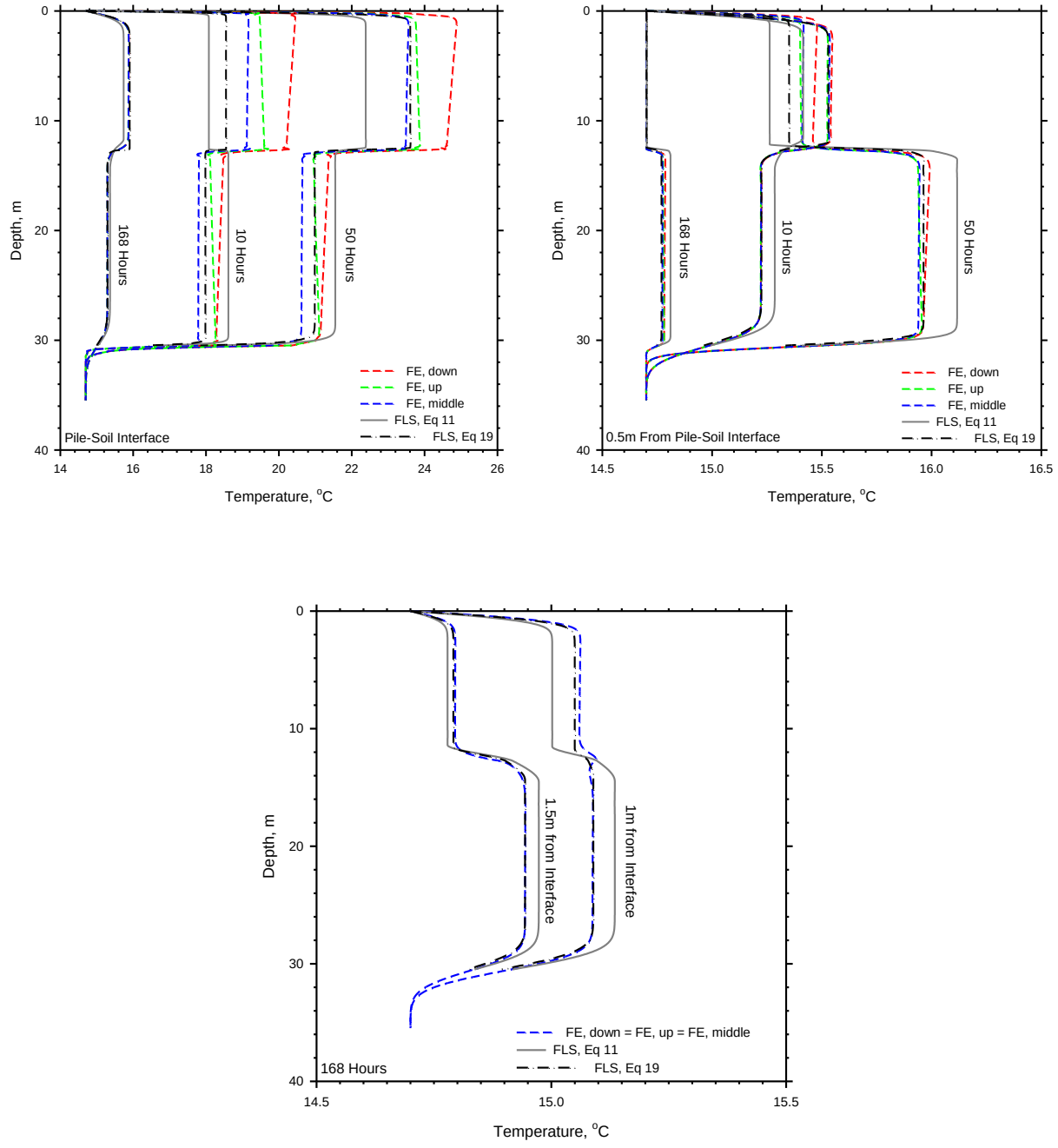

Figure 5-15. Selected temperature profiles as determined by the FE and FLS models at a) the pile-soil interface, b) 0.5m from the pile soil interface, and c) 168 hours at distances of 1.0 and 1.5m from the pile-soil interface.

Figure 5-15 shows the temperature profiles at select points in time for different radial distances from the pile. There are several important observations. First, the difference in temperatures between the down, up, and mid sides can be clearly seen. In fact, it can be seen that the temperature decreases with increasing depth on the down side and decreases with decreasing depth on the up side. This is representative of the temperature of the heat carrier fluid decreasing along its path through the energy pile. The mid side of the pile has the lowest temperatures as it is the furthest from the circulation tubes. It can again be observed that the temperature difference between locations decreases with increasing time and distance from the pile interface.

Also shown in Figure 5-15 are the temperatures calculated using the finite line source model. The agreement between the numerical and analytical models is particularly good at distances further from the energy pile. This is important as the closest observation well to Pile 1, where the majority of the TMTs and TCTs took place, is 1m away. There are a couple of differences between the analytical and numerical temperature profiles that must be explained, most notably what occurs at the pile-soil interface after 10 hours of heating. Not only is there a difference of several degrees between the two models, the temperature trend is actually reversed when using Equation 5-11. The numerical model shows the temperature of the upper layer relatively higher than the temperature of the lower layer, whereas the analytical model using Equation 5-11 shows the temperature of the lower layer relatively higher than the temperature of the upper layer. The cause of this has been discussed previously, and it is the difference in heating rates between the two layers. As shown in Figure 10, the difference in heating rates between the analytical and numerical models is greatest at early times. Thus, due to the relatively lower heating rate used in the upper layer of the analytical model as compared to the numerical model (and relatively higher heating rate in the lower layer), the temperature profiles are different. The FLS profile created using Equation 5-19, however, does not display this trend as it is able to account for the time dependence of the heating rate. In general, the profiles created using Equation 5-19 produced much better agreement with the profiles from the FE model than the FLS model using Equation 5-11.

5.7.2. Analytical Model

After validating the analytical model, it was used to back calculate the thermal properties of the soil layers at the experimental site. As shown in Table 5-1, the depth of the silty sand layer varies somewhat between the piles and boreholes. This is important as it will affect the effective thermal properties along the path length. Currently, while the analytical model can account for layers with different thermal properties, it has no method of accounting for varying layer thicknesses with distance from the heat source. Even if it did, it would be of little consequence in this case because though the depths are known at the locations of the piles and observation wells, the depth is not known in between the locations. Thus, less accuracy is expected along this transition layer, which is generally in the depths of 13-18 m. When selecting a depth for the silty sand layer, there are several options. The first is to use one representative value of the site. Two ways were performed with this method. The first was to use the value of depth at Pile 2 (12.8 m) as the majority of the heating tests used that pile. The second was to use an average of values from the site as recorded at the piles and observation wells. Another option for selecting the depth of the silty sand layer would be to have a value that changes based on the depth of whichever pile is emitting energy, or a value that changes based on whichever observation well is being used. It was found that it mattered little which method was used for depths less than 12.2 m and greater than 15.2 m, rather only the transition layers were affected. Amongst these depths, using the depth of the silty sand as recorded at the locations of the observation well produced the best agreement between experimental and measured results.

5.7.2.1. Depths Less than 12.2 m (40 ft)

The depths less than 12.2 m were also subject to temperature variation due to heat exchange between the surface of the ground and the atmosphere. Thus, the correction given by Equation 5-22 was applied. Figure 5-16 compares no correction in the upper layer with the correction applied for each observation well at a depth of 3.0m for both sets of ground thermal properties in Table 5-4. Also shown is the temperature change in the ground from Equation 5-22 only, which is essentially the temperature change in the ground as predicted by Kusada and Achenbach (1965) due solely to heat exchange with the ambient environment (i.e. there is no heat exchanger in the ground). Thus, one is able to see the predominant mode of influence on temperature. For example, in Figure 5-16a, the influence from the TCTs and TMTs is about equal to that of the atmosphere, on the magnitude of 4°C. However, in OW 2 (Figure 5-16b), the influence of the atmosphere far surpasses the influence of the heating operations, which is only about 0.2°C.

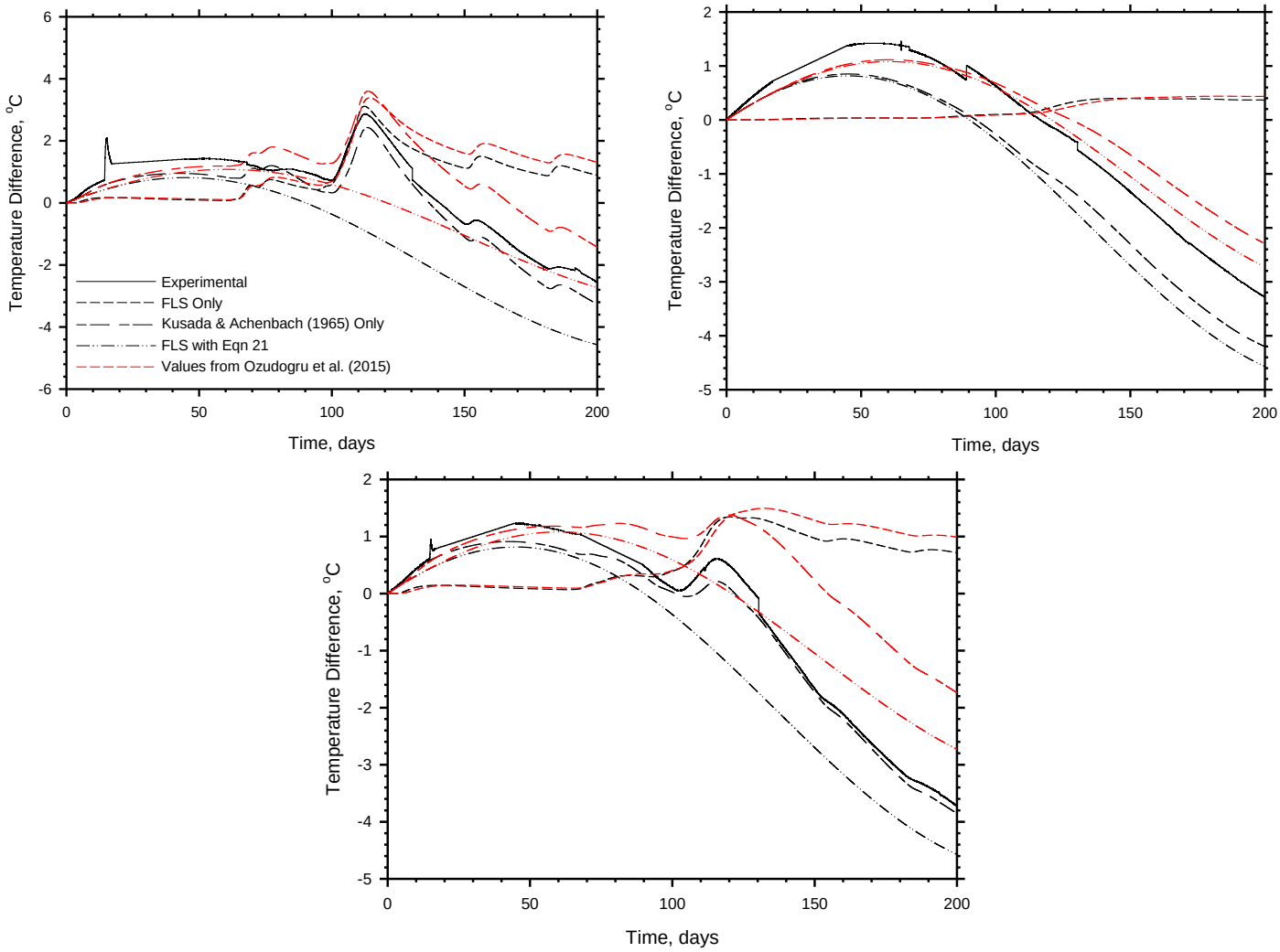

Figure 5-16. Temperature change in the ground over time for experimental results as compared to the predicted temperature change from the FLS model for a depth of 3.0 m at a) OW 1, b) OW 2, and c) OW 4.

There are several additional items to notice from Figure 5-16. First notice that the temperature change resulting from each TCT or TMT can be observed as a representative temperature spike or series of spikes. However, due to the influence of the heat exchange with the environment, it is hard to distinguish between the tests. The individual tests will be easier to separate at deeper observation points. Secondly, though Equation 5-22 does a good job of predicting the temperature change, it is not able to completely capture it, especially in OWs 1 and 4 which are closer to the energy piles. When combined with the FLS model, however, very good agreement between the observed and predicted temperature changes results.

A third observation is that the set of ground thermal properties proposed in this paper do a better job of predicting the temperature change in the ground than do the values in Ozudogru et al. (2015) for OWs 1 and 4, but not for OW 2. The trend using the values proposed in this paper, however, more closely resembles the trend observed from the experimental data in OW 2. This will be further discussed in a subsequent section.

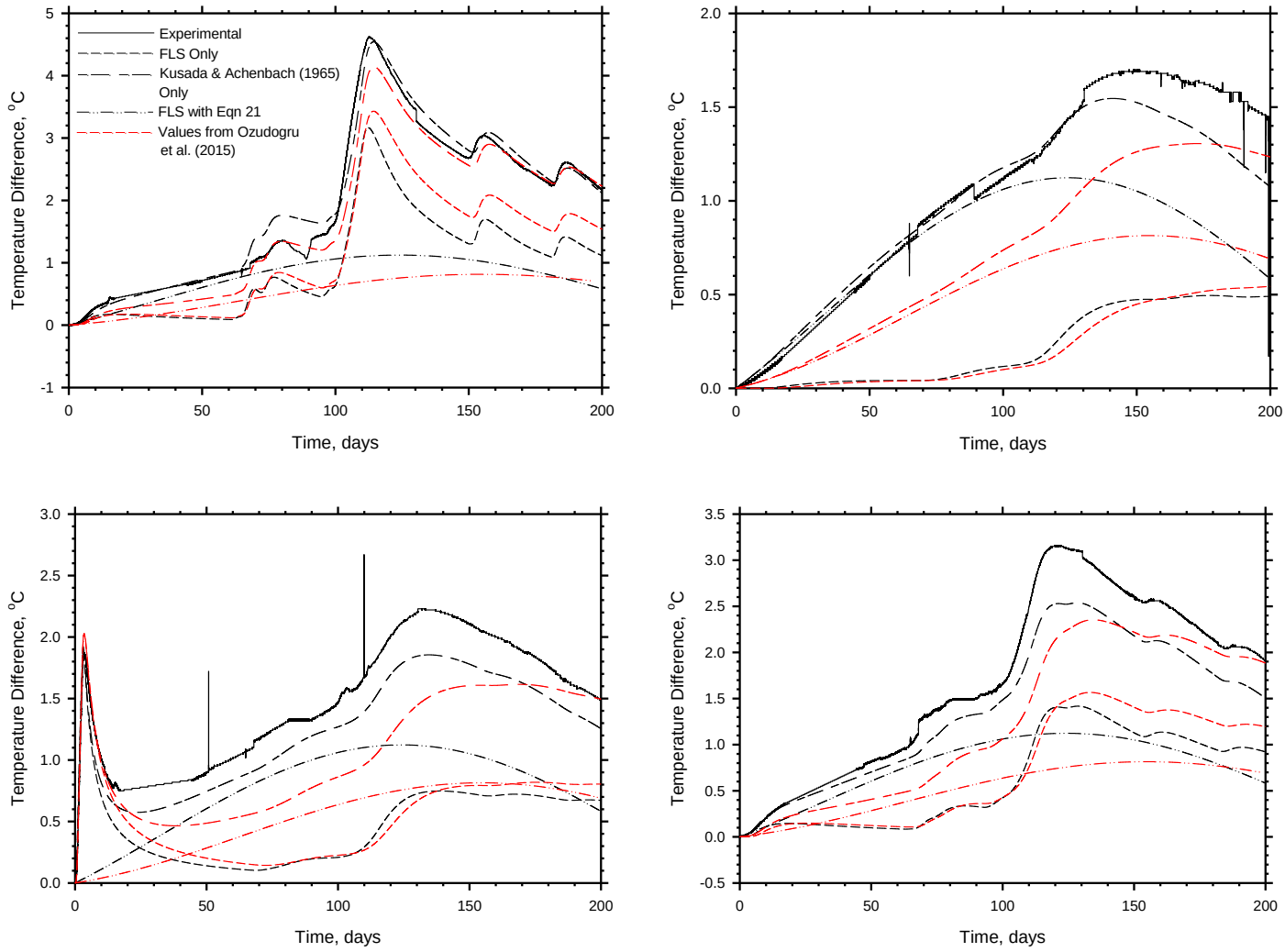

Figure 5-17. Temperature change in the ground over time for experimental results as compared to the predicted temperature change from the FLS model for a depth of 6.1 m at a) OW 1, b) OW 2, c) OW 3, and d) OW 4.

Figure 5-17 shows the temperature change in the ground for all OWs at a depth of 6.1 m. Note that OW 3 is only 0.5 m from Pile 3, which is where the first TCT takes place, thus it is the closest OW to a pile. Again, there is good agreement when utilizing Equation 5-22. Again, the second set of values from Table 5-4 do a better job of predicting the temperature change in the ground and in this case, that holds true for OW 2 as well as OWs 1, 3, and 4.

Figure 5-18 shows the temperature changes in the ground at a depth of 9.1 m for each OW except OW 3, which is at a depth of 10.7 m. At this depth, the influence of the TCTs and TMTs on temperature change outweighs the effects of the atmospheric heat exchange. In fact, for OWs 1, 2, and 3, better agreement between the FLS and experimental results occurs without the use of Equation 5-22. When Equation 5-22 is used, the first set of values from Table 5-4 yield better agreement to the observed values with the exception of OW 4. When it is not used, the second set of values yield better agreement. In both cases the second set of values produce trends that more closely align with what was observed experimentally.

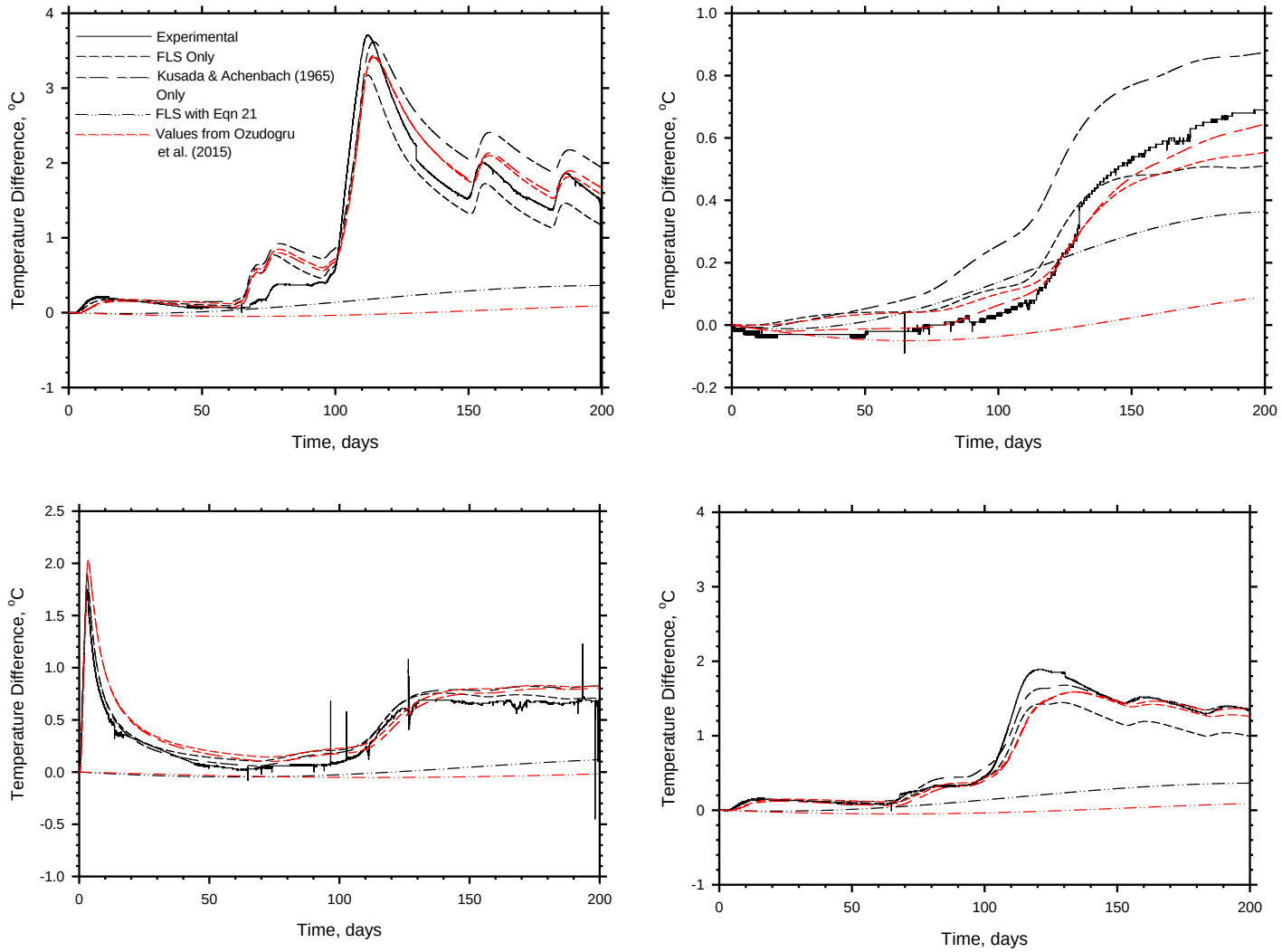

Figure 5-18. Temperature change in the ground over time for experimental results as compared to the predicted temperature change from the FLS model for a depth of 9.1 m at a) OW 1, b) OW 2, c) OW 3 (10.7m), and d) OW 4.

5.7.2.2. Depths Between 12.2 m (40 ft) and 18.3 m (60 ft)

The depths between 12.2 m and 18.3 m are in the transition zone where the silty sand turns to shale and it is beyond the influence of atmospheric heat exchange. As shown in Table 5-1, the transition occurs at a different depth for each pile and observation well. Thus, different methods for defining the depth of the transition zone were utilized as explained earlier and the best method was used to produce the figures. The comparisons between the observed temperature changes at OWs 1, 2, and 4 and the predicted temperature changes using the FLS model are shown in Figure 5-19, Figure 5-20, and Figure 5-21 for depths of 12.2 m, 15.2 m, and 18.3 m respectively.

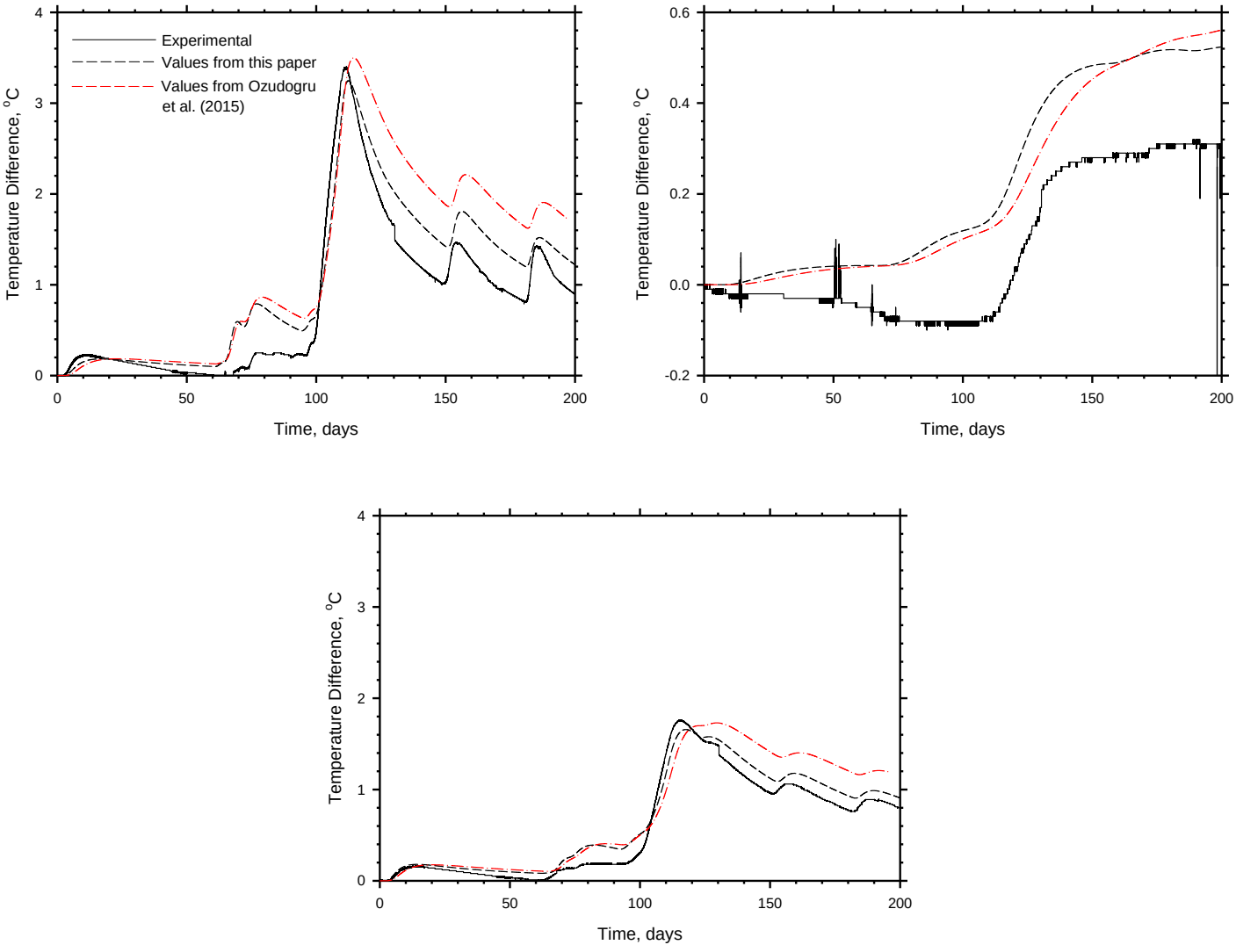

Figure 5-19. Temperature change in the ground over time for experimental results as compared to the predicted temperature change from the FLS model for a depth of 12.2 m at a) OW 1, b) OW 2, and c) OW 4.

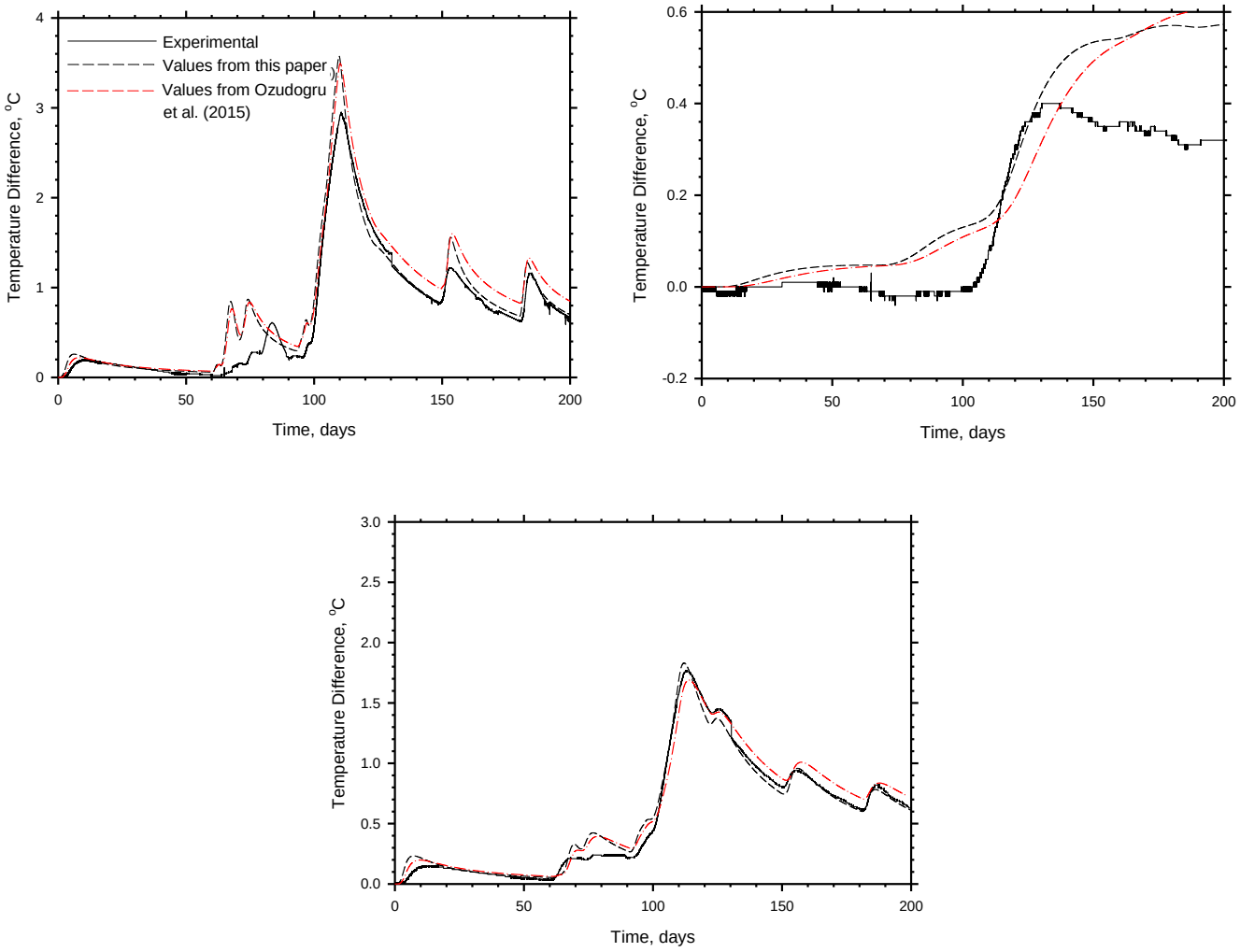

Figure 5-20. Temperature change in the ground over time for experimental results as compared to the predicted temperature change from the FLS model for a depth of 15.2 m at a) OW 1, b) OW 2, and c) OW 4.

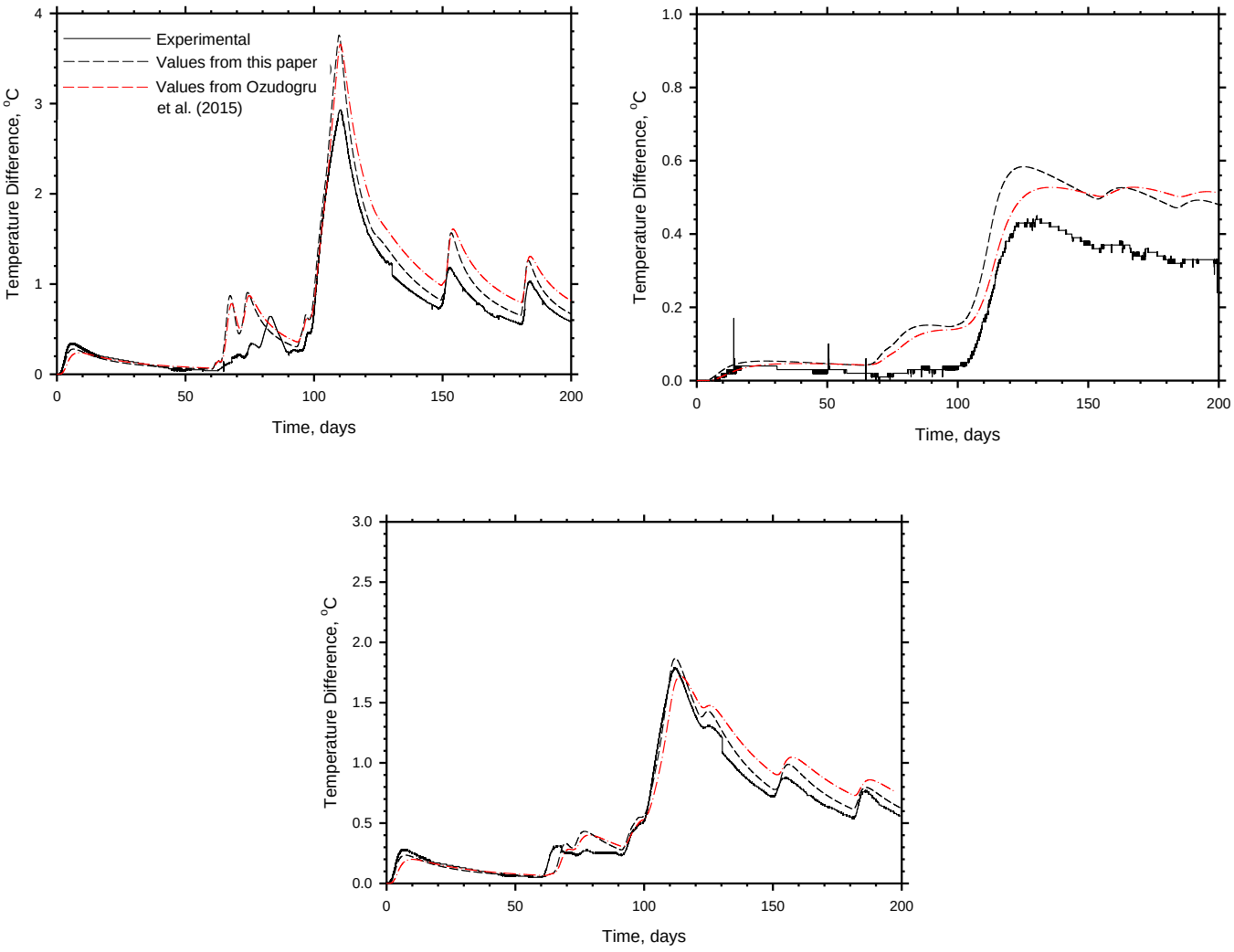

Figure 5-21. Temperature change in the ground over time for experimental results as compared to the predicted temperature change from the FLS model for a depth of 18.3 m at a) OW 1, b) OW 2, and c) OW 4.

In general there is good agreement between the predicted and observed temperature changes, despite the transition zone. In fact, at some depths the results from the FLS model are identical to what was observed. Similar to the shallower depths, the second set of thermal from Table 5-4 provide better agreement with observed results, especially for OWs 1 and 4. Note that for OW 2, the second set of thermal properties from Table 5-4 still more accurately replicate the trend experimentally observed, even if at some points in time the first set provides FLS results closer to what was observed. For OW 2, also note that the values are only off by a few tenths of a degree.

5.7.2.3. Depths Greater than 18.3 m (60 ft)

Depths greater than 18.3 m are beyond the transition zone and have no atmospheric influence. Thus it is expected that the FLS temperature predictions at these depths would produce good agreement with the experimental results. Figure 5-22, Figure 5-23, and Figure 5-24 show this. Figure 5-22 shows the depths at 18.3 m for OW 4 and 22.9 m for OWs 1 and 2. The second set of thermal properties in Table 5-4 produce very good agreement with the observed results for each OW, including OW 2 which was not always the case for the shallower depths. These observations also hold true for the results displayed in Figure 5-23, which shows OWs 1, 2 and 4 at a depth of 27.4m, and in Figure 5-24, which shows the same OWs at a depth of 30.4 m. The different TCTs and TMTs are easier to recognize at these depths, which is a function of the shale having material properties that lend themselves to more extreme and rapid temperature changes than the silty sand layer, as well as there being no atmospheric influence.

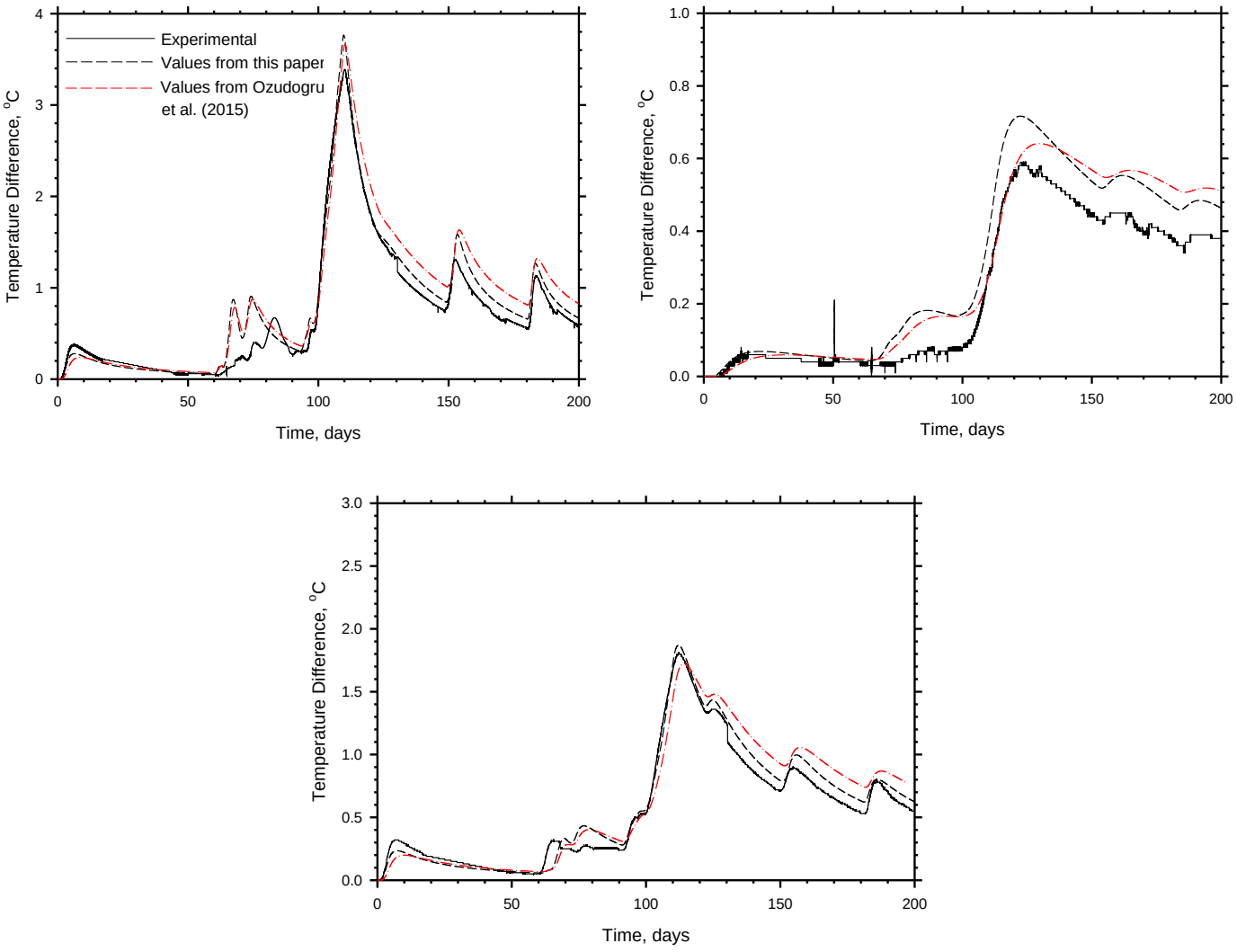

Figure 5-22. Temperature change in the ground over time for experimental results as compared to the predicted temperature change from the FLS model for a depth of 22.9 m at a) OW 1 and b) OW 2, and a depth of 21.3 m at c) OW 4.

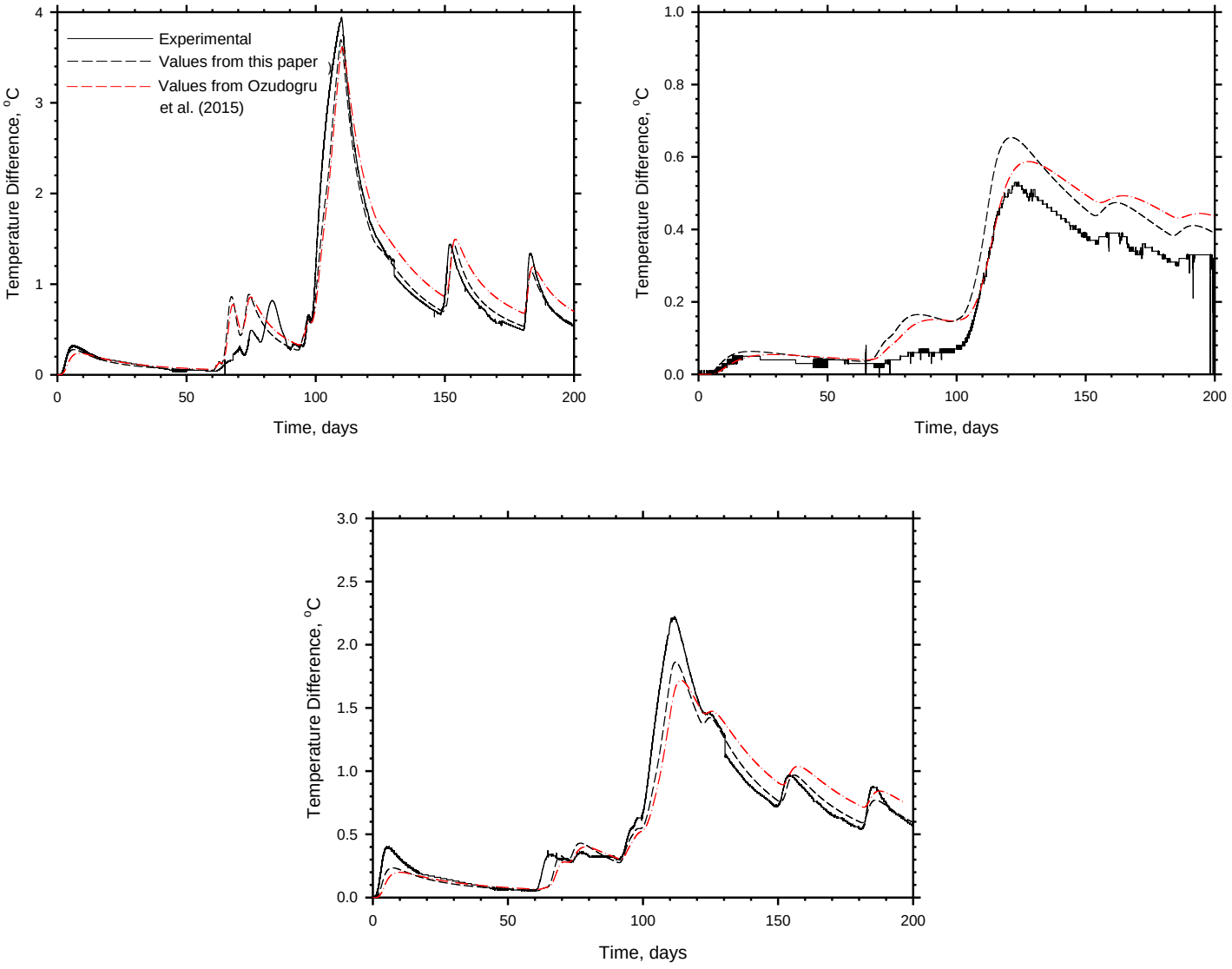

Figure 5-23. Temperature change in the ground over time for experimental results as compared to the predicted temperature change from the FLS model for a depth of 27.4 m at a) OW 1, b) OW 2, and c) OW 4.

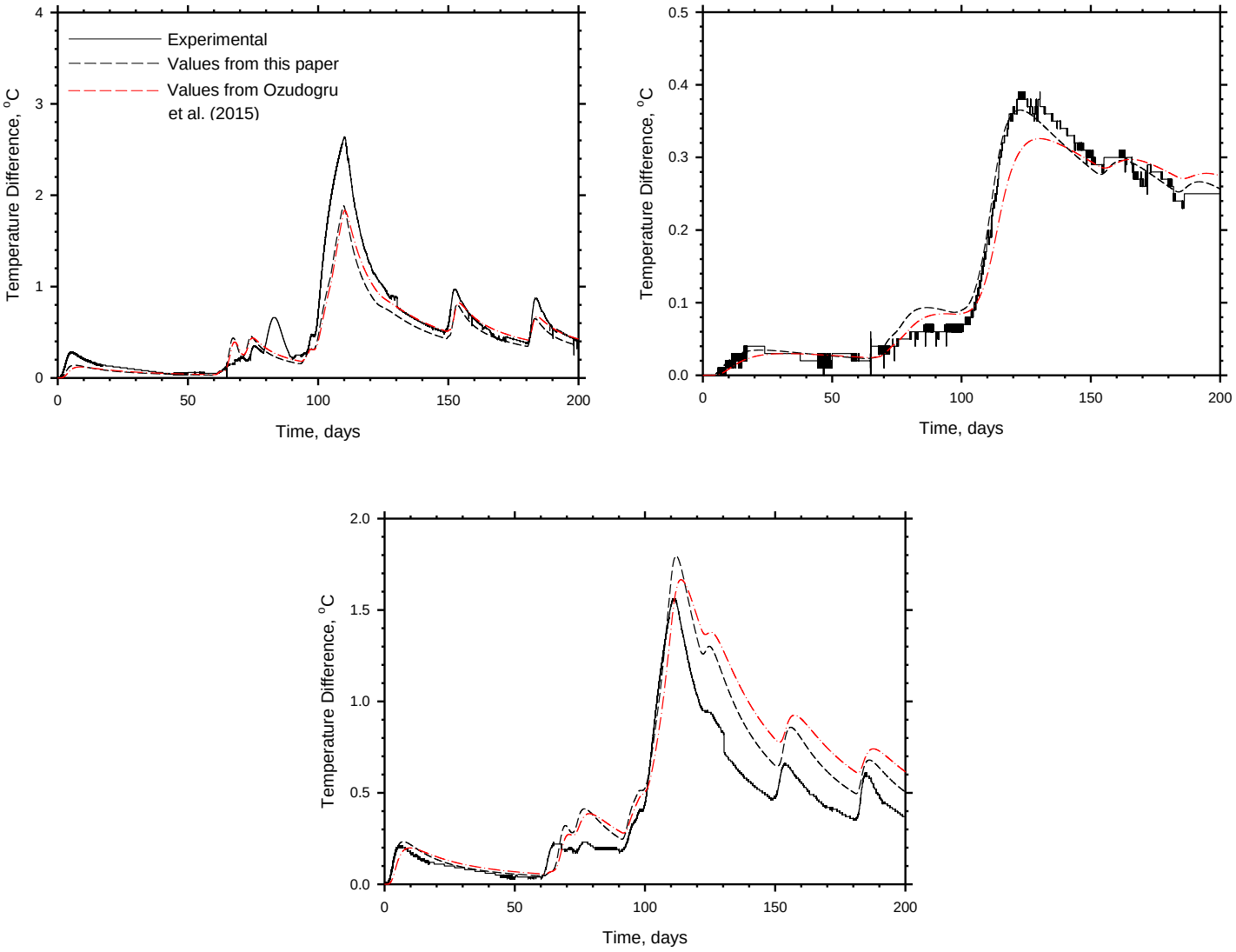

Figure 5-24. Temperature change in the ground over time for experimental results as compared to the predicted temperature change from the FLS model for a depth of 30.4 m at a) OW 1, b) OW 2, and c) OW 4.

5.7.2.4. Discussion

In comparing the temperature predictions from the FLS model with the observed values, there is poor agreement for TMT 1 for almost every depth and OW. This is especially true for OWs 1 and 4, which are closest to Pile 2, where TMT 1 took place. The energy values used to represent TMT 1, whose resulting temperature changes can generally be seen between days 60 and 110, are found in Figure 5-3. Due to the good agreement with TMT 2 as well as the TCT tests, there is most likely some discrepancy between the reported results and what actually took place. Abdelaziz (2013) mentions difficulties in obtaining accurate fluid temperature measurements for some of the tests and that may have occurred during TMT 1. The main discrepancy between the FLS and observed values is that the FLS shows both higher and more abrupt temperature changes, whereas the observed values are lower and more gradual. However, in almost every case the FLS and observed values do converge before increasing again as a result of TCT 4. This

indicates that the total amount of energy used in the FLS model was probably similar to the amount that was actually injected.

In general, for every other test, the FLS model does a good job at both predicting the peak temperature change as well as the rate of increase and decrease, both of which are important in SGE applications. This is also where the second set of values from Table 3 display a clear advantage over the values used in Ozudogru et al. (2014a). The correlation between the predicted and observed values using the second set of thermal properties is especially strong in the OWs that are closest to the piles, namely OWs 1, 3, and 4. TCT 1, which utilized Pile 3, occurred only 0.5 m from OW 3. From Figure 5-17c and Figure 5-18c, it can be seen that very good agreement exists for this test in both the peak temperature change and rates of temperature increase and decrease.

Thus, the FLS model accurately predicts the temperature change in the ground at both different depths and distances from the heat source. For example, OW 1 is 1 m from Pile 2, 1.7 m from Piles 1 and 3, and 2.3 m from Pile 4. Yet, the temperature change that resulted from the tests on the piles is accurately represented at different depths. This demonstrates the utility of this model in being able to accurately represent field conditions.

The apparent lack of accuracy between the predicted and observed values that occurred at OW 2 is from several factors. First, it is described as 'apparent' lack of accuracy in that the values were off by only a few tenths of a degree, which is about what it was for the other OWs. However, in terms of total temperature change, a few tenths of a degree is at some points in time, more than 100% of the total temperature change at OW 2. The discrepancy between the predicted and observed results is most likely a result of path effects. This manifests in several ways. First, as discussed previously, the method in accounting for the changing transition zone depth that produced the closest agreement between observed and predicted temperature changes was the one that used the depth as measured at the particular OW. For OWs 1 and 4, this is of little consequence as the depths of the silty-sand layer at their locations was within 1.5 m of each other and Pile 2, which is where the majority of the energy was exchanged. The depth of the sitly-sand at OW 2, however, is much lower (17.7 m). Thus, when this lower depth is assumed for the entire site, it not only affects the thermal properties along the path length (see Equation 5-8) which is compounded by the fact that path length is relatively great between OW 2 and the energy piles. The assumed lower depth also affects the layer dependent heat rate (Equation 5-19), which will ultimately affect the change in temperature. And because the change in temperature at this distance is relatively small, small variations from actual conditions can have a large impact in terms of percent difference between the FLS predictions and observed values.

Less accuracy was also observed in the upper 13 m. As previously discussed, this is due to atmospheric influence and Equation 5-22 can help account for this. A downfall of the atmospheric influence is that it is more difficult to establish accurate thermal properties of the silty-sand layer, especially since it does not extend beyond the zone of atmospheric influence. The results observed at OW 3 were primarily used in determination of the thermal properties as TCT 1 occurred very close to OW 3, thus most of the temperature change at that location will be from heat injection as opposed to atmospheric influence. Furthermore, this was the first test meaning that it is easier to isolate the temperature change from the test from that of the atmosphere because there was less time for the atmosphere to influence results (as opposed to TCT 5, which occurred near the end of the 200 day period). As shown and explained previously, good agreement between predicted and observed values exists for OW 3.

There is also less accuracy for the depths that occurred in the transition layer, though not at as much as may be expected. The differences are due to both path effects as discussed previously, as well as the limitations of using exponential functions and a pseudo-static approach for estimating the temperature change at the layer interface (see Abdelaziz et al. 2014). These effects can be mitigated through utilizing different methods to account for this depth, but they cannot be eliminated. Ultimately a SGE designer may only have one boring upon which to base a depth rendering selection of a transition layer depth a non-issue.

Finally, the effects of the differing thermal properties between the layers can be seen in both the predicted and experimental results. The thermal properties in the silty-sand layer result in a lower heat rate (see Figure 5-14) as well as less of a temperature change and slower rates of temperature increase and decrease as compared to the shale layer.

5.8. CONCLUSIONS

A finite line source model that can account for multiple, homogeneous subsurface layers as well as non-constant heating rates has been presented. It improves upon previous models by taking into account heat exchange between the ground and atmosphere. It also presents an improved method for determining the layer dependent heating rate by considering the thermal and geometric properties of the heat exchanger as well as time-rate effects. The FLS model was validated using a finite element model. The finite element model was calibrated to a field thermal conductivity test. The FLS model was then used to predict the temperature change in the ground from a series of thermo-mechanical and thermal conductivity field tests that occurred over the course of 200 days. Good agreement was observed between observed temperature changes in the ground and those predicted by the FLS model.

5.9. ACKNOWLEDGEMENTS

This material is based upon work supported by the National Science Foundation under grants CMMI-0928807 and CMMI-1100752 as well as by the Mid-Atlantic Universities Transportation Center (MAUTC). The first author started working on this study as an undergraduate researcher and is currently supported by the National Science Foundation as a graduate research fellow. All this support is greatly appreciated. Any opinions, conclusions or recommendations expressed herein are those of the authors and do not necessarily reflect the views of these agencies.

5.10. REFERENCES

Abdelaziz, S. L. (2013). "Deep Energy Foundations: Geotechnical Challenges and Design Considerations." Ph.D. Thesis, Virginia Polytechnic Institute and State University.

Abdelaziz, S. L., Ozudogru, T. Y., Olgun, C. G., and Martin, J. R. (2014). "Multilayer finite line source model for vertical heat exchangers." Geothermics, 51, 406-416.

Beck, M., Bayer, P., de Paly, M., Hecht-Mendez, J., and Zell, A. (2013). "Geometric arrangement and operation mode adjustment in low-enthalpy geothermal borehole fields for heating." Energy, 49(1), 434-443.

Bourne-Webb, P. J., Amatya, B., Soga, K., Amis, T., Davidson, C., and Payne, P. (2009). "Energy pile test at lambeth college, London: Geotechnical and thermodynamic aspects of pile response to heat cycles." Geotechnique, 59(3), 237-248.

Bowers, Jr., G., Olgun, C. and Ozudogru T. (2016). “Geometric Optimization of Shallow Geothermal Energy Systems through Select Borehole Utilization.” Applied Thermal Energy. Submitted.

Bowers, Jr., G., and C. Olgun. (2016). “The Thermal Performance of a Small-Scale Bridge Deck Deicing System Under Bridge Deck Deicing and Thermal Recharge Operations..” ASCE Journal of Cold Regions Engineering. Submitted.

Brandl, H. (2006). "Energy foundations and other thermo-active ground structures." Geotechnique, 56(2), 81-122.

Churchill, S.W. (1977). “Friction factor equations spans all fluid-flow regimes.” Chemical Engineering, 84, 91–92.

COMSOL. (2015). “COMSOL MultiphysicsTM Version 5.1: User’s Guide and Reference Manual.” COMSOL Inc., Burlington, MA.

De Paly, M., Hecht-Mendez, J., Beck, M., Blum, P., Zell, A., and Bayer, P. (2012). "Optimization of energy extraction for closed shallow geothermal systems using linear programming." Geothermics, 43, 57-65.

Dupray, F., Chao, L., and Laloui, L. (2014a). "Heat-exchanger piles for the de-icing of bridges." Acta Geotechnica, 9(3), 413-423.

Ingersoll, L. R., and Plass, H. J. (1948). "Theory of ground pipe heat source for heat pump." Heating, Piping and Air Conditioning, 20(7), 119-122.

Kusuda, T., and Achenbach, P.R. (1965). “Earth Temperature and Thermal Diffusivity at Selected Stations in the United States.” *ASHRAE Transactions.* 71(1): 61-65.

Minsk, L. (1999). "Heated Bridge Technology: Report on ISTEA Sec. 6005 Program." Special Report. FHWA, U.S. Department of Transportation.

Lazzari, S. 2010. “Long-term performance of BHE (borehole heat exchanger) fields with negligible groundwater movement.” Energy, 35(12), 4966-4974.

Loveridge, F., and Powrie, W. (2013). "Temperature response functions (G-functions) for single pile heat exchangers." Energy, 57, 554-564.

Loveridge, F., and Powrie, W. (2014). “2D Thermal Resistance of Pile Heat Exchangers.” *Geothermics*. 50: 122-135.

Lund, J. W., and Boyd, T. L. (2016). "Direct utilization of geothermal energy 2015 worldwide review." Geothermics, 60, 66-93.

Ozudogru, T. Y., Ghasemi-Fare, O., Olgun, C. G., and Basu, P. (2014a). "Numerical Modeling of Vertical Geothermal Heat Exchangers Using Finite Difference and Finite Element Techniques." Geotechnical and Geological Engineering, 33(2), 291-306.

Ozudogru, T. Y., Olgun, C. G., and Senol, A. (2014b). "3D numerical modeling of vertical geothermal heat exchangers." Geothermics, 51, 312-324.

Wood, C. J., Liu, H., and Riffat, S. B. (2009). "Use of energy piles in a residential building, and effects on ground temperature and heat pump efficiency." Geotechnique, 59(3), 287-290.

Yang, W., Mingheng, S., and Zhenqian, C. "A variable heat flux line source model for boreholes in ground coupled heat pump." Proc., 2009 Asia-Pacific Power and Energy Engineering Conference, APPEEC 2009,

March 27, 2009 - March 31, 2009, Inst. of Elec. and Elec. Eng. Computer Society, Wuhan University; IEEE Power and Energy Society; Chinese Society for Electrical Engineering; Scientific Research Publishing.

Zeng, H. Y., Diao, N. R., and Fang, Z. H. (2002). "A finite line-source model for boreholes in geothermal heat exchangers." Heat Transfer-Asian Research, 31(7), 558-567.

6. GEOMETRIC OPTIMIZATION OF SHALLOW GEOTHERMAL ENERGY SYSTEMS THROUGH SELECT BOREHOLE UTILIZATION

6.1. ABSTRACT

Shallow geothermal energy systems (SGES) are becoming more common due to their ability to assist in efficient heating and cooling of buildings. These heat exchanger systems are also being integrated within building foundations and allowing the creation of thermoactive foundations, which do not require the additional installation cost of a borehole field. Despite the popularity of SGES, several challenges remain that must be addressed. One challenge is subjecting SGES to unbalanced heating and cooling loads during the year. If more energy is required for either heating or cooling, the in-situ ground temperature could potentially change over time, thus negatively affecting the efficiency of the system. This is especially challenging in heating or cooling dominated climates such as Chicago, Miami, or Houston, and when energy demand profiles are such that they only require energy for heating, such as bridge deck deicing or grain drying. This paper explores selective operation of boreholes within a typical geothermal borehole grid field to minimize the amount of energy lost in the ground. The study utilizes a calibrated numerical model to investigate different combinations of heat injection and extraction alternatives. The findings from the analyses are evaluated to establish a practical solution to the problem that would not require an advanced control system or significant oversight from a system operator.

6.2. INTRODUCTION

Shallow geothermal energy systems (SGES) are becoming more common due to their ability to assist in efficient heating and cooling of buildings. These heat exchanger systems are also being integrated within building foundations and allowing the creation of thermoactive foundations, which do not require the additional installation cost of a borehole field (Brandl 2006). Furthermore, SGES applications are extending beyond traditional heating and cooling of buildings to bridge deck deicing, grain drying, and district water heating. Despite the popularity of SGES, several challenges remain that must be addressed. One challenge is subjecting SGES to unbalanced heating and cooling loads during the year. If more energy is required for either heating or cooling, the in-situ ground temperature could potentially change over time, thus negatively affecting the efficiency of the system. This is especially challenging in heating or cooling dominated climates such as Chicago, Miami, or Houston, and when energy demand profiles are such that they only require energy for heating, such as bridge deck deicing or grain drying.

Abdelaziz et al. (2015) numerically simulated 30 years of heating/cooling operations for an office building at three selected locations in the United States including Charlotte, NC, Chicago, IL, and Austin, TX. These studies included building physics simulations, which considered the climatic conditions at these selected locations to evaluate building and ground thermal loads. Heating and cooling loads are somewhat balanced in Charlotte with ground thermal loads of similar amplitude and duration. Similar amplitude heating episodes in the winter and cooling episodes in the summer are indicative of symmetrical ground thermal demands, which would have little impact on the in-situ ground temperatures. However unbalanced conditions are prevalent in Chicago and Austin with heating and cooling dominant ground thermal loads, respectively. These simulations over the 30 years of operation indicate that the average temperature of the ground progressively cooled in Chicago and warmed in Austin. The authors note that temperature change of the ground would decrease system efficiency and also it could potentially affect

the soil's compressibility and strength which would be important if the deep foundations of the building are utilized as heat exchangers.

One of the possible ways to mitigate the problem of unbalanced heat extraction is to selectively inject energy into the ground to offset unequal heating/cooling demands. In bridge deck deicing this is accomplished by operating the system during the summer to collect the thermal energy from the bridge deck and inject it into the ground, thereby heating the ground and creating an energy reserve for use during the winter. The SERSO project in Switzerland, which is the world's first shallow geothermal heated roadway, utilizes this concept (Eugster, 2007). Since the beginning of its operation in 1994 it has been able to inject more energy in the summer than it extracts in the winter, thus increasing the efficiency of the system. The authors report that another advantage of injecting thermal energy during the summer is reduction of extreme bridge deck temperatures in the summer and significant stabilization of the bridge deck surface temperatures.

Thermal energy storage can also be accomplished for buildings in heating dominated climates by collecting thermal energy from the building's roof and/or facade. For example, Yin et al. (2013) designed a building panel that combines photovoltaic modules with circulation tubes that can collect both electricity and thermal energy. The added advantage of this system is that it helps control indoor temperatures by collecting the thermal energy before it is transferred to the interior of the building, thereby reducing the amount of energy required for cooling.

Thus, there are many advantages to collecting and storing thermal energy aside from increasing SGES efficiency for both buildings and bridges. However, there are limitations to underground thermal energy storage that arise from the ground's ability to store energy as well as the climatic conditions that determine how much energy can be injected. Thus, thermal energy storage combined with efficient operation of the system is paramount in creating the most sustainable system.

6.3. BACKGROUND

Efficient operation of the SGES application involves the optimization of both energy injection and extraction. Presumably in regards to energy injection, it is best to inject as much energy as possible, which would involve operating all heat exchangers to full capacity (i.e. injecting energy into all boreholes). Optimization may be possible, however, by redistributing the energy within the borehole field, such as concentrating it towards the center or perimeter, to prevent the energy from leaving the geothermal footprint area and ensure that it is still available for extraction when needed. When considering energy extraction, different scenarios may exist that impose a higher extraction rate to certain boreholes during selected periods. These scenarios would both prevent energy from leaving the geothermal footprint area and make the stored energy easily accessible. The system will achieve the greatest efficiency if the stored energy is extracted directly as opposed to it being used to recharge the system. In the case of recharge, energy is extracted from the ground, lowering the ground temperature, and then the stored energy redistributes and stabilizes ground temperatures. Direct extraction results in higher fluid temperatures, which increases system efficiency when the energy is being used for heating.

Optimization of energy extraction has been explored by de Paly et al. (2012), Beck et al. (2013), and Bayer et al. (2014). De Paly et al. (2012) developed an algorithm that utilizes linear programming to optimize the energy extraction by minimizing the temperature decrease in the ground by varying the heat fluxes (heat extraction rates) at each borehole. Their model uses an analytical line heat source equation to represent

each borehole, and through superposition they are able to determine the change in temperature in the ground due to multiple boreholes. For the same amount of energy extracted per year and for a system in operation for 30 years, the authors were able to reduce the temperature decrease in the subsurface by 18%. Practically, this system would be difficult to implement requiring either an advanced control system or a very attentive system operator to constantly monitor and adjust the heat extraction rate of each borehole.

Beck et al. (2013) looked at optimizing the borehole geometrical arrangement of a given field with and without optimized heat flux as described in de Paly et al. (2012) to minimize the temperature decrease in the ground. The authors also represented the boreholes using an analytical line heat source equation. For a given set of ground parameters, they determined the optimum borehole configuration. They tested various optimization schemes that included equal heat extraction in all boreholes and several variations of an optimized heat flux scheme. Once again, this strategy is not necessarily practical for several reasons. One, if the ground parameters were estimated incorrectly, the geometric configuration obtained using this algorithm may negatively impact system performance as opposed to helping it. Furthermore, this scheme would lead to additional complexities for the borehole driller, which may increase the installation cost, and hence, the return period for investment.

Bayer et al. (2014) combined the model developed in De Paly et al. (2012) for determining changes in ground temperature with a scheme that reduces the number of boreholes used in a given field in such a way that the boreholes around which occur the maximum change in ground temperatures are eliminated. The loads to the other boreholes are increased to make up for eliminated boreholes. The authors report this method as being successful in reducing the temperature change in the ground when equal heat loads are applied to all boreholes. There is a point at which the increased borehole heat loads cause a change in ground temperature greater than what is prevented by eliminating interfering boreholes.

It is interesting to note that the most efficient geometrical arrangements in Beck et al. (2013) involved distributing the boreholes along the perimeter and the boreholes that were eliminated to optimize the system were the interior boreholes in Bayer et al. (2014). This is due to the fact that the perimeter boreholes are able to directly access the surrounding ground. Considering the goal of this study is to maximize heat storage and achieve the greatest temperature in the ground, these previous studies seem to indicate that heat storage should be concentrated in the interior of the borehole group.

This paper explores selective operation of boreholes within a typical geothermal borehole grid field to minimize the amount of energy lost in the ground. The study utilizes a calibrated numerical model to investigate different combinations of heat injection and extraction alternatives. The findings from the analyses are evaluated to establish a practical solution to the problem that would not require an advanced control system or significant oversight from a system operator.

6.4. NUMERICAL ANALYSIS AND MODEL DEVELOPMENT

A series of numerical simulations was performed to investigate different heat injection and extraction scenarios in the context of SGES efficiency. A two-dimensional model was developed for performing the thermal energy storage analyses using COMSOL Multiphysics™, a finite element simulation environment (COMSOL, 2015). This numerical analyses framework is based on the modeling approach developed and calibrated by Bowers et al. (2016) and Ozudogru et al. (2014). The model geometry consists of a 6x6 grid of 15cm diameter boreholes spaced 8m center-to-center as shown in Figure 6-1. The model utilizes a

horizontal cross-section of the borehole-soil system and it consists of several components These components include the fluid circulation pipes, an equivalent solid inside the circulation pipes to represent the fluid, the thermal grout and the soil surrounding the boreholes.

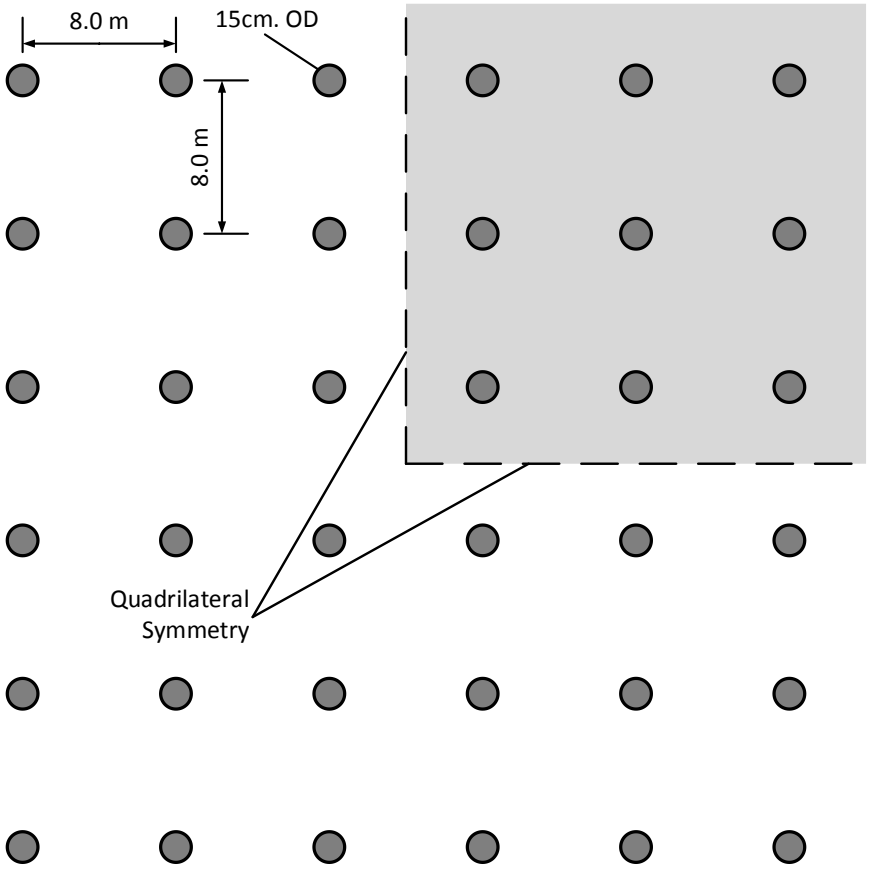

Figure 6-1. The modeled borehole field. Note the symmetric boundaries that allow for only a quarter of the above field to be modelled.

Each borehole has a single PEX U-loop with an inner diameter of 3.404 cm and an outer diameter of 4.171 cm (i.e. wall thickness t = 3.8 4mm) as shown in Figure 6-2. The material properties of the pipes, borehole, and soil are given in Table 6-1. The finite element mesh discretization of the model is performed using triangular elements. Quadrilateral symmetry is used in the model to reduce computational effort, since the geometry and physical process in the model is symmetrical. As such, Neumann boundary conditions with zero heat flux exist at the symmetry boundaries. The meshed domain around the boreholes and quadrilateral symmetry approach are shown in Figure 6-3 and Figure 6-4. The soil domain extends 60m from the center of the borehole footprint area in the x and y directions. A constant temperature equal to the initial ground temperature is applied to the outer boundary. In the models, the heat flux at this boundary was monitored to ensure it remained at zero, indicating that there was no thermal interference from the boundary conditions.

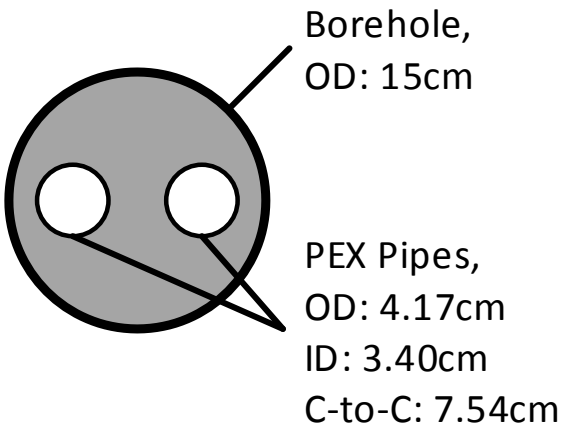

Figure 6-2. Cross section of the borehole and circulation pipes.

Table 6-1. Material properties used in the finite element model.

Material Property	**Value**	**Unit**
Soil		
Density*	1500	kg/m^3
Specific Heat Capacity*	1500	J/(kg·K)
Thermal Conductivity*	2.00	W/(m·K)
Initial Temperature*	15.0	^oC
Borehole Grout		
Density	1600	kg/m^3
Heat Capacity	1500	J/(kg·K)
Thermal Conductivity	1.00	W/(m·K)
Circulation Tube		
Density	960	kg/m^3
Heat Capacity	2300	J/(kg·K)
Thermal Conductivity	0.41	W/(m·K)
Effective Thermal Conductivity	0.37	W/(m·K)
Circulation Fluid		
Density	999.62	kg/m^3
Heat Capacity	4186.92	J/(kg·K)
Thermal Conductivity	0.59	W/(m·K)
Effective Thermal Conductivity	1000	W/(m·K)

*Values used for all analyses except those in the parameter study

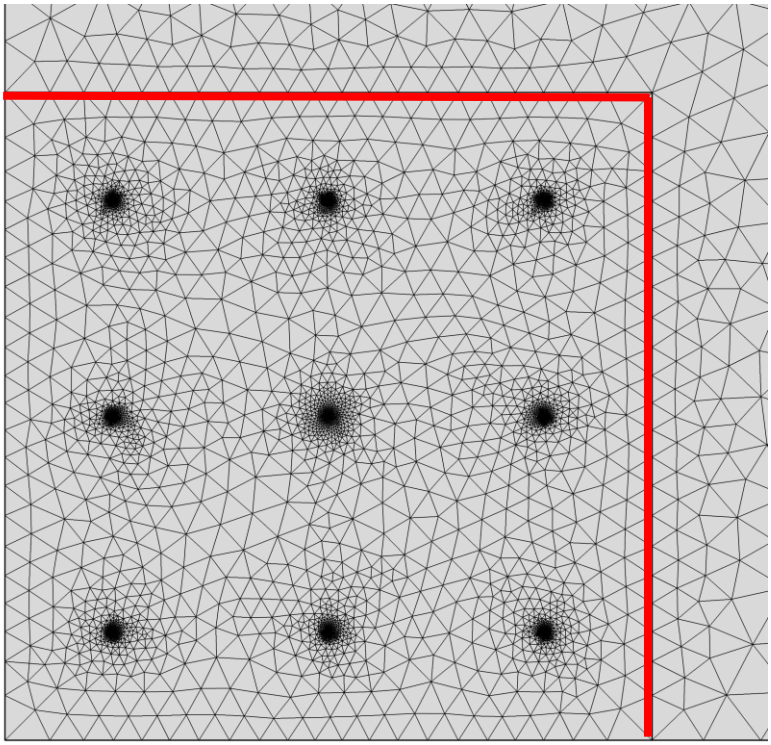

Figure 6-3. Meshing of the domain around the borehole footprint area, which is only a quarter of the entire borehole field due to quadrilateral symmetry with . Also observe the borehole footprint area outlined in red.

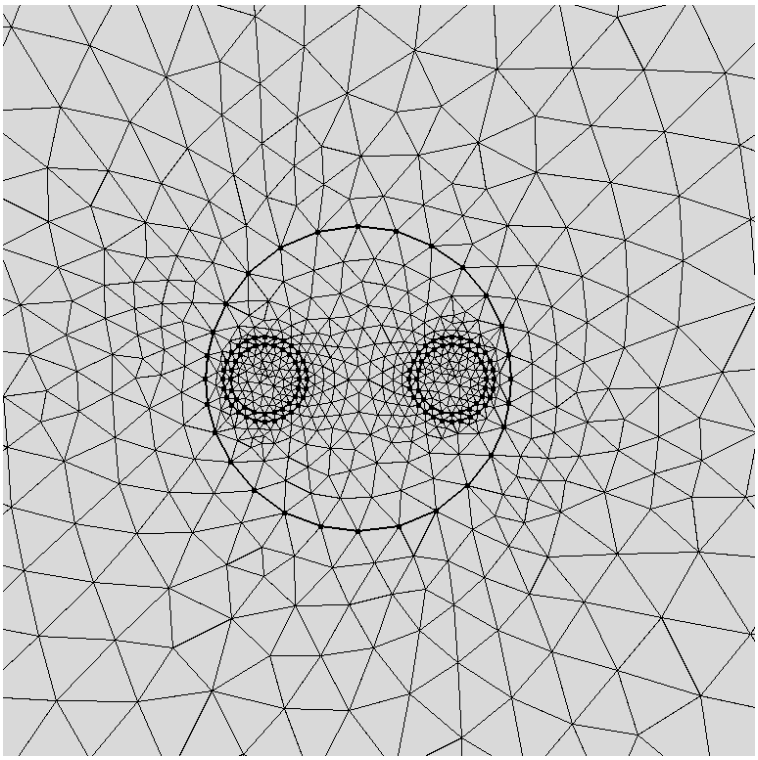

Figure 6-4. A close-up view of the meshing of a borehole and the circulation tubes.

The variation of temperature distribution along the vertical direction will be relatively small as the dominant direction of heat exchange is horizontal towards and away from the boreholes. Therefore, any vertical process is assumed to have negligible influence on the long-term thermal borehole operation and the 3D heat transfer problem is reduced to a 2D time-dependent heat conduction problem.

Because of the 2-dimensional nature of the model, the fluid flow in the pipes cannot be modeled directly. Lazzari et al. (2010) proposed using an equivalent solid with internal heat generation that can reproduce the same power per unit length that the borehole heat exchanger (BHE) is subjected to. To accomplish this, the equivalent solid has the same unit density and specific heat capacity as the carrier fluid, but contains a very high thermal conductivity (k_{eqs} = 1000 W/m-K), which will result in an almost uniform temperature distribution within the cross section of each circulation tube. The convective thermal resistance, which occurs between the carrier fluid and the tube wall can be accounted for by using an effective thermal conductivity of the pipe material, $k_{p,eff}$, (Lazzari et al. 2010), such that:

$$k_{\mathrm{p\,eff}} = \frac{\ln\left(d_{\mathrm{po}}/d_{\mathrm{pi}}\right)}{\frac{2}{d_{\mathrm{pi}}h_{\mathrm{int}}} + \frac{\ln\left(d_{\mathrm{po}}/d_{\mathrm{pi}}\right)}{k_{\mathrm{p}}}}$$

The internal convection coefficient, h_{int}, depends on the flow characteristics and can be determined using the correlations developed by Gnielinski (1976) and Churchill (1977). To simulate heat extraction, a constant heat extraction rate was applied to the equivalent water domain inside the circulation pipe. To simulate heat injection, a constant temperature was applied to the inner surface of the pipe wall. This constant temperature was applied for a certain length of time. In actuality, the process is much more complicated as a) the circulation fluid will not maintain a constant temperature over time but is likely to vary in response to the temperature of the heat collector, thus the applied temperature can be thought of as an average fluid temperature over the given injection interval; and b) the circulation fluid travelling in the downward flowing pipe will have a higher temperature than the circulation fluid travelling in the upward flowing pipe, thus the applied temperature can be thought of as the average temperature of the circulation fluid in the downward and upward pipes.

6.5. MODELING APPROACH: HEAT INJECTION AND EXTRACTION SCENARIOS

A series of thermal storage analyses is performed using this model geometry for several different heat injection and extraction scenarios. The analyses considered a variety of heat injection and extraction alternatives that utilized different sequences of borehole utilization. In general, heat injection was performed for 3 months during the summer (June-August). Following heat injection are two months of no net heat injection or extraction (September-October). Beginning in November are 5 months of heat extraction (November-March). During the final 2 months of the operational year (April-May) there is no operation.

The base case analysis was designed to represent a typical borehole system configuration that is similar to the current state of practice. In the base case, heat was injected into all the boreholes during the first 3 months, or 90 days. In the model, this was accomplished by applying 25°C fluid temperature to the inner pipe wall as described previously. This was applied for 6 hours per day followed by 18 hours of inactivity. The temperature and duration of heat injection was selected to represent heat collection from a solar thermal collector during the summer. This corresponds to a total of 891 MJ of energy injected for the

quarter-section of the borehole group (3564 MJ for the entire borehole group) during the considered heat injection episode.

Following the 90 day period of heat injection was a 60 day idle period where heat was neither injected nor extracted. This was selected to represent the seasonal episodes where the outside temperatures are not high enough to perform heat injection, yet there is not typically a demand for heat extraction from the ground. After the end of the first idle period, heat was extracted from all the boreholes at a rate of 20 W/m per length of each borehole for 8 hours per day. This corresponds to a total extraction rate of 180W/m for the quarter-section of the borehole group (720 W/m for the entire borehole group). In all, a total of 856 MJ of energy was extracted for the quarter-section of the borehole group (3424 MJ for the entire borehole group) during the considered heat extraction episode.

Figure 6-5 represents a year's worth of operation and shows the temperatures of the water, borehole domain, and the borehole surface to demonstrate how heat is injected and extracted. As mentioned earlier, temperature of the water in the circulation pipe is almost constant as a result of the modeling approach. The injection, extraction, and idle periods as well as the corresponding temperatures and heat fluxes are indicated in the Figure. Figure 6-6a and Figure 6-6b display the first week of injection and extraction, respectively. It must be noted that during heat injection, which is temperature controlled, the inner pipe surface has a constant temperature of 25^{o}C for 6 hours a day as energy is being injected into the ground. During extraction, however, the temperatures of the water, borehole domain, and borehole surface decrease for 8 hours/day as 20 W/m heat is extracted from each borehole. These temperatures partially recover at the idle time during the day when heat is not being extracted from the borehole. These figures are presented to describe the general process of heat injection and extraction operations. Further discussion of the ground temperatures and heat retention rates that were evaluated from the base case will be provided in the subsequent sections when the analyses results are presented in detail.

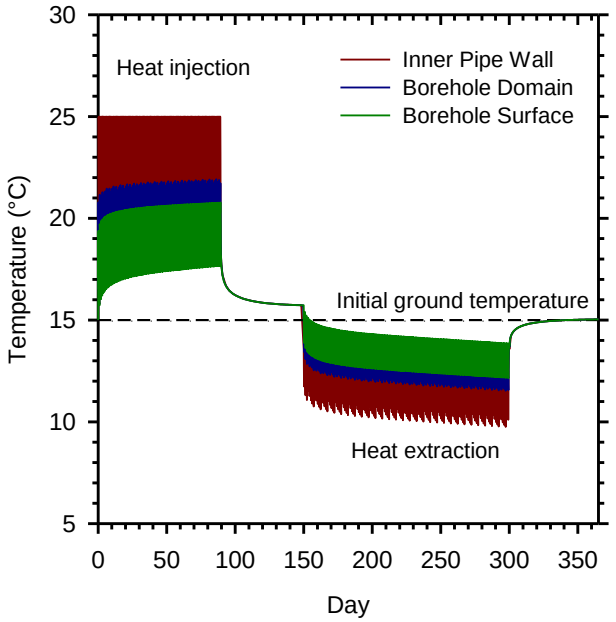

Figure 6-5. Temperatures at the inner pipe wall, borehole domain, and borehole surface during one year of operation. Heat is injected by imposing a constant temperature at borehole contact with the soil domain whereas heat is extracted by imposing a constant heat rate per in-plane length of the borehole

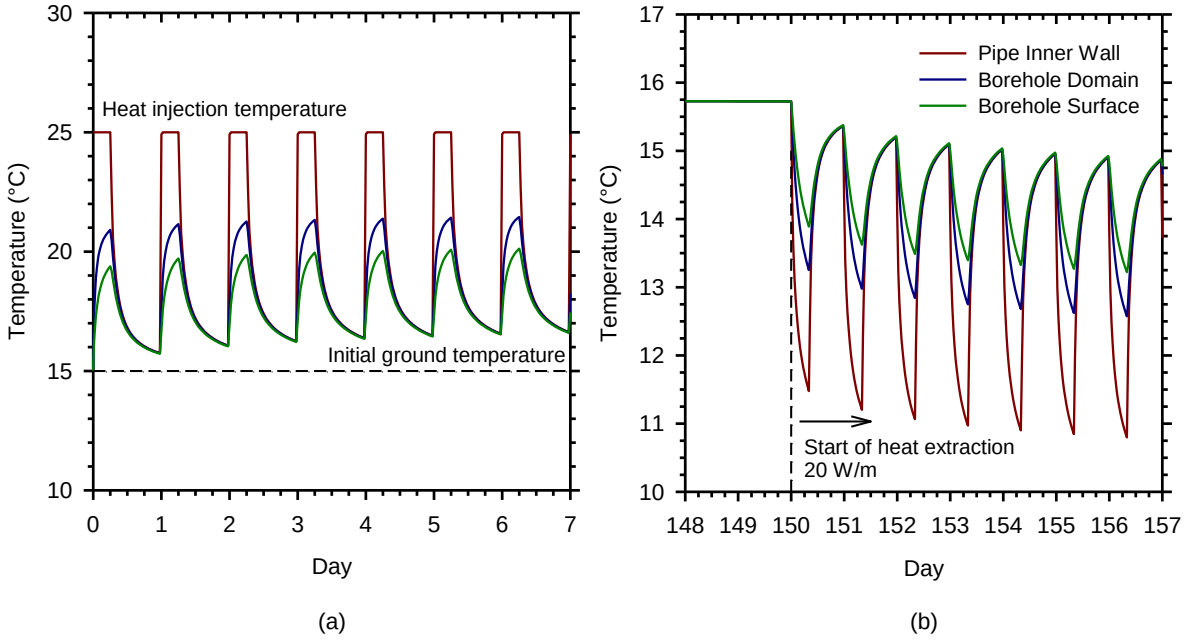

Figure 6-6. Temperatures of the pipe inner wall, borehole domain, and the borehole surface during the first week of heat injection (a), and during the first week of heat extraction (b).

Additional cases that used different sequences of borehole utilization were then compared to the results obtained from the base case. A total of two alternative heat injection scenarios (Table 6-2) and seven alternative extraction scenarios (Table 6-3) were tested. The main purpose of the additional analyses is to provide a comparison of different heat injection and extraction scenarios as well as present the effect of different model parameters on overall response and system efficiency in terms of thermal storage operations. In these analyses, sequencing and distribution of borehole utilization are varied systematically and the effect on thermal storage is investigated. Furthermore, model parameters such as initial ground temperature, fluid injection temperature, the soil's thermal conductivity and volumetric heat capacity are also varied to benchmark the effect of material properties.

Table 6-2. Summary of the alternative injection schemes considered.

Case	Inner		Middle		Outer		Hrs/Day	
	H	I	H	I	H	E	H	Flux
Basic Injection	25	-	25	-	25	-	6	-
Injection Redistribution 1	25	7.5	25	7.5	25	6	6	6
Injection Redistribution 2	25	25	25	25	25	20	6	6

H = Temperature of the circulating fluid (°C)
I = Rate of injection (W/m)
E = Rate of extraction (W/m)

Table 6-3. Summary of the alternative extraction schemes considered. 3a refers to the first 15 days of the 3rd month and 3b refers to the last 15 days of the 3rd month.

Extraction	Inner						Middle						Outer					
	1	2	3a	3b	4	5	1	2	3a	3b	4	5	1	2	3a	3b	4	5
Equal Extraction	20	20	20	20	20	20	20	20	20	20	20	20	20	20	20	20	20	20
Inside-Outside	45	45	45	-	-	-	45	45	45	-	-	-	-	-	-	36	36	36
Outside-Inside	-	-	-	45	45	45	-	-	-	45	45	45	36	36	36	-	-	-
Outside-Inside Optimized	-	-	-	-	45	45	-	-	-	-	45	45	36	36	36	36	-	-
Different Extraction Rates 1	33	33	33	33	33	33	24	24	24	24	24	24	15	15	15	15	15	15
Different Extraction Rates 2	7	7	7	7	7	7	16	16	16	16	16	16	25	25	25	25	25	25
Different Extraction Rates 3	26.5	26.5	26.5	26.5	26.5	26.5	22	22	22	22	22	22	17.5	17.5	17.5	17.5	17.5	17.5
Different Extraction Rates 4	13.5	13.5	13.5	13.5	13.5	13.5	18	18	18	18	18	18	22.5	22.5	22.5	22.5	22.5	22.5

Table 6-4. Summary of the alternative injection and extraction schemes considered including those from the parametric study.

	Injection			Extraction							
Parameter	Base	IR1	IR2	Base	In-Out	Out-In	Out-In Opt	DE 1	DE 2	DE 3	DE 4
Soil Temperature (°C)	13, 15	15	15	13, 15	15	15	15	15	15	15	15
Fluid Injection Temperature (°C)	25, 30	25	25	25, 30	25	25	25	25	25	25	25
Thermal Conductivity (W/mK)	1.0, 1.5, 2.0, 2.5	2.0	2.0	1.0, 1.5, 2.0, 2.5	2.0	2.0	1.5, 2.0	2.0	1.0, 1.5, 2.0	2.0	2.0
Volumetric Heat Capacity (J/m^3K)	1000, 1500, 2250, 3000	2250	2250	1000, 1500, 2250, 3000	2250	2250	1000, 1500, 2250	2250	1000, 1500, 2250	2250	2250
Year 2 Considered	Yes			Yes			Yes				
Total	**11**	**1**	**1**	**11**	**1**	**1**	**5**	**1**	**6**	**1**	**1**

In considering different cases, the boreholes within the group were divided into one of three groups: inner, middle, or outer as shown in Figure 6-7. The parameters for the two alternative injection scenarios are given in Table 6-2. In both cases, 25°C was applied to the inner pipe wall for 6 hours/day to the inner, middle, and outer boreholes which is the same as the base case. However, during the 18 hours between injection operations, energy is redistributed within the borehole group by extracting energy from the outer boreholes and then injecting that energy into the inner and middle boreholes. The difference between the two alternative cases is the rate at which the energy was extracted and injected. Following 6 hours of injection, and then 6 hours of inactivity, energy was extracted from the outer boreholes at a rate of 6 W/m for the Injection Redistribution Case 1 (IR1) and injected into the inner and middle boreholes at a rate of 7.5 W/m. For Injection Redistribution Case 2 (IR2) energy was extracted at a rate of 20 W/m from the outer boreholes and injected at a rate of 25 W/m into the inner and middle boreholes. Following the period of redistribution, there was another 6 hours of inactivity before injection began the next day.

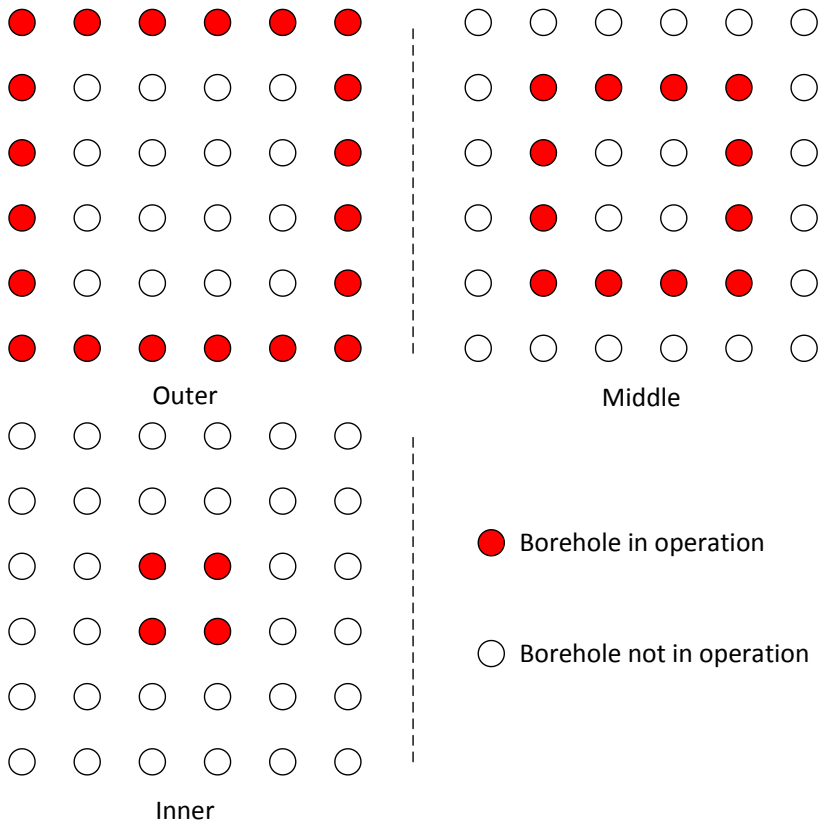

Figure 6-7. Locations of the 'outer', 'inner', and 'middle' boreholes for the alternative injection and extraction cases.

Table 6-3 lists the different heat extraction cases and which borehole group (inner, middle, outer) was operated during each extraction scenario and for what length of time during the 5 months (150 days) of extraction. For the base case of equal extraction, all three borehole groups were operated for the entire 5 months with an extraction rate of 20 W/m per borehole. The 'Inside-Outside' scenario involved operating only the inner and middle borehole groups for the first 75 days with an extraction rate of 45

W/m and then only operating the outer borehole group for the remaining 75 days with an extraction rate of 36 W/m. The 'Outside-Inside' scenario is the opposite of the 'Inside-Outside' where the outer borehole group is operated for the first 75 days with an extraction rate of 36 W/m followed by the inner and middle borehole groups with an extraction rate of 45 W/m. 'Outside-Inside Optimized' is a variation of 'Outside-Inside' where the outer borehole group is operated at the same extraction rate (36 W/m), but for a longer period of time (90 days). This results in the inner and middle borehole groups operated for a shorter period of time (60 days) with an extraction rate of 45 W/m.

There are four 'Different Extraction Rates' cases, each of which involves subjecting the inner, middle, and outer borehole groups to a different extraction rate for the entire 150 days of extraction. That is, all the boreholes are operated for the full 5 months of extraction as in the base case, but each group has a different load. For example, Different Extraction Rates Cases 1 (DE1) and 3 (DE3) subjected the inner borehole group to the highest extraction rate (33 W/m for DE1, 26.5 W/m for DE3), followed by the middle borehole group (24 W/m for DE1, 22 W/m for DE3), and the outer borehole group had the lowest extraction rate (15 W/m for DE1, 17.5 W/m for DE3). Different Extraction Rates Cases 2 (DE2) and 4 (DE4) subjected the outer borehole group to the highest rates (25 W/m for DE2, 22.5 W/m for DE4), followed by the middle borehole group (16 W/m for DE2, 18 W/m for DE4), and then the inner borehole group (7 W/m for DE2, 13.5 W/m for DE4).

In all the additional extraction cases, heat extraction rates were applied for a period of 8 hours/day. They were also adjusted so that the same amount of energy (180 W/m) was extracted over time, allowing for a direct comparison of all cases to the base case. Such an adjustment was necessary because the number of utilized boreholes for heat injection varied for different analysis cases. For example, the 'Inside-Outside' case involved operating the inner and middle borehole groups for the first 75 days with an extraction rate of 45 W/m per borehole and the outer borehole group was left alone. Because the inner and middle borehole groups contain a combined total of 4 boreholes per quarter of the borehole grid, at an extraction rate of 45 W/m, the total extraction rate of the group is 180 W/m. During the last 75 days only the outer borehole group was operated and because there are 5 boreholes in the outer group, an extraction rate of 36 W/m per borehole yields a total extraction rate of 180 W/m. This results in a total of 825 MJ of extracted energy per meter of depth and per quarter of the borehole grid. Note that 778 MJ is the exact amount determined from the application of the heat extraction resulting from 180 W/m being applied for 8 h/day over a period of 150 days (5 months). An additional 47 MJ was consumed in the ramping of loads as they were applied to the water domain.

A parametric study was also performed to determine how the soil's thermal conductivity, volumetric heat capacity, and initial temperature as well as the injected fluid temperature affect the performance of the borehole field. For the cases in which the changed parameters resulted in an energy deficit within the borehole group after one year of operation, the alternative scenarios were employed to try and mitigate the negative effects, some of which are decreased average ground temperatures and lower temperatures within the boreholes during extraction.

Additionally, a second year of operation was performed for the base case as well as the 'Outside-Inside Optimized' scenario in order to examine multi-year operational effects. Table 6-4 lists all of the cases performed. In all, a total of 29 cases were analyzed. This includes 13 different injection and 27 different extraction cases.

In all analyses the temperatures of the inner and outer circulation pipe wall, fluid domain, circulation pipe domain, borehole-soil interface, borehole domain, and the geothermal footprint area were monitored. In 2-dimensions, the boundaries of the geothermal footprint area extend outward from the perimeter boreholes a distance one-half the center-to-center spacing (4m) of the boreholes (Figure 6-3a). This definition was chosen to include the tributary area of each borehole, assuming a square-shaped area. Additionally, the heat flux between the geothermal footprint area and surrounding ground was monitored.

6.6. DISCUSSION OF RESULTS

Several metrics are employed to compare the alternative cases against the base case and amongst each other. The metrics are interrelated and simply offer different ways of analyzing the results. For example, temperature and energy are directly related, however both are valuable. The net change of energy within the geothermal footprint area, which is a function of the change in average temperature and volumetric heat capacity of the soil, can be used to determine success or failure in terms of net energy loss or gain. Temperatures at select locations, however, can give an indication as to where the energy is located within the geothermal footprint area. Furthermore, the heat flux at the boundaries of the geothermal footprint area can be used to determine how much energy is leaving/entering the system from the surrounding soil.

Several additional metrics have been developed for shallow geothermal energy systems. The Efficiency Factor developed by Zhang et al. (2012) is the ratio of the amount of energy injected to the amount of energy extracted. A value of 1 indicates that equal amounts of energy are being injected and extracted resulting in no net energy change within the ground. A ratio greater than 1 indicates more energy is being injected than extracted, which will result in progressively increasing ground temperatures, which will increase the efficiency of the system for heat extraction operations. A ratio less than 1 indicates more energy is being extracted than injected, thus resulting in a net decrease in ground temperature as well as decreased system efficiency for heat extraction operations. Because the same amount of energy was extracted for every scenario, all have the same Efficiency Factor, thus the efficiency factor alone is not a good indication of the performance of the system.

Baser and McCartney (2015) introduced the Temperature Density, which is the average temperature of the soil over the volume of soil. This value is dependent on both the initial temperature of the soil as soil with a higher initial temperature will have a greater initial temperature density, as well as the volume of soil chosen. As long as the volume of soil is consistent, as is the case with the defined geothermal footprint area, it does allow for direct comparison between the cases.

6.6.1. Base Injection/Extraction

Figure 6-8 contains contour plots of the temperature at select points in time during the operational year. From this figure, one can observe that at the end of heat injection, the majority of the temperature increase in the ground occurs very close to the boreholes. By the beginning of extraction, the energy has more evenly dissipated throughout the geothermal footprint area. At middle of extraction and end of extraction, the majority of the temperature decrease in the ground occurs very close to the boreholes and it appears that the energy stored between the boreholes is not accessed. By the end of 1 operational year, the remaining energy has more evenly distributed itself within the geothermal footprint.

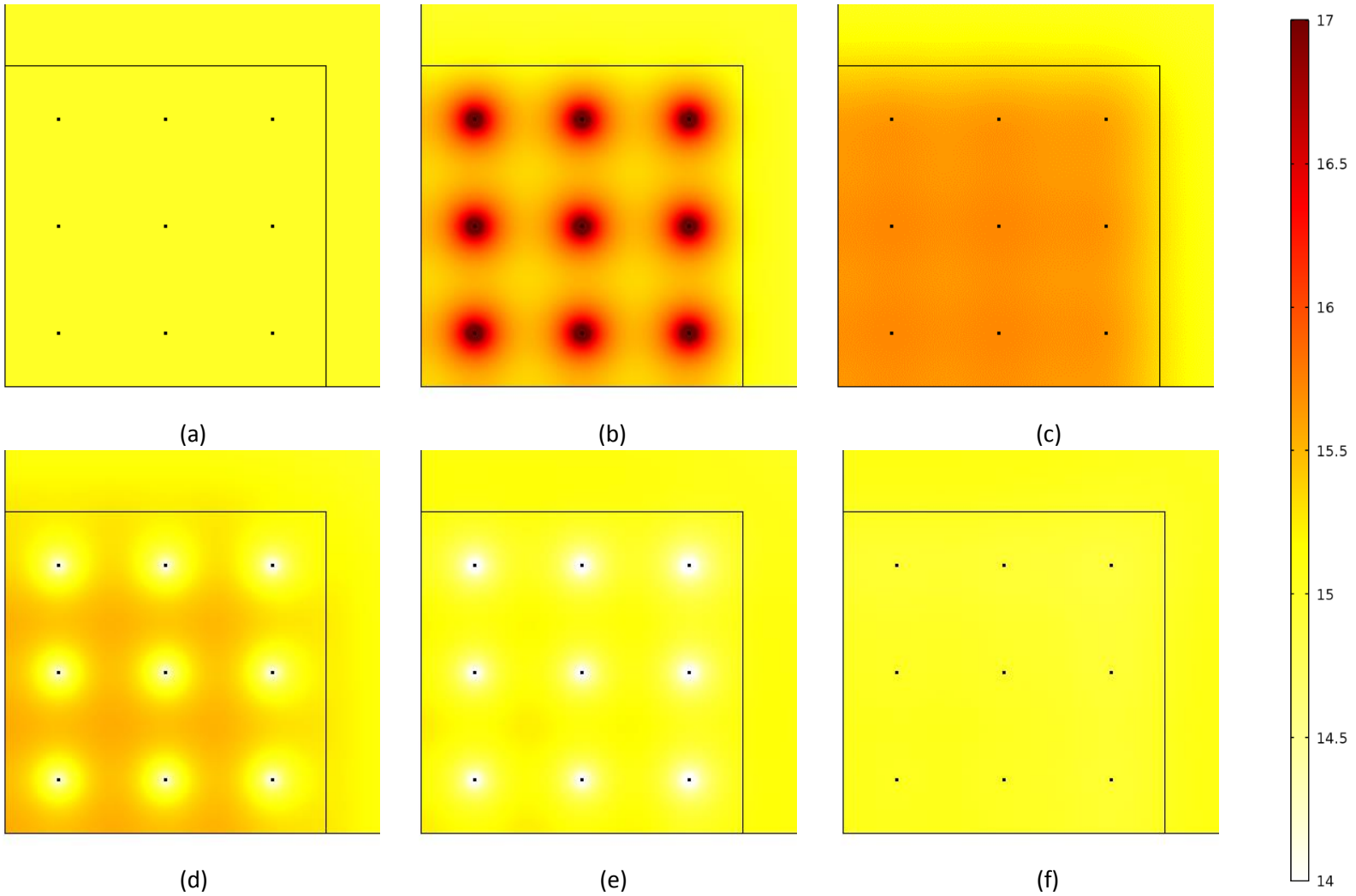

Figure 6-8. Temperature contours over time for base heating and extraction: a) beginning of heating, b) end of heating (3 months), c) beginning of extraction (5 months), d) middle of extraction (7.5 months), e) end of extraction (10 months), f) end of 1 operational year (12 months).

To better understand how the temperatures at certain locations within the geothermal footprint change over time, Figure 6-9 shows the locations of points labeled center, corner, and middle within the domain. The temperatures of these points over time as well as the average ground temperature, maximum ground temperature observed during extraction, and the minimum ground temperature observed during injection, are given in Figure 6-10. As expected, the average ground temperature continuously increases during the injection period to reach its highest value at the end of injection. It then decreases during the first idle period and during extraction until it reaches its lowest value at the end of extraction, which is less than the initial temperature. During the second idle period the temperature does increase slightly as energy flows back into the geothermal footprint from the surrounding ground. At the end of one year of operation the average temperature still has not recovered to its initial value, indicating an energy loss within the geothermal footprint area.

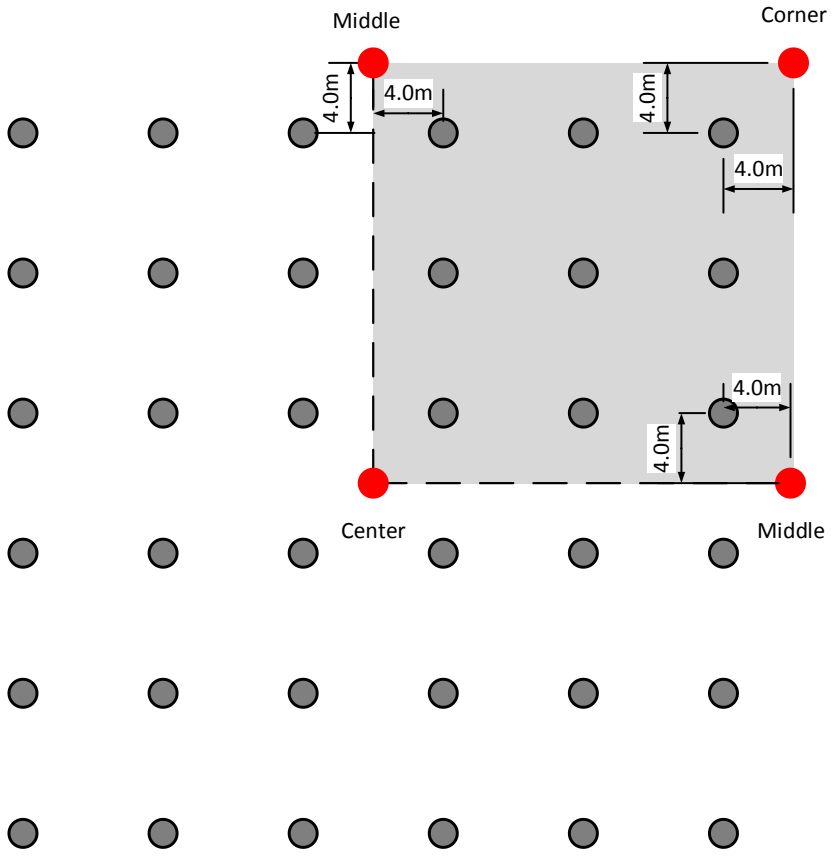

Figure 6-9. Locations of the center, corner, and middle points that were monitored during the analysis. Note that *center* refers to the center of the borehole group, *corner* refers to the corner of the borehole group geothermal footprint, and *middle* refers to the middle location along the borehole group geothermal footprint boundary. Note that there are two *middle* points because of symmetry.

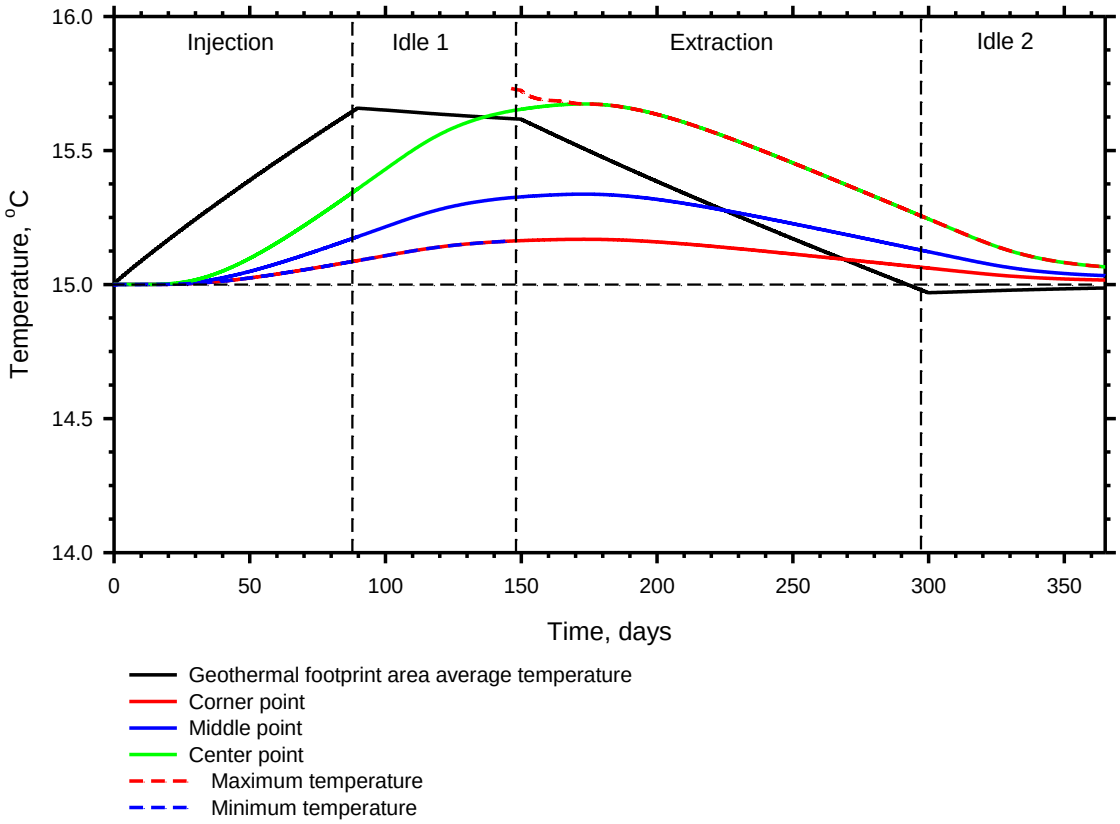

Figure 6-10. Temperatures over time of the corner, center, and middle points in the borehole geothermal footprint for the base extraction and injection cases. Also shown is the average, maximum, and minimum temperatures of the soil domain within the geothermal footprint area.

Due to thermal interference, the center of the borehole group heats more than the middle and corner points, which are located at the edges. The corner, center, and middle points are all 5.66m to the closest borehole, meaning they represent the furthest points between adjacent boreholes. Thus, they are the last points within the geothermal footprint to heat, which is why they are all lower than the average temperature during injection and most of the first idle period. It is also why they continue to increase even into the extraction period as the energy more evenly dissipates throughout the footprint area. Due to lack of interference, the corner point is the last to heat. During injection and the first idle period, the corner location corresponds to the minimum temperature within the geothermal footprint. At the end of one year of operation, the temperatures within the geothermal footprint have become more uniform as the average, center, corner, and middle points begin to converge. But it is not completely uniform and the highest temperatures within the footprint exist at the points between the boreholes. In fact, after the beginning of the extraction period and continuing throughout the rest of the operational year, the maximum temperature in the geothermal footprint is the center point.

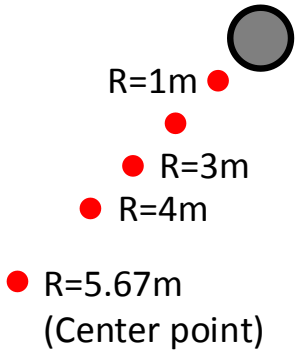

Figure 6-11. Locations of the calculated temperatures shown in Figure 6-12 around the inner borehole.

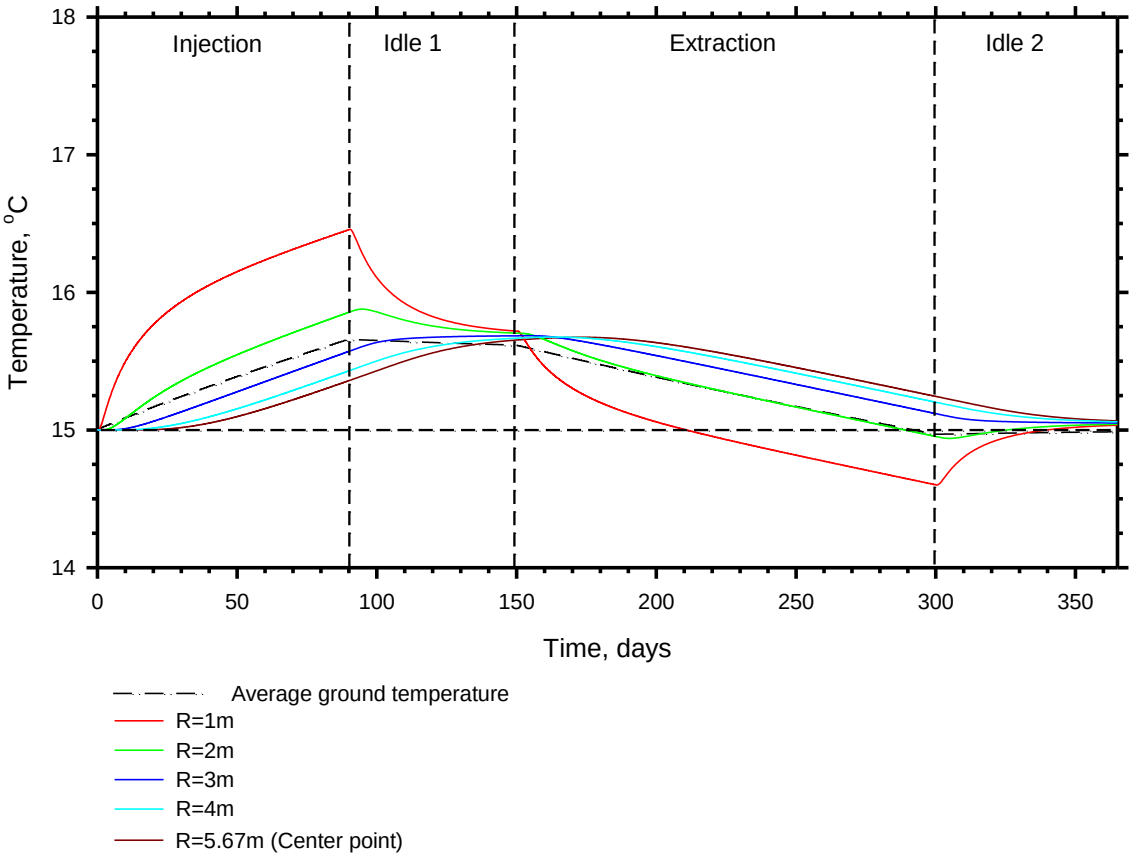

Figure 6-12. Temperature vs time for select points around the inner borehole.

The average temperature of the ground as well as the temperature of several locations around a borehole in the center of the grid (locations shown in Figure 6-11) are given in Figure 6-12. From this figure, it can be seen that the ground heats first from the center of the pile and then radiates outwards. At the end of the injection period, the ground immediately around the borehole is heated more than the ground at the furthest distance between boreholes, the center point. However, at the end of the first idle period the temperatures have mostly converged as the heat more evenly distributes throughout the footprint. Likewise, during the extraction period the points closest to the borehole decrease the most but after the

second idle period have begun to converge again. A temperature decrease below the initial temperature is observed in the ground up to a radial distance slightly greater than 2m from the borehole. Thus, the rate of extraction of energy from the borehole is greater than the rate at which the surrounding ground can supply energy to the borehole. In general, as the points increase in distance from the borehole, the temperature change is both delayed and the amplitude is reduced. Also observe from Figure 6-12 that the temperatures of the points surrounding the borehole in the center of the borehole grid converge to a value higher than the average temperature after the end of the first and second idle periods indicating that center of the borehole grid stores more heat energy than other locations.

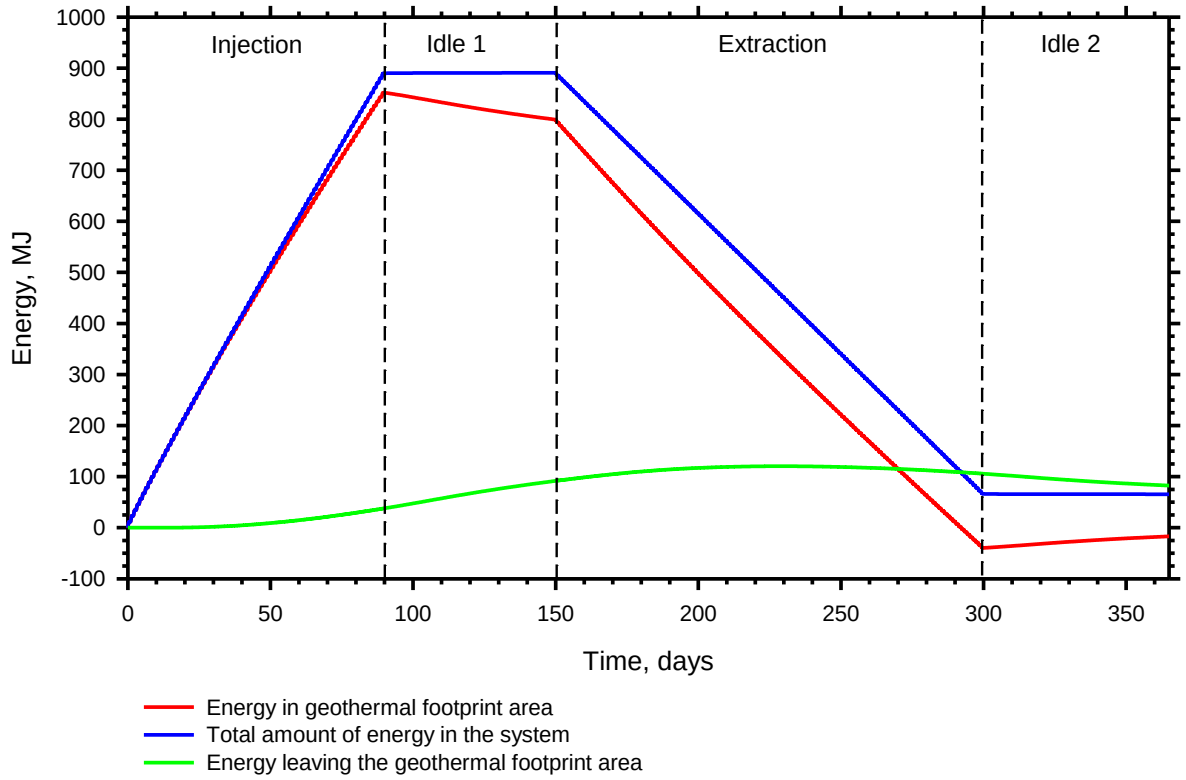

Figure 6-13. The amount of energy in the geothermal footprint, as well as the amount of energy leaving the geothermal footprint over time for base injection and extraction.

Figure 6-13 presents the total amount of energy injected into the ground, the amount of energy lost across the geothermal footprint boundary, as well as the amount of energy that remains in the geothermal footprint area. Note that these are the energy values representative of the quarter-section of the borehole group and subsequent energy values refer to the quarter-section. The values of the entire borehole group can be obtained by multiplying the energy values by 4. During the first and second idle periods, the total amount of energy stays constant because no energy is being injected or extracted. However, the amount of energy within the geothermal footprint changes as energy migrates across the boundary. There are several points in time during the operational year from which energy values can be taken from Figure 6-13 and used to characterize system operation. These values are given in Table 6-5 for the base case. The times are end of injection (EOI), beginning of extraction (BOE), end of extraction (EOE), and the end of one operational year (EOY). At EOI, it can be seen that a total of 891 MJ of energy was

injected into the system, which is more than enough energy to supply the 826 MJ required for extraction. However, 92 MJ of the injected energy left the geothermal footprint area by BOE and thus only leaving 799 MJ. This initial energy loss, combined with continued energy loss across the boundary during extraction results in an energy loss within the geothermal footprint area of 40 MJ at EOE. By EOY, some energy has reentered the geothermal footprint area, but it is not enough to bring the net amount of energy above 0 MJ, resulting in an energy loss of 17 MJ after the end of the first year of operation.

Table 6-5. Energy (MJ) results within the geothermal footprint area for basic injection and extraction.

Energy Values	Base Case	
	Year 1	No Inj
Total Energy Injected	891	-
Energy Loss After End of Injection	38	-
Net Energy After End of Injection	853	-
Energy Loss After 1st Idle Period	92	-
Net Energy After 1st Idle Period	799	-
Total Energy Extracted	-825	-826
Energy Loss After End of Extraction	106	-58
Net Energy After End of Extraction	-40	-767
Energy Loss After 1 Year	83	-103
Net Energy After 1 Year	-17	-723

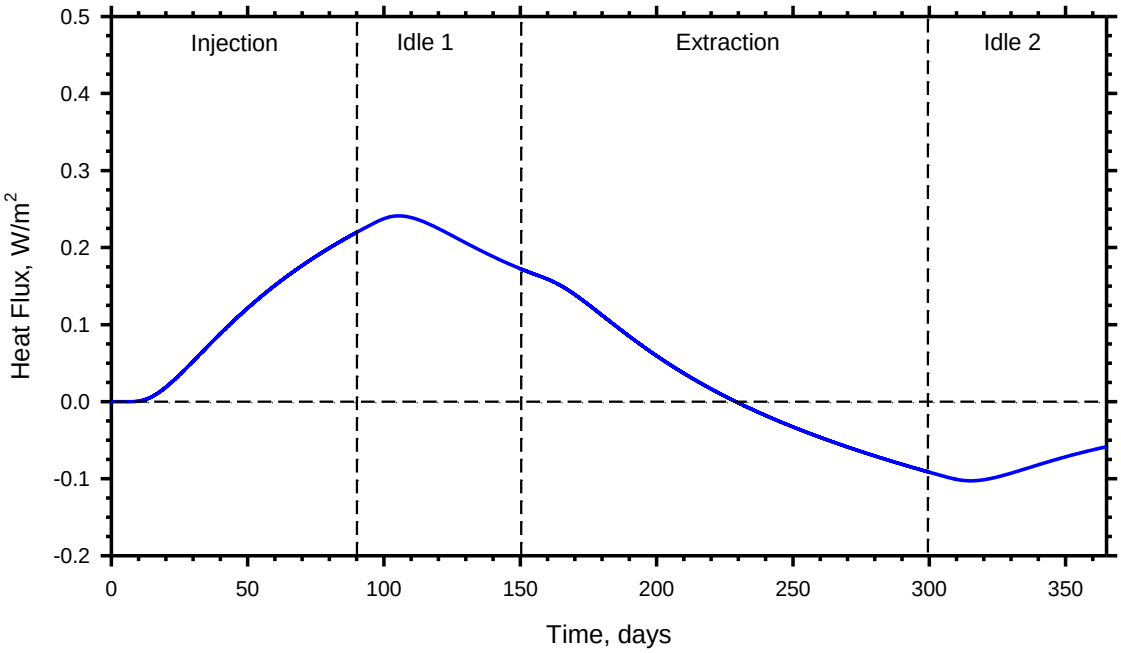

Figure 6-14. The Average rate of energy loss across the geothermal footprint boundary. A positive rate indicates energy leaving the geothermal footprint area and a negative rate indicates energy is entering the geothermal footprint area. The area under the curve multiplied by the length of the geothermal footprint boundary yields the net amount of energy leaving/entering the geothermal footprint area.

Figure 6-14 shows the rate at which energy is traveling across the boundary where positive rate indicates energy leaving and a negative rate indicates energy entering the footprint area from the surrounding ground. This figure explains the migration of energy across the geothermal footprint boundary and it is apparent that most of the energy leaves the system during the injection and first idle period. It is also seen that there is a net flux of energy into the geothermal footprint during about the middle of heat extraction episode as a result of the reduced temperature within the footprint causing an inward thermal gradient. This inward heat migration continues during the second idle episode following heat extraction.

6.6.2. Influence of Soil Thermal Properties

Soil properties including the thermal conductivity and volumetric heat capacity govern how thermal energy is stored and transported in the ground. Thus, an investigation as to their effects on shallow geothermal energy systems and if any of the methods explored could be used to mitigate detrimental effects was performed. Additional analyses were performed with soil thermal conductivity values of 1.0, 1.5, and 2.5 W/m·K and with volumetric heat capacities of 1000, 1500, and 3000 J/m^{3}K. For all additional thermal conductivity analyses, the standard volumetric heat capacity of 2250 J/m^{3}K was used and for all additional volumetric heat capacity analyses the standard thermal conductivity value of 2.0 W/m·K was used.

6.6.2.1. Thermal Conductivity

Lower thermal conductivity values prevent as much energy from being injected and result in lower temperatures in the boreholes as energy is extracted as shown in Figure 6-15. For thermal conductivity values of 1.5 and 1.0 W/m·K, enough energy (797 MJ and 669 MJ, respectively) was not even injected to account for what was extracted. These cases resulted in a net energy loss of 87 MJ and 193 MJ, respectively, within the geothermal footprint area. An increase in thermal conductivity to 2.5 W/m·K allowed more energy to be injected (964 MJ) and ultimately resulted in a net increase in energy in the geothermal footprint area of 32 MJ at the end of one year with base extraction.

Figure 6-16 compares the efficiency factors for the different values of thermal conductivity. It appears that for the amount of energy required from this borehole grid, a thermal conductivity value of approximately 1.8 W/m·K results in an efficiency factor of 1. This value is slightly misleading, however, as the base thermal conductivity value of 2.0 W/m·K yields an efficiency factor greater than 1, but still results in a net loss of energy within the geothermal footprint.

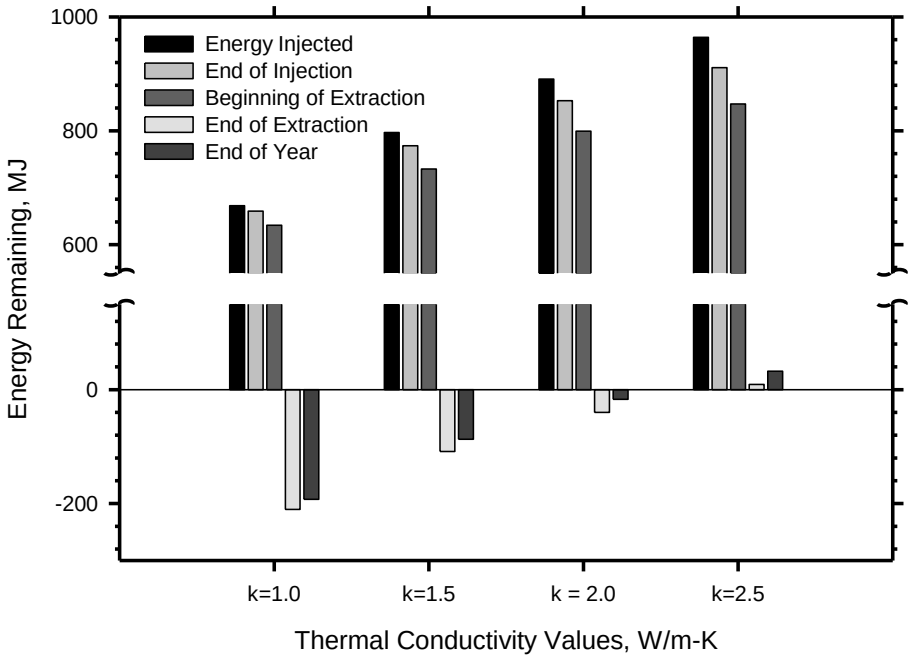

Figure 6-15. The amount of energy injected as well as the amount of energy remaining within the geothermal footprint area at EOI, BOE, EOE, and EOY for different values of soil thermal conductivity.

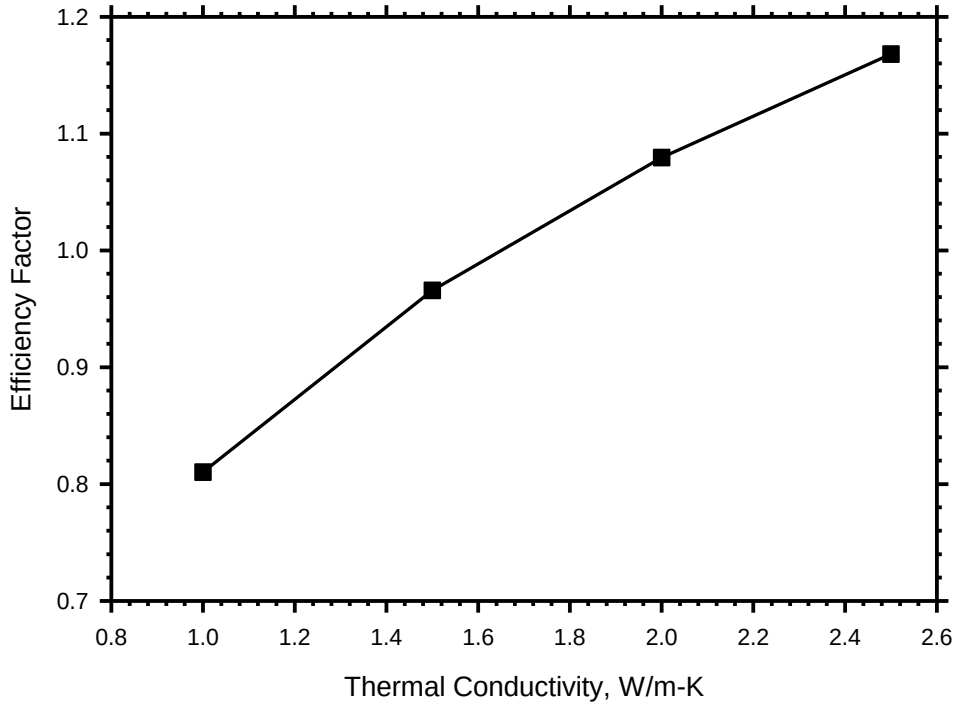

Figure 6-16. The efficiency factor of the system as a function of the soil's thermal conductivity.

6.6.2.2. Volumetric Heat Capacity

The higher the volumetric heat capacity, the larger the amount of energy a given volume of soil can hold. For temperature controlled energy injection, this results in more stored energy and less migration of energy away from the boreholes. Figure 6-17 presents the injection results for the four different values of volumetric heat capacity. Table 6-6 shows the percentages of energy that was both retained and lost to total injected energy. Even as the total amount of injected energy decreases, the relative amount of energy that was lost increases as the volumetric heat capacity decreases. For example, even though 914 MJ was injected for VH=3000 J/m^3·K, only 8%, or 73 MJ, was lost after the end of the first idle period whereas 18%, or 145 MJ, of the 823 MJ of injected energy was lost for VH=1000 J/m^{3}K. This demonstrates that as the volumetric heat capacity decreases, a larger volume is required in order to store the same amount of energy resulting in more energy leaving the geothermal footprint area.

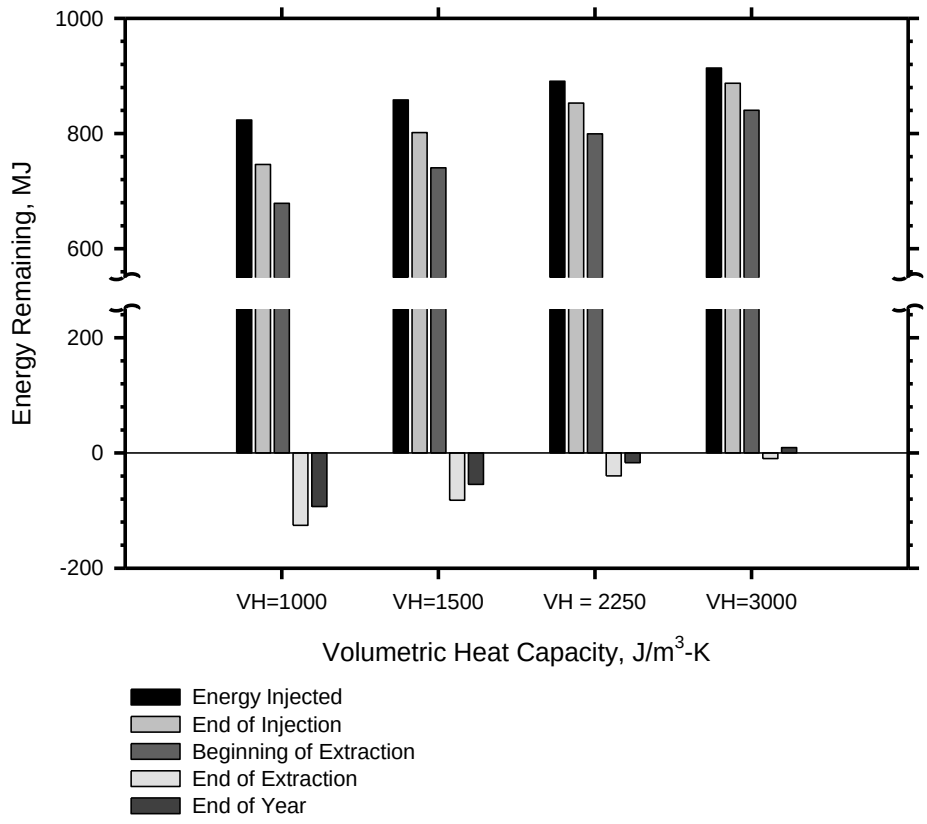

Figure 6-17. The amount of energy injected as well as the amount of energy remaining in the geothermal footprint area at EOI, BOE, EOE, and EOY for different values of soil volumetric heat capacities.

Table 6-6. Percent of the injected energy (MJ) that was retained and lost in the geothermal footprint area for different volumetric heat capacity (J/m^3·K) values.

Energy Values	$\rho \cdot C_p$ = 1000		$\rho \cdot C_p$ = 1500		$\rho \cdot C_p$ = 3000	
	Energy	% of Inj	Energy	% of Inj	Energy	% of Inj
Total Energy Injected	823	100%	858	100%	914	100%
Energy Loss After End of Injection	77	9%	57	7%	26	3%
Net Energy After End of Injection	746	91%	801	93%	887	97%
Energy Loss After 1st Idle Period	145	18%	118	14%	73	8%
Net Energy After 1st Idle Period	679	82%	740	86%	840	92%
Total Energy Extracted	-826	-100%	-825	-96%	-825	-90%
Energy Loss After End of Extraction	124	15%	115	13%	99	11%
Net Energy After End of Extraction	-126	-15%	-82	-10%	-10	-1%
Energy Loss After 1 Year	90	11%	87	10%	79	9%
Net Energy After 1 Year	-93	-11%	-54	-6%	9	1%

Figure 6-18 presents the efficiency factors as a function of soil's volumetric heat capacity. Even for the low VH value of 1000 J/m^3·K, the efficiency factor is very close to 1. This value is again misleading as even though the efficiency factor is just under 1, the energy decrease within the geothermal footprint area is 93 MJ. Higher volumetric heat capacities do not significantly alter the efficiency factor as a VH value of 3000 J/m^{3}K only increases the efficiency factor by 0.1. This indicates that the amount of energy that can be injected into the ground is not as dependent on volumetric heat capacity as thermal conductivity, as evidenced by the steeper curve efficiency factor curve for thermal conductivity in Figure 6-16.

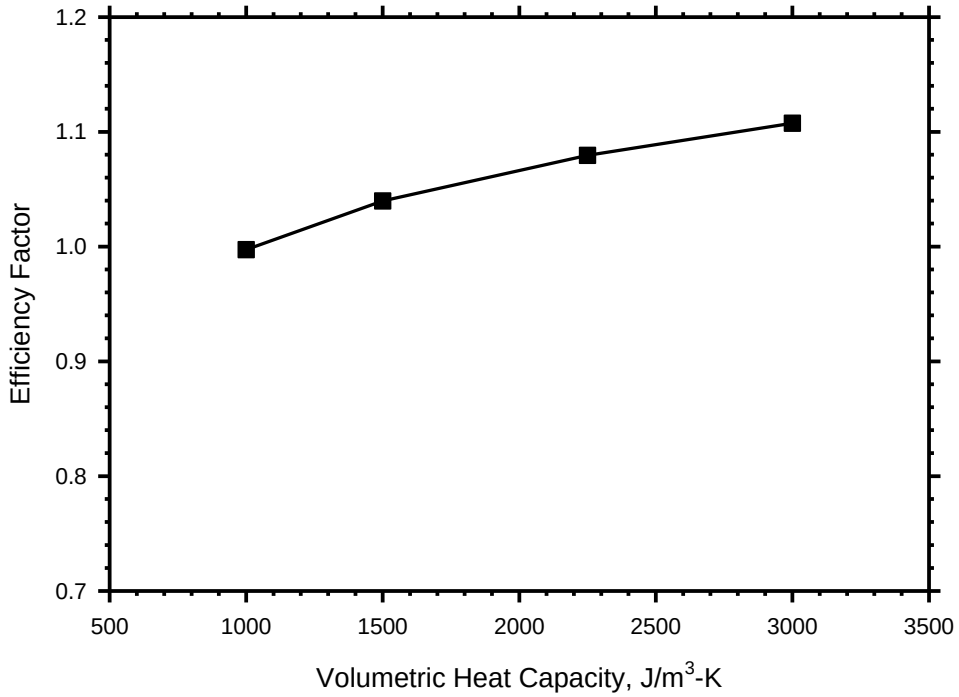

Figure 6-18. The efficiency factor of the system as a function of the soil's volumetric heat capacity.

In comparison with the thermal conductivity analyses results for k=1.5 W/mK, the VH=1000 J/m^{3}K case retained less energy within the geothermal footprint area after injection (679 MJ as compared to 733 MJ), yet at the end of one year of operation, only had a slightly larger energy loss (93 MJ as compared to 87 MJ). This is due to the ability of the VH=1000 J/m^{3}K case to draw large amounts of heat back into the geothermal footprint area during and after extraction. This again suggests that thermal conductivity is more influential than volumetric heat capacity when it comes to storing and extracting energy. For cases in which the volumetric heat capacity is low, a high thermal conductivity which allows energy to leave the geothermal footprint boundary more easily is actually a benefit. As long as the thermal conductivity is sufficiently high, it will allow more heat energy to be injected as the energy will simply occupy a larger volume of soil. While this will initially cause more energy to leave the geothermal footprint area than in cases with lower thermal conductivity, the energy appears to re-enter the geothermal footprint rather easily when needed.

6.6.2.3. Initial Ground and Injection Fluid Temperatures

Several other initial conditions were tested including an initial ground temperature of 13^{o}C and a fluid temperature of 30^{o}C. The results are given in Figure 6-19. For all cases with the higher fluid temperature, more than enough energy was injected into the ground and after extraction, there was still a net increase in energy in the geothermal footprint area. An increase an energy was also seen for the case with 25^{o}C fluid and 13^{o}C initial ground temperature. The lower initial ground temperature created a higher temperature gradient with the fluid thus resulting in more energy being injected.

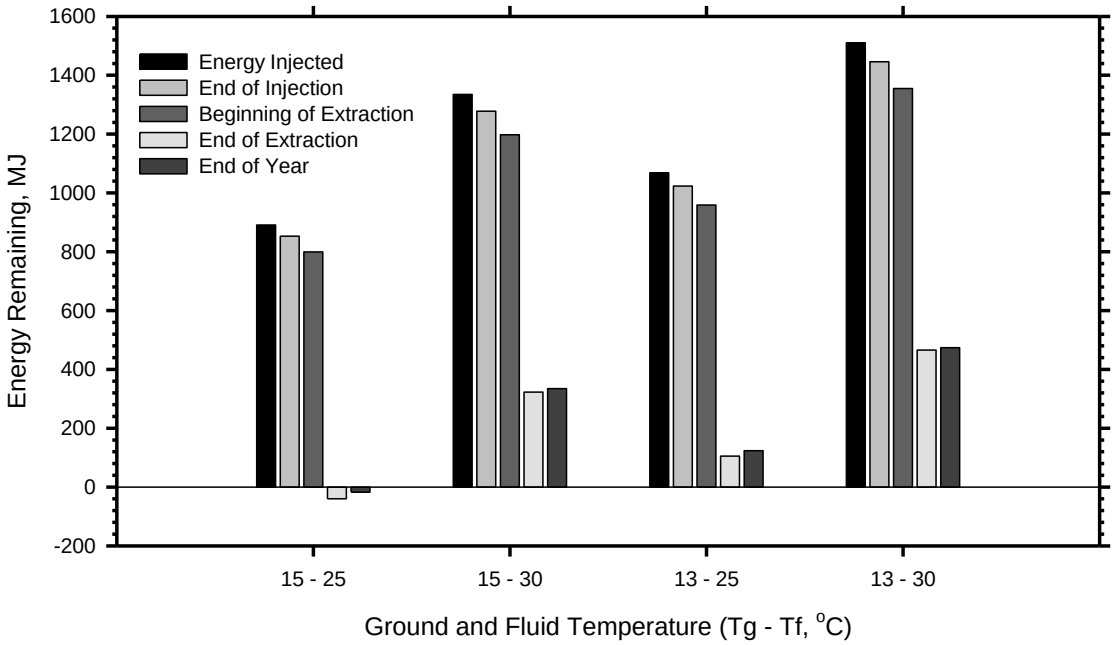

Figure 6-19. The amount of energy injected as well as the amount of energy remaining within the geothermal footprint area at EOI, BOE, EOE, and EOY for different values of initial soil temperatures and fluid injection temperatures

There are several implications to these results. The first is that if a high enough temperature gradient exists between the initial ground temperature and the fluid temperature during injection, an energy loss

in the system may not be a problem. Alternatively, by using alternative extraction scenarios to maximize the system's efficiency, more heat could be stored in the geothermal footprint area resulting in more efficient operation of the system for heat extraction and/or the size of the system could be reduced, which would reduce the overall cost.

6.6.3. Alternative Injection and Extraction Scenarios

Figure 6-20 compares the net change in energy within the geothermal footprint area at EOE and EOY for all of the alternative scenarios. As can be seen, only three of the scenarios tested resulted in a positive change in energy at the end of one operational year: IR2, Outside-Inside Optimized, and DE2. None of the scenarios had a net positive amount of energy at the end of extraction. Each alternative is discussed in more detail below.

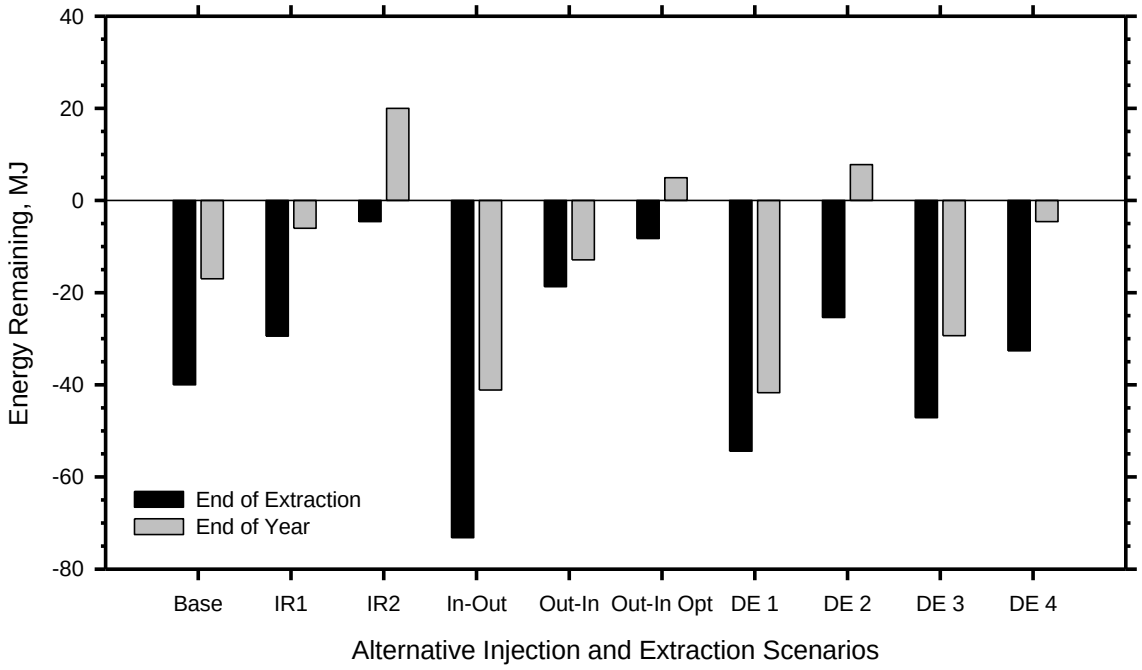

Figure 6-20. Comparison of the amount of energy remaining within the geothermal footprint at the end of extraction and end of one operational year between all the alternative injection and extraction scenarios

6.6.3.1. Alternative Injection Scenarios

Most of the energy leaves the geothermal footprint area during injection and the first idle period as shown earlier in Figure 6-13. Thus, the potential for the greatest energy savings occurs during this time period. However, it would not be advantageous to selectively operate certain boreholes during the injection period because it is temperature controlled and inherently assumed that there is a sufficient amount of heat for any selected number of boreholes. Therefore, selective operation would result in less total energy being injected if a number of boreholes less than the total was selectively utilized. The opportunity for energy savings exists in energy redistribution, which is moving energy from one area of the geothermal footprint to another. This can be accomplished by extracting heat from certain boreholes and then

injecting it into others. Note that the physical mechanism by which to accomplish this has not been developed. Rather, if this method shows potential for a significant increase in system efficiency, physical mechanisms can be developed.

Because energy leaves the geothermal footprint area due to the temperature gradient created across the boundary, it is advantageous to reduce that temperature gradient. The temperature gradient can be reduced by extracting the energy from the outer boreholes and injecting it into the center boreholes, thus reducing the amount of energy around the outer boreholes and thereby reducing the temperature. The end of the energy redistribution period was selected to coincide with the end of the injection period in order to give the temperatures around the boreholes time to stabilize (as shown by the convergence of temperatures at the points surrounding the borehole shown in Figure 6-12). Otherwise, lower temperatures will exist around the outer boreholes at the beginning of the extraction period, which will be lowered even further during extraction and result in decreased system efficiency.

As shown in Figure 6-21, the alternative injection scenarios were successful in retaining more injected energy within the geothermal footprint boundary. The same amount of total energy was injected for each case (891 MJ), which is the amount of energy that was injected for the base case. However, at the end of the injection period, 856 MJ of energy remained within the borehole footprint area for IR1 and 862 MJ remained for IR2 as compared to 853 MJ for basic injection. At the end of the first idle period, IR1 contained only 7 MJ of additional energy within the geothermal footprint area as compared to the base case, however IR2 contained 23 MJ more.

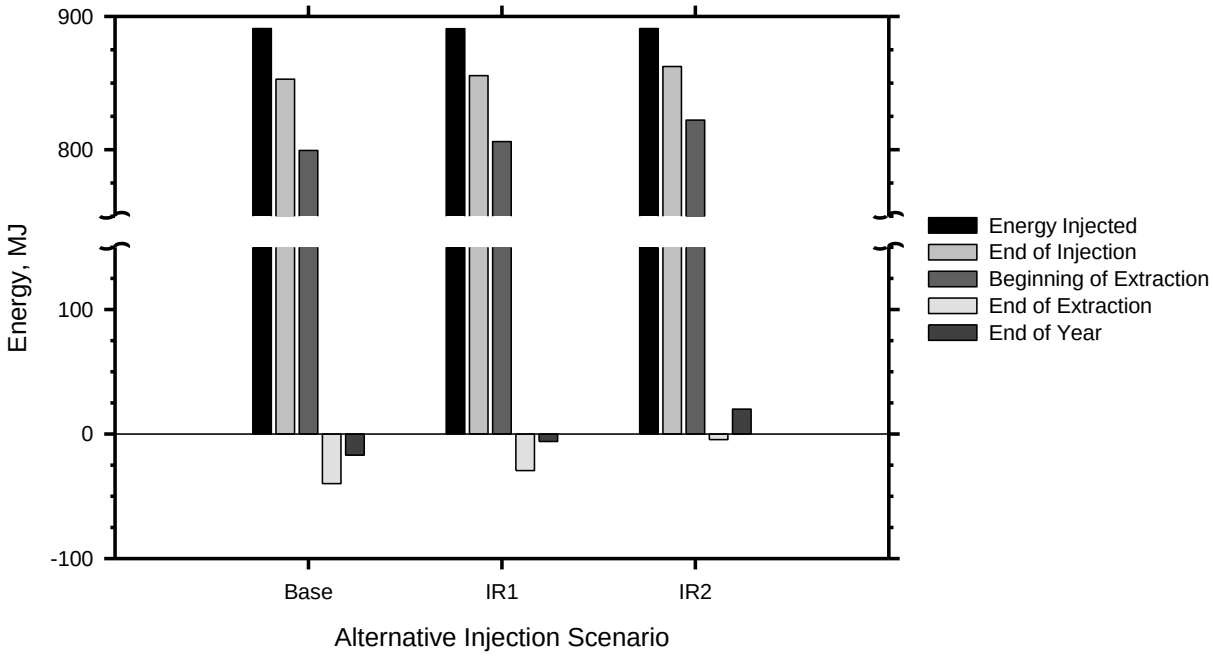

Figure 6-21. Comparison of the amount of energy within the geothermal footprint at EOI, BOE, EOE, and EOY between all the alternative injection scenarios after being subjected to base extraction.

Whereas there is a difference at BOE between IR1 and IR2 as compared to the base case, the real difference can be seen after extraction. Basic extraction was applied to each injection redistribution

scenario and compared with the base case. After 1 year of operation, there was 11 MJ more energy within the geothermal footprint area for IR1 and 37 MJ more energy for IR2 when compared to the base case. In fact, IR2 was able to prevent a net energy loss within the geothermal footprint area as seen in the base case.

Figure 6-22 compares the flux across the geothermal footprint boundary for IR1, IR2 and the base case. IR1 and IR2 decrease the flux during the injection and first idle periods. During extraction and the second idle period, IR1 closely resembles that of the base case indicating that the temperature gradient was not significantly reduced across that boundary. However, IR2 both lowers the flux across the boundary and reaches the point of drawing energy back into the geothermal footprint area before IR1 and the base case. At the end of the second idle period, the flux of IR2 appears to be very similar to IR1 and the base case.

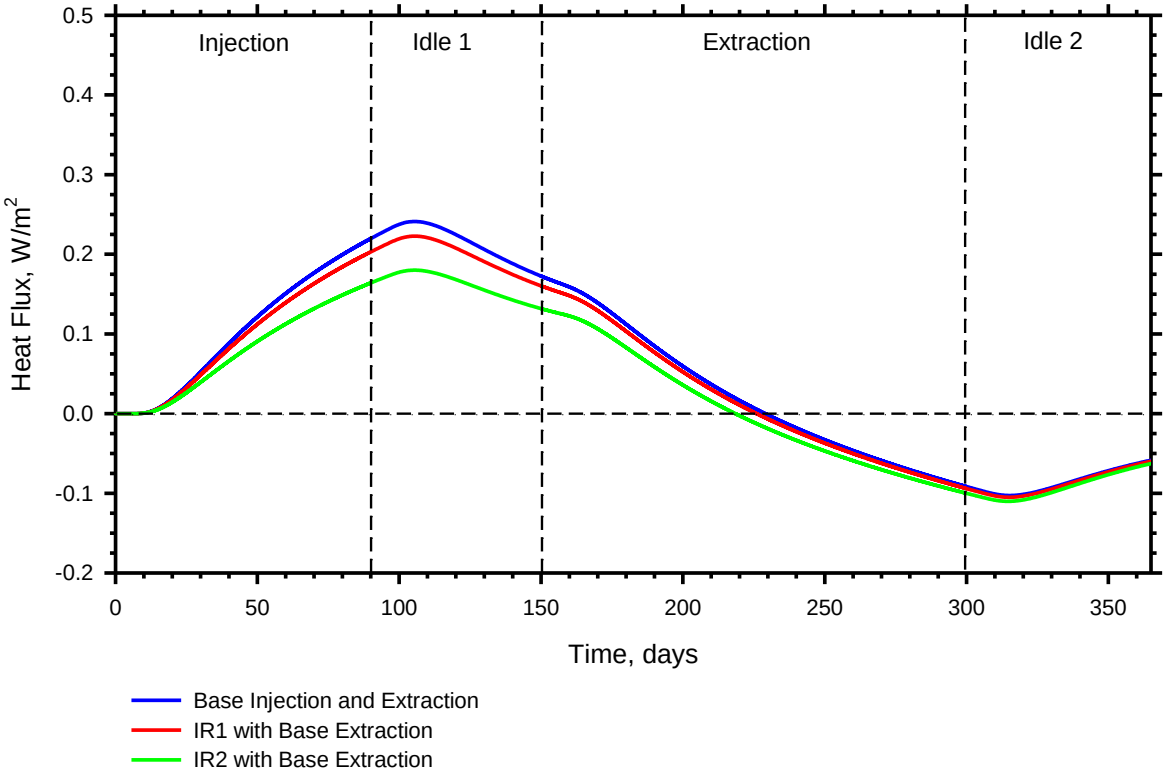

Figure 6-22. Average heat flux across the boundary footprint for the alternate injection scenarios, where positive is defined as an outward pointed vector normal to the borehole footprint boundary.

Figure 6-23 compares the temperature contours of the different injection scenarios with the base case at the end of injection and at the end of the first idle period. It is evident that there is more energy distributed around the interior boreholes at the end of injection for IR1 and IR2, with IR2 containing more. At the end of the first idle period, a concentration of energy can clearly be seen in the interior of the geothermal footprint for IR2. There is also a concentration of energy for IR1, though it is not as evident.

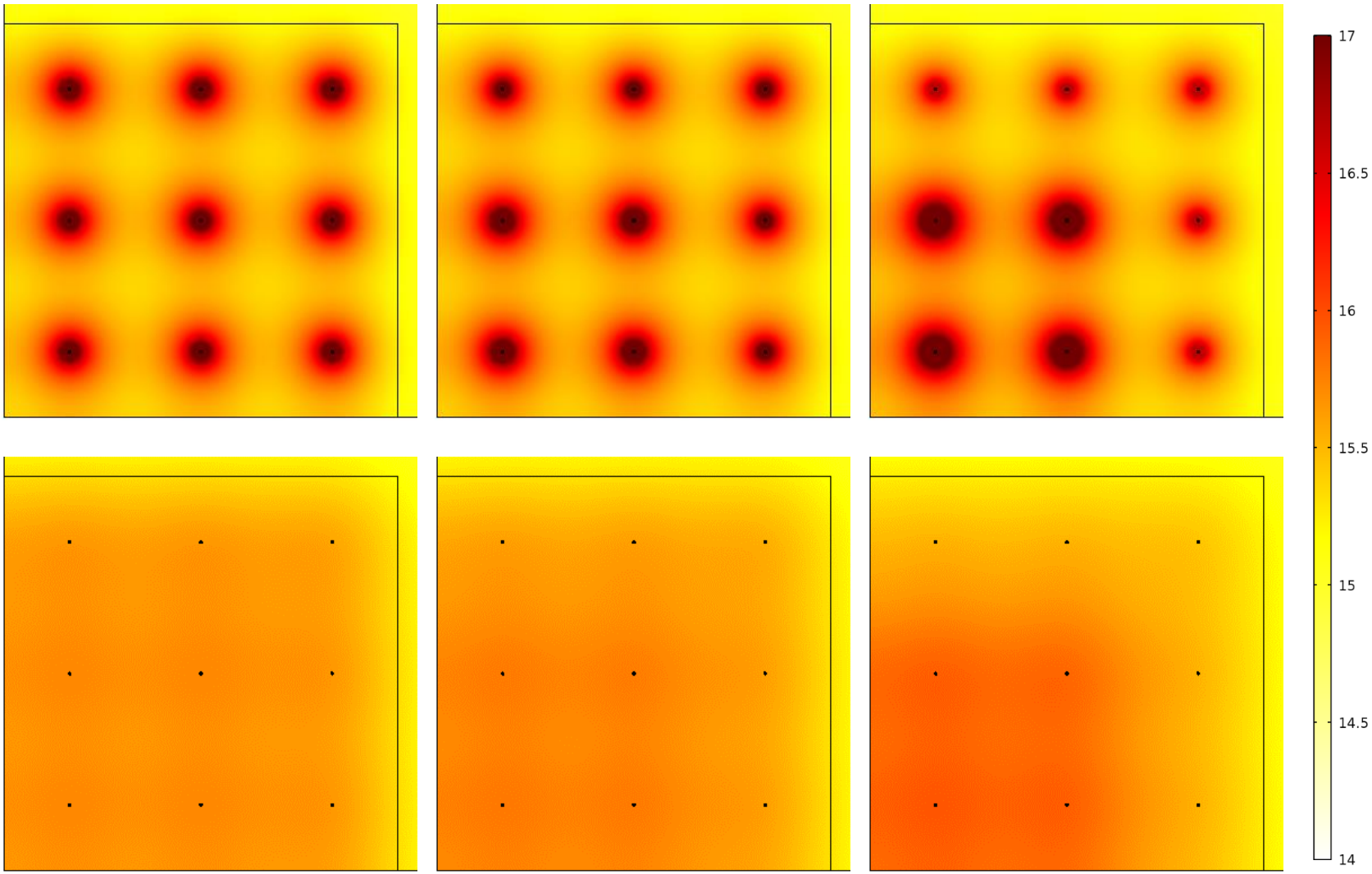

(a) (b) (c)

Figure 6-23. Temperature contours over time comparing end of injection (top) and end of the first idle period (bottom) of a) base injection, b) IR1, and c) IR2.

To discover how successful the alternative injection cases were in redistributing the energy, their center, middle, and corner point values are compared with the base case and is shown in Figure 6-24. As expected, the center points are higher for IR1 and IR2 when compared to the base case, and their middle and corner points are lower. Furthermore, it appears that the difference in temperature between the respective points and their base cases remains fairly constant after the end of the first idle period indicating that perhaps the energy in the center of the geothermal footprint is not being fully utilized.

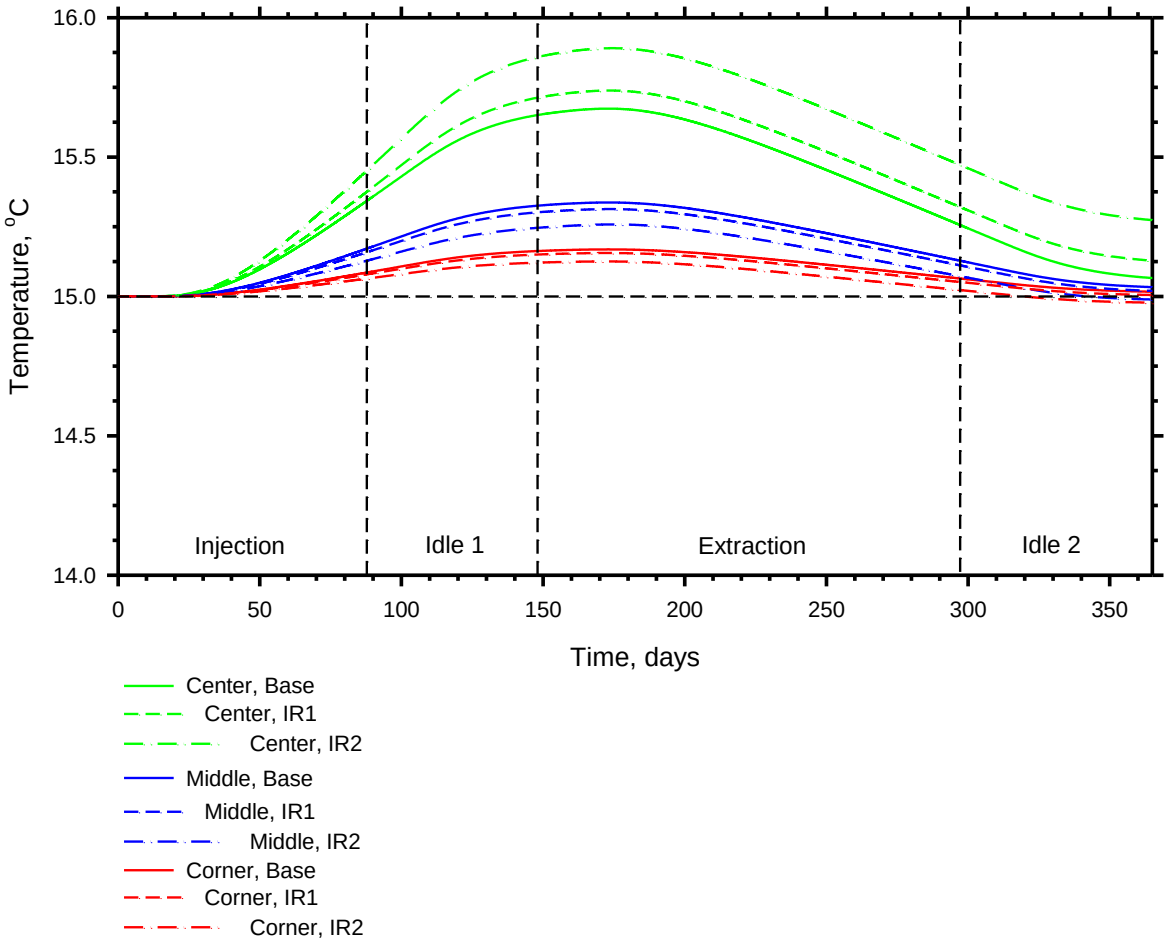

Figure 6-24. Temperatures over time of the corner, center, and middle points in the borehole geothermal footprint for the base extraction and injection cases as well as the alternative injection scenarios, IR1 and IR2.

6.6.3.2. Alternative Extraction Scenarios

6.6.3.2.1. Outside-Inside and Inside-Outside

By first extracting energy from the outer boreholes and then moving to the interior boreholes, more energy was retained within the geothermal footprint area. The net energy loss at the end of one year was 13 MJ as compared to 17 MJ for the base case (see Figure 6-20). Alternatively, extracting energy first from the interior boreholes and then extracting from the outer boreholes results in a net loss of 41 MJ at the end of one year. Figure 6-25 shows the heat flux across the geothermal footprint boundary for the outside-

inside and inside-outside cases compared with the base case. As observed, the outside-inside case is able to both prevent as much energy from leaving (by reaching 0 W/m^2 sooner than the base case), and is able to draw more energy back into the footprint. The inside-outside case, however, does exactly the opposite and thus results in a greater energy loss.

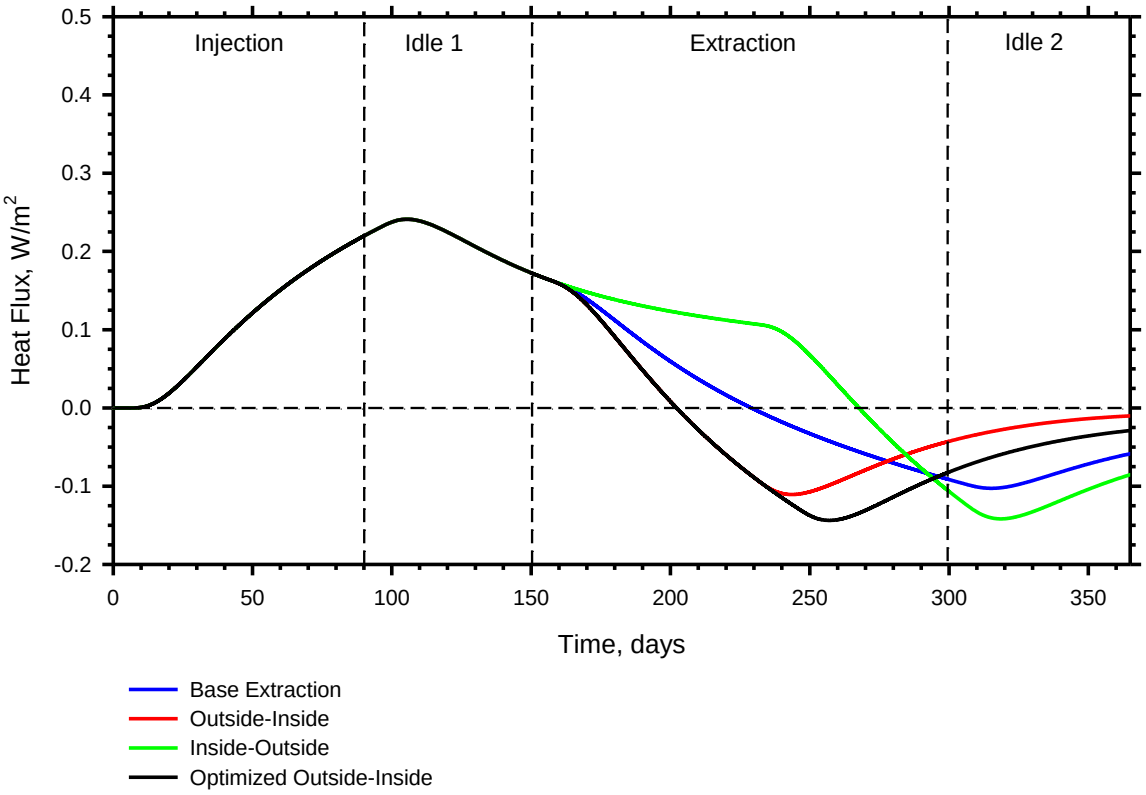

Figure 6-25. Average heat flux across the boundary footprint for cases E6, E7, and E8, where positive is defined as an outward pointed vector normal to the borehole footprint boundary.

The outside-inside case is able to retain more energy within the geothermal footprint area because of two primary factors. The first is that by extracting energy from the outer boreholes, it is able to utilize it before it leaves the footprint area. Secondly, due to the lower temperatures that exist around the outer boreholes, a negative gradient is created across the boundary which draws energy in from the surrounding ground. The negative gradient is larger than that of the base case and is reached more quickly.

One of the concerns in extracting energy from the boreholes at a higher rate is incurring too low of temperatures which can both decrease the efficiency, and in the case of energy foundations, lead to freezing the piles. Low temperatures decrease efficiency because though the same amount of energy is being extracted from the ground, a system must expend more energy to retrieve that energy when lower temperatures are incurred. Figure 6-26 shows the average temperatures of the interior and outer boreholes at the inner pipe surface, which is the location within the boreholes with the lowest temperature. As expected, the interior boreholes display a larger temperature drop than the outer boreholes due to the higher heat extraction rates they are subject to. The lowest temperature

experienced by the interior boreholes is 2.95°C whereas it is 5.43°C for the outer boreholes, which is shown in Table 6-7.

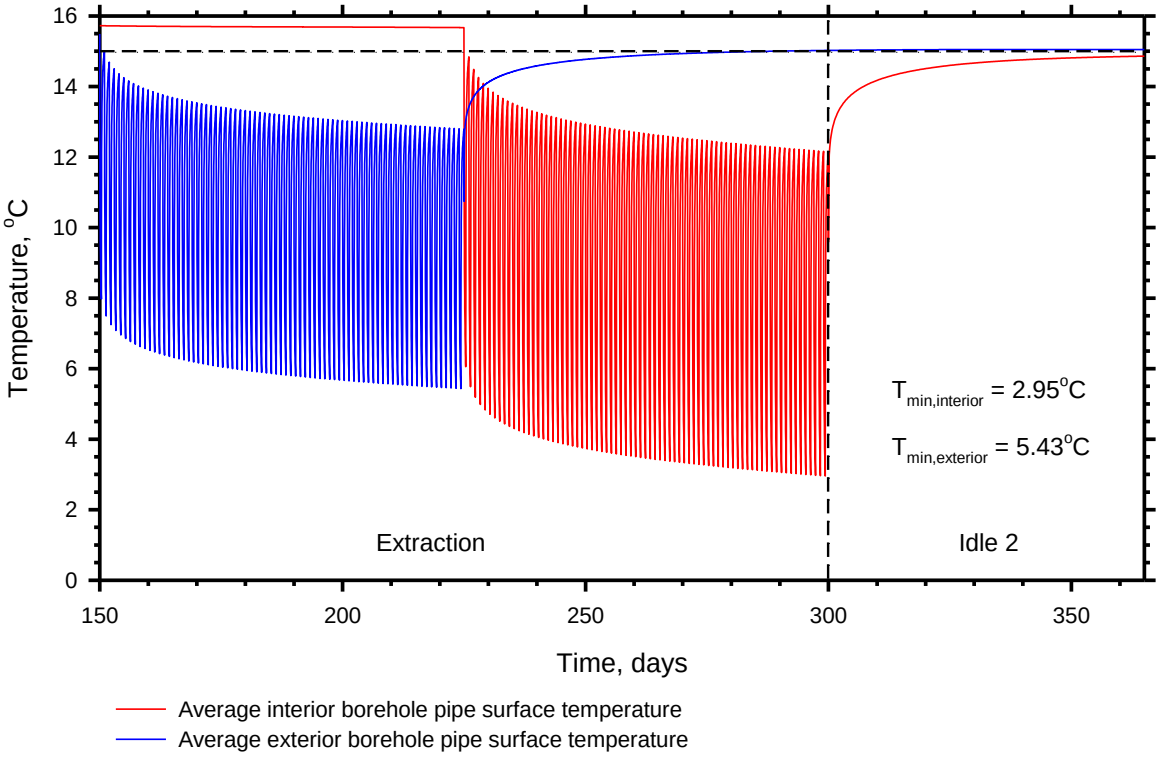

Figure 6-26. Average pipe surface temperatures in the interior and exterior boreholes for the outside-inside extraction scenario.

Table 6-7. Lowest temperature (°C) during extraction for the outside-inside and different extraction rate extraction scenarios.

Location	Outside – Inside		Different Extraction Rates			
	Standard	Optimized	Case 1	Case 2	Case 3	Case 4
Inner	2.95	3.10	5.91	13.57	7.82	11.65
Middle			8.54	10.90	9.13	10.31
Outer	5.43	5.31	11.05	8.13	10.32	8.86

While these temperatures are not below freezing, 2.95°C is low. Because the temperatures progressively lower as seen in Figure 6-26, if the operational period of the interior boreholes was shortened, it would result in higher minimum temperatures. Furthermore, as this scenario would require lengthening the operational period for the outer boreholes, the gradient across the footprint boundary will be even greater possibly allowing more energy to enter the geothermal footprint area and increasing the overall efficiency of this operation. Thus, a variation of the outside-inside scheme known as 'optimized outside-inside' was tested where the outer boreholes were operated for the first 3 months (90 days) and then the interior boreholes were operated for 2 months (60 days).

As shown in Figure 6-20, by operating the outer boreholes for an additional 15 days, the net energy after 12 months is 5 MJ as compared to -13 MJ for the outside-inside scenario. Furthermore, the minimum temperature in the interior boreholes is 3.11°C, which is greater than it was for the outside-inside scenario, while the lowest temperature in the outer boreholes was only reduced from 5.43°C to 5.31°C. Figure 24 also compares the heat flux of the optimized outside-inside scenario at the geothermal footprint boundary with the other cases. Though the optimized version of the outside-inside scenario does not prevent any additional heat from leaving the footprint area, it does generate a larger flux across the boundary to draw more energy back into the footprint area by EOY.

6.6.3.2.2. Different Extraction Rates

Applying different extraction rates to the boreholes is similar to the outside-inside approach except that all boreholes are operated the entire extraction period. The highest rates are applied to the outer boreholes to both prevent energy from leaving the geothermal footprint and to create a negative temperature gradient, which will draw energy in. DE2 and DE4 did this whereas DE1 and DE3 applied the larger extraction rate to the interior of the group for comparison.

From Figure 6-20, it is evident that both DE2 and DE4 performed better than the base case by retaining 8 MJ and -5 MJ, respectively, as opposed to -17 MJ. The case that used a larger difference (9 W/m) between extraction rates (DE2) yielded better results than the case that used a smaller difference (4.5 W/m – DE4). Both DE1 and DE3 performed worse than the base case by retaining -42 MJ and -29 MJ, respectively. In this instance, the case with the lower difference between rates (4.5 W/m – DE3) performed better than the case with larger difference between rates (9 W/m – DE1) because it allowed a larger extraction rate to be applied to the outer boreholes (17.5 W/m for DE3 as opposed to 15 W/m for DE1).

Figure 6-27 compares the heat flux over time across the geothermal footprint boundary for the four extraction cases as compared to the base case. DE2 and DE4 reach a negative flux before the base case, DE1, and DE3 preventing as much energy from leaving the footprint area and drawing more energy back in. The lowest temperatures in the outer, middle, and inner boreholes for all these cases are given in Table 6-7. Notice that in all cases, the lowest temperature is 5.91°C, which is greater than the lowest temperature from the outside-inside and optimized outside-inside cases. Furthermore, the lowest temperature in DE2 is only 8.13°C, which is much greater than the lowest temperature for the optimized outside-inside case of 3.10°C.

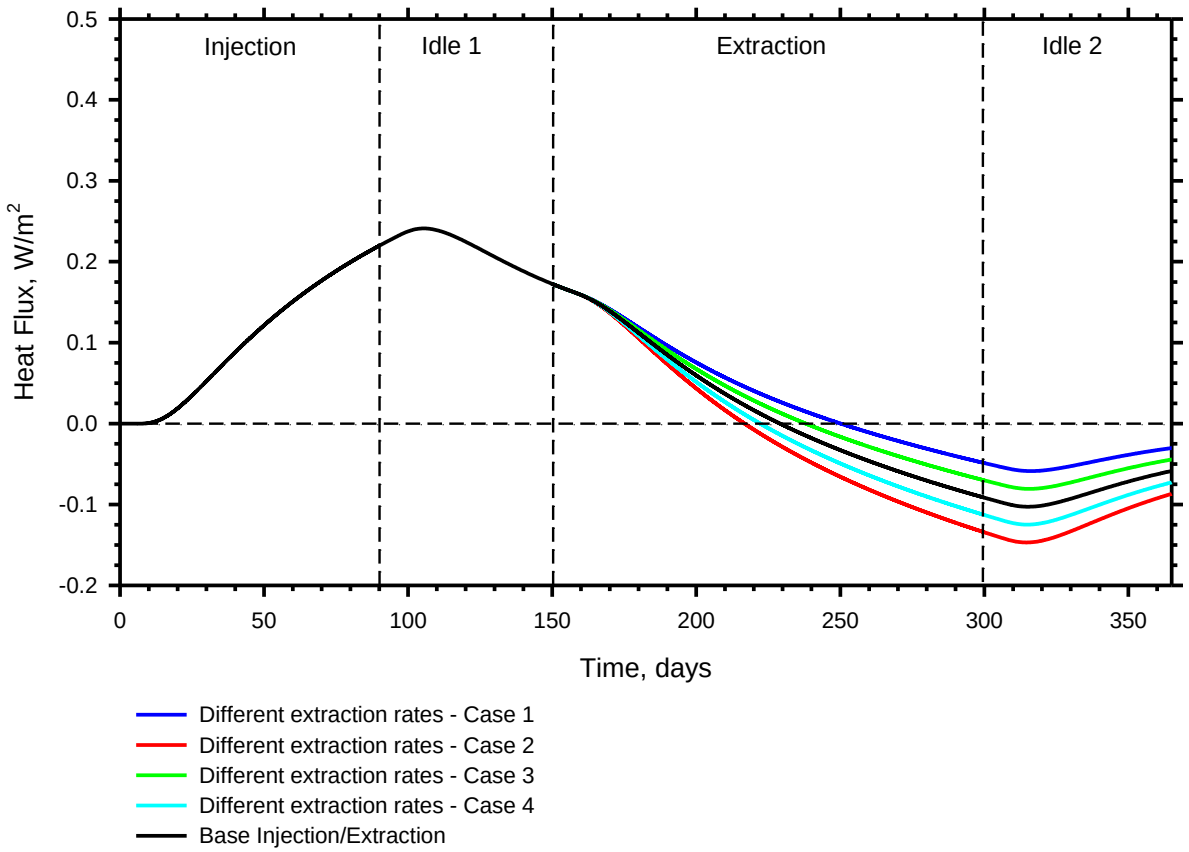

Figure 6-27. Average heat flux across the boundary footprint for the four different extraction rate scenarios, where positive is defined as an outward pointed vector normal to the borehole footprint boundary.

In terms of energy, DE2 also performed better than both the outside-inside scenario and the optimized outside-inside scenario. DE4 performed better than the outside-inside scenario. The most likely reason for this is that by extracting energy from the outer boreholes for the full 150 days as opposed to 75 (Out-In) or 90 (Op Out-In), the temperatures around the outer boreholes do not have as long to recover, resulting in a larger gradient for a longer length of time. Indeed, Figure 6-28 which compares the heat flux over time across the geothermal footprint boundary of DE2 and DE4 with that of the outside-inside and optimized outside-inside cases, confirms this.

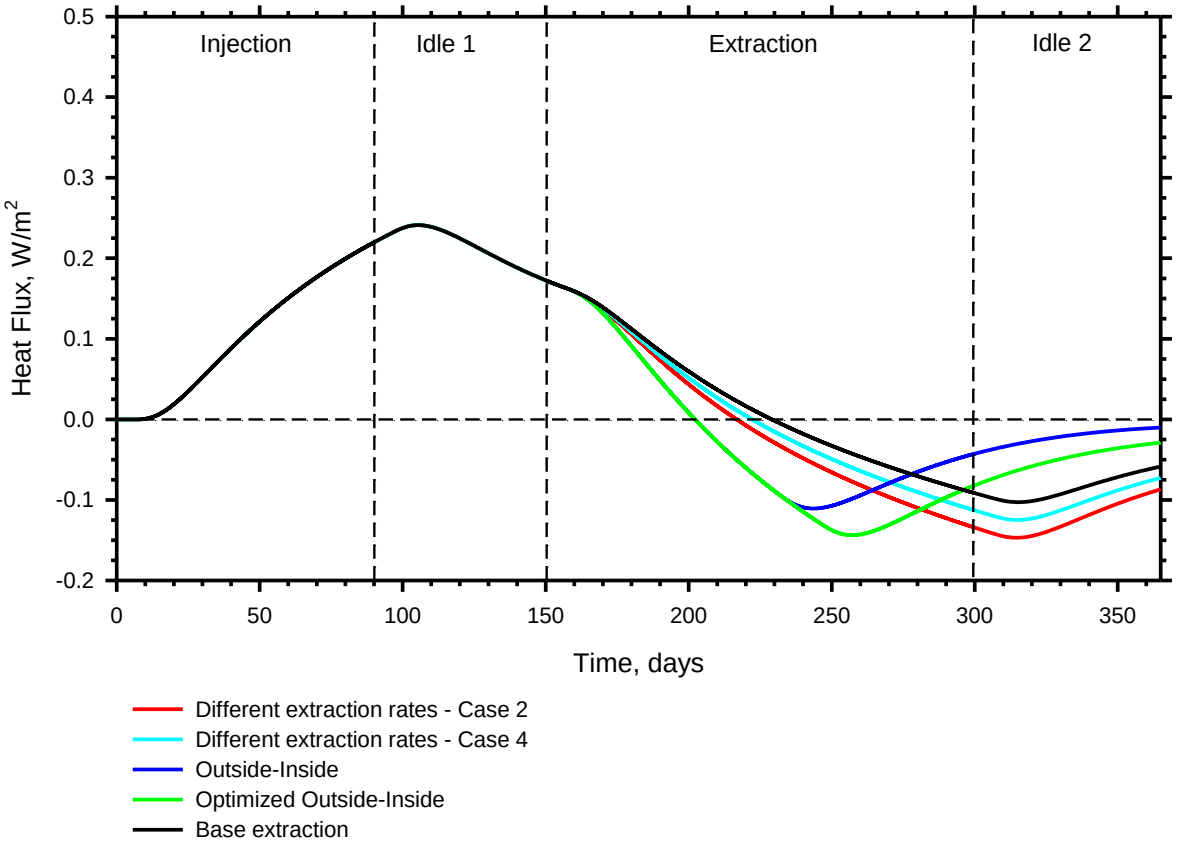

Figure 6-28. Average heat flux across the boundary footprint comparing cases 2 and 4 of the different extraction rate scenarios with the outside-inside and optimized outside-inside scenarios, where positive is defined as an outward pointed vector normal to the borehole footprint boundary.

Figure 6-29 compares the center, corner, and middle temperatures of the optimized outside-inside and DE2 scenarios. Interestingly, the center points are both greater than the base case with the center temperature of the optimized outside-inside case continuing to increase during extraction. This is due to no extraction taking place in the interior during the first three months of injection allowing the energy from directly around the piles to more evenly dissipate, thereby raising the center point. The higher center point temperature over time for DE2 is a result of lower extraction rates in the interior as compared to the base case. The middle and center temperatures of both alternative extraction scenarios are lower than the base case. The optimized outside-inside temperatures are the lowest temperatures at EOE and the DE2 temperatures are lowest at EOY. These results suggest that DE2 does not do a good job of utilizing the energy within the geothermal footprint as a large amount of energy still exists in the center after the end of the second idle period at the expense of temperatures lower than the initial temperature at the corner and middle points.

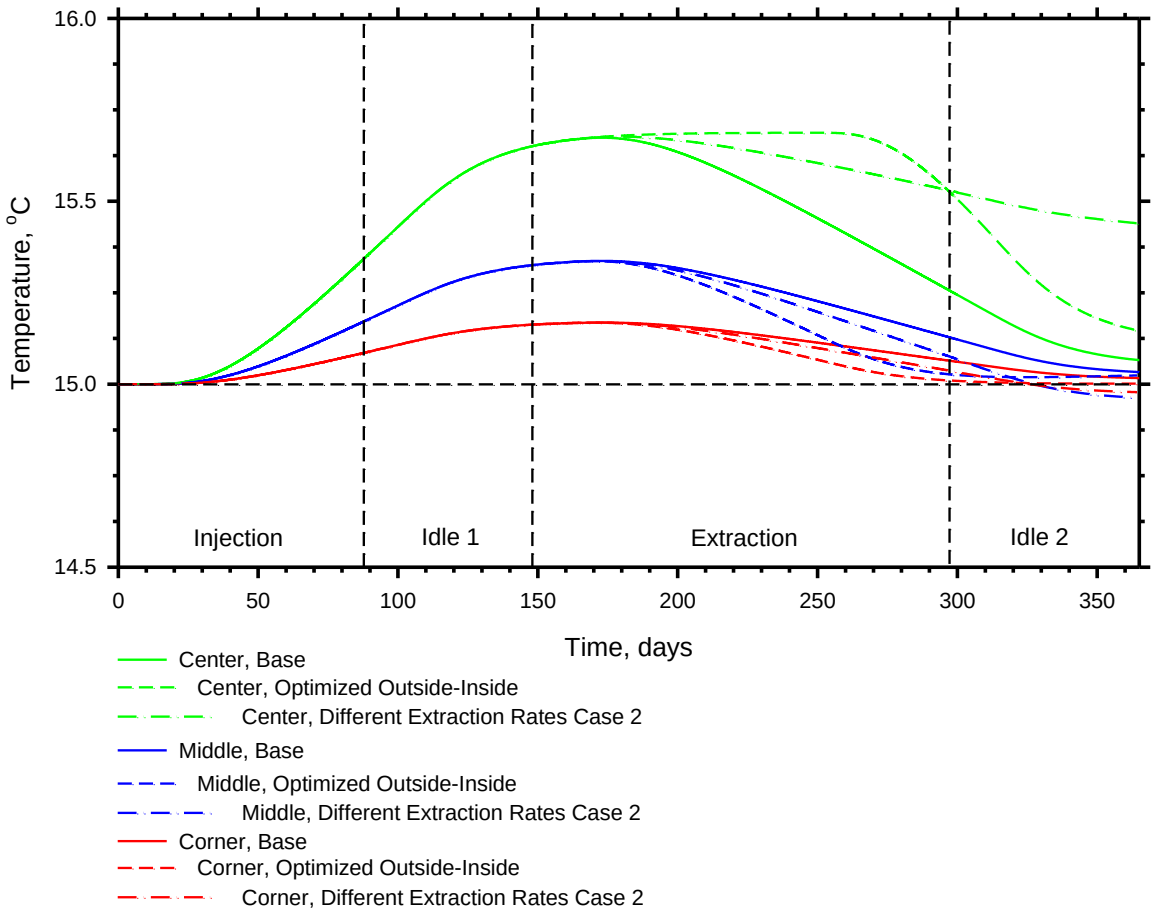

Figure 6-29. Temperatures over time of the corner, center, and middle points in the borehole geothermal footprint for the base extraction and injection cases as well as the optimized outside-inside and case 2 of the different heat extraction rate scenarios, IR1 and IR2.

Figure 6-30 visually represents this as it shows the temperature contours at EOE and EOY for these cases. As shown, at EOY the additional energy that was present after EOE for the optimized outside-inside case was used to recharge the interior boreholes. However, the additional energy present at the EOE was not needed to charge the interior boreholes for DE2 and is still present after one year of operation. Presumably, DE2 could be made more efficient by increasing the extraction rate of the interior borehole. However, this is what was done in DE4 as it was increased from 7 W/m to 13.5 W/m. This, however, resulted in a net energy loss in the geothermal footprint area (Table 6-7).

Applying different extraction rates to the boreholes, with higher rates to the outer boreholes increases the amount of energy retained within the geothermal footprint. Furthermore, this method results in less of a temperature decrease in the boreholes, which can lead to more efficient operation. However, the outside-inside scenarios are much easier to practically operate and appear to more efficiently utilize the energy within the geothermal footprint.

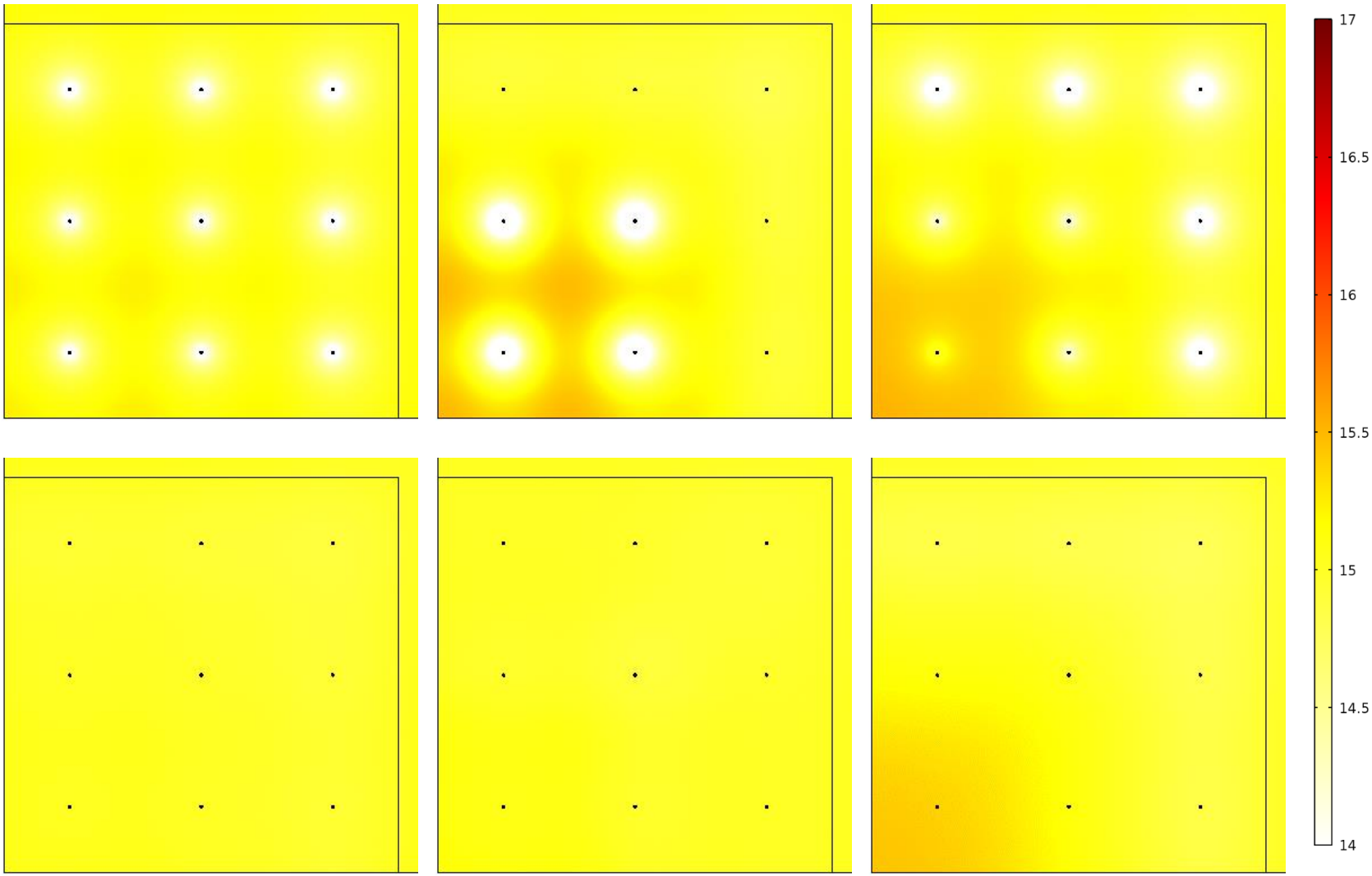

(a) (b) (c)

Figure 6-30. Temperature contours over time comparing end of extraction (top) and end of the second idle period (bottom) of a) base injection, b) optimized outside-inside, and c) case 2 of different heating rates

6.6.4. Use of Alternative Extraction Scenarios to Reduce Energy Loss in the Geothermal Footprint Area for Different Soil Properties

Two of the alternative extraction scenarios, the optimized outside-inside and DE2, were implemented in the cases in which changing soil properties resulted in a net loss of energy within the geothermal footprint to see if some of the energy loss could be mitigated. IR2, which was also successful in reversing the energy loss within the geothermal footprint area was not applied because of the lack of practicality in its implementation.

6.6.4.1. Mitigating the Influence of Thermal Conductivity

Figure 6-31 compares the energy values at EOI, BOE, EOE, and EOY for the different soil thermal conductivity values for the base and alternative extraction cases. The optimized outside-inside scenario as well as DE2 was used for the k=1.5 W/m·K analyses to see if some of the energy loss within the geothermal footprint could be mitigated (it cannot be eliminated as enough energy is not injected to account for what is extracted – in actuality, this system is under-designed for the extraction load required). Through the use of these alternative extraction scenarios the energy loss was reduced from -87 MJ to -66 MJ and -67 MJ for the optimized outside-inside and DE2 cases, respectively. Both alternatives yielded about the same result in terms of energy, but when looking at temperatures within the boreholes, there are clear differences.

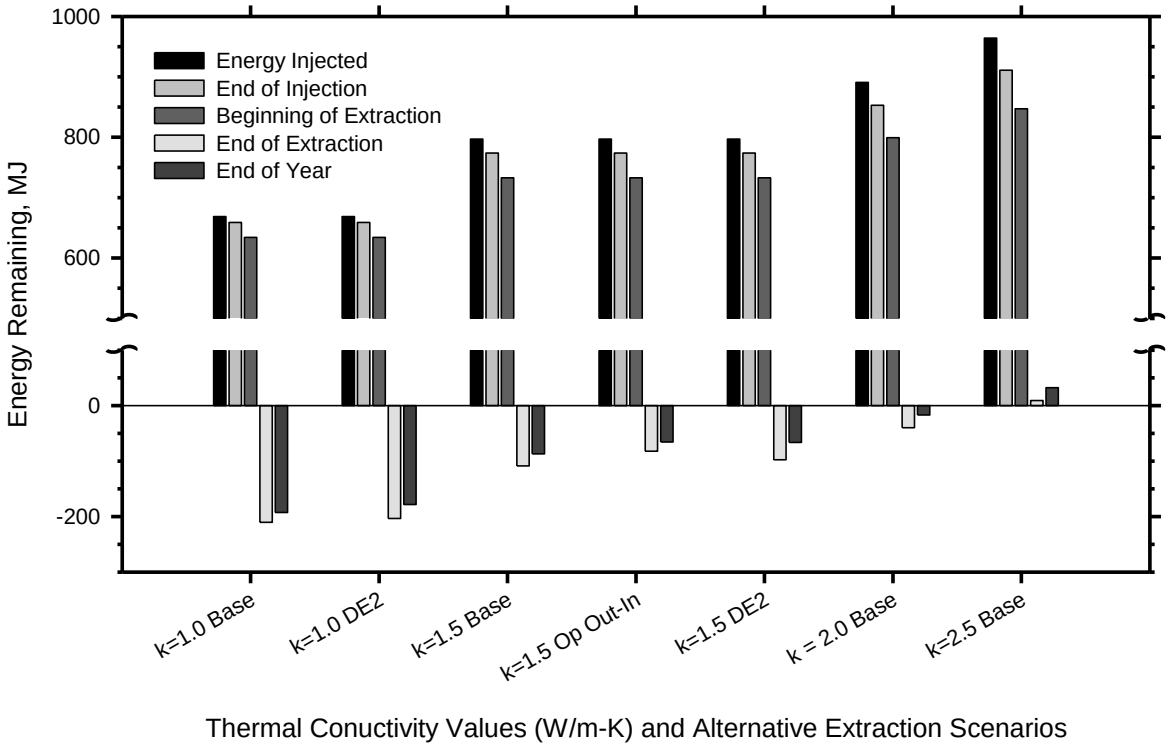

Figure 6-31. Comparison of the amount of energy within the geothermal footprint at EOI, BOE, EOE, and EOY between cases with differing thermal conductivity values

The minimum temperatures in the boreholes are shown in Table 6-8. Notice that the minimum temperatures in the inner and middle boreholes for the optimized outside-inside scenario with k=1.5 W/m·K are between 1.3 and 1.4°C, which is very low. Due to the low thermal conductivity, a greater temperature difference is required to extract the same amount of energy, resulting in the low temperatures. The minimum temperature for DE2 occurs in the outer boreholes and is only 7.1°C. Thus in terms of temperature, utilizing continuous but different heat extraction rates has a clear advantage over operating select boreholes with higher extraction rates when it comes to lower thermal conductivity values.

Table 6-8. Lowest temperature (°C) during extraction for the outside-inside and different extraction rate extraction scenarios for a soil thermal conductivity value of 1.5 W/m·K.

Location	Out-In Op	DE2
Inner	1.33	13.23
Middle		10.19
Outer	3.83	7.06

Due to the low temperatures in the boreholes from the optimized outside-inside scenario with k=1.5 W/m·K, only DE2 was used for k=1.0 W/m·K in an attempt to mitigate the energy loss. It succeeded in lowering the energy loss within the geothermal footprint area from -193 MJ to -178 MJ. The lowest temperature within the boreholes occurred in the outer boreholes and was 5.1°C. It is very likely that the minimum temperatures would be below 0°C if the optimized outside-inside scenario was tested.

6.6.4.2. Mitigating the Influence of Volumetric Heat Capacity

Figure 6-32 compares the energy values at EOI, BOE, EOE, and EOY for the different soil volumetric heat capacity values for the base and alternative extraction cases. Both the optimized outside-inside scenario and DE2 were used for extracting energy for VH values of 1000 J/m^{3}K and 1500 J/m^{3}K to retain more energy in the geothermal footprint area after the end of one year. For the case of VH=1500 J/m^{3}K, more than enough energy was injected into the ground to account for what was extracted. In the case of VH=1000 J/m^{3}K, the amount of injected energy was only 3 MJ less than what was extracted. Yet in both cases there is a net decrease in the amount of energy in the geothermal footprint area after one year and a reduction in the average ground temperature.

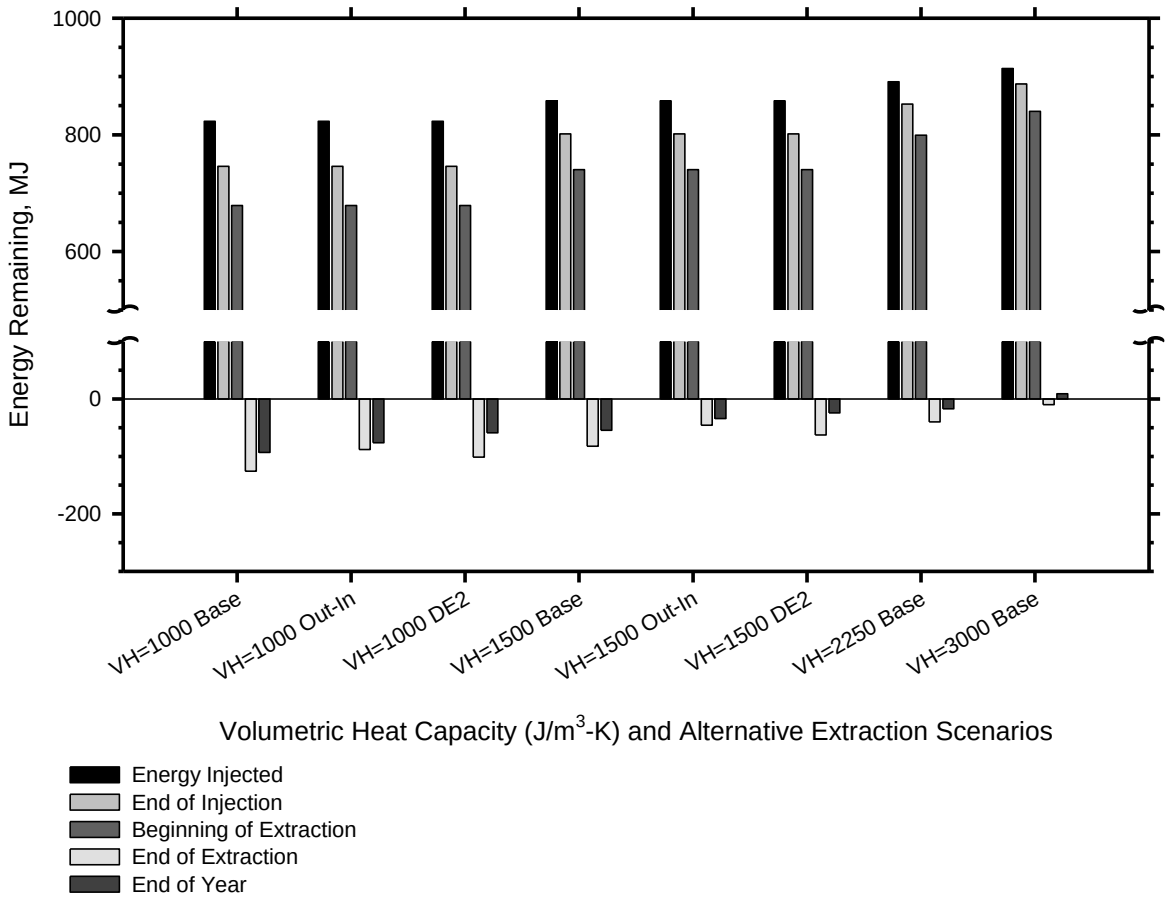

Figure 6-32. Comparison of the amount of energy within the geothermal footprint at EOI, BOE, EOE, and EOY between cases with differing volumetric heat capacity values.

Both alternative extraction scenarios decreased the amount of energy lost within the geothermal footprint area when compared with the base case. For both volumetric heat capacities utilizing DE2, more energy was retained than with the optimized outside-inside scenario. When using the different extraction rates, for a VH=1000 J/m^{3}K, the net energy loss was reduced from -93 MJ to -59 MJ and for a VH=1500 J/m^{3}K the net energy loss was reduced from -54 MJ to -24 MJ.

Low temperatures in the borehole are also observed in the optimized outside-inside scenarios for VH=1000 and 1500 J/m^{3}K, as shown in Table 6-9. For VH=1000 J/m^{3}K the lowest temperature was 2.17^{o}C whereas it was only 7.55^{o}C for the DE2 extraction scenario. Likewise, for VH=1500 J/m^{3}K, the lowest temperature was 2.69^{o}C, whereas it was only 7.87^{o}C for the DE2 extraction scenario. Similar to the thermal conductivity results, though the optimized outside-inside and DE2 extraction scenarios yield similar results in terms of energy, there is a clear advantage in favor of DE2 when it comes to temperature, and ultimately efficiency.

Table 6-9. Lowest temperature (°C) during extraction for the optimized outside-inside and DE2 extraction scenarios for soils with differing volumetric heat capacities.

Location	VH = 1000J/m³K			VH = 1500J/m³K		
	Base	Out-In Op	DE2	Base	Out-In Op	DE2
Inner	9.41	2.17	13.74	9.61	2.69	13.66
Middle	9.29		10.61	9.55		10.79
Outer	9.15	4.69	7.55	9.39	5.01	7.87

6.6.5. Multi-Year Operations

Shallow geothermal systems are often designed to operate for 30 years. Thus, some understanding of how these systems behave beyond the first year of operation is beneficial. A second year of injection and extraction was performed for the base case as well as the optimized outside-inside case. As shown in Table 6-10, in both cases almost the same amount of energy was injected (891 MJ, which was also the same as the injection case for year 1). The second year of operation for the base case was better than the first in that there was more energy within the geothermal footprint area at BOE and EOY. Though there was more net energy at the end of 1 year, there is still a net loss of energy (6 MJ) within the geothermal footprint area.

Table 6-10. Energy (MJ) results for multi-year operations of the base case and the optimized outside-inside scenario.

Energy Values	Base Case		Optimized Out-In	
	Year 1	Year 2	Year 1	Year 2
Total Energy Injected	891	892	891	891
Energy Loss After End of Injection	38	25	38	31
Net Energy After End of Injection	853	850	853	865
Energy Loss After 1st Idle Period	92	73	92	82
Net Energy After 1st Idle Period	799	802	799	814
Total Energy Extracted	-825	-825	-826	-826
Energy Loss After End of Extraction	106	81	74	60
Net Energy After End of Extraction	-40	-31	-8	11
Energy Loss After End of Year	83	56	60	45
Net Energy After End of Year	-17	-6	5	25

When looking at energy loss during the second year for the base case, less energy was lost overall (56 MJ as opposed to 83 MJ) to the surrounding ground. Though less energy was lost during the injection and first idle period during the second year (73 MJ as opposed to 92 MJ), 17 MJ of the injected energy was required to make up for the loss that was incurred from year 1.

The optimized outside-inside scenario succeeded in preventing more energy loss the second year (45 MJ for year two as opposed to 60 MJ for year one) and in retaining an even greater amount of energy within the geothermal footprint area after the first year of operation (25 MJ as opposed to 5 MJ).

Figure 6-33 compares the heat flux across the footprint boundary for years 1 and 2 of the base case and optimized outside-inside case. Several observations can be made. The first is that besides starting at different values, the second year of operation closely resembles the first year for each of the scenarios. In fact, at the end of the second year of operation, the fluxes are almost exactly what they were during the first year, which indicates that the third year of operation will be very similar to the second year of operation. Secondly, the fluxes for the second year of each case are slightly less than that of the first year for each case. This results in less energy being lost from and more energy being drawn into the geothermal footprint area, which is what was observed and discussed previously. Finally, though the base case starts with a larger flux drawing energy back into the footprint area at the beginning of the year, the optimized case is still able to draw more energy back into the footprint area during the extraction and idle period making it superior to the base case.

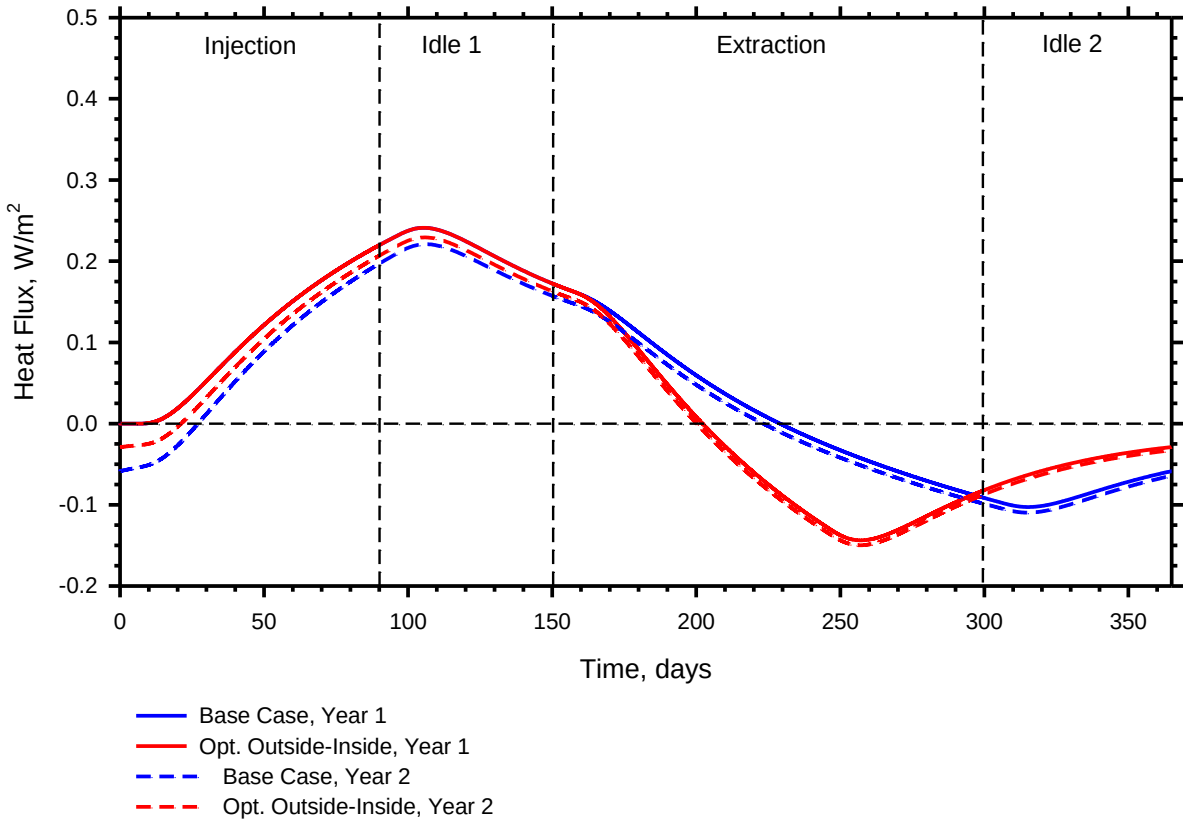

Figure 6-33. Average heat flux across the boundary footprint comparing the base case and optimized outside-inside scenarios for their first and second years of operation, where positive is defined as an outward pointed vector normal to the borehole footprint boundary.

Figure 6-34 shows the temperatures at the center, middle, and corner points for each year of operation. For each location, the temperatures were higher the second year, which corresponds to the observed increase in energy that was seen within each case's geothermal footprint area. Furthermore, it appears the largest temperature increase occurs at the center point. There was a relatively large difference between the starting and ending temperatures after the first year of operation. However, the difference

is not as great for the second year, which again indicates that the third year is likely to be similar to the second in operation.

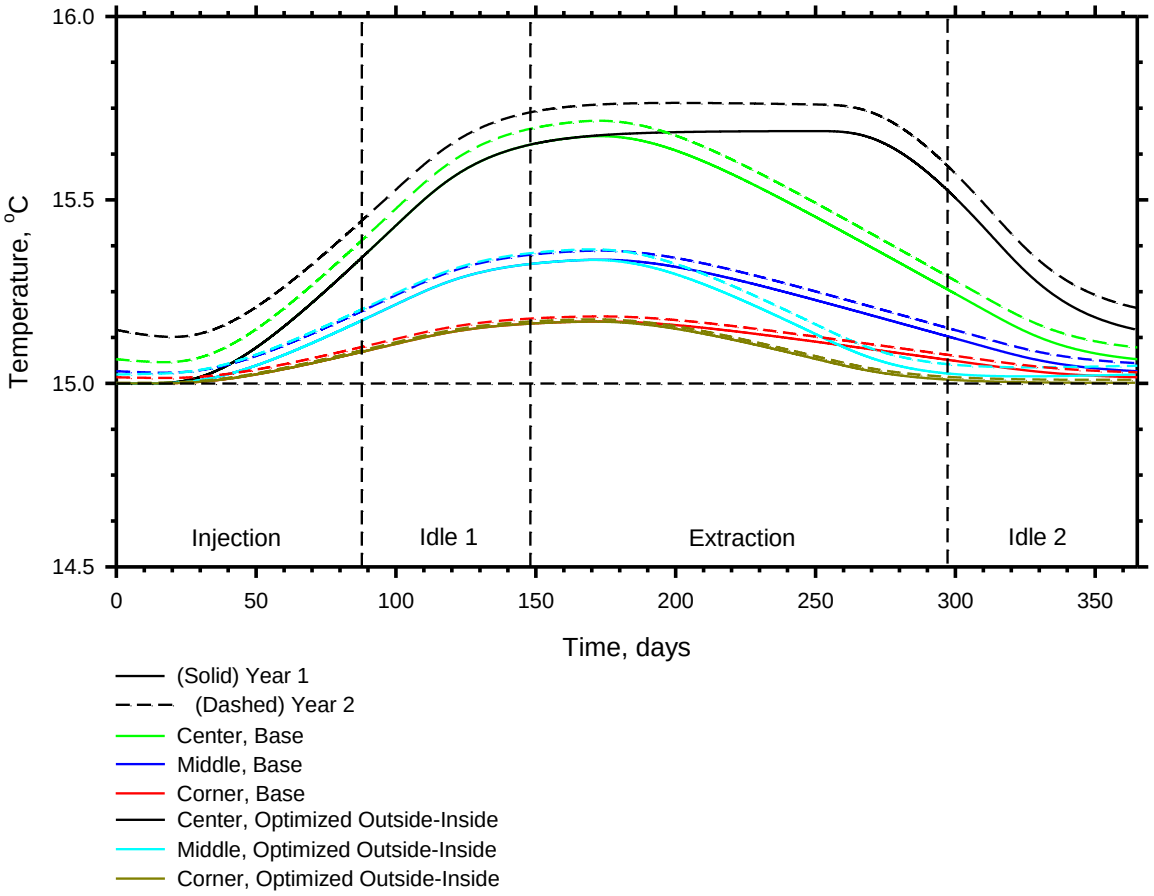

Figure 6-34. Temperatures over time of the corner, center, and middle points in the borehole geothermal footprint for the first and second years of operation of the base case and the optimized outside-inside scenario

6.7. CONCLUSIONS AND RECOMMENDATIONS FOR OPERATION

6.7.1. Conclusions

From the operations discussed in this paper, the following conclusions can be drawn regarding the optimization of shallow geothermal systems. First, when compared to a basic injection/extraction operation, there are methods that can reduce the amount of energy lost within the immediate distance of the geothermal boreholes, or the geothermal footprint area. The methods that work most efficiently are the ones that both prevent energy from leaving the geothermal footprint area and the ones that are able to draw energy into the footprint area from the surrounding soil. One alternative injection scenario that involved redistributing injected heat from the perimeter boreholes to the interior boreholes, IR2, was able to do this effectively, however, the physical mechanism by which this can be accomplished is yet to be developed.

Two alternative extraction scenarios were able to eliminate the energy loss that occurred in the geothermal footprint area. The first and simplest method to implement called optimized outside-inside involves extracting energy first from the perimeter boreholes, and then extracting energy from the interior boreholes. This method can be improved by lengthening the operation period of the perimeter boreholes, which results in a shorter operational period for the interior boreholes. The caveat to this method is that it results in lower temperatures within the borehole, which may interfere with the efficiency of the system.

The second extraction scenario allows all boreholes to be operated the entire extraction period but the outer boreholes are subject to a higher extraction rate. In order to make this method more efficient, larger differences in extraction rates between the outer, middle, and inner boreholes are required. The low borehole temperatures observed in the optimized outside-inside scenario are eliminated in this scenario, however, all of the energy within the geothermal footprint area may not be utilized as efficiently as possible.

These alternative extraction methods can also be used to reduce the adverse effects that lower soil thermal conductivities and volumetric heat capacities may have on these systems. In instances where there are no adverse effects, such as where higher thermal conductivities or volumetric heat capacities exist, the alternative injection and extraction methods may be used to reduce the size of the system and thus, the installation and operational cost. They may also be used to reduce the size of systems where higher gradients exist between the injection fluid temperature and the initial ground temperature.

6.7.2. Implementation Considerations

When implementing alternative injection and/or extraction schemes, several considerations should be taken into account including acceptable fluid and borehole temperatures as well as the amount of system oversight available. Utilizing different extraction rates results in less of a temperature drop in the fluid and boreholes, however it requires distributing extraction loads unevenly to the boreholes, which increases the complexity of the system. It could be accomplished in situations where there are several ground-coupled heat pumps by giving the perimeter boreholes a higher heat pump-to-borehole ratio, which would result in a higher load per borehole. The optimized outside-inside scenario results in lower fluid and borehole temperatures, but would require no complex automation or control beyond a maintenance operator turning a couple valves on and off three times a year (before injection, after injection, during extraction).

6.7.3. Applications

The applications of this research could prove especially valuable in situations where the average temperature of the ground cannot be significantly changed and in situations where the amount of subsurface available for SGE systems is limited. These methods can be used to prevent the progressive temperature change in the ground over the lifetime of these systems by more effectively balancing operations. Furthermore, many situations exist where there is a limited volume of subsurface available for SGE systems, such as the case of energy foundations (where the volume is limited by the size of the foundation), and crowded urban environments where the volume is limited to the footprint of the building and where competing SGE systems may exist. These methods can be used to more efficiently take advantage of the available volume as well as, in the case of competing urban systems, prevent interference and large-scale heating or cooling of the ground.

6.7.4. Future Work

Further research should be conducted to investigate the long term performance of these systems beyond two years. It would be beneficial to investigate a full 30 year lifespan to see the total impact alternative injection/extraction scenarios can have. Additionally, in this study the extraction rate to the borehole group was constant throughout the duration of the extraction period. In actuality, this rate fluctuates with energy demand and generally reaches a peak during the middle of the extraction period (Abdelaziz et al. 2015). Thus it would be beneficial to see how the alternative operation scenarios work under a variety of actual heating loads. Further research should also be conducted to determine the influence of geometric parameters, such as borehole spacing, on the effectiveness of alternative operation schemes. Furthermore, alternative injection scenarios and energy redistribution present a large potential for energy savings, but their practical implementation should be further explored.

6.8. REFERENCES

Abdelaziz, S.L., Olgun, C.G., and Martin J.R. (2015). “Equivalent energy wave for long-term analysis of ground coupled heat exchangers.” Geothermics, 53, 67-84.

Baser, T. and McCartney, J. (2015). “Development of a Full-Scale Soil-Borehole Thermal Energy Storage System.” Presentation. International Foundations Congress and Equipment Expo. San Antonio, TX. March 20, 2015.

Bayer, P., de Paly, M., and Beck, M. (2014). "Strategic optimization of borehole heat exchanger field for seasonal geothermal heating and cooling." Appl Energy, 136, 445-453.

Beck, M., Bayer, P., de Paly, M., Hecht-Mendez, J., and Zell, A. (2013). "Geometric arrangement and operation mode adjustment in low-enthalpy geothermal borehole fields for heating." Energy, 49(1), 434-443.

Bowers, G.A., Ozudogru, T.Y., and Olgun, C.G. (2016). “Numerical and Analytical Investigation of Subsurface Response to Heat Exchange Operations in Shallow Geothermal Energy Systems.” Geothermics. Submitted.

Brandl, H. (2006). "Energy foundations and other thermo-active ground structures." Geotechnique, 56(2), 81-122.

Churchill, S.W. (1977). “Friction factor equations spans all fluid-flow regimes.” Chemical Engineering, 84, 91–92.

COMSOL. (2015). “COMSOL Multiphysics™ Version 5.1: User’s Guide and Reference Manual.” COMSOL Inc., Burlington, MA.

De Paly, M., Hecht-Mendez, J., Beck, M., Blum, P., Zell, A., and Bayer, P. (2012). "Optimization of energy extraction for closed shallow geothermal systems using linear programming." Geothermics, 43, 57-65.

Eugster, W., J. "Road and Bridge Heating Using Geothermal Energy - Overview and Examples." Proc., European Geothermal Congress.

Gnielinski, V. (1976). “New equations for heat and mass transfer in turbulent pipe and channel flow.” International Journal of Chemical Engineering 16, 359–368.

Lazzari, S. 2010. “Long-term performance of BHE (borehole heat exchanger) fields with negligible groundwater movement.” Energy, 35(12), 4966-4974.

Ozudogru, T.Y., Ghasemi-Fare, O., Olgun, C.G., and Basu, P. (2014) “Numerical Modeling of Vertical Geothermal Heat Exchanger Using Finite Difference and Finite Element Techniques.” Journal of Geotechnical and Geological Engineering, Special Issue on Thermo-hydro-mechanical Behavior of Soils and Energy Geostructures, 33(2), 291-306.

Yin, H. M., Yang, D. J., Kelly, G., and Garant, J. (2013). "Design and performance of a novel building integrated PV/thermal system for energy efficiency of buildings." Sol Energy, 87(Journal Article), 184-195.

Zhang et al., 2012. R. Zhang, N. Lu, Y.S. Wu. (2012). “Efficiency of a community-scale borehole thermal energy storage.” Proceedings of GeoCongress 2012 (2012), pp. 4386–4395.

7. 3-DIMENSIONAL BRIDGE DECK DEICING NUMERICAL MODEL: DEVELOPMENT AND VALIDATION

7.1. ABSTRACT

The icing of bridge decks during the winter, which often occurs before that of roadways, presents dangerous conditions for motorists and lead to accidents every year. A possible solution to these problems is to heat the bridge deck during the winter storms using shallow geothermal energy. In order to design such systems, an accurate understanding of the heating requirements and expected performance is needed. To this end a 3D finite element model was created of the bridge deck component of a geothermally heated bridge deck deicing system. This paper describes the development of the model and presents the results from two validation exercises where the model was used to replicate the performance of an actual bridge deck deicing system. The validation exercises show that this model can be used to reasonably estimate surface and internal bridge deck temperatures as well as provide an accurate representation of the heating rates these systems are capable of during heating operations and the amount of energy consumed. Both the versatility and limitations of the model are discussed.

7.2. INTRODUCTION

The icing of bridge decks in the winter, which often occurs before that of roadways, presents dangerous conditions for motorists that are attributed to accidents every year (Friar and Decker 1999). Furthermore, the deterioration and associated costs from the deicing chemicals that are often used by transportation authorities to try and prevent the accumulation of frozen precipitation has been well documented (AASHTO, 2008; Koch et al., 2002; Yunovich et al., 2003; Virmani et al., 1983, 1984; Baboian, 1992; White et al., 2005; Granata and Hartt, 2009; Naito et al., 2010). A possible solution to these problems is to heat the bridge deck during winter storms to prevent icing.

Heating bridge decks using ground-sourced thermal energy alone is promising because it does not require the same level of system oversight or energy requirements as many other methods such as heat pipe, boiler powered, or ground-sourced heat pumps (Minsk 1999). Furthermore, recent advancements in the geotechnical engineering profession are allowing deep and shallow foundation elements, such as those used to support bridges, to function for both foundation support and for harvesting shallow geothermal energy (Brandl, 2006, Bourne-Webb et al. 2009, Katzenbach et al. 2014).

The concept is shown schematically in Figure 7-1. The pile foundation and approach embankment are converted to an ‘energy foundation’ through the installation of fluid circulation tubes. During the winter the ground below a depth of about 6-10 m (Kusada and Achenbach 1965) is typically warmer than that of the atmosphere. As fluid is circulated through the foundation elements, it is warmed by the ground. The heated fluid is then circulated through the bridge deck, heating the deck. In the summer the thermal energy stored in the deck as it is heated by the sun can be collected by the fluid and then injected into the ground to both replace the energy that was used during the winter and to possibly raise the temperature of the ground for more efficient heating.

These systems have been shown to work experimentally (Bowers and Olgun 2016), however the authors note there are limitations. Thus, before any system is installed a basic understanding as to how the system will perform is desirable. This paper presents a 3D numerical model that can be used to estimate bridge deck deicing system performance. This model is then validated using the results from several experimental

bridge deck heating tests. A parametric analysis is then performed to provide a basic understanding of how these systems will perform under a variety of weather conditions.

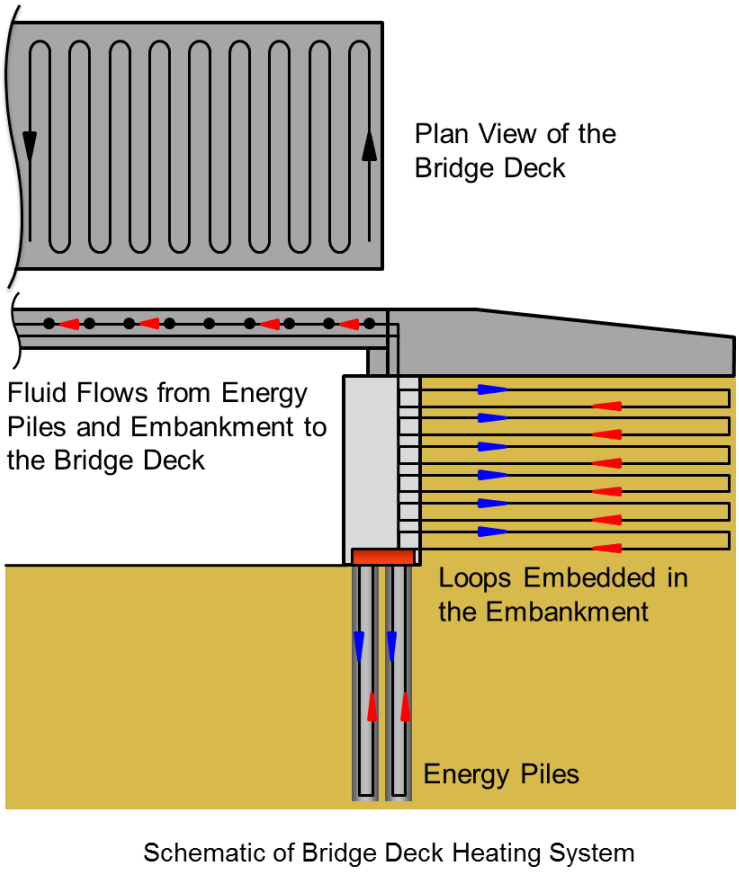

Figure 7-1. Conceptual schematic of ground-source bridge deck deicing (redrawn after Bowers and Olgun 2014).

7.3. BACKGROUND

In general, previous bridge deck deicing and pavement snow melting models can be grouped into two categories: those used for the determination of design values and those used to represent the actual slab heating and snow melting processes. The models within both groups vary with respect to dimension (1D, 2D, 3D) and time (steady-state, transient, semi-transient) and as such employ different assumptions and boundary conditions.

Many of the early models and the one that is currently recommended by ASHRAE (2011) is a 1D steady-state method that is used to develop a design value of required heat flux at the surface (Adlam 1950; Chapman 1952; Chapman 1956; Kilkis 1994a,b; Schnurr and Rogers 1970; Williams 1976; Williamson 1967) however some early 2-dimensional models did consider transient behavior (Regis et al. 1973; Schnurr and Falk 1973). The current design methodology presented in ASHRAE (2011) is based on the work of Ramsey et al. (1999), and is a 1-dimensional steady-state analysis. The 1-D models essentially perform a heat balance at the surface of a slab and account for relevant heat fluxes including convection, radiation, and the sensible and latent fluxes associated with snow melting. The models mainly differed in their determination of the design fluxes.

Several recent, numerical studies have considered both the transient and two-dimensional components of a hydronic heating system. Rees et al. (2002) developed a two-dimensional numerical model that accounted for the transient effects of the snow melting process on a pavement snow melting system's performance. The authors modeled a cross section of the slab that included one-half of the heating element and extended to a distance directly between two heating elements. The slab was situated on soil, the temperature of which was defined based on the analytical relationship given in Kusada and Achenbach (1965). In defining the initial conditions, the authors developed a 1D model (essentially the 2D model without a deicing tube) and subjected it to the boundary conditions for a period of two weeks before the start of any heating operation. The temperature gradient at the end of the two week initialization period was then applied to the 2-D domain six hours before the start of operation, which was then subject to the boundary conditions until the operation began.

The surface boundary condition was controlled by a surface boundary model that accounted for 7 possible surface conditions including dry, wet, dry snow, slush, snow and slush, solid ice, and solid ice and water. This boundary condition model allowed for the model to both predict what surface condition was present and then determine the appropriate surface boundary heat flux. The advantage of this model is that it can accurately account for the complex snow melting process and thus predict how a system will perform. The disadvantage is that it is 2D and only accounts for a small part of heated slab.

Liu et al. (2003) improved upon the model found in Rees et al. (2002) to simulate hydronic heating of a bridge deck over a lifetime as opposed to singular storm events and incorporated a ground-source heat pump. The entire model consisted of four sub-models: a hydronically heated bridge deck model, a ground loop heat exchanger model, a water to water heat pump model, and a system control model. The model was then experimentally validated with a hydronic ground-source bridge deck deicing system installed in an experimental bridge at Oklahoma State University. The deck is 18.3 m long by 6.1 m wide with 19 mm hydronic tubing installed on 0.3 m centers at a depth of 89 mm. The system is designed to control the bridge deck temperature in the range of 4.4-5.6^{o}C (40-42^{o}F) when there is a risk of snowfall. The model did a good job in predicting the average bridge surface temperatures and fluid exiting temperature but slightly over predicted the surface temperatures. The authors highlight the difficulty of numerically accounting for the long-wave radiation and convective heat fluxes.

Liu and Spitler (2004) utilize the simulation from Liu et al. (2003) and perform a parametric study to investigate the effects of idling time, pipe spacing, slab insulation, and control strategies on system performance. Among their findings are that preemptive heating is required to achieve the expected snow-melting performance when using the tabulated ASHRAE surface heat fluxes. Furthermore, preheating the slab with full heating capacity before snowfall can significantly improve the system's performance. This model has been further refined (Liu et al. 2007a) and validated (Liu et al. 2007b).

More recent work has been performed by Wang et al. (2010). The focus of their study was determining the temperature distribution within an asphalt layer when using a hydronic system to collect the solar heat energy. Their two-dimensional finite element model accounted for several asphalt layers on top of a soil base. The geometry was such that it accounted for several hydronic tubing elements as opposed to just one as the previous models have done. The authors varied several parameters in the model including thermal conductivity of the asphalt pavement, distance between the pipes, and the pipes' diameters. They then reported the temperature changes that took place in the slab.

Chen et al. (2011) used the model created by Wang et al. (2010) to study deicing in order to design a pavement hydronic deicing system. Snow melting was substituted by ice melting and it was assumed that whenever the temperature of the ice reached 0°C, that part of the ice had been melted. The chosen inlet fluid temperature for this model was 25°C, which is the assumed temperature of the 'thermal bank' that is providing the heat energy. They varied the thermal conductivity of the asphalt as well as the pipe depth and then reported the time of initiation of ice-melting. The results were then used to design an experimental system, however the results from the experiment were not used to validate the model.

7.4. NUMERICAL MODELING OF THE BRIDGE DECK

A three-dimensional numerical model was created to further explore bridge deck heating and deicing. This section describes how that model was developed and presents the results of some parametric analyses that utilized this model.

7.4.1. The Process of Bridge Deck Heating and Deicing

In order to create an accurate and useful model, the process of bridge deck heating and deicing must be understood. Bridge deck heating and deicing is a complicated process that involves many different heat transfer components. Figure 7-2 below summarizes these components, after which is a description of the relevant processes.

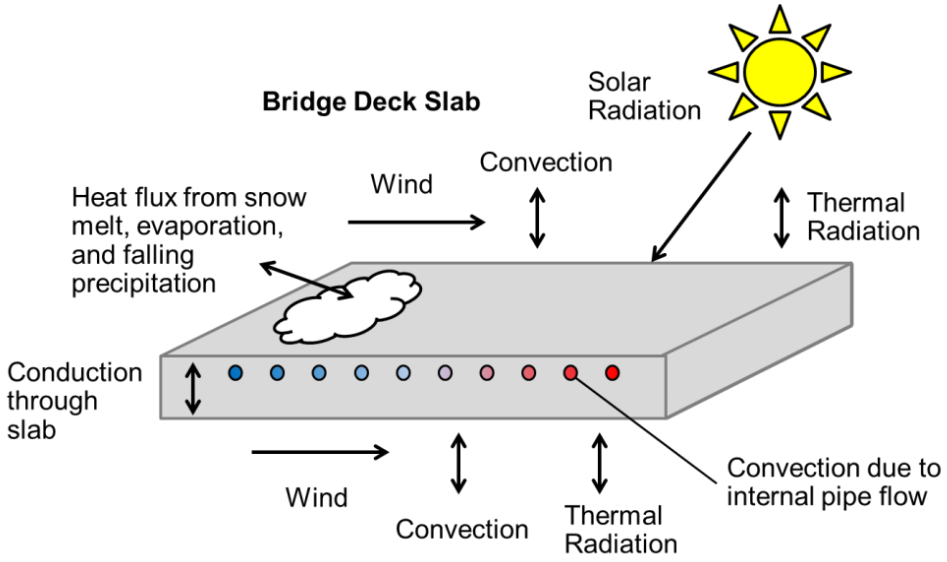

Figure 7-2. Thermal processes involved in bridge deck deicing operations.

Conduction: Conduction occurs in and between the circulation tube, the concrete bridge deck, and any precipitation on the bridge deck. Conduction also occurs between falling precipitation and either the bridge deck or accumulated precipitation on the bridge deck.

Convection: The four types of convection are forced, natural, boiling, and condensation. The two of concern for the bridge deck are natural and forced. Natural convection occurs when the flow is driven purely by the buoyancy forces that are created from variations in the fluid's density, which is a result of temperature differences in the fluid. Forced convection occurs when the fluid flow is caused by some external means (i.e. wind).

Radiation: Although radiation is one of the most important mechanisms in energy transfer between a bridge deck and its environment, it is also one of the most variable. A bridge deck absorbs solar radiation and longwave radiation from the atmosphere and also emits longwave radiation back to the atmosphere. The amount of radiation a bridge absorbs or emits is influenced by the temperature, cloud cover, the type of surface on the bridge deck, time of day, time of year and if the bridge deck is shielded or shaded. Capturing these variations is explained more fully in Section 7.4.3, which covers boundary conditions.

Additional Heat Flux Considerations: Several additional heat fluxes impact the thermal response of the bridge deck during certain operations. Mass is added to the system whenever precipitation falls on either the bridge deck or on the accumulated precipitation that is already on the bridge deck. Unless the temperature of the falling precipitation is the same as that of the surface on which it is falling, the precipitation's heat energy will affect the thermal equilibrium of the system. This requires consideration of the falling precipitation's mass and specific heat. Evaporation and melting are phase change processes that also require significant heat energy. Evaporation may take place during snow melting operations. Quantifying these additional considerations is explained more completely in Section 7.4.3, which covers boundary conditions.

7.4.2. Model Development

The model was created using COMSOL Multiphysics™, a finite element simulation environment (COMSOL, 2015). The bridge deck concrete slab was modeled directly as a solid. The circulation loops were also modeled using a solid domain, however it was modified through the use of 'pseudo-pipe' elements, which will be explained in Section 7.4.2.2. The fluid flow through the pipes was modeled by simplifying the 3D fluid flow equation to 1D approach, and the coupling the temperature domains directly. Weather conditions, including snowfall, were applied through the use of appropriate boundary conditions.

7.4.2.1. Governing Differential Equations

Assuming there is no internal heat generation, heat conduction through the solid domains (slab, tube) is governed by the following differential equation:

$$\rho c_p \frac{\partial T}{\partial t} + \nabla \cdot (-\mathbf{k}\nabla T) = 0 \qquad \text{Equation 7-1}$$

Several boundary conditions can exist. For completely insulated, or adiabatic surfaces of the bridge deck, a Neumann boundary condition exists, which specifies the heat flux at the respective boundary is 0:

$$q" = (-\mathbf{k}\nabla T) = 0 \qquad \text{Equation 7-2}$$

The top and bottom deck surfaces, unless insulated, are exposed to the environment, in which case they will experience both radiation and convection. Convection can be experienced on all surfaces of a bridge deck, depending on its exposure to the environment. On any exposed surface, the governing equation is:

$$-\mathbf{n} \cdot (-\mathbf{k}\nabla T) = h \cdot (T_{ext} - T) \qquad \text{Equation 7-3}$$

In the equation above, the determination of the convective heat transfer coefficient, h, is critical in accurately representing the effect of wind on the temperature of the bridge deck. Development of this coefficient is discussed in Section 7.4.3.2.

Radiation between the surface and the environment is expressed as:

$$-\mathbf{n}\cdot(-\mathbf{k}\nabla T) = \varepsilon\sigma(T_{ext}^4 - T^4) \quad \text{Equation 7-4}$$

Just as the determination of h is critical for convection, the determination of the appropriate external temperature, T_{ext} is critical for an accurate representation of radiation. Development of a proper T_{ext} is discussed in Section 7.4.3.1.1.

7.4.2.2. Fluid Flow and Pseudo Pipe Elements

Directly modeling fluid flow is a computationally expensive process and being able to directly model the flow of the fluid through the circulation pipes is not within the objectives of the model. Rather, the transfer of thermal energy between the fluid and the slab is of concern. Thus, a 1D approximation of the fluid flow process was utilized using COMSOL's non-isothermal pipe flow module. An explanation of the process is given below.

The energy equation that governs an incompressible fluid flowing in a pipe with no internal heat source is (COMSOL, 2015):

$$\rho A C_p \frac{\partial T}{\partial t} + \rho A C_p \mathbf{u}\cdot\nabla T = \nabla\cdot Ak\nabla T + f_D\frac{\rho A}{2d_h}|\mathbf{u}|^3 + Q_{wall} \quad \text{Equation 7-5}$$

In the equation above, the second term on the right hand side represents the friction heat dissipated due to viscous shear. The Darcy friction factor, f_D, can be estimated using the equation from Churchill (1997):

$$f_D = 8\left[\left(\frac{8}{\mathrm{Re}}\right)^{12} + (\mathrm{C_A}+\mathrm{C_B})^{-1.5}\right]^{\frac{1}{12}} \quad \text{Equation 7-6}$$

C_A and C_B are given by:

$$\mathrm{C_A} = \left[-2.457\ln\left(\left(\frac{7}{\mathrm{Re}}\right)^{0.9} + 0.27\left(\frac{e}{d_h}\right)\right)\right]^{16} \quad \text{Equation 7-7}$$

$$\mathrm{C_B} = \left(\frac{37530}{\mathrm{Re}}\right)^{16} \quad \text{Equation 7-8}$$

The absolute surface roughness coefficient, e, is 0.0015 mm for plastic pipes. The Reynold's number, Re, is given by:

$$\mathrm{Re} = \frac{\rho_f u d_h}{\mu_f} \quad \text{Equation 7-9}$$

In Equation 7-5, Q_{wall} is the radial heat transfer from the surroundings into the pipe and includes the effects of both the internal film resistance and thermal resistance from the pipe itself. It is given as:

$$Q_{wall} = (hZ)_{eff}(T_{ext} - T) \quad \text{Equation 7-10}$$

T_{ext} is the external temperature, in this case the temperature of the slab domain, and is what allows coupling of Equation 7-5 directly with the 3D heat transfer. In this case, the 3D model treats the fluid flow

as a 1D line heat source. The $(hZ)_{eff}$ is the effective value of the heat transfer coefficient h, which includes the effects of the internal film resistance and the pipe thermal resistance, multiplied by Z, the wall perimeter. For circular, non-layered pipe cross sections, $(hZ)_{eff}$ is given by:

$$(hZ)_{eff} = \frac{2\pi}{\frac{1}{r_i h_{int}} + \frac{\ln(r_o/r_i)}{k_p}} \quad \text{Equation 7-11}$$

Important to understand are two key assumptions in the determination of $(hZ)_{eff}$. The first is that there is an equal temperature distribution around the pipe and the second of which is that heat transfer through the pipe is quasi-static, or that it immediately assumes the temperature distribution across the pipe. In the equation above, the determination of h_{int}, the internal film heat transfer coefficient, is given by:

$$h_{int} = \mathrm{Nu}\frac{k_f}{2r_i} \quad \text{Equation 7-12}$$

Nu is the Nusselt number. For laminar pipe flow it is defined as 3.66 for circular pipe cross sections. For turbulent flow, it is determined as:

$$\mathrm{Nu} = \frac{(f_D/8)(\mathrm{Re} - 1000)\mathrm{Pr}}{1 + 12.7(f_D/8)^{1/2}(\mathrm{Pr}^{2/3} - 1)} \quad \text{Equation 7-13}$$

Pr is the Prandtl number and is given by:

$$\mathrm{Pr} = \frac{C_{p,f}\mu_f}{k_f} \quad \text{Equation 7-14}$$

As mentioned previously, the way the 1D pipe flow is typically coupled within the 3D numerical model is by integrating it as a line source element along the centerline of the tube. Ozudogru et al. (2014) points out that this simplification produces two main coupling errors. The first is that by assuming the pipe is a 1D linear element, the temperature field of the slab is coupled directly at that element whereas it should be coupled at a distance equal to pipe's outer radius. Secondly, by assuming the pipes themselves are linear elements, their volumetric heat capacities are neglected. Thus, Ozudogru et al. (2014) develop a 'pseudo-pipe' approach to account for these coupling errors, which was implemented in this model.

Under this approach a volumetric domain equal in size to the outer pipe radius is created. The domain consists of pseudo pipe elements, which have effective densities, defined by:

$$\rho_{p,eff} = \rho_p\left(\frac{d_{po}^2 - d_{pi}^2}{d_{po}^2}\right) \quad \text{Equation 7-15}$$

The heat capacity of the pseudo pipe elements is equal to that of the actual pipe. The thermal conductivity, however, is anisotropic and is set to be very high (1000 W/(m*K)) in the radial direction as defined by the pipe's centerline and zero in the tangential direction.

7.4.3. Boundary Conditions

Both convective and radiative boundary conditions are present at a bridge deck's surfaces, and the governing equations have been presented Equation 7-3 in and Equation 7-4. Determining the appropriate variables for those equations, however, is essential to an accurate representation of boundary conditions.

7.4.3.1. Radiation

7.4.3.1.1. Longwave (Incident)

Bridge decks exchange energy with the environment in the form of radiation, as dictated by Equation 7-4. In Equation 7-4, two parameters must be specified: the surface emissivity constant, ε, and the external temperature, T_{ext}.

The external temperature is not necessarily equal to the ambient air temperature, but rather is a factor of cloud cover and if there is any falling precipitation. The external temperature is defined by ASHRAE in their snow-melting design chapter as the mean external temperature, T_{MR}, which is the mean temperature of the surroundings. This term will be useful in conceptualizing the concept as applied to the experimental site, explained in Section 7.4.3.3.

Ramsey et al. (1999) defines the mean radiant temperature as:

$$T_{MR} = \left[T_{cloud}^4 F_{sc} + T_{sky\ clear}^4 (1 - F_{sc})\right]^{1/4} \quad \text{Equation 7-16}$$

F_{sc} is the fractional portion of the sky that is covered in clouds. The equivalent blackbody temperature of a clear sky, $T_{sky\ clear}$, depends on both the ambient air temperature and the water content of the atmosphere. Ramsey et al. (1982) estimates it as:

$$T_{skyclear} = T_a - [1.1058 \times 10^3 - 7.562(T_a) + 7.407 \times 10^{-2}(T_a)^2 - 31.292\phi + 14.58\phi^2] \quad \text{Equation 7-17}$$

The temperature of the clouds is based on the assumption the cloud height is at 3048m and that the temperature based on altitude decreases 6.38K per 1,000m. Thus:

$$T_{cloud} = T_a - 19.4 \quad \text{Equation 7-18}$$

However, the authors readily admit that when the atmosphere contains a high water content (such as during precipitation events), the temperature of the clear sky may be warmer than that calculated at the base of the clouds. Upon that condition, the authors say to set $T_{cloud} = T_{skyclear}$.

Liu (2005), in development of an algorithm for estimate the surface temperature of a hydronically heated slab, observed that the determination of T_{MR} from Ramsey et al. (1999) provided too low of a temperature during precipitation events as when compared to measured values. They determined that the algorithm proposed by Martin and Berdahl (1984) to provide a better estimate of the sky temperature when compared with measured values.

The Martin and Berdahl (1984) relationship determines the sky emissivity, from which the temperature depression (difference in temperature between the sky temperature and the ambient air temperature) can be determined. The monthly average clear sky emissivity, corrected for elevation of the observing station and hour of the day, is determined based on the dew point temperature:

$$\varepsilon_{sky,clear} = 0.711 + 0.56\left(\frac{T_{dp}}{100}\right) + 0.73\left(\frac{T_{dp}}{100}\right)^2 + 0.013\cos\left[2\pi\frac{t_h}{24}\right] + 0.00012(P - 1000) \quad \text{Equation 7-19}$$

Cloud cover increases the total sky emissivity. The emissivity of the clouds is given by:

$$\varepsilon_{cloud} = \varepsilon_{sky,clear} + (1 - \varepsilon_{sky,clear}) \sum_i n_i \varepsilon_{c,i} \Gamma_i \quad \text{Equation 7-20}$$

Where n_i is the fractional area of the sky covered at the i^{th} level, $\varepsilon_{c,I}$ is the hemispherical emissivity of the cloud at the i^{th} level, and Γ_i is the cloud factor at the i^{th} level. The authors note that low and mid-level clouds (clouds with bases less than 4km) are generally opaque ($\varepsilon_c = 1$) whereas high level clouds generally have emissivity values around 0.4. The cloud factor, Γ, depends on the cloud base temperature and is expected to be small for cold clouds. It can be defined by:

$$\Gamma_i = e^{-h_i/h_o} \quad \text{Equation 7-21}$$

From Equation 7-21, the cloud factor is determined using the cloud base height, h_i, and the reference base height, h_o = 8.2km. Finally, the sky temperature can be calculated by:

$$T_{sky} = T_a \varepsilon_{cloud}{}^{1/4} \quad \text{Equation 7-22}$$

The surface emissivity constant has been well defined for various materials, and though a direct value was not measured for the experimental bridge deck, a range can be determined.

7.4.3.1.2. Solar Radiation

Solar radiation from the sun can be accounted for:

$$-\mathbf{n} \cdot (-\mathbf{k} \nabla T) = \alpha I \quad \text{Equation 7-23}$$

Note that I is the direct radiation incident to a horizontal surface. This changes both throughout the year and throughout each day. The angle of incidence to a horizontal surface was determined using the relationships provided in ASHRAE (2013).

The absorptivity coefficient, α, is dependent on the surface condition. Ideally this coefficient can be measured using a 4-component net radiometer that measures the incoming and outgoing radiation to a surface.

7.4.3.2. Convection

There are two types of convection, forced and free. Forced convection is due to wind and free convection occurs as the buoyancy forces resulting from temperature differences in the air induce convection at the surface. The determination of the convective coefficient from Equation 7-3, h_c, differs depending which type of convection is present. Generally, if wind is present, forced convection dominates. Liu (2005) calculated the convective coefficient for both conditions and used whichever was greater. In this methodology, free convection is used whenever wind is not present and the air is calm. The convective coefficient is a function of the thermal conductivity of the air, the characteristic length, and the Nusselt number of the air:

$$h_c = \mathrm{Nu} \frac{k_{air}}{L} \quad \text{Equation 7-24}$$

For free convection from the upper surface of a heated plate or the lower surface of a cooled plate, Nu can be determined by (Incropera and Dewitt 2002):

$$\mathrm{Nu} = 0.54\mathrm{Ra}^{1/4}$$ (10^4 < Ra < 10^7 – Laminar flow) Equation 7-25

$$\mathrm{Nu} = 0.15\mathrm{Ra}^{1/3}$$ (10^7 < Ra < 10^{11} – Turbulent flow) Equation 7-26

The Nusselt number for forced convection over a horizontal surface can be determined by (Incropera and DeWitt 2002):

$$\mathrm{Nu} = 0.664\mathrm{Re}^{1/2}\mathrm{Pr}^{1/3}$$ (Re < 5x10^5 – Laminar flow) Equation 7-27

$$\mathrm{Nu} = 0.037\mathrm{Re}^{4/5}\mathrm{Pr}^{1/3}$$ (5x10^5 < Re < 10^8 – Turbulent flow) Equation 7-28

ASHRAE (2013) notes that the Prandtl number for air can be taken to be 0.7. The Rayleigh and Reynold's numbers can be determined as:

$$\mathrm{Re} = \frac{VL}{\nu_{air}}$$ Equation 7-29

$$\mathrm{Ra} = \frac{gB}{\nu_{air}\alpha_{air}}(T_s - T_a)L^3$$ Equation 7-30

Note that the Rayleigh number is a function of the surface and air temperatures. As such, it changes over time. Additionally, the properties of the air are to be taken at $(T_s + T_a)/2$ (ASHRAE 2013).

Several items must be realized. First, these equations assume an isothermal, horizontal surface. This is not the case during deck heating as the surfaces above the pipes will be warmed more than the surfaces between. Additionally, by just using one convection coefficient for the entire slab, the flow regime (laminar or turbulent) is assumed to be constant across the entire slab. Lastly, in determination of both the Reynold's number and the Rayleigh number, it requires a characteristic length. For the case of free convection with turbulent flow, Incropera and DeWitt (2002) also state that improved accuracy can be obtained by taking defining the characteristic length in determining the Nusselt number as:

$$L_c = A_s/P$$ Equation 7-31

But as ASHRAE (2011) notes, the characteristic length affects the heat transfer coefficient by $L^{-0.2}$ for forced convection and turbulent flow meaning longer snow melting snow-melting slabs will have a lower h_c value. It also means that depending on the length chosen for the bridge (transverse or longitudinal), a different h_c value will result. For design purposes, the conservative option is to define the characteristic length using the shortest dimension unless it is known that air flow will occur in the other direction. For replication of experimental tests, however, this can create a bit of a challenge if the wind direction is not known. However, as will be shown in a subsequent section, the convective heat loss is a small part of the overall heat requirements of these systems except for very high wind speeds.

7.4.3.3. Experimental Site Specific Considerations

Several conditions exist at the site that make the boundary conditions difficult to quantify, specifically in regards to the correct external temperature, T_{ext}, as well as correctly accounting for the effects of wind in regards to convective heat loss.

7.4.3.3.1. Determination of T_{ext}

The external temperature had to be determined for both the top and bottom surfaces of the experimental bridge deck. Due to the lack of a radiometer to measure the sky temperature directly, the

recommendation from Liu (2005) was followed in using the correlation proposed by Martin and Berdahl (1984) for the sky temperature that was used as T_{ext} in the radiation exchange with the top surface of the bridge deck. In determination of the mean radiant temperature of the surroundings, however, all surroundings must be accounted for. Thus, $T_{sky} = T_{MR}$ only if the bridge is isolated and there are no nearby structures/objects. That is not the case for the field site. There is a maintenance shed on one side of the deck, a mound of soil on another side, and another building and trees about 7 m from the deck. Thus, when considering the hemisphere above the deck and all the surroundings that may contribute to T_{MR}, over 25% is not the sky. This will raise the T_{MR} slightly from T_{sky}.

The bottom of the deck is not subject to the sky temperature, thus the T_{MR} is a different value. Thermal images of the surface underneath the deck show that it 1) generally lags behind the ambient temperature, and 2) does not reach the extremes the ambient temperature experiences. That is, during the day as the ambient temperature rises, the ground surface temperature under the deck also rises, but not to the degree of the ambient temperature. Additionally, at night when the ambient temperature begins to decrease, the ground surface temperature under the deck first reaches a peak, and then begins to decrease. Much of this change in temperature is due to radiation between the deck and the ground as the deck radiates the heat energy it captured during the day back to the ground and vice-versa.

In regards to numerical modeling, in the validation analyses it ended up mattering little in regards to the top surface temperature if the ambient temperature or a dampened version was used for T_{ext} at the bottom of the deck. Thus, the ambient air temperature was used as a lower bound for the analyses. As a result, the predicted bottom surface temperatures sometimes differed from that which was observed during heating tests. The ambient air temperature is also a good lower bound to use in the parametric studies because the underside of bridges that are elevated more than the one in this study will not be subject to T_{sky} but to a value closer to $T_{ambient}$.

7.4.3.3.2. Determination of h_c

As explained in Chapter 2, the deck is raised only 16" off the ground. Furthermore, the position of the deck supports and objects surrounding the bridge deck prevent almost any air flow underneath, thus there is no convection applied to the bottom surface in the replication of the experimental tests. This seems to matter little as the exact T_{ext} is not known as previously discussed. Furthermore, the flow of air at the top surface of the deck is also restricted by the various surroundings, and it was found that a reasonably accurate replication of results could be performed by considering free convection only. Forced convection should be considered, however, for most bridges and it is considered in the parametric studies discussed in Chapter 8.

7.4.4. Accounting for Snow

The purpose of this model was not to fully replicate the extremely complex snow melting process, although others have (see Liu (2005), Liu et al. (2007a)). Rather, this model sought to employ a reasonably accurate understanding of the energy required to melt falling or accumulated snow that can be applied directly to the surface of the deck. In consideration of this concept, three conditions can exist:

1. There is enough energy present at the surface of the deck to melt the falling snow, in which case the heat flux at the surface of the deck from snowmelt is equal to the mass snowfall rate

multiplied by the heat of fusion of snow. Radiative and convective heat fluxes would still be present.

2. There is enough energy present at the surface of the deck to melt the falling snow, but not at a rate that can match the rate at which the snow is falling, thus it begins to accumulate. After it begins to accumulate the snow acts as an insulator eliminating the radiative and convective fluxes. The heat flux from snowmelt is then equal to the sum of the conductive heat flux and the latent heat flux.
3. There is not enough energy present at the surface of the deck to melt the falling snow, in which case the snow begins to accumulate and serves to insulate the deck surface, creating a Neumann boundary condition.

To further complicate the process, all three of the conditions can exist at the same time on different parts of the bridge deck as it heats unevenly due to the configuration of the circulation tubes and drainage conditions. And if Conditions 2 and/or 3 exist, some method of accounting for the accumulated snow must be present.

Realizing that the intent of the model is to predict system performance and understand the range in which these systems are applicable, a method was chosen that in essence, is able to bound the results. In this case, a simple heat flux is applied to the surface given by the equation below:

$$q" = \dot{m}_s[H_{f,s} + C_{p,s}(-T_a) + c_1 C_{p,w}] \qquad \text{Equation 7-32}$$

Note that the flux applied is equal to the mass rate of snowfall, $\dot{m}_s$ (kg/s), multiplied by the sum of several terms. The first term of Equation 7-32 is the heat of fusion of snow, $H_{f,s}$ (334 kJ/kg). This is the energy required to actually melt the snow. The second term is the heat capacity of snow, $C_{p,s}$, multiplied by the difference in the ambient temperature and 0°C. This accounts for the energy required to raise the temperature of the snow to the freezing point by assuming the temperature of the falling snow is at ambient. The third terms accounts for the energy required to raise the temperature of the melted snow by 1°C to the liquid film temperature. The term c_1 is a constant with units of K that converts the mass rate of snowfall into its equivalent water content (assumed in this study to be 1/10) and account for the unit temperature change. 1°C was chosen for the liquid film temperature because it assumes some drainage. It assumes that the melted snow will be heated to a certain point and will then disappear (perfect drainage). Note that even in complex snow melting models, the assumption of perfect drainage is often employed (Liu et al. 2007a).

The flux from Equation 7-32 assumes that all three processes (heating the snow to freezing, melting, and heating the liquid film) occur instantaneously. In terms of the individual finite volumes of snow, this is not correct as the finite volume will have to be heated, melted, and heated again. However, when considered as a system all three processes will be occurring simultaneously as previously fallen snow is being melted and heated to the liquid film temperature and presently falling snow is being heated. Thus, only at the beginning and the end of the storm, as well as periods when the snowfall rate changes will the heat flux be incorrect. The rate can be somewhat corrected at the beginning and end by ramping it over a given time step as opposed to applying it all at once. And as will be mentioned in Section 7.6.1, error is already introduced regarding changing rates during the storm due to the frequency of data collection unless continuous data is provided. Finally, the heat flux from Equation 7-32 also assumes that the snow is

homogeneous with respect to material and thermal properties both throughout time (duration of the storm) and space (extent of the slab face).

Any area of the deck that remains above freezing after this flux is applied will have successfully melted the snow. Any area of the deck that did not remain above freezing was not able to melt the snow, and thus snow will begin to accumulate on that portion of the deck. If this occurs in a particular model, the model can be rerun assuming that the deck is not able to melt any of the snow, in which case Neumann boundary conditions exist. If after rerunning the model with Neumann boundary conditions it is found that the surface temperature of the deck is still not above freezing, the system is unable to heat the slab to a sufficient point to melt any snow and Condition 3 exists. If, while under the Neumann boundary condition, the surface temperature of the deck rises above freezing, then Condition 2 exists.

This model will be accurate if the deck is able to melt the snow completely (Condition 1) or if the deck is not able to melt the snow at all (Condition 3). However, if Condition 2 exists, the model will be accurate up until the point snow begins to accumulate (surface temperatures drop below 0°C) and it then breaks down as the actual flux at the surface will tend towards 0 W/m^2 on areas where snow begins to accumulate. However, if the Neumann condition is then applied and the deck surface temperature is above freezing, it can be concluded that the system is still melting the snow, just at rate less than that of which it is falling.

The model accomplishes its purpose because based on the results, one will be able to ascertain whether the system is able to keep the deck completely free from snow, if the system will not work at all, or if the system will be able to melt the snow, just not at a rate fast enough to prevent accumulation. Furthermore, it will give an idea as to how much energy is being extracted from the fluid to heat the system, which is beneficial for determining the subsurface effects. This is summarized in Figure 7-3.

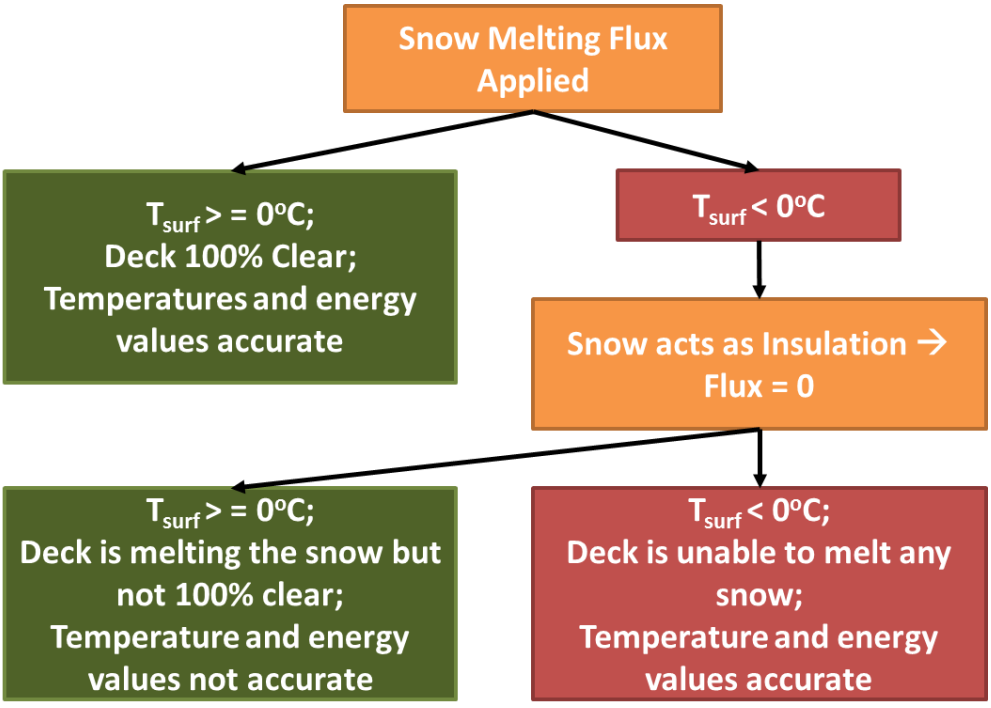

Figure 7-3. How the results of the model are to be interpreted after applying the snow melting flux.

7.5. EXPERIMENTAL AND NUMERICAL MODEL CONFIGURATION

7.5.1. Experimental Configuration

An experimental bridge deck deicing system was constructed at the Virginia Tech Geotechnical Research facility. The doubly reinforced concrete bridge deck is 2.6 m x 3.0 m x 25.4 cm and is elevated approximately 40 cm from the ground to allow for the heat loss that will occur at the underside of an actual bridge deck. The outer perimeter of the slab is insulated such that heat loss in mainly concentrated to the upper and lower surfaces. The deck consists of two 1.3 m x 3 m halves, separated by insulation so that each half can operate independently of the other. The fluid circulation tubes are connected to the top layer of reinforcement and are spaced 20 cm in one half, and 30 cm in the other. The circulation tube material is 3 mm thick cross-linked polyethylene (PEX) with 16 mm inner diameter. The deck is connected to a field of four energy piles, each 30.4 m deep. Further information regarding the configuration of the experimental system can be found in Chapter 2.

The bridge deck was equipped with thermistors to monitor the temperature throughout the bridge deck. The location of the experimental temperature measurements given in this paper are shown in Figure 7-4. In addition to the deck temperature, the inlet and outlet deck fluid temperature and fluid flow rate were also monitored.

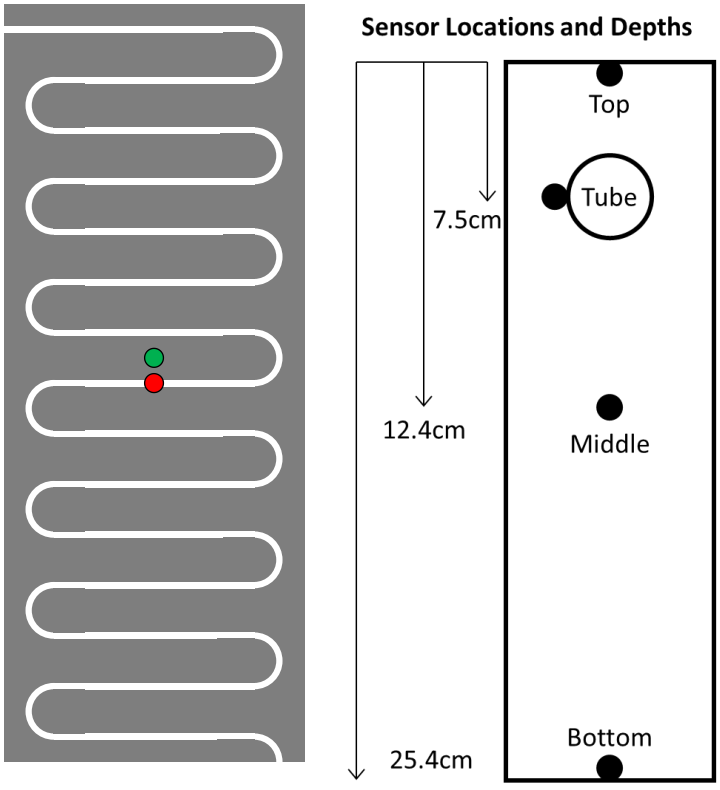

Figure 7-4. Locations of the recorded experimental and numerical temperature measurements in plan (left) and cross-section (right).

7.5.2. Numerical Model Configuration

The numerical model used for validation was configured after the experimental bridge deck deicing system described previously. The geometric dimensions and material properties are given in Table 7-1. Notice that only one half of the experimental bridge deck was modeled as each half was operated independently. Adiabatic conditions were applied to the edges of the bridge deck, as the experimental bridge deck was insulated. The upper and lower surfaces of the bridge deck were subject to adiabatic, convective, and/or radiative heat fluxes as necessary.

The concrete was modeled directly and the circulation tubes were modeled using the pseudo-pipe approach described previously. However, to increase the model's efficiency, the rebar was not modeled directly. Rather, a zoned weighted average approach was adopted in which the concrete domain of the bridge deck was separated into three zones, as shown in Figure 7-5. The middle zone consists of purely concrete, thus the material properties of that zone are that of concrete. The top and bottom zones consist of both concrete and rebar reinforcement, thus the material properties of those zones are a volumetric average of concrete and steel. The material properties used in these zones are also given in Table 7-1. Thus, in summary, the model consisted of four material domains: the pseudo-pipe domain, the top concrete-rebar domain, the pure concrete domain, and the bottom concrete-rebar domain. Meshing was accomplished using quadrilateral elements within each domain. The material domains and meshing of each are shown in Figure 7-6.

Table 7-1. Material and geometric properties of the experimental and numerical models.

Parameter	Experimental	Numerical	Unit
Bridge Deck Dimensions			
Length	3.0	3.0	m
Width	1.3	1.3	m
Height	25.4	25.4	cm
Depth of circulation tubes	7.45	7.45	cm
Circulation Fluid (20% Glycol)			
Flow rate	15.1	15.1	L/m
Dynamic viscosity	4.8	4.8	mPa·s
Thermal conductivity	0.4	0.4	W/m·K
Specific heat capacity	3538	3538	J/kg·K
Density	1070	1070	kg/m^3
Pipes (PEX)[1]			
Thermal conductivity	0.41	0.41	W/m·K
Effective thermal conductivity	-	{1000, 1000, 0}[2]	W/m·K
Specific heat capacity	2300	2300	J/kg·K
Density	950	950	kg/m^3
Effective density	-	447.52	kg/m^3
Pipe inner diameter	16	16	mm
Pipe wall thickness	3.0	3.0	mm
Pipe spacing (center-to-center)	20	20	cm

Concrete[3]			
Thermal conductivity	3.0	3.0	W/m·K
Specific heat capacity	880	880	J/kg·K
Density	2360	2360	kg/m^3
Rebar			
Thermal conductivity	45.4	45.4	W/m·K
Specific heat capacity	475	475	J/kg·K
Density	7850	7850	kg/m^3
Concrete/Rebar Zones			
Top height	-	7.45	cm
Bottom height	-	10.16	cm
Top thermal conductivity	-	3.65	W/m·K
Top specific heat capacity	-	873.82	J/kg·K
Top density	-	2443.8	kg/m^3
Bottom thermal conductivity	-	3.48	W/m·K
Bottom specific heat capacity	-	875.42	J/kg·K
Bottom density	-	2422.1	kg/m^3

[1]The material properties for the PEX pipe in this paper were taken directly from the manufacturer's data sheet. It did not give the thermal conductivity or heat capacity, thus typical values of PEX were used.
[2]Directions are in the cylindrical material r, ϕ, and z directions where z follows the axis of the circulation tube
[3]The density of the concrete was measured directly. The values for thermal conductivity and specific heat capacity were taken as typical values of limestone aggregate concrete from Rhodes (1978).

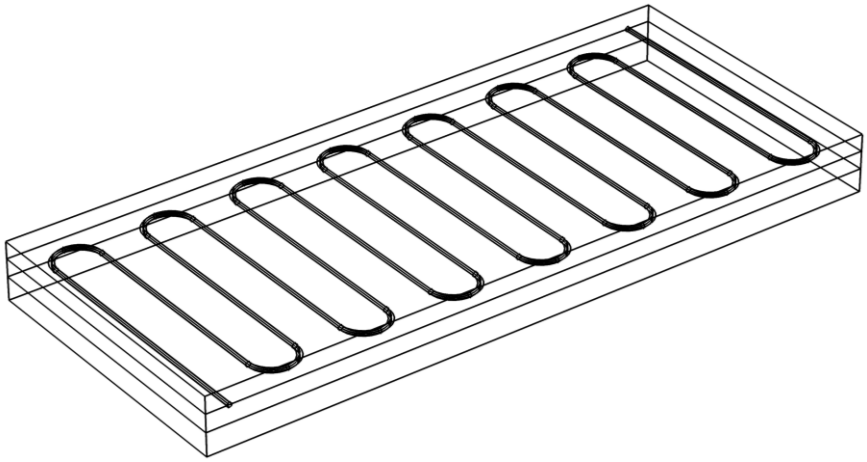

Figure 7-5. The bridge deck deicing slab geometry showing the concrete split into 3 zones – top, middle, and bottom – which allows for the more effective representation of the rebar.

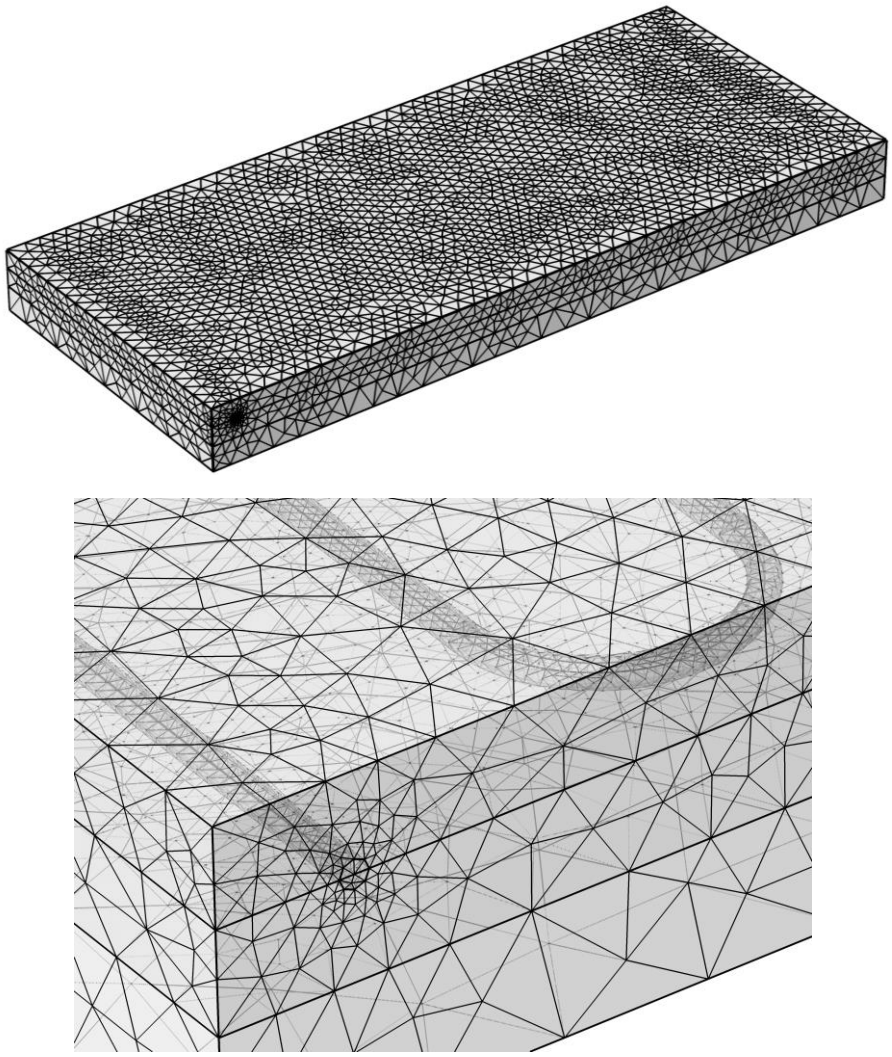

Figure 7-6. Numerical model geometry showing the meshed domains using quadrilateral elements (entire slab – top, close up of the tube elements – bottom).

A fluid flow rate and inlet temperature were applied to the model along with appropriate boundary conditions. For the model validation cases, these parameters were set equal to those that were observed experimentally.

As noted in Rees et al. (2002), correctly defining the initial conditions is as important as the boundary conditions. Because temperature sensors were installed in the cross section of the slab, the initial temperatures of the slab were defined as a function of depth at the locations given in Figure 7-4 before the start of any heating or cooling operation. The temperature of the slab at the locations given in Figure 7-4 as well as the outlet fluid temperature were then monitored over time so that a direct comparison could be made to the experimental model.

7.6. MODEL VALIDATION

7.6.1. Understanding the Experimental Uncertainties When Interpreting Results

Before the model validation is discussed, the uncertainties and how they are accounted for must be addressed. Several uncertainties relating to boundary conditions and how they were addressed has already been discussed. The remaining uncertainties can be grouped into two categories: materials properties of the bridge deck and accuracy of the weather data. In reference to the material properties of the bridge deck, several have the capability of greatly affecting the results. They include the thermal conductivity of the concrete, the emissivity values of the top and bottom surfaces, and the top surface absorptivity value. The thermal conductivity of concrete can vary depending on the density and type of aggregate used (Rhodes 1978). It also varies with moisture content meaning that concrete that is wet generally has a higher thermal conductivity than concrete that is dry (Rhodes 1978). Furthermore, as mentioned previously, because the rebar was not modeled directly, the resulting averaging of the material properties incurs some error. Other material properties that were not measured directly include the top and bottom surface emissivity values as well as the surface absorptivity coefficient. Though emissivity values are pretty standard, the absorptivity value can vary considerably and Lui et al. (2003) states that it can greatly influence the results.

The other group of uncertainty has to do with the weather data. Weather data was collected from two different weather stations. The first was taken at the Virginia Tech Airport, which is located about 4.2 miles from the research site. It reports data every 20 minutes. The second weather station was located at Kentland Farm, which is also about 4 miles from the research site, but in the opposite direction. Data from this station is only reported once an hour. The airport station was used for ambient temperature as well as for cloud height and dew point temperature in order to calculate the sky temperature because of the higher frequency of data. It, however, did not give values for solar radiation and precipitation amounts, thus those values were taken from the Kentland Farm station. Thus, both the distance of these stations to the research site, as well as the lack of frequency of data reporting, especially in regard to the solar radiation and precipitation measurements, will not be completely representative of the field research site conditions. This was found to be especially critical for solar radiation as the hourly values did not include the influence of occasional cloud cover, which reduces the value.

Because of these uncertainties, the experimental tests used for validation were chosen based on their ability to isolate and test certain boundary conditions. The first test was a heating test that occurred after there was snow already accumulated on the slab. As discussed previously, with an extremely low thermal conductivity snow is a very good insulator. Thus, with the top and side surfaces of the deck insulated, the early part of the test can be used to examine the actual heating process of the deck and to explore the effect of material properties and the lower surface boundary condition on results.

The second test occurred during a period of cold weather followed by snowfall. The first part of the test can be used to test the boundary conditions of the model as the deck was clear during this time and subject to radiation and convection with the environment. The second part of the test can be used to test the snowmelt model as the snow is falling. During this particular experimental test, the system was barely able to keep the deck free from accumulated snow. Thus, condition 1 exists and the experimental and numerical surface temperatures of the deck should agree.

7.6.2. Heating Test #1

The first model validation utilized an experimental test that occurred during a period of extremely cold weather that was preceded by a large winter storm. As a result of the winter storm, there was in excess of 20cm of snow accumulated on the slab. The details of the storm and experimental operation are given in Section 3.5.8. The snow served to act as an insulator to the top surface of the bridge deck, thus shielding it from the effects of radiative and convective heat fluxes. Due to the absence of these fluxes on the top surface, this operation allowed for the testing of the material properties and slab heating process.

Figure 7-7 compares the outlet fluid temperature from the numerical model with the one that was observed experimentally. It can be seen that very good agreement exists between the two measurements and the temperature difference between the inlet and outlet starts at about 0.6°C and is around 0.2°C by the end of the operation.

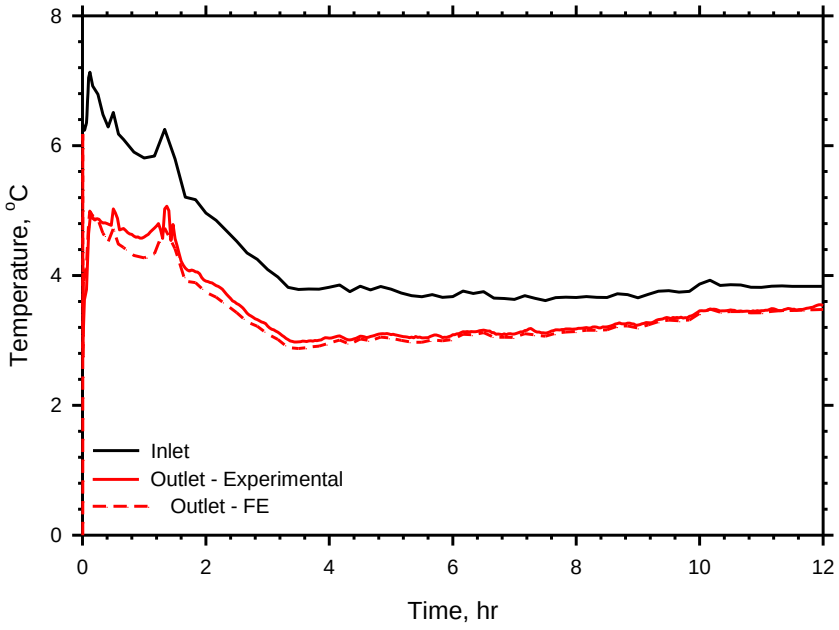

Figure 7-7. Inlet and outlet fluid temperatures of the bridge deck observed experimentally and predicted by the numerical model

From the inlet and outlet fluid temperatures, the heating rate and cumulative imparted energy can be determined. These values are shown in Figure 7-8. Again, there is good agreement between the experimental and numerical results. In general, both the amount of energy imparted to the bridge deck and rate at which it was imparted is slightly higher in the numerical model. Furthermore, the numerical model does not display some of the variability that is seen in the experimental heating rate. There could be several reasons for this. One of which is that the fluid temperature sensors were influenced by atmospheric conditions that caused slight variability. However, this variability would have affected both the inlet and outlet fluid temperature sensors. The most likely reason is that the time steps for the numerical model were set at 5 minutes for times greater than 1 hour. Fluid temperature readings, however, occurred every 2 minutes. Thus, some of the inlet fluid temperature variability was lost when inputting it into the numerical model.

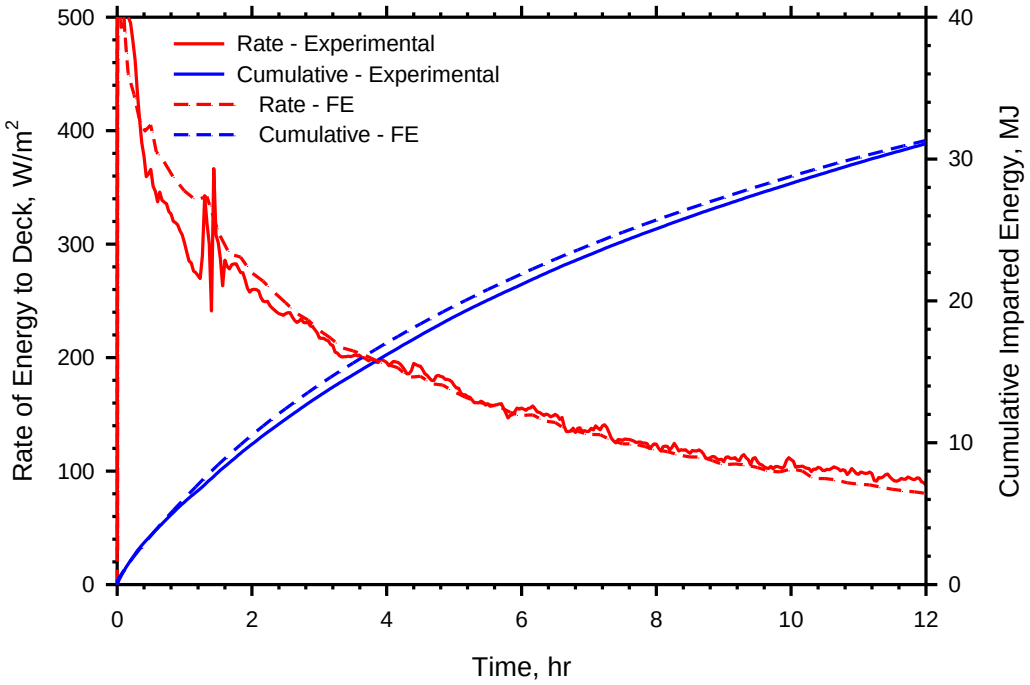

Figure 7-8. Rate at which energy is imparted to the bridge deck and the cumulative imparted energy to the bridge deck as observed experimentally and predicted by the numerical model.

Figure 7-9 displays the temperatures recorded at select points within the slab for a cross section containing a deicing tube (Figure 8a) and for a cross section containing no deicing tube (Figure 8b). Note there is no temperature sensor at the bottom of the deck between deicing tubes, which is why only the numerical value is shown in Figure 8b. In general, there is very good agreement between the experimental and numerical temperatures. Good agreement between the temperatures is key because it signifies that not only does the model do a good job of predicting the amount of energy required for heating, it is accurately predicting how that energy is distributed throughout the model.

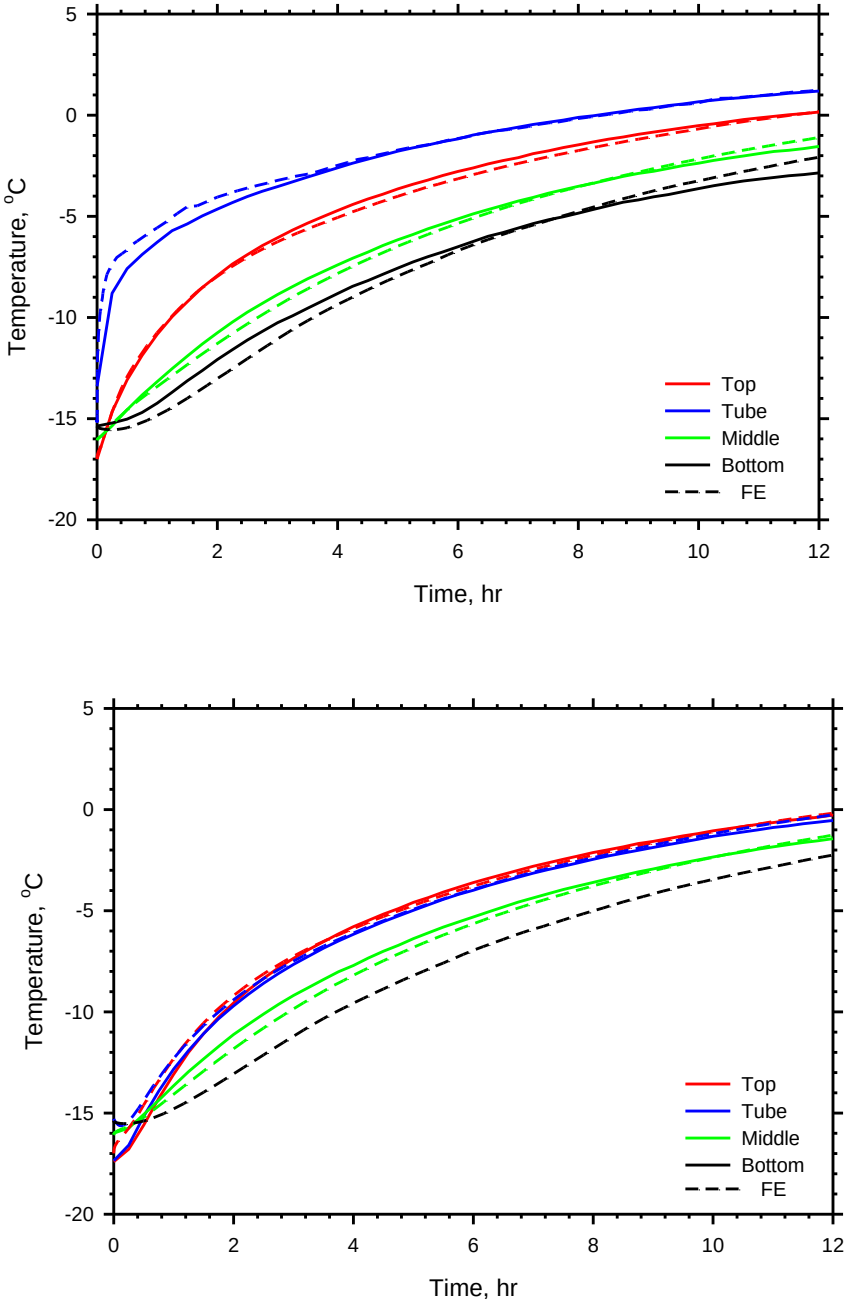

Figure 7-9. Comparison of experimental and numerically predicted temperature of the top, tube, middle, and bottom locations within the slab at cross sections with (a, top) and without (b, bottom) a deicing tube.

For points in a cross section with a deicing tube, the agreement between the FE and experimental results at the top and tube depths is very good. This is important as the temperature at the top surface is one of the primary metrics that will be used to numerically judge whether or not a deicing system succeeds or fails. The temperature progression trend at the top and tube depths is also very similar to what actually occurred. There is also good agreement between the temperatures at the middle and bottom depths,

however the agreement is not as close and the trends do not resemble the experimental trends with the same degree of accuracy as the top and tube depths.

The temperatures from the numerical model also closely match the experimental temperatures in a cross section with no deicing tube. In this case, the tube and top temperatures are practically identical, thus the results plot on top of each other. The agreement at the middle depth is actually better in this case, which is to be expected as it is further from the heat source, thus it will experience less variability.

The difference between the numerical and experimental results at the middle and bottom depths is not extremely significant, however, it is greater than the difference observed at the top and tube depths. The greater difference is likely caused from both not applying completely accurate boundary conditions to the bottom surface of the slab and from the effect of averaging the material properties in the bottom zone instead of modeling the rebar directly. In terms of applying the correct boundary conditions, as discussed previously the exact boundary conditions are not known. Due to the close agreement at the top and tube depths, it is doubtful that averaging the material properties of the concrete and rebar significantly contributed to error, however it would affect the middle and bottom depths more than the top and tube depths due to their relatively further distance from the heat source (deicing tube) and the fact that a larger volume was used in the averaging process for the bottom zone. Ultimately it appears that subjecting the bottom boundary to a radiative condition using the ambient temperature as T_{MR} and averaging the values of the rebar and the concrete does a fairly good job at representing what actually happens in the experimental slab.

Figure 7-10 shows the temperature progression of the top surface of the slab throughout the heating operation. At the beginning of operation (Figure 7-10a), the top surface temperature is a relatively uniform -17^{o}C. Four hours after the heating operation began (Figure 7-10b), the outline of the deicing tubes under the surface of the deck can be clearly seen as represented by higher surface temperatures. At this point the surface temperatures are between -5^{o}C and -8^{o}C and the coldest portions of the slab are those that are between the deicing tubes and the outer edges. Four hours later, which is 8 hours after the heating operation began (Figure 7-10c), the temperature of the surface is between -1^{o}C and -5^{o}C whereas after 12 hours (Figure 7-10d) the majority of the surface temperature is at 0^{o}C or above.

Figure 7-11 displays the temperatures in a cross section of the slab at various points throughout the heating operation. At the start of operation (Figure 7-11a), the cross sectional temperature in the slab was relatively uniform between -17 and -15^{o}C. After heating began, the temperatures immediately around the deicing tubes increased. The majority of this heat migrated to the surface as shown in Figure 10b, which is 4 hours after the heating operation began. At this point in time the temperature at the bottom of the slab was less than -10^{o}C whereas the top surface temperature was between -5 and -8^{o}C. Around the deicing tubes, however, the temperatures were as high as -3^{o}C. This cross sectional temperature variation can lead to the development of thermal stresses, which is explored in Chapter 3. The higher temperatures near the surface and around the deicing tubes relative to the bottom of the slab are also observed 8 hours after the operation begins (Figure 7-11c). After 12 hours (Figure 7-11d) there is still some variation, however the variation in cross sectional temperatures has significantly decreased.

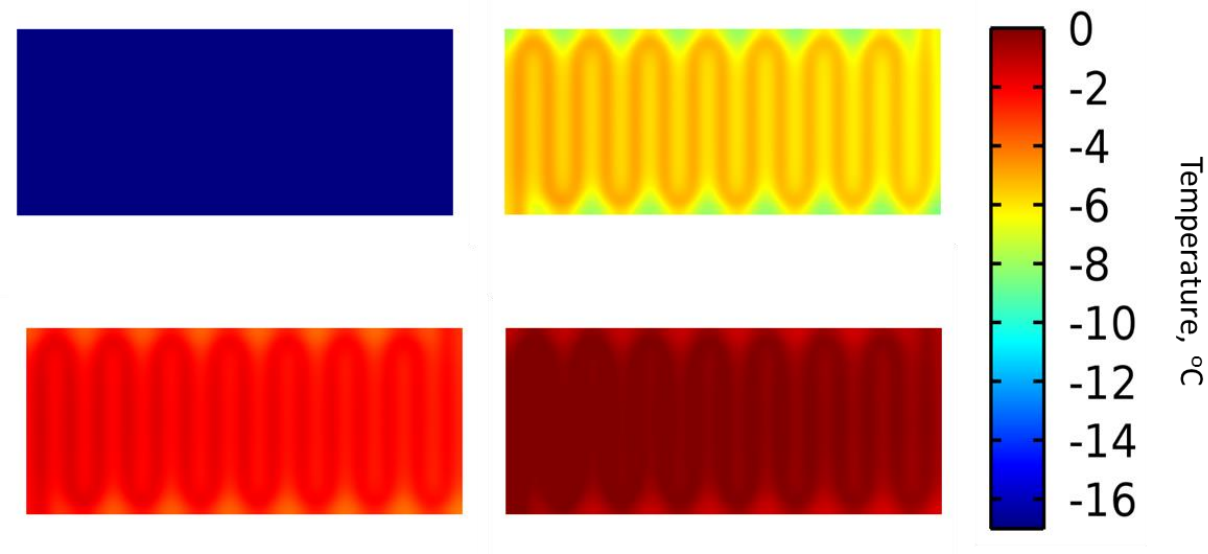

Figure 7-10. Progressions of the top surface temperature over time at a) start of heating, b) 4 hours, c) 8 hours, and d) 12 hours.

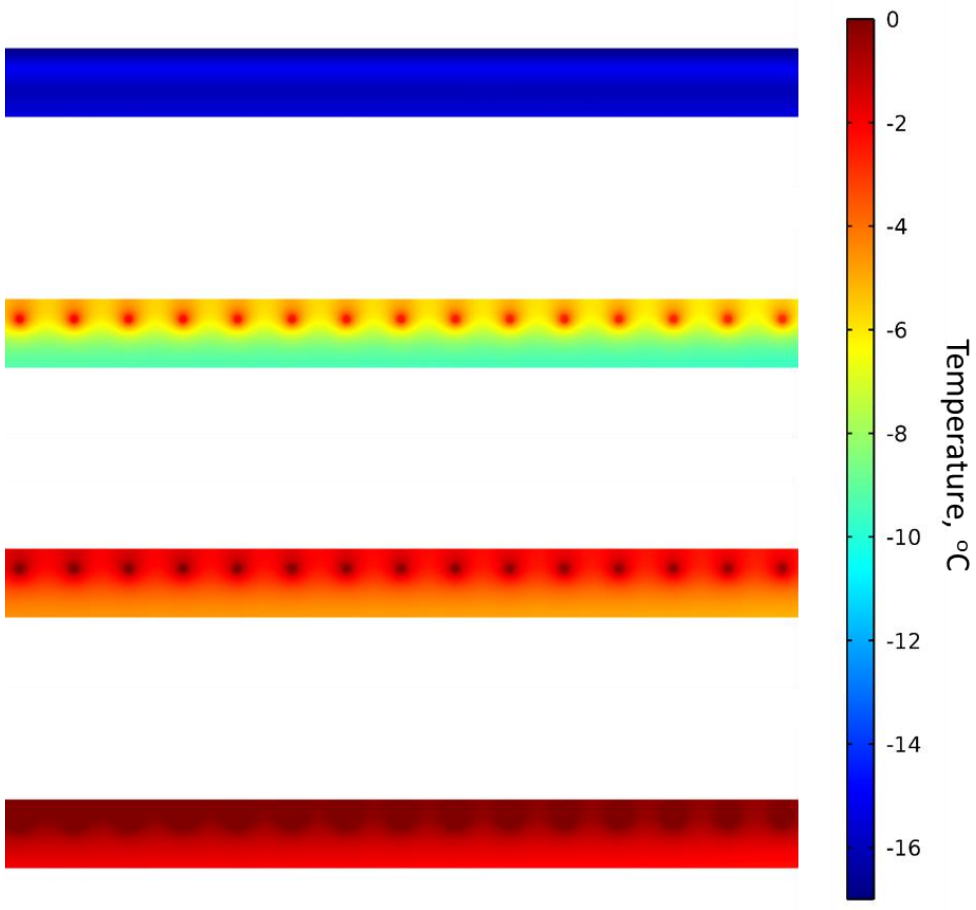

Figure 7-11. Progressions of the cross sectional temperature over time at a) start of heating, b) 4 hours, c) 8 hours, and d) 12 hours.

There are several implications from the results of this validation. First, the material properties used in the model appear to be representative of those in field. This is especially important in regards to the thermal conductivity and specific heat capacity values of the concrete, as this was not measured directly. Secondly, the method used to average the thermal properties of the concrete and rebar in the top and bottom zones allows for computational efficiency in being able to eliminate the rebar from the model without sacrificing significant accuracy in the results. Thirdly, and most importantly, the numerical model can be used to predict the resulting surface and internal temperatures of the bridge deck as well as the amount of energy required for heating.

7.6.3. Heating Test #2

The second model validation utilized a heating test that occurred during a winter storm where 7.6 cm of snow fell over the course of about 5 hours, and yet the system was able to keep the deck free from snow. The details of the storm can be found in Section 3.5.4. The conditions that were applied to the model are given Figure 7-12. This test was chosen for validation for several reasons. First, the system operated successfully in that it kept the deck free from snow. This allows the temperatures to be compared directly. Secondly, a variety of weather conditions were present before the storm occurred. The system was operated for over 12 hours before the storm which included periods of varying degrees of cloud cover (affecting T_{MR}) and solar radiation, as shown in Figure 7-12. Thus, it allows for the testing of the convective and radiative (both solar and longwave) heat fluxes at the surface of the slab.

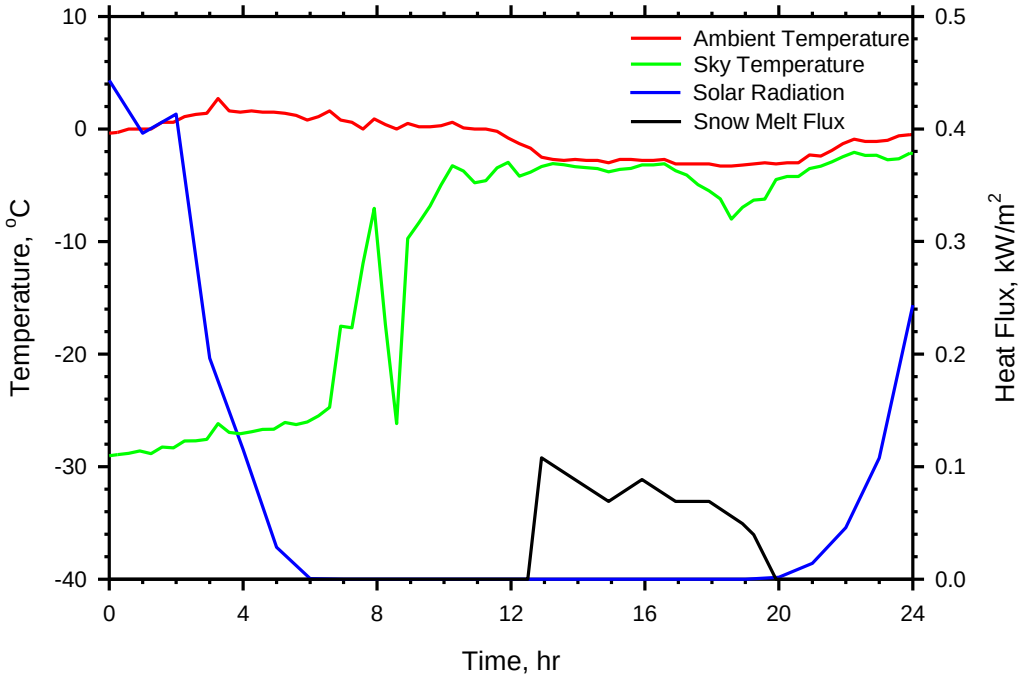

Figure 7-12. Input values to the numerical model that were used in the second validation exercise.

A comparison between the heating rate and cumulative imparted energy to the slab is shown in Figure 7-13. Not as good agreement exists for this validation as for the previous validation exercise, however that is to be expected. During this validation the top surface of the deck was subject to the environment meaning it was not only subject to the respective heat fluxes and boundary conditions, but also to the uncertainty in determining the parameters that govern the heat fluxes as discussed previously. The

heating rate of the bridge deck was lower in the numerical model than what was observed at early times and greater at later times. During the period of snow fall, which lasted from approximately 13 – 20 hours, the fluxes are very close. Additionally, the cumulative amount of heat energy, though starting out quite different, ends up being very similar.

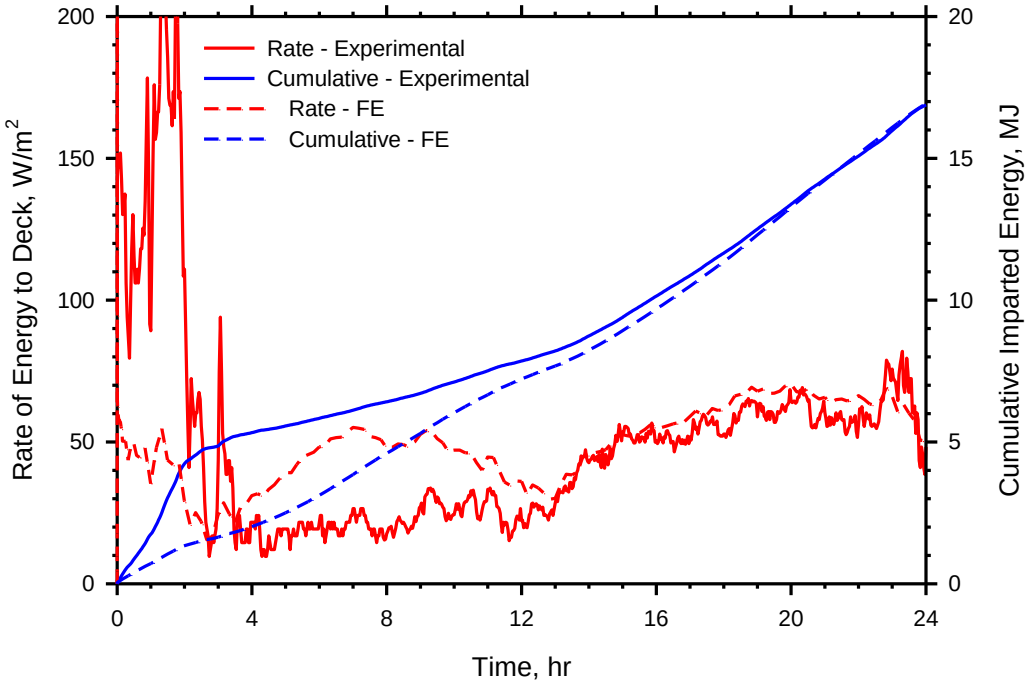

Figure 7-13. Rate at which energy is imparted to the bridge deck and the cumulative imparted energy to the bridge deck as observed experimentally and predicted by the numerical model.

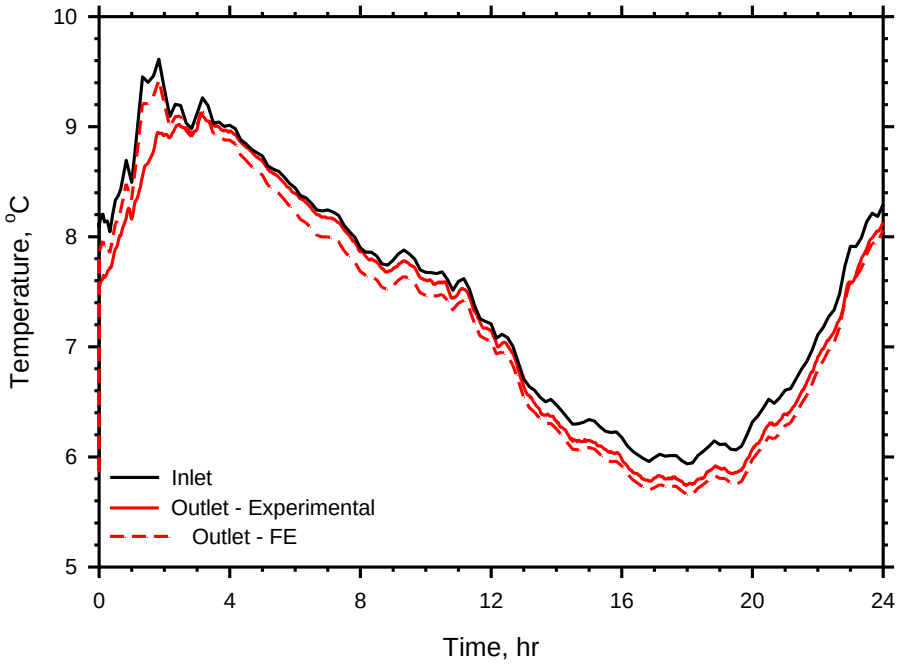

Figure 7-14. Inlet and outlet fluid temperatures of the bridge deck observed experimentally and predicted by the numerical model.

Figure 7-14, which shows the inlet and outlet fluid temperatures helps to explain the difference in the heating rates that are observed. Notice that there is a much greater temperature difference between the inlet and outlet fluids at the beginning of operation for the experimental test relative to the numerical model. This results in a much higher deck heating rate. Conversely, a larger temperature difference is then observed between the inlet and outlet of the FE model as compared to the experimental. The reason for these differences could, again, be the result of uncertainty in accounting for the atmospheric parameters and deck surface material properties. This will be explored more as the temperature comparisons are made.

The cross-sectional temperatures are compared in Figure 7-15. It can be seen that good agreement exists between the numerical model and experimental test in both actual temperatures and observed trends. By examining separate time intervals, different aspects of the model can be compared. Solar radiation existed between the hours of 0 and 5, which resulting in higher top surface temperature. The model does a good job of predicting the resulting temperature spike that occurs around hour 2, but then the largest difference between predicted and observed temperatures occurs on the top of the slab between hours 4 and 10. Notice from Figure 7-12 this is a period where the mean radiant temperature is very low. As discussed previously, in this model $T_{MR} = T_{clear,sky}$, which does not account for the contributions from the surroundings. Due to the solar radiation, it is likely that the surroundings are much warmer than the $T_{clear,sky}$, thus resulting in a higher T_{MR} than what was actually applied to the model between hours 2 and 7. Note that good agreement at the top surface is again achieved at hour 12, which is where $T_{MR} = T_{ambient}$ because of the cloud cover. The lower top temperature resulted in a lower tube, middle, and bottom temperature as energy was being lost from the surface of the slab. A similar trend can be observed in Figure 7-15b, which shows the temperatures in a cross section with no circulation tube, though the temperatures are slightly lower.

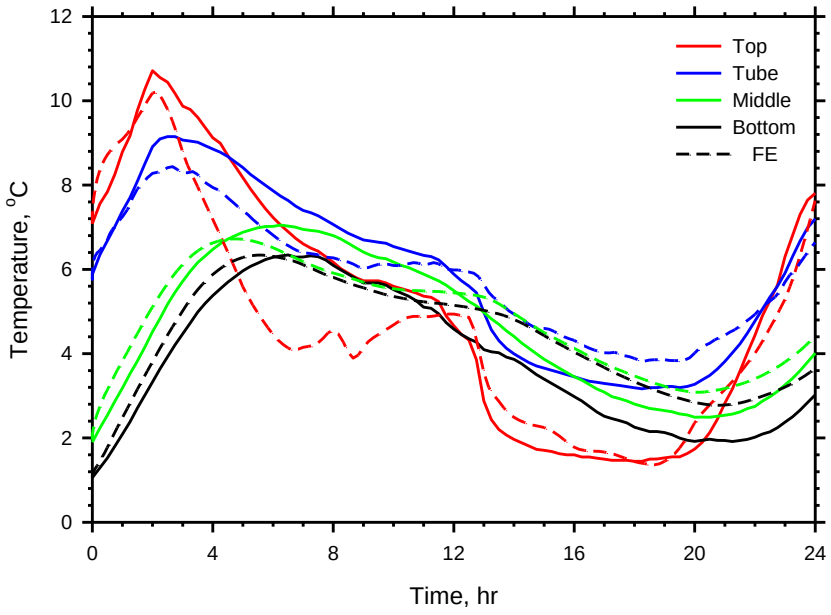

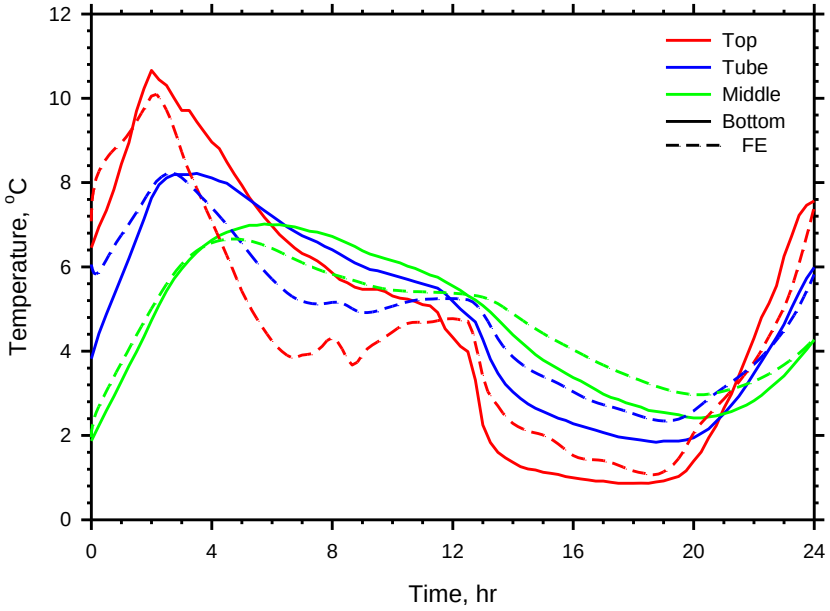

Figure 7-15. Comparison of experimental and numerically predicted temperature of the top, tube, middle, and bottom locations within the slab at cross sections with (a, top) and without (b, bottom) a deicing tube.

After the start of the storm at hour 12, the top temperature showed close agreement with what was observed experimentally. The predicted temperatures from the FE model for the other depths were slightly higher, though generally no more than 1°C. This is likely a result of not correctly accounting for the bottom surface boundary in that the actual T_{MR} at the bottom may have been colder than $T_{ambient}$, which was assumed. After the storm, the numerical and experimental temperatures for the tube, middle, and bottom depths began to match. Again, a similar trend in the correlation between the numerical and experimental results exists in the cross section between deicing tubes (Figure 7-15b).

An interesting observation can be made regarding the bridge deck heating rate and the cross sectional temperatures. Initially, it appears that a contradiction exists in that a higher numerical deck heating rate resulted in lower deck temperatures, especially the surface temperature, when compared to the experimental results. One may think that a higher heating rate would lead to more energy being imparted to the bridge deck and thus higher bridge deck temperatures. It was shown in Chapter 3 that the bridge deck heating rate is largely a function of the temperature gradient that exists between the bridge deck and the circulation fluid. That is why low fluid circulation temperatures were sometimes observed to produce higher bridge deck heating rates than higher fluid circulation temperatures. Consider the first validation where the circulation temperatures were between 3-5°C (Figure 7-7), whereas for this validation the temperatures were above 6°C and has high as 9.5°C (Figure 7-14). The heating rate for the first validation was between 100-400 W/m^2 (Figure 7) whereas it was generally less than 100 W/m^2 for this validation (Figure 7-13). This is possible because the starting bridge deck temperatures were below -15°C for the first validation (Figure 8), which creates a larger temperature gradient with the circulation fluid, than the gradient between the deck and the fluid in this validation, even though the temperature of the circulation fluid is higher in this validation.

Now consider that the same inlet fluid circulation temperature that was observed experimentally was applied to the numerical model. The boundary conditions of the numerical model induced temperature changes in the bridge deck which were more severe than what actually occurred. Thus, a larger temperature gradient existed between the bridge deck and the circulation fluid in the FE model than did in the experimental model. This is ultimately why a higher bridge deck heating rate was predicted numerically between the hours of 4 and 12, even though the numerical deck temperatures are lower than the experimental temperatures.

Figure 7-16 displays the top surface temperatures at key points during the heating operation. Figure 7-16a shows the temperature at the start of operation, which is a fairly uniform 7°C. Figure 7-16b, which is 3 hours after the heating operation begins and the point at which the highest top surface temperatures were observed (see Figure 7-15), shows that the areas above the deicing tubes are slightly warmer than the areas between the tubes, but not by much as solar radiation is the main source of thermal energy for the deck during this time. Figure 7-16c occurs 12 hours after the operation begins, which is the point in time at which the storm begins. At this point the entire deck surface is above 0°C, with the temperatures ranging between 5 and 6°C. Figure 7-16d shows the top surface at hour 16, which is during the middle of the storm and the point at which the top surface temperatures are near their coldest. The temperatures are obviously colder than at any other point during operation, however they are still above 0°C, with the outline of the deicing tubes still visible.

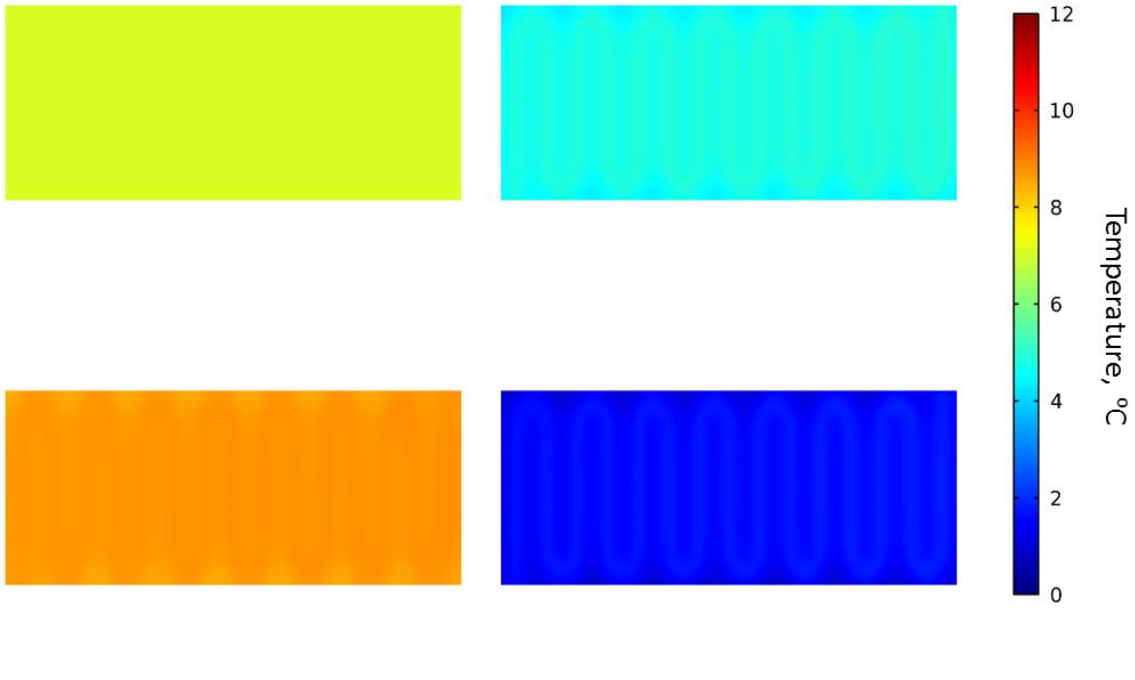

Figure 7-16. Progressions of the top surface temperature over time at a) start of heating, b) 3 hours, c) 12 hours (right before the onset of the storm), and d) 16 hours (during the storm).

The cross sectional temperatures of the slab are shown in Figure 7-17 for the same points in time as represented in Figure 7-17. There is a preexisting temperature gradient in the slab at time 0 Figure 7-17a).

Three hours later (Figure 7-17b) heat can be seen emanating from the deicing tubes, however that is not the warmest part of the cross section. The highest cross sectional temperatures are seen at the top of the slab, which is a direct result of being heated by solar radiation as discussed previously. The circulating fluid is still contributing thermal energy to the slab because the cross sectional temperatures near the deicing tubes are lower than the fluid temperatures (Figure 7-15). However, the rate of energy transfer is very low (Figure 7-13). Before the start of the storm (Figure 7-17c) the cross sectional temperatures are relatively uniform. Though the temperatures near the top and bottom of the slab have dropped, the temperatures near the bottom have dropped little compared to the top. The temperatures around the circulation tubes are still the warmest. During the middle of the storm (Figure 7-17d), the temperatures at the top of the slab are the coldest as energy is being utilized at the top surface for deicing operations. The temperatures near the bottom of the slab are relatively warm, which is in essence a store of thermal energy that is being utilized as the temperature gradient is drawing energy from that portion of the slab.

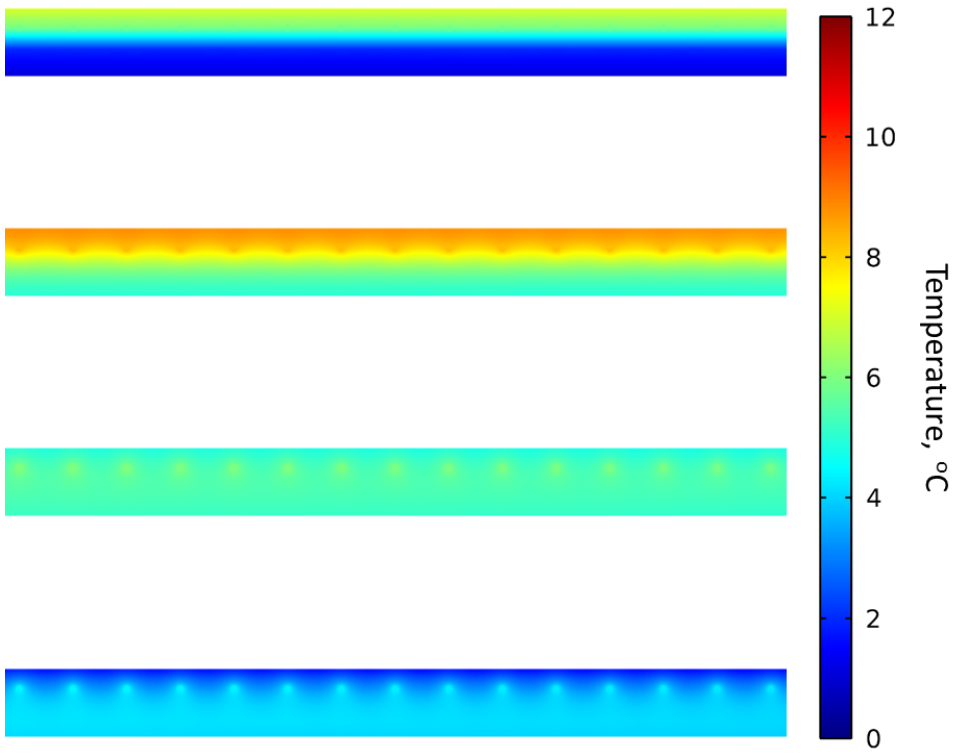

Figure 7-17. Progressions of the cross sectional temperatures over time at a) start of heating, b) 3 hours, c) 12 hours (right before the onset of the storm), and d) 16 hours (during the storm).

The advantage of the numerical model is that the energy in the system can be monitored. This is shown in Figure 7-18. The energy stored in the deck is representative of the amount of energy in the system relative to the start of operation. That is, it is a sum of all energy that has entered and left the deck up until that point. Initially the energy in the deck increases due to both energy from the fluid as well as energy from the environment, which is coming mainly from solar radiation. After hour 3, the environment stops imparting energy and the deck begins to lose energy to the environment. By hour 7 the net amount

energy imparted by the environment is negative. This is due to radiative and convective heat losses up until hour 12, and then it is losing energy to snow melt as well.

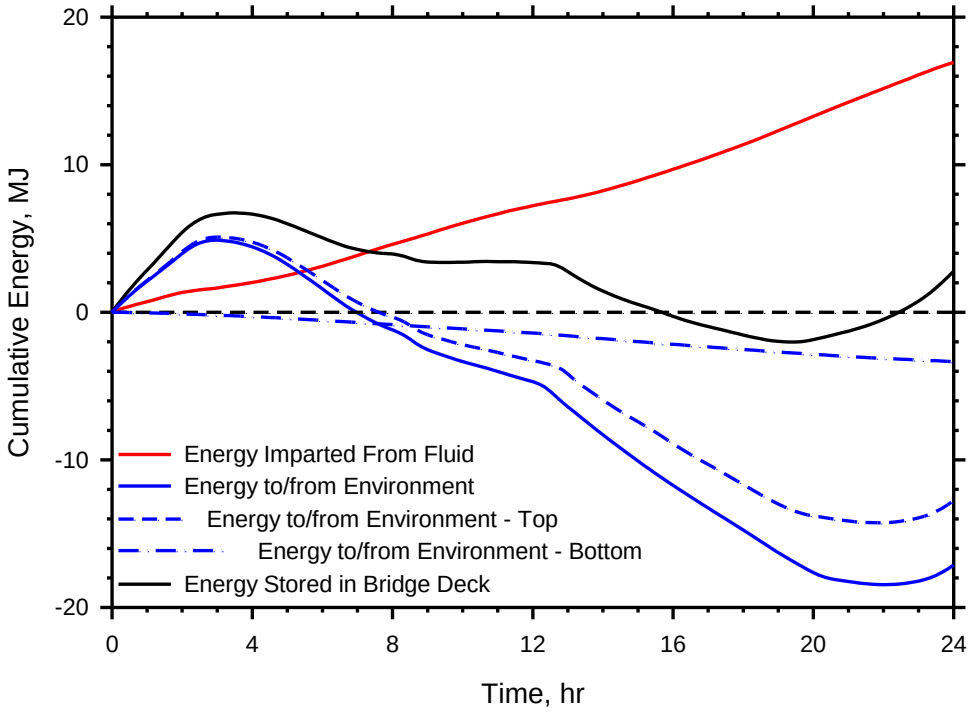

Figure 7-18. The amount of energy imparted to the slab from the circulation fluid, stored in the bridge deck, and lost to the environment relative to time t=0.

During the storm (hours 12 to 21) the energy in the deck decreases to less than what was there initially. This should not be confused with system failure or snow accumulation because this is simply the amount of energy in the deck relative to the start of the operation. Because the average deck temperature was initially above 0°C (see Figure 7-15), it contained stored energy with which it could melt snow. It does demonstrate why heating the deck beforehand is important. By heating the deck before the storm occurred, the deck was able to store energy which was then used during the storm to melt the falling snow. By the time the storm started the heating system had already imparted 8 MJ of energy to the deck. Had it not been turned on before the storm, it would not have had as much stored energy.

Also shown in Figure 7-18 is the amount of the total energy that was lost to the environment through the top and bottom surfaces. Observe that during a heating operation the vast majority of the energy exchange between the bridge deck and the environment occurs at the top surface. This suggests that the top surface boundary conditions of the model are more important that the bottom surface boundary conditions and will affect the accuracy of the model to a much higher degree. Also observe that whereas the energy exchange with the top surface varies – that is at some points the deck is receiving energy and at other points the deck is yielding energy – the energy exchange between the bottom surface and the environment is a constant loss of energy over time. This is expected as the bottom surface is not exposed to solar radiation like the top surface and during heating operations, when the deck is kept warmer than the ambient air temperature, energy loss through the bottom surface will occur in absence of insulation.

In this validation, there was less agreement between the numerical and experimental results as compared to the first validation exercise, though the agreement was still good. In fact, during the periods of time that are most important, which is during the storm event, the agreement in the top temperatures and bridge deck heating rate are extremely good. The disagreement that does exist is most likely a result of 1) not accurately accounting for the unknown boundary conditions, specifically T_{MR} at the top and bottom of the slab, and 2) the limitation of the weather data in both frequency and proximity to the site.

7.7. CONCLUSIONS

A 3-dimensional numerical model has been created that can accurately account for the thermal processes involved in bridge deck deicing. It has been used to replicate experimental tests from a model bridge deck deicing system and provides good accuracy in terms of replicating surface and internal temperatures, the deck heating rate, and the energy consumed during the operation. Thus, this numerical model provides a framework that engineers can use to estimate a given system's performance when designing bridge deck deicing systems. It should be noted that several simplifying assumptions were used in the development of the model, especially in regard to considering snow melt. Thus this model should not be used to exactly replicate the snow melt process and/or to estimate how much snow will be on the deck at a given time. It can, however, be used to determine system success or failure and if success, the corresponding deck temperatures, energy requirements, etc. There are several benefits to this approach. First, the simplifying assumptions allow for increased model efficiency. Secondly, winter storms and weather conditions are highly variable and rarely, if ever, replicate from year to year. Thus, modeling every detail of the snowmelt process during a given storm is somewhat futile as a system designer will have no way of knowing the exact parameters of a storm that will occur. At best, he/she will have an idea of what type of storm to expect. In other words, a model that replicates every aspect of the snow melt process is needlessly accurate because when considering future storms, the designer will not have the exact parameters to input into the model. And finally, when considering different design options, designers are primarily concerned with system success or failure as opposed to determining the exact operating performance during a given snow storm. Though it was validated within the context of ground-source bridge deck deicing systems, it should also work for estimating performance of higher temperature active systems as the underlying physics will not change. A follow up paper will investigate the performance of ground-source bridge deck deicing systems using this numerical model.

7.8. REFERENCES

Adlam, T. N. (1950). Snow melting: design, installation and control of systems for melting snow by hot water coils embedded beneath walks, roads, or other areas where snow is an obstruction or hazard, Industrial Press, New York.

American Association of State Highway and Transportation Officials (AASHTO) (2008). "Bridging the Gap: Restoring and Rebuilding the Nation's Bridges." American Association of State Highway and Transportation Officials.

American Society of Heating Refrigerating and Air-Conditioning Engineers (ASHRAE) (2011). 2011 ASHRAE Handbook - Heating, Ventilating, and Air-Conditioning Applications (SI Edition), American Society of Heating, Refrigerating and Air-Conditioning Engineers, Inc.

American Society of Heating Refrigerating and Air-Conditioning Engineers (ASHRAE) (2013). 2013 ASHRAE Handbook - Fundamentals (SI Edition), American Society of Heating, Refrigerating and Air-Conditioning Engineers, Inc.

Baboian, R. "Synergistic effects of acid deposition and road salts on corrosion." Proc., Symposium on Corrosion Forms and Control for Infrastruture, November 3, 1991 - November 4, 1991, Publ by ASTM, 17-29.

Bourne-Webb, P. J., Amatya, B., Soga, K., Amis, T., Davidson, C., and Payne, P. (2009). "Energy pile test at lambeth college, London: Geotechnical and thermodynamic aspects of pile response to heat cycles." Geotechnique, 59(3), 237-248.

Bowers, Jr., G. and Olgun, C. (2014). “Ground-Source Bridge Deck Deicing Systems Using Energy Foundations.” Geo-Congress 2014 Technical Papers: pp. 2705-2714.

Bowers, Jr., G., and C. Olgun. (2016). “The Thermal Performance of a Small-Scale Bridge Deck Deicing System Under Bridge Deck Deicing and Thermal Recharge Operations..” ASCE Journal of Cold Regions Engineering. Submitted.

Brandl, H. (2006). "Energy foundations and other thermo-active ground structures." Geotechnique, 56(2), 81-122.

Chapman, W. P. (1952). "Design of snow melting systems." Heating and Ventilating, 49(11), 88-91.

Chapman, W. P. (1956). "Heat requirements of snow melting systems." Heating, Piping and Air Conditioning, 28(2), 149-153.

Chen, M., Shaopeng, W., Hong, W., and Jizhe, Z. (2011). "Study of ice and snow melting process on conductive asphalt solar collector." Solar Energy Materials and Solar Cells, 95(12), 3241-3250.

Churchill, S.W. (1977). “Friction factor equations spans all fluid-flow regimes.” Chemical Engineering, 84, 91–92.

COMSOL. (2015). “COMSOL MultiphysicsTM Version 5.1: User’s Guide and Reference Manual.” COMSOL Inc., Burlington, MA.

Friar, S., and Decker, R. (1999). "Evaluation of a fixed anti-icing spray system." Transportation Research Record(1672), 34-41.

Granata, R. D., and Hartt, W. H. (2009). "Integrity of Infrastructure Materials and Structures." U. S. D. o. T. FHWA, ed., FHWA, U.S. Department of Transportation, United States, 90p.

Incropera, F. P., and DeWitt, D. P. (2002). Fundamentals of heat and mass transfer, J. Wiley, New York.

Katzenbach, R., Olgun, C.G., Loveridge, F.A., Sutman, M., Bowers, G.A., McCartney, J.S. Laloui, L., Dupray, F., Spitler, J.D., Clauss, F., Meyer, L.L., and Akrouch, G. (2014) “New Technologies and Applications; Materials and Equipment in Near Surface Geothermal Systems.” DFI Journal, The Journal of the Deep Foundations Institute, Special Issue on Energy Foundations. Vol. 8(2), pp. 93 – 107.

Kilkis, I. B. "Design of embedded snow-melting systems part 1: heat requirements - an overall assessment and recommendations." Proc., Proceedings of the ASHRAE Winter Meeting, January 23, 1994 - January 26, 1994, ASHRAE, 423-433.

Kilkis, I. B. "Design of embedded snow-melting systems: part 2, heat transfer in the slab - a simplified model." Proc., Proceedings of the ASHRAE Winter Meeting, January 23, 1994 - January 26, 1994, ASHRAE, 434-441.

Koch, G. H., Brongers, M. P. H., Thompson, N. G., Virmani, Y. P., and Payer, J. H. (2002). "Corrosion Cost and Preventive Strategies in the United States." FHWA, U.S. Department of Transportation, United States, 790p.

Kusuda, T., and Achenbach, P. R. (1965). "Earth temperature and thermal diffusivity at selected stations in the United States." ASHRAE Transactions, American Society of Heating, Refrigerating, and Air-Conditioning Engineers, Inc., New York, N.Y., 61-75.

Liu, X. (2005). “Development and Experimental Validation of Simulation of Hydronic Snow Melting Systems for Bridges.” Ph.D. Thesis. Oklahoma State University.

Liu, X., Rees, S. J., and Spitler, J. D. (2007a). "Modeling snow melting on heated pavement surfaces. Part I: Model development." Applied Thermal Engineering, 27(5-6), 1115-1124.

Liu, X., Rees, S. J., and Spitler, J. D. (2007b). "Modeling snow melting on heated pavement surfaces. Part II: Experimental validation." Applied Thermal Engineering, 27(5-6), 1125-1131.

Liu, X., Rees, S. J., and Spitler, J. D. (2003). "Simulation of a Geothermal Bridge Deck Anti-Icing System and Experimental Validation." 82nd Annual Meeting of the Transportation Research Board. Washington, DC.

Liu, X., and Spitler, J. D. (2004). "A Simulation Tool for the Hydronic Bridge Snow Melting System." 12th International Road Weather Conference. Bingen, Germany.

Martin, M., and Berdahl, P. (1984). "Summary of results from the spectral and angular sky radiation measurement program." Sol Energy, 33(3-4), 241-252.

Naito, C., Sause, R., Hodgson, I., Pessiki, S., and MacIoce, T. (2010). "Forensic examination of a noncomposite adjacent precast prestressed concrete box beam bridge." Journal of Bridge Engineering, 15(4), 408-418.

Ozudogru, T. Y., Olgun, C. G., and Senol, A. (2014). "3D numerical modeling of vertical geothermal heat exchangers." Geothermics, 51, 312-324.

Ramsey, J. W., Hewett, M. J., Kuehn, T. H., and Petersen, S. D. (1999). "Updated design guidelines for snow melting systems." ASHRAE Transactions, 105, PART 1.

Rees, S. J., Spitler, J. D., and Xiao, X. "Transient analysis of snow-melting system performance." Proc., ASHRAE Transactions 2002, June 22, 2002 - June 26, 2002, Amer. Soc. Heating, Ref. Air-Conditoning Eng. Inc., 406-423.

Regis, M., Leal, L. V., and Miller, P. L. (1973). "Transient temperature field in a plane slab with embedded cylindrical sources." Int J Heat Mass Tran, 16(6), 1319-1322.

Rhodes, J.A. (1978). “Chapter 17 – Thermal Properties.” Significance of Tests and Properties of Concrete and Concrete-Making Materials. American Society for Testing and Materials. Philadelphia.

Schnurr, N. M., and Falk, M. W. (1973). "TRANSIENT ANALYSIS OF SNOW MELTING SYSTEMS." ASHRAE Transactions, 79(Part 2), 159-166.

Schnurr, N. M., and Rogers, D. B. (1970). "HEAT TRANSFER DESIGN DATA FOR OPTIMIZATION OF SNOW MELTING SYSTEMS." ASHRAE Transactions, 76(pt 2), 257-263.

Virmani, Y. P., Clear, K. C., and Pasko, T. J. (1983). "Time-To-Corrosion of Reinforcing Steel in Concrete Slabs. Volume 5. Calcium Nitrite Admixture or Epoxy-Coated Reinforcing Bars as Corrosion Protection Systems." FHWA, U.S. Department of Transportation, United States, 80p.

Virmani, Y. P., Jones, W. R., and Jones, D. H. (1984). "Steel corrosion in concrete: pH at corrosion sites." Public Roads, 48(3), 96-102.

Wang, H., Shaopeng, W., Mingyu, C., and Yuan, Z. (2010). "Numerical simulation on the thermal response of heat-conducting asphalt pavements." Physica Scripta Volume T, 2010(T139), 014041 (014043 pp.).

White, D. J., Sritharan, S., Suleiman, M. T., Mekkawy, M. M., and Chulter, S. (2005). "Identification of the Best Practices for Design, Construction, and Repair of Bridge Approach Sections." Center for Transportation Research and Education, Iowa State University, 379.

Williams, G. P. (1976). "DESIGN HEAT REQUIREMENTS FOR EMBEDDED SNOW-MELTING SYSTEMS IN COLD CLIMATES." Transportation Research Record(576), 21-32.

Williamson, P. J. (1967). "The Estimation of Heat Outputs for Road Heating Installations."United States, 71p.

Yunovich, M., Thompson, N. G., and Virmani, Y. P. (2003). "Life Cycle Cost Analysis for Reinforced Concrete Bridge Decks. Paper No. 03309." Proc., CORROSION/03.

8. NUMERICAL INVESTIGATION OF SHALLOW GEOTHERMAL ENERGY BRIDGE DECK DEICING SYSTEMS

8.1. ABSTRACT

The icing of bridge decks in the winter creates dangerous conditions for motorists and is attributed to accidents every year. Shallow geothermal energy (SGE) is an alternative method of heating bridge decks that could potentially eliminate the need for deicing chemicals while not requiring a significant input of energy and/or labor. SGE powered systems take advantage of the relatively constant temperature of the earth, which exists below a depth of about 6-10 m. Previous studies have shown these systems to work, but do note that there are limitations. This paper utilizes a validated 3-dimensional numerical model as a design tool to estimate the performance of SGE systems under a variety of conditions. The results are presented in such a way as to allow the designer to estimate the performance of a given system for differing weather conditions, geometric configurations, and material properties.

8.2. INTRODUCTION

The icing of bridge decks in the winter creates dangerous conditions for motorists and is attributed to accidents every year (Friar and Decker 1999). The most common form of preventing and/or controlling the accumulation of frozen precipitation on both roads and bridges is the use of deicing chemicals. However, it has been shown that the use of the chemicals is harmful to the environment and contributes to accelerated bridge deck deterioration (AASHTO, 2008; Koch et al., 2002; Yunovich et al., 2003; Virmani et al., 1983, 1984). Although many alternative methods have been introduced to deice bridge decks, they are energy intensive and often necessitate the availability of an external power source.

Shallow geothermal energy (SGE) is an alternative method of heating bridge decks that could potentially eliminate the need for deicing chemicals while not requiring a significant input of energy and/or labor. SGE powered systems take advantage of the relatively constant temperature of the earth, which exists below a depth of about 5 m. After this depth, the temperature is approximately equal to the average yearly atmospheric temperature. Thus, in the winter the ground is warmer than the atmosphere and in the summer the ground is cooler. This energy has traditionally been accessed by geothermal borehole heat exchangers (BHE) which consists of one or more loops of tubing installed up to several hundred meters deep, within which a fluid is circulated. The loops are connected to a ground source heat pump (GSHP), which then uses the fluid as a heat source or heat sink to more efficiently heat or cool, respectively, buildings.

Energy piles enable one to economically access SGE by combining BHEs with already required deep foundation elements such as micropiles or drilled shafts, thus allowing the foundation of a building or structure to serve the dual purpose of structural support and thermal energy exchange with the subsurface. Because many bridges are supported on deep foundations, energy piles present an economical method of accessing SGE, which can then be used for bridge deck deicing. SGE has been successfully used to deicing bridge decks with a GSHP (Minsk, 1999, Liu, 2005, Liu et al. 2007a,b), though none of the studies utilized energy piles. The literature also records a few instances where SGE alone was used to successfully heat the bridge deck (i.e. the fluid was circulated directly from the ground to the deck without the use of a GSHP) (Minsk, 1999; Yoshitake et al. 2011). Eliminating the need for a GSHP is extremely desirable in that it significantly lessens the energy requirement of these systems as additional

energy will only be needed to run fluid circulation pumps. In most cases this energy could be provided from photovoltaic cells and allow the system to operate apart from the electric grid.

Bowers and Olgun (2016) used energy piles to deice an experimental bridge deck during several winter storms. They showed that SGE could be used without the aid of GSHP to keep the bridge deck free from snow/ice and melt existing snow/ice on the surface. They did note, however, that there are limitations to these systems and that engineers should be aware of such limitations when considering the expectations for the system they are designing. For example, it is unrealistic to expect these systems to be able to prevent snow and/or ice accumulation during severe winter storms when the temperatures are very low and/or the snow is falling at an accelerated rate. Though the system was unable to keep the deck free from snow during these storms, it was generally able to keep the deck surface above freezing, meaning that snow on the surface was being melted, just not at a rate equal to which it was accumulating. The authors point out that in these situations snow will accumulate on the roads despite the application of deicing chemicals necessitating mechanical removal (plowing).

Currently no benchmark exists upon which to estimate and/or evaluate the performance of SGE bridge deck deicing systems. The current design methodology under ASHRAE (2011) yields a design heating flux and assumes that a heating system will be installed capable of handling that flux. For SGE systems, however, the heat flux is limited. In other words, ASHRAE can help in *designing* a system but no current tool exists to *estimate the performance* a system. This paper utilizes a 3-dimensional numerical model as a design tool to estimate the performance of SGE systems under a variety of conditions. The results are presented in such a way as to allow the designer to estimate the performance of a given system for differing weather conditions, geometric configurations, and material properties.

8.3. NUMERICAL ANALYSIS

The analysis utilizes a 3-dimensional numerical model that was developed by Bowers and Olgun (Chapter 7). The development and calibration of the model including all assumptions, physics, and governing parameters are discussed in the aforementioned paper. It is important to note how it accounts for snow. Because snow melting is an extremely complicated process and the purpose of the model was to represent system performance as opposed to the melting of snow, a Boolean system of success/failure was adopted. To represent the energy required to melt snow, the flux shown in Equation 8-1 was applied:

$$q" = \dot{m}_s[H_{f,s} + C_{p,s}(-T_a) + c_1 C_{p,w}] \qquad \text{Equation 8-1}$$

The flux in Equation 1 accounts for the energy required to raise the temperature of the snow to 0°C, melt the snow, and then raise the temperature of the liquid film by 1°C. If after applying the flux the surface temperature of the slab dropped below 0°C, the system would not be able to keep the deck surface completely free from snow, thus snow would begin to accumulate. If snow were to begin to accumulate, because of its natural insulation characteristics, it would change the boundary condition at the surface of the deck. Thus, the model was rerun from the point at which the deck surface temperature dropped below 0°C with an updated surface boundary condition and no heat flux due to snow melt. If the system was still unable to keep the top surface above freezing, then the system would not be able to melt any of the snow that was falling. If the system was able to keep the deck surface temperature above 0°C after application of the new boundary conditions, then it could be stated that though the system was unable to keep the deck completely free from snow, it would be continually melting the snow just at a rate less than that of which it was falling. Because the melting of the snow was not directly modeled, the exact rate of snow

melt would be unknown. However, as mentioned previously, in the situations where the system was unable to keep the deck completely free from snow, mechanical removal is likely to be required anyway, thus the rate of snow melt is not needed.

The same methodology was followed in these analyses where, among other metrics, the system was evaluated as either being able to keep the deck completely free from snow, not able to melt any snow, or able to keep the deck above freezing and melt snow, but not at a rate fast enough to keep the deck clear.

8.3.1. Analysis Methodology

Many different parameters affect the performance of bridge deck deicing systems including factors both inside and outside of the system designer's control. Weather conditions, including ambient temperature, wind speed, and rate of snow fall cannot be controlled whereas tube spacing, flow rate, and to a degree, the thermal properties of the materials in the bridge deck can be controlled. Thus, several parameters were analyzed: ambient temperature, wind speed, inlet fluid temperature, tube spacing, fluid flow rate, thermal conductivity of the concrete, and heat capacity of the concrete. A base case was established from which to compare the other cases and to aid in presentation of results. Table 8-1 summarizes the values used in the base case and lists the additional values tested.

Table 8-1. Bridge deck properties assigned to numerical model for the base case heating scenario.

Parameter	Value	Unit
Bridge Deck Dimensions		
Length	4 x Pipe Spacing	m
Width	3.7	m
Height	25.4	cm
Depth of circulation tubes	7.45	cm
Circulation Fluid (20% Glycol)		
Flow rate	11.0	L/m
Dynamic viscosity	4.8	mPa·s
Thermal conductivity	0.4	W/m·K
Specific heat capacity	3538	J/kg·K
Density	1070	kg/m^3
Pipes (PEX)		
Thermal conductivity	0.41	W/m·K
Effective thermal conductivity	{1000, 1000, 0}[1]	W/m·K
Specific heat capacity	2300	J/kg·K
Density	950	kg/m^3
Effective density	447.52	kg/m^3
Pipe inner diameter	16	mm
Pipe wall thickness	3.0	mm
Pipe spacing (center-to-center)	20	cm
Concrete		
Thermal conductivity	3.0	W/m·K
Specific heat capacity	880	J/kg·K
Density	2360	kg/m^3

Rebar		
Thermal conductivity	45.4	W/m·K
Specific heat capacity	475	J/kg·K
Density	7850	kg/m^3
Concrete/Rebar Zones		
Top height	7.45	cm
Bottom height	10.16	cm
Top thermal conductivity	3.65	W/m·K
Top specific heat capacity	873.82	J/kg·K
Top density	2443.8	kg/m^3
Bottom thermal conductivity	3.48	W/m·K
Bottom specific heat capacity	875.42	J/kg·K
Bottom density	2422.1	kg/m^3

[1]Directions are in the cylindrical material r, ϕ, and z directions where z follows the axis of the circulation tube

The additional model parameters, including material properties and geometry, that were used for the base case as well as the other cases are given in Table 8-2. These values were based on the model bridge deck that was experimentally tested in Bowers and Olgun (2016) as well as what could be expected from an actual bridge. The width of the bridge deck was set at 3.7 m (12 ft), or one typical road lane width. The length of the bridge was set to be 4 times the tube spacing such that the same number of loops could be modeled for different loop spacing. Obviously actual bridges are much longer, however the modeling of an entire bridge is impractical due to the extremely large number of elements required. Several loops are enough to provide an accurate understanding of how the system works and associated heat requirements. The portion of the deck closer to the inlet of the circulation loop will be warmer than the portion of the deck near the end of the loop as the fluid will be losing energy along the path from inlet to outlet. This has been considered and will be discussed.

Table 8-2. Bridge deck and weather properties that were varied an compared against base case heating scenario.

Parameter	Base Case	Additional Values Tested	Insulated Values Tested
Tube Spacing (cm)	20	15, 25, 30	20
Inlet Fluid Temperature (°C)	12	4, 6, 8, 10, 14, 16, 18, 20	12
Ambient and Initial Temperature (°C)	-2	-0.5, -1.0, -1.5, -2.5, -3.0, -4.0, -6.0, -8.0, -10.0	-4.0, -6.0, -8.0, -10.0
Wind Speed (m/s)	0	2, 4, 6, 8, 10, 15, 20	2, 8, 15
Thermal Conductivity (W/m-K)	3	1.5, 2.0, 2.5, 3.5, 4.0	-
Heat Capacity (J/kg-K)	880	700, 1000	-

The performance of the bridge deck under the different configurations and conditions of Table 8-2. Bridge deck and weather properties that were varied an compared against base case heating scenario. was first evaluated in the absence of snow fall to evaluate the basic performance of bridge deck deicing systems. Considering these systems will spend a significant portion of their operating time in 'pre-heating' mode in preparation for a storm (Schnurr and Falk, 1973; Liu and Spitler, 2004; ASHRAE, 2013), it is critical to evaluate the performance of the bridge deck and investigate such metrics as energy requirements, how long it takes the bridge deck to heat, and surface temperatures.

Snow was then considered using three different snowfall rates symbolic of three types of observed storms from Bowers and Olgun (2016): mild, moderate, and severe as shown in Table 8-3. Table 8-3 also shows the cases that were tested with snow fall and the types of storms applied. Pre-heating was assumed for every case and the point at which the snow melting flux was applied was selected based on the average surface temperature. This was done to allow for a more direct comparison between the cases. Under actual operating conditions, the operator is not going to know exactly when snow will begin and/or how long it will take for the deck to reach a certain surface temperature but he/she will have an idea of when the storm is expected to start. Thus, the amount of time it takes the deck to reach a given surface temperature will also be presented.

Table 8-3. Rates of snowfall used to test in the numerical model.

Type of Storm	Snowfall Rate (cm/hr)	Snow Melting Flux[1] (W/m^2)
Mild	2	-19.3
Moderate	5	-48.1
Severe	10	-96.3

[1]Assuming an ambient temperature of -2°C. This value will change for the scenarios in which the ambient temperature changes.

Figure 8-1 shows the typical geometry as well as the discretization of the domain using quadrilateral elements. A zoned approach to account for the top and bottom layers of rebar reinforcement was adopted as explained in Bower and Olgun (Chapter 7). The top and bottom bridge deck surfaces were exposed to the environment and subject to both radiative and convective heat fluxes. The edges of the bridge deck were insulated. This was done to eliminate edge effects. Due to the parallel alignment of the circulation tubes beneath the surface of the deck as well as high ratio of top and bottom surface areas to side surface areas, the majority of the energy exchange between the bridge deck and environment will take place at the top and bottom surfaces. Due to the relatively small size of the numerical model with respect to an actual bridge deck, allowing heat exchange through the sides of deck in the numerical model could influence the results.

The boundary conditions, such as inlet fluid temperature, ambient air temperature, and wind speed were held constant. Natural weather does change over time and the previous paper has shown that the numerical model can accurately account for this. However, in order to develop a basic understanding of how these systems perform, it is advantageous to isolate variables and observe the system's response.

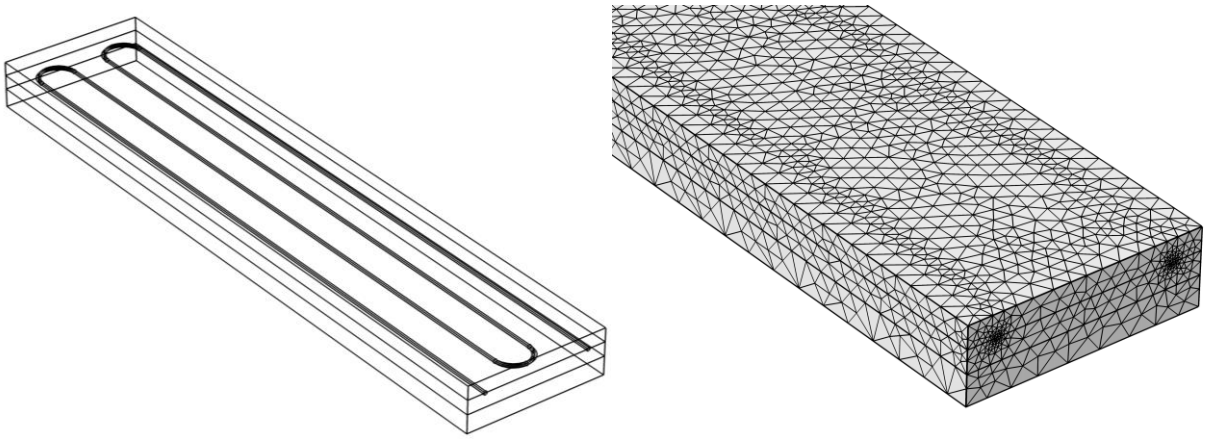

Figure 8-1. Typical geometry and discretized domain.

8.4. BASIC BRIDGE DECK BEHAVIOR

8.4.1. The Base Case

Figure 8-2 displays the average surface temperature of the bridge deck over time as it is subjected to the base conditions from Table 1. It takes about 0.7 hours for the average deck temperature to reach 0°C and after 10 hours, the average surface temperature is over 6°C. This would certainly indicate that as long as the deck temperature is not extremely cold and that relatively constant atmospheric conditions will exist (which often occur before the onset of a storm), a significant amount of pre-heating is not required for the associated inlet fluid temperature, wind speed, thermal properties, etc. However, the longer the deck is pre-heated, the higher the average surface temperature and potentially better system performance during snow fall.

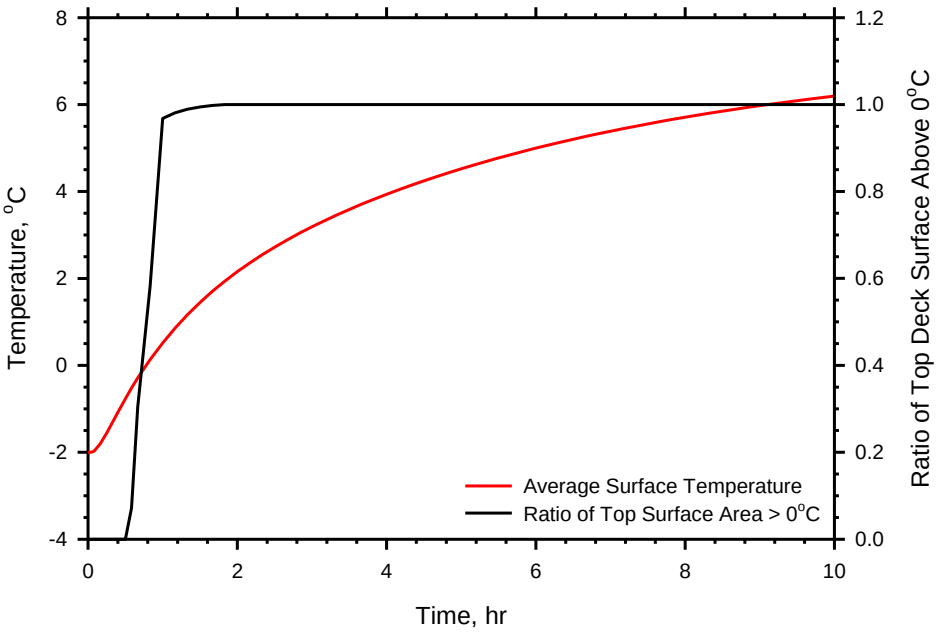

Figure 8-2. Average surface temperature and area of the top surface greater than 0°C over time for the base case.

The average surface temperature is not always a good indication of the true condition at the deck surface as high or low values can influence the average. Thus the fraction of the deck surface that is above 0°C is also shown in Figure 8-2. In this case, the portion of the deck that is above 0°C goes from 0 to 1 in just over 1 hour, and from 0 to 0.9 in about 30 minutes. This also occurs about the same time the average deck surface temperature reaches 0°C. It will be shown that this is not always the case.

Important in designing the SGE BDD systems is determining their energy requirements. Figure 8-3 displays the cumulative amount of energy imparted by the fluid to the slab over time. It also shows the amount of energy that is used to heat the deck and that is lost to the environment through radiation and convection. During the first hour of operation, almost all of the energy goes solely to deck heating and very little is lost to the environment. Over time, however, the amount that is lost to the environment increases with more energy being lost to radiation than to convection. Figure 8-3 shows that though it only takes an hour for the deck surface to heat to above 0°C, the longer the system operates, the more energy is transferred to the deck. For example, after 1 hour of heating, 2.9 MJ of energy have been transferred to the deck from the fluid and are still stored in the deck (not lost to the environment). After 5 hours of heating that value has increased to 9.3 MJ. Thus, after 5 hours the deck is storing an additional 6.4 MJ of energy that can be used to melt falling snow. This can significantly improve system performance as the greater the amount of energy that is stored in the deck before the storm, the less it will have to solely rely on the rate of energy transfer to the deck from the subsurface system component.

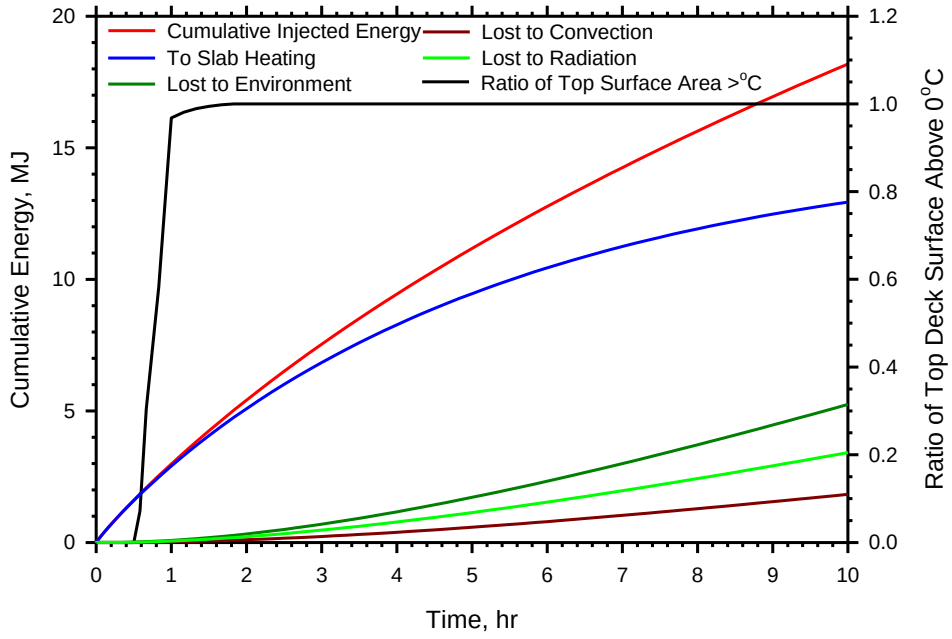

Figure 8-3. Cumulative injected energy to the slab amount of energy used for slab heating, radiation, and convection.

In order to better show where the energy is going, Figure 8-4 was created. Figure 8-4 shows the percentage of energy that goes towards heating the slab and the percentage of energy that is lost to the environment. The amount of energy going to slab decreases from 100% at the start of operation to around 71% after 10 hours whereas the amount of energy lost to the environment increases from 0% to 29%. Of the energy that is lost, Figure 8-4 shows that about 70% is to radiation and 30% is to convection. These

percentages are fairly constant over time. What is not constant is how much of the energy is lost through the top and bottom surfaces. For both radiation and convection, a significantly greater amount of energy is lost through the top surface as compared to the bottom surface. With regards to radiation, 100% of the energy is lost through the top surface at the beginning of operation and that percentage decreases to just under 80% after 10 hours. Likewise, in considering convection the percentage begins at 100% and decreases to 60% after 10 hours. This makes sense as the top of the bridge deck heats more quickly and to a higher temperature than the bottom surface of the bridge deck due to the placement of the deicing tubes under the top surface. This imbalance in temperatures between the top and bottom surfaces ultimately creates a higher temperature gradient with the environment at the top of the slab leading to more energy exchange with the environment.

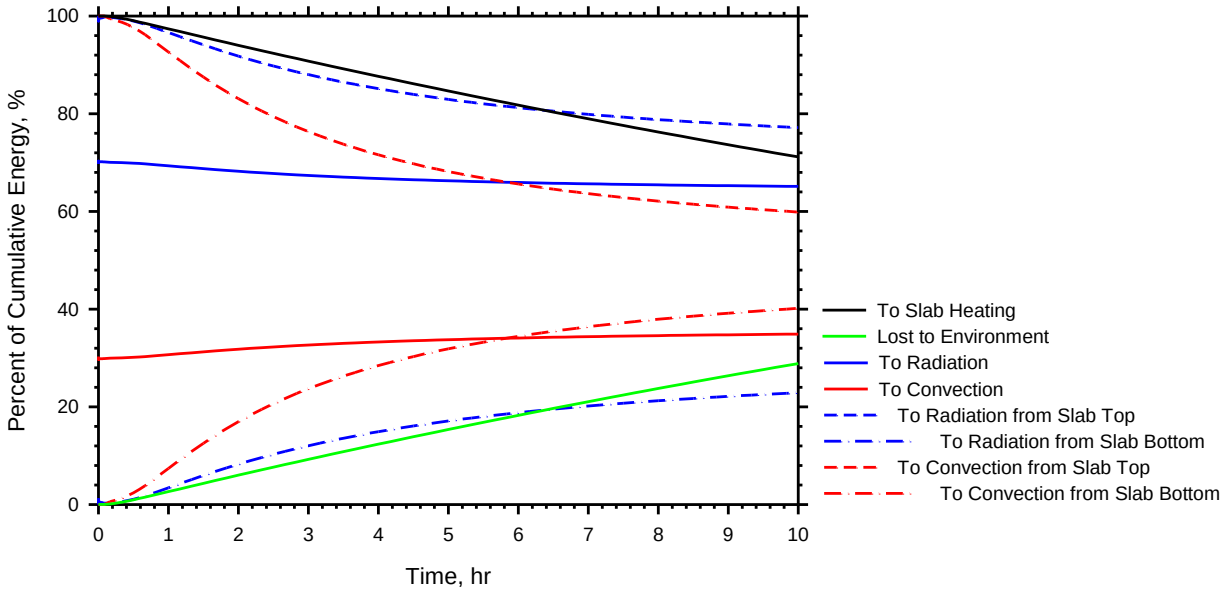

Figure 8-4. Distribution of injected energy to the slab and energy lost from the slab.

A useful parameter that can be used to compare different cases is the total heat flux per surface area, which is the rate at which energy is being transferred to the slab per unit surface area. This value is shown in Figure 8-6. It starts high at over 300 W/m^2 and then quickly decreases to below 120 W/m^2 after 10 hours. This is the rate at which energy will have to be supplied to the deck from the subsurface component of the system and can be used to determine the subsurface response separately from this analysis.

As mentioned previously, it is expected that portions of the bridge deck near the inlet will heat more quickly than those near the outlet as the fluid will be decreasing in temperature from inlet to outlet during a heating operation. In order to discern how this might affect the above values, specifically the percent of energy that is used for heating vs. lost and the value of the slab heating flux, a larger model was created. In this case the length of the slab was extended by 20% (which was the maximum size the computer was capable of handling) and the results were compared with the base case. Figure 8-5 compares the distribution of heat energy between the two cases and shows that they are identical. Thus it can be inferred that regardless of the length of the model, the distribution of energy will remain constant.

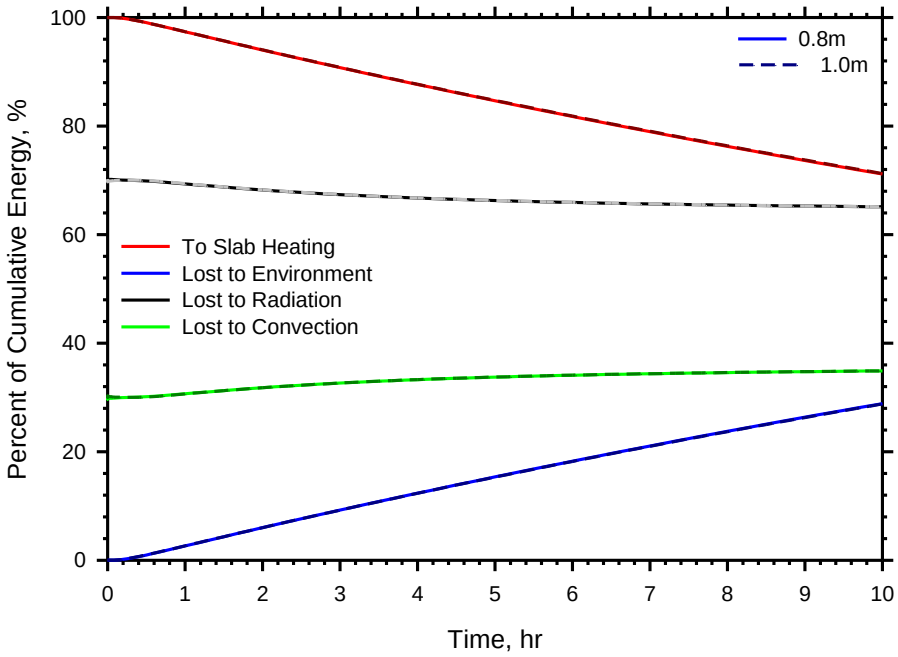

Figure 8-5. Distribution of energy for the base case with a slab length of 0.8 and 1.0 m.

What is may change, however, is the slab heat flux per surface area. They are compared in Figure 8-6. Again, the two are virtually identical though the flux from the larger model is slightly less – on the order of 1% or less. This implies that if the heated area per tube ratio is kept relatively small, there will not be a significant decrease in the average slab heating flux. Conversely, if a 50 m deck has one single inlet, than there will be a significant decrease in the heat flux along the deck from inlet to outlet. Keep in mind that at some point, the 'inlet' temperature to a particular deck section may have decreased to 10°C. In this way the deck can be envisioned as a collection of smaller decks with gradually decreasing inlet fluid temperatures. Obviously this is not a perfect representation as the fluid temperature at a particular location in the bridge deck is not constant over time, but this method can provide a useful approximation that is more conservative than using one inlet value for the whole deck. Figure 8-7 shows the difference between the two methodologies. Keep in mind that the actual inlet temperature will also be a function of the heat exchange operation with the ground, thus more inlets will not necessarily guarantee higher deck temperatures. For the same ground configuration, as the number of inlets increase the average inlet temperature decreases, which is also represented in Figure 8-7.

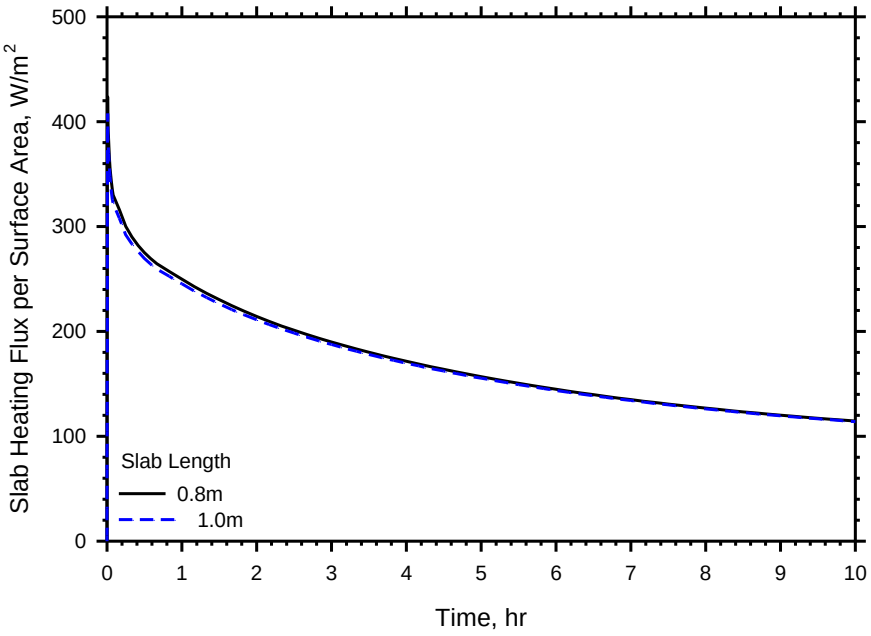

Figure 8-6. Slab heating flux per surface area of the base case comparing different slab lengths.

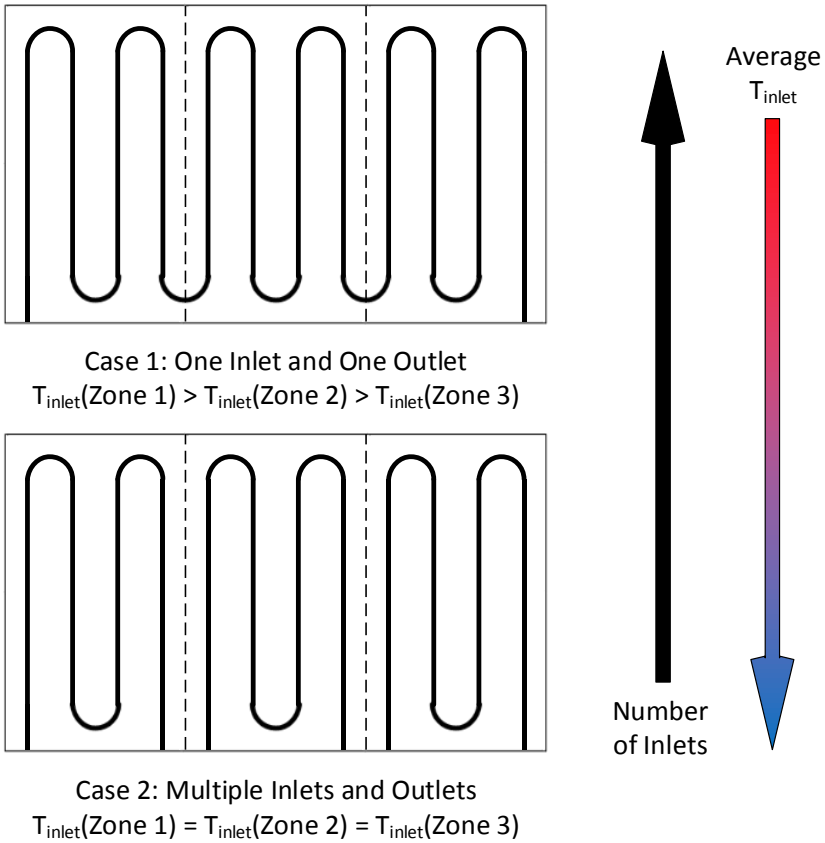

Figure 8-7. Comparison of methodologies to envision bridge deck heating.

8.4.2. Effects of Tube Spacing

One of the primary design factors that has potential to govern the deck heating behavior is tube spacing. From previous studies, tube spacing generally varies between 15 and 30 cm (6 and 12 inches). The effects of tube spacing on average surface temperature are shown in Figure 8-8. As can be seen, as the tube spacing increases the average surface temperature decreases while the amount of time it takes for the average surface temperature to reach 0°C increases. Also observe that for closer tube spacing the time it takes the average surface temperature to reach 0°C is close to the amount of time it takes 70 to 90% of the deck surface to increase above 0°C. However, as the tube spacing increases the difference between these two times increases such that the average deck surface temperature reaches 0°C before 70% and 90% of the deck is above 0°C. This is due to the fact that the surface area directly above the tubes heats more quickly relative to the surface area between the tubes. For wider tube spacing, the time it takes the heat energy to reach the spot between the middle of the deicing tubes is greater than it is for narrower tube spacing. This ultimately results in the surface temperature above the tubes increasing at a faster rate than the surface area between the tubes, with the difference in rates being greater for wider tube spacing. This is shown in Figure 8-9, which shows the surface temperature contours of the different tube spacing scenarios at the point in time the average surface temperature for each slab is 0°C. Notice the lower surface temperatures between the tubes for the wider tube spacing scenarios. There are also higher surface temperatures directly above the tubes for wider tube spacing because wider tube spacing scenarios require longer heating times for the average to reach 0°C, as discussed previously, thus giving the surface above the tubes more time to heat, resulting in higher surface temperatures relative to more closely spaced scenarios.

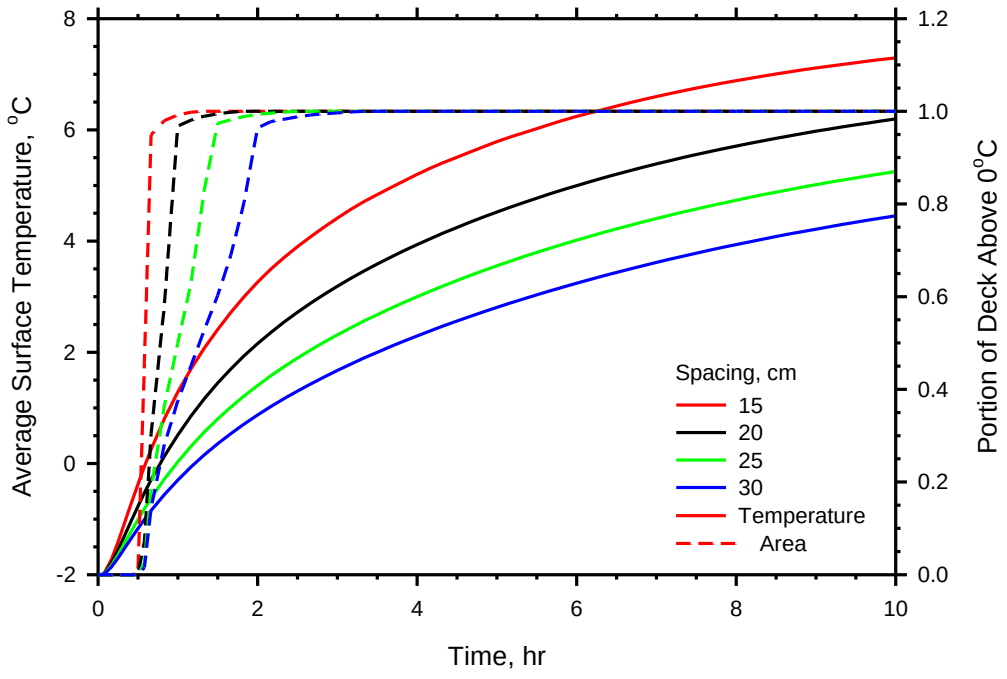

Figure 8-8. Average surface temperatures and area of deck surface above 0°C for different tube spacing scenarios.

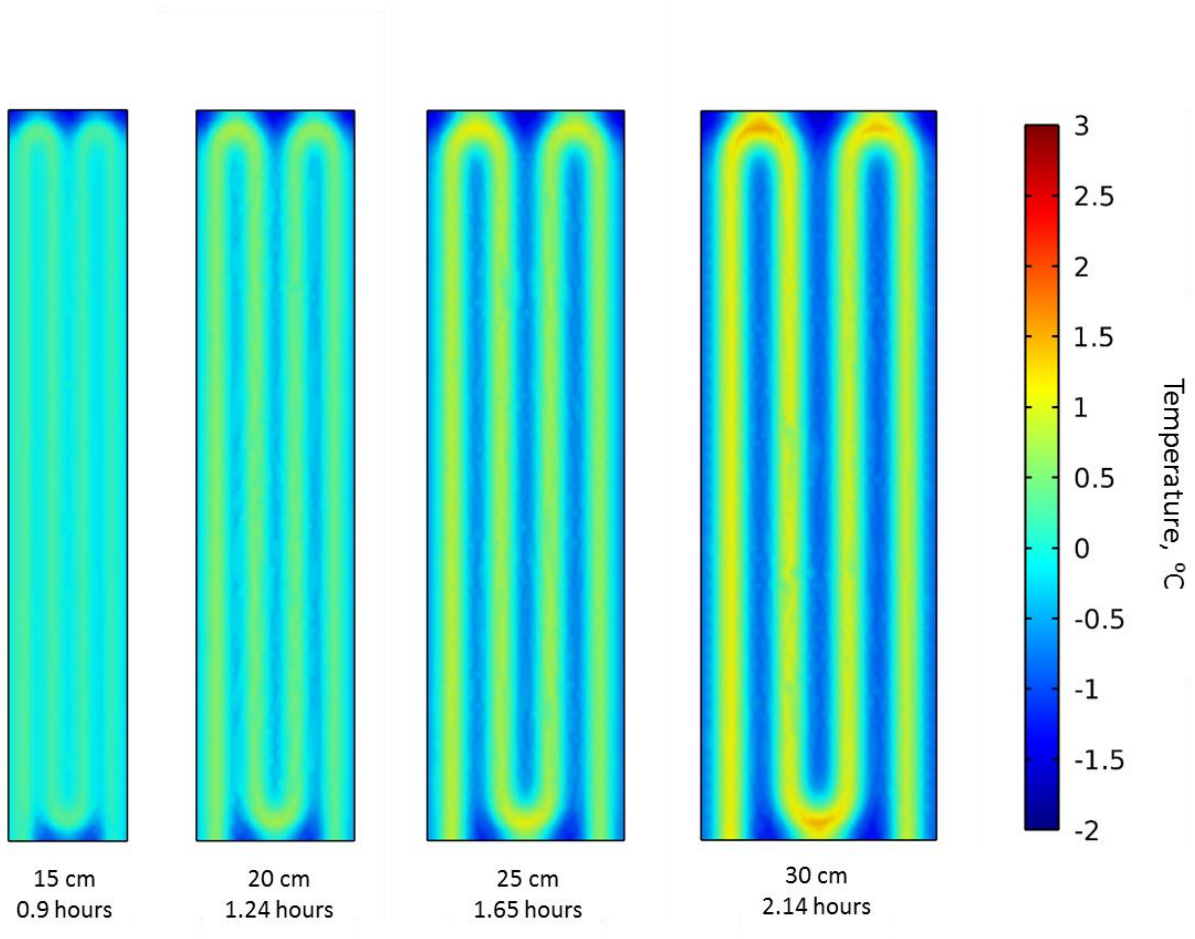

Figure 8-9. Comparison of surface temperature contours of the deck surface of different tube spacing scenarios at the point in time when the average surface temperature was 0°C.

In order to compare the energy distributions and heating flux for differing tube spacing scenarios, each energy value was normalized by the top surface area of the deck. These normalized values over time are shown for the cumulative amount of energy in Figure 8-10. As compared to the base case, the 15 cm tube spacing scenario injects more energy per surface area into the slab, and the 25 cm and 30 cm spacing scenarios each inject less. This makes sense given the fact there is a greater tube density per slab surface area for 15 cm spacing as compared to the base case.

Though the 15 cm spacing scenario injects the greatest amount of energy over time, the wider tube spacing scenarios actually inject more energy per tube length. Figure 8-10 also compares two different heating rates. One is normalized by the surface area and the other is normalized by the length of the tube in the slab. Whereas the heating rate per surface area is greater than the base case for the 15 cm tube spacing scenario, it is less than the base case when normalized by tube length. This is due to the fact that the wider tube spacing scenarios actually have more slab volume to heat per length of tube than do the narrower tube spacing scenarios. This results in a greater heating rate. Heating rate per surface area is more useful in terms of estimating system performance, however heating rate per tube length can aid in understanding how these systems work.

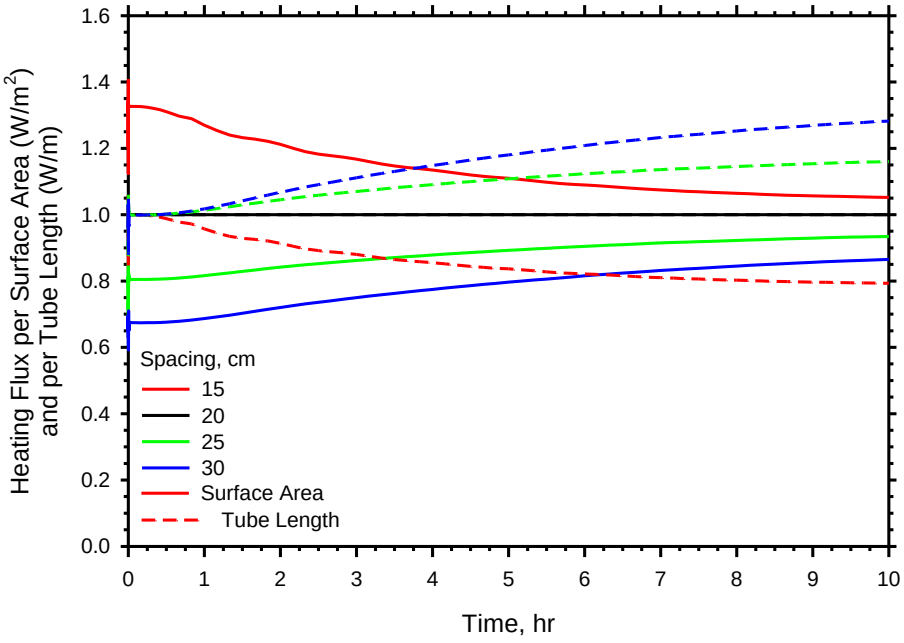

Figure 8-10. Heating flux per surface area and per tube length for different tube spacing scenarios.

Normalized values are shown in Figure 8-11a-f as a function of tube spacing for various energy and flux plots. Because the normalized values are not constant over time as shown in Figure 8-10, each plot has contours for several time intervals. When normalized by surface area, the amount of energy injected to the slab decreases as the tube spacing increases as shown in Figure 8-11b. This is also true for the amount of energy devoted to heating the slab (Figure 8-11c), the amount of energy lost (Figure 8-11d), and the amount of energy lost to radiation (Figure 8-11e) and convection (Figure 8-11f). However, in terms of the amount of energy used for slab heating and that was lost to the environment, Figure 8-11c and Figure 8-11d may not be the best comparison as not as much energy was delivered to the slab, thus the amounts going to heating and to the environment will be less than the base case. Figure 8-12 compares the percentages of the total energy that is going to slab heating and the environment, as well as the percent lost that goes to radiation and convection. As the tube spacing increases, the percent of energy that is lost decreases slightly. This means that wider tube spacing scenarios are slightly more efficient in terms of energy going to slab heating as opposed to being lost, however, not as much total energy is being injected to the slab (Figure 8-11b). It appears that tube spacing has no effect on the percentage of lost energy going to radiation or convection.

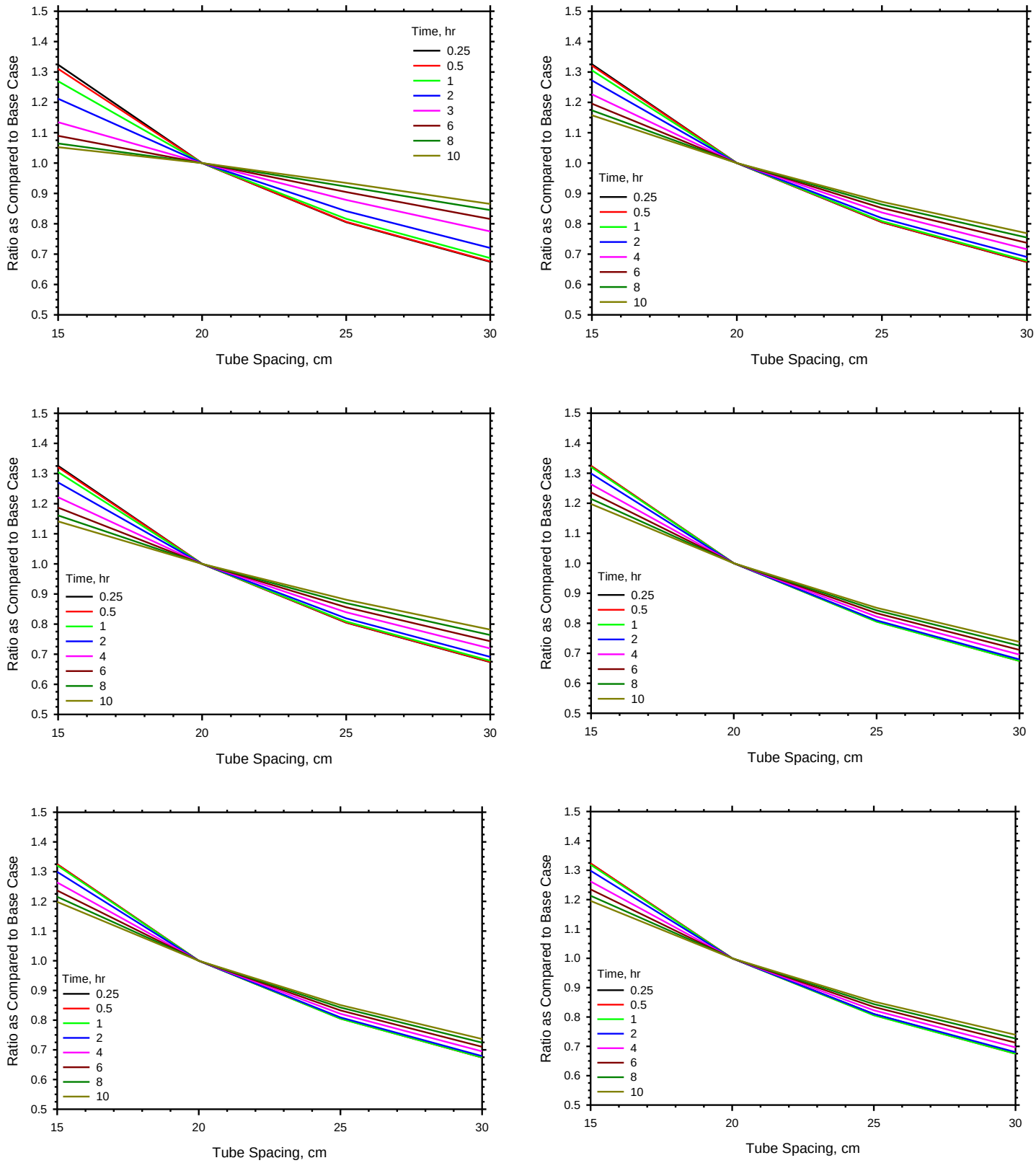

Figure 8-11. Ratio as compared to the base of slab heating flux per surface area (a-top left), cumulative energy injected to the slab (b-top right), energy used for slab heating (c-mid left), energy lost to the environment (d-mid right), energy lost to radiation (e-bottom left), and energy lost to convection (f-bottom right) as a function of tube spacing.

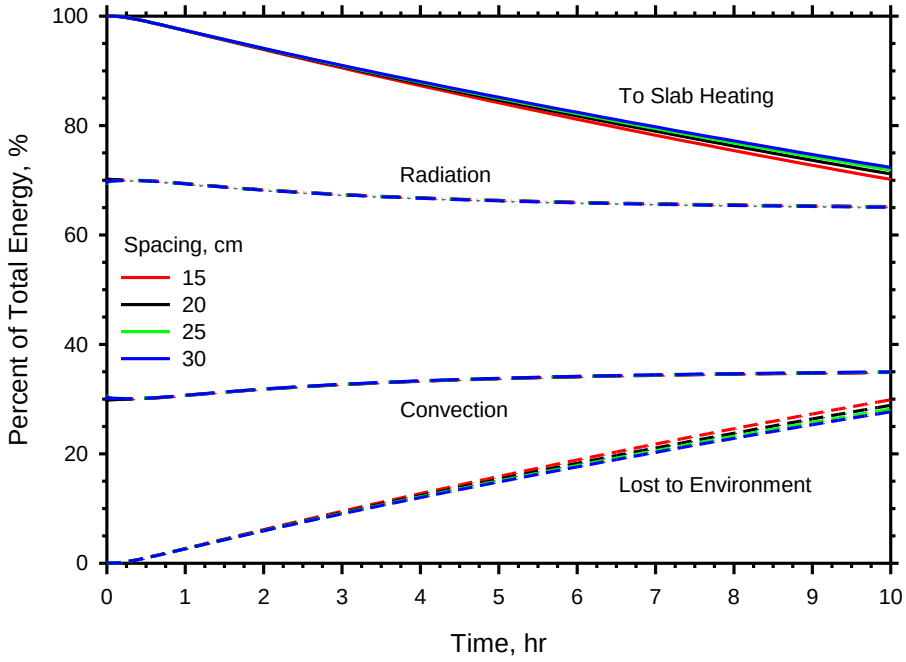

Figure 8-12. Distribution of injected energy to the slab and the mechanism by which energy was lost to the environment for different tube spacing.

8.4.3. Effects of Inlet Fluid Temperature

Inlet fluid temperature will vary both from site to site and throughout the storm depending on the temperature of the ground and energy demands of the system. Experimental tests in Chapter 3 have shown inlet fluid temperatures to vary from less than 4°C to over 9°C during deicing operations. Presumably higher inlet temperatures could be obtained in systems located in warmer climatic regions. To show how inlet fluid temperatures can affect the performance of a system, inlet temperatures ranging from 4°C to 20°C were applied to the model.

The average surface temperatures over time are shown in Figure 8-13. Notice that as the inlet fluid temperature increases, so does the average surface temperature. The portion of the deck that is above 0°C is also shown on Figure 8-13. As the inlet fluid temperature increases, the amount of time it takes for the surface of the deck to heat above 0°C decreases. This is not a linear progression as the time it takes for the majority of the surface area to heat above 0°C significantly decreases moving from an inlet fluid temperature of 4°C to 6°C, but not as significantly when moving from 6°C to 8°C. Thus the heating efficiencies of inlet fluid temperatures increase significantly when moving from 4°C to 10°C but not as much when moving from 10°C to 20°C.

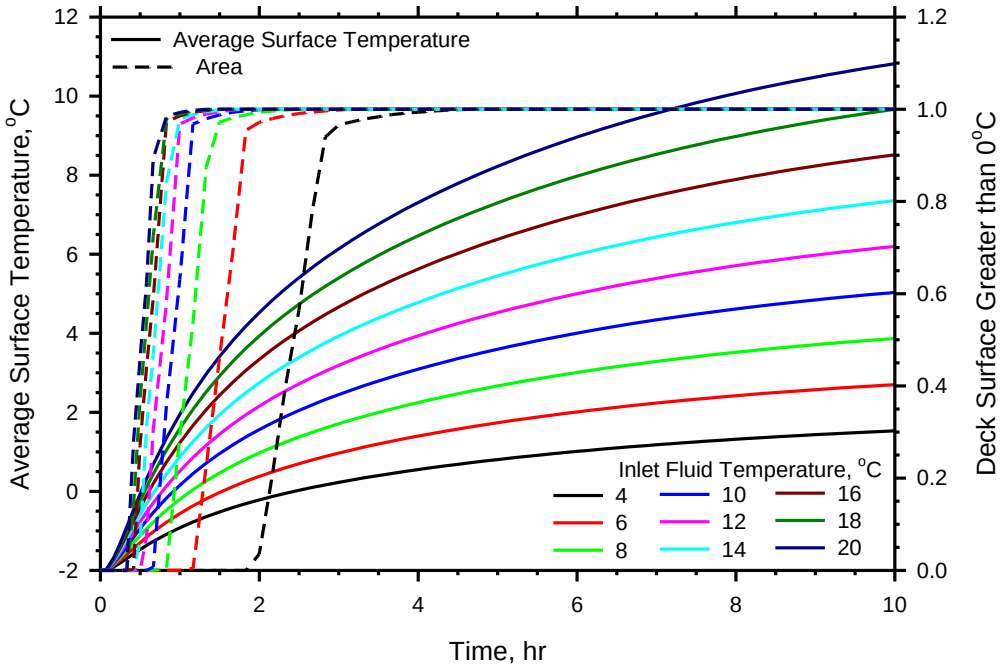

Figure 8-13. Average surface temperatures and area of deck surface above 0°C for different inlet fluid temperatures.

The cumulative amount of energy injected to the slab for each inlet fluid temperature was compared to the base case and shown in Figure 8-14. Notice the constant value over time for each inlet fluid temperature. The constant value for each inlet fluid temperature is then plotted as a function of inlet fluid temperature, as shown in Figure 8-15. Also shown in Figure 8-15 is the relationship to the base case in terms of the amount of energy that was lost, used for heating, and the slab heating flux, all of which displayed similar constant trends to Figure 8-14 when plotted as functions of time. Several observations can be made. First, all of the relationships with inlet fluid temperature are linear when compared to the base case. Secondly, the relationships practically plot on top of each other. For example, when increasing in inlet fluid temperature, the amount of cumulative energy injected to the slab relative to the base case increases. When increasing in inlet fluid temperature, the amount of energy lost and the amount of energy used for slab heating also increase relative to the base case, and they do so at almost the same rate as the increase in cumulative injected energy.

This shows that bridge deck deicing systems located in warmer climactic regions where higher ground temperatures are expected will be able to inject more energy to the slab than systems located in colder climactic regions. This is somewhat unfortunate as colder climactic regions are both more likely to need these systems as they experience lower ambient temperatures and more severe winter storms. However, this also shows that if the ground temperature can be increased through thermal recharge as discussed in Bowers and Olgun (2015a, 2015b), better system performance can be expected in terms of higher average surface temperatures, quicker heating times, and more energy being injected to the slab.

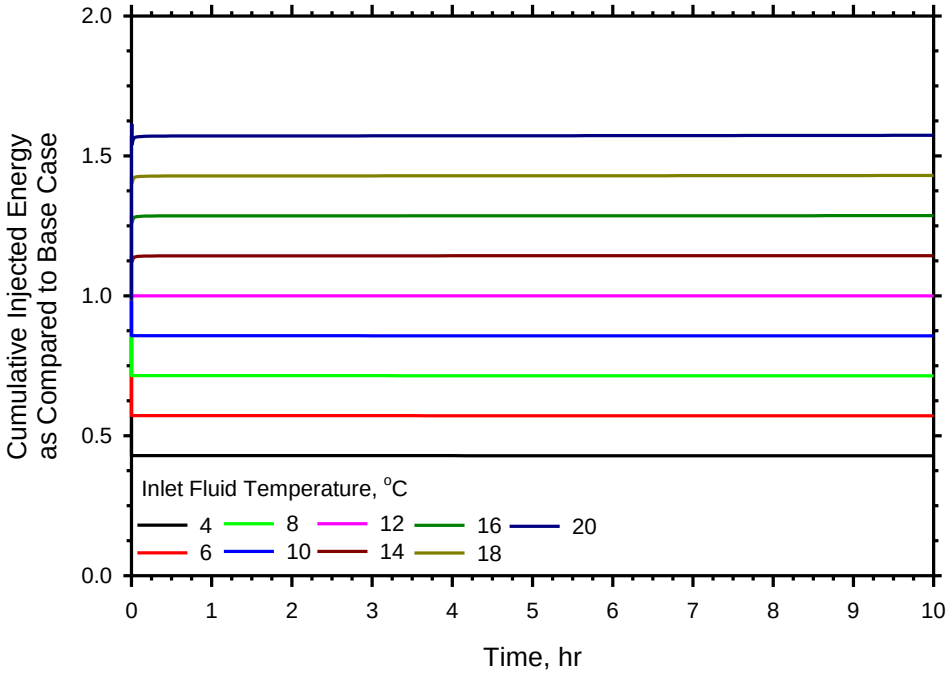

Figure 8-14. Ratio of the cumulative injected energy to the slab as compared to the base case for different inlet fluid temperatures.

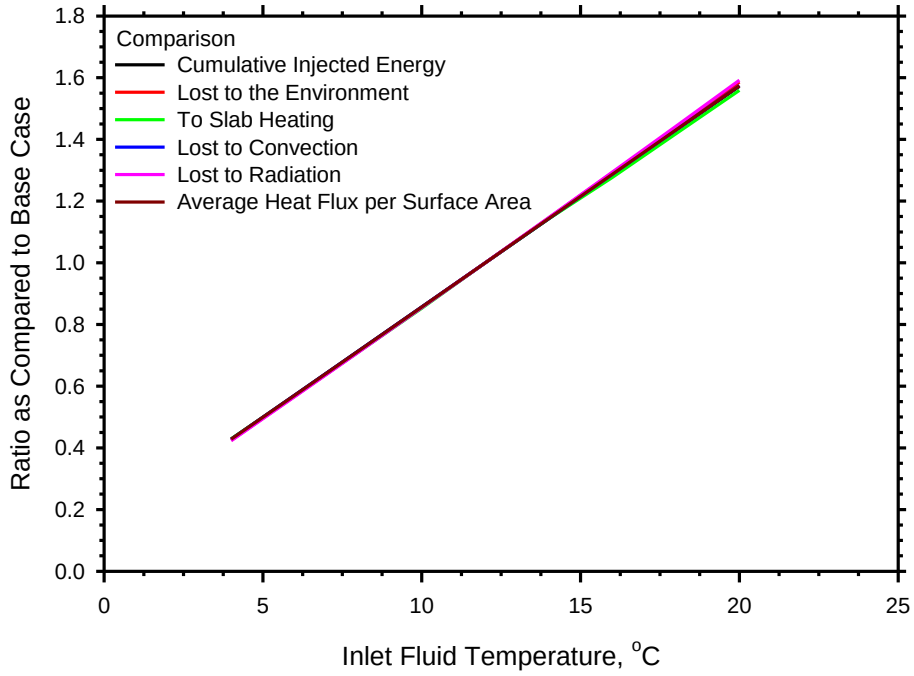

Figure 8-15. Ratio as compared to the base of slab heating flux per surface area, cumulative energy injected to the slab, energy used for slab heating, energy lost to the environment, energy lost to radiation, and energy lost to convection as a function of inlet fluid temperature.

8.4.4. Effects of Ambient and Initial Temperature

The ambient temperature of the environment will also affect the performance of the system as lower ambient temperatures will require a greater amount of energy to heat the slab. In this case, ambient temperatures can be thought of as the mean radiant temperature, which is discussed more fully in Chapter 7, and is a function of atmospheric temperature, the sky temperature, and the amount of cloud cover present. For 100% cloud cover, which is often the case before and during winter storms, the mean radiant temperature is usually equal to the ambient temperature. For these analyses, the initial slab temperature was assumed to be equal to the ambient temperature. This is not often the case as the initial slab temperature will not necessarily be constant with depth or across the slab length and width (see Chapter 3 for experimental results) and is a function of the prior environmental conditions. However, for the purpose of understanding deck heating behavior it is useful to set the initial temperature equal to the ambient temperature as lower ambient temperatures preceding a storm will likely result in lower initial bridge deck heating temperatures. Thus initial and ambient temperatures from -0.5°C to -10°C were investigated.

Figure 8-16 displays the average surface temperatures of the slab over time for different ambient and initial temperatures as well as the portion of the deck surface above 0°C. Not surprisingly, the lower the ambient temperature, the longer it takes the slab to heat the surface above 0°C. Higher ambient temperatures require very little time to heat the slab whereas ambient temperatures as low as 10°C require over 4 hours for the majority of the slab to heat above 0°C. Ultimately, the lower and the ambient temperature and/or initial bridge deck temperature preceding a storm, the longer it will take to heat the slab and this should be accounted for when operating the systems.

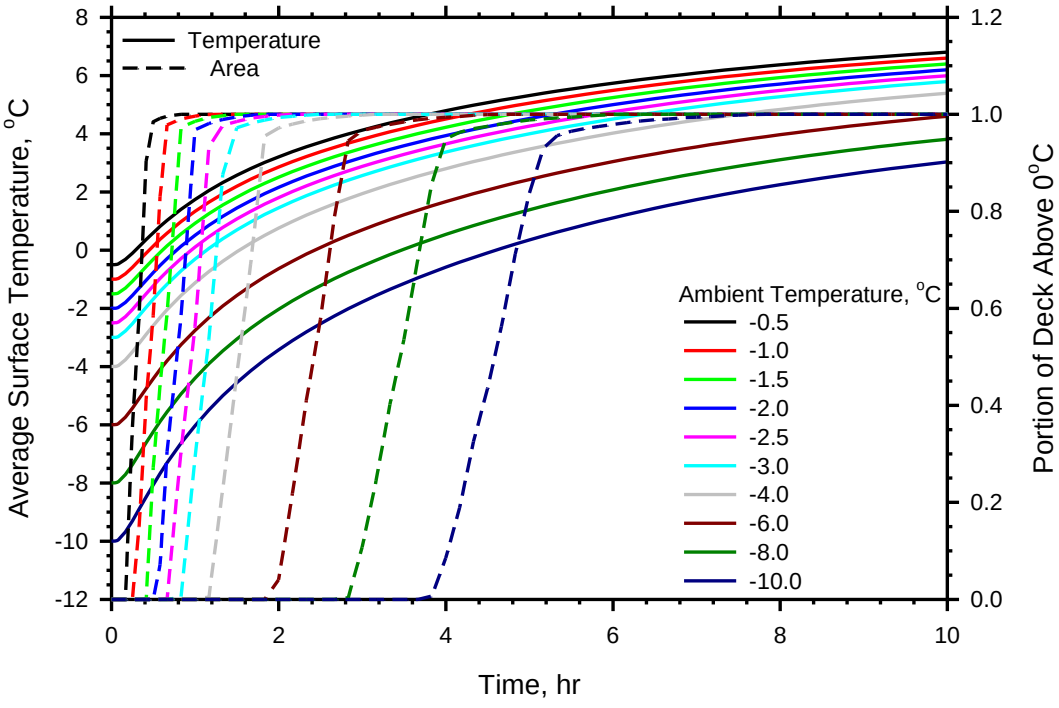

Figure 8-16. Average surface temperatures and area of deck surface above 0°C for different ambient temperatures.

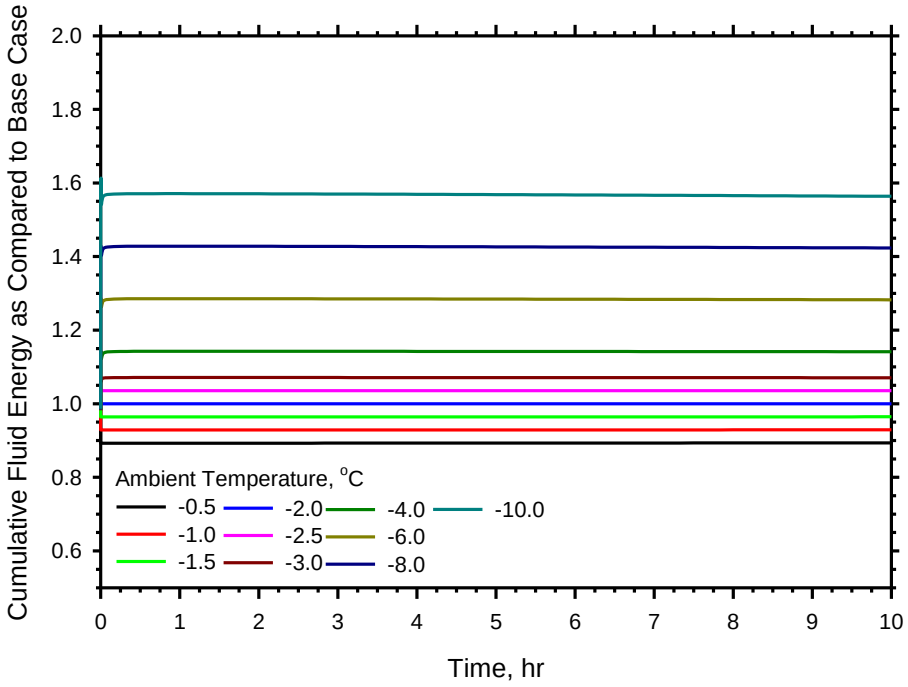

Figure 8-17. Ratio of the cumulative injected energy to the slab as compared to the base case for different ambient temperatures.

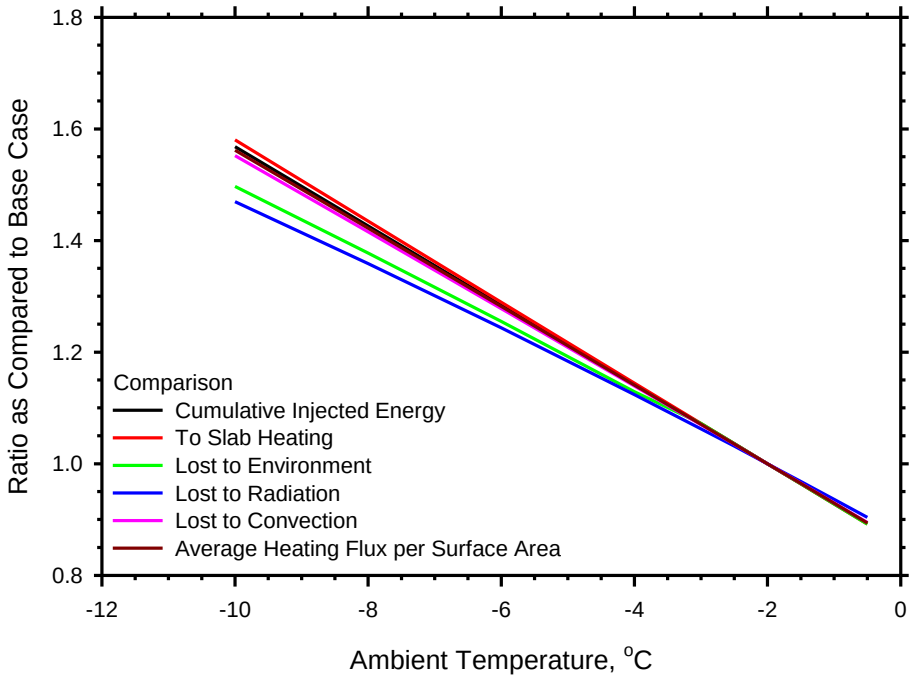

Figure 8-18. Ratio as compared to the base of slab heating flux per surface area, cumulative energy injected to the slab, energy used for slab heating, energy lost to the environment, energy lost to radiation, and energy lost to convection as a function of ambient temperature.

The cumulative amount of energy injected to the slab for each case in relation to the base case is shown in Figure 8-17. Notice that the values are constant over time, just as they were for the different inlet fluid temperature scenarios. This again allows them to be plotted as a function of ambient temperature, which is shown on Figure 8-18. As the ambient temperature decreases, the amount of energy injected to the slab increases. Likewise, the amount of energy devoted to slab heating and lost to the environment increases as the ambient temperature decreases. However, as can be seen from Figure 8-19, the percentage of the energy that is used to heat the slab and lost to the environment does not change with respect to ambient temperature.

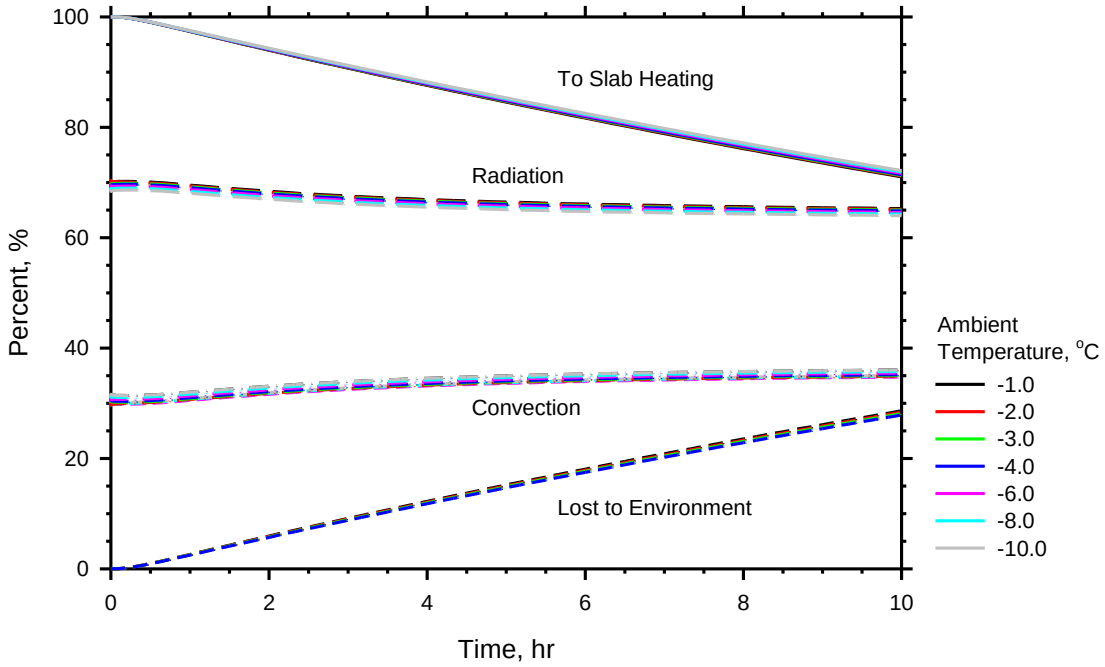

Figure 8-19. Distribution of injected energy to the slab and the mechanism by which energy was lost to the environment for different ambient temperatures.

8.4.5. Effects of Wind

Wind speed is rarely constant and can vary tremendously between storms and within a single storm. However, for the sake of this analysis they were held constant in order to better understand how sustained winds would affect the performance of a system. Wind speeds from 2 to 20 m/s were compared against the base case. Figure 8-20 compares the average surface temperatures and area of the deck surface above 0°C for the different cases. Wind speed does have effect on the average surface temperature, and in effect serves to limit what the upper extreme can be. Though each case was only observed for 10 hours, it is clear that for higher wind speeds the average temperature is approaching a constant value, which decreases with increasing wind speed. Furthermore, the wind speed significantly affects the amount of time it takes for the surface area of the deck to reach temperatures above 0°C. In fact, for wind speeds of 20 m/s, not every point on the surface of the deck reached temperatures greater than 0°C over the course of 10 hours.

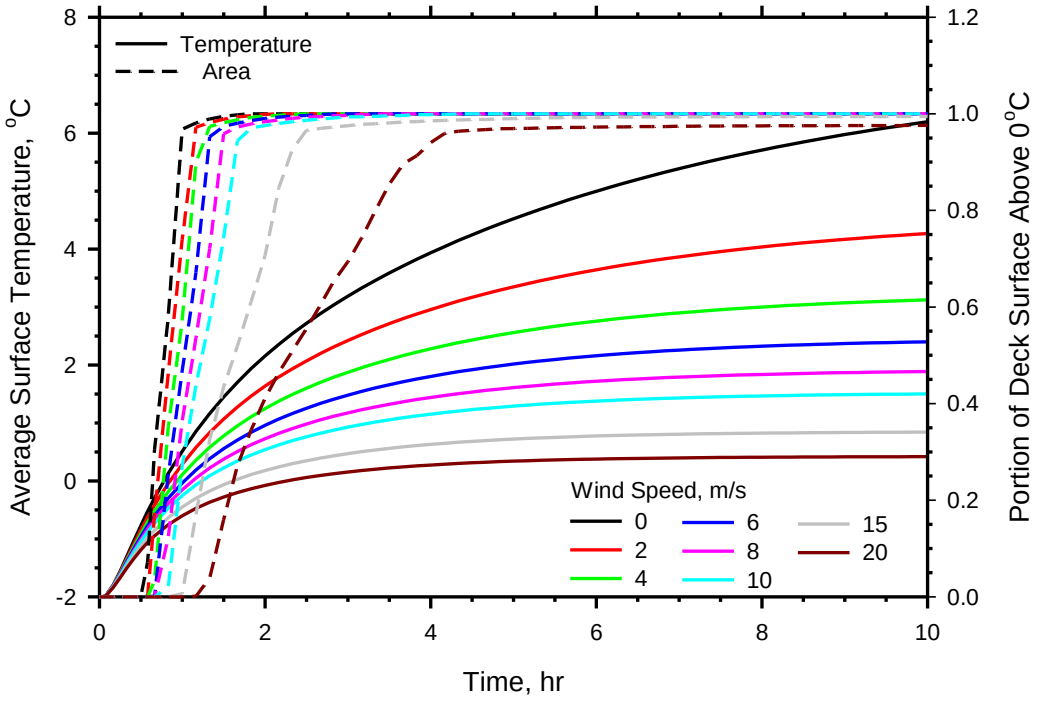

Figure 8-20. Average surface temperatures and area of deck surface above 0°C for different wind speeds.

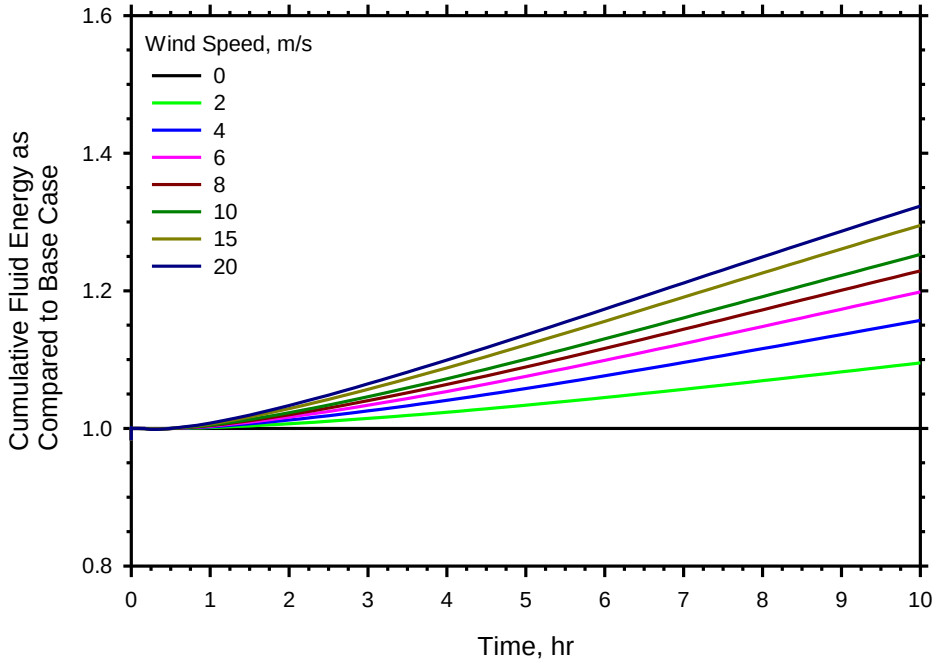

Figure 8-21. Ratio of the cumulative injected energy to the slab as compared to the base case for different wind speeds.

Figure 8-21 displays the cumulative amount of energy injected to the slab over time as compared to the base case for different wind speeds. Notice that the trends are not constant and increase at a non-linear rate over time. Figure 8-22a plots these curves as a function of wind speed using different time contours. As the wind speed increases, so does the amount of injected energy, however, the increase is most pronounced when moving from 0 to 5 m/s, and then becomes less pronounced with each 5 m/s increase in wind speed. The amount of injected energy also increases over time, and as it does so does the rate at which the injected energy increases vs wind speed. That is, when moving from the time contour of 0.25 hr to the time contour of 1 hr, not much additional energy is required, regardless of wind speed. However, when moving from the 1 hr to the 4 hr contours, not only does the amount of injected energy increase, but so does the rate of increase in that energy when moving from lower to higher wind speeds. This ultimately means that higher wind speeds not only require more energy, but will require significantly more energy the longer the system is operated and/or the longer the higher wind speeds persist.

The rate at which the energy is delivered to the deck as compared to the base case is compared in Figure 8-22b. The trends are nearly identical to those of the cumulative energy in that the longer the system operates and/or the higher the sustained wind speeds, the greater the rate at which energy is imparted to the deck. This can be significant as compared to the base case as ratios greater than 1.4 are observed for higher wind speeds at larger time intervals. This means that the subsurface component of the system must be able to supply the heat energy at a higher sustained rate over time with increasing wind speeds.

It is interesting to observe how energy is distributed in these systems with differing wind speeds. Figure 8-22c compares the amount of energy going to heat the slab as compared to the base case and Figure 8-22d compares the amount of energy that is lost to the environment through convection and radiation as compared to the base case. For increasing wind speeds the amount of energy going to the slab with respect to the base case decreases despite an increase in the amount of injected energy (see Figure 8-22a). This is because the amount of energy that is lost as compared to the base case increases with increasing wind speed as shown in Figure 8-22d. Observe the high ratios (greater than 2) observed in Figure 8-22d. The reason for these high ratios will be discussed shortly.

The amount of energy lost to radiation and convection as compared to the base case is shown in Figure 8-22e and Figure 8-22f, respectively. As the wind speed increases, the amount of energy lost to radiation decreases with respect to the base case, and this decrease becomes more pronounced with longer heating times. This can be attributed to the lower average deck surface temperatures (Figure 8-20) associated with higher wind speeds as the radiative heat flux depends on the temperature difference between the surface and the environment. The amount of energy lost to convection, however, increases with respect to the base case for higher wind speeds. This is due to the fact that the base case considered natural convection only whereas wind speeds 2 m/s and higher will induce forced convection and results in much higher convective heat fluxes with convective energy losses 10 to 25 times higher than that of the base case for higher wind speeds. The much higher convective losses are ultimately what cause the higher lost energy ratios observed in Figure 8-22d.

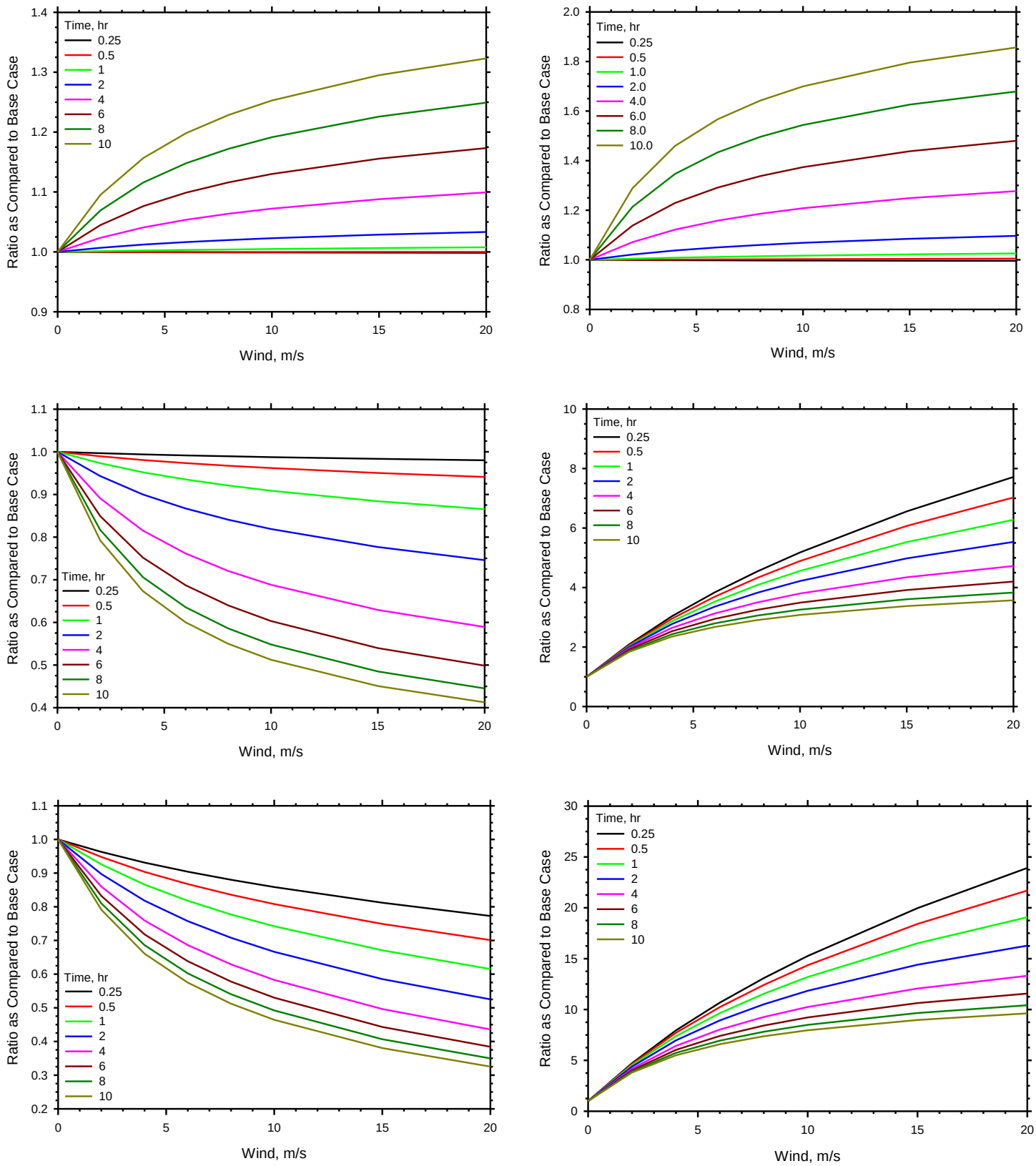

Figure 8-22. Ratio as compared to the base of cumulative energy injected to the slab (a-top left), cumulative energy injected to the slab (b-top right), slab heating flux per surface area (c-mid left), energy lost to the environment (d-mid right), energy lost to radiation (e-bottom left), and energy lost to convection (f-bottom right) as a function of wind speed.

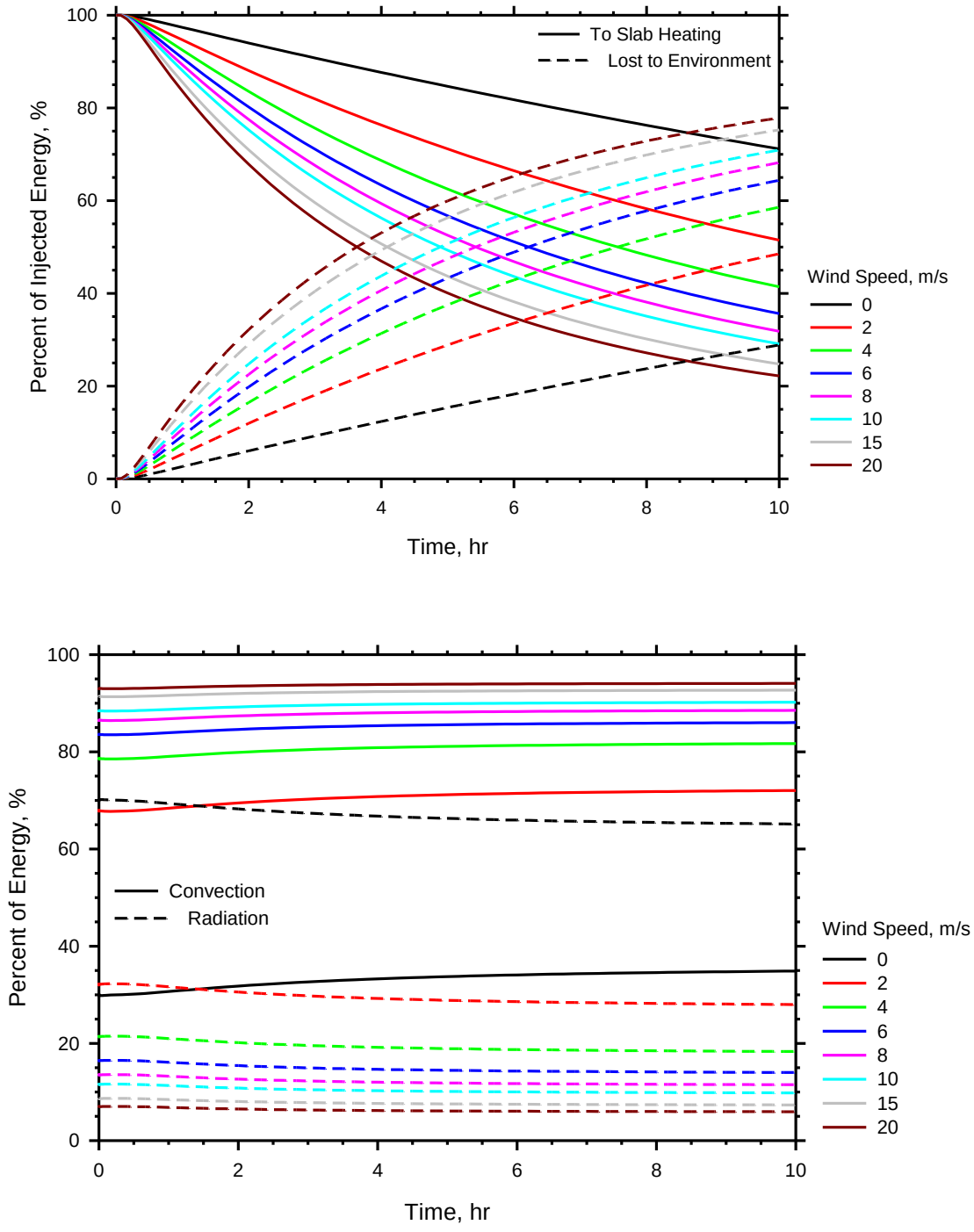

Figure 8-23. Distribution of injected energy to the slab (a-top) and the mechanism by which energy was lost to the environment (b-bottom) for different wind speeds.

This point is further confirmed by Figure 8-23a, which shows the percent of energy used to heat the slab as well as the percent of energy that was lost. The percent of the lost energy that went to convection and radiation is then shown in Figure 8-23b. For increasing wind speeds, the percent of energy that is lost

drastically increases. After 10 hours, the percent of energy that was lost for the base case is just under 30%, whereas it is over 75% for a wind speed of 20 m/s, and almost 50% for a wind speed of 2 m/s. Note that at times less than 3.5 hours, at least 50% of the injected energy is going to heat the slab, regardless of wind speed. From Figure 8-23b, it can be seen that for wind speeds of 2 m/s and greater, at least two times more energy is lost to convection than radiation. The percent lost is fairly constant over time. For wind speeds of 15 and 20 m/s, over 90% of the energy lost is due to convection. Of the 50% energy that is lost after 10 hours for a wind speed of 2 m/s, over 70% is from convection. This is compared to just 30% energy lost, and of that only 35% due to convection for the base case. This is why the convective energy loss ratios are so high in Figure 8-23b.

8.4.6. Effects of Circulation Fluid Flow Rate

Flow rate is often a factor within the system operator's control. Though there may be other variables that govern a given flow rate such as frictional resistance, cavitation, pump size, etc., it is helpful to understand how the flow rate may impact system performance. Flow rates ranging from 5 to 17 L/min were tested using the numerical model. Figure 8-24 compares the average surface temperature over time for the given flow rates. Higher flow rates yield higher average surface temperatures as well as quicker deck surface heating times. Though there is a big difference between a flow rate of 5 L/min and one of 8 L/min, there is not as much of a difference between a flow rate of 11 L/min and one of 17 L/min suggesting an upper limit to the flow rate where its influence on faster heating times diminishes. This will be discussed further.

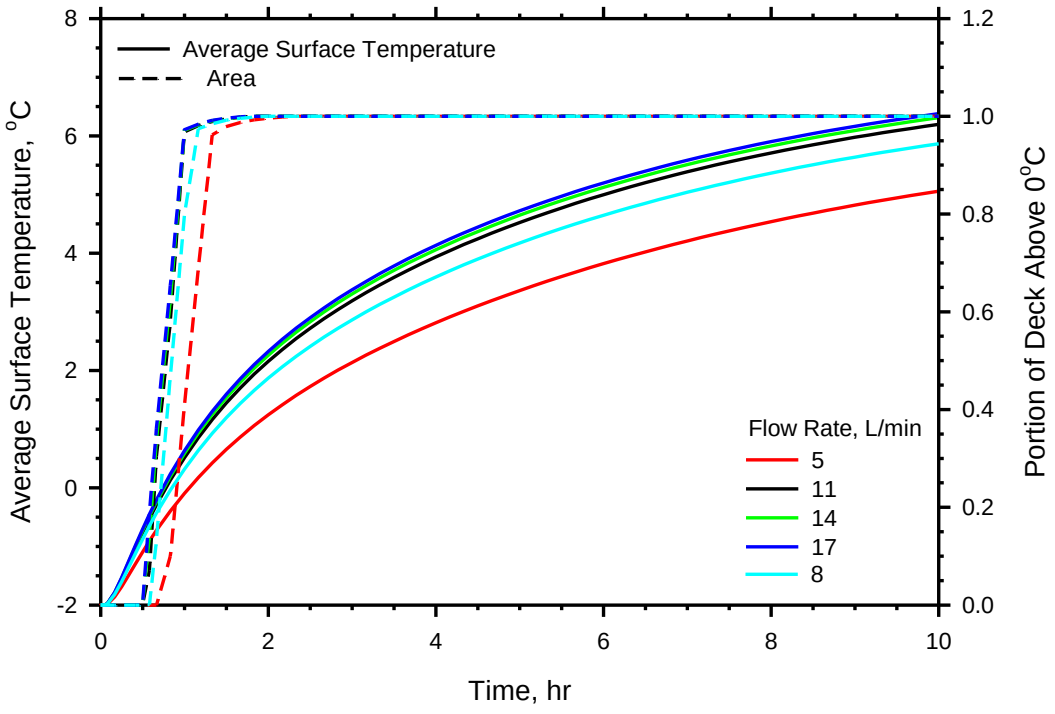

Figure 8-24. Average surface temperatures and area of deck surface above 0°C for different flow rates.

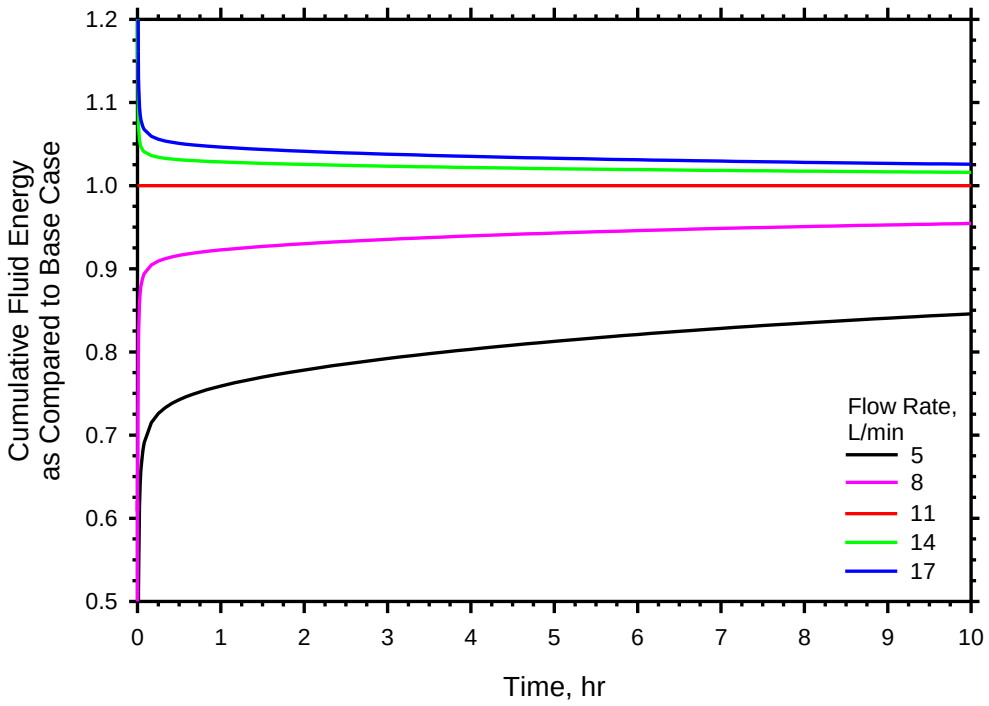

Figure 8-25. Ratio of the cumulative injected energy to the slab as compared to the base case for different flow rates.

When compared to the base case, the cumulative amount of energy delivered to the bridge deck is not constant with time, as shown in Figure 8-25. Lower flow rates deliver less energy to the deck and higher flow rates deliver more, but all values approach that of the base case with longer heating times. This is shown in Figure 8-26a which plots the cumulative amount of energy imparted to the deck relative to the base case as a function of flow rate for given time contours. As time increases the contours become flatter, that is, approach a ratio of one with the base case. It should also be noted from Figure 8-25 and Figure 8-26a that there is a large difference in the amount of imparted energy between flow rates of 5 L/min and 11 L/min, but not as much of a difference between flow rates of 11 L/min and 17 L/min. For instance, at heating times of 3 hours or less a flow rate of 5 L/min imparts less than 80% of the energy to the slab as the base case whereas a flowrate of 17 L/min only imparts 7% more. As shown in Figure 8-26b, lower flow rates impart energy to the bridge deck at a lower rate than higher flow rates. As noticed with both deck temperatures (Figure 8-24) and cumulative imparted energy (Figure 8-25), there is an upper threshold as to the rate of energy transfer to the slab.

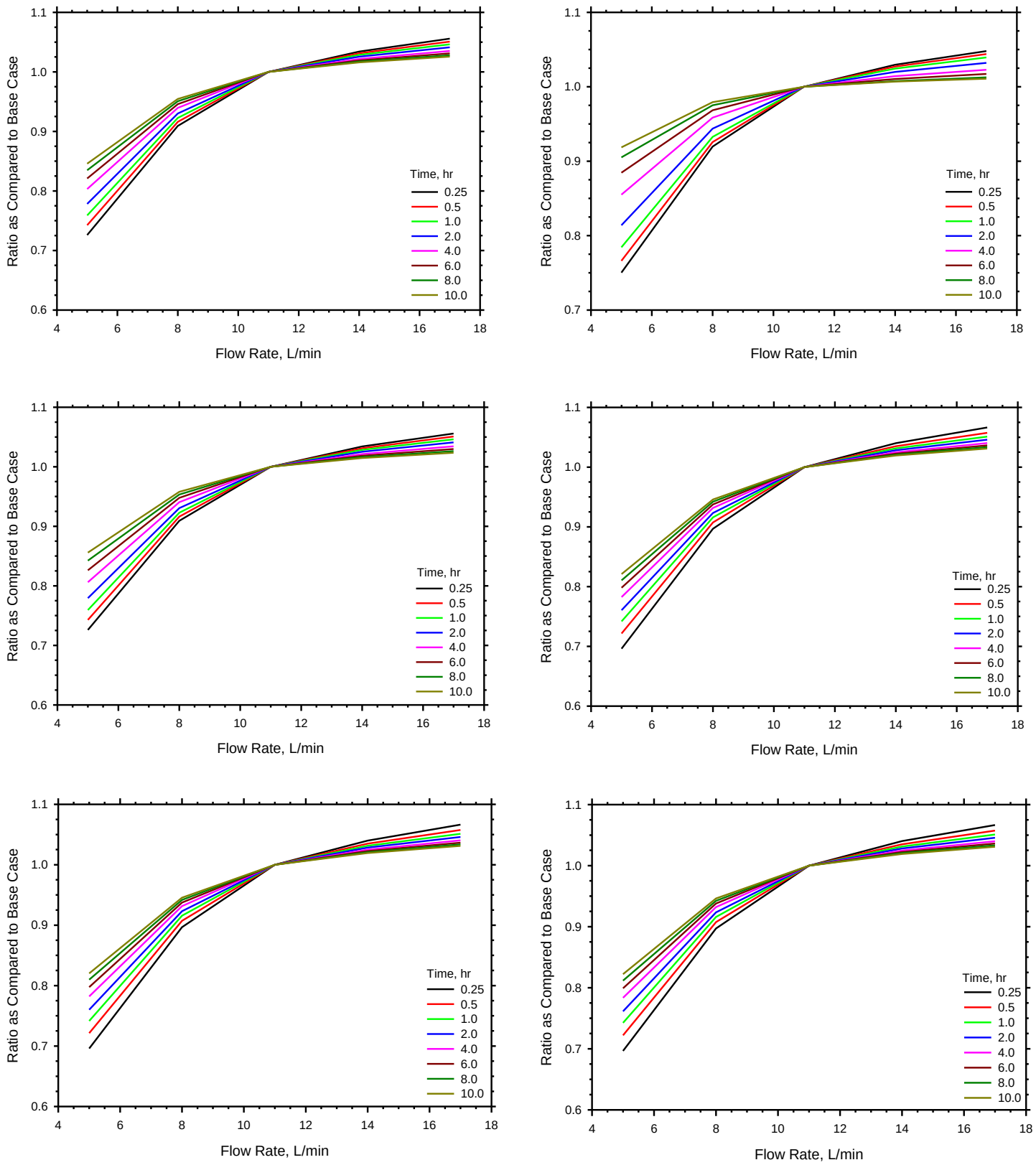

Figure 8-26. Ratio as compared to the base of cumulative energy injected to the slab (a-top left), cumulative energy injected to the slab (b-top right), slab heating flux per surface area (c-mid left), energy lost to the environment (d-mid right), energy lost to radiation (e-bottom left), and energy lost to convection (f-bottom right) as a function of flow rate.

Figure 8-26c-f compares the amount of energy going to heat the slab, the amount of energy lost, the amount of lost energy to radiation, and the amount of lost energy to convection. Their trends resemble that of Figure 8-26a and Figure 8-26b where the values approach that of the base case over time, and higher flow rates have ratios higher than the base case and lower flow rates have ratios lower than the base case. That is, higher flow rates impart more energy to the slab than the base case, but also lose more energy to the environment than does the base case.

Figure 8-27 shows the percent of energy distribution of each case. As can be seen, they are almost identical in terms of the percent of energy lost and the mechanism by which that energy is lost (convection or radiation). So even though lower flow rates lose less energy to the environment than the base case and cases with higher flow rates, they do not utilize a higher percent of the imparted energy for slab heating.

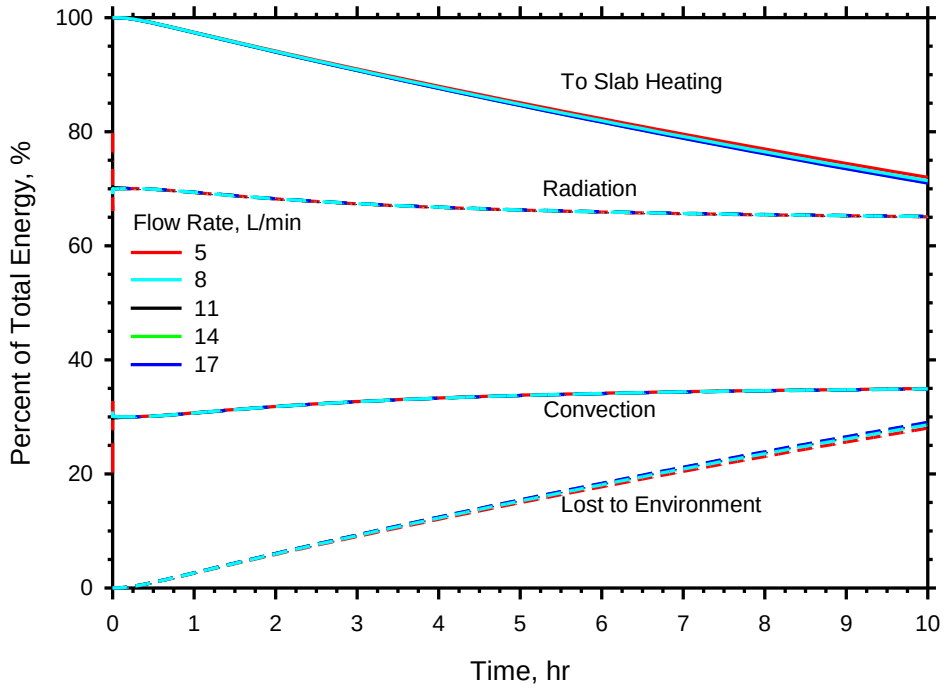

Figure 8-27. Distribution of injected energy to the slab and the mechanism by which energy was lost to the environment for different flow rates.

It has been noted that there appears to be an upper limit to the flow rate, where further increase adds little benefit to the system with regards to delivering more heat and faster heating times. To understand this, it is important to understand the mechanism of slab heating. The reason an increased flow rate is more effective at heating the system is because it is delivering energy to the system at a faster rate thus a higher flow rate will be able to heat the deck more quickly than a lower flow rate. However, the energy that is delivered to the deck is in the form of a heated fluid. At some point two factors will limit the amount of energy that can be transferred from the fluid to the deck: the thermal limitations of the fluid, pipe, and bridge deck; and thermal gradient between the circulation fluid and the bridge deck slab. Both of these factors govern how quickly the energy can be transferred from the fluid to the slab. As the flow rate increases so does the potential for higher amounts of energy to be delivered to the deck, but the amount

of energy actually transferred to the deck is a function of the thermal properties of the materials involved and temperature gradients within the deck.

This has several implications for practice. One is that the flow rate should be kept high enough that the deck is receiving as much energy as it can absorb for a given set of weather conditions. Beyond a certain point, however, the deck will largely be unable to absorb any more energy. More extreme conditions (ie. lower ambient temperatures, higher wind speeds, higher snow fall rates, lower inlet fluid temperatures, etc.) will allow for a higher flow rate as more extreme temperature gradients will exist between the circulation fluid and the bridge deck.

8.4.7. Effects of Thermal Conductivity

Various factors can influence the thermal conductivity of the concrete including type of cement and aggregate used, additives, moisture content, and saturation (Rhodes 1978). Figure 8-28 compares the average surface temperatures and surface heating times for thermal conductivity values ranging from 1.5 to 4.0 W/m-K. Higher thermal conductivities lead to higher average surface temperatures and shorter deck heating times as higher thermal conductivities facilitate the more efficient transfer of energy. As shown in Figure 8-29, when compared to the base case the cumulative imparted energy to the bridge deck is not constant over time. Lower thermal conductivities impart less energy and higher thermal conductivities impart more energy with the values decreasing and increasing, respectively, initially and then approaching the base case with increasing time. A thermal conductivity of 1.5 W/m-K only imparts 85% of the energy of the base case whereas a thermal conductivity of 4.0 W/m-K imparts about 5% more. When this ratio is plotted as a function of thermal conductivity at various points within the heating operation (Figure 8-30a), it can be seen that the contours initially become steeper before flattening out as the heating times increase. Figure 8-30b, which simply shows the rate of energy transfer for different time intervals and thermal conductivities, displays the same trends.

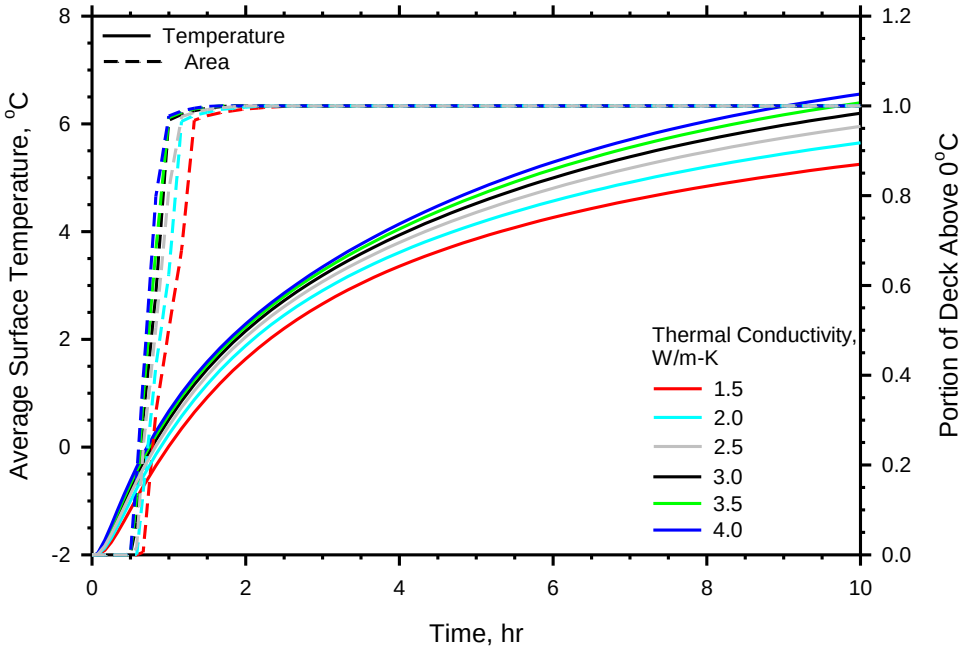

Figure 8-28. Average surface temperatures and area of deck surface above 0°C for different slab thermal conductivities.

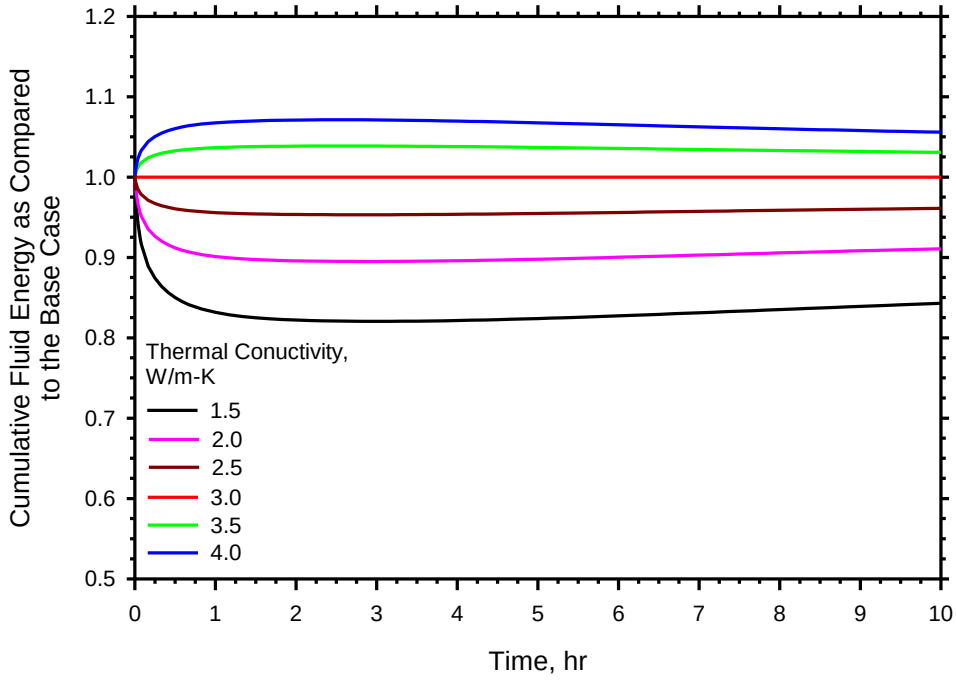

Figure 8-29. Ratio of the cumulative injected energy to the slab as compared to the base case for different slab thermal conductivities.

Figure 8-30c-f compares the amount of energy going to heat the slab, the amount of energy lost, the amount of lost energy to radiation, and the amount of lost energy to convection. Regarding the amount of energy going to heat the slab, the trend resembles that of Figure 8-30a in that the slopes initially steepen (deviate away from the base case) but then flatten with time (approach the base case). For the amount of energy lost and the associated convection and radiation, the trends are markedly different as they are initially quite steep (far from the base case) but then rapidly approach the base case within the first two hours. They then levels off with higher heating times.

The percent of injected energy going to heat the slab and lost to the environment changes little between the different thermal conductivities and is shown in Figure 8-31. Likewise, the percent of energy that is lost to the environment in the form of convection or radiation changes little. Ultimately, higher thermal conductivities do allow more energy to be imparted to the bridge deck and for the surface to both heat above 0^{o}C more quickly and to a higher temperature.

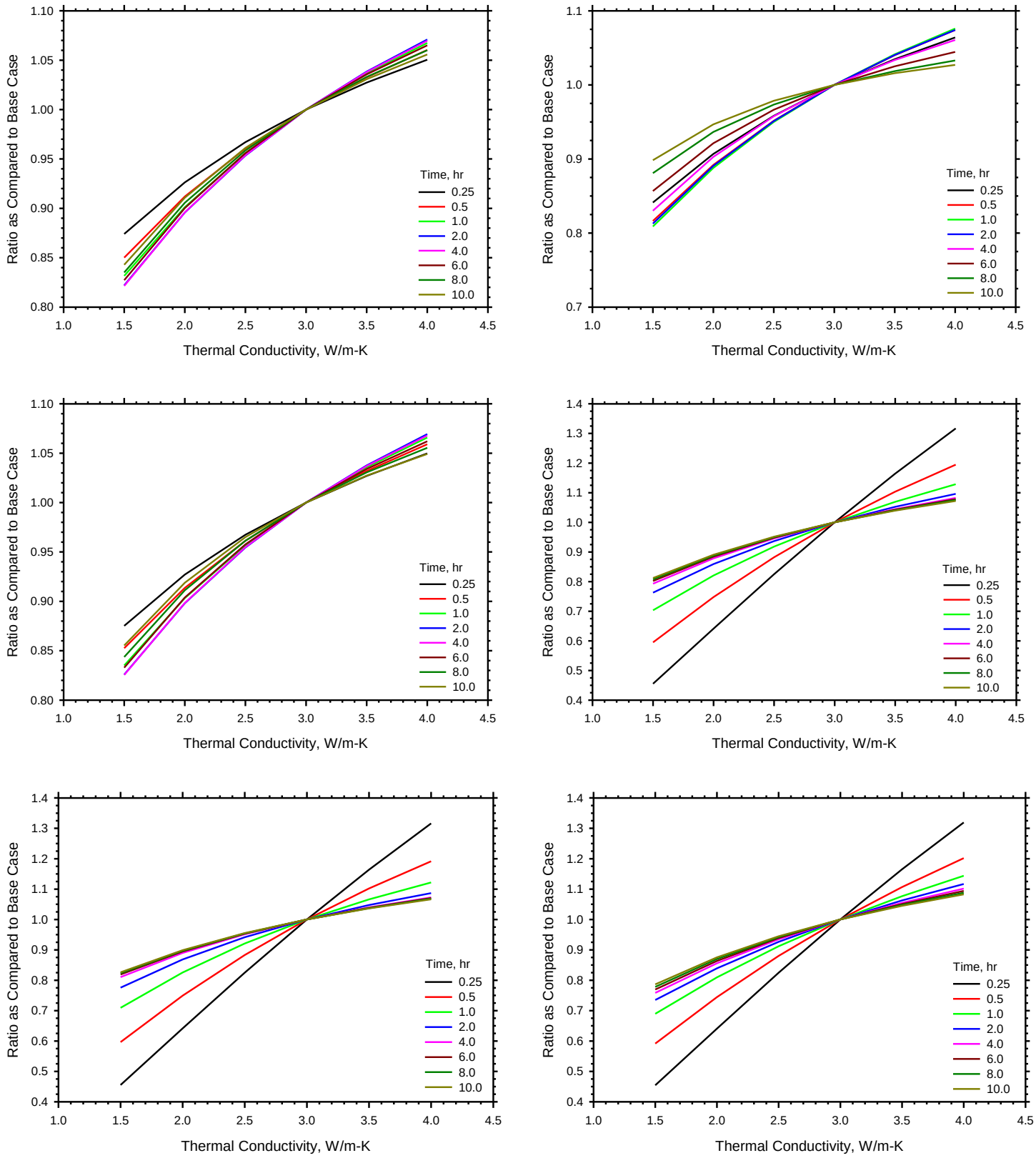

Figure 8-30. Ratio as compared to the base of cumulative energy injected to the slab (a-top left), cumulative energy injected to the slab (b-top right), slab heating flux per surface area (c-mid left), energy lost to the environment (d-mid right), energy lost to radiation (e-bottom left), and energy lost to convection (f-bottom right) as a function of thermal conductivity.

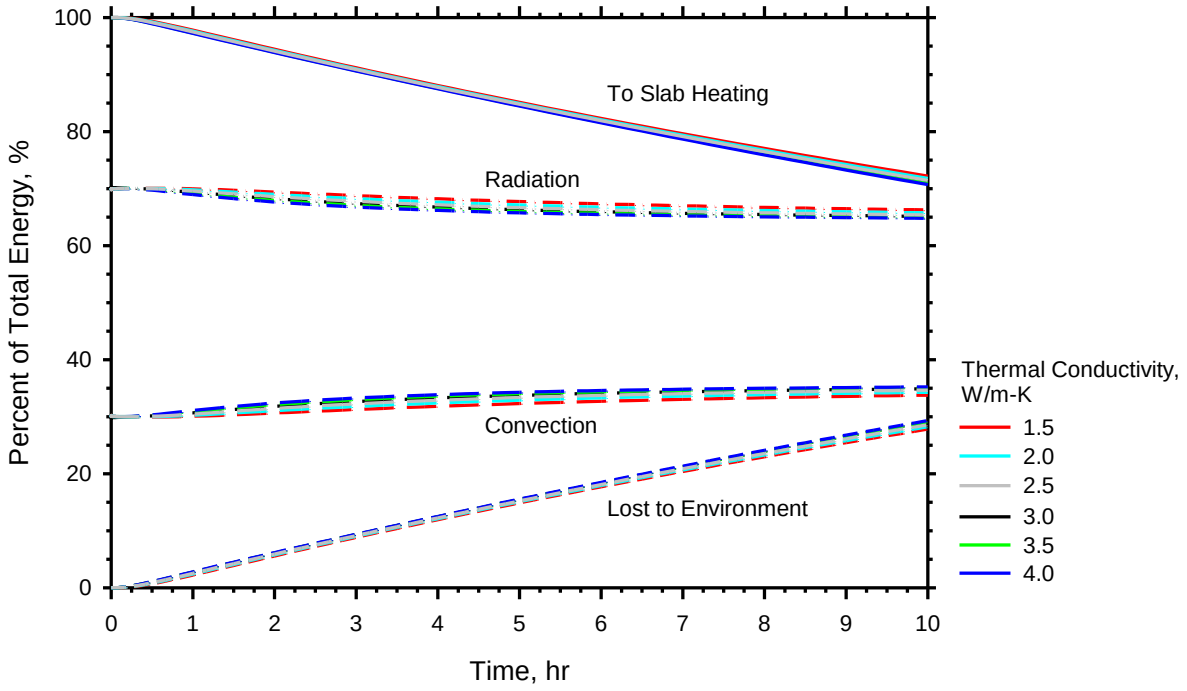

Figure 8-31. Distribution of injected energy to the slab and the mechanism by which energy was lost to the environment for different thermal conductivities.

8.4.8. Effects of Specific Heat Capacity

The specific heat capacity, like the thermal conductivity, is influenced by various factors. Two additional heat capacities were tested: 700 J/kg-K, and 1000 J/kg-K. The lower heat capacity allowed for quicker heating times and higher average surface temperatures as shown in Figure 8-32. It actually did this by imparting between 2 and 7% less energy to the slab as shown in Figure 8-33, whereas the higher heat capacity imparted between 1 and 5% more energy. When plotted as a function of heat capacity, the ratios approximately linearize for various time increments as shown in Figure 8-34a. As heating time increases, the values further deviate from the base case which means the higher heat capacity scenario continues to increase in the amount of imparted energy to the slab relative to the base case whereas the lower heat capacity scenario decreases in the same regard. Figure 8-34b displays the slab heating flux per surface area and also shows that as time increments increase, the fluxes continue to deviate from the base case. This phenomenon of observing increasing deck surface temperatures with less imparted energy will be discussed further.

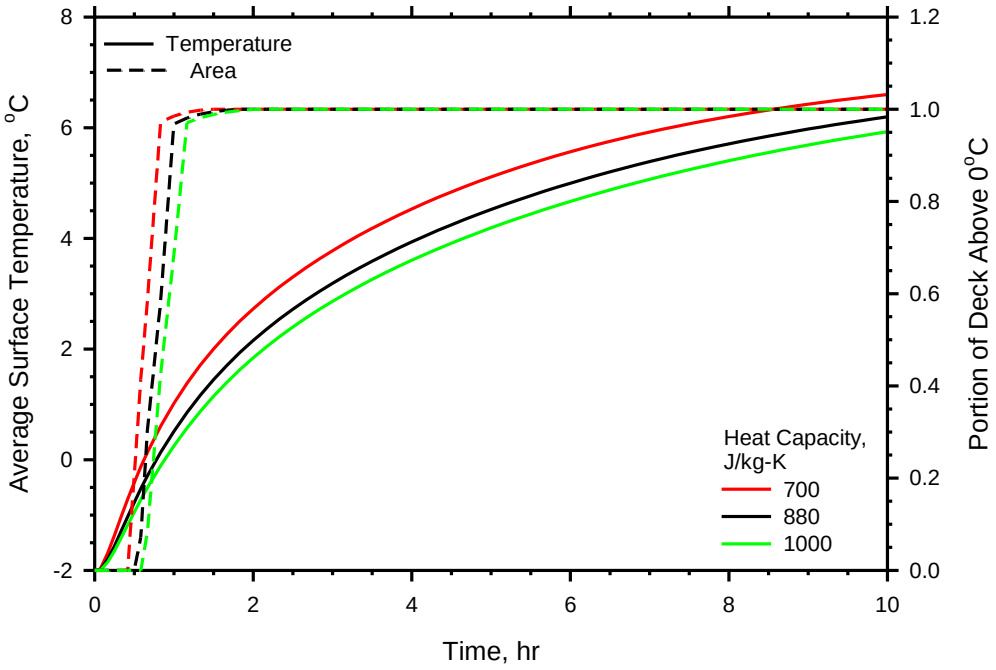

Figure 8-32. Average surface temperatures and area of deck surface above 0°C for different slab heat capacities.

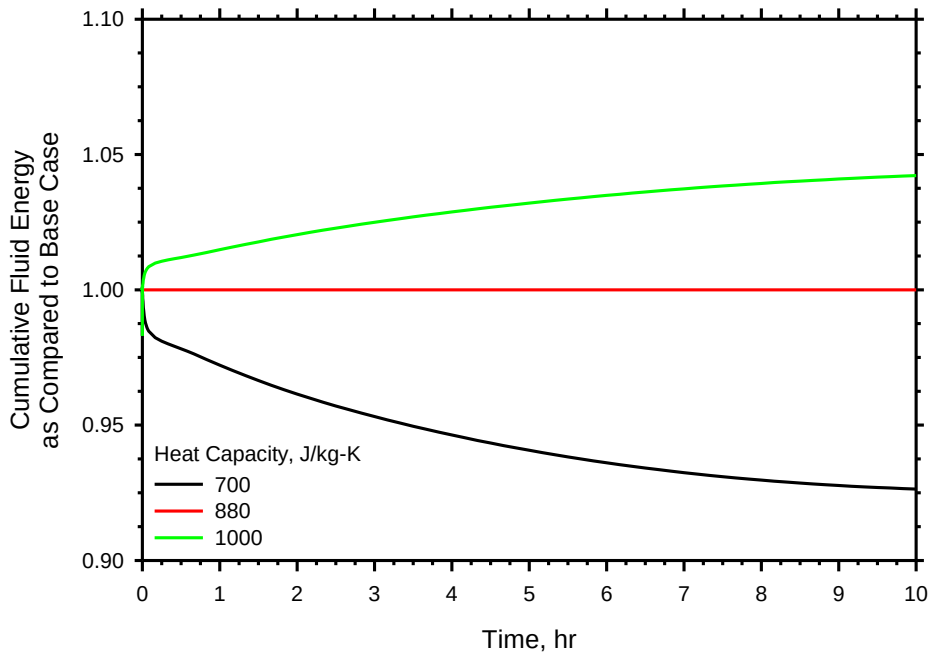

Figure 8-33. Ratio of the cumulative injected energy to the slab as compared to the base case for different slab heat capacities.

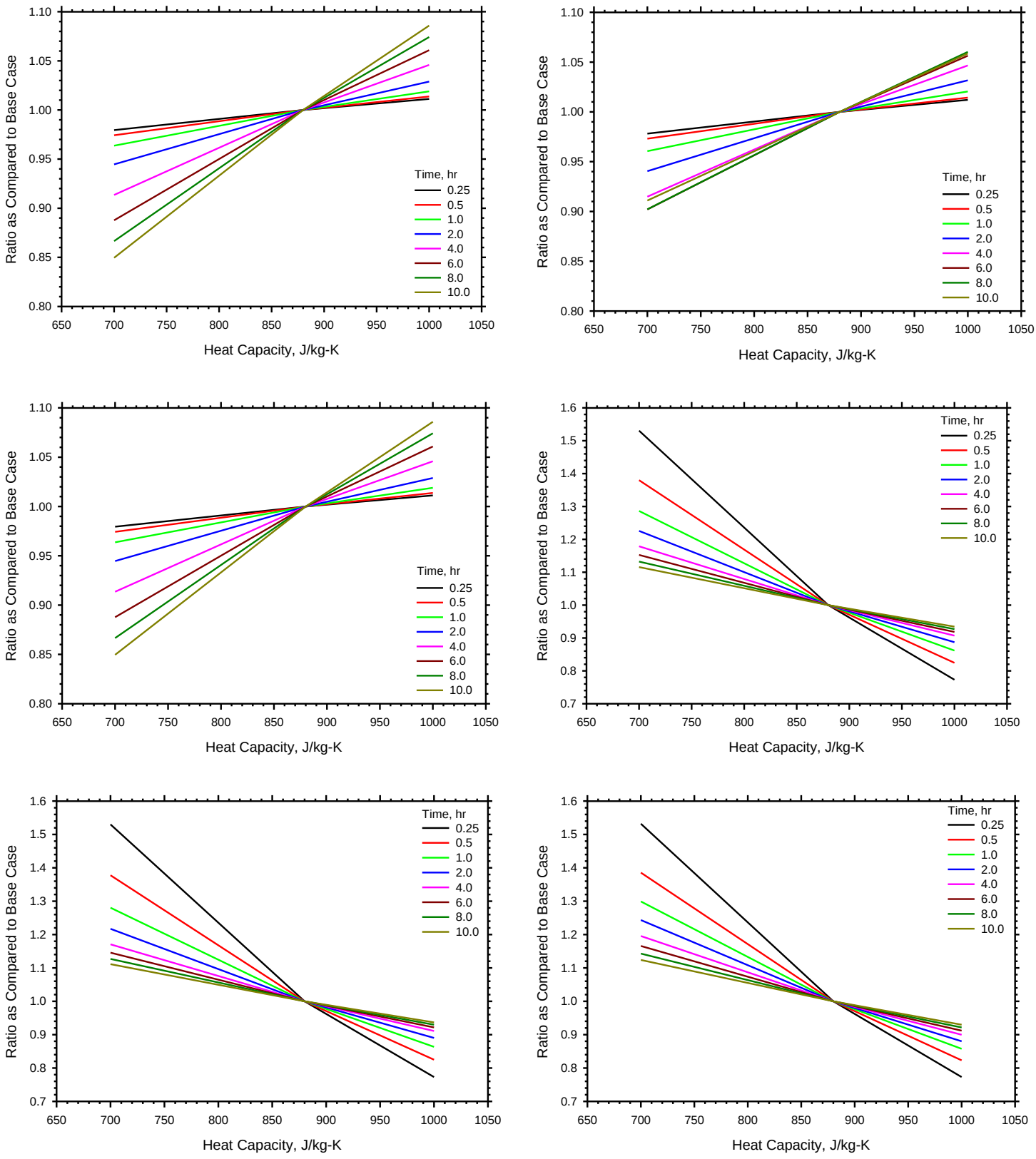

Figure 8-34. Ratio as compared to the base of cumulative energy injected to the slab (a-top left), cumulative energy injected to the slab (b-top right), slab heating flux per surface area (c-mid left), energy lost to the environment (d-mid right), energy lost to radiation (e-bottom left), and energy lost to convection (f-bottom right) as a function of heat capacity.

Figure 8-34c-f compares the amount of energy going to heat the slab, the amount of energy lost, the amount of lost energy to radiation, and the amount of lost energy to convection. The amount of energy used for slab heating increases relative to the base case as the heat capacity increases, and decreases as the heat capacity decreases. These trends become more extreme for longer heating times. However, the amount of energy lost to the environment increases with decreasing heat capacity and decreases with increasing heat capacity. These trends, however, become less extreme for longer heating times. The same is true for the amount of energy lost to convection and radiation relative to the base case.

The percent of injected energy that goes to deck heating and that is lost to the environment is shown in Figure 8-35. The amounts are not equal for differing heat capacities. Bridge decks with higher heat capacities are actually more efficient in that they lose less of their injected energy to the environment than do lower heat capacity bridge decks. Even though more energy is injected to bridge decks with higher heat capacities, percentagewise less of that injected energy is lost to the environment.

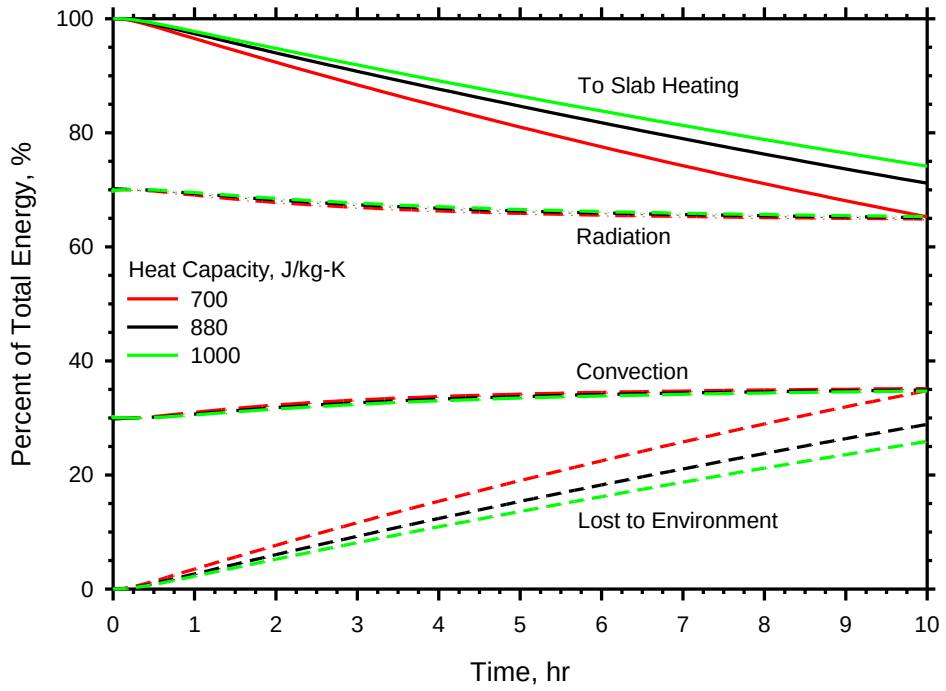

Figure 8-35. Distribution of injected energy to the slab and the mechanism by which energy was lost to the environment for different heat capacities.

Lower heat capacities allow the deck to heat more quickly and to a higher temperature than higher heat capacities because not as much energy is stored in the deck. As previously seen in Figure 8-34a, a higher portion of the imparted energy went to slab heating for the higher heat capacity scenario. This is due to the fact that decks with higher heat capacities store more energy and take longer to heat. As such, the temperatures at the surfaces will be lower resulting in less environmental losses. Thus higher heat capacities are more efficient, but require more energy to be injected and/or longer heating times in order to heat the slab to the same temperature as for lower heat capacities. Whereas lower heat capacities may be more desirable for more rapid heating of the deck, they can run into problems in storing energy. For

instance, two decks that have been heated to the same surface temperature begin to melt snow during a storm. The deck with the higher heat capacity will have more stored internal energy that can be used to melt the falling snow than will the deck with the lower heat capacity. Furthermore, decks with lower heat capacities will be more subject to thermal 'swings' in that when the ambient temperature rapidly changes, the deck will increase/decrease in temperature more quickly and to a greater degree than will a deck with a higher heat capacity.

8.4.9. Effect of Insulation Underneath the Slab

It has been mentioned previously that bridges lose energy from the top and bottom surfaces. If the bottom of the slab were insulated, it would prevent some of that energy loss. To determine the effect insulation on the bottom surface would have during heating operations, several cases from above were rerun with an insulated undersurface. The cases that were rerun include the base case; wind speeds of 2, 8, and 15 m/s; and ambient temperatures of -4, -6, -8, and -10^{o}C. The results are compared against their respective cases with no insulation.

8.4.9.1. Effect with Different Wind Speeds

The average surface temperatures as well as the time it takes the surface of the deck to heat above 0^{o}C for the cases of wind with insulation is shown in Figure 8-36. In each case, the average surface temperature of the case with insulation is greater than the average surface temperature of the comparative case with no insulation. However, this effect is mainly seen at later times as the time it takes the surface to heat above 0^{o}C remains virtually unchanged for each case. This indicates that insulation may not help immediately after the system is turned on in terms of heating the slab more quickly, however it can help in the longer term by retaining more energy, as represented by the higher slab surface temperatures. This is accomplished with a lower slab heating rates per surface area relative to the cases with no insulation as shown in Figure 8-37. Thus, insulation does increase the efficiency of these systems as the deck heats to a higher temperature using lower heating rates, and ultimately requiring less energy, which is shown in Figure 8-38.

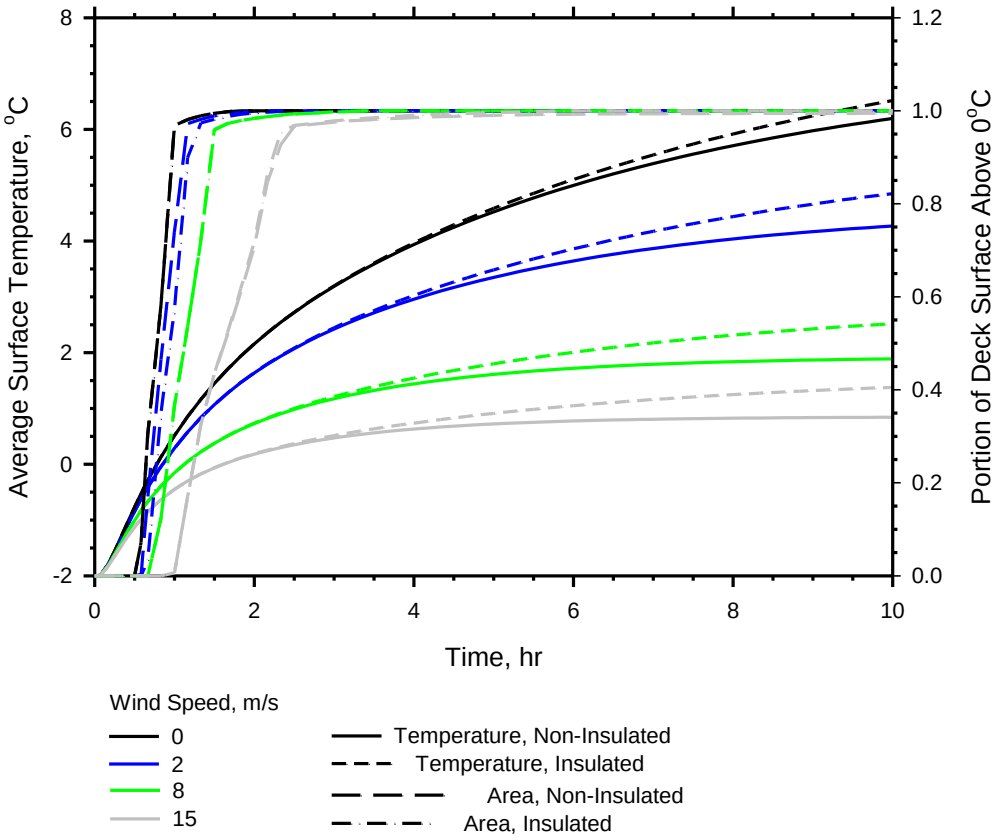

Figure 8-36. Average surface temperatures and area of deck surface above 0°C for different wind speeds comparing the effect of slab insulation.

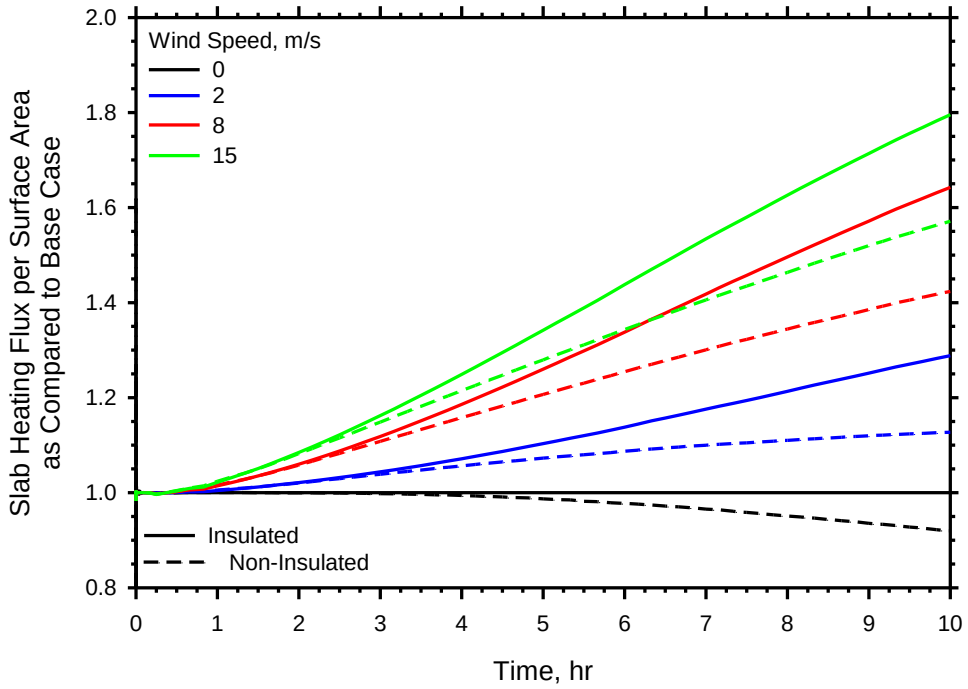

Figure 8-37. Average slab heating flux per surface area for different wind speeds comparing the effect of slab insulation.

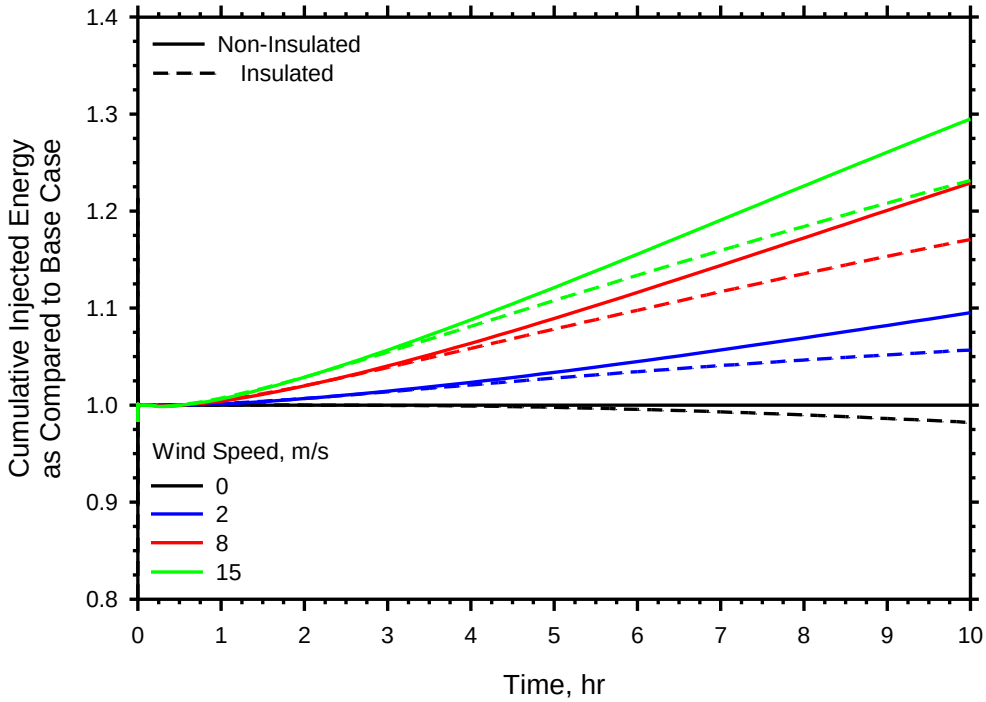

Figure 8-38. Cumulative injected energy for different wind speeds comparing the effect of slab insulation.

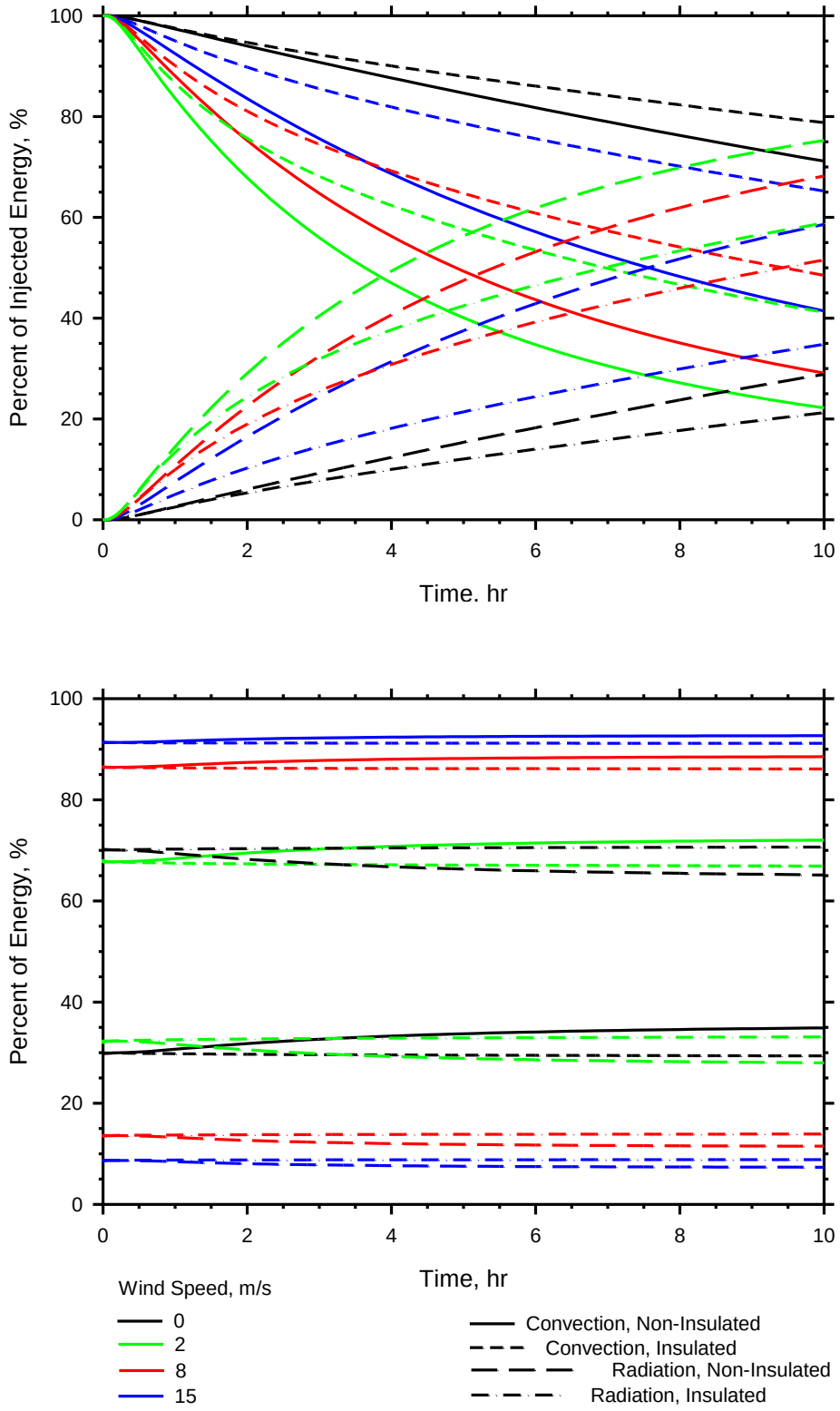

Figure 8-39. Distribution of injected energy to the slab (a-top) and the mechanism by which energy was lost to the environment (b-bottom) for different wind speeds comparing the effects of insulation.

Figure 8-39a displays the percentage of energy that is retained or lost for each of the cases. As shown, in every case insulation increases the amount of energy used for heating and decreases the amount of energy that is lost to the environment. Insulation helps by preventing energy from leaving the bottom of the slab to the environment which then allows more of the injected energy to heat the deck, increasing the efficiency and requiring less energy than cases with no insulation. Regarding the energy that is lost the environment, Figure 8-39b shows that there is a slight change in the amount that is lost due to convection or radiation in cases with insulation as less energy is lost to radiation and more is lost to convection. Because insulation prevents energy loss to both radiation and convection underneath the deck, it is not expected that these values will change significantly. It was shown in the base case that roughly the same percentage is lost to convection and radiation on the top and bottom of the deck.

8.4.9.2. Effect with Ambient Temperature

The average surface temperatures as well as the time it takes the surface of the deck to heat above 0^{o}C for the cases of different ambient temperatures with insulation is shown in Figure 8-40. Resembling the cases with wind, in each case, the average surface temperature of the case with insulation is greater than the average surface temperature of the comparative case with no insulation. However, the average surface temperatures of the cases with insulation are almost identical to the cases with no insulation for the first 3 to 4 hours. Likewise, the deck surface heating times are almost identical indicating that insulation has almost no effect on the amount of time it takes the deck surface to heat above 0^{o}C. When examining the amount of injected energy as compared to the base case, the insulated cases are almost identical to their respective non-insulated cases for the first 4 hours as shown in Figure 8-41. As heating time increases, the insulation appears to have more effect as the average surface temperatures increase relative to the non-insulated cases. The insulation is obviously helping as the average surface temperatures increase despite less energy being injected relative to their respective cases (Figure 8-41). This is shown in Figure 8-42a as a higher percentage of injected energy goes to heating for the cases with insulation. The percentages of energy that was lost to convection or radiation (Figure 8-42b) were almost identical for all of the insulated cases.

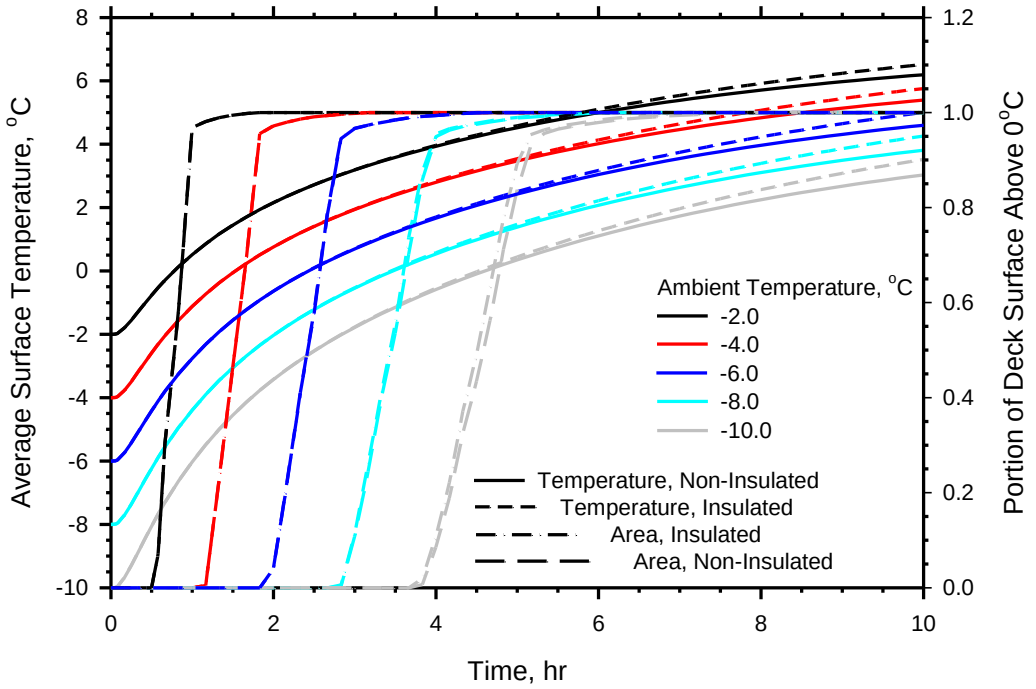

Figure 8-40. Average surface temperatures and area of deck surface above 0°C for different ambient temperatures comparing the effect of slab insulation.

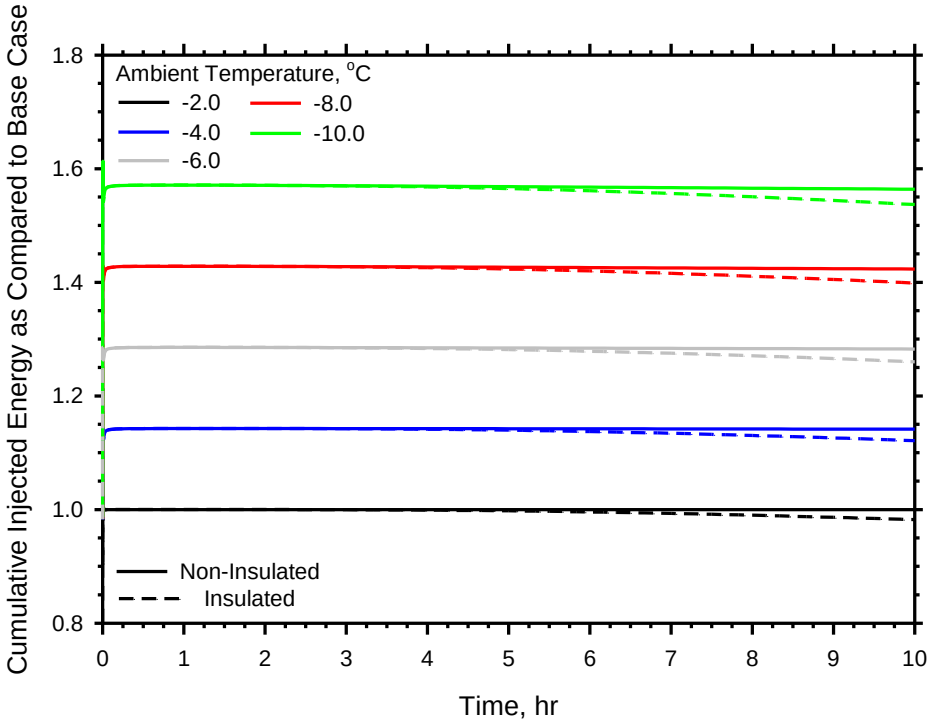

Figure 8-41. Cumulative injected energy for different ambient temperatures comparing the effect of slab insulation.

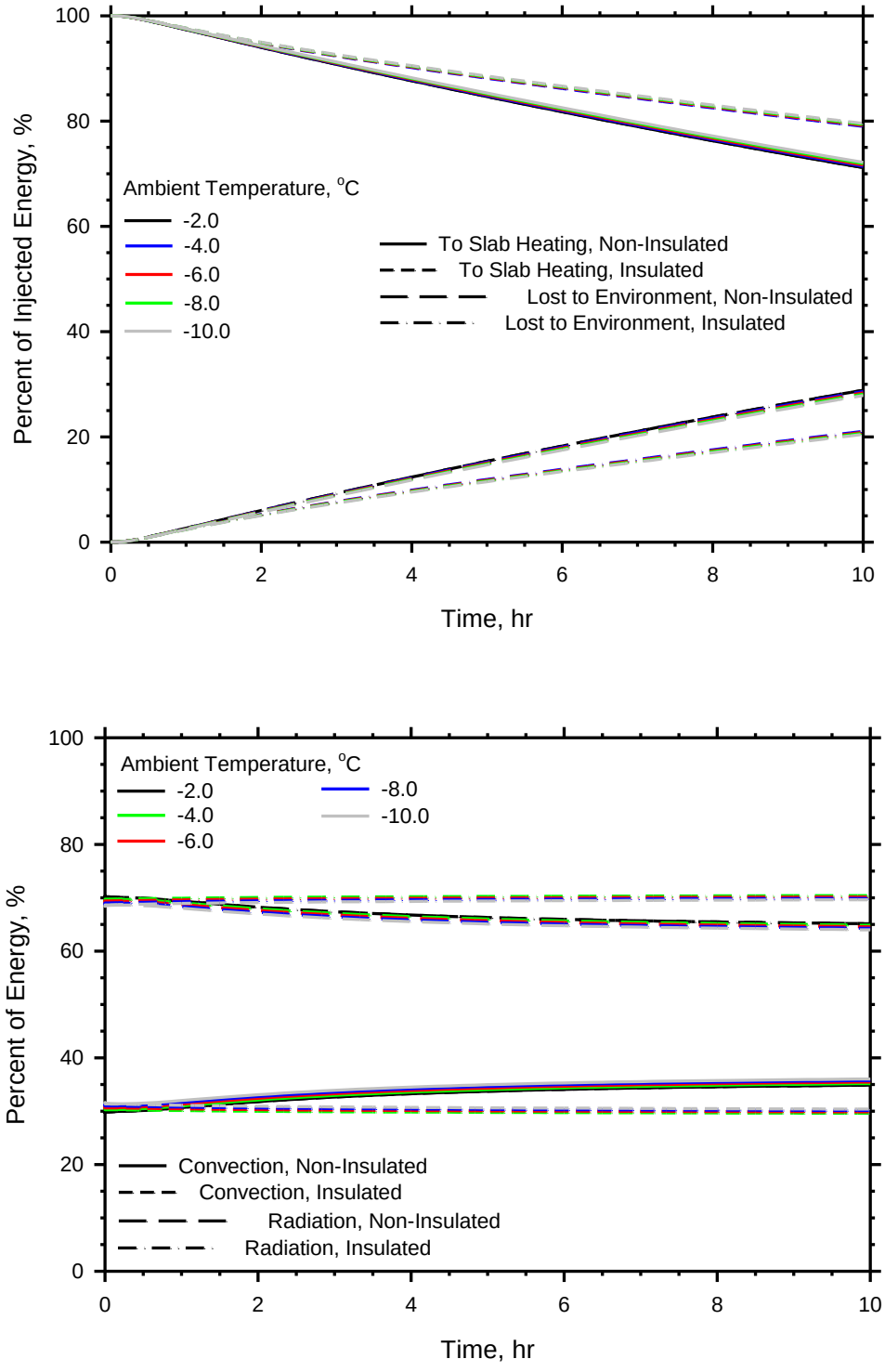

Figure 8-42. Distribution of injected energy to the slab (a-top) and the mechanism by which energy was lost to the environment (b-bottom) for different ambient temperatures comparing the effects of insulation.

The slab heating rates per surface area relative to the base case are shown in Figure 8-43. Over time, the cases utilizing insulation have lower slab heating rates than their respective cases with no insulation. It also seems that insulation does not have a proportionately greater effect for lower ambient temperatures than for higher ones as the trends are all identical from Figure 8-41 and Figure 8-43. Ultimately insulation does help in terms of allowing more of the injected energy to go to heating the slab as opposed to being lost, however the real benefits in terms of increased surface temperature are not realized until after several hours of heating, after the surface has already heated to above 0°C. Thus, it will help in terms of allowing the system to operate more efficiently but may not help it to initially heat more quickly.

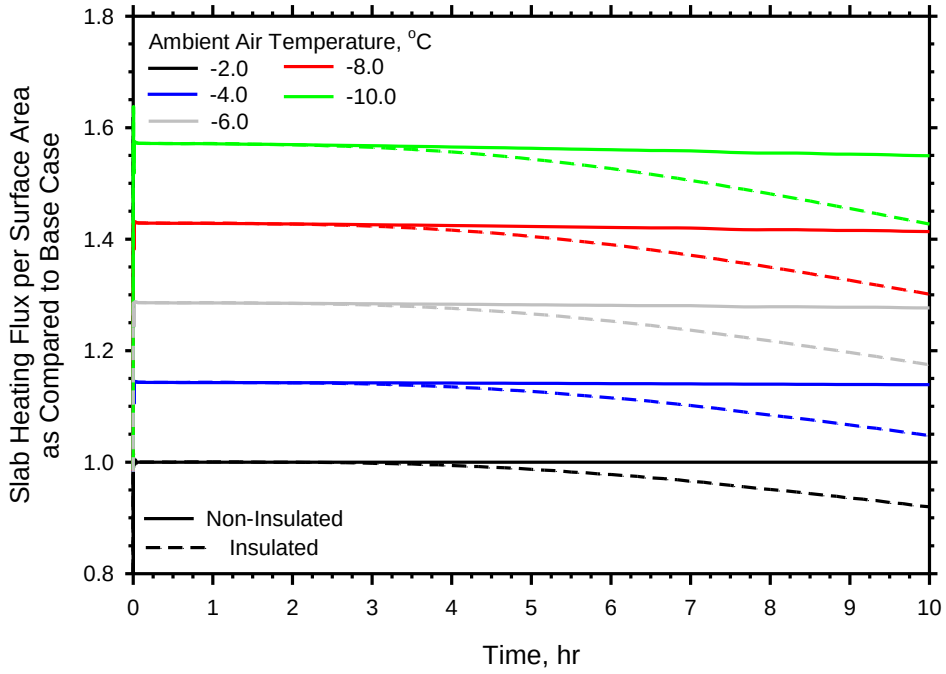

Figure 8-43. Average slab heating flux per surface area for different ambient temperatures comparing the effect of slab insulation.

8.5. BRIDGE DECK DEICING BEHAVIOR

8.5.1. The Base Case

8.5.1.1. Impact of Rate of Snowfall

As shown in Table 8-3, three different rates of snowfall were used: 2 cm/hr, 5 cm/hr, and 10 cm/hr. As will be seen, the severity of the storm is a function of more than just the rate of snowfall including ambient temperature and wind speed. However, the rate of snowfall does significantly affect the performance of the system. The average surface temperature of the slab after the fluxes were applied are shown in Figure 8-44 and several conclusions can be made. First, the surface temperature drops immediately after the snow melting flux is applied. The higher the rate of snowfall, the more the temperature drops. This is in agreement with the observed experimental results of Chapter 3. Secondly, after the temperature drops, it increases again. This is not a universal conclusion, rather a factor of the other system conditions (ambient temperature, thermal properties, etc.).

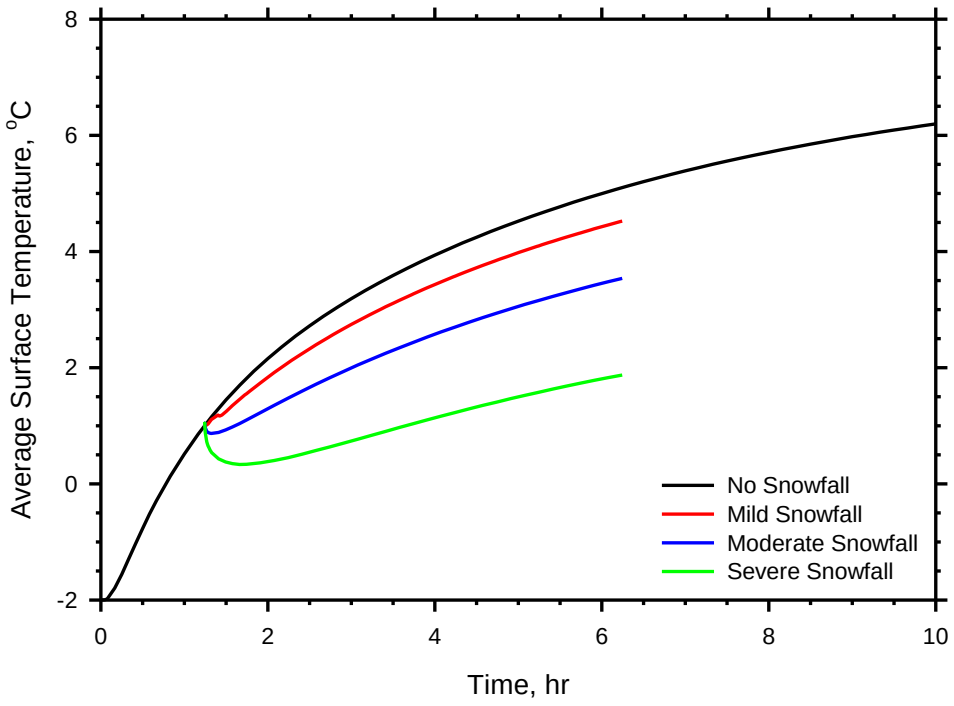

Figure 8-44. Average surface temperatures for varying rates of snowfall (Table 8-3).

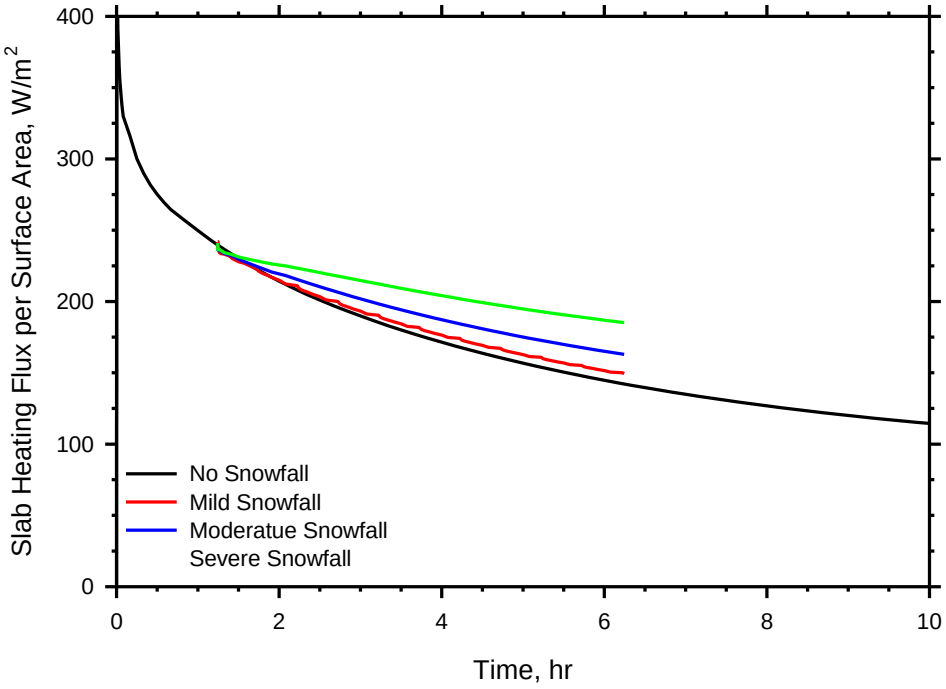

Figure 8-45. Slab heating fluxes per surface area for varying rates of snowfall (Table 8-3).

The slab heating fluxes per surface area are compared in Figure 8-45. The higher rates of snowfall command higher slab heating fluxes. Thus, assuming the system is capable of providing the same inlet fluid temperature, the system, in a sense, self-adjusts to the storm and/or weather conditions by delivering a higher slab heating flux. This was also observed experimentally in Chapter 3.

8.5.1.2. Impact of Initial Surface Temperature

If the slab has a higher initial surface temperature when the storm hits, it should perform better during the storm because it will have more stored energy in the bridge deck with which to melt snow, thus lessening the need for a higher slab heating flux. The average surface temperatures over time are shown in Figure 8-46. The higher initial surface temperatures do perform better in the sense that they maintain higher surface temperatures during the storm. However, whereas the average surface temperature for the cases with lower initial surface temperatures continue to increase after the snow melting flux is applied, it either does not increase (condition with an initial average temperature of 4°C with a severe snowfall rate) or increases at a much slower rate. This is because of slab heating fluxes and thermal gradients with the slab. Higher slab temperatures result in a lower gradient between it and the temperature of the circulating fluid, thus not allowing as much energy to be transferred, resulting in different trends with regard to the average surface temperature. However, the cases with the higher initial surface temperatures do not need to increase as greatly as the cases with the lower initial surface temperatures.

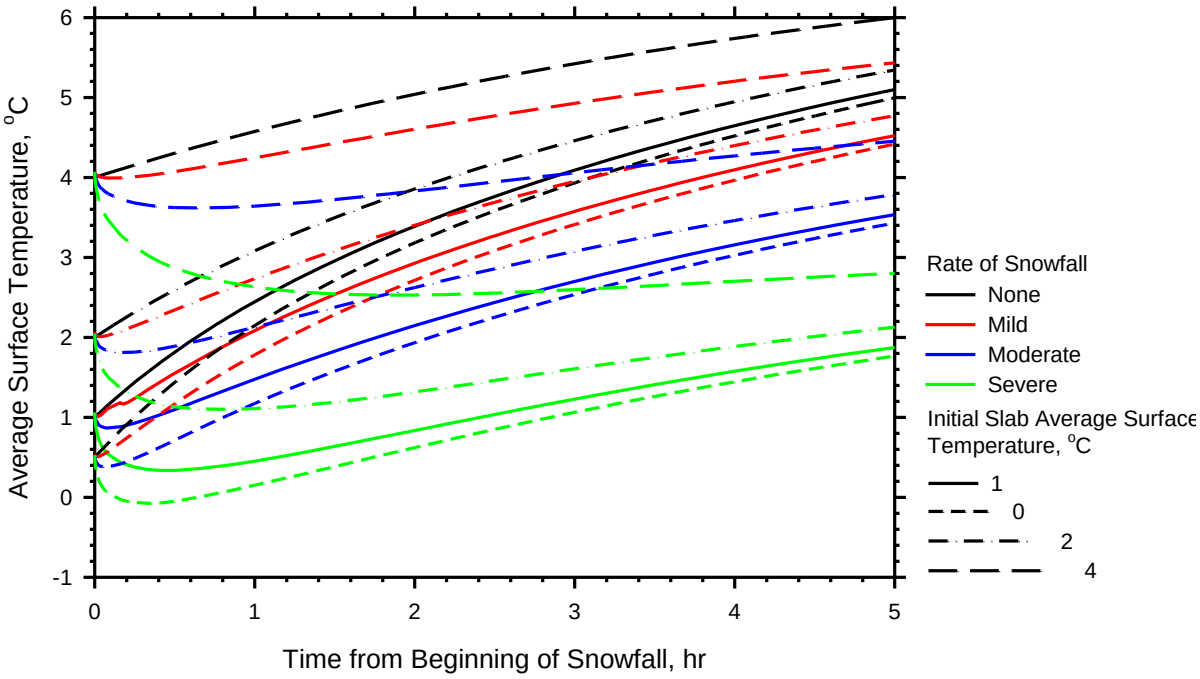

Figure 8-46. Average surface temperatures for varying rates of snowfall (Table 3) and initial surface temperatures.

Figure 8-47 compares the slab heating fluxes per surface area for different initial surface temperatures. Observe that lower initial average surface temperatures along with more severe storms display higher

slab heating fluxes, thus delivering more energy to the slab than the cases with higher initial surface temperatures. Again, it is seen that the system 'self-adjusts' to the given weather conditions. Though the system does adjust by delivering a higher flux, it is still better for the average surface temperature to be as high as possible before the snowfall begins.

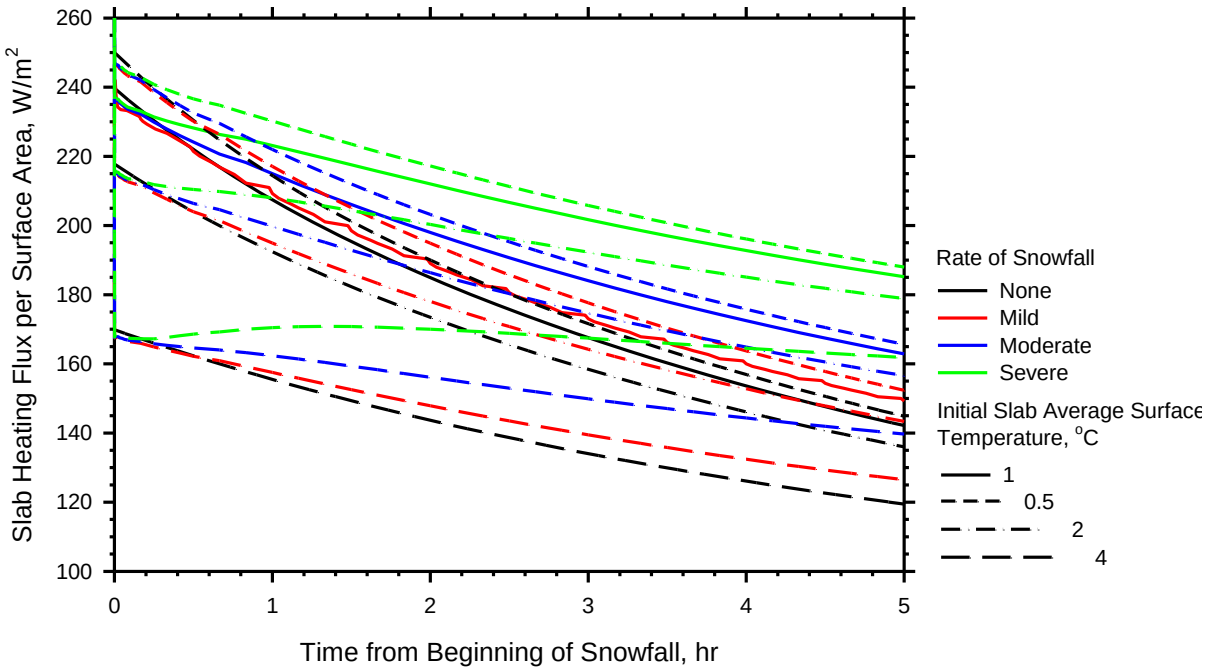

Figure 8-47. Slab heating fluxes per surface area for varying rates of snowfall (Table 3) and initial surface temperatures.

8.5.2. Performance

Table 8-4 and Table 8-5 provide a useful summary of some of the results above. Table 8-4 displays the amount of time it takes the average surface temperature to reach 1°C, 2°C, and 4°C and also presents the temperature of the surface of the slab above the deicing tubes as well as between them. Table 8-5 presents a given system's performance during snowfall. Several trends emerge from these tables. The first is that as the tube spacing increases, the time it takes for the average surface temperature increases as does the difference between the temperatures at the surface over a deicing tube and between the deicing tubes. This was discussed previously. It is also why the performance of the system decreases as the spacing increases. Notice from Table 8-5 that a spacing scenario of 15 cm can keep the deck clear even with a severe rate of snowfall, 20 cm and 25 cm spacing scenarios can keep the deck clear for mild and moderate rates of snowfall, and a 30 cm spacing scenario can only keep the deck clear for mild rates of snowfall. The trends for ambient temperature, inlet fluid temperature, and wind speed are similar in that as the conditions becomes more severe (ambient temperature decreases, inlet fluid temperature decreases, wind speed increases) the performance of the system decreases whereas the amount of time it takes the deck surface to heat to the same average surface temperature increases, it the particular case is able to reach it at all.

Table 8-4. Heating times for various system configurations and weather conditions.

System and Weather Conditions							Average Surface Temp = 1°C			Average Surface Temp = 2°C			Average Surface Temp = 4°C		
Tube Spacing (cm)	Inlet Fluid (°C)	Ambient Temp (degC)	Wind (m/s)	Thermal Conductivity (W/m-K)	Heat Capacity (J/kg-K)	Bottom Insulation	Time (hr)	Temp Above Tube (°C)	Surface Between Tubes (°C)	Time (hr)	Temp Above Tube (°C)	Surface Between Tubes (°C)	Time (hr)	Temp Above Tube (°C)	Surface Between Tubes (°C)
20	12	-2.0	0	3.0	880	No	1.24	1.50	0.62	1.88	2.47	1.67	4.10	4.39	3.76
20	12	-2.0	0	3.0	880	Yes	1.24	1.50	0.62	1.88	2.47	1.67	4.05	4.39	3.76
15	12	-2.0	0	3.0	880	No	0.90	1.27	0.85	1.30	2.28	1.88	2.59	4.25	3.94
25	12	-2.0	0	3.0	880	No	1.65	1.76	0.39	2.62	2.70	1.46	5.96	4.56	3.59
30	12	-2.0	0	3.0	880	No	2.14	2.00	0.20	3.50	2.91	1.29	8.22	4.71	3.45
20	12	-0.5	0	3.0	880	No	0.66	1.63	0.75	1.14	2.46	1.65	2.84	4.39	3.75
20	12	-1.0	0	3.0	880	No	0.84	1.50	0.60	1.37	2.46	1.65	3.25	4.39	3.75
20	12	-1.5	0	3.0	880	No	1.04	1.50	0.61	1.62	2.47	1.66	3.67	4.39	3.76
20	12	-2.5	0	3.0	880	No	1.46	1.51	0.62	2.16	2.48	1.67	4.55	4.39	3.76
20	12	-3.0	0	3.0	880	No	1.69	1.51	0.63	2.45	2.48	1.68	5.01	4.40	3.77
20	12	-4.0	0	3.0	880	No	2.18	1.52	0.64	3.06	2.49	1.69	5.97	4.40	3.77
20	12	-4.0	0	3.0	880	Yes	2.17	1.52	0.64	3.05	2.49	1.69	5.76	4.40	3.77
20	12	-6.0	0	3.0	880	No	3.29	1.54	0.66	4.41	2.49	1.70	8.09	4.40	3.79
20	12	-6.0	0	3.0	880	Yes	3.27	1.54	0.66	4.35	2.50	1.70	7.51	4.40	3.79
20	12	-8.0	0	3.0	880	No	4.52	1.55	0.67	5.88	2.50	1.72	N/A	N/A	N/A
20	12	-8.0	0	3.0	880	Yes	4.45	1.55	0.67	5.69	2.50	1.72	9.33	4.40	3.80
20	12	-10.0	0	3.0	880	No	5.85	1.55	0.69	7.50	2.50	1.73	N/A	N/A	N/A
20	12	-10.0	0	3.0	880	Yes	5.66	1.55	0.69	7.05	2.50	1.73	N/A	N/A	N/A
20	12	-2.0	2	3.0	880	No	1.45	1.47	0.65	2.41	2.43	1.70	7.77	4.34	3.79
20	12	-2.0	2	3.0	880	Yes	1.45	1.47	0.65	2.40	2.43	1.70	6.43	4.34	3.79
20	12	-2.0	4	3.0	880	No	1.72	1.44	0.68	3.27	2.40	1.73	N/A	N/A	N/A
20	12	-2.0	6	3.0	880	No	2.06	1.41	0.70	4.91	2.36	1.75	N/A	N/A	N/A
20	12	-2.0	8	3.0	880	No	2.54	1.39	0.72	N/A	N/A	N/A	N/A	N/A	N/A
20	12	-2.0	8	3.0	880	Yes	2.50	1.39	0.72	5.97	2.34	1.77	N/A	N/A	N/A
20	12	-2.0	10	3.0	880	No	3.28	1.37	0.74	N/A	N/A	N/A	N/A	N/A	N/A
20	12	-2.0	15	3.0	880	No	10.00	1.17	0.61	N/A	N/A	N/A	N/A	N/A	N/A
20	12	-2.0	15	3.0	880	Yes	5.63	1.32	0.77	N/A	N/A	N/A	N/A	N/A	N/A

20	12	-2.0	20	3.0	880	No	10.00	0.73	0.19	N/A	N/A	N/A	N/A	N/A	N/A
20	4	-2.0	0	3.0	880	No	5.96	1.15	0.92	N/A	N/A	N/A	N/A	N/A	N/A
20	6	-2.0	0	3.0	880	No	3.07	1.24	0.84	5.97	2.20	1.89	N/A	N/A	N/A
20	8	-2.0	0	3.0	880	No	2.04	1.33	0.77	3.51	2.29	1.82	N/A	N/A	N/A
20	10	-2.0	0	3.0	880	No	1.53	1.42	0.69	2.45	2.38	1.74	5.99	4.30	3.83
20	14	-2.0	0	3.0	880	No	1.05	1.59	0.54	1.54	2.56	1.59	3.08	4.48	3.69
20	16	-2.0	0	3.0	880	No	0.92	1.68	0.46	1.31	2.64	1.51	2.45	4.57	3.61
20	18	-2.0	0	3.0	880	No	0.82	1.77	0.38	1.14	2.73	1.44	2.04	4.66	3.54
20	20	-2.0	0	3.0	880	No	0.75	1.85	0.31	1.02	2.82	1.36	1.75	4.75	3.46
20	12	-2.0	0	3.0	700	No	0.99	1.50	0.62	1.50	2.47	1.67	3.27	4.39	3.76
20	12	-2.0	0	3.0	1000	No	1.41	1.50	0.62	2.13	2.47	1.67	4.65	4.39	3.76
20	20	-2.0	0	1.5	880	No	1.55	1.67	0.46	2.31	2.62	1.53	5.32	4.49	3.67
20	20	-2.0	0	2.0	880	No	1.40	1.61	0.52	2.10	2.56	1.58	4.70	4.45	3.70
20	20	-2.0	0	2.5	880	No	1.31	1.55	0.57	1.97	2.51	1.63	4.34	4.42	3.73
20	20	-2.0	0	3.5	880	No	1.20	1.47	0.65	1.82	2.44	1.70	3.93	4.37	3.78
20	20	-2.0	0	4.0	880	No	1.16	1.43	0.68	1.78	2.41	1.72	3.81	4.35	3.80

Table 8-5. Performance of various systems configurations and weather conditions after application of snow melting flux.

System and Weather Conditions				Start Conditions		Performance		
Tube Spacing (cm)	**Inlet Fluid (degC)**	**Ambient Temp (degC)**	**Wind (m/s)**	**Average Surface Temp (degC)**	**Time (hr)**	**Snowfall Rate[1]**	**Does surface temp drop below 0°C**	**If so, is snow still melting at surface?**
20	12	-2	0	0.5	0.99	Mild	No	N/A
						Moderate	No	N/A
						Severe	Yes	Yes
20	12	-2	0	1.0	1.24	Mild	No	N/A
						Moderate	No	N/A
						Severe	No	N/A
20	12	-2	0	2.0	1.88	Mild	No	N/A
						Moderate	No	N/A
						Severe	No	N/A
20	12	-2	0	4.0	4.10	Mild	No	N/A
						Moderate	No	N/A
						Severe	No	N/A
15	12	-2	0	1.0	0.90	Mild	No	N/A
						Moderate	No	N/A
						Severe	No	N/A
25	12	-2	0	1.0	1.65	Mild	No	N/A
						Moderate	No	N/A
						Severe	Yes	Yes
30	12	-2	0	1.0	2.14	Mild	Yes	N/A
						Moderate	No	Yes
						Severe	No	Yes
20	12	-4	0	1.0	2.18	Mild	Yes	N/A
						Moderate	Yes	N/A
						Severe	No	Yes
20	12	-6	0	1.0	3.29	Mild	Yes	N/A
						Moderate	Yes	N/A
						Severe	No	Yes

						Mild	Yes	N/A
20	12	-8	0	1.0	4.52	Moderate	Yes	N/A
						Severe	No	Yes
						Mild	Yes	N/A
20	12	-10	0	1.0	5.85	Moderate	Yes	N/A
						Severe	No	Yes
						Mild	No	N/A
20	12	-2	2	1.0	1.45	Moderate	No	N/A
						Severe	Yes	Yes
						Mild	No	N/A
20	12	-2	4	1.0	1.72	Moderate	No	N/A
						Severe	Yes	Yes
						Mild	No	N/A
20	12	-2	6	1.0	2.06	Moderate	No	N/A
						Severe	Yes	Yes
						Mild	No	N/A
20	12	-2	8	1.0	2.54	Moderate	No	N/A
						Severe	Yes	Yes
						Mild	No	N/A
20	12	-2	10	1.0	3.28	Moderate	No	N/A
						Severe	Yes	Yes
						Mild	No	N/A
20	12	-2	15	0.8	10.00	Moderate	Yes	Yes
						Severe	Yes	Yes
						Mild	Yes	Yes
20	12	-2	20	0.4	10.00	Moderate	Yes	Yes
						Severe	Yes	Yes
						Mild	No	N/A
20	4	-2	0	1.0	5.96	Moderate	Yes	Yes
						Severe	Yes	Yes
						Mild	No	N/A
20	6	-2	0	1.0	3.07	Moderate	No	N/A
						Severe	Yes	Yes

						Mild	No	N/A
20	8	-2	0	1.0	2.04	Moderate	No	N/A
						Severe	Yes	Yes
						Mild	No	N/A
20	10	-2	0	1.0	1.53	Moderate	No	N/A
						Severe	Yes	Yes
						Mild	No	N/A
20	14	-2	0	1.0	1.05	Moderate	No	N/A
						Severe	No	N/A
						Mild	No	N/A
20	16	-2	0	1.0	0.92	Moderate	No	N/A
						Severe	No	N/A
						Mild	No	N/A
20	18	-2	0	1.0	0.82	Moderate	No	N/A
						Severe	No	N/A
						Mild	No	N/A
20	20	-2	0	1.0	0.75	Moderate	No	N/A
						Severe	No	N/A

[1]See Table 8-3

Several conclusions can be drawn from Table 8-4 and Table 8-5. First, these systems are capable of operating successfully under a variety of system configurations and weather conditions. Though the temperatures are much lower than in actively heated systems, they are capable of keeping the deck free from snow if started in enough advance of oncoming storms. Secondly, those these systems can operate successfully, there are limitations. As weather conditions become more severe and/or site conditions become less suitable (i.e. inlet fluid temperature decreases) the performance of these systems decrease, and that should be expected. However, in most cases the conditions will be severe enough that mechanical removal will still be required (see Chapter 3 for a larger discussion). Thirdly, these systems must be turned on in advance of storms in order to be effective. Even the shortest heating times in Table 8-4 are around an hour, thus waiting until the storm occurs will be too late. More time will also be needed for harsher conditions. Finally, there are steps system designers can take to improve system performance and/or overcome unfavorable conditions. One step is as simple as selecting a closer tube spacing. Higher inlet fluid temperatures also improve the performance of the system, thus injecting thermal energy into the ground during the summer months to increase the ground temperature could have a significant and positive impact of system performance. Other factors such as more thermally conductive concrete, insulation, and higher flow rates can also be considered.

8.6. DESIGN CONSIDERATIONS

Table 8-4 and Table 8-5, in conjunction with the Figures presented in this paper, can be used for both design and system operation. For example, in design an engineer can use the heating times from Table 8-4 and performance values from Table 8-5 to determine whether or not they are acceptable for a given configuration. They can then refer to the Figures throughout this paper to get an idea of the average slab heating flux per surface area and energy requirements so that they can estimate the subsurface system performance.

During operation, these results allow the system engineer to estimate the length of time required to preheat a bridge deck for given system and weather conditions. The advantage of showing the temperatures above and between the deicing tubes is that it gives an idea of how sufficient the given average surface temperature is in preparation for snowmelt. For example, the temperatures above and between the deicing tubes for a tube spacing of 15 cm with the conditions shown in Table 8-4 are 1.27^{o}C, and 0.85^{o}C, respectfully, and it takes approximately 0.9 hours to achieve. However, for a tube spacing of 30 cm the temperature above and between the deicing tubes are 2.00^{o}C and 0.20^{o}C, respectfully, and it takes 2.14 hours to achieve. A temperature of 0.20^{o} is very close to 0^{o}C, thus an average surface temperature of 2^{o}C where the temperature between the deicing tubes is 1.46^{o}C may be more appropriate for the 30 cm tube spacing, which requires 3.50 hours for the given conditions. Likewise, from Table 8-5 it can be estimated whether or not mechanical removal is to be needed for the bridge. For example, a moderate storm for the base case will likely require no mechanical removal whereas a severe storm, though able to continually melt the snow, will require mechanical removal is it is not able to melt the snow at a fast enough rate.

Table 8-4 and Table 8-5 do not include all scenarios or possible conditions. For conditions not directly reported (for example, a system with a tube spacing of 25 cm, insulated undersurface, and an ambient temperature of -4^{o}C), the reader is encouraged to understand the basic system behavior and trends as reported previously in this paper and apply it to his/her particular system. For example, it is known that 25 cm tube spacing takes longer to heat than do 20 cm tube spacing and to a lower average surface

temperature, however it uses less energy. Insulation is not likely to initially shorten the amount of time it takes the deck surface to heat, but will allow it to achieve a higher surface temperature over time. An ambient temperature of 4^{o}C will require longer heating times. Furthermore, the numerical model that was used for these analyses is described in Chapter 7 and can be used to run additional analyses for given conditions as well as non-constant weather and system conditions (such as changing ambient temperature, inlet fluid temperature, wind speed, etc., over time), which are not reported in this paper.

8.7. CONCLUSIONS

Shallow geothermal energy can be successfully used to heat bridge decks during winter storms despite lower fluid temperatures than what is found in active systems. This has been shown using a 3-dimensional numerical model for a variety of system configurations and weather conditions. Imperative to the success of these systems, however, is pre-heating, which allows the deck to heat in anticipation of snow falling. There are limitations as to the severity of storms and weather conditions these systems can handle. Some of these limitations can be overcome through design by using closer tube spacing, higher flow rates, insulation, and/or more thermally conductive concrete. Table 8-4 and Table 8-5, as well as the various figures within the paper can assist in designing and operating these systems as well as giving a basic understanding of how the systems operate.

8.8. REFERENCES

American Association of State Highway and Transportation Officials (AASHTO) (2008). "Bridging the Gap: Restoring and Rebuilding the Nation's Bridges." American Association of State Highway and Transportation Officials.

American Society of Heating Refrigerating and Air-Conditioning Engineers (ASHRAE) (2011). 2011 ASHRAE Handbook - Heating, Ventilating, and Air-Conditioning Applications (SI Edition), American Society of Heating, Refrigerating and Air-Conditioning Engineers, Inc.

Bowers, Jr., G., and C. Olgun. (2016). "The Thermal Performance of a Small-Scale Bridge Deck Deicing System Under Bridge Deck Deicing and Thermal Recharge Operations.." ASCE Journal of Cold Regions Engineering. Submitted.

Friar, S., and Decker, R. (1999). "Evaluation of a fixed anti-icing spray system." Transportation Research Record(1672), 34-41.

Koch, G. H., Brongers, M. P. H., Thompson, N. G., Virmani, Y. P., and Payer, J. H. (2002). "Corrosion Cost and Preventive Strategies in the United States." FHWA, U.S. Department of Transportation, United States, 790p.

Liu, X. (2005). "Development and Experimental Validation of Simulation of Hydronic Snow Melting Systems for Bridges." Ph.D. Thesis. Oklahoma State University.

Liu, X., Rees, S. J., and Spitler, J. D. (2007a). "Modeling snow melting on heated pavement surfaces. Part I: Model development." Applied Thermal Engineering, 27(5-6), 1115-1124.

Liu, X., Rees, S. J., and Spitler, J. D. (2007b). "Modeling snow melting on heated pavement surfaces. Part II: Experimental validation." Applied Thermal Engineering, 27(5-6), 1125-1131.

Liu, X., and Spitler, J. D. (2004). "A Simulation Tool for the Hydronic Bridge Snow Melting System." 12th International Road Weather Conference. Bingen, Germany.

Minsk, L. D. (1999). "Heated Bridge Technology: Report on ISTEA Sec. 6005 Program." FHWA, U.S. Department of Transportation, 51.

Rhodes, J.A. (1978). “Chapter 17 – Thermal Properties.” Significance of Tests and Properties of Concrete and Concrete-Making Materials. American Society for Testing and Materials. Philadelphia.

Schnurr, N. M., and Falk, M. W. (1973). "TRANSIENT ANALYSIS OF SNOW MELTING SYSTEMS." ASHRAE Transactions, 79(Part 2), 159-166.

Virmani, Y. P., Clear, K. C., and Pasko, T. J. (1983). "Time-To-Corrosion of Reinforcing Steel in Concrete Slabs. Volume 5. Calcium Nitrite Admixture or Epoxy-Coated Reinforcing Bars as Corrosion Protection Systems." FHWA, U.S. Department of Transportation, United States, 80p.

Virmani, Y. P., Jones, W. R., and Jones, D. H. (1984). "Steel corrosion in concrete: pH at corrosion sites." Public Roads, 48(3), 96-102.

Yoshitake, I., Yasumura, N., Syobuzako, M., and Scanlon, A. (2011). "Pipe heating system with underground water tank for snow thawing and ice prevention on roads and bridge decks." Journal of Cold Regions Engineering, 25(2), 71-86.

Yunovich, M., Thompson, N. G., and Virmani, Y. P. (2003). "Life Cycle Cost Analysis for Reinforced Concrete Bridge Decks. Paper No. 03309." Proc., CORROSION/03.

9. CONCLUSIONS

9.1. GROUND-SOURCE BRIDGE DECK DEICING

It has been shown experimentally and numerically that bridge deck deicing systems can be powered by shallow geothermal energy alone, without the aid of a heat pump. These systems perform well during many storms and are often able to keep the deck completely free from snow. It was also observed that the rate at which the deck heats is a function of the deck and ground temperatures, thus allowing them to self-correct in that they supply a higher heat flux when needed. However, there are several points that must be clearly understood. The first of which is that in order for these systems to perform well, they must be turned on in advance of the storm so that they have time to heat the bridge deck. The rate at which the energy is imparted to the deck is not great enough to rapidly heat the deck requiring advance heating time. Secondly, there are limitations to the success. When conditions become extreme such as lower ambient temperatures, lower inlet fluid temperatures, higher wind speeds, and/or higher rates of snow fall, the ability of the system to keep the deck completely free from snow decreases. However, it was observed that in almost every case such conditions would have necessitated mechanical removal of the snow anyway and that though the deck was not completely free from snow, it was still able to melt the snow at the surface of the deck. One should not expect these systems to always be able to keep the deck clear, but they should be able to eliminate the need for deicing chemicals on bridges.

The performance of these systems can be enhanced through thermal recharge operations. From experimental tests, it was determined that the rate of bridge deck cooling was 2-3 times greater than the rate of bridge deck heating. This indicates that not as many hours of thermal recharge operation are needed relative to the amount of hours of bridge deck deicing operation in order to inject the same amount of energy that was extracted. For equal hours of thermal recharge operation as compared to bridge deck deicing operation, a net injection of thermal energy into the ground will occur such that the temperature of the ground will increase. Not enough recharge operations were performed over a long enough period of time to fully investigate its effect on the experimental system, however, it was observed experimentally and numerically that thermal recharge can increase the temperatures of the ground, which is advantageous for bridge deck deicing.

The operation of ground-source geothermal systems for bridge deck deicing and thermal recharge does impose thermal gradients within the bridge deck not normally experienced. In general, the negative gradients imposed more of a problem than the positive gradients due to the temperature reversal these systems cause within the bridge deck when compared to the natural gradients bridge decks typically experience. These adverse gradients can be mitigated, if not eliminated, by careful selection of operation start and end times. Furthermore, if operated correctly, bridge deck deicing systems can serve to stabilize the temperatures in the bridge deck and keep them from experiencing the severity of the normally occurring temperature gradients, which reduces the cyclic expansion and contraction that naturally occur.

9.2. SUBSURFACE RESPONSE TO GROUND-SOURCE BRIDGE DECK DEICING AND THERMAL ENERGY EXCHANGE

Bridge deck deicing and thermal recharge operations impose thermal loads on the pile used for thermal energy exchange with the ground. These loads were observed experimentally for heating and cooling operations. Bridge deck heating operations decreased the temperatures within the pile, and though the decrease in temperature was no more than 3-4^{o}C, it was enough to induce negative (tensional) axial

stresses within the pile that were up to 13% of the maximum axial pile capacity. This was due to the pile attempting to contract relative to the soil around it. Conversely, thermal recharge operations increased the temperature within the pile. Similar to bridge deck deicing operations, though the temperature increase within the pile was no more than 3-4^{o}C, it was enough to induce positive (compressive) axial stresses within the pile as the pile sought to expand relative to the soil around it. These values were compared against other experimentally observed values and a new parameter, the thermal modulus, was introduced as a way to quantify the change in axial stress. The thermal modulus value is not always constant with temperature change, but appears to vary depending of pile fixity conditions and load transfer mechanisms to the surrounding soil. Furthermore, it is a function of the pile's tangent modulus, which is not always constant with pile depth.

Bridge deck deicing and thermal recharge operations also induce temperature change in the surrounding ground. The temperature change is a function of the thermal properties of the subsurface material. An analytical model was presented as a way to estimate the temperature change in the ground. The model can be used for varying heat injection/extraction rates, a layered subsurface with different thermal properties, and multiple boreholes. The temperature changes predicted by the model were validated with a 3D numerical model, and then verified using the results from experimental tests. Good agreement was observed between the model and the experimental results. The model is ultimately a tool that can be used to accurately account for the temperature change within the subsurface without the computational inefficiencies of a 3D numerical model.

Methods of increasing the capacity of the subsurface for efficient thermal energy exchange were also explored. Many times in thermo-active foundations the size of the borehole/energy pile grid is controlled by the size of the foundation. Thus, methods by which to increase the efficiency of the system through selective utilization of boreholes was explored. It was found that methods that store thermal energy in the center of the borehole grid during idle periods with no energy injection/extraction and methods that prevent energy from leaving the geothermal footprint area are able to retain more thermal energy that can be accessed by the boreholes. The methods that are able to accomplish this either redistribute injected energy by concentrating it in the middle; operate the perimeter boreholes first with respect to the interior boreholes; or operate the perimeter boreholes at a higher rate with respect to the interior boreholes. Furthermore, these methods are able to reduce the impact that unfavorable thermal properties such as lower thermal conductivities and heat capacities have in efficient thermal energy storage and energy exchange. However, the practical considerations with regard to the ease of implementation of each method must be considered as well as fluid temperatures in the borehole that result from operation as both factors will impact system performance.

9.3. NUMERICAL MODELING OF BRIDGE DECK DEICING

To successfully model bridge deck deicing, all of the relevant heat transfer processes must be accounted for including conduction, convection, and radiation. In order to increase the efficiency of the model, simplifications can be made to eliminate the direct representation of reinforcing steel, fluid flow, and snow melt. The accuracy of the model is greatly affected by the selection of the appropriate boundary conditions and material properties. The model was ultimately used to successfully replicate two experimental field tests with good agreement between the model and the experimental results in terms of slab temperatures, injected energy to the slab, and success or failure of the system.

A parametric study utilizing the validated bridge deck numerical model investigated a wide range of system configurations and weather conditions. Factors such as circulation tube spacing, concrete thermal conductivity, concrete heat capacity, fluid flow rate, insulation of the slab's under-surface, ambient temperature, initial slab temperature, circulation fluid temperature, and wind speed on system performance was explored and correlations with regard to surface temperature, injected energy, slab heating rate, and amount of energy lost or used for heating were developed. The correlation of some factors, such as inlet fluid temperature, normalized over time such that one contour was representative over time whereas the correlations for other factors, such as wind speed, required multiple time contours. Different snow rates were also investigated and similar to the experimental studies, it was found that higher rates of snowfall were able to generate higher slab heating fluxes demonstrating the 'self-adjusting' nature of these systems as they are able to deliver a higher heating flux when needed. Ultimately the results were compiled into tables that can be used by engineers for design and system operation.